Reduced-order modeling and simulation of turbulent disperse two-phase flows : new theoretical and modeling approaches for reproducing intermittency, segregation and two-way coupling

Roxane Letournel

université PARIS-SACLAY

Reduced-order modeling and simulation of turbulent disperse two-phase flows : new theoretical and modeling approaches for reproducing intermittency, segregation and two-way coupling

Thèse de doctorat de l'université Paris-Saclay

École doctorale n°574 : mathématiques Hadamard (EDMH)
Spécialité de doctorat : Mathématiques aux interfaces
Graduate School : Mathématiques, Référent : CentraleSupélec

Thèse préparée dans l'unité de recherche Fédération de Mathématiques de CentraleSupélec, sous la direction de Frédérique LAURENT-NEGRE, chargée de recherche, la co-direction de Marc MASSOT, professeur, le co-encadrement d'Aymeric VIE, maître de conférences

Thèse soutenue à Gif-sur-Yvette, le 17 février 2022, par

Roxane LETOURNEL

Composition du jury

Pauline Lafitte Professeure, MICS, CentraleSupélec	Présidente
Gianluca Iaccarino Professeur, Université de Stanford	Rapporteur & Examinateur
Alain Pumir Directeur de recherche, ENS Lyon	Rapporteur & Examinateur
Olivier Simonin Professeur, IMFT, INP Toulouse	Rapporteur & Examinateur
Mireille Bossy Directrice de recherche, INRIA Sophia Antipolis	Examinatrice
Mikhael Gorokhovski Professeur, LMFA, Ecole Centrale Lyon	Examinateur
Cristian Marchioli Professeur, Université de Udine	Examinateur
Frédérique Laurent-Nègre Chargée de recherche, EM2C, CentraleSupélec	Directrice de thèse

THESE DE DOCTORAT
NNT : 2022UPASM003

université PARIS-SACLAY | ÉCOLE DOCTORALE de mathématiques Hadamard (EDMH)

Titre : Modélisation d'ordre réduit et simulation d'écoulements diphasiques dispersés turbulents : nouvelles approches théoriques et modèles pour la prédiction de l'intermittence, de la ségrégation et du couplage fort

Mots clés : Ecoulements à phase disperse, intermittence, ségrégation, couplage bi-directionnel, modèles stochastiques, modèles cinématiques

Résumé :

La capacité de modéliser et simuler les écoulements turbulents à phase dispersée est un enjeu crucial pour de nombreuses applications industrielles et environnementales, telles que les moteurs à combustion interne, le transport de polluants ou la formation de nuages. Cependant, si la résolution de l'ensemble des échelles de la turbulence par DNS (Direct Numerical Simulation) est possible sur des configurations académiques simples, elle devient inenvisageable pour des applications réalistes. Il faut alors recourir aux ROS (Reduced-Order Simulations), qui, en filtrant ou moyennant les équations, permettent de ne prendre en compte que les grandes échelles de l'écoulement. Bien que de récentes avancées aient permis d'améliorer la qualité des modèles de turbulence, ils ne rendent pas compte fidèlement de l'interaction avec la phase dispersée, du fait des couplages non résolus aux petites échelles.

Afin de lever ce verrou, l'objectif de cette thèse est d'identifier les phénomènes physiques négligés par les ROS dans la dynamique des particules, et d'en proposer une caractérisation complète. A partir de ces analyses physiques, nous avons développé des modèles cohérents mathématiquement, qui couplés aux ROS, permettent de retrouver les statistiques obtenues par DNS pour une efficacité de calcul équivalente voire supérieure.

La première lacune identifiée dans les ROS est la perte du phénomène d'intermittence, correspondant à de fortes fluctuations du champ de dissipation de l'écoulement turbulent. Une caractérisation mathématique de l'intermittence a été proposée pour un écoulement monophasique. Les modèles stochastiques visant à reproduire l'intermittence reposent sur les chaos Gaussiens multiplicatifs, dont plusieurs modèles existent dans la littérature. Nous avons proposé une méthode mathématique originale permettant de construire de tels processus de manière générique comme somme infinie de processus d'Ornstein-Uhlenbeck. Ce formalisme permet non seulement d'unifier l'écriture des processus existants, mais surtout d'en développer un nouveau plus générique et plus efficace en temps de calcul.

De plus, un écoulement turbulent peut engendrer une hétérogénéité dans la distribution spatiale des particules appelée ségrégation. En ne résolvant pas les petites échelles avec lesquelles les particules interagissent, les ROS représentent mal ce phénomène. Pour retrouver ces propriétés, nous avons proposé un nouveau modèle cinématique à base d'ondelettes à divergence nulle. En comparant ce modèle à des simulations DNS et aux modèles cinématiques de la littérature, nous avons pu montrer qu'il permet de retrouver les principales statistiques des deux phases et de s'adapter à différents écoulements.

Enfin, les transferts d'énergie entre phases et entre les échelles résolues et non-résolues ne sont pas correctement reproduits dans les ROS actuelles. Préalable essentiel à la conception d'un nouveau modèle palliant ces défauts, nous avons mené un important travail d'analyse de ces rétro-couplages à partir de simulations DNS et en unifiant les résultats de la littérature. Nous avons ainsi pu identifier les échelles et mécanismes privilégiés de ces transferts d'énergie, ainsi que les paramètres prépondérants permettant de caractériser ces phénomènes, comme la densité moyenne de particules. L'ensemble de ces travaux permet d'apporter un nouvel éclairage sur les interactions entre des particules et la turbulence. Cette thèse a ainsi permis de mener des analyses approfondies et de proposer des modèles originaux pour enrichir les ROS, ouvrant la voie à des simulations capturant fidèlement le rétro-couplage. Elle offre également de nombreuses perspectives pour la construction d'un modèle fluide couplé cohérent pour la simulation d'écoulements diphasiques turbulents.

Title : Reduced-order modeling and simulation of turbulent disperse two-phase flows : new theoretical and modeling approaches for reproducing intermittency, segregation and two-way coupling

Keywords : Disperse phase flows, intermittency, segregation, two-way coupling, stochastic models, kinematic simulation

Abstract : The ability to model, simulate, and predict turbulent disperse two-phase flows is crucial for various industrial and environmental issues, such as internal combustion engines, pollutant transports or clouds formation. However, if the resolution of all scales of turbulence by DNS (Direct Numerical Simulation) is possible in academic configurations, it becomes unrealistic for industrial applications. The use of Reduced-Order Simulation (ROS) allows, by filtering or averaging the equations, to take into account only the large scales of the flow and to make the simulation of real systems accessible. Although recent advances have made these models predictive for single-phase flows, they do not accurately account for the interaction with the disperse phase due to small-scale unresolved couplings.

In order to overcome this problem, the objective of this thesis is to identify the physical phenomena neglected by ROS for the dynamics of particles and to propose a complete characterization of them. Based on these physical analyses, we develop mathematically consistent models, which, when coupled to the ROS, recover the statistics obtained by DNS while maintaining or even improving the computational efficiency.

The first shortcoming identified in ROS is the loss of the intermittency phenomenon, corresponding to violent fluctuations of the dissipation field of the turbulent flow. A mathematical characterization of intermittency has been proposed for a single-phase flow. Stochastic models aiming at reproducing the intermittency are based on multiplicative Gaussian chaos, of which several models exist in the literature. We have proposed an original mathematical method to construct such processes in a generic way as an infinite sum of Ornstein-Uhlenbeck processes. This formalism allows not only to unify the writing of the existing processes but also to develop a new one, more versatile and more efficient in computation time.

In addition, a turbulent flow can generate a heterogeneous spatial distribution of inertial particles, namely the preferential concentration. The ROS poorly captures these dynamics by not solving the small scales with which the particles interact. To recover the properties of the unresolved scales, we have proposed a new kinematic model based on divergence-free wavelets. By comparing this model with DNS and kinematic models from the literature, we have shown that it can recover the main statistics of the two phases and can be adapted to different flows.

Finally, the energy transfers between phases and between resolved and unresolved scales are not correctly reproduced in the current ROS. As an essential prerequisite to designing a new model to overcome these shortcomings, we have carried out an important work of analysis of these reverse couplings from DNS and unified the literature results. We were thus able to identify the scales and mechanisms of these energy transfers, as well as the main parameters that characterize these phenomena, such as the number density of particles. A measure of heterogeneity has also been developed in order to identify the characteristic regimes of flows with low particle loadings, which have been little studied until now.

These works provide new insights into the interactions between particles and turbulent flows. This thesis has thus allowed us to carry out in-depth analyses and to propose original models to enrich the ROS, paving the way for accurate two-way coupled simulations. It also opens perspectives for the construction of a coherent coupled fluid model for turbulent particle-laden flows.

Remerciements

Si ce manuscrit est consacré aux principaux résultats scientifiques, ces quelques lignes témoignent de ma reconnaissance envers les personnes qui m'ont accompagnée tout au long de ma thèse.

Lorsque j'ai poussé la porte du laboratoire EM2C il y a plus de six ans, mon intention était de découvrir le monde de la recherche à l'interface entre les mathématiques appliquées et la physique. Sur les conseils de Francis Dupoirieux, je me suis tournée vers l'équipe de mathématiques à l'EM2C qui est devenue trois ans plus tard mon équipe encadrante de thèse, et que je voudrais aujourd'hui remercier.
Ma directrice de thèse tout d'abord, Frédérique Laurent-Nègre, pour son soutien, sa disponibilité et sa bienveillance tout au long de ces trois ans. Je tiens également à remercier chaleureusement Marc Massot, pour la vision et les conseils qu'il m'a apportés sur l'orientation de mes travaux, et l'interdisciplinarité qu'il a promue et soutenue tout au long de ma thèse. Aymeric Vié enfin, avec qui cette aventure a débuté et qui m'a accompagnée, soutenue, encouragée depuis ce projet de deuxième année à Centrale. Je voudrais ici lui adresser un immense merci pour son encadrement scientifique, son ouverture sur des nouveaux sujets ou outils, notamment mathématiques, et la motivation et l'enthousiasme qu'il a toujours su me communiquer.

L'équipe encadrante s'est renforcée de quelques collaborateurs, notamment de Rémi Zamansky que je remercie pour sa bienveillance, nos discussions et sa patience pour la relecture de plusieurs chapitres de mon manuscrit. Merci également à Ludovic Goudenège, et Alexandre Richard pour les discussions riches autour des modèles stochastiques que nous avons pu partager et qui me tiennent particulièrement à cœur : elles reflètent l'interdisciplinarité de ma thèse entre mathématiques et physique des fluides.

Enfin, pour la conclusion de cette aventure, je voudrais remercier les rapporteurs, qui ont accepté de relire mon manuscrit de thèse sans se douter du poids du paquet qu'ils recevraient pour Noël. Je les remercie pour leurs retours précieux et leur lecture attentive. Merci à Alain Pumir pour nos nombreux échanges l'intérêt porté à mes contributions, merci à Olivier Simonin pour ses remarques pertinentes et constructives qui ont mis en lumière des perspectives intéressantes pour mes travaux et merci à Gianluca Iaccarino, entre autres grâce à qui je me suis lancée dans l'aventure après un stage dans son équipe à Stanford en 2016. Merci également aux examinateurs pour leurs nombreuses remarques et questions lors de la soutenance, Mickael Gorokhovski, Cristian Marchioli, Mireille Bossy, ainsi que Pauline Lafitte d'avoir accepté de présider le jury.

Une thèse c'est aussi un laboratoire d'accueil, et je tiens à remercier plus généralement tous mes collègues de l'EM2C. L'ambiance y est particulièrement stimulante : on peut se retrouver au détour d'un couloir aussi bien à discuter quantification d'incertitudes ou modèles de combustion, qu'à

débriefer la dernière soirée raclette ou la dernière série Netflix. Merci aux doctorants qui ont su rendre ces trois ans joyeux, souvent drôles et régulièrement mémorables. Merci pour les pauses café, pour votre patience face à mes critiques du restaurant universitaire, pour les séances de basket ou parties de fléchettes le midi (je n'aurai finalement blessé personne !), pour les nombreuses excuses pour apporter des viennoiseries le matin, ou encore pour les afterworks tous les premiers jeudis de la semaine.
Merci en particulier à Jean, Victorien, Valentin, Luc, Ulysse, Guilhem, Karl, Corentin, Pierre, Artur, Victor, Lorella, Théa, Augustin, Aurélien, Junghwa, Maxime, Alexandre, Yuri, Geoffrey, Laurent, Moises, sans oublier l'inimitable "Team EB202" : Erwan, Arthur et Nicolas qui sont devenus des amis précieux. Vous arrivez à garder un magnifique équilibre entre sérieux dans le travail et humour dans le quotidien, et ça m'a beaucoup aidée à me lever le matin ces trois dernières années, un grand merci pour qui vous êtes (et bon courage à ceux qui restent pour la fin de leur thèse… ainsi qu'Erwan) !
Merci à Ruben et Alberto, avec qui j'ai partagé des moments magiques à Rio, à Udine et de nombreuses soirées à Paris. Merci pour vos histoires improbables, vos passions que vous transmettez avec succès au travers de projets ambitieux, et votre fidèle amitié.
Merci aussi à mes amis qui ont suivi de près ou de loin cette aventure, en particulier Iris et Sarah pour les séances de danse, de padel, les voyages, les soirées animées ou les soirées au thé.

Enfin, merci à ma famille de m'avoir accompagnée et soutenue non seulement ces 3 dernières années, mais aussi depuis 26 ans. Merci de m'avoir encouragée dans ces études scientifiques, de m'avoir donné les meilleures chances de réussir, et bon courage à Eloïse qui prend la relève pour la thèse !

Et finalement, Louis, mon "copain" en première année, mon "fiancé" en deuxième année et désormais mon "mari" ! Merci pour ton soutien infaillible, mais aussi pour ta passion et ton enthousiasme pour de si nombreux sujets techniques : j'ai la chance de pouvoir partager ma vie et certains problèmes scientifiques avec toi !

Abstract

The ability to model, simulate, and predict turbulent disperse two-phase flows is crucial for various industrial and environmental issues, such as internal combustion engines, pollutant transports or clouds formation. However, if the resolution of all scales of turbulence by DNS (Direct Numerical Simulation) is possible in academic configurations, it becomes unrealistic for industrial applications. The use of Reduced-Order Simulation (ROS) allows, by filtering or averaging the equations, to take into account only the large scales of the flow and to make the simulation of real systems accessible. Although recent advances have made these models predictive for single-phase flows, they do not accurately account for the interaction with the disperse phase due to small-scale unresolved couplings.

In order to overcome this problem, the objective of this thesis is to identify the physical phenomena neglected by ROS for the dynamics of particles and to propose a complete characterization of them. Based on these physical analyses, we develop mathematically consistent models, which, when coupled to the ROS, recover the statistics obtained by DNS while maintaining or even improving the computational efficiency.

The first shortcoming identified in ROS is the loss of the intermittency phenomenon, corresponding to violent fluctuations of the dissipation field of the turbulent flow. A mathematical characterization of intermittency has been proposed for a single-phase flow. Stochastic models aiming at reproducing the intermittency are based on multiplicative Gaussian chaos, of which several models exist in the literature. We have proposed an original mathematical method to construct such processes in a generic way as an infinite sum of Ornstein-Uhlenbeck processes. This formalism allows not only to unify the writing of the existing processes but also to develop a new one, more versatile and more efficient in computation time.
In addition, a turbulent flow can generate a heterogeneous spatial distribution of inertial particles, namely the preferential concentration. The ROS poorly captures these dynamics by not solving the small scales with which the particles interact. To recover the properties of the unresolved scales, we have proposed a new kinematic model based on divergence-free wavelets. By comparing this model with DNS and kinematic models from the literature, we have shown that it can recover the main statistics of the two phases and can be adapted to different flows.
Finally, the energy transfers between phases and between resolved and unresolved scales are not correctly reproduced in the current ROS. As an essential prerequisite to designing a new model to overcome these shortcomings, we have carried out an important work of analysis of these reverse couplings from DNS and unified the literature results. We were thus able to identify the scales and mechanisms of these energy transfers, as well as the main parameters that characterize these phenomena, such as the number density of particles. A measure of heterogeneity has also been developed in order to identify the characteristic regimes of flows with low particle loadings, which have been little studied until now.

These works provide new insights into the interactions between particles and turbulent flows. This thesis has thus allowed us to carry out in-depth analyses and to propose original models to enrich the ROS, paving the way for accurate two-way coupled simulations. It also opens perspectives for the construction of a coherent coupled fluid model for turbulent particle-laden flows.

Résumé

La capacité de modéliser et simuler les écoulements turbulents à phase dispersée est un enjeu crucial pour de nombreuses applications industrielles et environnementales, telles que les moteurs à combustion interne, le transport de polluants ou la formation de nuages. Cependant, si la résolution de l'ensemble des échelles de la turbulence par DNS (Direct Numerical Simulation) est possible sur des configurations académiques simples, elle devient inenvisageable pour des applications réalistes. Il faut alors recourir aux ROS (Reduced-Order Simulations), qui, en filtrant ou moyennant les équations, permettent de ne prendre en compte que les grandes échelles de l'écoulement. Bien que de récentes avancées aient permis d'améliorer la qualité des modèles de turbulence, ils ne rendent pas compte fidèlement de l'interaction avec la phase dispersée, du fait des couplages non résolus aux petites échelles.

Afin de lever ce verrou, l'objectif de cette thèse est d'identifier les phénomènes physiques négligés par les ROS dans la dynamique des particules, et d'en proposer une caractérisation complète. A partir de ces analyses physiques, nous avons développé des modèles cohérents mathématiquement, qui couplés aux ROS, permettent de retrouver les statistiques obtenues par DNS pour une efficacité de calcul équivalente voire supérieure.

La première lacune identifiée dans les ROS est la perte du phénomène d'intermittence, correspondant à de fortes fluctuations du champ de dissipation de l'écoulement turbulent. Une caractérisation mathématique de l'intermittence a été proposée pour un écoulement monophasique. Les modèles stochastiques visant à reproduire l'intermittence reposent sur les chaos Gaussiens multiplicatifs, dont plusieurs modèles existent dans la littérature. Nous avons proposé une méthode mathématique originale permettant de construire de tels processus de manière générique comme somme infinie de processus d'Ornstein-Uhlenbeck. Ce formalisme permet non seulement d'unifier l'écriture des processus existants, mais surtout d'en développer un nouveau plus générique et plus efficace en temps de calcul.

De plus, un écoulement turbulent peut engendrer une hétérogénéité dans la distribution spatiale des particules appelée ségrégation. En ne résolvant pas les petites échelles avec lesquelles les particules interagissent, les ROS représentent mal ce phénomène. Pour retrouver ces propriétés, nous avons proposé un nouveau modèle cinématique à base d'ondelettes à divergence nulle. En comparant ce modèle à des simulations DNS et aux modèles cinématiques de la littérature, nous avons pu montrer qu'il permet de retrouver les principales statistiques des deux phases et de s'adapter à différents écoulements.

Enfin, les transferts d'énergie entre phases et entre les échelles résolues et non-résolues ne sont pas correctement reproduits dans les ROS actuelles. Préalable essentiel à la conception d'un nouveau modèle palliant ces défauts, nous avons mené un important travail d'analyse de ces rétrocouplages à partir de simulations DNS et en unifiant les résultats de la littérature. Nous avons ainsi pu identifier les échelles et mécanismes privilégiés de ces transferts d'énergie, ainsi que les paramètres prépondérants permettant de caractériser ces phénomènes, comme la densité moyenne de particules.

L'ensemble de ces travaux permet d'apporter un nouvel éclairage sur les interactions entre des particules et la turbulence. Cette thèse a ainsi permis de mener des analyses approfondies et de proposer des modèles originaux pour enrichir les ROS, ouvrant la voie à des simulations capturant fidèlement le rétro-couplage. Elle offre également de nombreuses perspectives pour la construction d'un modèle fluide couplé cohérent pour la simulation d'écoulements diphasiques turbulents.

Contents

Abstract **vii**

Résumé **ix**

Nomenclature **xix**

Introduction **1**
1 Contexte 1
1.1 Écoulements diphasiques dispersés turbulents dans les applications industrielles et environnementales 1
1.2 Expériences et simulations 2
2 Simulation numérique d'écoulements diphasiques turbulents à phase dispersée . . . 3
2.1 Simulation numérique de la turbulence 4
2.2 Simulation numérique de la phase dispersée 5
2.2.1 Approches lagrangiennes déterministes 5
2.2.2 Méthodes basées sur la cinétique 6
2.2.3 Méthodes des moments eulériens 7
2.3 Quelques éléments clés de la physique des écoulements à phase dispersée et leur modélisation 7
3 Défis liés à la modélisation point-particule dans une simulation de turbulence d'ordre réduit 9
3.1 Statistiques intermittentes 10
3.2 Ségrégation 11
3.3 Couplage inverse 11
4 La contribution de la thèse 12
5 Plan du manuscrit 13

Introduction **15**
6 Context 15
6.1 Turbulent disperse two-phase flows in environmental and industrial contexts 15
6.2 Experiments and simulations 16
7 Numerical simulation of turbulent disperse two-phase flows 17
7.1 Numerical simulation of turbulence 17
7.2 Numerical simulation of the disperse phase 18
7.2.1 Deterministic Lagrangian approaches 18
7.2.2 Kinetic-based methods 19
7.2.3 Eulerian moment methods 20

7.3 Some key physics of disperse phase flows and their modeling 20
8 Modeling challenges for point-particle with reduced-order turbulence simulation . 23
8.1 Intermittent statistics 23
8.2 Segregation 24
8.3 Two-way coupling 24
9 The thesis contribution 25
10 Outline of the manuscript 26

I Turbulent flows **29**

1 Physics and theories of turbulent flows **33**
1.1 Fluid dynamic equations 33
1.1.1 From molecules to continuous medium 33
1.1.2 Navier-Stokes equations 34
1.1.3 The Reynolds number 35
1.1.4 Richardson's energy cascade and energy spectrum 36
1.1.5 Lagrangian framework for fluid particles 38
1.1.6 The random nature of turbulence 38
1.1.6.1 Probability space for turbulent flows 40
1.1.6.2 Ergodicity 41
1.2 Statistical description of turbulence 42
1.2.1 One-point, one-time statistics 42
1.2.2 One-point, two-time statistics 43
1.2.3 Two-point, one-time statistics 44
1.2.4 Characteristic scales of turbulence 45
1.2.5 Structure functions 45
1.3 The quest for turbulence universality 46
1.3.1 Origins and properties of the intermittency 47
1.3.1.1 K 41: the global- similarity hypotheses 47
1.3.1.2 K62: the refined similarity hypotheses 48
1.3.1.3 Eulerian framework for intermittency 50
1.3.2 The cascade model of Yaglom 50
1.3.3 Acceleration statistics 51

2 Modeling and simulation of turbulent flows **57**
2.1 Direct numerical simulation 57
2.2 Dimensionality reduction strategies for turbulence 58
2.2.1 Reynolds averaged Navier-Stokes 60
2.2.2 Large Eddy Simulation 61
2.2.3 A general framework for reduced-order simulations (ROS) 65
2.3 Homogeneous isotropic turbulence 65
2.3.1 Initialization 66
2.3.2 Model spectrum 66
2.3.3 Turbulence forcing 68
2.4 Numerical framework 69
2.4.1 Asphodele code: DNS of decaying HIT 69

2.4.2 Fieldz code: DNS and LES of stationary HIT . . . 70
2.4.3 DNS dataset of Lanotte et al. (2011): stationary HIT . . . 72
2.4.4 Main numerical tools and challenges . . . 72

II Reproducing intermittency in turbulent flows 75

3 Intermittency in stochastic models for turbulence 79
3.1 Introduction to stochastic processes . . . 80
3.1.1 Definition of stochastic process . . . 80
3.1.2 Definition of Gaussian process . . . 80
3.1.3 Wiener process . . . 81
3.1.4 Itô calculus . . . 81
3.1.5 Ornstein-Uhlenbeck process . . . 82
3.1.6 Fractional Brownian motion . . . 84
3.1.7 Some properties of stochastic processes . . . 85
3.1.7.1 Self-similar process . . . 85
3.1.7.2 Kolmogorov continuity theorem . . . 85
3.2 Stochastic models for turbulent flows consistent with K41 . . . 86
3.2.1 First-order model . . . 87
3.2.2 Closures of the parameters . . . 89
3.2.3 Second-order model . . . 89
3.2.4 Higher-order models . . . 92
3.3 Stochastic models for turbulent flows consistent with K62 . . . 92
3.3.1 Local dissipation modeled by an Ornstein-Uhlenbeck process . . . 92
3.3.2 Conditional Gaussian velocity . . . 93
3.3.3 Conditional Gaussian acceleration . . . 93
3.3.4 Conditional Non-Gaussian acceleration . . . 94
3.3.5 Velocity-conditioned acceleration . . . 95
3.3.6 Conclusion on models compliant with K62 . . . 95
3.4 Intermittent stochastic models . . . 95
3.4.1 Modeling the pseudo-dissipation . . . 96
3.4.2 Multifractal properties of the pseudo-dissipation . . . 96
3.4.3 General formalism for the pseudo-dissipation . . . 97
3.4.4 A review of existing dissipation processes . . . 99
3.4.4.1 An Ornstein-Uhlenbeck process . . . 99
3.4.4.2 Log-correlated processes . . . 99
3.4.4.3 Comparison of models with DNS . . . 101
3.4.5 Extension to the LES framework . . . 102

4 A new mathematical framework for the Gaussian multiplicative chaos 105
4.1 Construction of a stochastic process with intermittent statistics . . . 105
4.1.1 Gaussian multiplicative chaos . . . 106
4.1.2 A fractional Ornstein-Uhlenbeck process X^τ based on W^τ . . . 106
4.1.3 Regularized fractional Brownian motion . . . 107
4.1.4 Representation in the Laplace domain . . . 108
4.1.4.1 Laplace representation of W^τ . . . 108

4.1.4.2 Laplace representation of W^H . . . 110
4.2 A new framework for FBM . . . 111
4.2.1 A generic representation encompassing existing FBM . . . 111
4.2.2 Computation of covariance of $\mathcal{W}$ . . . 112
4.3 A new framework for approximated GMC . . . 114
4.3.1 Generic representation of X^τ . . . 114
4.3.2 General stationary Ornstein-Uhlenbeck processes . . . 116
4.3.2.1 Covariance of the general stationary Ornstein-Uhlenbeck processes . . . 117
4.3.2.2 The general stationary OU process as a solution to a SDE . . . 119
4.4 Convergence to the Gaussian multiplicative chaos . . . 120
4.4.1 The limit covariance . . . 120
4.4.2 Convergence to the log-correlated process . . . 123

5 An original and versatile numerical approach for intermittent stochastic processes 127
5.1 Infinite sum of correlated Ornstein-Uhlenbeck processes . . . 127
5.1.1 A new stochastic process with appropriate regularizations . . . 128
5.1.2 Autocorrelation function of X_t^∞ . . . 129
5.1.3 A framework encompassing existing processes . . . 132
5.2 Finite sum of correlated Ornstein-Uhlenbeck processes . . . 134
5.2.1 Quadrature . . . 134
5.2.2 Discussion . . . 136
5.2.2.1 Physical interpretation . . . 136
5.2.2.2 Implementation . . . 138
5.2.2.3 A causal multi-fractal process for pseudo-dissipation . . . 138

III One-way coupled turbulent disperse two-phase flows 143

6 Transport of particles by turbulence 147
6.1 A particle in a flow . . . 147
6.1.1 Forces acting on a particle . . . 148
6.1.2 The Stokes drag for point-particle tracking . . . 149
6.2 Eulerian description of the disperse phase . . . 149
6.2.1 Particle preferential concentration . . . 151
6.2.1.1 Evidence of particle preferential concentration . . . 151
6.2.1.2 Measure of particle preferential concentration . . . 153
6.2.2 Particle velocity dispersion . . . 154
6.2.2.1 Evidence of particle trajectory crossing . . . 154
6.2.2.2 Measure of particle velocity dispersion . . . 155

7 Modeling and simulation of the disperse phase 159
7.1 Dimensionality reduction for the disperse phase . . . 160
7.1.1 Microscopic approaches . . . 160
7.1.2 Mesoscopic approaches . . . 160
7.1.3 Macroscopic approaches . . . 161
7.2 Particles dynamics in under-resolved turbulence . . . 162

7.2.1 Impact of under-resolved turbulence on particles dynamics . . . 163
7.2.1.1 Simulation set-up: Euler-Lagrange disperse flows . . . 163
7.2.1.2 Intermittency . . . 165
7.2.1.3 Segregation . . . 166
7.2.2 Overview of existing particle sub-filter scale models . . . 167
7.2.2.1 Stochastic models . . . 168
7.2.2.2 Structural models . . . 169
7.2.3 Capturing reduced-order statistics of the disperse phase . . . 170

IV Reproducing segregation and intermittency in turbulent disperse two-phase flows 175

8 Two-phase flow stochastic models 179
8.1 Criteria for the assessment of stochastic models . . . 179
8.2 Stochastic models for particle velocity . . . 180
8.3 Stochastic models for particle acceleration . . . 181
8.3.1 Velocity along inertial particle trajectory . . . 182
8.3.2 Stochastic models for the velocity seen . . . 183
8.3.3 Stochastic model for the acceleration . . . 184
8.4 Dissipation along inertial particle trajectory . . . 185
8.4.1 An Ornstein-Uhlenbeck process for the dissipation seen by particles . . . 185
8.4.2 A multifractal process for the dissipation seen by particles . . . 187

9 Wavelet-based kinematic simulation 191
9.1 Fourier-based kinematic simulation . . . 191
9.2 Multiresolution Analysis . . . 194
9.2.1 Introduction to wavelets . . . 194
9.2.2 Multi-dimensional wavelets . . . 195
9.2.2.1 Decomposition of a scalar field . . . 197
9.2.2.2 Decomposition of a vector field . . . 198
9.2.3 Divergence-free wavelets . . . 199
9.2.3.1 Definition . . . 199
9.2.3.2 Change of basis . . . 202
9.2.3.3 Extension to the 3D case . . . 203
9.3 A new kinematic simulation based on wavelets . . . 203
9.3.1 Construction of a new synthetic velocity field . . . 203
9.3.1.1 Energy spectrum and characteristic length scales . . . 205
9.3.1.2 Characteristic time scales . . . 207
9.3.1.3 Validation with 2D frozen turbulence . . . 210
9.3.2 Evolution of the wavelet field . . . 211
9.4 Validation with DNS . . . 212

10 Particles dynamics in wavelet-based kinematic simulation 219
10.1 Influence of the Reynolds number . . . 219
10.1.1 Particle preferential concentration . . . 221
10.1.2 Random uncorrelated motion . . . 221

10.2 Validation with 2D frozen turbulence . . . 223
10.3 Influence of λ . . . 224
10.4 Validation with DNS of 3D HIT and comparison with Fourier-based KS . . . 226

11 Perspectives for wavelet-based kinematic simulation 231
11.1 Intermittency in wavelet-based KS . . . 231
11.1.1 Comparing intermittency in kinematic simulations . . . 231
11.1.2 Towards an intermittent cascade of wavelets . . . 232
11.1.3 An overview of discrete cascade models . . . 233
11.1.4 A perspective for intermittent KS . . . 235
11.2 Towards reduced-order simulations . . . 236
11.2.1 Compression of the wavelet field . . . 236
11.2.2 Truncated normal distribution . . . 236
11.2.3 Sinusoidal temporal evolution of coefficients . . . 239
11.2.4 A sub-grid velocity model for LES . . . 241

V Towards two-way coupling in turbulent disperse two-phase flows 245

12 Modeling two-way coupling 249
12.1 Impact of volume and mass fractions . . . 250
12.2 Overview of existing studies . . . 250
12.3 Modeling and numerical frameworks . . . 251
12.3.1 Fluid and particles equations . . . 251
12.3.2 Coupling equations . . . 253
12.3.3 Numerical methods . . . 253
12.4 Target configuration and parameter sets . . . 254
12.4.1 Homogeneous isotropic turbulence . . . 254
12.4.2 Key-parameters and dimensional analysis . . . 256

13 Modulation of turbulence by particles 261
13.1 A measure of disperse phase spatial heterogeneity . . . 261
13.1.1 Box counting measure . . . 261
13.1.2 Voronoï measure . . . 263
13.1.3 Identification of isolated particles . . . 265
13.1.4 Summary of proposed measures . . . 266
13.2 Modulation of turbulence by particles: an exhaustive study . . . 268
13.2.1 Methodology . . . 268
13.2.2 Two-way interaction energy rate . . . 268
13.2.3 Spectral space analysis of two-way coupling energy rate . . . 273
13.2.4 Particle field heterogeneity . . . 276
13.2.4.1 Preferential concentration . . . 276
13.2.4.2 Collective and isolated regimes . . . 278
13.2.4.3 Scale by scale convergence . . . 279

14 Towards two-way coupling 283
14.1 Challenges with two-way coupled simulations . . . 283

14.2 Statistically-consistent two-phase formalisms with two-way coupling 285
14.2.1 Interactions between unresolved and resolved scales in ROS 285
14.2.2 Consequences of two-way coupling on the statistical description 286
14.2.3 A classification of possible strategies 286
14.3 Extension of kinematic simulation for two-way coupled flows 288
14.3.1 Global statistics 289
14.3.2 Global spectrum 289
14.3.3 Local two-way coupling 290
14.3.4 Next steps 291

Conclusion **295**

A Eulerian moment methods **301**
A.1 Mesoscopic approach 301
A.2 Some notations and definitions 302
A.3 Moments equation 304
A.4 Closures 305
A.4.1 Algebraic closures 305
A.4.2 Assumed NDF shape 306
A.4.2.1 Monokinetic closure 306
A.4.2.2 Anisotropic Gaussian closure 306
A.4.2.3 Isotropic Gaussian closure 307
A.4.2.4 Comparison of the methods on HIT 307

B Kinematic simulation with Gaussian fields **311**
B.1 Construction of a new synthetic velocity field 311
B.2 Temporal evolution of the velocity field 313
B.3 Particle segregation in the Gaussian-based KS 314
B.4 Compatibility with LES framework 315

C Impact of the coupling kernel **319**

D Convergence of the box counting measure **323**

References **341**

Nomenclature

Upper-case Roman characters :

A_f	Set of fluid flow field
B_f	Set of possible external forces
C	Unspecified constant
$\mathcal{C}$	Courant-Friedrich-Lewy number
C_D	Drag coefficient
C_S	Smagorinsky constant
$\mathcal{C}_0$	Universal Kolmogorov constant
D_p^E	Eulerian velocity structure function of order p
D_p^L	Lagrangian velocity structure function of order p
$D(\kappa)$	Spectral viscous dissipation rate
$E(\kappa)$	Energy spectrum
$\mathcal{E}$	Set of events
$\boldsymbol{F}_D$	Drag force of the fluid on a particle
$\boldsymbol{F}_p$	Drag force per unit mass of the fluid on a particle
Kn	Knudsen number
H	Hurst parameter
H_n	Standardized moment of order n
$\mathcal{L}$	Size of the domain
L	Largest scale in the flow (injection of energy)
N_d	Number of physical dimensions
N_p	Number of particles

N_x	Number of grid points in one direction
N_t	Number of total time steps
N_κ	Number of modes in the Fourier-based kinematic simulation
$\mathcal{N}$	Gaussian distribution
$\mathcal{N}_T$	Truncated Gaussian distribution
$\mathbb{P}$	Probability measure
Re	Reynolds number
Re_L	Turbulence Reynolds number
Re_η	Reynolds Kolmogorov scales
Re_ℓ	Local Reynolds number
Re_λ	Taylor-scale Reynolds number
Re_p	Particle Reynolds number
R_E^u	Eulerian one-point velocity correlation function
$R_{E,ij}^u$	Eulerian two-point velocity correlation function
R_L^u	Lagrangian velocity correlation function
S_{ij}	Deformation-rate tensor
$\|S\|$	Norm of the strain rate tensor
St_η	Stokes number based on the Kolmogorov scales (also denoted St)
St_L	Stokes number based on the integral scales
St_Δ	Stokes number based on the cut-off scale
$T(\kappa)$	Spectral energy-transfer rate
T_E	Eulerian time scale of velocity correlation: eddy turnover time
$T_{E,j}$	Eddy turnover time (in wavelet-based KS)
T_L	Lagrangian integral time scale
$T_L^\star$	Lagrangian integral time scale of fluctuating velocity
$T_L^{\star@p}$	Lagrangian integral time scale of fluctuating velocity along particle trajectory
$\mathcal{V}$	Volume of control
V_j	Sub-space of MRA

W_j	Supplementary sub-space of MRA
$\mathcal{W}$	Generalized fractional Brownian motion
W_t^ϵ	Regularized FBM
$\mathcal{X}$	General stationary solution of fractional Ornstein-Uhlenbeck
X_t	Zero-average Gaussian variable
X_t^ϵ	Regularized log-correlated Gaussian variable
Y_t^x	Standard Ornstein-Uhlenbeck process with zero mean and speed reversion x

Lower-case Roman characters :

$\boldsymbol{a}$	Fluid acceleration
a_0	Constant in the K41 model
$\overline{a_0}$	Universal constant in the K62 model
a_η	Kolmogorov acceleration
d_p	Particle diameter
$d_{j,\boldsymbol{k}}^\varepsilon$	Wavelet coefficient
f	Particle number density function (NDF)
$\boldsymbol{f}$	Force exerted by particle per unit mass applied on the fluid
$\boldsymbol{f}_{ext}$	External force per unit mass applied on the fluid
g	Cutting function (e.g. Heaviside function)
$\boldsymbol{g}$	Gravitational force per unit mass
k	Local fluid turbulent kinetic energy
k_ϵ	Regularized kernel (or κ_ϵ).
k_{sgs}	Sub-grid scale energy
$j_{\min}$	Minimum level in wavelet-based KS
$j_{\max}$	Maximum level in wavelet-based KS
ℓ	Typical length scale
ℓ_j	Typical length scale associated to level j (wavelet-based KS)
ℓ_S	Smagorinsky length scale

m_p	Mass of particle
$n(\boldsymbol{x}, t)$	Particle number density field
n_0	Dimensionless particle number density
n_η	Dimensionless particle number density
$p(\boldsymbol{x}, t)$	Fluid pressure field
$t^\star_\eta$	Smallest time scale for fluctuating velocity
$t_{\chi@p}$	Smallest time scale for dissipation along particle trajectory
$\boldsymbol{u}(\boldsymbol{x}, t)$	Fluid velocity field
$\boldsymbol{u}_{@p}(t)$	Undisturbed fluid velocity at particle position
$\boldsymbol{u}_p(t, \boldsymbol{x})$	Average particle velocity
u_η	Kolmogorov velocity scale
$\boldsymbol{v}_p(t)$	Lagrangian particle velocity

Upper-case Greek characters :

Δ	Filter width or cut-off length (LES)
$\Delta_\tau u$	Lagrangian velocity increment
Δx	Spatial discretization step
Δt	Time discretization step
$\Delta(\boldsymbol{x})$	Projection kernel function
Ψ_p	Spectral two-way coupling (fluid–particle drag interaction) energy rate
Ω	Set of possible outcomes

Lower-case Greek characters :

α	Volume fraction
α_i	Random variable in cascade models
$\delta\theta_p$	Kinetic energy of the random uncorrelated-motion
ε	Local fluid energy dissipation rate
$\varepsilon_\star$	Dissipation of fluctuating scale (ROS)
$\varepsilon_{\star@p}$	Dissipation of fluctuating scale (ROS) along particle trajectory

$\varepsilon_{\mathrm{sgs}}$	Sub-grid scale dissipation rate (LES)
ε_ℓ	Dissipation averaged over a ball of size ℓ
ε^τ	Dissipation averaged along a particle path during a time τ
φ	Scaling function (MRA)
φ	Pseudo-dissipation
φ^τ	Locally-averaged pseudo-dissipation
ϕ	Mass loading
ψ	Wavelet function (MRA)
ψ_p	Two-way interaction energy rate
η	Kolmogorov length scale
$\boldsymbol{\kappa}$	Wavenumber
κ_0	First resolved wavenumber
$\kappa_{\max}$	Maximum resolved wavenumber
κ_c	Cut-off wavenumber
λ	Mean free path
λ	Constant scale ratio
λ	Factor of eddy turnover velocity
λ_f	Taylor's microscopic length scale
λ_I	Intermittency parameter
μ	Shear viscosity coefficient
μ_t	Turbulent eddy (dynamic) viscosity
ν	Fluid dynamic viscosity
ν_t	Turbulent eddy (kinematic) viscosity
ρ	Fluid density
ρ_p	Particle density
$\rho_p(t, \boldsymbol{x})$	Particle density field
τ	Characteristic time scale

τ_{sgs}	Sub-grid time scale
τ_{ij}	Viscous stress tensor
τ_{ij}^R	Residual viscous stress tensor (RANS)
τ_{ij}^r	Sub-grid-scale stress tensor (LES)
τ_η	Kolmogorov time scale
τ_p	Particle relaxation time
σ_u^2	Variance of fluid velocity
$\sigma_\star$	Variance of fluctuating velocity (ROS)
σ_{sgs}	Sub-grid velocity (LES)
ω	Frequency
ω	Realization
ω_j	Eddy turnover frequency (wavelet-based KS)
χ	Logarithm of the normalized (pseudo-)dissipation rate
$\chi_@$	Logarithm of the normalized (pseudo-)dissipation along particle trajectory
$\xi(p)$	Intermittency exponent

Notation:

$s \wedge t$	$= \min(s,t)$, minimum between s and t
$s \vee t$	$= \max(s,t)$, maximum between s and t
$\mathbb{E}[\bullet]$	Expectancy of a random variable $\bullet$
$\mu_\bullet$	Mean of the process $\bullet$
$\sigma_\bullet^2$	Variance of the process $\bullet$
$\langle\bullet\rangle$	Reynolds average (ensemble average)
$\overline{\bullet}$	Filtered quantity
U	Reduced quantify (Reynolds average or filtered)
u'	Residual (fluctuating) part
$\mathrm{d}\bullet$	Differential of $\bullet$
$\partial\bullet$	Partial derivative with respect to $\bullet$
$\nabla_{\boldsymbol{x}}$	Notation for $(\partial_x, \partial_y, \partial_z)$

$\nabla_{\boldsymbol{v}}$	Notation for $(\partial_{v_x}, \partial_{v_y}, \partial_{v_z})$
$\Re\{\}$	Real part
$.^*$	Complex conjugate
$\hat{.}$	Fourier transform
$\times$	Cross product
$\otimes$	Outer product
$\otimes_s$	Symmetric tensor outer product

Abbreviations :

ADM	Approximate Deconvolution Method
DNS	Direct Numerical Simulation
DPS	Discrete Particle Simulation
EMEF	Extended Mesoscopic Eulerian Formalism
FBM	Fractional Brownian Motion
GMC	Gaussian Multiplicative Chaos
HIT	Homogeneous Isotropic Turbulence
K41	Kolmogorov 1941 theory
K62	Kolmogorov and Obukhov 1962 theory
KS	Kinematic Simulation
LES	Large Eddy Simulation
MEF	Mesoscopic Eulerian Formalism
MCE	Mean Correlated Energy
MRA	Multiresolution Analysis
MTE	Mean Total Energy
NDF	Number Density Function
ODE	Ordinary Differential Equation
PDF	Probability Density Function

PPC	Particle Preferential Concentration
PTC	Particle Trajectory Crossing
RANS	Reynolds Averaged Navier-Stokes
ROS	Reduced-Order Simulation
RPP	Random Poisson Process
RUM	Random Uncorrelated Motion
SDE	Stochastic Differential Equation
SFS	Sub-Filter Scale
WBE	Williams-Boltzmann equation

Introduction (français)

1 Contexte

1.1 Écoulements diphasiques dispersés turbulents dans les applications industrielles et environnementales

Les écoulements diphasiques dispersés turbulents sont au cœur de nombreux phénomènes naturels tels que les nuages, dans lesquels la condensation des gouttelettes est contrôlée par la turbulence, la formation des planètes et des disques protoplanétaires par l'agrégation de particules de poussière (voir Fig. 1(a)), ou encore la sédimentation des océans. Ils sont également impliqués dans un grand nombre de considérations environnementales, notamment le transport de particules dans l'atmosphère. Ces particules peuvent avoir des origines et des propriétés diverses, par exemple les fumées d'incendie, les cendres volcaniques (voir Fig. 1(b)) ou divers polluants (particules fines, suie, ...).

Ils constituent également un élément clé dans de nombreuses applications industrielles. En particulier, l'efficacité de beaucoup de processus de production et de conversion d'énergie est régie par la dynamique des écoulements multiphasiques. L'exemple le plus emblématique est la combustion de carburant dans les moteurs thermiques, pour lesquels des efforts de recherche importants sont réalisés en vue d'améliorer leur efficacité énergétique et ainsi de réduire les émissions polluantes associés. Ainsi, le spray de carburant résultant de l'atomisation constitue un élément essentiel du fonctionnement des moteurs, puisque ces gouttelettes, en s'évaporant, produisent le mélange carburant/oxydant qui alimente la combustion. Une compréhension détaillée de ces phénomènes complexes combinée à des modèles efficaces est donc essentielle pour aider à concevoir les futures générations de moteurs thermiques, offrant une combustion plus efficace et des moyens de transport plus propres.
La diversité et l'importance des domaines où interviennent les écoulements diphasiques dispersés font de leur modélisation un sujet de grand intérêt pour les communautés scientifiques et industrielles. Bien qu'il s'agisse d'un domaine d'étude intensif depuis des décennies, de nombreuses questions scientifiques doivent encore être abordées pour compléter notre compréhension de ces phénomènes. La complexité du problème étudié provient d'abord de la nature de la phase porteuse, qui est le plus souvent turbulente, ce qui permet un meilleur mélange entre les deux phases. La turbulence, par nature instationnaire et multi-échelle, est déjà un défi dans les écoulements monophasiques, et le couplage avec la phase dispersée introduit des difficultés supplémentaires pour comprendre et modéliser efficacement ces phénomènes.

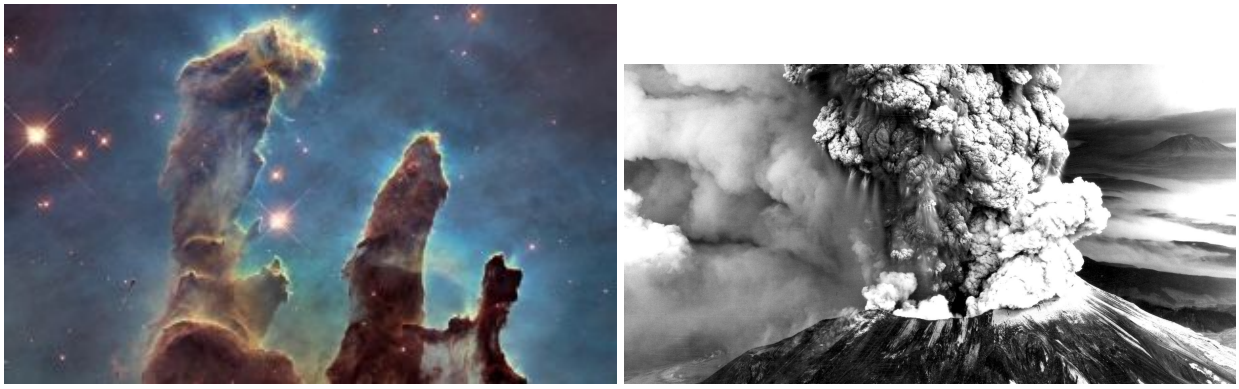

(a) (b)

Figure 1. (a) Gaz et poussière interstellaires dans la nébuleuse de l'Aigle, d'une longueur d'environ 4 années-lumière, à quelques 7 000 années-lumière de la Terre. NASA, ESA. (b) Photographie de l'éruption du Mont St. Helens, le 18 mai 1980

1.2 Expériences et simulations

L'ambition de la recherche sur les écoulements diphasiques dispersés est de prédire avec précision l'évolution et le comportement de tels écoulements dans une configuration donnée, par exemple une chambre de combustion dans un moteur thermique. Les études expérimentales et les essais sur banc sont longtemps restés la principale approche pour évaluer, analyser, comprendre et concevoir des systèmes impliquant des écoulements diphasiques. S'ils sont toujours considérés comme une référence, ils présentent néanmoins plusieurs inconvénients. En effet, contrairement aux simulations numériques, les études expérimentales ne permettent pas d'avoir une connaissance complète du système étudié (certaines mesures peuvent être intrusives ou très difficiles à réaliser), et certaines configurations ou conditions environnementales peuvent être difficilement reproductibles. De façon générale, les ressources et le temps que requièrent les expériences réelles limitent la quantité de données qui peut être générée pour comprendre ou concevoir un système.
Les simulations numériques sont un complément idéal aux études expérimentales : à partir de modèles, c'est-à-dire d'un ensemble d'équations dont les solutions reproduisent le plus fidèlement possible la réalité, il est possible de faire des prédictions sur un système avec un coût et une précision raisonnables. Développés à partir de bases théoriques et mathématiques, les modèles permettent ainsi de reproduire des expériences, de tester différentes configurations, et même d'explorer des mécanismes physiques difficiles à observer expérimentalement. Dans la plupart des cas, la résolution des équations du modèle nécessite une simulation numérique. Une comparaison entre une expérience et une simulation de turbulence homogène est donnée dans la Fig. 2.
Grâce aux développements récents de modèles fiables et d'architectures de calcul massif, les simulations numériques d'écoulements turbulents diphasiques dispersés sont rapidement devenues un sujet d'intérêt pour les communautés académiques et industrielles.

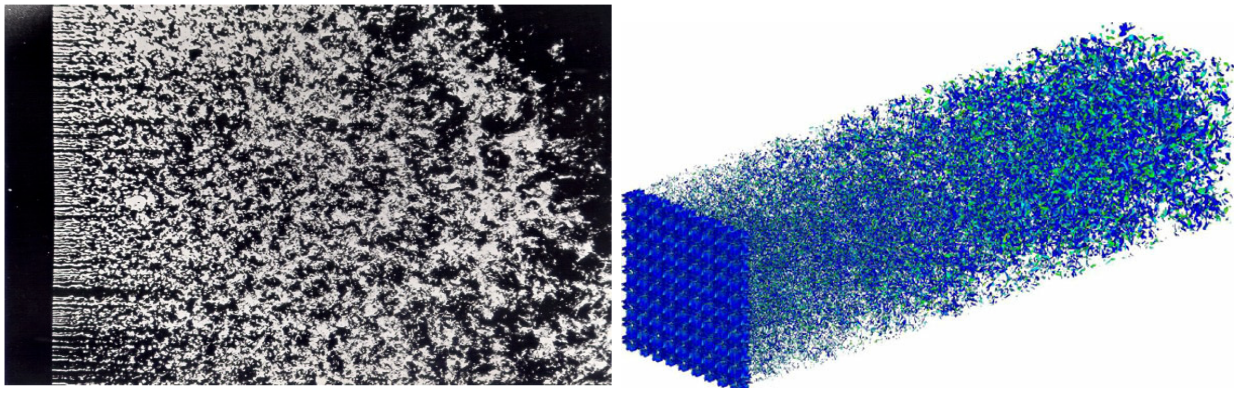

(a) (b)

Figure 2. Turbulence homogène derrière une grille. (a) Photographie tirée de Van Dyke, Album of Fluid Motion n°153 ; (b) Simulation tirée de Vassilicos and Laizet (2010).

2 Simulation numérique d'écoulements diphasiques turbulents à phase dispersée

La modélisation de tels écoulements doit relever un double défi : la description de la turbulence (la phase porteuse) et la description de la phase dispersée. Dans les deux cas, il s'agit de problèmes multi-échelles qui nécessitent des modèles d'ordre réduit : pour un système d'injection de carburant liquide, le diamètre de la particule est typiquement de $0,1 - 10$ μm alors que les dimensions de la chambre de combustion sont d'environ 10 cm. Le niveau de description définit les détails du champ d'écoulement qui est résolu dans les deux phases.

L'utilisation de modèles d'ordre réduit présente un double intérêt. Le premier découle de la haute dimensionnalité du problème, restreignant le recours à la simulation haute fidélité à un nombre limité de particules ou à une turbulence peu développée. Les simulations d'ordre réduit (ROS) permettent de diminuer le temps de calcul, mais cette réduction a un coût : la perte d'information aux plus petites échelles ne peut être compensée que par un effort de modélisation supplémentaire. La deuxième motivation est liée à la nature chaotique de ces écoulements complexes. Un changement minime dans les conditions initiales de l'une des deux phases peut conduire à des perturbations considérables à long terme. La résolution d'un écoulement donné peut donc être remise en question puisque la connaissance de l'écoulement initial des positions et vitesses des particules ne sera jamais parfaite, la modélisation introduit des hypothèses simplificatrices et la simulation peut générer des erreurs numériques. Il est donc inutile de chercher à obtenir une description détaillée des deux phases mais il est plus pertinent d'en faire une description statistique.

Nous présenterons tout d'abord les stratégies de réduction en ordre concernant la phase turbulente porteuse seule, puis celles liées à la description de la phase dispersée. Enfin, nous aborderons les questions liées au couplage de ces deux phases.

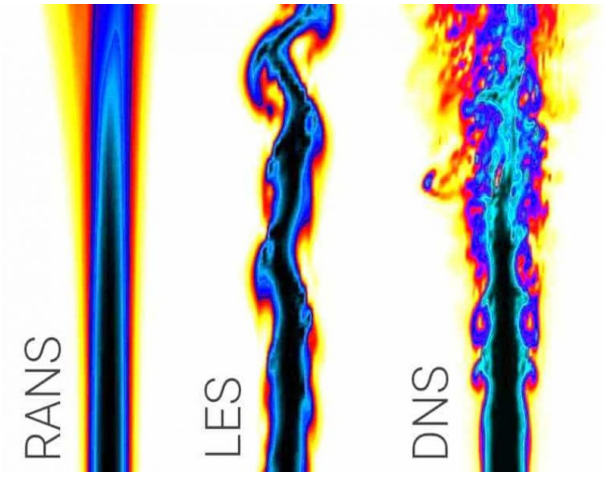

Figure 3. Simulations numériques d'un jet turbulent pour différents modèles (Agence italienne pour les technologies des énergies nouvelles 2006).

2.1 Simulation numérique de la turbulence

Les écoulements turbulents monophasiques sont des problèmes hautement multi-échelles. Le rapport entre les échelles de production et de dissipation d'énergie est donné par le nombre de Reynolds, qui caractérise la turbulence. Cette séparation d'échelle est à l'origine du coût numérique puisque la résolution des plus petites échelles sur de grands domaines peut alors exploser pour de grands nombres de Reynolds. Il existe différentes stratégies de résolution, qui sont illustrées pour le cas d'un jet turbulent dans la Fig. 3.

Simulation numérique directe
La description la plus précise de la turbulence est donnée par la résolution de l'ensemble de l'écoulement, en utilisant la simulation numérique directe (Direct Numerical Simulation : DNS). L'image DNS de la Fig. 3 est en effet très détaillée, elle résout les échelles les plus fines de l'écoulement. Cependant, le coût de ces méthodes est inaccessible dans un cadre industriel : le nombre de Reynolds typique dans une chambre de combustion est d'environ $10^5 - 10^6$. Par conséquent, les DNS sont limitées à de petits domaines et reposent sur des architectures de calcul massivement parallèles.

Simulation d'ordre réduit
Afin de permettre une résolution du problème, bien que cela implique une perte d'information sur les petites échelles, des modèles d'ordre réduit sont proposés. Les simulations d'ordre réduit (Reduced-Order Simulation : ROS) permettent de réaliser des simulations prédictives et efficaces en temps de calcul sur des configurations industrielles. Cependant, elles ne peuvent capturer que les dynamiques à grande échelle, qui sont entièrement résolues, et ignorent les plus petites échelles, qui nécessitent une modélisation pour être prises en compte. Deux stratégies principales sont couramment utilisées pour construire de tels modèles. Une opération de moyennage peut être appliquée aux équations de Navier-Stokes pour obtenir les équations moyennes des écoulements de fluides appelées équations de Reynolds Averaged Navier-Stokes (RANS). Cette approche est la plus économique et la plus répandue dans les applications industrielles actuelles. Cependant, il peut être nécessaire pour certaines applications de résoudre une partie des échelles turbulentes plutôt que de les modéliser. Les simulations aux grandes échelles (Large Eddy Simulation : LES)

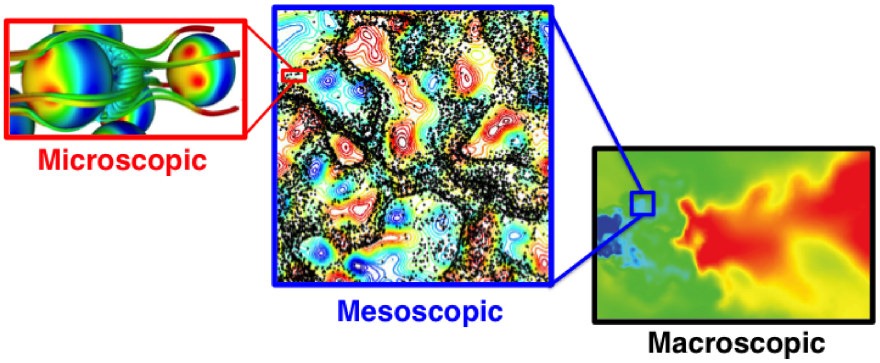

Figure 4. Différents niveaux de description de la phase dispersée : microscopique (à gauche), mésoscopique (au centre) et macroscopique (à droite).

consistent à filtrer les équations de Navier-Stokes, pour ne résoudre que les grandes échelles de la turbulence. La figure 3 montre que la méthode RANS fournit une image moyenne et symétrique du jet, très diffuse. D'autre part, la simulation LES est un intermédiaire, elle reproduit les grandes échelles instationnaires du jet mais les plus petites sont filtrées.

Bien que les modèles d'ordre réduit fournissent un niveau raisonnable de prédiction de l'écoulement purement gazeux, leur fidélité doit être évaluée pour les configurations diphasiques dans lesquelles la phase dispersée interagit avec les structures turbulentes.

2.2 Simulation numérique de la phase dispersée

Différentes approches existent dans la littérature pour décrire la phase dispersée, et une attention particulière doit être portée au choix de la modélisation afin de reproduire les comportements physiques à un coût minimal pour les applications industrielles. Dans cette section, nous considérons des simulations non réduites de la turbulence : la phase porteuse est supposée entièrement résolue pour nous concentrer sur la modélisation des particules.

2.2.1 Approches lagrangiennes déterministes

Pour les gouttelettes liquides, la résolution exacte de l'ensemble de la phase dispersée nécessiterait la connaissance de l'écoulement à l'intérieur de chaque gouttelette et en tout point de l'interface avec la phase porteuse. Une telle simulation correspond donc à une simulation numérique directe pour chaque particule (Boniou 2021). Sous certaines hypothèses, ou pour des particules solides, le problème est simplifié en imposant des conditions aux limites à la surface de chaque particule (Xu and Subramaniam 2010), la particule peut par exemple être assimilée à une sphère. Ce niveau "microscopique" est illustré dans la Fig. 4, dans l'encadré supérieur gauche, où le terme "microscopique" fait référence au cadre de la théorie cinétique des gaz (Ferziger, Kaper, and Kaper 1972).

Dans la plupart des applications industrielles, on fait l'hypothèse d'une particule ponctuelle lagrangienne : il s'agit de la Simulation de Particules Discrètes (Discrete Particule Simulation : DPS) (Riley and Patterson Jr 1974). Les particules sont suivies individuellement, et leur interaction avec la phase porteuse est modélisée par des forces telles que la loi de traînée de Stokes appliquée au centre de masse de la particule. Dans une telle modélisation, le volume occupé par la

phase dispersée est négligeable par rapport à celui occupé par la phase porteuse.

La simulation lagrangienne est relativement intuitive et simple à mettre en œuvre numériquement (résolution d'une équation différentielle ordinaire pour chaque particule), bien qu'elle nécessite une attention particulière dans les calculs parallèles puisqu'ils exigent l'utilisation d'un équilibrage de la charge de calcul (Marta 2009). C'est pourquoi elle est la méthode la plus répandue dans la littérature pour étudier le comportement des particules inertielles (Squires and Eaton 1991; Elghobashi and Truesdell 1992) et dans les applications de combustion (par exemple Mesquita, Vié, Zimmer, and Ducruix (2021)).

La précision de ces méthodes dépend directement de la modélisation de ces forces mais aussi de l'évaluation de la vitesse du fluide non perturbé à la position de la particule (Horwitz and Mani 2016; Ireland and Desjardins 2017; Poustis, Senoner, Zuzio, and Villedieu 2019). De plus, une seule réalisation de la phase dispersée est obtenue dans chaque simulation. Il est alors nécessaire d'effectuer plusieurs simulations lagrangiennes pour obtenir des variables statistiques globales, ce qui devient excessivement coûteux. On peut alors s'appuyer sur une description cinétique (ou mésoscopique) de la phase dispersée, dans l'esprit de l'équation de Boltzmann obtenue dans la limite Boltzmann-Grad de l'équation de Liouville.

2.2.2 Méthodes basées sur la cinétique

Les approches mésoscopiques fournissent des statistiques de la phase dispersée en dérivant la fonction de densité de nombre (Number Density Function : NDF) de la phase dispersée. Cette fonction donne la probabilité de trouver une particule dans un état donné de l'espace des phases (qui est composé d'un ensemble de variables internes telles que la vitesse, la taille des particules, la température, etc.) L'évolution de la NDF est régie par l'équation de Williams-Boltzmann (Williams-Boltzmann Equation : WBE). La figure 4 montre une réalisation de l'approche mésoscopique, avec une densité initiale de particules uniforme, obtenue avec le suivi lagrangien.

Deux stratégies de résolution de la WBE peuvent être considérées : la première consiste à intégrer l'équation dans l'espace des phases afin de réduire la dimensionnalité du problème et donc de transporter les moments : ceci est décrit plus en détail dans la section suivante. La seconde stratégie est basée sur des méthodes lagrangiennes :

- La méthode de simulation Monte-Carlo directe (Bird 1994) approxime la NDF par un échantillon de particules statistiques discrètes représentant une particule. Il faut donc un grand nombre de particules numériques, chacune d'entre elles étant censée représenter une fraction de la particule physique. Ces particules sont suivies selon le même système d'équations différentielles ordinaires que dans la DPS et la méthode présente donc les mêmes inconvénients de convergence statistique lente.
- La méthode des "parcels" stochastiques consiste au contraire à représenter un groupe de particules aux propriétés identiques par une seule particule numérique, appelée parcelle (O'Rourke 1981). En diminuant le nombre de particules à suivre, cette méthode réduit évidemment le coût de calcul, mais celui-ci reste proportionnel au nombre de particules réelles.

Les deux méthodes lagrangiennes stochastiques présentées ci-dessus rencontrent des difficultés dans un contexte de couplage inverse : en effet, les particules ne sont pas représentées individu-

ellement et l'effet local qu'elles peuvent avoir sur l'écoulement turbulent ne peut être reproduit fidèlement.

2.2.3 Méthodes des moments eulériens

En intégrant la WBE dans l'espace des phases par rapport à un ensemble de polynômes de degré limité, nous obtenons des quantités, appelées moments, qui peuvent être liées à des quantités macroscopiques telles que la concentration de particules ou le champ de vitesse des particules, comme représenté dans l'encart en bas à droite de la Fig. 4. Dans cette approche, les particules ne sont pas décrites individuellement, mais par des champs eulériens qui satisfont des équations différentielles partielles.

Cette méthode est intrinsèquement statistiquement convergente, et le temps de calcul ne dépend pas du nombre de particules. Le cadre eulérien simplifie le couplage avec la phase porteuse puisque les termes d'échange sont alors écrits dans le même formalisme. De plus, cette méthode peut être efficacement implémentée en calcul parallèle puisqu'elle est similaire aux outils habituels de dynamique des fluides numérique.

En revanche, une attention particulière doit être portée à la modélisation de la dispersion en vitesse ou en taille des particules, et les champs résultants dépendent des termes de fermeture considérés. De plus, des méthodes numériques adéquates doivent être développées car cette approche peut conduire à des champs hypercompressifs (De Chaisemartin 2009) et à des singularités.

2.3 Quelques éléments clés de la physique des écoulements à phase dispersée et leur modélisation

Parmi les éléments critiques impliqués dans la modélisation des écoulements diphasiques dispersés, la reproduction de la dynamique des particules est au coeur de cette thèse, et en particulier les statistiques intermittentes, la concentration préférentielle des particules, et le couplage inverse :

- Une simulation lagrangienne peut reproduire fidèlement la dynamique typique d'un écoulement diphasique, et en particulier ses événements rares. La figure 5 montre la simulation d'un brûleur à pulvérisation avec évaporation de gouttelettes. Le passage d'une gouttelette à travers la flamme peut considérablement modifier son front et apporte une perturbation locale qui ne peut pas être capturée par des simulations eulériennes basées sur des moyennes globales. De tels événements extrêmes peuvent être générés par l'intermittence de la phase turbulente, dont les fluctuations de vitesse peuvent varier brutalement et fortement.
- La concentration préférentielle des particules correspond à une accumulation de particules dans certaines régions de l'écoulement, causée par l'interaction des particules avec les tourbillons turbulents. Ceci est illustré dans la Fig. 6, où la position des particules est représentée pour différents nombres de Stokes, ce dernier caractérisant l'inertie des particules. En fonction de ce paramètre adimensionné, la phase dispersée peut être plus ou moins hétérogène. De telles inhomogénéités de concentration jouent un rôle fondamental dans la dynamique de ces systèmes ; par exemple l'accumulation de particules chauffées dans un fluide entraîne un chauffage local plus intense ; et pour les applications de combustion, la ségrégation peut générer des points chauds et des déformations du front de flamme. Ce phénomène est bien

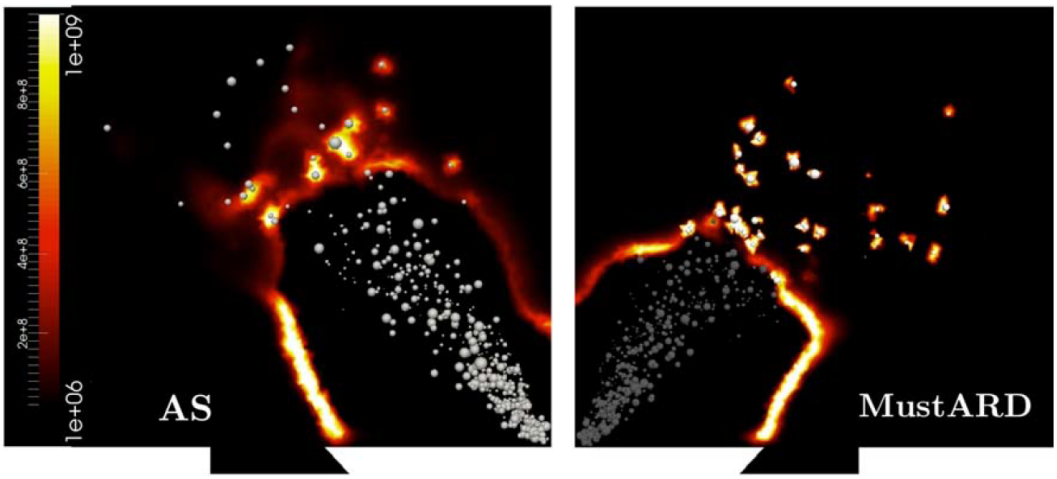

Figure 5. Dégagement de chaleur instantané, avec superposition de gouttelettes pour deux simulations lagrangiennes différentes d'un brûleur à pulvérisation

.

reproduit dans les simulations déterministes lagrangiennes, tandis qu'une résolution très fine est nécessaire pour observer le niveau correct de ségrégation avec les méthodes eulériennes. (Sabat 2016).

- L'influence de la phase dispersée sur la phase porteuse doit également être considérée, en particulier lorsque le chargement massique est important (Elghobashi 1991). Par exemple, des structures turbulentes auto-entretenues ont été observées dans une large gamme de biofluides tels que dans les environnements bactériens ou les eaux de surface océaniques, en raison de petits organismes actifs (bactéries, plancton) générant un mouvement chaotique à petite échelle (Dunkel, Heidenreich, Drescher, Wensink, Bär, and Goldstein 2013; Abraham 1998). Ce phénomène est connu sous le nom de couplage inverse et des termes sources supplémentaires de masse, de quantité de mouvement et d'énergie doivent alors être pris en compte dans la résolution de la phase turbulente. Pour les approches lagrangiennes, les termes d'échange entre le fluide et la phase dispersée doivent être traités avec une attention particulière, car l'information doit être transférée entre les particules ponctuelles et le maillage eulérien du fluide. De nombreux travaux récents sur le sujet proposent des stratégies de régularisation pour éviter ce problème numérique (Capecelatro and Desjardins 2013; Zamansky, Coletti, Massot, and Mani 2014; Poustis, Senoner, Zuzio, and Villedieu 2019). L'implémentation numérique du couplage inverse est plus simple pour les simulations eulériennes puisque les deux phases partagent le même cadre. Cependant, elles ne considèrent qu'un couplage inverse global, à l'échelle de la maille résolue. L'impact de particules isolées n'est pas bien reproduit, alors que ces événements extrêmes peuvent être critiques, comme dans l'exemple d'une gouttelette de carburant évaporée. Dans ce cas, la nécessité d'un couplage inverse local est préférentiellement traitée par une approche lagrangienne : (Doisneau 2013).

En pratique, pour la plupart des configurations industrielles, une approche lagrangienne point-particule est utilisée car elle permet une modélisation fidèle d'une phase polydispersée et utilise des schémas numériques simples qui n'introduisent pas de diffusion numérique, contrairement aux méthodes eulériennes. Néanmoins, certaines méthodes de moments ont été développées ces dernières années (Kaufmann et al. 2008; Laurent et al. 2012; Masi et al. 2014; Sabat 2016;

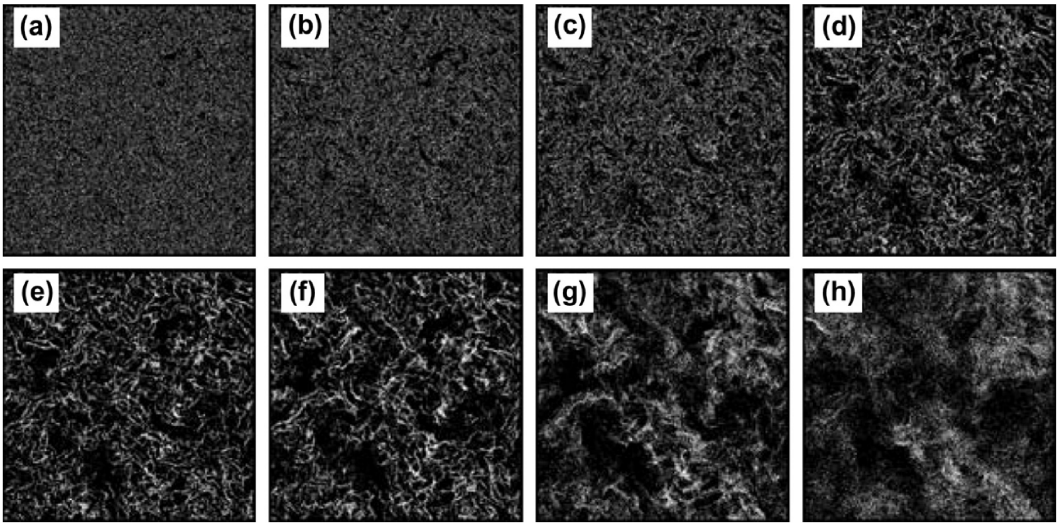

Figure 6. Distribution spatiale des particules à l'intérieur d'une couche mince pour huit nombres de Stokes différents. (a) St = 0,05, (b) 0,1, (c) 0,2, (d) 0,5, (e) 1, (f) 2, (g) 5 et (h) 10. Simulation tirée de Yoshimoto and Goto (2007).

Sabat et al. 2019) dans le but de reproduire le plus fidèlement possible la dynamique de la phase dispersée. Par exemple, dans les réacteurs à lit fluidisé, les approches de modélisation Euler-Euler sont privilégiées en raison du nombre élevé de particules impliquées (Neau, Pigou, Fede, Ansart, Baudry, Mérigoux, Laviéville, Fournier, Renon, and Simonin 2020). Cependant, elles ont rarement été appliquées aux configurations industrielles pour les applications de combustion, et les simulations lagrangiennes restent les simulations de référence. Pourtant, les avantages des simulations lagrangiennes doivent être nuancés car ils ne s'appliquent qu'aux phases dispersées. Afin de décrire un spray d'injection complet, les méthodes lagrangiennes, lorsqu'elles sont utilisées, doivent être couplées à un modèle eulérien pour les écoulements à phases séparées : (Drui 2017; Cordesse 2020; Di Battista 2021; Loison 2024).

En plus de ces questions physiques, nous devons également rappeler que dans un contexte industriel, il est inenvisageable de résoudre toutes les échelles de la phase turbulente, et des simulations d'ordre réduit sont donc utilisées. Il est alors essentiel de modéliser l'effet des échelles non résolues de la sous-maille sur la dynamique des particules. De plus, avec le couplage inverse, il est également nécessaire d'intégrer la rétroaction des particules sur ces mêmes échelles de sous-maille. Dans ce qui suit, nous énonçons les défis de modélisation des approches point-particule avec une turbulence d'ordre réduit comme une première étape vers la réduction dimensionnelle de la phase dispersée, qui peut éventuellement conduire à des méthodes Euler-Euler réduites.

3 Défis liés à la modélisation point-particule dans une simulation de turbulence d'ordre réduit

La dynamique de la phase dispersée est intrinsèquement liée à l'interaction entre les particules et la turbulence à l'échelle de la particule. Cependant, les opérations de réduction (moyenne ou filtre) empêchent les particules d'interagir avec les structures fluides non résolues. Dans certaines applications, les échelles non résolues de la vitesse du fluide ont un effet significatif sur le mou-

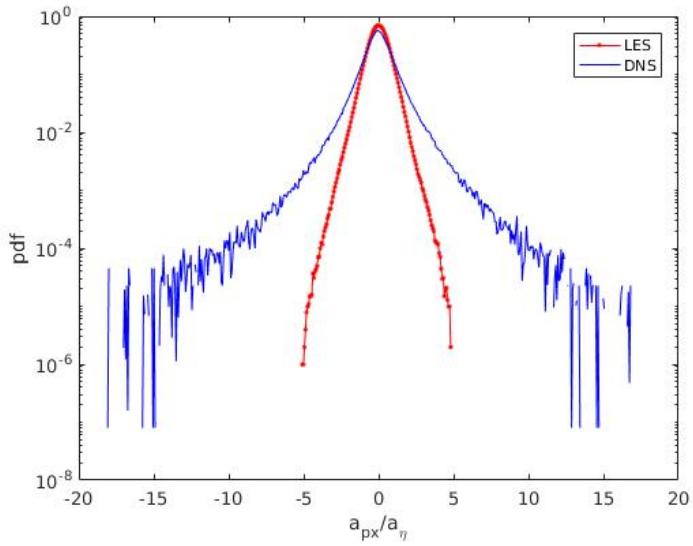

Figure 7. Fonction de densité de probabilité (Probability Density Function : PDF) de l'accélération des particules fluides dans un écoulement turbulent résolu avec un maillage DNS de 1024^3 (ligne bleue) et un maillage LES de 64^3 (ligne rouge), avec $Re_\lambda = 200$. Figure tirée de Zhang (2019).

vement des particules. Dans ce cas, deux modèles de sous-filtre doivent être considérés, l'un pour les équations régissant le fluide, l'autre pour les équations du mouvement des particules.
Les principaux défis consistent à reproduire les statistiques correctes de la phase dispersée (telles que l'énergie cinétique des particules ou l'intermittence), la concentration préférentielle des particules, et à modéliser correctement les termes de couplage inverse.

3.1 Statistiques intermittentes

Les statistiques de la phase dispersée telles que la vitesse, l'accélération et la dispersion des particules sont modifiées par la réduction de la phase porteuse, en particulier lorsqu'une partie importante de l'énergie cinétique de la turbulence est supprimée par la réduction (Fede and Simonin 2006). Des efforts de modélisation ont été fournis pour reproduire le comportement non-gaussien de l'accélération des particules observé dans les expériences et la simulation numérique directe (Bini and Jones 2007).

Plus précisément, la première lacune identifiée dans les simulations d'ordre réduit est la perte du phénomène d'intermittence, inhérent à la nature turbulente du fluide, correspondant à de violentes fluctuations du champ de dissipation de l'écoulement. Un exemple de ce phénomène est observé dans la Fig. 7 avec les statistiques non-gaussiennes de l'accélération du fluide dans un champ turbulent résolu par DNS. Avec une approche d'ordre réduit, les queues de distribution sont beaucoup plus faibles, et les événements extrêmes liés à une forte accélération des particules ne se produisent plus. Pourtant, si l'accélération (et donc les forces sous-jacentes qui s'appliquent sur les particules) manque de reproduire les événements extrêmes, alors les phénomènes de dispersion, par exemple, ne peuvent être simulés, même si les valeurs moyennes sont correctes. D'un point de vue plus général, cette méthode est également importante pour les accumulations de particules, l'évaporation, la combustion et tous les phénomènes se déroulant à petite échelle.

De nombreuses études sur l'analyse des données d'intermittence dans la turbulence révèlent la nature multifractale de la dissipation, et des modèles ont été développés pour tenter de la reproduire (Pope and Chen 1990; Borgas 1993; Frisch 1995; Sreenivasan and Antonia 1997). Cependant, tous les modèles à statistiques non gaussiennes ne sont pas nécessairement intermittents et une caractérisation rigoureuse doit être établie. Le chaos gaussien multiplicatif (Gaussian Multiplicative Chaos : GMC) (Kahane 1985; Robert and Vargas 2010) fournit un cadre approprié pour les processus stochastiques intermittents, car il correspond à un modèle de cascade continue pour la dissipation conforme à la théorie de Kolmogorov (1962). Quelques modèles basés sur le GMC ont été développés (Chevillard 2017; Schmitt and Marsan 2001; Pereira, Moriconi, and Chevillard 2018) mais leur analyse mathématique et leur implémentation numérique ne sont pas simples.

3.2 Ségrégation

La perte d'information due à la simulation d'ordre réduit de la phase porteuse a un impact sur la dynamique des particules puisqu'elle modifie les petites échelles et donc l'interaction des particules inertielles avec celles-ci.

Fede and Simonin (2006) ont constaté que les taux d'accumulation et de collision des particules sont considérablement influencés lorsque le temps de relaxation des particules est inférieur aux échelles de temps caractéristiques de la simulation d'ordre réduit. Pozorski and Apte (2009) ont également étudié l'effet des champs filtrés sur la ségrégation des particules et ont observé des changements significatifs dans la structure de la phase dispersée. Si les modèles stochastiques diffusifs ne sont pas capables de reproduire des structures cohérentes de sous-maille, une autre stratégie est alors possible. Les modèles structurels visent à reconstruire les échelles de sous-maille de l'écoulement. Parmi eux, on trouve les modèles de déconvolution approximative, l'interpolation fractale ou les simulations cinématiques. Cependant, ces approches ne réussissent pas entièrement à retrouver les schémas de concentration préférentielle d'une DNS (Cernick, Tullis, and Lightstone 2015) (voir Sec. 2.3).

3.3 Couplage inverse

Les transferts d'énergie entre les deux phases aux échelles résolues et non résolues doivent être correctement reproduits dans les ROS. Ceci nécessite une compréhension des échelles d'interaction entre les deux phases, ainsi que des mécanismes de couplage, ce qui n'est pas encore complètement établi dans la littérature, même avec des études DNS (Squires and Eaton 1990; Elghobashi 1994; Squires and Eaton 1994; Boivin et al. 1998; Ferrante and Elghobashi 2003; Abdelsamie and Lee 2012).

A notre connaissance, peu de recherches ont été menées sur le couplage inverse dans les simulations d'ordre réduit avec l'approche point-particule. Boivin, Simonin, and Squires (2000) ont réalisé des LES d'écoulements gaz-solide dans une turbulence homogène isotrope forcée avec un couplage inverse. Tant que le temps de relaxation des particules reste supérieur à l'échelle de temps caractéristique de la turbulence à l'échelle de la sous-maille, certains modèles LES (modèles mixtes) sont capables de capturer le flux d'énergie local entre les mouvements résolus et non résolus. Cependant, les applications avec des particules à faible inertie sont fréquentes et plus délicates en raison de la concentration préférentielle des particules, et nécessitent également des

efforts de modélisation dans un contexte de couplage inverse.

Comme première étape vers des modèles à couplage inverse, le formalisme mésoscopique eulérien étendu introduit par Mercier (2020) étudie les conséquences du couplage inverse sur la description statistique des écoulements turbulents chargés de particules, et il a été identifié que des statistiques conditionnées à grande échelle doivent être utilisées dans ce contexte. Même si ce travail a clarifié certaines conditions pour permettre une description statistique avec LES, un modèle entièrement cohérent reste à construire.

4 La contribution de la thèse

L'objectif de cette thèse est d'identifier et de caractériser les phénomènes physiques négligés par les modèles d'ordre réduit qui peuvent altérer la dynamique des particules et de proposer des modèles de sous-maille de particules appropriés.
Les nouveaux éléments que nous apportons à ces questions sont obtenus par l'analyse des DNS, qui nous permettent de comprendre les mécanismes impliqués dans l'intermittence, la ségrégation et le transfert de quantité de mouvement. A partir de ces analyses physiques, nous sommes en mesure de développer des modèles mathématiquement cohérents, qui couplés avec les ROS, permettent d'obtenir des statistiques de type DNS tout en gardant la même efficacité de calcul, voire en l'améliorant. Le cas test réalisé est une turbulence homogène isotrope 3D qui est un cas académique canonique.

Dans cette thèse, les contributions sont de trois types :

- Nous établissons une caractérisation de l'intermittence pour les écoulements monophasiques, cohérente à la fois avec les théories de la turbulence et les définitions mathématiques. Nous proposons une méthode originale pour construire de tels processus de manière générique et élégante, basée sur une somme infinie de processus Ornstein-Uhlenbeck. Ce formalisme permet non seulement d'unifier l'écriture des différents processus existants, mais aussi d'en développer un nouveau, plus versatile et plus efficace en temps de calcul grâce à la simplicité de simulation des processus Ornstein-Uhlenbeck.
- Nous proposons une nouvelle stratégie, dans l'esprit de la modélisation cinématique de la turbulence, pour laquelle nous mettons en évidence les limites des modèles actuels. Des champs de vitesse aléatoires, corrélés spatialement et temporellement, sont générés à l'aide d'ondelettes à divergence nulle. Le modèle cinématique basé sur les ondelettes est d'abord validé en 2D et 3D en utilisant les statistiques de la turbulence. Ensuite, les statistiques de la phase dispersée sont étudiées et nous nous concentrons sur la concentration préférentielle des particules. Les résultats sont comparés aux simulations DNS et aux simulations cinématiques classiques de la littérature.
- Nous nous intéressons à l'impact des particules sur un écoulement turbulent (couplage inverse), à partir de simulations numériques directes, afin de mieux comprendre et caractériser ces interactions. Nous mettons en évidence l'importance de la densité moyenne du nombre de particules à travers une analyse dimensionnelle. Nous étudions différents outils pour mesurer l'hétérogénéité de la phase dispersée et donnons de nouvelles perspectives sur ce phénomène. La méthodologie mise en œuvre a également l'avantage de constituer un outil de comparaison des études de la littérature, et permet d'unifier leurs résultats. Les résultats

nous permettent d'étendre le modèle cinématique à des cadres de couplage inverse avec différents niveaux de couplage.

Cette thèse fournit de nouvelles perspectives sur les interactions entre les particules et les écoulements turbulents. En effectuant des analyses approfondies, nous proposons des modèles originaux pour enrichir les ROS, ouvrant ainsi la voie à des simulations couplées bidirectionnelles précises.

Publications et conférences

Ces contributions ont été publiées dans quatre articles et actes de conférences, ainsi que dans deux articles en préparation :

- Impact of particle field heterogeneity on the dynamics of turbulent two-way coupled particulate flows (Letournel, Laurent, Massot, and Vié 2019), *10th International Conference on Multiphase Flow, ICMF 2019*.
- Modulation of homogeneous and isotropic turbulence by sub-Kolmogorov particles: Impact of particle field heterogeneity (Letournel, Laurent, Massot, and Vié 2020), *International Journal of Multiphase Flow*.
- Reproducing segregation and particle dynamics in Large Eddy Simulation of particle-laden flows (Letournel, Laurent, Massot, and Vié 2021), *International Conference on Liquid Atomization and Spray Systems (ICLASS)*.
- Revisiting the framework for intermittency in Lagrangian stochastic models for turbulent flows: a way to an original and versatile numerical approach (Letournel, Goudenège, Zamansky, Vié, and Massot 2021), *Physical Review E*.
- A new mathematical framework for the construction of stochastic processes with the ability to reproduce intermittency in turbulent flows (Goudenège, Letournel, and Richard 2022), *in preparation*.
- Wavelet-based kinematic simulation of particle-laden turbulent flows (Letournel, Massot, and Vié 2022), *in preparation*.

En outre, les résultats de ce travail ont été présentés dans plusieurs conférences et séminaires internationaux, dont l'orateur est souligné dans ce qui suit :

- On the accurate prediction of preferential concentration in Large Eddy Simulation of particle-laden flow (Letournel, Laurent, Massot, Vié), *French conference INCA (Advanced Combustion Initiative)*, April 7-8 2021.
- Reproducing segregation and particle dynamics in Large Eddy Simulation of particle-laden flows (Letournel, Laurent, Massot, Vié), *invited to BICTAM-CISM Symposium on Dispersed Multiphase Flows : from Measuring to Modeling*, March 2-5 2021.
- Intermittency in Lagrangian stochastic models for turbulent flows : genuine characterization and design of a versatile numerical approach (Letournel, Goudenège, Zamansky, Vié, Massot), *14th World Congress on Computational Mechanics, ECCOMAS Congress*, January 11-15 2021.

5 Plan du manuscrit

- La partie I traite des écoulements turbulents, des aspects physiques à la modélisation et à la simulation. En particulier, le Chap. 1 introduit les notions fondamentales à l'étude de la turbulence à travers les outils statistiques, les quantités caractéristiques et les principales

théories liées à la turbulence. Le chapitre 2 présente les différents modèles de turbulence, et les techniques de simulation numérique associées. Les modèles haute-fidélité et d'ordre réduit sont présentés et discutés. Le cadre numérique de cette thèse est également introduit.

- Part II est consacrée plus spécifiquement à l'étude de l'intermittence dans les écoulements turbulents. Le chapitre 3 propose une classification des modèles stochastiques existants pour les particules fluides selon le niveau de modélisation, le type d'équation stochastique et l'adéquation de chaque modèle avec les théories classiques de la turbulence. Des propriétés spécifiques à l'intermittence du champ de dissipation sont mises en évidence et permettent d'établir une liste d'exigences pour l'évaluation des modèles existants ou le développement de nouveaux modèles. Le chapitre 4 fournit un cadre mathématique nouveau et original pour les processus stochastiques intermittents s'appuyant sur le chaos gaussien multiplicatif. Sur la base de ce cadre mathématique, nous introduisons au Chap. 5 un nouveau modèle stochastique qui permet de reproduire les statistiques de dissipation. Par rapport aux modèles existants, son implémentation numérique est simple et efficace et sa versatilité le rend particulièrement intéressant dans le cadre des LES.
- Part III traite des écoulements diphasiques dispersés sans couplage inverse. Le chapitre 6 présente la physique d'une phase dispersée sous un ensemble d'hypothèses permettant la formulation d'un modèle lagrangien simplifié. Un formalisme eulérien est introduit pour étudier le comportement collectif des particules (par exemple la ségrégation). Le chapitre 7 passe en revue les principaux modèles et simulations de la phase dispersée associés aux stratégies de réduction de la dimensionnalité. Dans le contexte de la turbulence sous-résolue, la nécessité de développer des modèles de particules se fait sentir et les stratégies existantes sont discutées.
- La partie IV de cette thèse se concentre sur les stratégies de modélisation des particules à l'échelle non-résolue. Le chapitre 8 passe en revue les modèles stochastiques existants pour les particules, et un nouveau modèle intermittent adapté aux particules inertielles est proposé. Le chapitre 9 introduit une autre stratégie, la simulation cinématique, classiquement basée sur une représentation de Fourier d'un écoulement synthétique. Nous proposons un nouveau type de simulation cinématique, basé sur des ondelettes à divergence nulle, qui préserve les avantages de la simulation cinématique classique, à savoir une représentation analytique, une structure spatiale cohérente, et la reproduction d'un spectre d'énergie donné, tout en apportant des améliorations : évolution temporelle du champ et localité de l'information. La simulation cinématique à base d'ondelettes est validée pour la dynamique des phases dispersées, et notamment pour la concentration préférentielle des particules dans le Chap. 10. Les améliorations et perspectives futures concernant l'intermittence et le coût numérique de la simulation sont discutées au Chap. 11.
- Enfin, la partie V ouvre la voie à la simulation couplée inverse. Le chapitre 12 présente les principaux défis liés au traitement du couplage inverse dans les approches Euler-Lagrange, et le chapitre 13 donne une étude complète de l'influence des paramètres adimensionné sur le transfert d'énergie entre les deux phases. Le chapitre 14 donne quelques indications pour adapter les modèles développés dans cette thèse au couplage inverse ou pour développer de nouvelles stratégies basées sur des modèles unifiés.

Introduction (english)

6 Context

6.1 Turbulent disperse two-phase flows in environmental and industrial contexts

Turbulent disperse two-phase flows are at the heart of various natural phenomena such as clouds, in which droplets condensation is controlled by turbulence, the formation of planets and protoplanetary disks by the aggregation of dust particles (see Fig. 8(a)), or ocean sedimentation. They are involved in a large number of environmental considerations, in particular through the transport of particles in the atmosphere. Such particles can have different origins and properties, for example fire smoke, volcanic ashes (see Fig. 8(b)) or various pollutants (fine particles, soot,...).

They are also a key element in many industrial applications. In particular, the efficiency of a lot of energy production or conversion processes is governed by the dynamics of multiphase flows. The most iconic example is the fuel combustion in thermal engines for which significant research efforts are being made to improve their energy efficiency in order to reduce the pollutant emissions associated with this activity. The evolution of the fuel spray resulting from the atomization constitutes a typical example of disperse phase flows and an essential element of the operation of the engines, since these droplets, by evaporating, produce the fuel/oxidant mixture which will supply the combustion. A detailed understanding of these complex phenomena combined with cost-efficient models is thus essential to help design the future generations of thermal engines,

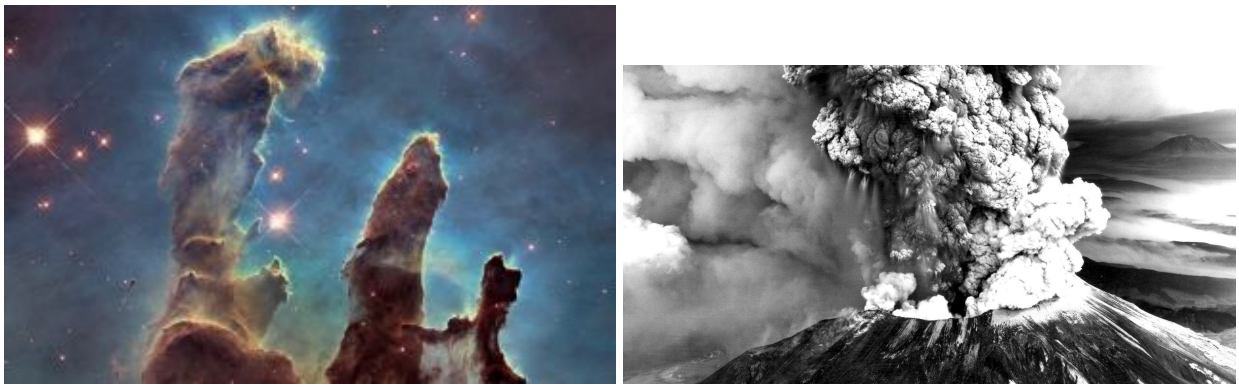

(a) (b)

Figure 8. (a) Interstellar gas and dust in the Eagle Nebula of about 4 light-year in length, at some 7,000 light years from Earth. NASA, ESA. (b) Photograph of the eruption of Mount St. Helens, May 18 1980

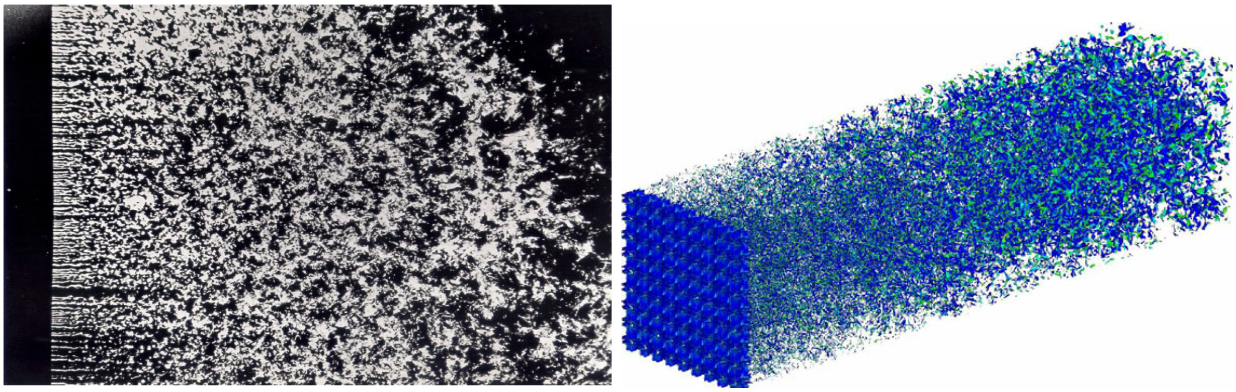

(a) (b)

Figure 9. Homogeneous turbulence behind a grid. (a) Photograph from Van Dyke, Album of Fluid Motion n°153 ; (b) Simulation from Vassilicos and Laizet (2010).

providing more efficient combustion and cleaner means of transportation.

The diversity and importance of the areas where disperse two-phase flows are involved make their modeling a topic of great interest for both the scientific and industrial communities. Despite being an intensive field of study for decades, many scientific questions still need to be addressed to complete our understanding of these phenomena. The complexity of the problem studied first arises from the nature of the carrier flows, which are mostly turbulent, as this improves the mixing between the two phases in energetic systems. Turbulence, by nature unsteady and multi-scale, is already a challenge in single-phase flows, and the coupling with the disperse phase introduces additional difficulties to understand and efficiently model these phenomena.

6.2 Experiments and simulations

The ambition of disperse two-phase flow research is to accurately predict the evolution and behavior of such flows in a given configuration, e.g., a combustion chamber in a thermal engine. Experimental studies and bench testing have long remained the main approach to assessing, analyzing, understanding, and designing systems involving two-phase flows. If they are still considered as a reference, they also have some severe limitations. Indeed, unlike numerical simulations, experimental studies do not provide the full knowledge of the system under study (some measures can be intrusive or very challenging to perform). Some configurations or environmental conditions can also be hard to reproduce, and experiments are generally time and resource-consuming, thus limiting the amount of data that can be generated to understand or design a system.

Numerical simulations are an ideal complement to experimental studies: from models, i.e. a set of equations, whose solutions reproduce as faithfully as possible the reality, predictions can be made on a system with reasonable cost and accuracy. Developed from theoretical and mathematical bases, models thus allow to reproduce experiments, test different configurations, and even explore physical mechanisms that are difficult to observe experimentally. In most cases, the resolution of the model equations requires numerical simulation. A comparison of experiment and simulation of homogeneous turbulence is given in Fig. 9. Thanks to the development of both reliable models and massive computing architectures, the interest in numerical simulations of disperse two-phase

turbulent flows has been growing rapidly for academic and industrial purposes.

7 Numerical simulation of turbulent disperse two-phase flows

The modeling of such flows must tackle a twofold challenge: the description of the turbulence (the carrier phase) and the description of the disperse phase. In both cases, these are multi-scale problems that require reduced-order models: for liquid fuel injection system, the diameter of particle is typically $0.1 - 10$ μm whereas the dimensions of the combustion chamber is about 10 cm. The level of description defines the details of the flow field that is resolved in both phases.

We can see two motivations for the use of reduced-order models. The first one arises from the high dimensionality of the problem, limiting the use of high fidelity simulations to a limited number of particles or poorly developed turbulence. The reduced-order simulations (ROS) help improving computing time. This reduction comes at a cost: the loss of information at the smallest scales can only be compensated by an additional modeling effort. The second motivation is related to the chaotic nature of such complex flows. An insignificant change in the initial conditions of one of the two phases can lead to considerable long-term perturbations. The resolution of a given flow can therefore be questioned since the knowledge of the initial flow or the positions and velocities of the particles will never be perfect, not to mention the modifications introduced by the different models and assumptions. It is thus pointless to obtain a detailed description of the two phases but more relevant to describe them with a statistical approach.

We present the reduction strategies first regarding the turbulent carrier phase alone, then those related to the description of the disperse phase. Finally, we specify the reasons underlying the choice in this thesis for the coupling of the two phases.

7.1 Numerical simulation of turbulence

Single-phase turbulent flows are highly multi-scales problems. The range between the scales of energy production and dissipation is given by the Reynolds number, which characterizes turbulence. This separation of scale drives the numerical cost since the resolution of the smallest scales on large domains can then explode for large Reynolds numbers. Different resolution strategies exist, as illustrated in the case of a turbulent jet in Fig. 10.

Direct numerical simulation
The most accurate description of turbulence is given by the resolution of the entire flow, using direct numerical simulation (DNS). The DNS snapshot in Fig. 10 is indeed very detailed, it resolves the finest scales of the flow. However, the cost of these methods is unreachable in an industrial framework: typical Reynolds number in a combustion chamber is about $10^5 - 10^6$. Hence, DNS are limited to small domains and rely on massively parallel computing architectures.

Reduced-order simulation
In order to still enable a resolution of the problem, although it implies losing information on the details of the flow, reduced-order models are derived. Reduced-order simulations (ROS) allow for predictive and CPU-efficient simulations on industrial configurations. However, they can only capture large-scale dynamics, which are fully resolved, and discard the smallest scales, which require

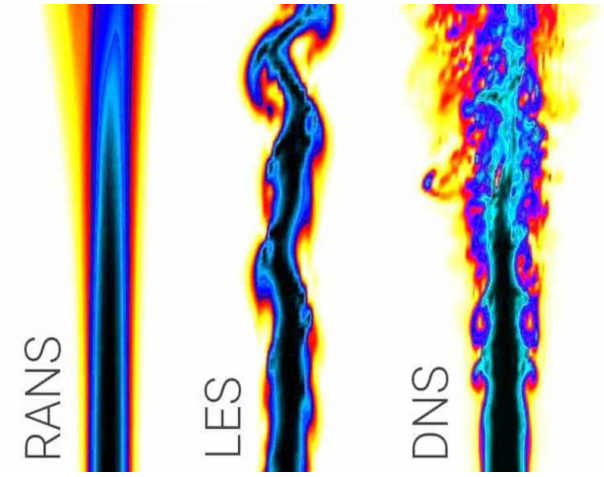

Figure 10. Computational fluid dynamics modeling of a turbulent jet using different approaches (Italian Agency For New Energy Technologies 2006).

modeling to be accounted for. Two main strategies are commonly used for deriving such models. An averaging operation can be applied to the Navier-Stokes equations to obtain the mean equations of fluid flows called Reynolds Averaged Navier-Stokes (RANS) equations. This is the most economical and widespread approach in industrial applications today. However, it may be required for some applications to solve part of the turbulent scales rather than model them. The large eddy simulations (LES) consists in filtering the Navier-Stokes equations, to solve only the large scales of the turbulence. Figure 10 shows that RANS method provides an averaged, symmetrical image of the jet, highly diffuse. On the other hand, the LES simulation is an intermediary, it reproduces the large unsteady scales of the jet but the smallest ones are filtered.

Although reduced-order models provide a reasonable level of prediction of the purely gaseous flow, their fidelity must be assessed for multiphase configurations in which the disperse phase interacts with the turbulent structures.

7.2 Numerical simulation of the disperse phase

Different approaches exist in the literature to describe the disperse phase, and particular attention must be paid to the choice of modeling in order to reproduce the correct physics at minimal cost for industrial applications. In this section, to give a global picture, we consider non-reduced simulations of turbulence: we assume the carrier phase is fully resolved to focus on particle modeling.

7.2.1 Deterministic Lagrangian approaches

For liquid droplets, the exact resolution of the whole disperse phase would require the solution of the flow inside each droplet and at any point of the interface with the carrier phase. Such a simulation therefore corresponds to a direct numerical simulation for each particle (Boniou 2021). Under some assumptions, or for solid particles, the problem is simplified by imposing boundary conditions on the surface of each particle (Xu and Subramaniam 2010), for instance the particle is assimilated to a sphere. This “microscopic” level is illustrated in Fig. 11, in the top left figure, where microscopic relates to the framework of kinetic theory of gases (Ferziger, Kaper, and Kaper

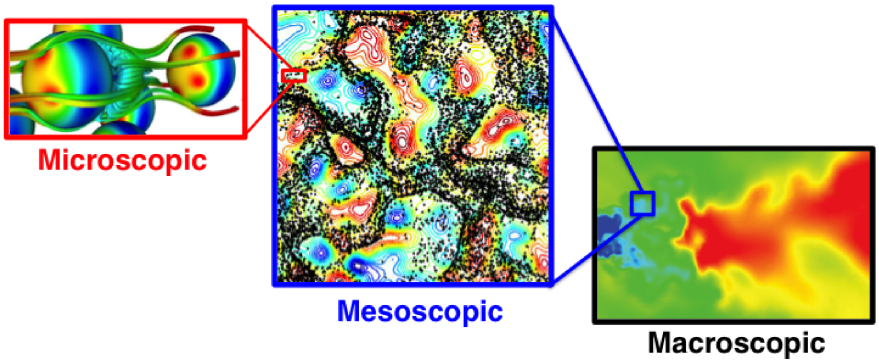

Figure 11. Different levels of description of the disperse phase from microscopic (left), mesoscopic (center) to macroscopic (right).

1972).

In most industrial applications, a Lagrangian point-particle assumption is considered: this is the Discrete Particle Simulation (DPS) (Riley and Patterson Jr 1974). The particles are tracked individually, and their interaction with the carrier phase is modeled through forces such as the Stokes drag law applied at the center of mass of the particle. In such modeling, the volume occupied by the disperse phase is negligible compared to the one occupied by the carrier phase.

Lagrangian simulation is relatively intuitive and straightforward to implement numerically (solving an ordinary differential equation for each particle), although it requires special attention in parallel computations since they demand the use of a computational load balancing (Marta 2009). That is why it is the most widespread method in the literature to study the behavior of inertial particles (Squires and Eaton 1991; Elghobashi and Truesdell 1992) and in combustion applications (for instance Mesquita, Vié, Zimmer, and Ducruix (2021)).

The accuracy of these methods depends directly on the modeling of these forces but also on the evaluation of the undisturbed fluid velocity at the position of the particle (Horwitz and Mani 2016; Ireland and Desjardins 2017; Poustis, Senoner, Zuzio, and Villedieu 2019). Moreover, only one realization of the disperse phase is obtained in each simulation. It is then necessary to perform several Lagrangian simulations to obtain global statistical variables, which becomes excessively expensive. One can instead rely on a kinetic (or mesoscopic) description of the disperse phase, in the spirit of the Boltzmann equation obtained in the Boltzmann-Grad limit of the Liouville equation.

7.2.2 Kinetic-based methods

Mesoscopic approaches provide statistics of the disperse phase by deriving the number density function (NDF) of the disperse phase. This function gives the probability of finding a particle in a given state of the phase space (which is composed of a set of internal variables such as velocity, particle size, temperature etc.). The evolution of the NDF is governed by the Williams-Boltzmann equation (WBE). Figure 11 shows one realization of the mesoscopic approach, with an initial uniform particle density, obtained with Lagrangian tracking.

Two strategies for solving this WBE can be considered: the first consists in integrating the WBE in the phase space in order to reduce the dimensionality of the problem and thus transport moments: this is further described in next section. The second strategy is based on Lagrangian methods:

- The direct Monte-Carlo simulation method (Bird 1994) approximates the NDF by a sample of discrete statistical particles representing a particle. Therefore, a large number of numerical particles is needed, each of them supposed to represent a fraction of the physical particle. Those particles are tracked following the same system of ordinary differential equations (ODE) than in DPS and the method thus has the same drawbacks of slow statistical convergence.
- The stochastic parcel method consists on the contrary in representing a group of particles with identical properties by a single numerical particle, called parcel (O'Rourke 1981). By decreasing the number of particles to follow, this method obviously reduces the computational cost, but it remains proportional to the number of real particles.

Both stochastic Lagrangian methods presented above face difficulties in a two-way coupling context: indeed, the particles are not represented individually and the local effect they may have on the turbulent flow cannot be faithfully reproduced.

7.2.3 Eulerian moment methods

By integrating the WBE in the phase space against a set of polynomials of limited degree, we obtain quantities, called moments, which can be related to macroscopic quantities such as the concentration of particles or the particle velocity field, as given by the bottom right snapshot in Fig. 11. In this approach particles are not described individually, but through Eulerian fields which satisfy partial differential equations.

This method is intrinsically statistically convergent, and the computation time does not depend on the number of particles. The Eulerian framework simplifies the coupling with the carrier phase since the exchange terms are then written in the same formalism. Furthermore, this method can be efficiently implemented in parallel computation since it is similar to usual computational fluid dynamics tools.

On the other hand, particular attention must be paid to the modeling of dispersion in velocity or size of the particles, and the resulting fields depend on the closure terms considered. Moreover, adequate numerical methods must be developed because this approach can lead to hypercompressive fields (De Chaisemartin 2009) and singularities.

7.3 Some key physics of disperse phase flows and their modeling

Among the critical elements involved in the modeling of disperse two-phase flows, the reproduction of particle dynamics will be the focus of this thesis, and in particular intermittent statistics, the preferential concentration of particles, and the two-way coupling:

- A Lagrangian simulation can faithfully reproduce the typical dynamics of a two-phase flow, and in particular its rare events. Figure 12 shows the simulation of a spray burner with evaporation of droplets. The passage of a droplet through the flame can considerably modify its front and brings a local perturbation which cannot be considered in the case of Eulerian simulations based on global averages. Such extreme events can be generated by the inter-

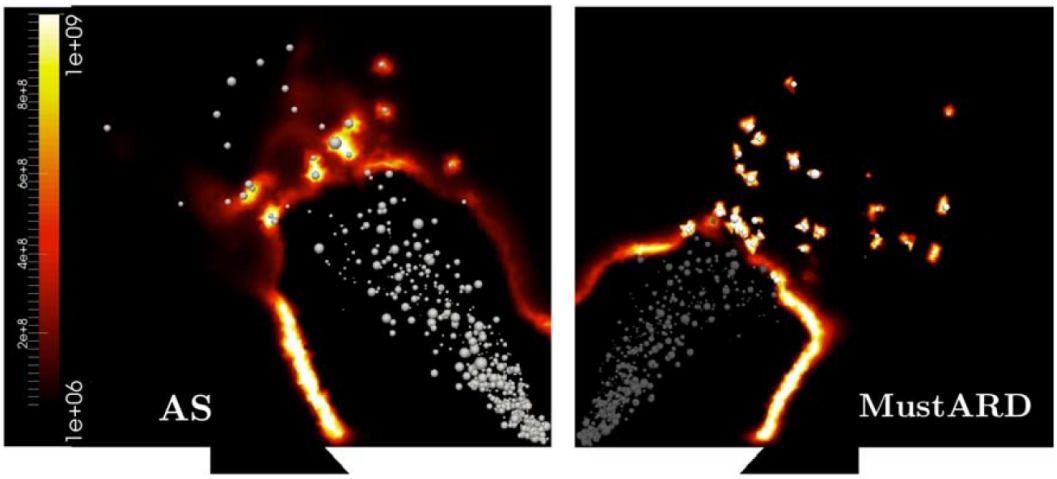

Figure 12. Instantaneous heat release, with over-imposition of droplets for two different Lagrangian simulations of a spray burner (Paulhiac 2015).

mittency of the turbulent phase, whose velocity fluctuations can vary brutally and strongly.

- The preferential concentration of particles corresponds to an accumulation of particles in certain regions of the flow, caused by particles interaction with turbulent eddies. This is illustrated in Fig. 13, where snapshots of particles are given for different particle Stokes numbers, which characterizes particle inertia. Depending on this dimensionless parameter, the disperse phase can be highly heterogeneous. Such concentration inhomogeneities are essential for the dynamics of the system, for example particle clustering of heating particles in a dilute suspension which results in more intense local heating (Zamansky, Coletti, Massot, and Mani 2016); and for combustion applications, segregation can generate hot spots and deformations of the flame front. This phenomenon is well reproduced in deterministic Lagrangian simulations, whereas a high resolution is required to observe the correct level of segregation with Eulerian methods (Sabat 2016).

- The influence of the disperse phase on the carrier phase must also be considered, in particular when the mass loading is important (Elghobashi 1991). For example, self-sustained turbulent structures have been observed in a wide range of living fluids such as bacterial environments or oceanic surface waters, due to small active organisms (bacteria, plankton) generating small-scale chaotic motion (Dunkel, Heidenreich, Drescher, Wensink, Bär, and Goldstein 2013; Abraham 1998). This is known as two-way coupling and additional source terms of mass, momentum and energy must then be taken into account in the resolution of the turbulent phase. For Lagrangian approaches, the exchange terms between the fluid and the disperse phase must be treated carefully, as information must be transferred between the singular point particles and the Eulerian mesh of the fluid. Many recent works on the subject propose regularization strategies to avoid numerical problems (Capecelatro and Desjardins 2013; Zamansky, Coletti, Massot, and Mani 2014; Poustis, Senoner, Zuzio, and Villedieu 2019). The numerical implementation of two-way coupling is more straightforward for Eulerian simulations since the two phases share the same framework. However, they only consider a global reverse coupling, at the scale of the resolved mesh. The impact of isolated particles is not well reproduced, while these extreme events can be critical, such as the evaporated fuel from a droplet. In that case, the need for a local two-way coupling is

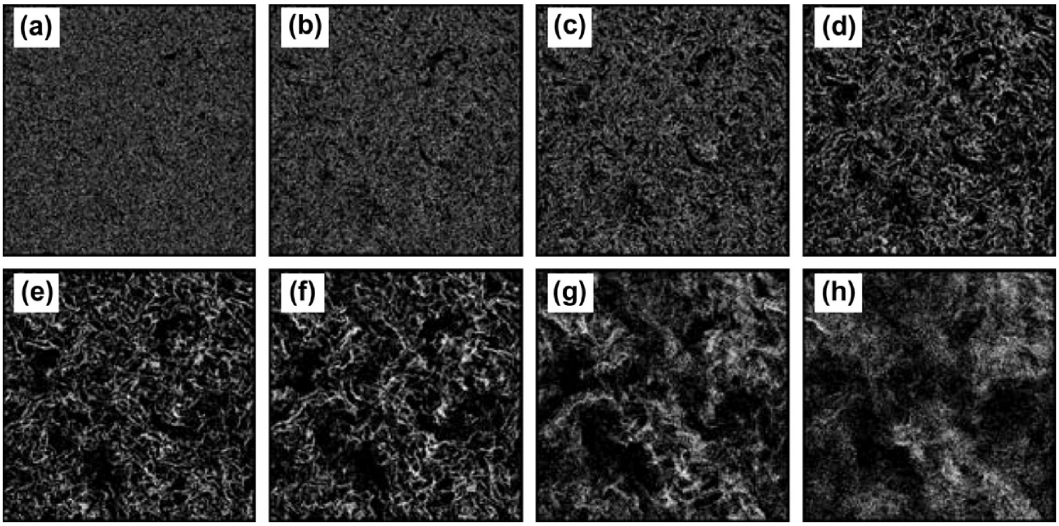

Figure 13. Spatial distribution of particles inside a thin layer for eight different Stokes numbers. (a) St = 0.05, (b) 0.1, (c) 0.2, (d) 0.5, (e) 1, (f) 2, (g) 5 and (h) 10. Simulation from Yoshimoto and Goto (2007).

preferentially addressed with a Lagrangian approach (Doisneau 2013).

In practice, for most industrial configurations, a Lagrangian point-particle approach is used since it allows faithful modeling of a polydisperse phase and uses simple numerical schemes that do not introduce numerical diffusion, as opposed to Eulerian methods. Nonetheless, some methods of moments have been developed in recent years (Kaufmann et al. 2008; Laurent et al. 2012; Masi et al. 2014; Sabat 2016; Sabat et al. 2019) with the aim of reproducing the dynamics of the disperse phase as faithfully as possible. For instance, in fluidized-bed reactors, Euler-Euler modeling approaches are preferred due to the high number of particles involved (Neau, Pigou, Fede, Ansart, Baudry, Mérigoux, Laviéville, Fournier, Renon, and Simonin 2020). However, they have rarely been applied to industrial configurations for combustion applications, and Lagrangian simulations are still the reference simulations. Still, the Lagrangian benefits have to be nuanced since it is only applicable to disperse phases. In order to describe a complete spray injection, Lagrangian methods, when they are used, have to be coupled with an Eulerian model for separated phase flows (Drui 2017; Cordesse 2020; Di Battista 2021; Loison 2024).

On top of these physical issues, we also must recall that in an industrial context, it is impracticable to solve all the scales of the turbulent phase, and reduced-order simulations are therefore used. It is then essential to model the effect of the unresolved scales on particle dynamics. Moreover, with two-way coupling, it is also necessary to integrate the feedback of the particles on these same scales. In the following, we state the modeling challenges of point-particle approaches with reduced-order turbulence as a first step towards the dimensional reduction of the disperse phase, which may eventually lead to reduced Euler-Euler methods.

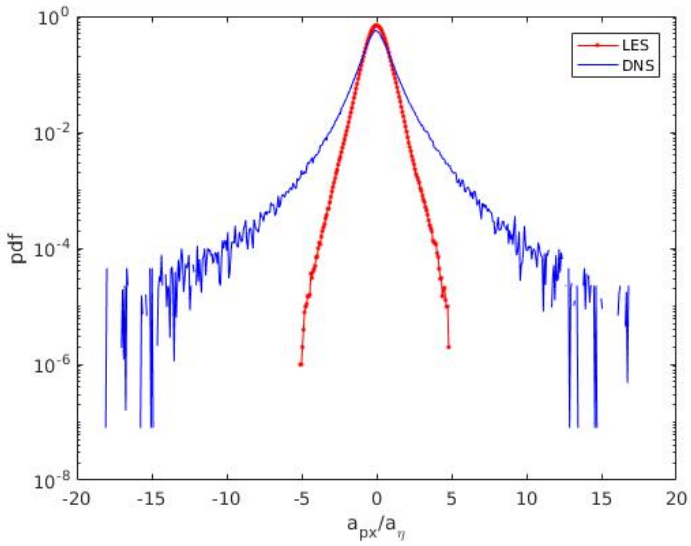

Figure 14. Probability density function (PDF) of fluid particle acceleration in a turbulent flow resolved with DNS mesh 1024^3 (blue line) and LES mesh 64^3 (red line), with $Re_\lambda = 200$. Figure from Zhang (2019).

8 Modeling challenges for point-particle with reduced-order turbulence simulation

The dynamics of the disperse phase is intrinsically bound to the interplay between the particles and the turbulence at the particle scale. However, averaging or filtering operations prevent particles from interacting with unresolved fluid structures. In some applications the unresolved scales of the fluid velocity have a significant effect on the particle motion. In this case, two sub-filter scale models must be considered, one for the equations governing the fluid, and another for the particle motion equations.

The main challenges are to retrieve the correct statistics of the disperse phase (such as particle kinetic energy or intermittency), particle preferential concentration, and to correctly model the two-way coupling terms.

8.1 Intermittent statistics

Statistics of the disperse phase such as velocity, acceleration, and dispersion of the particles are altered by the filtering of the carrier phase, in particular when a significant part of the kinetic energy of the turbulence is removed by the filter (Fede and Simonin 2006). Modeling efforts have been done to reproduce the far-from-Gaussian behavior of the particle acceleration observed in experiments and direct numerical simulation (Bini and Jones 2007).

More precisely, the first shortcoming identified in reduced-order simulations is the loss of the intermittency phenomenon, inherent to the turbulent nature of the fluid, corresponding to violent fluctuations of the flow dissipation field. An example of this phenomenon is observed in Fig. 14 with the highly non-Gaussian statistics of fluid acceleration in a DNS-resolved turbulent field.

With a reduced-order approach, the distribution tails are much lower, and extreme events related to high particle acceleration no longer occur. Yet, if the acceleration (and thus the underlying forces that apply on particles) misses the extreme events, then the dispersion phenomena, for example, cannot be reproduced, even if the average values are correct. On a broader view, it is also important for particles clusters, evaporation, combustion, and all phenomena taking place at small scales.

Numerous studies on data analysis of intermittency in turbulence reveal the multifractal nature of the dissipation, and models were developed in attempt to reproduce it (Pope and Chen 1990; Borgas 1993; Frisch 1995; Sreenivasan and Antonia 1997). However, not all models with non-Gaussian statistics are necessarily intermittent and a rigorous characterization must be established. The Gaussian multiplicative chaos (GMC) (Kahane 1985; Robert and Vargas 2010) provides an appropriate framework for intermittent stochastic processes, since it corresponds to a continuous cascade model for the dissipation consistent with the theory of Kolmogorov (1962). Few models based on the GMC were developed (Chevillard 2017; Schmitt and Marsan 2001; Pereira, Moriconi, and Chevillard 2018) but their mathematical analysis and numerical implementation are not straightforward.

8.2 Segregation

The loss of information due to the reduced-order simulation of the carrier phase has an impact on the dynamics of the particles since it modifies the small scales and hence the interaction of inertial particles with them.

Fede and Simonin (2006) found that particle accumulation and collision rates are significantly influenced when the particle relaxation time is smaller than characteristic time scales of the reduced-order simulation. Pozorski and Apte (2009) also studied the effect of filtered fields on particle segregation and observed significant changes in the disperse phase structure. If diffusive stochastic models are not able to reproduce coherent unresolved structures, another strategy is then possible. Structural models aim at reconstructing the unresolved scales of the flow. Among them are the approximate deconvolution models (ADM), the fractal interpolation or kinematic simulations (Murray, Lightstone, and Tullis 2016a). However, these approaches are not entirely successful in retrieving the preferential concentration patterns of a DNS (Cernick, Tullis, and Lightstone 2015), which is a primary concern in most applications (see Sec. 7.3).

8.3 Two-way coupling

Energy transfers between the two phases at resolved and unresolved scales must be correctly reproduced in ROS. This requires an understanding of the interaction scales between the two phases, as well as the coupling mechanisms, which is not yet fully established in the literature, even with DNS studies (Squires and Eaton 1990; Elghobashi 1994; Squires and Eaton 1994; Boivin et al. 1998; Ferrante and Elghobashi 2003; Abdelsamie and Lee 2012).

To our knowledge, little research has been conducted on the two-way coupling in reduced-order simulations with point-particle approach. Boivin, Simonin, and Squires (2000) performed LES of gas-solid flows in forced homogeneous isotropic turbulence with two-way coupling. As long as particle relaxation time remains larger than the characteristic time scale of the sub-grid scale

turbulence, some LES models (mixed-models) are able to capture the local energy flux between resolved and unresolved motions. However, applications with lower inertia particles are frequent and more challenging due to particle preferential concentration, and also require modeling efforts in two-way coupling context.

As a first step towards two-way coupled models, the extended mesoscopic Eulerian formalism (EMEF) introduced by Mercier (2020) investigates the consequence of two-way coupling on the statistical description of turbulent particle-laden flows, and it has been identified that large-scale conditioned statistics must be used in this context. Even if this work clarified some conditions to enable a statistical description with LES, a fully-consistent model is still to be built.

9 The thesis contribution

The objective of this thesis is to identify and characterize the physical phenomena neglected by the reduced-order models that can alter the dynamic of particles and to propose appropriate particle sub-filter scale (SFS) models.
The new elements we bring to these questions are obtained by analysis of DNS, which allow us to understand the mechanisms involved in intermittency, segregation, and transfer of momentum. From these physical analyses, we are able to develop mathematically consistent models, which coupled with the ROS, allow to obtain DNS-like statistics while keeping the same computational efficiency, or even improving it. The conducted test case is a 3D homogeneous isotropic turbulence (HIT) which is a canonical academic case.

In this thesis, the contributions are of three types:

- A characterization of intermittency for single-phase flows is established, consistent with both turbulence theories and mathematical definitions. We propose an original method to construct such processes in a generic and elegant way based on an infinite sum of Ornstein-Uhlenbeck processes. This formalism allows not only to unify the writing of the different existing processes, but also to develop a new one, more versatile and more efficient in computation time thanks to the simplicity of simulation of Ornstein-Uhlenbeck processes.
- We propose a new strategy, in the spirit of kinematic modeling of turbulence, for which we highlight the limits of the current models. Random velocity fields, spatially and temporally correlated, are generated using divergence-free wavelets. The wavelet-based KS is first validated in 2D and 3D using turbulence statistics. Then, the disperse phase statistics are investigated and we focus on particle preferential concentration. Results are compared with DNS and Fourier-based kinematic simulations.
- We are interested in the impact of particles on a turbulent flow (two-way coupling), from direct numerical simulations, in order to better understand and characterize these interactions. We highlight the importance of the average particle number density through a dimensional analysis. We investigate different tools for measuring the disperse phase heterogeneity and give new insights on this phenomenon. The methodology implemented also has the advantage of constituting a tool for comparison of the studies of the literature, and allows to unify their results. The results allow us to extend the kinematic model to two-way coupling frameworks with different levels of couplings.

This thesis provides new insights into the interactions between particles and turbulent flows. By carrying out in-depth analyses, we propose original models to enrich the ROS, paving the way for accurate two-way coupled simulations.

Publications and conferences

These contributions were published in four papers and conferences proceedings along with two articles in preparation:

- Impact of particle field heterogeneity on the dynamics of turbulent two-way coupled particulate flows (Letournel, Laurent, Massot, and Vié 2019), *10th International Conference on Multiphase Flow, ICMF 2019*.
- Modulation of homogeneous and isotropic turbulence by sub-Kolmogorov particles: Impact of particle field heterogeneity (Letournel, Laurent, Massot, and Vié 2020), *International Journal of Multiphase Flow*.
- Reproducing segregation and particle dynamics in Large Eddy Simulation of particle-laden flows (Letournel, Laurent, Massot, and Vié 2021), *International Conference on Liquid Atomization and Spray Systems (ICLASS)*.
- Revisiting the framework for intermittency in Lagrangian stochastic models for turbulent flows: a way to an original and versatile numerical approach (Letournel, Goudenège, Zamansky, Vié, and Massot 2021), *Physical Review E*.
- A new mathematical framework for the construction of stochastic processes with the ability to reproduce intermittency in turbulent flows (Goudenège, Letournel, and Richard 2022), *in preparation*.
- Wavelet-based kinematic simulation of particle-laden turbulent flows (Letournel, Massot, and Vié 2022), *in preparation*.

In addition, the results of this work were presented in several international conferences and seminars, where the presenter is underlined in the following:

- On the accurate prediction of preferential concentration in Large Eddy Simulation of particle-laden flow (Letournel, Laurent, Massot, Vié), *French conference INCA (Advanced Combustion Initiative)*, April 7-8 2021.
- Reproducing segregation and particle dynamics in Large Eddy Simulation of particle-laden flows (Letournel, Laurent, Massot, Vié), *invited to BICTAM-CISM Symposium on Dispersed Multiphase Flows : from Measuring to Modeling*, March 2-5 2021.
- Intermittency in Lagrangian stochastic models for turbulent flows : genuine characterization and design of a versatile numerical approach (Letournel, Goudenège, Zamansky, Vié, Massot), *14th World Congress on Computational Mechanics, ECCOMAS Congress*, January 11-15 2021.

10 Outline of the manuscript

- Part I deals with turbulent flows, from physical aspects to modeling and simulation. In particular, Chap. 1 introduces the fundamental notions to the study of turbulence through statistical tools, characteristic quantities and the main theories related to turbulence. Chapter 2 presents the different turbulent models, and the associated numerical simulation techniques. The high fidelity and reduced-order models are presented and discussed. The numerical framework of

this thesis is also introduced.

- Part II is devoted more specifically to the study of intermittency in turbulent flows. Chapter 3 proposes a classification of the existing stochastic models for fluid particles according to the level of modeling, the type of stochastic equation and the adequation of each model with classic turbulent theories. Properties specific to the intermittency of the dissipation field are highlighted and are used to establish a list of requirements for the evaluation of existing models or the development of new ones. Chapter 4 provides a new and original mathematical framework for intermittent stochastic processes relying on the Gaussian multiplicative chaos. Based on this mathematical framework, we introduce in Chap. 5 a new stochastic model which allows to reproduce the statistics of dissipation. Compared to existing models, its numerical implementation is simple and efficient and its versatility makes it particularly interesting in the LES framework.
- Part III deals with one-way coupled disperse two-phase flows. Chapter 6 presents the physics of a disperse phase under a set of assumptions allowing the formulation of a simplified Lagrangian model. An Eulerian formalism is introduced to study the collective behavior of particles (for example segregation). Chapter 7 reviews the main models and simulations of the disperse phase associated with dimensionality reduction strategies. In the context of under-resolved turbulence (ROS), the need to develop particle models arises and existing strategies are discussed.
- Part IV of this thesis is focuses on strategies for particle sub-filter scale modeling. Chap. 8 reviews existing stochastic models for particles, and a new intermittent model adapted to inertial particles is proposed. Chapter 9 introduces another strategy, the kinematic simulation, classically based on a Fourier representation of a synthetic flow. We propose a new type of kinematic simulation, based on divergence-free wavelets, which preserves the advantages of the classical kinematic simulation, i.e. an analytical representation, a coherent spatial structure, and the reproduction of a given energy spectrum, while bringing improvements: temporal evolution of the field and locality of the information. Wavelet-based KS is validated for the disperse phase dynamics, and especially for particle preferential concentration in Chap. 10. Future improvements and perspectives regarding the intermittency and the numerical cost of the wavelet-based KS are discussed in Chap. 11.
- Finally, Part V paves the way to two-way coupled simulation. Chapter 12 introduces the main challenges for handling two-way coupling in Euler-Lagrange approaches, and Chap. 13. gives a comprehensive study of the influence of the dimensionless parameters on the energy transfer between the two phases. Chapter 14 gives some guidelines for adapting the models developed in this thesis to the two-way framework or for developing new strategies based on unified models.

Part I

Turbulent flows

This part deals with turbulent flows, their main characteristics and their modeling. In particular, Chap. 1 presents the issues and difficulties related to the description of turbulence, which by its chaotic nature requires a statistical treatment. The notions of ensemble averages are defined and simplified under the assumption of homogeneous isotropic turbulence (HIT). One and two-point statistics of the velocity field are derived and provide information on the flow's characteristic lengths, times, and velocities. The main theories governing the universality of turbulence are exposed, in particular the Richardson cascade principle, the K41 and K62 theories of Kolmogorov and Obukhov, and the Yaglom cascade model, which introduce the concept of intermittency in turbulence. Chapter 2 deals with the modeling and simulation of turbulent flows. While direct numerical simulation (DNS) gives the most accurate representation, its numerical cost does not allow its use in industrial or physical configurations with high Reynolds numbers. Reduced-order models such as RANS or LES are introduced, and we detail their equations and some of the most commonly used closures. An accurate understanding of the loss of information associated with ROS computations is fundamental to assess their efficiency and try improving them.

Chapter 1

Physics and theories of turbulent flows

Many physical phenomena are turbulent: the agitated current in a river, a waterfall, the flow behind a car or an airplane, the motion of the wind, the smoke of a fire, the plume of a rocket engine... The main visible characteristics of such flows are instability, irregularity, randomness and seemingly chaotic character, the presence of vortices of different shapes and sizes. Indeed, dealing with structures of various sizes (ranging from the characteristic length of the geometry of the system to the smallest scales) represents one of the great difficulties for the numerical simulation of such flows. On the other hand, the highly chaotic behavior of turbulence makes it practically hopeless to attempt to reproduce a given realization of such flows as observed in an experiment. Turbulence is only reproducible through its statistics.

This chapter aims at giving the reader some tools to understand turbulent flows, and their main characteristics. Many quantities are introduced, as well as methods and notations, which will be essential to the reading of this thesis.

In this chapter, we first establish in Sec. 1.1 the equations governing the evolution of the fluid. We present the properties of a turbulent flow and the associated metrics. We give the mathematical keys to understand such flows from a statistical point of view. In Sec. 1.2, the characteristic quantities of interest for the statistical study are introduced, as well as the associated characteristic scales. Eventually, in Sec. 1.3, we introduce a fundamental and intrinsic property of turbulence: the intermittency. The original theories of Kolmogorov and Obukhov are presented, and their implications on the introduced metrics and statistics are established.

1.1 Fluid dynamic equations

1.1.1 From molecules to continuous medium

The resolution of a flow from a microscopic point of view consists in studying all the molecules of the fluid interacting with each other. However, such level of description is both complex and computationally expensive, and the fluid is generally treated as continuous media.
Indeed, the time and length scales of molecular motion are extremely small compared to the resolution scales of flows. For example, the mean free path of ambient air is $\lambda \sim 7 \times 10^{-8}$m. It is the average distance traveled between two successive collisions with other moving particles of air. On the other hand, the smallest length scales of interest present in the flows are rather of the order of magnitude $\ell \sim 0.1$mm. There are thus more than three orders of magnitude of separation.

The separation of the scales is quantified by the Knudsen number, $\mathrm{Kn} := \lambda/\ell$. For $\mathrm{Kn} < 0.01$, a continuous approach can be considered whereas for $\mathrm{Kn} > 10$, the system is in free molecular flow. In the ambient air for example, the Knudsen number is less than 10^{-3} and we will consider that this assumption is also largely verified for the flows described in this thesis.

Two strategies can be considered for the derivation of continuous Eulerian equations. In continuum mechanics, they can be obtained by mass, momentum and energy balances on a control volume (Pope 2000). For very small Knudsen numbers on the other hand, thanks to the scale separation, it is possible to define a volume of typical size $\ell_\star^3$ such that $\lambda \ll \ell_\star \ll \ell$. Thus, the macroscopic quantity defined at point $\boldsymbol{x}$ and time t is the average of all the microscopic quantities of the fluid particles present in such volume. The kinetic and statistic theories, considering a distribution function and in the limit of $\mathrm{Kn} \ll 1$ also yields a mixed hyperbolic-parabolic system (Bardos, Golse, and Levermore 1993; Lions and Masmoudi 2001).

1.1.2 Navier-Stokes equations

For low values of Mach number, the incompressible Navier-Stokes equations are a system of non-linear second order partial differential equations, with independent variables: position $(\boldsymbol{x})$ and time (t). They provide the evolution of the fluid velocity $\boldsymbol{u}$ at a point $\boldsymbol{x}$ in time t. The equations can be derived from the basic principles of continuity of mass and momentum, applied to a finite arbitrary volume and assuming constant density:

$$\begin{cases} \dfrac{\partial u_i}{\partial x_i} &= 0, \\ \rho \dfrac{\partial u_i}{\partial t} + \rho u_j \dfrac{\partial u_i}{\partial x_j} &= \rho f_{ext,i} - \dfrac{\partial p}{\partial x_i} + \dfrac{\partial \tau_{ij}}{\partial x_j}, \end{cases} \tag{1.1}$$

where we use the Einstein notation. The first equation is the conservation of mass and the second one is the conservation of momentum. The fluid density is given by ρ. We define the pressure p, the external force per unit mass applied on the fluid $\boldsymbol{f}_{ext}$ and the viscous stress tensor τ_{ij}, given as:

$$\tau_{ij} := 2\mu S_{ij}, \tag{1.2}$$

where μ is the dynamic viscosity and S_{ij} is the deformation-rate tensor defined by:

$$S_{ij} := \frac{1}{2}\left(\frac{\partial u_i}{\partial x_j} + \frac{\partial u_j}{\partial x_i}\right). \tag{1.3}$$

The local kinetic energy and dissipation rate are respectively defined by:

$$k := \frac{1}{2} u_i u_i, \tag{1.4}$$

$$\varepsilon := 2\nu S_{ij} S_{ij}, \tag{1.5}$$

where $\nu = \mu/\rho$ is the fluid kinematic viscosity.

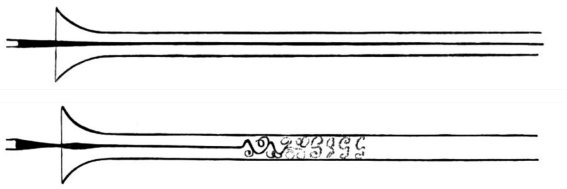

Figure 1.1. A sketch from Reynolds (1883) illustrating the Reynolds number influence on the flow. A fluid is flowing in a tube, and ink is injected at the entrance to visualize the flow. In the top figure, the regime is laminar, the fluid is flowing straightforward. In the bottom figure, the regime becomes turbulent after a certain distance in the tube. The ink reveals eddies, vortices in the flow.

No analytical solution of the Navier-Stokes equations is known today, except in very simplified configurations. This is because of the non-linearity of the partial differential equations, and the mathematical existence and uniqueness of solutions of the Navier-Stokes equations is not yet proven (Temam 2001). Nevertheless, numerical simulations are the only mean to get understanding of realistic fluid systems.

Depending on the terms present in the equation, different regimes for the behavior of the flow are identified, among which a particularly unstable one, called turbulence. This regime is defined for a criterion related to the Reynolds number.

1.1.3 The Reynolds number

We consider that to a typical length scale ℓ is associated a characteristic time scale τ_ℓ and velocity u_ℓ, related by $u_\ell = \ell/\tau_\ell$. In Eq.(1.1), we can identify two particular terms:

- a force of inertia: $\dfrac{\rho u_\ell^2}{\ell}$;
- a viscous dissipation force: $\dfrac{\mu u_\ell}{\ell^2}$;

as well as two characteristic times, obtained by dimensional argument:

- a dynamic time: ℓ/u_ℓ;
- a dissipation time: ℓ^2/ν.

The ratio of these two forces, which is also the ratio of these two times, gives the local Reynolds number:

$$\mathrm{Re}_\ell = \frac{\ell u_\ell}{\nu}. \tag{1.6}$$

Based on the largest scales in the flow, Re_L can be defined as $\mathrm{Re}_L := \dfrac{L\sigma_u}{\nu}$, where σ_u represents the characteristic velocity of large scales. The influence of the Reynolds number is illustrated on the sketch of Fig. 1.1.

When Re_L is small, dissipation blocks all development of the flow. If there is a permanent forcing, a stable flow is established (laminar at the limit), which will not interest us in the following. Such laminar flow is represented in the top figure of Fig. 1.1.

When Re_L is large, the forces of inertia prevail over the forces of dissipation. The motion is unstable, erratic and difficult to characterize in terms of shapes or patterns. Under an external forcing, the turbulence is maintained and one can observe the typical eddies in the bottom Fig. 1.1.

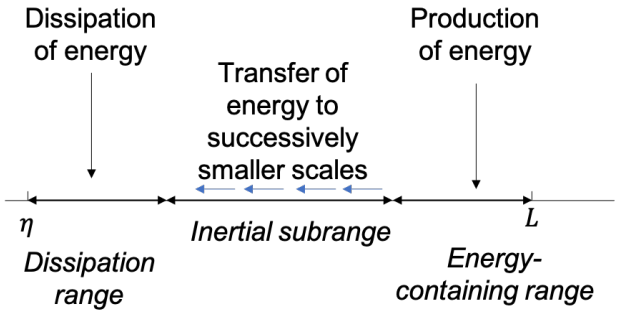

Figure 1.2. A schematic diagram of the energy cascade at very high Reynolds number.

1.1.4 Richardson's energy cascade and energy spectrum

This mechanism, proposed in the 1920s, describes the way energy is produced, distributed and then dissipated in turbulent flow. Richardson postulates that:

- energy is injected at a large scale L;
- the energy transfers from scale to smaller scale (the vortices give birth to smaller vortices by stretching and folding);
- it is dissipated when the "dissipation time" is of the order of "dynamic time", which defines the Kolmogorov scale.

There are thus three ranges of scales in the flow, as represented in Fig. 1.2:

- the large scales L, T_L and σ_u which are sensitive to external phenomena (boundary conditions, forcing, etc...);
- the very small scales, where viscosity dominates. Those are called the Kolmogorov scales: the length scale η, the time scale τ_η and the velocity u_η. At the smallest scales, inertia and viscous effects are in balance $\mathrm{Re}_\eta = u_\eta \eta/\nu = 1$;
- the intermediate scales, dominated by dynamics, and where most of the turbulence develops.

Richardson assumes that for the intermediate scales ℓ, the dissipation rate of energy is conserved. By dimensional analysis, it is defined as $\varepsilon_\ell = E_\ell/\tau_\ell$, where $E_\ell = u_\ell^2$ is the kinetic energy associated to these scales. Therefore we have conservation of the energy dissipation rate from the largest (L and T_L) to the smallest scales (η and τ_η):

$$\varepsilon_\ell \sim \frac{u_\ell^2}{\tau_\ell} \sim \frac{u_\ell^3}{\ell} \sim C. \tag{1.7}$$

The inertial zone extends between the length scales η and L (respectively the time scales τ_η and T_L). Reynolds numbers are a measure of scale separation because by applying this conservation of energy to $\dfrac{\sigma_u^3}{L} \sim \dfrac{u_\eta^3}{\eta}$ and $\dfrac{\sigma_u^2}{T_L} \sim \dfrac{u_\eta^2}{\tau_\eta}$, we easily obtain:

$$\frac{L}{\eta} \sim \mathrm{Re}_L^{3/4}, \quad \frac{T_L}{\tau_\eta} \sim \mathrm{Re}_L^{1/2}. \tag{1.8}$$

Therefore, the Reynolds number is directly related to the scale separation (in time and space).

Also note that Richardson's picture of turbulence relies on the assumption that ε_ℓ has small fluctuations and can be considered as a constant. This vision of turbulence will be further developed

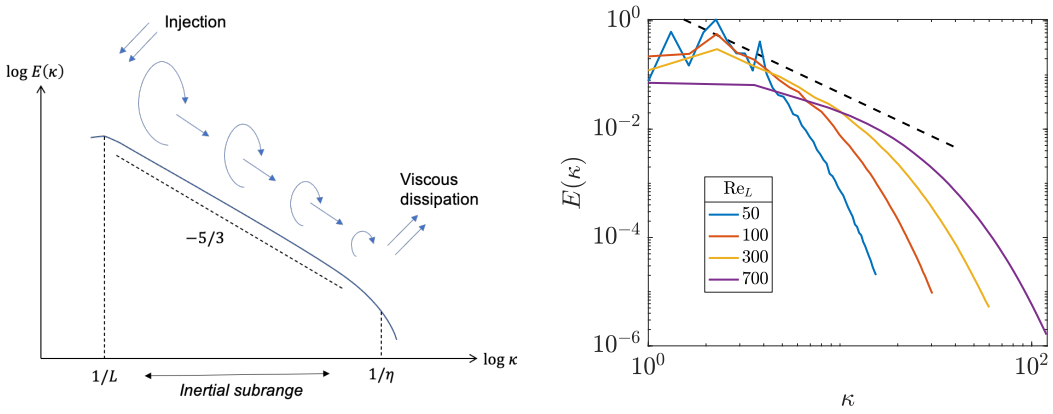

(a) (b)

Figure 1.3. (a) A scheme of the energy spectrum at very high Reynolds number ; (b) Energy spectra in log-log scale for different Reynolds numbers Re_L. The dashed lines represent a $-5/3$-slope.

by Kolmogorov (1941b). However, if fluctuations are strong, this universal picture of turbulence must be revised (Kolmogorov 1962) and in that case, intermittency must be taken into account (see Sec. 1.3.1).

The energy spectrum provides insight into the distribution of turbulent kinetic energy among the eddies of different sizes. We define the Eulerian energy spectrum $E(\kappa)$ as the kinetic energy per unit mass and unit wavenumber κ of a velocity field. Let us consider a series of discrete scales such as

$$\ell_n = \ell_0 2^{-n}, \quad n = 0, 1, 2...$$

and the associated wavenumbers $\kappa_n = \ell_n^{-1}$. The kinetic energy per unit mass in scales ℓ_n is defined as:

$$E_n = \int_{\kappa_n}^{\kappa_{n-1}} E(\kappa)\,\mathrm{d}\kappa \sim E(\kappa_n)\Delta\kappa_n, \tag{1.9}$$

where $\Delta\kappa_n = \kappa_{n+1} - \kappa_n = 2\kappa_n - \kappa_n = \kappa_n$. Therefore, we have: $E_n \sim E(\kappa_n)\kappa_n$. We have seen that ε_n can be considered constant throughout the inertial range: $\varepsilon_n \sim C$. This yields:

$$u_n \sim (C\ell_n)^{1/3}, \quad E_n \sim (C\ell_n)^{2/3}. \tag{1.10}$$

Finally, $E_n \sim E(\kappa_n)\kappa_n$, and we obtain the well-known behavior of the energy spectrum in the inertial range: $E(\kappa) \sim \kappa^{-5/3}$.

Figure 1.3(a) shows the Richardson cascade model, with a logarithmic spectral representation of the turbulent energy. At large scales, i.e. at small wavenumbers, is the injection zone. At small scales, the energy dissipation takes place and produces the collapse of the energy of the fluid. In between is established the inertial zone, which is characterized by the average dissipation rate.

In practice, the energy spectrum is obtained with a Fourier transform of the velocity. We consider the cube of length $\mathcal{L}$ in physical space. The smallest wavenumber is $\kappa_0 = 2\pi/\mathcal{L}$ and the wavenumber vector is defined by : $\boldsymbol{\kappa} = \kappa_0 \boldsymbol{n}$, for $\boldsymbol{n} \in \mathbb{Z}^3$.

The Fourier decomposition of the flow gives:

$$\boldsymbol{u}(\boldsymbol{x},t) = \sum_{\boldsymbol{\kappa}} e^{i\boldsymbol{\kappa}\boldsymbol{x}} \hat{\boldsymbol{u}}(\boldsymbol{\kappa},t), \tag{1.11}$$

where $\hat{u}(\boldsymbol{\kappa},t)$ are the Fourier coefficients. The energy spectrum tensor is defined as:

$$E(\boldsymbol{\kappa},t) = \frac{1}{2}|\hat{u}_i(\boldsymbol{\kappa},t)|^2. \tag{1.12}$$

Its spectral density gives the energy spectrum:

$$E(\kappa,t) = \sum_{\kappa \leq |\boldsymbol{\kappa}| \leq \kappa+1} E(\boldsymbol{\kappa},t). \tag{1.13}$$

Figure 1.3(b) shows the energy spectrum for different Reynolds numbers computed from three-dimensional numerical simulations performed with Fieldz, a code introduced in Zamansky, Coletti, Massot, and Mani (2016) and detailed in Sec. 2.4. The inertial zone is only visible at high Reynolds numbers, when there is clear scale separation.

1.1.5 Lagrangian framework for fluid particles

Until now, only an Eulerian description of the fluid motion has been introduced. However, it is sometimes useful to define the Lagrangian description of the flow, which consists of following the motion of "fluid particles" (or tracers). The fluid particle is defined in Monin and Yaglom (1975) by a *volume of fluid having linear dimensions which are very large compared to the average distance between molecules*. Therefore, the framework of continuum medium mechanics still applies, but the dimensions of the fluid particles are so small that the velocity and pressure inside its volume are considered as constant.

In this framework, the evolution equation of a fluid particle is the following:

$$\frac{\mathrm{D}\boldsymbol{u}}{\mathrm{D}t} = -\nabla p + \nu \nabla^2 \boldsymbol{u}, \tag{1.14}$$

where $\dfrac{\mathrm{D}\boldsymbol{u}}{\mathrm{D}t} := \dfrac{\partial \boldsymbol{u}}{\partial t} + (\boldsymbol{u}\cdot\nabla)\boldsymbol{u}$ is the particle acceleration, transported and advected by the flow $\boldsymbol{u}$.

We will see in the following that such framework defines complementary statistics to those of the Eulerian fields and also allows us to model the behavior of fluid particles by stochastic processes (see Chap. 3), considering the random nature of turbulence.

1.1.6 The random nature of turbulence

Fig. 1.4(a) represents a turbulent field, obtained from a numerical simulation which data are available in Lanotte et al. (2011) and about which details are given in Sec. 2.4. By following fluid particles in this kind of flow, we obtain the type of temporal evolution for the velocity, acceleration or dissipation plotted in Figs 1.4(b), 1.4(c) and 1.4(d). They seem random, and reflect the chaotic behavior of the flow.

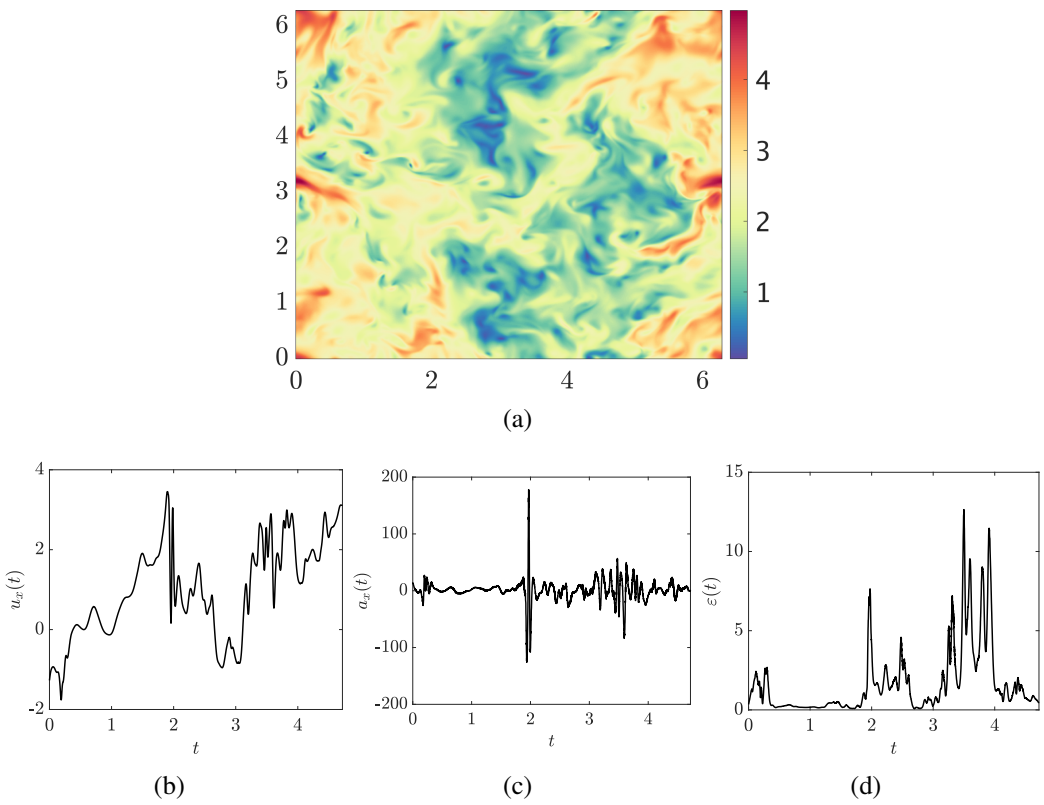

Figure 1.4. Snapshot of the velocity field obtained by numerical simulation (a) ; Evolution of a velocity component (b), an acceleration component (c) and the dissipation (d) of a fluid particles in turbulence. Dataset from Lanotte et al. (2011).

In turbulent flow, the velocity field $\boldsymbol{u}(\boldsymbol{x}, t)$ is random, although the Navier-Stokes equations are deterministic in nature. Indeed, in any turbulent flow, there are inevitably perturbations related to the accuracy of the initial conditions, the boundary conditions or the fluid properties, and the turbulent flow is extremely sensitive to these perturbations. The initial conditions being imprecisely known, they cannot univocally determine the evolution of a turbulent flow. The chaotic nature of turbulence has long been investigated (Benzi, Paladin, Parisi, and Vulpiani 1984; Ottino 1990).

Thus, it is hopeless to try to find an expression for the time-dependence of the macroscopic fields of a single individual flow, the remaining possibility being a statistical description of turbulence. This means that a probability measure can be associated with the turbulent flow, as introduced by Drew and Passman (2006) and presented in next section.

1.1.6.1 Probability space for turbulent flows

This section presents how to build a probability measure associated to turbulence. Let us start by defining a probability space.

Definition 1.1.1 *A probability space is a tuple $(\Omega, \mathcal{E}, \mathbb{P})$ of three elements:*

- *the set of possible outcomes Ω,*
- *the set of events, which is a σ-algebra:*
  - *$\emptyset \in \mathcal{E}$ and $\Omega \in \mathcal{E}$*
  - *$\mathcal{E}$ is closed under complements, $\forall e \in \mathcal{E}, \quad (\cap e) \in \mathcal{E}$,*
  - *and $\mathcal{E}$ is closed under countable unions*

$$\forall \left(e_i\right)_{i\in\mathbb{N}} \in \mathcal{E}^{\mathbb{N}}, \quad \left(\bigcup_{i=1}^{\mathbb{N}} e_i\right) \in \mathcal{E}$$

- *and $\mathbb{P}$, the probability measure on $\mathcal{E}$:*
  - *$\mathbb{P}[\emptyset] = 0$ and $\mathbb{P}[\Omega] = 1$*
  - *For any $\left(e_i\right)_{i\in\mathbb{N}} \in \mathcal{E}^{\mathbb{N}}$, such that for any $i, j \in \mathbb{N}$ with $i \neq j$ one has $e_i \cap e_j = \emptyset$,*

$$\mathbb{P}\left[\bigcup_{i=1}^{\mathbb{N}} e_i\right] = \sum_{i=1}^{\mathbb{N}} \mathbb{P}\left[e_i\right]$$

Definition 1.1.2 *A random variable Y is a measurable function from a set of possible outcomes Ω to a measurable space.*

Definition 1.1.3 *When it exists, the expectation of a random variable Y is given by:*

$$\mathbb{E}\left[Y\right] := \int_{\Omega} Y(\omega) \mathrm{d}\mathbb{P}[\omega]. \tag{1.15}$$

The variance is defined as:

$$\mathrm{Var}[Y] := \mathbb{E}\left[\left(Y - \mathbb{E}\left[Y\right]\right)^2\right]. \tag{1.16}$$

For a deterministic system of equations such as the Navier-Stokes equations, there are several ways to introduce a probability space and we give two examples:

- **The initial conditions**:
  Let us call A_f the set of turbulent fluid fields. We consider that initial conditions are a measurable function which depends on the outcome of a random phenomenon:

$$\begin{aligned} \boldsymbol{u}_0 :&\Omega \to A_f \\ &\omega \mapsto \boldsymbol{u}_0(\omega; \boldsymbol{x}) \end{aligned}$$

  Therefore, the initial conditions of the fluid $\boldsymbol{u}_0$ define a random field. Applying Navier-Stokes to this random variable propagates the distribution of initial conditions through time.

- **The external forcing**:
  In stationary turbulence, an external force $\boldsymbol{f}_{ext}(\boldsymbol{x}, t)$ must maintain the stationarity of the flow in the Navier-Stokes equation. Let us call B_f the set of possible forces $\boldsymbol{f}_{ext}(\boldsymbol{x}, t)$ and we consider that this forcing is a measurable function which depends on ω, a random event:

$$\begin{aligned} \boldsymbol{f}_{ext} :&\Omega \to B_f \\ &\omega \mapsto \boldsymbol{f}_{ext}(\omega; \boldsymbol{x}, t) \end{aligned}$$

  Each outcome is therefore a random external force $\boldsymbol{f}_{ext}(\omega; \boldsymbol{x}, t)$ introduced in the Navier-Stokes equation.

Other possible sources of randomness can be introduced following the same approach, for instance those related to uncertainties on boundary conditions.

By introducing such probabilistic framework in the Navier-Stokes equations, we define a solution of the equation which is itself random: $\boldsymbol{u}(\omega; \boldsymbol{x}, t)$. It is thus possible to apply to it the operators of expectation and variance. However, in practice, we cannot compute $\mathbb{E}\left[\boldsymbol{u}(\omega; \boldsymbol{x}, t)\right]$ analytically and we rather estimate the statistics by ensemble means, i.e. by performing a large number of simulations and randomly drawing the corresponding random variables.

We now define the ensemble mean $\langle . \rangle$, as an estimator of $\mathbb{E}\left[.\right]$ with respect to the corresponding statistical ensemble (for example those associated with the choice of the initial conditions or the external forcing).

$$\begin{aligned} \langle \phi \rangle (\boldsymbol{x}, t) &\approx \mathbb{E}\left[\phi(\omega; \boldsymbol{x}, t)\right] \\ \sigma^2_\phi(\boldsymbol{x}, t) &\approx \mathrm{Var}[\phi(\omega; \boldsymbol{x}, t)]. \end{aligned} \tag{1.17}$$

1.1.6.2 Ergodicity

Computing ensemble means is unrealistic since it consists in repeating experiments or numerical simulation a large number of times. For experiments on geophysical flows, it is not possible because we cannot ask the nature to repeat a weather pattern. For numerical simulations, the computational cost is rapidly too high.

A strategy to avoid repeating those experiments consists in taking advantage of the ergodicity of the flow: an ergodic process is a stochastic process for which the statistics can be approximated by studying a single sufficiently long realization. The underlying assumption is therefore to consider that a trajectory occupies a region of the phase space which corresponds to all possible sets of

the initial phases and which, in the course of time, covers practically all the points in the region. Therefore, the turbulent motion which arises in this case is "ergodic" and in time, the fluid will pass through states as close as desired to any possible state of motion (Monin and Yaglom 1975).

Under certain assumptions, we can estimate the ensemble means through time and/or spatial means. The advantage of ergodicity is that we can explore the same events within a single simulation as the one obtained by averaging over a large number of simulations. There are different types of ergodicity, depending on the properties of the studied turbulence:

- **Homogeneity:** Turbulence is homogeneous if all the mean quantities are invariant under any spatial translation. Then the ergodicity hypothesis allows an ensemble average to be calculated as a spatial average for a single flow realization ω_0

$$\langle \phi \rangle (t) \approx \frac{1}{|\mathcal{V}|} \int_{\mathcal{V}} \phi(\omega_0; \boldsymbol{x}, t) \, \mathrm{d}\boldsymbol{x}, \tag{1.18}$$

  where $\mathcal{V}$ is the domain of fluid simulated and $|\mathcal{V}|$ its volume.
- **Isotropy:** Turbulence is isotropic if all the mean quantities are invariant under any arbitrary rotation of coordinates: $\langle u_x \rangle = \langle u_y \rangle = \langle u_z \rangle$.
- **Stationarity:** Turbulence is stationary if all mean quantities are invariant under a translation in time.

$$\langle \phi \rangle (\boldsymbol{x}) \approx \frac{1}{T} \int_{[0,T]} \phi(\omega_0; \boldsymbol{x}, t) \, \mathrm{d}t. \tag{1.19}$$

In the following, we will study homogeneous isotropic turbulence (HIT) and unless otherwise stated, stationary turbulence. The ergodicity allows us to have access to mean flow quantities defined by:

$$\langle \phi \rangle = \frac{1}{|\mathcal{V}|} \frac{1}{3} \frac{1}{T} \int_{[0,T]} \int_{\mathcal{V}} (\phi_x(\omega_0; \boldsymbol{x}, t) + \phi_y(\omega_0; \boldsymbol{x}, t) + \phi_z(\omega_0; \boldsymbol{x}, t)) \, \mathrm{d}\boldsymbol{x} \, \mathrm{d}t. \tag{1.20}$$

One can note the dependency of $\langle \phi \rangle$ with $\boldsymbol{x}$ and t because the flow is homogeneous, and stationary and we drop the component indice because the flow is isotropic.
In the case of non stationary flow, we will keep the dependency on time $\langle \phi \rangle (t)$ and compute the averaging on the spatial dimension only. We will make use of the ergodicity assumption to define statistical properties of turbulence.

1.2 Statistical description of turbulence

Since turbulence is random in nature, a perfect knowledge of a flow would be given by the statistics in N points and N times of the velocity field: $\langle u(\boldsymbol{x}_1, t_1) u(\boldsymbol{x}_2, t_2) ... u(\boldsymbol{x}_N, t_N) \rangle$. In practice, it is not possible to predict the behavior of all of these statistics, and studies are generally limited to the statistics at one or two points (or times) (Pope 2000). One or two-point statistics gather important information on space and time characteristics, therefore they represent the main focus for the modeling of turbulent flows.

1.2.1 One-point, one-time statistics

Homogeneous isotropic turbulence is qualified by a small number of global metrics. The characteristic velocity σ_u can be defined in HIT from the variance of the velocity field: $\sigma_u^2 = \left\langle u^2 \right\rangle$. It is

related to the global fluid turbulent kinetic energy which can be defined by averaging Eq. (1.4):

$$\langle k \rangle = \frac{1}{2} \langle u_i u_i \rangle = \frac{3}{2} \sigma_u^2. \tag{1.21}$$

And so is defined the global energy dissipation rate $\langle \varepsilon \rangle = \langle \varepsilon(\boldsymbol{x}, t) \rangle = 2\nu \langle S_{ij} S_{ij} \rangle$.

In a periodic domain and in the absence of an external forcing, turbulence is decaying and the time evolution equation of turbulent kinetic energy is obtained by multiplying fluid momentum equation by u_i and ensemble averaging. We note here that the flow is not stationary, therefore the ensemble mean can only be calculated with a volume average using spatial ergodicity, and the time dependencies of the global variables must appear:

$$\frac{d \langle k \rangle (t)}{dt} = - \langle \varepsilon \rangle (t). \tag{1.22}$$

For stationary flows with forcing, the time derivatives are null and $\langle k \rangle$ and $\langle \varepsilon \rangle$ are characteristics constants of the flow.

1.2.2 One-point, two-time statistics

One-point correlations are used to determine the time scale (life time) of large eddies. They can be calculated in an Eulerian or in a Lagrangian frame.

Eulerian measure

Eulerian one-point correlations are defined as:

$$R_E^u(\tau) := \frac{1}{3} \langle u_i(\boldsymbol{x}, t) u_i(\boldsymbol{x}, t + \tau) \rangle , \tag{1.23}$$

and the time scale related to the Eulerian correlation is defined as:

$$T_E := \frac{1}{R_E^u(0)} \int_0^\infty R_E^u(\tau) \, \mathrm{d}\tau. \tag{1.24}$$

T_E is the time scale during which the fluctuating velocity decorrelates from itself. A practical calculation of Eulerian one-point correlations involves the evolution of the fluid velocity at a large number of arbitrarily distributed points in the flow domain and using the spatial averages. The fluid velocities are stored at the spatial grid points therefore, a practical way of calculating the correlations is the consideration of the velocities at grid points. Using the stationarity in forced turbulence, the correlations can further be improved by using time averages for the correlations calculated for a certain number of realizations separated by a decorrelation time interval.

Lagrangian measure

Lagrangian one-point correlations can be computed along fluid particles trajectories and are defined similarly:

$$R_L^u(\tau) := \frac{1}{3} \langle u_i(\boldsymbol{x}_f(t), t) u_i(\boldsymbol{x}_f(t + \tau), t + \tau) \rangle . \tag{1.25}$$

The Lagrangian integral time scale is defined accordingly:

$$T_L := \frac{1}{R_L^u(0)} \int_0^\infty R_L^u(\tau)\,\mathrm{d}\tau, \tag{1.26}$$

which is the time scale during which the large eddy complete their rotation.

1.2.3 Two-point, one-time statistics

In a stationary turbulence, the Eulerian two-point velocity correlation function is defined by:

$$R_{E,ij}^u(\mathbf{r}) := \langle u_i(\mathbf{x}) u_j(\mathbf{x}+\mathbf{r})\rangle. \tag{1.27}$$

We have the following properties:

- $R_{E,ij}^u(\mathbf{r}) = 0$ if $r \to \infty$: the velocities are uncorrelated at infinity.
- $R_{E,ii}^u(r\mathbf{e}_i) = \sigma_u^2$ when $r \to 0$
- $R_{E,ij}^u(\boldsymbol{r}) = 0$ for $i \neq j$

Since $R_{E,ij}^u$ is homogeneous to a square velocity and tends towards σ_u^2 for $r = 0$, it can be written as the product of this value by a dimensionless function that describes the variation as a function of r:

- $R_{E,ij}^u(r\mathbf{e}_k) = \sigma_u^2 f(r)$ for $i = j = k$
- $R_{E,ij}^u(r\mathbf{e}_k) = \sigma_u^2 g(r)$ for $i = j$, and $k \neq i$

where

$$\begin{aligned} f(r) &= \frac{1}{3}\frac{\langle u_i(\boldsymbol{x}) u_i(\boldsymbol{x}+r\boldsymbol{e}_i)\rangle}{\sigma_u^2}, \\ g(r) &= \frac{1}{3}\frac{\langle u_i(\boldsymbol{x}) u_i(\boldsymbol{x}+r\boldsymbol{e}_j)\rangle}{\sigma_u^2}, \quad i \neq j. \end{aligned} \tag{1.28}$$

These two correlations allow the definition of two space scales, namely: longitudinal and transversal large scales. They can be calculated by:

$$\begin{aligned} L_f &:= \int_0^\infty f(r)\,\mathrm{d}r \\ L_g &:= \int_0^\infty g(r)\,\mathrm{d}r. \end{aligned} \tag{1.29}$$

Using the incompressibility condition, Von Karman and Howarth (1938) give a relation connecting these two correlations. It is written:

$$g(r) = \frac{1}{2r}(r^2 f(r))' = f(r) + \frac{1}{2} r f'(r). \tag{1.30}$$

Thus, in isotropic turbulence the two-point correlation $R_{E,ij}^u(r)$ is completely determined by the longitudinal autocorrelation function $f(r)$. Another length scale, λ_f, can be defined from f, characterizing its behavior near 0. We can find a development according to r of the function $f(r)$ in the form:

$$\begin{aligned} f(r) &= 1 + r f'(0) + \frac{r^2}{2} f''(0) + O(r^2) \\ &= 1 - \frac{r^2}{\lambda_f^2} + O(r^2), \end{aligned} \tag{1.31}$$

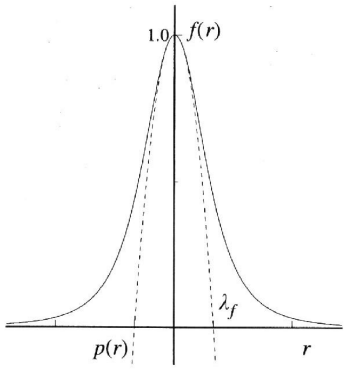

Figure 1.5. A sketch of the longitudinal velocity autocorrelation function showing the definition of the Taylor microscale, λ_f. Sketch from Pope (2000).

where $f'(0) = 0$ because f is an even function. This expression can be used as a definition of Taylor's microscopic length scale $\lambda_f := \left[-\frac{1}{2}f''(0)\right]^{-1/2}$, which is therefore the typical scale in the inertial cascade. A Reynolds number associated to this characteristic scale can be introduced, it is the Taylor-scale Reynolds number: $\mathrm{Re}_\lambda = \frac{\sigma_u \lambda_f}{\nu}$. The scheme in Fig. 1.5 illustrates what this characteristic length represents. If the correlation function f is assimilated to a parabola centered at 0, then this parabola cuts the abcissa axis at λ_f. This is therefore the typical correlation length of the longitudinal velocity. Pope (2000) shows that the Reynolds number based on Taylor microscale λ_f is directly proportional to the ratio of the time scales : $\mathrm{Re}_\lambda \sim T_L/\tau_\eta$.

1.2.4 Characteristic scales of turbulence

Now that we have introduced these length and time scales, we can specify the intervals and the parameters introduced in Sec. 1.1.4.

- The large scales are thus characterized by the length scale L, the time scale T_L and the velocity σ_u. The conservation of the dissipation rate gives: $L \sim \sigma_u^3/\langle\varepsilon\rangle$ and $T_L \sim \sigma_u^2/\langle\varepsilon\rangle$.
- The smallest scales of the flow, η, τ_η and u_η are already related by the equilibrium of the viscous and inertial forces $\mathrm{Re}_\eta = 1$ and moreover, the conservation of the dissipation rate gives: $\frac{u_\eta^2}{\tau_\eta} \sim \frac{u_\eta^3}{\eta} \sim \langle\varepsilon\rangle$. Thus, the three parameters of Kolmogorov are:

$$\eta := \left(\nu^3/\langle\varepsilon\rangle\right)^{1/4}, \quad u_\eta := \left(\langle\varepsilon\rangle\,\nu\right)^{1/4}, \quad \tau_\eta := \left(\nu/\langle\varepsilon\rangle\right)^{1/2}. \tag{1.32}$$

1.2.5 Structure functions

Experimental studies show that the velocity $\mathbf{u}$ and its components have a quasi-Gaussian distribution. This is expected: when we consider the whole fluid, there are a large number of events that are independent of each other. The velocity at each point therefore contributes independently and the law of large numbers predicts this Gaussian behavior.
That is not the case for velocity increments. The Lagrangian velocity increment is defined by:

$$\Delta_\tau u(t) := u(t+\tau) - u(t), \tag{1.33}$$

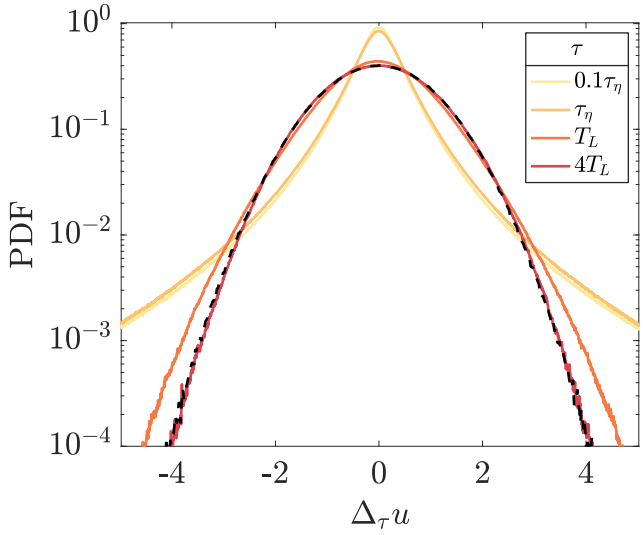

Figure 1.6. PDF of the velocity increments for different values of τ. The PDF is normalized for unit variance and compared with the Gaussian distribution in black dashed line. Dataset from Lanotte et al. (2011).

where u refers to any component of $\boldsymbol{u}$. The pth-order moment of $\Delta_\tau u(t)$ is, by definition, the pth-order Lagrangian velocity structure function:

$$D_p^L(\tau) := \langle [\Delta_\tau u]^p \rangle \,, \tag{1.34}$$

where we have dropped the time dependency because of the stationarity of the flow.

Figure 1.6 shows the distribution of Lagrangian velocity increments for different values of increments τ. For time increments of the order of magnitude of τ_η, and very small compared to T_L, the probability density function (PDF) of the velocity increments exhibits very large tails, far from the Gaussian distribution. Correlation effects are strong and extend quite far across the domain. For larger time increments, velocities are uncorrelated and the distribution is closer to the Gaussian one, as expected.

The structure functions are used to study the non-Gaussianity of the velocity increments, often by comparing the standardized moments:

$$H_n(\tau) := \frac{D_n^L(\tau)}{D_2^L(\tau)^{n/2}}. \tag{1.35}$$

The non-Gaussian behavior of small scales is confirmed in Fig. 1.7(a) by the evolution of the flatness H_4 of the velocity increments which gradually decreases to 3 for the larger scales.
In the following section, the well-known Kolmogorov theory is presented, in particular from the perspective of characterizing these Lagrangian structure functions.

1.3 The quest for turbulence universality

In an attempt to unify statistical properties of turbulent flows, several fundamental theories were developed concerning the universal behavior of statistics introduced in the previous section. In this section, we outline the main ones:

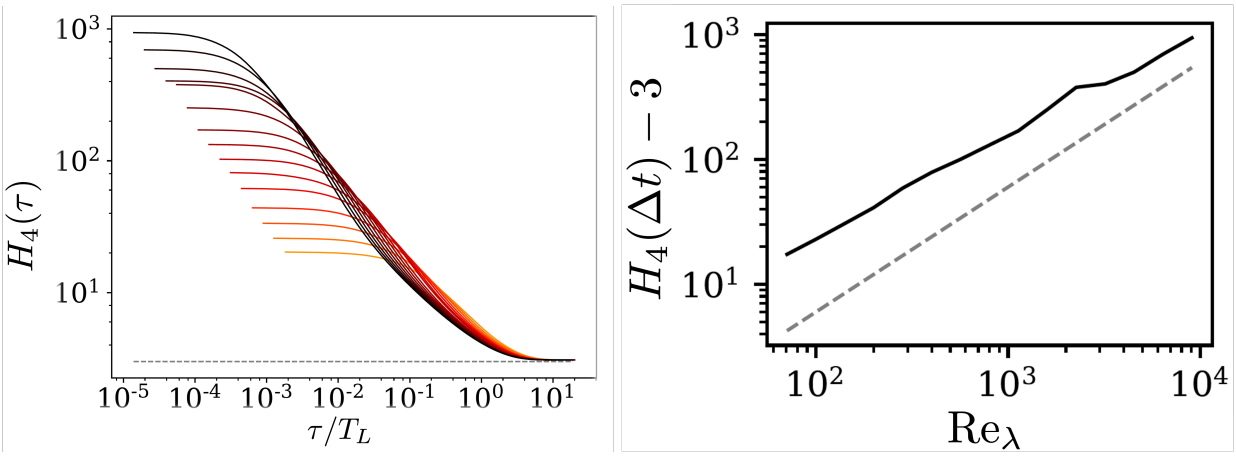

(a) (b)

Figure 1.7. (a) Evolution of the flatness of the velocity increments H_4 versus the time shift for $\mathrm{Re}_\lambda = 70$ to 9000 from orange to black and (b) evolution of the flatness of the acceleration with the Reynolds number and comparison with the linear law. Figure from Zamansky (2021).

- Kolmogorov (1941b), hereafter referred as K41, formalized this universality of turbulence with a self-similar description of velocity fluctuations in the inertial range (see Sec.1.3.1.1);
- Kolmogorov (1962), hereafter referred as K62, developed a vision based on local and scale-dependent variables which are more relevant to describe velocity fluctuations (see Sec.1.3.1.2);
- the model of Yaglom (1966), presenting the turbulence as a cascade involving embedded vortices of decreasing size (see Sec. 1.3.2).

The consequences of these theories in terms of acceleration statistics are specified in Sec.1.3.3. These properties will be retained as a fundamental basis for the stochastic models that will be developed in Part I I.

1.3.1 Origins and properties of the intermittency

Although originally developed in an Eulerian framework for the corresponding structure functions, we present below the fundamental assumptions of Kolmogorov's turbulence theories in a Lagrangian framework, the equivalence having been previously established by Monin and Yaglom (1975), Borgas (1993) and others.

1.3.1.1 K 41: the global- similarity hypotheses

Kolmogorov (1941b) first formalized the vision of Richardson cascade by introducing the similarity hypothesis. He stated that for high Reynolds numbers Re_L, turbulence is universal and velocity fluctuations statistics are expected to be independent of the large scales. His theory is based on two hypotheses:

- **The first hypothesis of similarity**
  For $\tau \ll T_L$, velocity increments statistics are independent on the forcing mechanism. The structure functions only depend on the mean dissipation and the viscosity ν. Because $D_2^L(\tau)$ is homogeneous to a squared velocity, it can be written in the form:

$$D_2^L(\tau) = u_\eta^2 \beta_0, \tag{1.36}$$

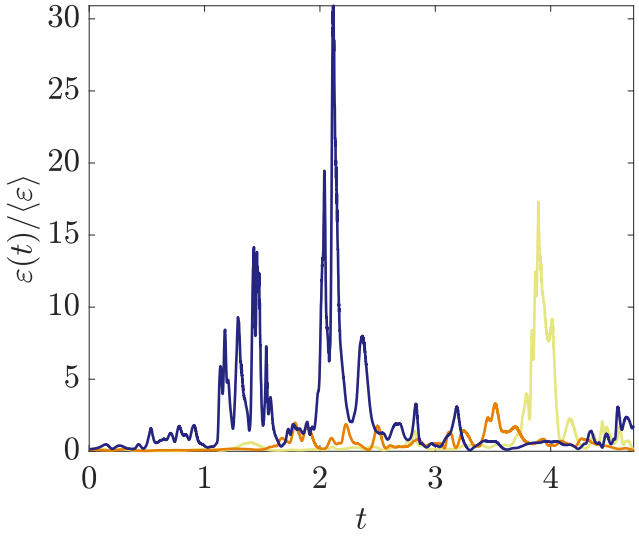

Figure 1.8. Temporal evolution of the dissipation ε along three particle trajectories. Dataset from Lanotte, Calzavarini, Toschi, Bec, Biferale, and Cencini (2011).

where we recall that $u_\eta = (\nu \langle\varepsilon\rangle)^{1/4}$ and $\beta_0 = \beta_0(\tau/\tau_\eta)$ is a universal function. An expansion around 0 gives:

$$u(t+\tau) - u(t) = \tau \frac{\mathrm{d}u}{\mathrm{d}t} + O(\tau). \tag{1.37}$$

Therefore, by dimensional analysis, $\beta_0(x) = a_0 x^2$ for $x \ll 1$ i.e. $\tau \ll \tau_\eta$ and we have in the dissipative range:

$$D_2^L(\tau) = a_0 \langle\varepsilon\rangle^{3/2} \nu^{-1/2} \tau^2, \tag{1.38}$$

where a_0 is assumed universal.

- **The second hypothesis of similarity**
  For $\tau_\eta \ll \tau \ll T_L$, velocity increments statistics are also independent on the viscosity:

$$D_2^L(\tau) = \nu^{1/2} \langle\varepsilon\rangle^{1/2} \beta_0 = \tau_\eta \langle\varepsilon\rangle \beta_0. \tag{1.39}$$

  Therefore, in the inertial range, $\beta_0(x) = \mathcal{C}_0 x$ for $x \gg 1$: there is a complete similarity (the exact definition is given in Sec. 3.1.7.1). $\mathcal{C}_0$ is the universal Kolmogorov constant. The K41 theory in the inertial range leads to:

$$D_2^L(\tau) = \mathcal{C}_0 \langle\varepsilon\rangle \tau. \tag{1.40}$$

However, it was pointed out by Landau and Lifshitz (1987) that this theory is flawed at small scales by the intermittent fluctuations of the energy dissipation, in contradiction with the homogeneity assumed in K41.

1.3.1.2 K62: the refined similarity hypotheses

Landau, Lifshitz, and Holbrow (1963), Monin and Yaglom (1975), Yeung and Pope (1989) found that "constants" of the K41 model $\mathcal{C}_0$ and a_0 were not universal but Reynolds-dependent. Furthermore the scaling of Lagrangian velocity structure functions cannot be extended to higher order

moments of the velocity increments because the instantaneous dissipation intermittently reaches very high values and so the global average of ε is not the relevant scale. This is illustrated in Fig. 1.8 where the dissipation along fluid particle paths ε is plotted and exhibits brief and sudden high fluctuations. The long-range correlation of the dissipation indicates that the large scales of the flow influence the local dissipation rate thus raising the question of the universality of the flow. These remarks, raised by Landau and Lifshitz (1944), led Kolmogorov (1962) to the refined similarity hypothesis with the consideration of a locally-averaged dissipation:

$$\varepsilon^\tau(t) := \frac{1}{\tau}\int_t^{t+\tau} \varepsilon(s)\mathrm{d}s, \tag{1.41}$$

where, the upperscript τ represents the time scale of the locally-averaged variable. Local velocity, scales and Reynolds numbers can be introduced: $u_\tau = (\varepsilon^\tau \tau)^{1/2}$, $\ell_\tau = \tau v_\tau = \varepsilon^\tau \tau^{3/2}$ and $\mathrm{Re}_\tau = \dfrac{u_\tau \ell_\tau}{\nu}$.

- **The first refined similarity hypothesis**
  The first local similarity hypothesis states that the Lagrangian velocity structure functions conditioned by local dissipation should be independent on the large forcing scales for $\tau \ll T_L$:

  $$\langle (\Delta_\tau u)^p | \varepsilon^\tau \rangle = u_\tau^p \beta_p, \tag{1.42}$$

  where $\beta_p = \beta_p(\mathrm{Re}_\tau)$ hence depends on the viscosity ν.

- **The second refined similarity hypothesis**
  Moreover, in the inertial range, the behavior of the velocity increments does not depend on the viscosity and therefore $\beta_p = C_p$, a constant. We obtain:

  $$\langle (\Delta_\tau u)^p | \varepsilon^\tau \rangle = C_p (\varepsilon^\tau \tau)^{p/2}. \tag{1.43}$$

  The unconditional statistics of the velocity increments therefore depend on the statistics of the locally-averaged dissipation:

  $$\langle [\Delta_\tau u]^p \rangle = C_p \tau^{p/2} \left\langle (\varepsilon^\tau)^{p/2} \right\rangle. \tag{1.44}$$

- **The third refined similarity hypothesis**
  Such velocity structure functions have been studied and characterized in Mordant et al. (2004), Xu et al. (2006), Biferale et al. (2008), Arnèodo et al. (2008). In K62, it was also suggested a log-normal distribution for ε^τ, with a logarithm scaling for the variance of $\log \varepsilon^\tau$:

  $$\sigma^2_{\log \varepsilon^\tau} \sim \log \frac{T_L}{\tau}. \tag{1.45}$$

  This prediction is in reasonable agreement with experimental data (Mordant, Delour, Léveque, Arnéodo, and Pinton 2002) and is reproduced in the "Cascade model" of Yaglom (1966), presented in Sec. 1.3.2. This model is at the basis of all the existing cascade models.

Since the publication of the refined similarity hypotheses, many studies have been devoted to data analysis, most of them focusing on energy dissipation. Consistently with these hypotheses, it was observed that the dissipation has a log-normal distribution and presents long-range power-law correlation (Yeung and Pope 1989; Pope and Chen 1990; Yeung, Pope, Lamorgese, and Donzis 2006; Dubrulle 2019).

1.3.1.3 Eulerian framework for intermittency

It should be pointed out that the similarity hypotheses have above been derived within a Lagrangian framework but were originally presented in an Eulerian context, considering local spatial averages of the dissipation. Indeed, in the literature, it is more common (Benzi, Ciliberto, Tripiccione, Baudet, Massaioli, and Succi 1993) to exhibit intermittency on the Eulerian velocity increments, defined by:

$$\Delta_\ell u(x,t) := u(x+\ell,t) - u(x,t). \tag{1.46}$$

And the Eulerian velocity structure functions:

$$D_p^E(\ell) := \langle [\Delta_\ell u(x,t)]^p \rangle \,. \tag{1.47}$$

The K41 similarity hypothesis in the Eulerian framework can be written as:

$$\forall \eta \ll \ell \ll L, \quad D_p^E(\ell) \propto \langle \varepsilon \rangle^{p/3} \, \ell^{p/3}. \tag{1.48}$$

And the K62 similarity hypothesis becomes:

$$\forall \eta \ll \ell \ll L, \quad D_p^E(\ell) \propto \left\langle \varepsilon^{p/3} \right\rangle \ell^{p/3} \propto \ell^{\xi(p)}, \tag{1.49}$$

where $\xi(p)$, the intermittency exponent is $\xi(p) = p/3$ in K41 and deviates from the linear behavior in the refined theory K62.

The K41 hypothesis is only verified for the first moments of the Eulerian velocity structure functions:

- for $p = 2$, the hypothesis explains the $-5/3$ slope of the energy spectrum, as demonstrated in Sec. 1.1.4;
- for $p = 3$, the scaling is rigorously demonstrated from the Navier-Stokes equations and results in the $4/5$ scaling. An exact relation between D_2^E and D_3^E was obtained by Kolmogorov (1941a), starting with equations for homogeneous isotropic turbulence $D_3^E = -\frac{4}{5} \langle \varepsilon \rangle \, \ell + 6\nu \frac{\partial D_2^E}{\partial \ell}$. In the inertial range, the viscous term can be neglected and reduces to the $4/5$ law: $D_3^E(\ell) = -\frac{4}{5} \langle \varepsilon \rangle \, \ell$;
- for larger p, Benzi, Ciliberto, Tripiccione, Baudet, Massaioli, and Succi (1993) showed that scaling properties of the velocity increments can be extended up to the dissipative range under the form $D_p^E \propto \left(D_3^E\right)^{\xi(p)/\xi(3)}$, where $\xi(p)$ substantially deviates from the linear K41 law.

Many models have been proposed to explain the intermittency in $\xi(p)$. The most famous are the log-normal model (the distribution of the energy dissipation is log-normal) (Kolmogorov 1962; Yaglom 1966), and the multifractal model (the energy dissipation has a multifractal measure) (Frisch 1985). In the following section, we present the cascade model of Yaglom (1966), a multiplicative cascade which formalism has been adopted by all later models.

1.3.2 The cascade model of Yaglom

In the Eulerian framework, discrete cascade models and later continuous random fields were developed. Yaglom (1966) proposed a model of multiplicative cascade where eddies can be seen as

an ensemble of cells. The largest scale is represented by a unique cell of size L and is then divided into smallest cells of size $\ell_1 = L/\lambda$ where λ is the constant scale ratio of the cascade model. This process is repeated until the smallest scales are reached, with the subdivision $\ell_N = \eta = L/\lambda^N$. The energy is transferred from one cell generation to the next with a positive ratio given by a random variable α_i with $\langle \alpha_i \rangle = 1$ that are independent and identically distributed. We can define for each cell of size ℓ_n the energy dissipation rate through it:

$$\varepsilon_{\ell_n} = \alpha_1 \alpha_2 ... \alpha_n \langle \varepsilon \rangle . \tag{1.50}$$

Following the independence of the random variables α_i, it is straightforward to calculate the moments of any coarse-grained dissipation ε_{ℓ_n}:

$$\begin{aligned} \langle (\varepsilon_{\ell_n})^p \rangle &= \langle \varepsilon \rangle^p \prod_{i=1}^{n} \langle (\alpha_i)^p \rangle \\ &= \langle \varepsilon \rangle^p \langle \alpha_i^p \rangle^n \\ &= \langle \varepsilon \rangle^p \left(\frac{\ell_n}{L} \right)^{K(p)}, \end{aligned} \tag{1.51}$$

where we used $n = \ln_\lambda (L/\ell_n)$ and $K(p) = -\ln_\lambda \langle \alpha^p \rangle$. Finally, the exponents $K(p)$ and $\xi(p)$ are related to each other according to the refined similarity hypothesis of Eq. (1.49):

$$D_p^E(\ell) \propto \left\langle \varepsilon^{p/3} \right\rangle \ell^{p/3} = \langle \varepsilon \rangle^{p/3} \left(\frac{\ell}{L} \right)^{K(p/3)} \ell^{p/3} = \ell^{\xi(p)}. \tag{1.52}$$

And therefore $\xi(p) = K(p/3) + p/3$.

Depending on the distribution of the α_i, different forms of $\xi(p)$ are found (Frisch et al. 1978; Benzi et al. 1984; Meneveau and Sreenivasan 1987)). Consistent with K62, $\varepsilon = \varepsilon_\eta = \alpha_1 \alpha_2 ... \alpha_N \langle \varepsilon \rangle$ is log-normal according to the central limit theorem, assuming it applies.

Yaglom (1966) assumed a log-normal distribution for α. We retrieve a quadratic form for $K(p) = \frac{\lambda_I}{2}(p^2 - p)$, where we denote $\lambda_I = K(2)$ the so-called intermittency parameter. The structure function exponent is

$$\xi(p) = \frac{p}{3} - \frac{\lambda_I}{18}(p^2 - 3p). \tag{1.53}$$

Other discrete models were also formulated later and the reader is referred to the exhaustive review of Seuront, Yamazaki, and Schmitt (2005).

1.3.3 Acceleration statistics

The statistics of Lagrangian velocities and accelerations of fluid particles in turbulence have been the focus of several experimental works (Voth et al. 1998; La Porta et al. 2001; Mordant et al. 2001; Mordant et al. 2004) and numerical studies (Yeung 1997; Vedula and Yeung 1999; Biferale et al. 2005; Yeung et al. 2006; Yeung et al. 2007). Numerous works in these fields attempt to develop a stochastic model capable of reproducing these statistics, and in particular their intermittent

nature.

The fluid particle acceleration $\boldsymbol{a}(t)$ in a turbulent flow can be defined as:

$$\boldsymbol{a}(t) := \lim_{\tau \to 0} \frac{\Delta_\tau \boldsymbol{u}(t)}{\tau}. \tag{1.54}$$

Therefore we expect the acceleration properties to inherit from previous properties of the velocity increments.

Acceleration variance consistent with K41

According to Eq. (1.38), valid in the dissipation range, we have $\left\langle (\Delta_\tau u)^2 \right\rangle = a_0 \left\langle \varepsilon \right\rangle^{3/2} \nu^{-1/2} \tau^2$. With the definition of acceleration, we obtain:

$$\left\langle a^2 \right\rangle = a_0 \left\langle \varepsilon \right\rangle^{3/2} \nu^{-1/2} = a_0 a_\eta^2. \tag{1.55}$$

It has been observed that a_0 has a strong Reynolds-number dependence: The agreement with DNS $a_0 = 0.13 \mathrm{Re}_\lambda^{0.64}$ found by Sawford (1991) was later improved in Sawford, Yeung, Borgas, Vedula, La Porta, Crawford, and Bodenschatz (2003) as $a_0 = 5/(1 + 110/\mathrm{Re}_\lambda)$. We investigate if this Reynolds-number dependence can be explained by K62.

Conditional acceleration consistent with K62

According to K62, acceleration is conditionned by the local dissipation value:

$$\left\langle a^2 | \varepsilon \right\rangle = \overline{a_0} \varepsilon^{3/2} \nu^{-1/2}, \tag{1.56}$$

where $\overline{a_0}$ is a universal constant. This yields:

$$\left\langle a^2 \right\rangle = \overline{a_0} \left\langle \varepsilon^{3/2} \right\rangle \nu^{-1/2}. \tag{1.57}$$

Acceleration variance consistent with K62

To match the two acceleration predictions of the theories Eq. (1.55) and (1.57), we are looking for a relation between $\left\langle \varepsilon^{3/2} \right\rangle$ and $\left\langle \varepsilon \right\rangle^{3/2}$. This is provided by the third hypothesis of K62 or by the model of Yaglom (1966), which both assume $\log \varepsilon \sim \mathcal{N}(\mu_{\log \varepsilon}, \sigma^2_{\log \varepsilon})$ and based on Eq. (1.45), $\sigma^2_{\log \varepsilon} = a + b \log \mathrm{Re}_\lambda$. Therefore, one can easily derive the moments of ε (calculations will be detailed in Sec. 3.4.3) and obtain:

$$\left\langle \varepsilon^{3/2} \right\rangle = \left\langle \varepsilon \right\rangle^{3/2} \exp\left(\frac{3}{8} a\right) \mathrm{Re}_\lambda^{b\frac{3}{8}}. \tag{1.58}$$

Matching Eq. (1.55) and (1.57), we find a correction term for the pseudo-universal constant of K41:

$$a_0 = \overline{a_0} \frac{\left\langle \varepsilon^{3/2} \right\rangle}{\left\langle \varepsilon \right\rangle^{3/2}} = \overline{a_0} \exp\left(\frac{3}{8} a\right) \mathrm{Re}_\lambda^{b\frac{3}{8}}. \tag{1.59}$$

This dependency of a_0 with the Reynolds number was reported in Pope and Chen (1990), Sawford (1991).

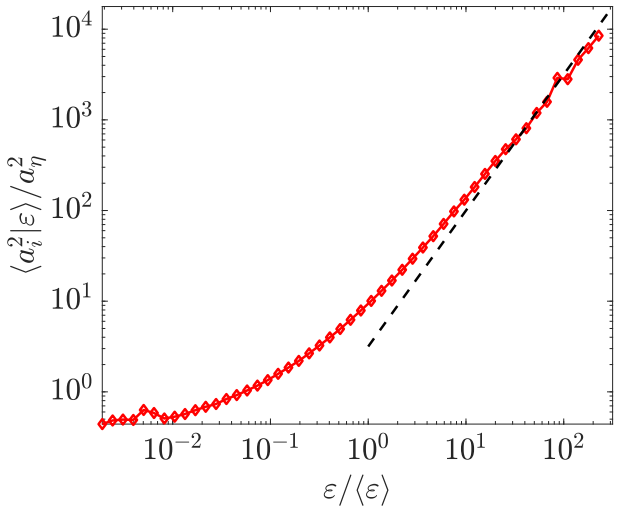

Figure 1.9. Variance of the acceleration of a fluid particle conditioned by the local value of the dissipation rate. The black dashed line represents a 3/2 slope. Dataset from (Lanotte, Calzavarini, Toschi, Bec, Biferale, and Cencini 2011).

Scaling of acceleration variance with local dissipation

Figure 1.9 shows the normalized conditional acceleration as a function of the local dissipation. It is expected to scale as a power law of $3/2$ since:

$$\frac{\langle a^2|\varepsilon\rangle}{a_\eta^2} \sim \frac{\varepsilon^{3/2}}{\langle\varepsilon\rangle^{3/2}}. \tag{1.60}$$

For large values of ε fluctuations, we notice that the conditional variance follows a power law in $\varepsilon^{3/2}$ for $\varepsilon \gg \langle\varepsilon\rangle$. For small fluctuations, we find that the value of the conditional acceleration seems to tend toward an asymptotic value, which depends on the Reynolds number (Zamansky 2021).

Conclusion

In this chapter, we have introduced turbulent flows, in particular their random nature and consequently the need for a statistical description. One and two-point statistics have been derived and lead to the definition of characteristic times and scales of turbulence. The extreme scales (Kolmogorov and integral scales) define an interval on which turbulence can be universally characterized.

We have introduced the founding theories of turbulence, and have in particular exposed the notion of intermittency. The main theories and models are recalled in Table 1.1 and we distinguish the behavior in the inertial range and in the dissipative range.

All the turbulent models discussed and developed throughout this thesis will be validated according to the main metrics, properties and theories discussed in this chapter. In the next chapter, we introduce the main turbulence models and simulations used in literature.

Theory	**Inertial range**	**Dissipative range**
Cascade of Richardson	$\langle\varepsilon\rangle \sim \frac{u_\ell^2}{\tau_\ell} \sim \frac{u_\ell^3}{\ell} \sim C$	$\mathrm{Re}_\eta = \frac{u_\eta \eta}{\nu} = 1$
Energy Spectrum	$E(\kappa) \sim \kappa^{-5/3}$	
K41	$\langle[\Delta_\tau u]^p\rangle = \mathcal{C}_0 \langle\varepsilon\rangle^{p/2} \tau^{p/2}$ $\langle[\Delta_\ell u]^p\rangle \sim \langle\varepsilon\rangle^{p/3} \ell^{p/3}$ verified for first moments only	$\left\langle[\Delta_\tau u]^2\right\rangle = a_0 \nu^{-1/2} \langle\varepsilon\rangle \tau^2$ $\rightarrow \left\langle a^2\right\rangle = a_0 a_\eta^2$ but a_0 Reynolds dependent
K62	$\langle[\Delta_\tau u]^p \vert \varepsilon^\tau\rangle = \mathcal{C}_p (\varepsilon^\tau)^{p/2} \tau^{p/2}$ $\langle[\Delta_\tau u]^p\rangle \sim \left\langle(\varepsilon^\tau)^{p/2}\right\rangle \tau^{p/2} \sim \tau^{\xi(p)}$ with ε^τ log-normal	$\left\langle a^2 \vert \varepsilon\right\rangle = \overline{a_0} \varepsilon^{3/2} \nu^{-1/2}$ $\rightarrow a_0 = f(\overline{a_0}, \mathrm{Re}_\lambda)$
Yaglom Cascade	$\varepsilon_{\ell_n} = \alpha_1 ... \alpha_n \langle\varepsilon\rangle$ where α_i iid $\rightarrow \varepsilon$ log-normal	

Table 1.1. Summary of the main theories in turbulence.

Chapter 2

Modeling and simulation of turbulent flows

Navier-Stokes equations governing the fluid motion take into account properly all the interactions in the motion of the fluid. However, no analytical solution exists for the general Navier-Stokes equations, except for some specific cases such as inviscid flows. Therefore, their resolution requires numerical methods and high performance computing.

In this chapter, we present the main approaches to turbulence simulation, from the most accurate and expensive (DNS) to reduced-order models, such as RANS or LES. We discuss the advantages and drawbacks of each, in terms of fidelity, modeling needs and computational costs. We also introduce the numerical framework of this thesis, the homogeneous isotropic turbulence (HIT), while the presentation of the different computational codes and database used in this thesis is provided in Sec. 2.4.

2.1 Direct numerical simulation

The direct numerical simulation (DNS) consists in solving all the scales of the flow. Each simulation corresponds to a single realization of the flow. This is the simplest approach since it does not require an additional physical model but only a numerical method strategy for solving the Navier-Stokes equation. It is also the most accurate and detailed approach in level of description. However, the computational cost of a simulation is largely determined by the resolution requirements (Pope 2000), i.e. spatial and temporal discretizations.

Regarding the spatial discretization:

- The grid spacing Δx must be small enough to resolve the dissipative scales: $\Delta x \lessapprox \eta$. More precisely, Yeung and Pope (1989) have shown that $\kappa_{\max}\eta \geq 1.5$ is the criterion for good resolution of the smallest scales but this threshold actually depends on the numerical scheme.
- The domain of simulation must be large enough to represent the energy-containing motions of size L, hence the number of points N_x in a given direction of the mesh must verify $N_x \Delta x > L$.

The two previous conditions imply $N_x^3 \geq \mathrm{Re}_L^{9/4}$, and the dependence of the number of mesh points on the Reynolds number thus becomes explicit.

For the temporal discretization, the time step Δt used to advance the solution is also limited by considerations of numerical accuracy.

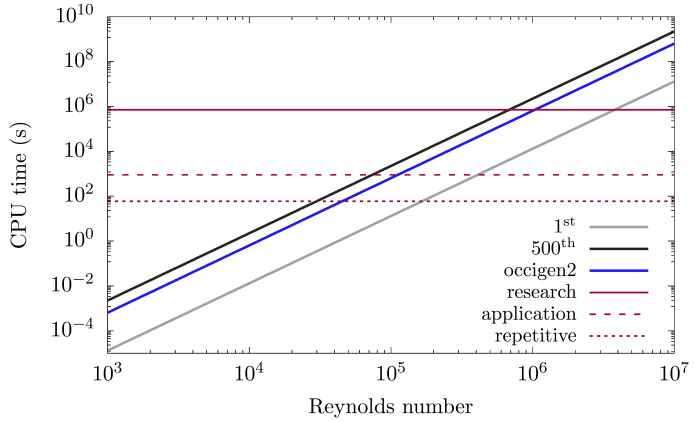

Figure 2.1. CPU time of different computers to compute homogeneous isotropic turbulence according to Reynolds numbers. Times deemed acceptables for research (200 hours), applications (15 minutes) and repetitive computations (1 minute) are indicated as a reference. Figure from Mercier (2020).

- Due to the intrinsically multi-scale nature of the problem, the fast scales are usually unresolved by implicit strategies. An explicit time integration scheme must respect the Courant-Friedrichs-Lewy (CFL) condition, which imposes a criterion for the time discretization step: $\mathcal{C} = \sigma_u \Delta t / \Delta x < 1$;
- The total simulation time interval must be larger than the Lagrangian integral time scale $T_L \sim L/\sigma_u$, hence $N_t \Delta t > T_L$.

Again, combining those two conditions, we get that the total number of time step N_t is proportional to $L/\mathcal{C}\eta$ and using the relation of Eq. (1.8), $N_t \sim \mathrm{Re}_L^{3/4}/\mathcal{C}$ and consequently, the number of time steps grows also as a power law of the Reynolds number.

To give an example of a typical academic simulation, Fig. 2.1 gives the CPU time required to compute homogeneous isotropic turbulence (HIT) for increasing Reynolds numbers on different computers. Even with the best computers, the range of turbulence simulations is very limited.

To give an example of industrial order of magnitude, if we want to solve the external flow at the end of the fuselage of an Airbus A380 of length $\mathcal{L} = 80$ m, flying at Mach speed $M = 0.85$, under pressure $P = 2.5\ 10^4$ Pa and temperature $T = 220$ K, the Reynolds number of such flow is $\mathrm{Re} = 5.7\ 10^8$. The number of points necessary to solve the problem is therefore $5\ 10^{19}$. Many industrial applications are therefore not possible with such an approach, which can only be accessible for flows with low or moderate Reynolds numbers. For this reason, its usage is limited to the academic field and is mainly considered as a numerical experiment tool.

2.2 Dimensionality reduction strategies for turbulence

In realistic configurations, the multi-scale character of the flows does not allow to simulate all the scales of the problem, and the DNS is therefore too expensive. Reduced-order methods have therefore been developed in order to reduce computational costs. The idea of this section is to introduce the classical strategies of reduced-order turbulence representations. An example of such reduced-order simulation (ROS) is given in Fig. 2.2(b) and can be compared to a DNS resolution in Fig. 2.2(a).

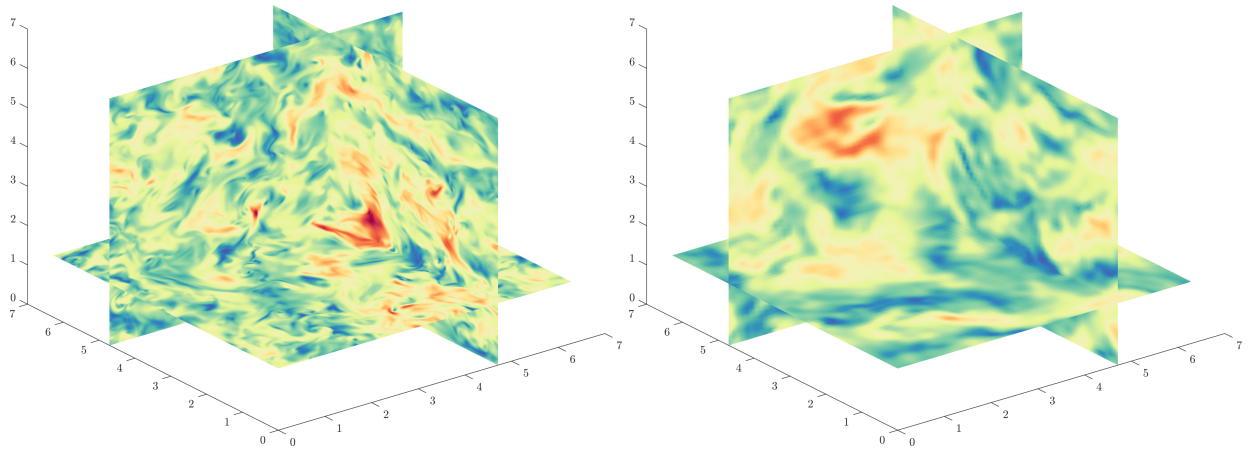

(a) DNS (b) LES

Figure 2.2. Snapshot of velocity field from a DNS (a) and LES (b) simulations performed with Fieldz code and corresponding to $\mathrm{Re}_\lambda = 140$.

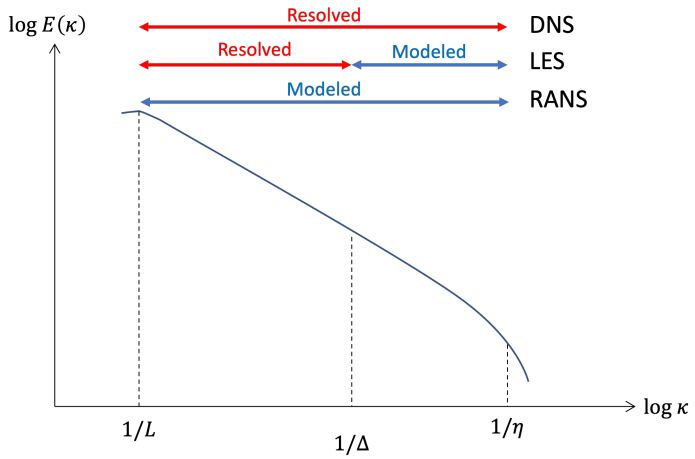

Figure 2.3. Scheme of the energy spectrum resolved or modeled depending on the turbulence simulation (DNS, LES, RANS).

We have seen in Chap. 1 that the fluid is described by its velocity and pressure field, which are discretized on a very large number of points due to scale separation: $\mathrm{Re}_L \sim (T_L/\tau_\eta)^2$. This gives the problem its high dimensionality and its very high numerical cost.

Therefore, the objective of the reduction strategies is to reduce the number of degrees of freedom and hence assume a more regular solution. This operation is performed using ensemble averaging or filtering operators. In the rest of the manuscript, we will generally refer to a reduced-order fluid description to encompass the various possible reduction techniques indifferently.
In the following, we present two classical reduction strategies: the Reynolds Averaged Navier-Stokes (RANS) and the Large Eddy Simulation (LES). Figure 2.3 is a scheme of typical turbulent energy spectrum and it shows the resolved and modeled scales for the three strategies introduced in the chapter: DNS, which resolved all scales, RANS, which models all scales of turbulence, and LES, which resolved only large scales of the flow while modeling the smallest ones.

2.2.1 Reynolds averaged Navier-Stokes

Reynolds decomposition

The use of the Reynolds decomposition is justified when dealing with a phenomenon whose spectrum can be separated into two clearly distinct parts:

- a band of low frequencies or quasi-permanent regime, with an average contribution that is if not constant, at least varies little over time;
- a band of transient regimes of high frequency and zero average contribution.

The Reynolds decomposition of the velocity field gives:

$$\boldsymbol{u}(\boldsymbol{x},t) = \langle \boldsymbol{u}(\boldsymbol{x},t)\rangle + \boldsymbol{u'}(\boldsymbol{x},t), \tag{2.1}$$

where the notation $\langle \boldsymbol{u}(\boldsymbol{x},t)\rangle$ here is the ensemble or time average, and $\boldsymbol{u'}(\boldsymbol{x},t)$ designates the fluctuating part. The same holds for other scalar quantities such as pressure:

$$p(\boldsymbol{x},t) = \langle p(\boldsymbol{x},t)\rangle + p'(\boldsymbol{x},t). \tag{2.2}$$

The RANS equations are obtained by substituting expressions of this form for the flow variables into the instantaneous continuity and momentum equations taking a time (or ensemble) average. For incompressible flows, we can average the Navier-Stokes equation Eq. (1.1) and we obtain:

$$\begin{cases} \dfrac{\partial \langle u_i\rangle}{\partial x_i} &= 0, \\ \dfrac{\partial \langle u_i\rangle}{\partial t} + \dfrac{\partial \langle u_j\rangle \langle u_i\rangle}{\partial x_j} &= \langle f_{ext,i}\rangle - \dfrac{1}{\rho}\dfrac{\partial \langle p\rangle}{\partial x_i} + \nu \dfrac{\partial^2 \langle u_i\rangle}{\partial x_j \partial x_j} + \dfrac{1}{\rho}\dfrac{\partial \tau_{ij}^R}{\partial x_j}. \end{cases} \tag{2.3}$$

The last term introduces the Reynolds stress tensor, very similar to the viscous stress tensor τ_{ij} defined in Eq. (1.2):

$$\tau_{ij}^R := -\rho \left\langle u_i' u_j' \right\rangle. \tag{2.4}$$

It represents the effects of turbulence and it must be modeled in order to close Eq. 2.3.

RANS closures

The Boussinesq hypothesis is the most common method to relate the turbulence stresses to the mean flow:

$$\begin{aligned} \tau_{ij}^R + \frac{1}{3}\tau_{kk}^R \delta_{ij} &= 2\mu_t \left\langle S_{ij}\right\rangle, \\ \tau_{ij}^R &= 2\mu_t \left\langle S_{ij}\right\rangle - \frac{2}{3}\left\langle k\right\rangle \delta_{ij}. \end{aligned} \tag{2.5}$$

Note that a new proportionality constant $\mu_t > 0$, the turbulence eddy viscosity, has been introduced. Models of this type are known as eddy viscosity models.

The Boussinesq hypothesis is used in many models: the Spalart-Allmaras model, the $k-\varepsilon$ model and the $k-\omega$ model. It has the advantage of being computationally affordable since it only requires the additional calculation of this turbulent viscosity. In the case of the Spalart-Allmaras

model, only one additional equation is required, and for the other models, two additional transport equations are solved. Then, μ_t is obtained as a function of these two transported variables. In strongly anisotropic cases however, other types of models will be preferred because of the isotropy of the μ_t term. In this case, each term in the Reynolds tensor must be solved separately.

Stochastic Lagrangian classically used in PDF methods can also lead to Reynolds-stress models (Haworth and Pope 1986). In particular, Pope (1994) has shown that to every stochastic Lagrangian model there is a unique corresponding second-moment closure. Stochastic models are discussed in Chap. 3.

2.2.2 Large Eddy Simulation

In LES, large scales are solved directly, while small scales must be modeled (see Fig. 2.3). The LES is thus a compromise between the DNS and the RANS simulation in terms of resolved scales. LES is attractive since mass, momentum, and energy are mainly transported by large eddies. These eddies strongly depend on the type of problem: geometry, boundary conditions, etc. On the contrary, the small scales are less dependent on the geometry: we have already established the universality of these scales, which allows us to develop consistent models. The resolution of large scales naturally allows coarser meshes and larger time steps than for DNS, but still more refined than for RANS simulations.

Filtering operation

The principal idea for LES is to reduce the computational cost by ignoring the smallest length scales, which are the most computationally expensive to resolve, via low-pass filtering of the Navier–Stokes equations. Such a low-pass filtering, which can be viewed as a time- and/or spatial-averaging, effectively removes small-scale information from the numerical solution. This information is not irrelevant, however, and its effect on the flow field must be modeled, a task which is an active area of research for problems in which small-scales can play an important role. The filtered field, denoted with a bar, is defined as:

$$\overline{\phi(\boldsymbol{x},t)} = \int_{-\infty}^{\infty}\int_{-\infty}^{\infty} \phi(\boldsymbol{r},t')G(\boldsymbol{x}-\boldsymbol{r},t-t')\,\mathrm{d}t'\,\mathrm{d}\boldsymbol{r}, \tag{2.6}$$

where G is a convolution kernel: $\overline{\phi} = \phi * G$. The filter kernel G uses cutoff length and time scales, denoted Δ and τ_c, respectively. Scales smaller than these are eliminated from $\overline{\phi}$. Using this definition, any field ϕ may be decomposed into a filtered and sub-filtered (denoted with a prime) contribution, as:

$$\phi = \overline{\phi} + \phi'. \tag{2.7}$$

The filtering operation removes scales associated with high frequencies, and the operation can accordingly be interpreted in Fourier space. For a scalar field $\phi(\boldsymbol{x},t)$, its Fourier transform is $\hat{\phi}(\boldsymbol{k},\omega)$, where $\boldsymbol{k}$ and ω are the spatial wavenumber and temporal frequency. $\hat{\phi}$ can be filtered by the corresponding Fourier transform of the filter kernel, denoted $\hat{G}(\boldsymbol{k},\omega)$.

$$\overline{\hat{\phi}(\boldsymbol{k},\omega)} = \hat{\phi}(\boldsymbol{k},\omega)\hat{G}(\boldsymbol{k},\omega). \tag{2.8}$$

Filter	Physical space	Spectral space
Box filter	$G(\boldsymbol{x}-\boldsymbol{r}) = \begin{cases} \frac{1}{\Delta}, & \text{if } \mid \boldsymbol{x}-\boldsymbol{r} \mid \leq \frac{\Delta}{2} \\ 0, & \text{otherwise} \end{cases}$	$\hat{G}(\boldsymbol{k}) = \frac{\sin(1/2k\Delta)}{1/2k\Delta}$
Gaussian filter	$G(\boldsymbol{x}-\boldsymbol{r}) = \left(\frac{6}{\pi\Delta^2}\right)^{\frac{1}{2}} \exp\left(-\frac{6(\boldsymbol{x}-\boldsymbol{r})^2}{\Delta^2}\right)$	$\hat{G}(\boldsymbol{k}) = \exp\left(-\frac{\boldsymbol{k}^2\Delta^2}{24}\right)$
Sharp filter	$G(\boldsymbol{x}-\boldsymbol{r}) = \frac{\sin(\pi(\boldsymbol{x}-\boldsymbol{r})/\Delta)}{\pi(\boldsymbol{x}-\boldsymbol{r})}$	$\hat{G}(\boldsymbol{k}) = H\left(k_c - \mid k \mid\right), \quad k_c = \frac{\pi}{\Delta}$

Table 2.1. Some classic LES filters and their Fourier spectral representation.

The filter width Δ has an associated cutoff wavenumber $\boldsymbol{\kappa}_c$ and a temporal filter width τ_c associated to a frequency cutoff ω_c.

There are three filters ordinarily used for spatial filtering in LES. The definition of $G(\boldsymbol{x})$ and $\hat{G}(\boldsymbol{k})$ are given in Tab. 2.1. Figure 2.4(a) is a velocity field of HIT produced by a DNS performed with the code Fieldz. Figure 2.4(b) is the same velocity field filtered using a Gaussian filter. The large scales are still clearly identifiable in the second snapshot, but all the small scales have been removed, and the obtained velocity field is smoother. Their turbulent energy spectra are compared in Fig. 2.4(c) and shows the effect of the filtering operation: energy of the large scales is well preserved whereas small scales are filtered out and their energy is considerably reduced.

The filtered Navier-Stokes equations are obtained:

$$\begin{aligned} \frac{\partial \overline{u}_i}{\partial x_i} &= 0 \\ \frac{\partial \overline{u}_i}{\partial t} + \frac{\partial \overline{u}_i \overline{u}_j}{\partial x_j} &= \overline{f_{ext,i}} - \frac{1}{\rho}\frac{\partial \overline{p}}{\partial x_i} + \nu \frac{\partial^2 \overline{u}_i}{\partial x_j \partial x_j} + \frac{1}{\rho}\frac{\partial \tau_{ij}^r}{\partial x_j}, \end{aligned} \tag{2.9}$$

where the sub-grid scale stress tensor is defined as:

$$\tau_{ij}^r = -\rho\left(\overline{u_i u_j} - \overline{u_i}\,\overline{u_j}\right). \tag{2.10}$$

LES closures

Sub-grid scale (SGS) models consist in modeling the unclosed term τ_{ij}^r. This term must account for the interactions among all scales, including filtered and unfiltered scales. Two categories of closures exist, and the reader is referred to Sagaut (2006) for an exhaustive review of classical closure techniques.

- **Functional models**: knowing that the regularized version of the resolved field dissipates less energy than the real flow, the sub-grid scales can be assimilated to an additional diffusion process. Although these models perfectly reproduce the effect of the tensor, they are not derived directly from the exact term, and it is difficult to guarantee their use for a wide range of flow configurations.
- **Structural models**: they do not attempt to recover the unresolved information but rather to reproduce the structure of the sub-grid tensor (Bardina, Ferziger, and Reynolds 1980). We find, among others, the approximate deconvolution, the fractal interpolation, the kinematic simulation...

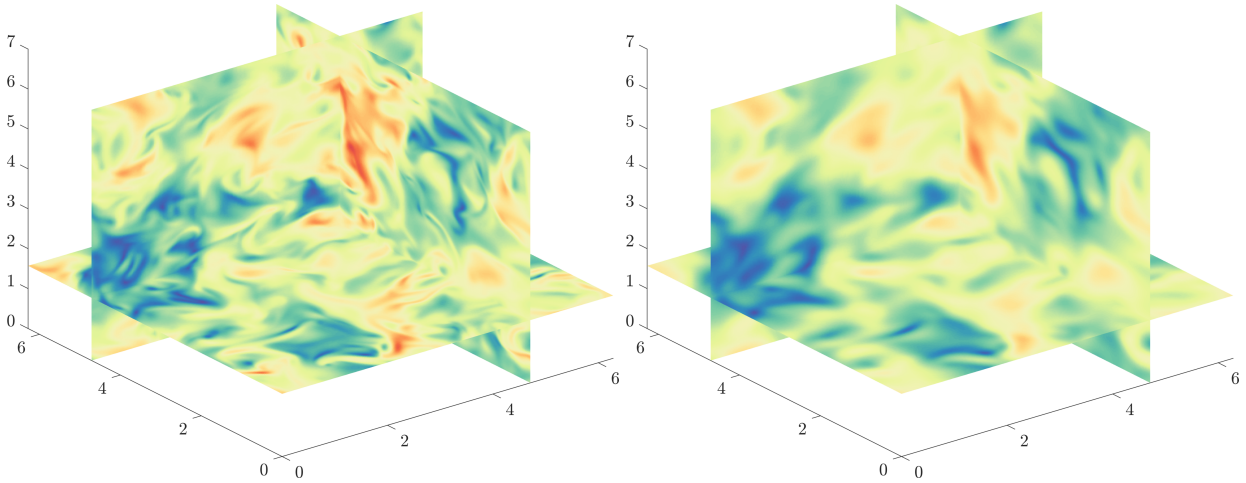

(a) DNS (b) Gaussian-filtered DNS

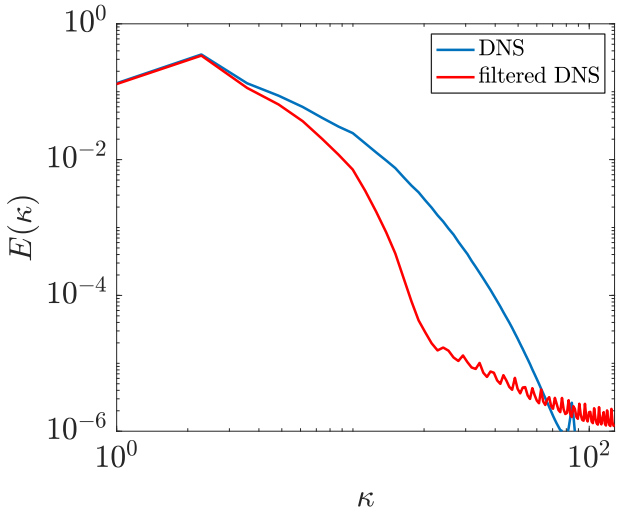

(c) Energy spectrum

Figure 2.4. Snapshots of velocity field obtained by DNS performed with Fieldz at $\mathrm{Re}_\lambda = 140$ (a) ; corresponding filtered velocity field with Gaussian filter (b) ; and associated energy spectra (c).

The functional approach is the most widely used in industrial applications and the most common sub-grid models are based on an eddy viscosity approach, where the effects of sub-grid turbulence are treated by analogy with molecular diffusion, using the Boussinesq hypothesis. The sub-grid scale stress tensor is modeled with:

$$\tau_{ij}^r - \frac{1}{3}\tau_{kk}^r \delta_{ij} = 2\mu_t \overline{S_{ij}}, \tag{2.11}$$

where μ_t is the sub-grid scale turbulent viscosity. $\overline{S_{ij}}$ is the strain rate tensor for the resolved scales. Similarly to the RANS models, there are different LES models depending on how the turbulent viscosity term is modeled or transported.

The simplest model has been proposed by Smagorinsky (1963), in which the eddy viscosity is modeled by:

$$\nu_t = \rho\mu_t = \ell_S^2 |\overline{S}|, \tag{2.12}$$

where ℓ_S is the mixing-length for sub-grid scales and $|\overline{S}| = \sqrt{2\overline{S_{ij}}\ \overline{S_{ij}}}$. The characteristic sub-grid length scale is defined as $\ell_S = C_S\Delta$, where C_S is the Smagorinsky constant and Δ the cut-off length of the LES.

Several studies attempt to derive the value of C_S, but it was found to be not universal. Nonetheless, a value of around 0.1 gives the best results for a wide range of flows. Other models are developed in which the Smagorinsky constant C_S is dynamically computed (Germano, Piomelli, Moin, and Cabot 1991; Lilly 1992).

For sufficiently large Reynolds numbers, the LES cut-off scale is assumed to be in the inertial range, and thus the smallest resolved scales ℓ_S can actually capture the energy rate transferred by the cascade. There is a local equilibrium between the transferred energy through the grid-filter scale Δ and the dissipation of kinetic energy at small sub-grid scales (i.e. up to η). Thus, from the similarity equation Eq. (1.7), we can define the rate of the energy dissipation from these scales:

$$\varepsilon_{\text{sgs}} = 2\nu_t \overline{S_{ij}}\ \overline{S_{ij}} = \nu_t |\overline{S}|^2. \tag{2.13}$$

Consistently, the characteristic sub-grid time scale is defined as:

$$\tau_{\text{sgs}} = |\overline{S}|^{-1}. \tag{2.14}$$

And the characteristic sub-grid velocity is $\sigma_{\text{sgs}} = \sqrt{2/3 k_{\text{sgs}}}$ where

$$k_{\text{sgs}} \propto \Delta^2 |\overline{S}|^2. \tag{2.15}$$

Such eddy viscosity model is completely dissipative and fails to predict any energy transfer from the small scales towards larger ones (backscatter of energy, which can happen in the presence of particles or near walls).

LES is therefore more accurate than RANS simulations, and allows to adapt the cost of the simulation according to the chosen cut-off length scale (taking $\Delta = \eta$, we can retrieve the DNS

equations). Moreover, the unsteady effects are captured. On the other hand, the simulation is more expensive than for RANS, and often requires significant CPU resources.

In turbulence, near-wall flows are significantly affected in a non-trivial way: no-slip boundary conditions modify the mean flow properties such as velocity. Viscosity reduces velocity fluctuations very close to the wall, while shear gradients introduced near the wall induce energy production in regions far from the wall. Near-wall modeling is a challenge for numerical simulation because the characteristic scales of energy production are very small, and the classical scale separation must be revised. Thus, specific models such as Wall Modeled LES must be developed to perform high fidelity wall-bounded simulations. Another solution in this case is the Detached Eddy Simulation approach, in which the unsteady RANS models are employed in the boundary layer, while the LES treatment is applied to the separated regions.

2.2.3 A general framework for reduced-order simulations (ROS)

At first sight, the concepts of Reynolds averaging and spatial filtering seem incompatible, as they yield to different additional terms in the momentum equations (Reynolds stress and sub-grid stress). However, one can note the similarity of their equations: once a turbulence model is introduced into the momentum equations, they no longer contain any information regarding their derivation.
Furthermore, note that the most popular models in both RANS and LES are eddy viscosity models that are used to replace the Reynolds or sub-grid stress tensor. After the introduction of turbulent/eddy viscosity, the RANS and LES momentum equations are formally identical. The only difference lies in the size of the eddy-viscosity provided by the corresponding turbulence model. In this perspective, DNS corresponds to a LES with 100% of the energy of the flow in the reduced flow field, whereas RANS corresponds to a LES with 0% of the energy of the flow in the reduced flow field.

In the rest of the manuscript, we will therefore refer more generally to reduced-order simulation (ROS), which encompasses both RANS and LES simulations, and the term “sub-filter” can also be applied to the RANS model, in the sense that it models all scales of turbulence. In the framework of ROS, the instantaneous fluid velocity is decomposed as:

$$\boldsymbol{u}(\boldsymbol{x},t) = \boldsymbol{U}(\boldsymbol{x},t) + \boldsymbol{u'}(\boldsymbol{x},t), \tag{2.16}$$

where $\boldsymbol{U}$ is numerically solved, and $\boldsymbol{u'}$ requires modeling.

2.3 Homogeneous isotropic turbulence

Homogeneous isotropic turbulence, already introduced in Chap. 1, is an idealized case of turbulence widely studied in the literature (Orszag and Patterson Jr 1972; She, Jackson, and Orszag 1990; George 1992; Wang and Maxey 1993). All the studies carried out in this thesis are based on HIT simulations, either stationary or unsteady, performed in a periodic cubic domain of size $\mathcal{L}$. The simulation of a HIT requires few inputs, including initial data or forcing in the stationary case, that we detail below.

2.3.1 Initialization

In addition to the intrinsic properties of the fluid, such as the viscosity ν, initial information on large scales must also be given. This is usually introduced with the root-mean-square of the turbulence velocity fluctuations, σ_u, or the turbulence kinetic energy $\langle k \rangle$. The energy dissipation rate is also specified, $\langle \varepsilon \rangle$. Thus, the largest scales (integral scale) $L \sim \sigma_u^3 / \langle \varepsilon \rangle$ and the smallest scales (Kolmogorov scale) $\eta = (\nu^3 / \langle \varepsilon \rangle)^{1/4}$ are determined.

2.3.2 Model spectrum

The solution of the Navier-Stokes equations requires initial conditions in the whole domain. Most of the time, in HIT, this will be set with a randomly drawn energy spectrum.
Several models are available to represent the turbulent spectra, all consistent with the Richardson cascade. At high Reynolds, the characteristic slope of the inertial zone in $\kappa^{-5/3}$ must be found. Very simple models, not taking into account the small effects of intermittency on the spectrum can be used for kinematic simulations for example (such models will be used in Part. IV) (Fung, Hunt, Malik, and Perkins 1992):

$$E(\kappa) = \begin{cases} \alpha_k \langle \varepsilon \rangle^{3/2} \kappa^{-5/3}, & \text{for } \kappa_c < \kappa < \kappa_\eta \\ 0 \quad \text{otherwise.} \end{cases} \tag{2.17}$$

In most cases, more realistic energy spectra are used to initialize or force HIT. This is the case for the model of Overholt and Pope (1998):

$$E(\kappa) = C \langle \epsilon \rangle^{2/3} \kappa^{-5/3} f_L(\kappa L) f_\eta(\kappa \eta), \tag{2.18}$$

with :

$$f_L(\kappa L) = \left(\frac{\kappa L}{[(\kappa L)^2 + c_L]^{1/2}} \right)^{5/3+P_0}, \tag{2.19}$$

$$f_\eta(\kappa \eta) = \exp\Big(- \beta[((\kappa \eta)^4 + c_\eta^4)^{1/4} - c_\eta] \Big). \tag{2.20}$$

Functions f_L and f_η characterize the turbulence regions of production and dissipation of energy.
For specified values of $\langle k \rangle$, $\langle \varepsilon \rangle$, and ν, the model spectrum is determined by Eqs. (2.18), (2.19) and (2.20) with $C = 1.5$ and $\beta = 5.2$. The constants c_L and c_η are determined by the requirements that $E(\kappa)$ and $2\nu\kappa^2 E(\kappa)$ integrate to $\langle k \rangle$ and $\langle \varepsilon \rangle$, respectively : $\langle k \rangle = \int_0^\infty E(\kappa)\, \mathrm{d}\kappa$ and $\langle \varepsilon \rangle = \int_0^\infty 2\nu E(\kappa) \kappa^2\, \mathrm{d}\kappa$.

One can confirm the influence of c_L and c_η coefficients in Figs. 2.5(a) and 2.5(b) respectively for low and high wavenumbers. In particular, c_L controls the most energetic scales, defining the maximum of the spectrum whereas c_η controls the smallest wavenumbers. The sensitivity to P_0 coefficients, defined above is plotted in Fig.2.5(c). P_0 controls the slope of the energy spectrum for low wavenumbers.

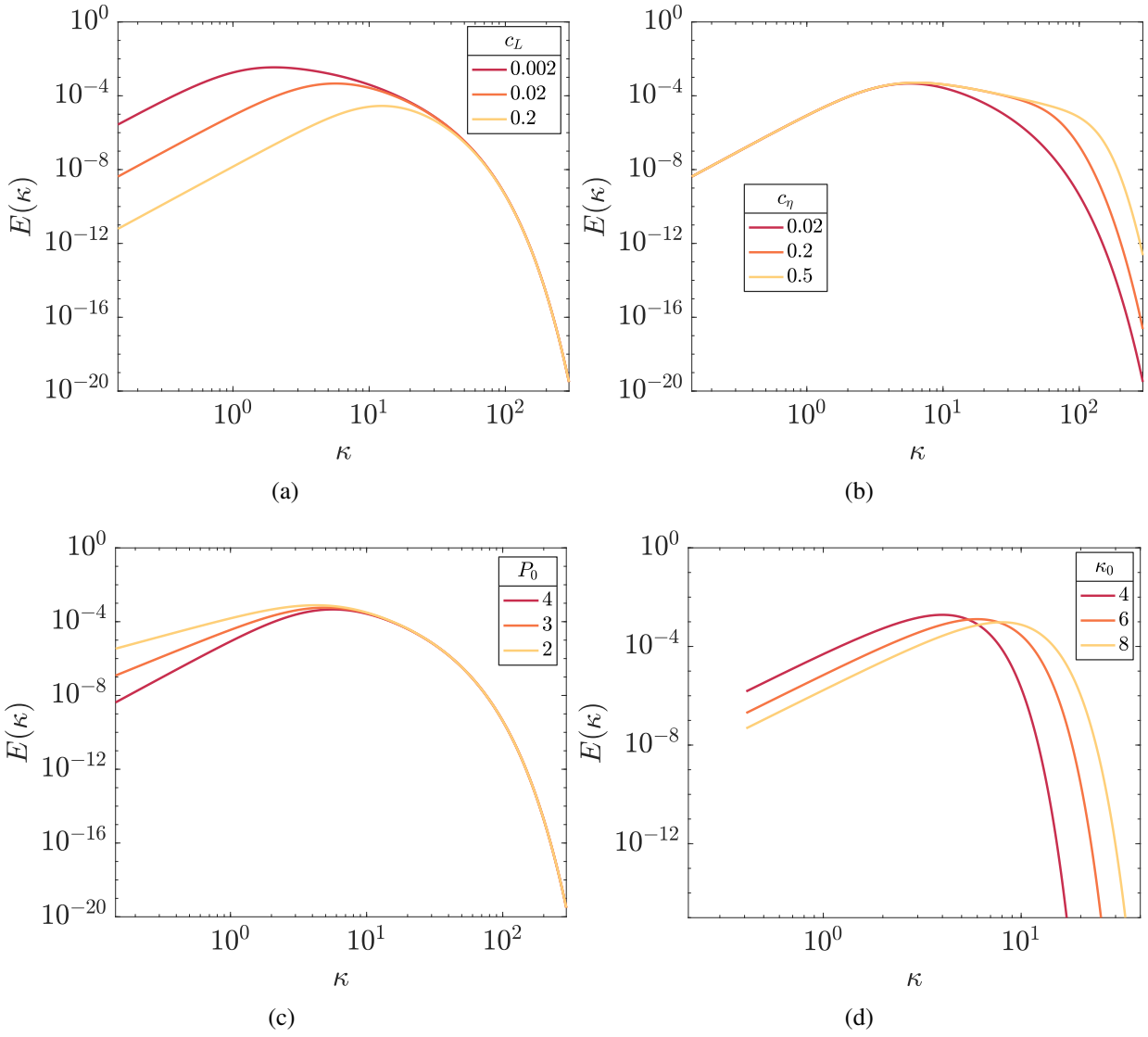

Figure 2.5. Energy spectra obtained with the model of Overholt and Pope (1998) with different parameters c_L (a), c_η (b), P_0 (c), κ_0 (d).

For low Reynolds numbers, isotropic velocity field can also be generated with the Passot-Pouquet spectrum (Passot and Pouquet 1987), which is written as:

$$E(\kappa) = \frac{16\sigma_u^2}{\sqrt{\pi/2}} \frac{\kappa^4}{\kappa_0^5} \exp\left(-\frac{2\kappa^2}{\kappa_0^2}\right), \tag{2.21}$$

where κ_0 is the wavenumber at which the maximum of $E(\kappa)$ occurs and the sensitivity of the model to this parameter is plotted in Fig. 2.5(d).

2.3.3 Turbulence forcing

The isotropic homogeneous turbulence is not stationary, and energy must be added at large scales, in order to simulate energy production and to balance the viscous dissipation. This can be achieved through various forcing methods:

- spectral forcing schemes, developed by Eswaran and Pope (1988) and also used in Février (2000), which requires the inverse fast fourier transform (FFT);
- linerar forcing schemes (Lundgren 2003; Rosales and Meneveau 2005; Toutant 2006), whose ability to reproduce isotropic homogeneous turbulence has been shown to be less efficient than for spectral models by Zeren (2010).

Focusing on the spectral stochastic forcing, the large scales of the flow are forced to maintain a certain energy level. The scale separation and high Reynolds number universality principles described in the previous chapter ensure that the small-scales quantities do not depend on the dynamics of the large scales, and thus on the type of forcing.

The spectral stochastic forcing allows to maintain the stationarity of the flow by acting only on the large scales. Eswaran and Pope (1988) have proposed the following stochastic model, based on a Langevin equation (see Chap. 3 for more details):

$$\mathrm{d}\boldsymbol{b}_m = -\frac{1}{T_F}\boldsymbol{b}_m \,\mathrm{d}t + \sqrt{\frac{2\sigma_F^2}{T_F}}\,\mathrm{d}\boldsymbol{W}_t, \tag{2.22}$$

where $m = 1, 2$ is the real and imaginary part of the 3-component coefficient $\boldsymbol{b}$. T_F and σ_F are respectively the forcing time scale and amplitude of the forcing. This equation is solved for large wavenumbers only and Eswaran and Pope (1988) proposed to perform a projection to ensure the divergence-free property of the fluid:

$$a_i^F = b_i - \kappa_i \frac{\kappa_j b_j}{\boldsymbol{\kappa}^2}. \tag{2.23}$$

Coefficients a_i^F are finally added to the Navier-Stokes equations in spectral space:

$$\frac{\partial u_i}{\partial t}(\boldsymbol{\kappa}, t) = a_i(\boldsymbol{\kappa}, t) + a_i^F(\boldsymbol{\kappa}, t), \tag{2.24}$$

where $a_i(\boldsymbol{\kappa}, t)$ is the convection, diffusion and pressure gradient. The coefficients are then converted to the physical space using inverse Fourier transform and we obtain the forcing term $\boldsymbol{f}_{ext}$.

	N_x	Re_L	Re_λ	η	Δx	$\langle\varepsilon\rangle$	ν	τ_η
t_0	256	21.13	15.9	0.018	0.019	0.0089	0.047	0.335
t_f	256	13.47	12.7	0.037	0.019	0.00052	0.047	1.38

Table 2.2. Properties of the fluid at initial and final time.

2.4 Numerical framework

In this thesis, we are interested in the study of homogeneous isotropic turbulence (HIT) and we have used several simulation tools:

- **Asphodele** is a DNS solver coupled with a Lagrangian solver for the disperse phase. We have used it in our study of the impact of particles on the carrier phase in the two-way coupling context.
- **Fieldz** is a DNS and LES solver developed by Rémi Zamansky. It was used in this work to evaluate the impact of reduced-order models (LES) on the disperse phase.
- Lanotte, Calzavarini, Toschi, Bec, Biferale, and Cencini (2011) provided a database of a stationary HIT, resolved by DNS. The time and spatial steps provide high resolution of velocity dynamics at small scales, and we have relied on this dataset especially to study intermittent statistics.

All of these codes were parallelized and Fieldz and Asphodele were run using HPC resources from:

- the mesocentre computing center of CentraleSupélec and Ecole Normale Supérieure Paris-Saclay supported by CNRS and Region Ile-de-France (http://mesocentre. centralesupelec.fr/);
- CINES under the allocation A00 62B0 6172 made by GENCI (Grand Equipement National de Calcul Intensif).

2.4.1 Asphodele code: DNS of decaying HIT

Asphodele is a code developed by Reveillon and Demoulin (2007) at CORIA laboratory, devoted to the simulation of spray combustion. Direct numerical simulation is performed to solve the unsteady three-dimensional Navier-Stokes and continuity equations with Asphodele using a low Mach formulation of the Navier-Stokes equations (Guichard, Réveillon, and Hauguel 2004). The time resolution is provided by a third order explicit Runge Kutta scheme and spatial evolution is done with a finite difference scheme, the derivatives being computed with a Pade 6th order scheme (Lele 1992).

The domain is a cubic periodic box of size $\mathcal{L} = 5$ meshed with N_x^3 cubic cells, $N_x \in \{128, 256, 512\}$. The initial turbulence field is generated using an isotropic random mode generation and inverse Fourier transform. The initial condition for the carrier phase is set using a Pope spectrum, described in Sec. 2.3.2. The initial parameters of the spectrum are $C = 1.5$, $\beta = 5.2$ and $p_0 = 4$, $c_L = 0.019$, $c_\eta = 0.051$.

The turbulence characteristics of the decaying HIT are given in Table 2.2 for initial time t_0, and final time t_f of simulation. Adequate resolution of statistics is verified with the parameter $\kappa_{max}\eta = 2.9 \geq 1$ (Yeung and Pope 1989). We verify the convergence of the spectra for different grid sizes in Fig. 2.6. Spectra overlapped in their definition domain, which ensures that the smallest scales

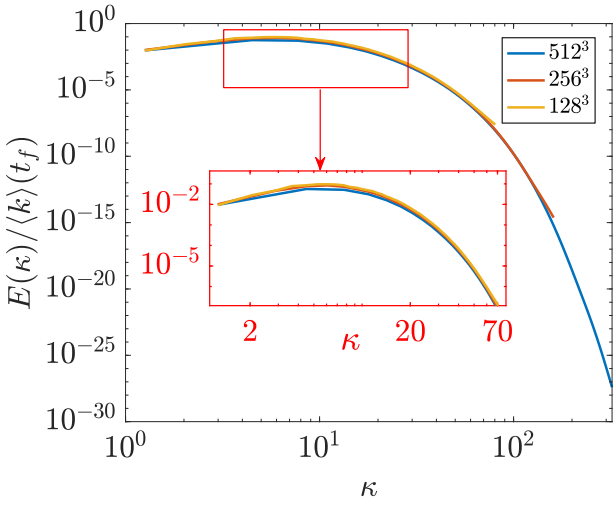

Figure 2.6. Comparison of the normalized energy spectrum for different size of meshgrids. The inset displays a zoom around the largest scales.

are always appropriately resolved.
All the values of the variables presented in this work are dimensionless and the normalizing Reynolds number is $\mathrm{Re} = u_{\mathrm{ref}} L_{\mathrm{ref}}/\nu = 10^3$. The reference velocity u_{ref} and length L_{ref} based on the macroscopic characteristics of the computational domain allow to define a reference time scale for the carrier phase: $t_{\mathrm{ref}} = L_{\mathrm{ref}}/u_{\mathrm{ref}}$. We provide dimensional quantities for illustration purposes, based on an estimated velocity of $u_{\mathrm{ref}} = 1\mathrm{m/s}$ and $L_{\mathrm{ref}} = 1\mathrm{m}$.

Asphodele features a Lagrangian DPS approach for the disperse phase. At initial time, particles are uniformly distributed throughout the domain with the same initial velocity as the carrier phase and periodic boundary conditions are considered.

The solver uses a second-order trilinear algorithm to compute the carrier phase quantities at particle location and projection of Lagrangian quantities on Eulerian fields are performed using a PSI-Cell method (Crowe, Sharma, and Stock 1977). We also developed a Gaussian projection method to compare the influence of projection kernels for two-way coupling contexts.

Also note that Asphodele has been successfully coupled to MUSES3D, a code developed by De Chaisemartin (2009) and the EM2C Math team for the evaluation of Eulerian spray models and methods. MUSES3D was used in the context of this thesis to compare Euler-Euler and Euler-Lagrange strategies in a one-way coupling context in App. A.

2.4.2 Fieldz code: DNS and LES of stationary HIT

The Fieldz code, introduced in Zamansky, Coletti, Massot, and Mani (2016), is considered to transport particles in a stationary incompressible HIT.

This numerical code solves the Navier-Stokes equations in a three-dimensional box with periodic boundary conditions and by applying the divergence-free constraint. Thanks to the periodicity, the different fields can be represented in Fourier space which allows a simplicity and an efficiency of

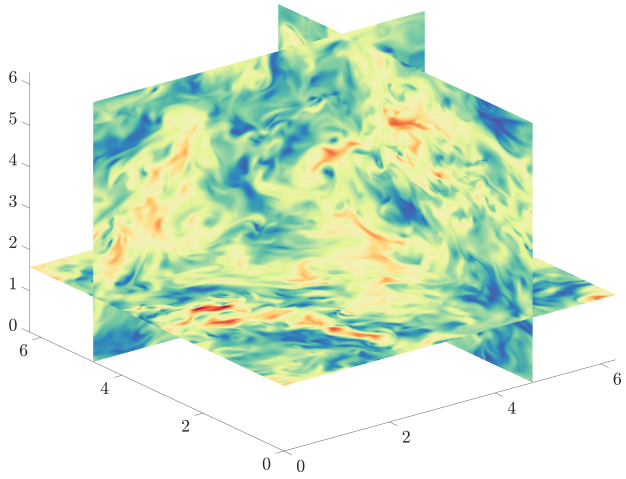

Figure 2.7. Snapshot of velocity field from a simulation performed with Fieldz code and corresponding to $\mathrm{Re}_\lambda = 150$.

	N_x	Re_λ	η	Δx	$\langle\varepsilon\rangle$	ν	τ_η
DNS	1024	235	0.0057	0.006	0.5	0.0008	0.04
DNS	512	150	0.011	0.012	0.5	0.002	0.06
DNS	256	100	0.022	0.024	0.5	0.005	0.1
LES	64	140	0.011	0.098	0.5	0.002	0.06

Table 2.3. Turbulence characteristics of Fieldz

the calculations of the spatial derivatives. The non-linear terms, on the other hand, are computed in physical space, which requires multiple Fourier transforms and inverse transforms at each time step.

A pseudo-spectral approach is used, based on the P3DFFT library, the time integration is done by the second order Adams-Bashford method and the forcing of the flow is ensured with the model of Chen, Doolen, Kraichnan, and She (1992), by forcing only the smallest wavenumbers to maintain the stationarity of the flow.

The flow is either simulated through DNS or with LES, using the standard Smagorinsky model for which the constant is set to $C_S = 0.19$. The turbulence characteristics of the stationary HIT are given in Table 2.3. One can note that statistics obtained with a $N_x = 64$ grid point in LES need to be simulated with a $N_x = 512$ grid points in DNS. Figure 2.7 shows a snapshot of the velocity field obtained with Fieldz with a DNS meshing 512^3.

Lagrangian tracking is used to obtain the evolution of the particle position and velocity. The carrier phase properties at particle location is estimated from cubic spline interpolation (Yeung and Pope 1988). A Gaussian shape regularization is used to project Lagrangian quantities. All simulations are initiated with particles randomly distributed in space.

N_x	Re_λ	η	Δx	$\langle\varepsilon\rangle$	ν	τ_η	Δt
2048	400	3×10^{-3}	3×10^{-3}	0.9	3.5×10^{-4}	2×10^{-2}	1.2×10^{-4}

Table 2.4. (Lanotte et al. 2011)

Being constrained by the numerical cost of DNS, Fieldz and Asphodele have been used in this thesis for low Reynolds number studies, preferring to repeat simulations for parametric studies rather than to perform a high Reynolds number simulation. In order to study such turbulence, we used the dataset described in the following.

2.4.3 DNS dataset of Lanotte et al. (2011): stationary HIT

The dataset of Lanotte, Calzavarini, Toschi, Bec, Biferale, and Cencini (2011) is mentioned throughout this thesis as a reference DNS with fluid particles (tracers) and inertial particles. The Navier-Stokes equations are solved on a cubic grid with periodic conditions. The turbulence is homogenous, isotropic and is forced stationary with a spectral forcing described in Chen, Doolen, Kraichnan, and She (1992). Consistent with Sec. 2.3.1, the viscosity is set to ensure $\Delta x \approx \eta$. A pseudo-spectral algorithm with second-order Adams–Bashforth time-stepping is used. The high spatial Eulerian resolution ensures a smooth differentiable velocity field. The turbulence characteristics of the stationary HIT are given in Table 2.4.

Particle dynamics is updated with a time step from 10 to 1000 times smaller than the Stokes time, providing an accurate resolution of the particle trajectories. Carrier phase velocity at the particle position is determined with a tri-linear interpolation. The Stokes numbers available are: $\mathrm{St} \in \{0; 0.16; 0.6; 1; 2; 3; 5; 10; 20; 30; 40; 50; 70\}$. The trajectory length is $4720\Delta t$ and the total number of particles is 203776.

2.4.4 Main numerical tools and challenges

In this section, we review the different numerical challenges met throughout our work. We briefly present the different codes and post-processing tools that we have implemented, the computational cost involved in terms of memory (RAM) and CPU time.

Regarding the DNS performed with the Fieldz and Asphodele codes, here are some of the numerical challenges related to the nature of our studies:

- In order to observe intermittent statistics in the inertial zone, the scale separation must be sufficiently large, and therefore simulations with large Reynolds numbers must be conducted. To give some orders of magnitude, a DNS running $10T_L$ with Fieldz in 512^3 lasts 22h (40h for a simulation with inertial particles), and a 1024^3 simulation takes 11 days running on 512 processors.
- Each of these simulations must be performed for fluid particles and inertial particles with different Stokes numbers. In particular, the two-way study, a parametric study consisting in varying the three dimensionless parameters, Stokes number, mass loading, number of particles, has required more than 350 different simulations (Chap. 13).

- Lagrangian tracking requires high memory storage. Some of these simulations, with high density in number of particles, required extensive memory access (3000 GB) during the calculation. The storage of some simulation data for post-processing was also essential, and in total, more than 6 To of data were stored during the thesis.

A few developments carried out within these codes can be mentionned: filtering of velocity field in Asphodele and Fieldz to produce *a priori* LES; implementation of a Gaussian projection of Lagrangian quantities onto Eulerian fields in Asphodele; implementation of some stochastic models in Fieldz LES.

The post-processing tools developed during this thesis are numerous but did not raise any major difficulties. In particular, we can mention the statistical analysis tools allowing to obtain the autocorrelation functions, the standardized moments, the conditioned PDF. Different segregation measures have also been implemented: box counting, the Voronoi measure and the interparticle distance.

Finally, most of the numerical efforts of this thesis were focused on the development of new numerical codes implemented in Matlab. Among them:

- Stochastic schemes have been implemented in Matlab, with Euler–Maruyama method. If the Ornstein-Uhlenbeck are very simple to implement, other stochastic processes such as fractional Brownian motion are more challenging (Chevillard 2017).
- The implementation of the Fourier-based kinematic simulation, whose modes are constrained by the periodicity condition.
- The implementation of the 2D and 3D wavelet kinematic simulation, for which numerical details and pseudo codes are available in the thesis of Deriaz and Perrier (2006).

Conclusion

In this chapter, we have presented the main numerical strategies to solve turbulent flows along with the test case of homogeneous isotropic turbulence considered throughout this thesis.
High fidelity methods like DNS have been introduced and criteria on the time and spatial steps have been derived. We have shown how the high-dimensionality of turbulent flows makes their computation over-expensive.

Reduction techniques are therefore required to make reachable the computation of high-Reynolds-number flows. Averaging or filtering the Navier-Stokes equations yields the classical reduced-order models RANS and LES respectively. However, in both cases, the obtained equations require closures of the non-linear Reynolds-stress tensor. Many models have been developed to reproduce the effect of sub-filter scales on the resolved flow.

ROS are well suited for applications dealing with turbulent or reactive flows dominated by large scales. However, the modeling capabilities are more questionable for flows where these processes occur at smaller scales, which is the case, for example, for chemical reactions in turbulent combustion. Therefore, we are interested in the next section in stochastic models to reproduce the small scales statistics, particularly the intermittency, of a fluid particle in a turbulent flow.

Part II

Reproducing intermittency in turbulent flows

Intermittency refers to the extreme variability of a signal that can suddenly and briefly have a high intensity. In turbulence, intermittency is related to energy transfer between scales and it is measured on velocity fluctuations or dissipation statistics. Reproducing the intermittency of turbulence is a major challenge for the modeling of disperse phase flows, since it leads to the occurrence of extreme events. In combustion chambers for example, an isolated particle strongly accelerated by the intermittent turbulent field can locally deform the structure of the flame front. This part aims to introduce a stochastic framework to reproduce the intermittency statistics of a fluid particle in a turbulent flow. Chapter 3 proposes a set of definitions and mathematical tools for this purpose and reviews the stochastic models in the literature by assessing their compatibility with turbulence theories and thus with intermittency. In particular, acceleration and velocity models conditioned on local dissipation are studied, and the intermittent properties of dissipation are highlighted. Chapter 4 introduces a rigorous mathematical framework for constructing such a process based on the Gaussian multiplicative chaos (GMC). We propose an original and elegant formalism to derive families of regularized and then stationarized fractional Brownian motions (FBM) used in the GMC. Chapter 5 establishes the link between the regularization scales introduced in the mathematical formalism and the physical scales of turbulence. A new stochastic model is proposed, reproducing accurate intermittency and combining versatility and computational efficiency.

Chapter 3

Intermittency in stochastic models for turbulence

The stochastic nature of turbulence and the statistical behaviors of velocity fluctuations have been widely investigated, for example by Minier, Chibbaro, and Pope (2014) in order to understand and then reproduce its properties on reduced-order turbulence models. Indeed, we have seen in Chap. 2 that reduced-order models only solve the large scales of the turbulent flow and therefore can give insight into mean velocity fields, their variance (turbulent kinetic energy) or their dissipation at best at the resolved scale. Also, the higher order moments of velocity fluctuations are not systematically recovered, especially the intermittency phenomena.

Deriving stochastic models on fluid particles can have two purposes:

- use stochastic mathematical tools in order to reproduce particular statistics such as high order moments of velocity fluctuations. Thus, Minier and Peirano (2001) shows that by deriving the probability distribution function of stochastic Lagrangian models, it allows to establish particular closures for the ROS models;
- establish relevant stochastic models for fluid particles, in order to adapt them to inertial particles in Chap. 8.

The present chapter first aims at verifying the adequacy of existing models to Kolmogorov theories of turbulence, introduced in Chap. 1. We propose a classification of models relying on both the level of the model (velocity, acceleration, acceleration derivative, etc.) and the type of associated stochastic model (Gaussian, conditioned Gaussian, non-Gaussian). By unifying the notations between the models presented in this chapter, we emphasize the compatibility of the models with K41 or K62, regardless of the type of reduced-order model (indifferently RANS or LES).

In a second step, we properly identify and characterize the intermittent properties of the turbulence. Intermittency refers, in common parlance, to a property of a strongly fluctuating signal, with sudden and brief high activity. When applied to turbulence, the notion of intermittency is often misused to refer to any statistic that is clearly non-Gaussian. Actually it comes from the large fluctuations in the energy transfer between eddies of different scales. Although the non-Gaussianity is a direct consequence, it is not a sufficient characterization, and it should be appropriately defined in this context. We therefore propose a framework with consistent heuristics for assessing intermittency of turbulence statistics.

The chapter is organized as follows: in Sec. 3.1, we introduce the fundamental tools for stochastic

calculus which will be used throughout this thesis. Classical processes such as Ornstein-Uhlenbeck processes are studied, and we also focus on less common processes with interesting properties for our modeling, such as fractional Brownian motion (FBM). In Sec. 3.2, a classification of stochastic models is proposed according to the order of differentiability of the velocity. The closure of these processes is ensured by the stationarity on the one hand, and the consistency with the K41 theory on the other. Yet, these processes do not have intermittent statistics. In Sec. 3.3, the same classification is revisited, this time confronting the models with the K62 theory. The use of dissipation-conditioned statistics hence requires the development of appropriate stochastic models for dissipation. These are the subject of Sec. 3.4.

3.1 Introduction to stochastic processes

This section is mainly inspired from the course on stochastic processes given by Sarah Lemler at Ecole CentraleSupélec.

In the following, $\mathcal{T}$ is a set of indices representing time. Classically, we consider $\mathcal{T} = \mathbb{R}, \mathbb{R}^+, [a, b]$. We will then note $(X_t)_{t\in\mathcal{T}}$ the random process indexed by the t in $\mathcal{T}$. In the following, we consider the probability space $(\Omega, \mathcal{F}, \mathbb{P})$.

3.1.1 Definition of stochastic process

Let (E, d) be a metric space and $\mathcal{E}$ its Borellian set.

Definition 3.1.1 *We call a stochastic process, any family of random variables $(X_t)_{t\in\mathcal{T}}$ defined on a same probability space $(\Omega, \mathcal{F}, \mathbb{P})$ and having values in $(E, \mathcal{E})$.*

Definition 3.1.2 *Let $(X_t)_{t\geq 0}$ be a process defined on $(\Omega, \mathcal{F}, \mathbb{P})$ and having values in E. We say that $(X_t)_{t\geq 0}$ is continuous (or with continuous paths) if for any $\omega \in \Omega, t \mapsto X_t(\omega)$ is continuous.*

3.1.2 Definition of Gaussian process

Definition 3.1.3 (Gaussian random variable) *A random variable $X : \Omega \to \mathbb{R}$ is Gaussian if and only if its probability density function is:*

$$f_{\mu,\sigma^2}(x) = \frac{1}{\sqrt{2\pi}\sigma} \exp\left(-\frac{(x-\mu)^2}{2\sigma^2}\right) \quad \forall x \in \mathbb{R}, \tag{3.1}$$

with $\mathbb{E}(X) = \mu$ and $\mathrm{Var}(X) = \mathbb{E}\left[(X-\mu)^2\right] = \sigma^2$.

Definition 3.1.4 (Gaussian vector) *Let $X_1, \ldots, X_n$ be random variables of $(\Omega, \mathcal{F}, \mathbb{P})$ in $(E, \mathcal{E})$. We say that $X = (X_1, \ldots, X_n)$ is a Gaussian vector if any linear combination of its components follows a Gaussian distribution, i.e. if for any $(\alpha_1, \ldots, \alpha_n) \in \mathbb{R}^n, \alpha_1 X_1 + \cdots + \alpha_n X_n$ follows a Gaussian distribution.*

A Gaussian vector $X = (X_1, \ldots, X_n)$ is entirely determined by its mean

$$\mu = \mathbb{E}(X) = (\mathbb{E}(X_1), \ldots, \mathbb{E}(X_n))$$

and its covariance matrix

$$\Sigma = \mathrm{Cov}(X) = (\mathrm{Cov}(X_i, X_j))_{1\leq i,j\leq n}$$

.

Definition 3.1.5 (Gaussian process) *A process $(X_t)_{t\in\mathcal{T}}$ is Gaussian if for any $(t_1,\dots,t_n)\in\mathcal{T}^n$, $(X_{t_1},\dots,X_{t_n})$ is a Gaussian vector.*
We define its mean (function) μ by $\mu(t) := \mathbb{E}(X_t)$ and its covariance (function) Σ by $\Sigma(s,t) := \mathbb{E}[(X_s-\mu(s))(X_t-\mu(t))] = \mathbb{E}(X_sX_t)-\mu(s)\mu(t)$.

Remark 3.1.6 *The distribution of a Gaussian process is characterized by its mean function and its covariance function.*

3.1.3 Wiener process

Brownian motion is associated to the description of trajectories that evolve in such a disordered way that it seems complicated to predict their evolution, even in a very short time interval. It plays a central role in the theory of stochastic processes. In many theoretical or applied problems, Brownian motion or its associated diffusion processes provide simple models for which calculations of statistics are generally explicit.

Brownian motion was introduced in 1827 by the Scottish botanist Robert Brown to describe the motion of fine organic particles suspended in a gas or fluid. In 1905, Albert Einstein built a probabilistic model to describe the motion of a particle that diffuses: he found that the law of the position at time t of the particle knowing that the initial state is x admits a density that verifies the heat equation and is therefore Gaussian. In 1923, Norbert Wiener rigorously constructed the random Brownian motion with continuous trajectories. Paul Lévy then discovered, with other mathematicians, many properties of Brownian motion and introduced a first form of stochastic differential equations (SDE), the study of which was later systematized by Kiyoshi Itô.

Definition 3.1.7 (Brownian motion) *We call Brownian motion any Gaussian process $W=(W_t)_{t\geq 0}$ with zero mean function and covariance function $\Sigma(s,t)=\min(s,t),\quad \forall t,s\geq 0$.*
If the process is moreover continuous, it is called standard Brownian motion. Three realizations of such process are plotted in Fig. 3.1.

Proposition 3.1.8 *Let $(W_t)_{t\geq 0}$ be a Brownian motion. Then:*
- *The increments of $(W_t)_{t\geq 0}$ are independent, i.e. for all $0\leq t_0<\cdots<t_n$, the variables $\left(W_{t_{k+1}}-W_{t_k}\right)_{0\leq k\leq n}$ are independent.*
- *The increments of $(W_t)_{t\geq 0}$ are stationary, i.e. for all $u>0$, the variables $(W_{u+t}-W_t)_{t\geq 0}$ have the same distribution, namely $\mathcal{N}(0,u)$.*

3.1.4 Itô calculus

The Itô integral is one of the fundamental tools of stochastic calculus. It generalizes the Stieltjes integral in a stochastic way. Let us introduce a Wiener process (or Brownian motion) $W:[0,T]\times\Omega\to\mathbb{R}$, and $X:[0,T]\times\Omega\to\mathbb{R}$ a stochastic process adapted to the natural filtration associated to W_t, then the Itô integral

$$Y_t=\int_0^t X_s\,\mathrm{d}W_s \tag{3.2}$$

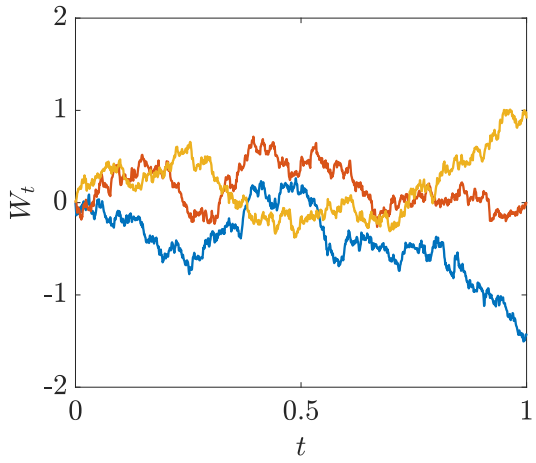

Figure 3.1. Example of three Wiener processes simulated with the following numerical scheme: $W_{t+\Delta t} = W_t + \sqrt{\Delta t}\xi$, where $\xi \sim \mathcal{N}(0,1)$.

is defined by the root mean square limit of

$$\sum_{i=0}^{k-1} X_{t_i} \left(W_{t_i+1} - W_{t_i}\right), \tag{3.3}$$

when the step of the partition $0 = t_0 < t_1 < \cdots < t_k = T$ of $[0,T]$ tends to 0.

An Itô process is defined to be an adapted stochastic process that can be expressed as the sum of an integral with respect to Brownian motion and an integral with respect to time,

$$X_t = X_0 + \int_0^t \sigma_s \,\mathrm{d}W_s + \int_0^t \mu_s \,\mathrm{d}s. \tag{3.4}$$

An important result for the study of Itô processes is Itô's lemma.
Theorem 3.1.9 (Itô Lemma) *For any $f \in \mathcal{C}^2(\mathbb{R})$ and X_t an Itô process as described above, $f(X)$ is itself an Itô process satisfying*

$$\mathrm{d}f(X_t) = f'(X_t)\,\mathrm{d}X_t + \frac{1}{2} f''(X_t)\sigma_t^2 \,\mathrm{d}t. \tag{3.5}$$

3.1.5 Ornstein-Uhlenbeck process

Definition 3.1.10 (Ornstein-Uhlenbeck process) *The Ornstein-Uhlenbeck process is a stochastic process described by the stochastic differential equation:*

$$\begin{cases} \mathrm{d}Y_t = \theta(\mu - Y_t)\,\mathrm{d}t + \Sigma\,\mathrm{d}W_t \\ Y_0 = y, \end{cases} \tag{3.6}$$

where θ, μ and Σ are deterministic parameters.
We are looking for solutions Y_t to this stochastic equation. Let us apply Itô's lemma to the function $f(Y_t, t) = Y_t e^{\theta t}$ to obtain:

$$\mathrm{d}f\,(Y_t, t) = \theta Y_t e^{\theta t}\,\mathrm{d}t + e^{\theta t}\,\mathrm{d}Y_t = e^{\theta t}\theta\mu\,\mathrm{d}t + \Sigma e^{\theta t}\,\mathrm{d}W_t. \tag{3.7}$$

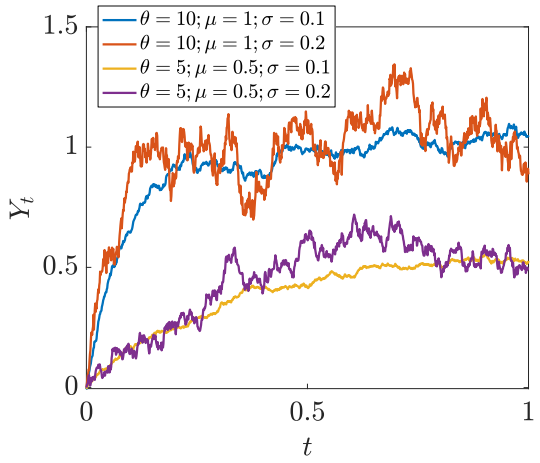

Figure 3.2. Example of Ornstein-Uhlenbeck processes.

Integrating from 0 to t, we obtain

$$\begin{aligned} Y_t e^{\theta t} &= Y_0 + \int_0^t e^{\theta s} \theta \mu \, \mathrm{d}s + \int_0^t \Sigma e^{\theta s} \, \mathrm{d}W_s \\ Y_t &= Y_0 e^{-\theta t} + \mu \left(1 - e^{-\theta t}\right) + \int_0^t \Sigma e^{\theta (s-t)} \, \mathrm{d}W_s. \end{aligned} \tag{3.8}$$

Thus, the first moment is given (assuming Y_0 is a constant) by:

$$\mathbb{E}\left[Y_t\right] = Y_0 e^{-\theta t} + \mu \left(1 - e^{-\theta t}\right). \tag{3.9}$$

In stationary regime (i.e. $t \to \infty$), we have: $\mathbb{E}[Y_t] = \mu$.

We can use the Itô isometry to calculate the covariance:

$$\begin{aligned} \mathrm{cov}\left(Y_s, Y_t\right) &= \mathbb{E}\left[\left(Y_s - \mathbb{E}\left[Y_s\right]\right)\left(Y_t - \mathbb{E}\left[Y_t\right]\right)\right] \\ &= \mathbb{E}\left[\int_0^s \Sigma e^{\theta (u-s)} \, \mathrm{d}W_u \int_0^t \Sigma e^{\theta (v-t)} \, \mathrm{d}W_v\right] \\ &= \Sigma^2 e^{-\theta (s+t)} \mathbb{E}\left[\int_0^s e^{\theta u} \, \mathrm{d}W_u \int_0^t e^{\theta v} \, \mathrm{d}W_v\right] \\ &= \frac{\Sigma^2}{2\theta} e^{-\theta (s+t)} \left(e^{2\theta (\min(t,s))} - 1\right). \end{aligned} \tag{3.10}$$

In stationary regime, the autocorrelation function becomes:

$$\mathrm{cov}\left(Y_t, Y_{t+\tau}\right) = \sigma^2 \mathrm{e}^{-\theta \tau}, \tag{3.11}$$

Figure. 3.2 shows examples of Ornstein-Uhlenbeck processes with different parameters: it is clear that the processes tend towards the mean value μ. Moreover, the characteristic time scale to reach the stationary regime is given by θ^{-1}, and the variance σ determines the roughness of the process.

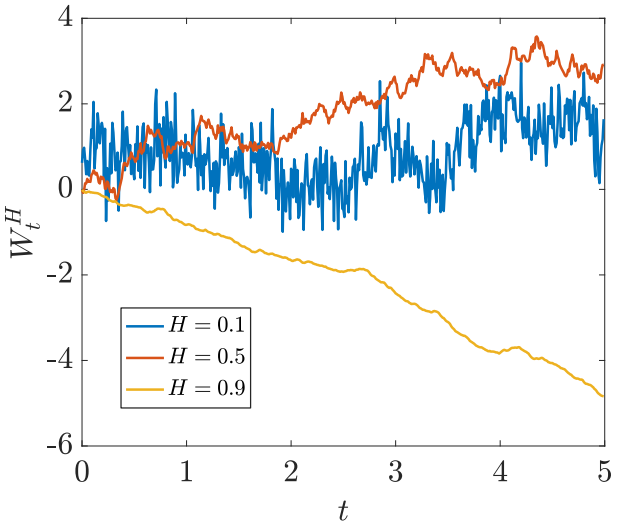

Figure 3.3. Three examples of FBM for different values of H.

3.1.6 Fractional Brownian motion

The fractional Brownian motion (FBM) is a generalization of Brownian motion (Mandelbrot and Van Ness 1968). The field of applications of FBM is wide. Indeed, it is used for example to recreate certain natural landscapes, in particular mountains, but also in hydrology, telecommunications, economy, physics. Unlike those of classical Brownian motion, the increments of such processes are not independent.

Definition 3.1.11 (Fractional Brownian motion) *The FBM is a continuous-time Gaussian process W_t^H on $[0, T]$, that starts at zero, has expectation zero for all t in $[0, T]$, and has the following covariance function:*

$$\mathbb{E}\left[W_t^H W_s^H\right] = \frac{1}{2}(|t|^{2H} + |t-s|^{2H} - |s|^{2H}), \tag{3.12}$$

where H is a real number in $(0, 1)$, called the Hurst index or Hurst parameter.

The Hurst exponent describes the roughness of the resultant motion, with a higher value leading to a smoother motion. Three examples of FBM are plotted in Fig. 3.3, with different values of H. The value of H determines what kind of process the FBM is:

- if $H = 1/2$, the process is a Brownian motion (or Wiener process); it has no memory, its increments are uncorrelated. We denote $W_t^{1/2} = W_t$;
- if $H > 1/2$, the increments of the process are positively correlated. The process is not Markovian but it has long-term memory, because its increments are correlated. The evolution of the series tends to follow trends. If the series has increased previously, there is a strong probability that it will continue to do so. Persistent series have a long-term memory, i.e. there is a long-term correlation between current and future events. Each observation carries the memory of the events that preceded it.
- if $H < 1/2$ then the increments of the process are negatively correlated. The process is not Markovian and has also memory. In this case the successive increases tend to be negatively correlated. An increase in the variable tends to be followed by a decrease, and vice versa.

Mandelbrot and Van Ness (1968) have introduced the following expression of FBM:

$$W_t^H = \int_{-\infty}^{0} \left[(t-s)^{H-1/2} - (-s)^{H-1/2}\right] \mathrm{d}W_s + \int_0^t \left[(t-s)^{H-1/2}\right] \mathrm{d}W_s. \tag{3.13}$$

Without the first integral, the increments of this process are not stationary. McCauley, Gunaratne, and Bassler (2007) have clarified the characterization of long-time correlation, by attributing it not to the scaling property, but rather to the stationarity of the increments of the process.

3.1.7 Some properties of stochastic processes

3.1.7.1 Self-similar process

The self-similarity of a fractal object refers to the fact that the object can be decomposed into sub-units, and then into sub-subunits, which have the same statistical properties as the overall object. Whatever the scale of observation, identical characteristics are therefore observed.

Definition 3.1.12 (Self-similarity) *A stochastic process X_t is said to scale with Hurst exponent α if*

$$X_{at} \sim a^\alpha X_t. \tag{3.14}$$

The best evidence for scaling is to examine the scaling of its density function but in practice, one can look for scaling of the moments:

$$\mathbb{E}\left[X_t^n\right] = \mathbb{E}\left[X_1^n\right] t^{n\alpha} = c_n t^{n\alpha}. \tag{3.15}$$

Note that self-similar processes are necessarily strongly nonstationary by looking at their moments in Eq. (3.15). However, they might have stationary increments.

Example 3.1.13 The fractional Brownian motion is self-similar with Hurst exponent H, since in terms of probability distributions, $W_{at}^H \sim |a|^H W_t^H$.

3.1.7.2 Kolmogorov continuity theorem

The Kolmogorov continuity theorem (Chentsov 1956) guarantees the continuity of a stochastic process (or, more precisely, that it has a "continuous version"), under certain constraints on the moments of its increments:

Theorem 3.1.14 (Kolmogorov continuity) *Suppose that $\left(\Omega, \mathcal{F}, \mathbb{P}, (X_t)_{t\geq 0}\right)$ is a stochastic process with state space $\mathbb{R}^d$. If there are $\alpha, \beta, c > 0$ such that*

$$\mathbb{E}\left(|X_t - X_s|^\alpha\right) \leq c|t-s|^{1+\beta}, \quad s,t \in \mathbb{R}^+, \tag{3.16}$$

then the stochastic process admits a continuous modification $\tilde{X}$ such that:

- *$\tilde{X}$ is sample-continuous;*
- *$\forall t, \quad \mathbb{P}(X_t = \tilde{X}_t) = 1$;*
- *The paths of $\tilde{X}$ are locally γ-Hölder-continuous for every $0 < \gamma < \dfrac{\beta}{\alpha}$.*

Example 3.1.15 The FBM is continuous since its increments $W_t - W_s$ are Gaussian variables with zero mean and with variance:

$$\begin{aligned}\mathbb{E}\left[(W_t - W_s)^2\right] &= \mathbb{E}\left[W_t^2\right] + \mathbb{E}\left[W_s^2\right] - 2\mathbb{E}\left[W_t W_s\right] \\ &= |t|^{2H} + |s|^{2H} - \left(|t|^{2H} + |s|^{2H} - |t-s|^{2H}\right) \\ &= |t-s|^{2H}.\end{aligned} \tag{3.17}$$

Moments of the increments scale like a Gaussian variable with standard deviation $|t-s|^H$:

$$\mathbb{E}\left[|W_t - W_s|^p\right] = \mathbb{E}\left[|N|^p\right]|t-s|^{pH}, \tag{3.18}$$

where $N \sim \mathcal{N}(0,1)$. The Kolmogorov theorem ensures that the FBM has a continuous modification which, with probability one, is locally γ-Hölder continuous for all $\gamma < H - 1/p < H$.

The mathematical tools introduced in this section provide us with basic stochastic models that could be used to reproduce statistics of fluid particle trajectories.
In the following section, we introduce Gaussian stochastic processes that mimics the behavior of fluid particles in stationary HIT. Variance and characteristic time scales can be retrieved according to turbulence theories introduced in Chap. 1.

3.2 Stochastic models for turbulent flows consistent with K41

In a Lagrangian framework, according to the Navier-Stokes equations, in an infinitesimal time interval $\mathrm{d}t$, the velocity of a fluid particle can be predicted by:

$$\begin{cases} \mathrm{d}x_{f,i} &= u_{f,i}\,\mathrm{d}t \\ \mathrm{d}u_{f,i} &= \left(-\dfrac{1}{\rho}\dfrac{\partial p}{\partial x_i} + \nu\dfrac{\partial^2 u_j}{\partial x_j \partial x_j}\right)\mathrm{d}t = a_i\,\mathrm{d}t. \end{cases} \tag{3.19}$$

As introduced in Chap. 2, in a framework of reduced description of turbulence, the instantaneous fluid velocity is decomposed as: $\boldsymbol{u}(\boldsymbol{x},t) = \boldsymbol{U}(\boldsymbol{x},t) + \boldsymbol{u'}(\boldsymbol{x},t)$, where $\boldsymbol{U}$ is numerically solved, but $\boldsymbol{u'}$ requires modeling. With this approach, the trajectory of a Lagrangian fluid element is written by Haworth and Pope (1986) as:

$$\mathrm{d}u_{f,i} = \left(-\frac{1}{\rho}\frac{\partial P}{\partial x_i} + \nu\frac{\partial^2 U_j}{\partial x_j \partial x_j}\right)\mathrm{d}t + \left(-\frac{1}{\rho}\frac{\partial p'}{\partial x_i} + \nu\frac{\partial^2 u'_j}{\partial x_j \partial x_j}\right)\mathrm{d}t \tag{3.20}$$

The first parenthesis is known because the resolved fields P and $\boldsymbol{U}$ are given. However, we need to model the second member, which corresponds to the fluctuating part filtered by the reduced model.

Stochastic models appear to be a powerful tool to model this random part, which we will henceforth note $\mathrm{d}u'_i$ or $a'_i\,\mathrm{d}t$, depending on the level of modeling chosen. In this section, we present first-order models (modeling velocity fluctuations), second order models (modeling acceleration fluctuations), and higher-order models, and we derive closures of these models consistently with K41 hypotheses.

3.2.1 First-order model

An elementary model consists in writing a stochastic Langevin equation on the velocity fluctuations $\mathrm{d}\boldsymbol{u'}$:

$$\mathrm{d}\boldsymbol{u'} = \mathbb{A}\mathbf{u}'\,\mathrm{d}t + \mathbb{B}d\mathbf{W}_t. \tag{3.21}$$

The tensors $\mathbb{A}$ and $\mathbb{B}$ can be simplified as $A\delta_{ij}$ and $B\delta_{ij}$ because of the isotropy of the flow field. In such cases, we will drop the index i in the notation of the components and consider the general following form:

$$\mathrm{d}u' = Au'\,\mathrm{d}t + B\,\mathrm{d}W_t, \tag{3.22}$$

where the reader can recognize an Ornstein-Uhlenbeck process with zero mean as described in Sec. 3.1.5. To identify A and B with physical terms, we use two arguments: the stationarity of the flow and the Kolmogorov similarity hypotheses.

Stationarity

First, let us notice that by dimensional analysis, it is necessary for A to have the dimension of inverse time:

$$A = -1/T_L^\star, \tag{3.23}$$

where $T_L^\star$ is a characteristic time of the fluctuating unresolved scales[1].

We have seen in Sec. 3.1.5 that for such Ornstein-Uhlenbeck processes to be stationary, B is necessarily in the form:

$$B = \sqrt{\frac{2\sigma_\star^2}{T_L^\star}}, \tag{3.24}$$

where $\sigma_\star = \sqrt{\mathbb{E}\left[u'^2\right]}$ represents the characteristic velocity scale of the non-resolved flow scales that must be modeled.

Kolmogorov similarity hypothesis

According to Sec. 3.1.5, the autocorrelation function of this Ornstein-Uhlenbeck process in stationary regime is:

$$R_L^{u'}(\tau) = \mathbb{E}\left[u'(t)u'(t+\tau)\right] = \sigma_\star^2 \exp(-\tau/T_L^\star), \tag{3.25}$$

and it is related to the Lagrangian velocity structure function defined in Eq. (1.34)

$$D_2^L(\tau) = \mathbb{E}\left[\left(u'(t) - u'(t+\tau)\right)^2\right] = 2\left(\sigma_\star^2 - R_L^{u'}(\tau)\right) = 2\sigma_\star^2\left(1 - \exp(-\tau/T_L^\star)\right). \tag{3.26}$$

For small time increments τ compared to $T_L^\star$, we can write a first order expansion of $\exp(-\tau/T_L^\star)$ and we obtain:

$$D_2^L(\tau) \approx 2\sigma_\star^2\tau/T_L^\star. \tag{3.27}$$

[1] The exponent $\star$ refers to a parameter of the unresolved scales, which depends on the reduction applied to the fluid.

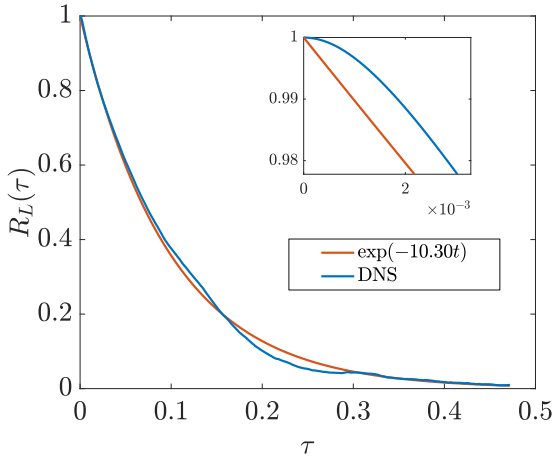

Figure 3.4. Lagrangian autocorrelation of the velocity, compared to an exponential decay. Dataset from Lanotte et al. (2011)

In the inertial range, the Kolmogorov theories predict the behavior of $D_2^L(\tau) = \mathcal{C}_0\varepsilon_\star\tau$, where $\varepsilon_\star$ is either the global or the locally-averaged dissipation. This gives a relation between the three parameters:

$$D_2^L(\tau) = 2\sigma_\star^2\tau/T_L^\star = \mathcal{C}_0\varepsilon_\star\tau. \tag{3.28}$$

We have an expression for $T_L^\star$ and B:

$$T_L^\star = \frac{2\sigma_\star^2}{\mathcal{C}_0\varepsilon_\star}, \quad B = \sqrt{\mathcal{C}_0\varepsilon_\star}. \tag{3.29}$$

Closures for $\sigma_\star$ and $\varepsilon_\star$ will be discussed in Sec. 3.2.2 and depends on the type of ROS.

This first order model has been widely used in literature for RANS or LES applications (Haworth and Pope 1986; Shotorban and Mashayek 2006; Pope and Chen 1990). Yet, first-order models have some limitations, and their validity may become questionable regarding some aspects:

- In particular, they model a non-differentiable velocity process whereas actual fluid particle acceleration cannot be infinite. This deviation from the actual behavior of the velocity autocorrelation is shown in Fig. 3.4, in the inset of the figure, which displays a zoom at the origin.
- Also, the simulated process has Gaussian increments, while experiments and DNS show that the time increments are strongly non-Gaussian (as seen in Sec. 1.3).
- According to K41, inertial range scaling only applies for time increments τ such that $\tau_\eta \ll \tau \ll T_L$, while the scaling produced by the Langevin model of Eq. (3.22) is verified for any time increments[2]. This shows that the Langevin equation provides a physically realistic model of fluid particle behavior only for times $\tau_\eta \ll t \ll T_L$ and these models neglect high time-frequency behavior. However, at low Reynolds numbers, the separation of time scales $\tau_\eta \ll T_L$ is not verified anymore and the need to introduce a second time scale has been addressed with second order models, derived in Sec. 3.2.3.

[2]However, it is necessary to simulate the process by ensuring that the time step is smaller than the characteristic time $\Delta t \ll T_L$

Before introducing other models, we give some hints on the closure of the parameters we have introduced: $\sigma_\star$, $T_L^\star$ and $\varepsilon_\star$, considering the statistics of the resolved fields obtained from reduced-order simulations of turbulence.

3.2.2 Closures of the parameters

We have introduced three parameters to describe the fluctuating scales: $\sigma_\star$, $T_L^\star$ and $\varepsilon_\star$. Consistent with Kolmogorov scaling, we have obtained a relation between them in Eq. (3.29): $T_L^\star = 2\sigma_\star^2/\mathcal{C}_0\varepsilon_\star$. Depending on the type of reduced-order simulation, one can propose models for $\sigma_\star$ and $\varepsilon_\star$.

For stationary HIT, RANS simulation immediately yields $U = \langle u \rangle = 0$ and the stochastic model on u' should be able to reproduce on its own the entire turbulent field. Let us assume for example that the total turbulent kinetic energy $\langle k \rangle$ and the energy dissipation rate $\langle \varepsilon \rangle$ are given . They can be taken as the input of the model: $\sigma_\star = \sigma_u = \sqrt{2/3\,\langle k \rangle}$ and $\varepsilon_\star = \langle \varepsilon \rangle$.

The stochastic equation for $\boldsymbol{u}$ is an Ornstein-Uhlenbeck process:

$$\mathrm{d}\boldsymbol{u}' = -\frac{1}{T_L}\boldsymbol{u}'\,\mathrm{d}t + \sqrt{\mathcal{C}_0\,\langle \varepsilon \rangle}\,\mathrm{d}\boldsymbol{W}_t, \tag{3.30}$$

where T_L is the Lagrangian integral time scale of the flow.

For RANS simulation of inhomogeneous flows, we obtain the generalized Langevin model (Haworth and Pope 1986):

$$\mathrm{d}\boldsymbol{u}' = \left(\frac{-1}{\rho}\nabla P + \nu\nabla^2\boldsymbol{U}\right)\mathrm{d}t - \frac{1}{T_L}\left(\boldsymbol{u}' - \boldsymbol{U}\right)\mathrm{d}t + \sqrt{\mathcal{C}_0\,\langle \varepsilon \rangle}\,\mathrm{d}\boldsymbol{W}_t. \tag{3.31}$$

In LES simulations, $\sigma_\star$ and $\varepsilon_\star$ can be estimated at the sub-grid scale by σ_{sgs} and $\varepsilon_{\mathrm{sgs}}$, depending on the LES model. For model of Smagorinsky, we have $\sigma_{\mathrm{sgs}} \propto |\overline{S}|^2$ and $\varepsilon_{\mathrm{sgs}} \propto |\overline{S}|^3$ (see Sec. 2.2.2).

More advanced and realistic closures have been introduced in the works of Shotorban and Mashayek (2006), Fede, Simonin, Villedieu, and Squires (2006), Knorps and Pozorski (2015) to take into account inhomogeneous, wall-bounded flows, and the reader is referred to the review of Marchioli (2017) for further details.

3.2.3 Second-order model

In order to overcome the limitations of the velocity model discussed above, we can write the velocity as the derivative of an acceleration process. In that case, the fluctuating part in Eq. (3.20) is not modeled using $\mathrm{d}u'$ but rather with $a'\,\mathrm{d}t$. This is for example the case of the second-order model suggested by Sawford (1991):

$$d\boldsymbol{Z} = \mathbb{A}\boldsymbol{Z}\,\mathrm{d}t + \boldsymbol{B}\,\mathrm{d}W_t, \tag{3.32}$$

where $\boldsymbol{Z} = [\boldsymbol{u'}, \boldsymbol{a'}]^T$ is the vector of stochastic process for velocity and acceleration. The drift matrix and diffusion vector can be written as:

$$\mathbb{A} = \begin{pmatrix} 0 & 1 \\ \alpha_1 & \alpha_2 \end{pmatrix} \quad \boldsymbol{B} = \begin{pmatrix} 0 \\ b \end{pmatrix}. \tag{3.33}$$

Let us denote β_1 and β_2 the eigenvalues of $\mathbb{A}$, such that $\alpha_1 = -\beta_1\beta_2$ and $\alpha_2 = (\beta_1 + \beta_2)$. One can also derive: $\alpha_1 = -\dfrac{\sigma_{a'}^2}{\sigma_\star^2}$ and $\alpha_2 = \dfrac{-b^2}{2\sigma_{a'}^2}$.

We follow the same approach as in the previous section: first, the stationarity condition gives a relation between the coefficient b, the coefficients of $\mathbb{A}$, and the variance of the sub-filter velocity $\sigma_\star^2 = \mathbb{E}\left[u'^2\right]$. Secondly, we determine the time scales β_1 and β_2 from the physical parameters, consistent with the first and second hypotheses of Kolmogorov's theories.

Stationarity and reformulation of the process in terms of imbricated Ornstein-Uhlenbeck

Proposition 3.2.1 *Sawford's second-order model can be formulated with imbricated Ornstein-Uhlenbeck in the form:*

$$\begin{cases} \mathrm{d}u' = \beta_1 u' \,\mathrm{d}t + f \,\mathrm{d}t \\ \mathrm{d}f = \beta_2 f \,\mathrm{d}t + b \,\mathrm{d}W_t \end{cases} \tag{3.34}$$

Proof 3.2.2 We introduce f the process defined by $f = a' - \beta_1 u'$ such that

$$\mathrm{d}u' = (\beta_1 u' + f)\,\mathrm{d}t. \tag{3.35}$$

By differentiating f, we have:

$$\mathrm{d}f = \mathrm{d}a' - \beta_1 a' \,\mathrm{d}t = \alpha_1 u' \,\mathrm{d}t + \alpha_2 a' \,\mathrm{d}t + b \,\mathrm{d}W_t - \beta_1 a' \,\mathrm{d}t. \tag{3.36}$$

After identification with the eigenvalues, we obtain:

$$\mathrm{d}f = \beta_2(a' - \beta_1 u')\,\mathrm{d}t + b\,\mathrm{d}W_t = \beta_2 f \,\mathrm{d}t + b\,\mathrm{d}W_t. \tag{3.37}$$

We recognize an Ornstein-Uhlenbeck equation for the process f, with zero mean. Therefore, to ensure the stationarity of the process, we have $b = \sqrt{-2\sigma_f^2\beta_2}$.

We must now determine $\sigma_f^2 = \mathbb{E}\left[f^2\right]$. By multiplying $\mathrm{d}u'$ by u' and averaging, we obtain a relation between $\langle f u' \rangle$ and $\sigma_\star^2$:

$$\frac{1}{2}\frac{\mathrm{d}\mathbb{E}\left[u'^2\right]}{\mathrm{d}t} = \beta_1 \mathbb{E}\left[u'^2\right] + \mathbb{E}\left[f u'\right]. \tag{3.38}$$

By stationarity, it follows that $\mathbb{E}\left[f u'\right]$ is constant. We then multiply Eq. (3.35) by f and Eq. (3.36) by u' and sum both expressions:

$$\begin{aligned} f\,\mathrm{d}u' &= \beta_1 u' f \,\mathrm{d}t + f^2 \,\mathrm{d}t \\ u\,\mathrm{d}f &= \beta_2 u' f \,\mathrm{d}t + b u' \,\mathrm{d}W_t \\ \mathrm{d}(f u') &= (\beta_1 + \beta_2) f u' \,\mathrm{d}t + f^2 \,\mathrm{d}t + b u' \,\mathrm{d}W_t. \end{aligned} \tag{3.39}$$

We take the ensemble average and we replace the constant $\mathbb{E}\left[f u'\right]$ by its value obtained in Eq. (3.38):

$$\left\langle f^2 \right\rangle = \beta_1(\beta_1 + \beta_2)\mathbb{E}\left[u'^2\right]. \tag{3.40}$$

Finally, we obtain: $b = \sqrt{2\alpha_1\alpha_2\sigma_\star^2}$. ■

Kolmogorov similarity hypothesis

Sawford (1991) derives the expression of the velocity autocorrelation for the second-order model:

$$R_L^{u'}(\tau) = \sigma_\star^2 \frac{\beta_2 \exp(\beta_1 \tau) - \beta_1 \exp(\beta_2 \tau)}{\beta_2 - \beta_1}, \tag{3.41}$$

and we recall that: $D_2(\tau) = 2\sigma_\star^2 \left(1 - R_L^{u'}(\tau)/\sigma_\star^2\right)$.

The second time scale enables the identification with the two different regimes defined in K41 and K62, assuming separation of scales $\beta_2 \ll \beta_1$:

- In the inertial range, $D_2^L(\tau) = \mathcal{C}_0 \varepsilon_\star \tau$. An asymptotic development for $-\beta_1^{-1} \ll \tau \ll -\beta_2^{-1}$ gives the following identification

$$\beta_1 \tau = -\mathcal{C}_0 \varepsilon_\star \frac{\tau}{2\sigma_\star^2}. \tag{3.42}$$

- In the dissipation range, K41 first hypotheses give: $D_2^L(\tau) = a_0 \varepsilon_\star^{3/2} \nu^{-1/2} \tau^2$. An asymptotic development for $\tau \ll -\beta_1^{-1}, -\beta_2^{-1}$ gives the following identification

$$\beta_1 \beta_2 \frac{\tau^2}{2} = a_0 \varepsilon_\star^{3/2} \nu^{-1/2} \frac{\tau^2}{2\sigma_\star^2}. \tag{3.43}$$

Finally:

$$\beta_1 = -\frac{\mathcal{C}_0 \varepsilon_\star}{2\sigma_\star^2} = -\frac{1}{T_L^\star}, \quad \beta_2 = -\frac{2a_0}{\mathcal{C}_0} \left(\frac{\varepsilon_\star}{\nu}\right)^{1/2} = -\frac{1}{t_\eta^\star} \tag{3.44}$$

We retrieve the Lagrangian integral time scale $T_L^\star$, characteristic of the fluctuating scales, and similar to the one obtained with the first-order model. The second time scale $t_\eta^\star$ involves either the Kolmogorov time scale τ_η or a local one τ_η^{sgs}, depending on whether the model is applied to RANS or LES. It characterizes the velocities in the dissipation range, i.e., the correlation time for very small increments. Hence, it can be viewed as the characteristic time scale of the acceleration.

Note that the model for $\varepsilon_\star$ is given at a coarse scale in ROS: either at the global one (RANS) or sub-grid one (LES). It is therefore not possible to apply the first hypothesis of K62 since the local dissipation is not known, and for such increments, we have $\tau \ll \tau_\eta \ll \tau_\Delta$.

A very close formulation was proposed more recently by Innocenti, Mordant, Stelzenmuller, and Chibbaro (2020) for RANS framework:

$$\begin{cases} \mathrm{d}u' &= \beta_1 u' \,\mathrm{d}t + a' \,\mathrm{d}t \\ \mathrm{d}a' &= \beta_2 a' \,\mathrm{d}t + b \,\mathrm{d}W_t. \end{cases} \tag{3.45}$$

One can notice that the acceleration plays here the same role as f in the model of Sawford (1991). By stationarity, we have seen that $b = \sqrt{-2\beta_1\beta_2(\beta_1 + \beta_2)\sigma_u^2}$. Knowing that $\beta_1 = -1/T_L$ and in accordance with the K41 theory, they fixed $\beta_2 = -1/\tau_\eta$.

This second-order model tackles some of the limitations of the Langevin velocity model. By introducing this second characteristic time of acceleration, the stochastic model is in agreement with the theory of K41 in the dissipation range and the velocity of the fluid particle is now differentiable. On the other hand, its acceleration is not and models of higher orders have hence been developed.

3.2.4 Higher-order models

Viggiano, Friedrich, Volk, Bourgoin, Cal, and Chevillard (2020) consider similarly n additional layers instead of a single one. All time scales associated with order higher than 1 are equal to τ_η.

$$\begin{cases} \mathrm{d}u' & = -\dfrac{1}{T_L^\star} u' \,\mathrm{d}t + f_1 \,\mathrm{d}t \\ \mathrm{d}f_1 & = -\dfrac{1}{\tau_\eta} f_1 \,\mathrm{d}t + f_2 \,\mathrm{d}t \\ & \dots \\ \mathrm{d}f_{n-1} & = -\dfrac{1}{\tau_\eta} f_{n-1} \,\mathrm{d}t + b \,\mathrm{d}W_t. \end{cases} \tag{3.46}$$

For $n \to \infty$ the process is therefore infinitely differentiable at a given Reynolds number. By simulating differentiable accelerations, third-order or higher-order models produce Lagrangian acceleration autocorrelation functions that are analytic at the origin, in accordance with experiment (Voth, Satyanarayan, and Bodenschatz 1998).

However, this process remains Gaussian. Sawford and Innocenti models also both assume a Gaussian Lagrangian acceleration PDF and thus do not account for the intermittency of acceleration observed in experiments. Non-Gaussian features of Lagrangian turbulence must be reproduced and in the following, we extend the construction of these processes to include intermittent nature of the fluctuations. Velocities and accelerations statistics must be conditioned by the local value of dissipation, as introduced in the K62 theory.

3.3 Stochastic models for turbulent flows consistent with K62

The models seen in the previous section have been established consistent with the Kolmogorov theory of 1941. However, the Gaussianity of the velocity or acceleration PDF is in contradiction with experiments and K62 theory (see Chap. 1) and do not reproduce the intermittent character of turbulence.

In this section, we review some existing models that improve first and second-order models already introduced in previous section by conditioning the velocity or the acceleration to the local dissipation. However, in ROS, the local dissipation is not fully resolved and must be modeled. The most common dissipation model is the one introduced by Pope and Chen (1990).

3.3.1 Local dissipation modeled by an Ornstein-Uhlenbeck process

Pope and Chen (1990) originally suggested to model the dissipation process $\varepsilon_\star$ by a log-normally correlated process by mean of Ornstein-Uhlenbeck process . The stochastic equation they proposed for $\chi_t = \ln\left(\varepsilon_\star / \mathbb{E}\left[\varepsilon_\star\right]\right)$ is the following:

$$\mathrm{d}\chi_t = -\left(\chi_t + \frac{1}{2}\sigma_\chi^2\right)\frac{\mathrm{d}t}{T_\chi} + \left(2\frac{\sigma_\chi^2}{T_\chi}\right)^{1/2} \mathrm{d}W_t, \tag{3.47}$$

where W_t is a Wiener process, T_χ is the Lagrangian integral time scale of χ, extracted from DNS and found to be close to the Lagrangian integral time scale of the velocity T_L. The parameter σ_χ^2 is Reynolds number dependent and is also chosen accordingly to DNS data.
This process was widely used in the literature for modeling the dissipation in conditional models: Pope and Chen (1990), Reynolds (2003a), Lamorgese, Pope, Yeung, and Sawford (2007).

3.3.2 Conditional Gaussian velocity

First order models can be immediately extended and made compatible with the K62 framework since the velocity increments are now conditioned on the local and not on the global dissipation:

$$\begin{cases} \mathrm{d}u' = -\dfrac{1}{T_L^\star}u'\,\mathrm{d}t + \sqrt{\mathcal{C}_0\mathbb{E}\left[\varepsilon_\star\right]\exp\chi_t}\,\mathrm{d}W_t, \\ \mathrm{d}\chi_t = -\left(\chi_t + \dfrac{1}{2}\sigma_\chi^2\right)\dfrac{\mathrm{d}t}{T_\chi} + \left(2\dfrac{\sigma_\chi^2}{T_\chi}\right)^{1/2}\mathrm{d}W_t, \end{cases} \tag{3.48}$$

We verify that this refined Langevin model (Pope and Chen 1990) is compatible with K62 theory because for small time intervals τ, the diffusion term dominates in the expression and gives:

$$\mathbb{E}\left[(\Delta_\tau u)^2|\varepsilon_\star\right] = \mathcal{C}_0\varepsilon_\star\tau. \tag{3.49}$$

3.3.3 Conditional Gaussian acceleration

Similarly, Reynolds (2003a), Reynolds (2003b) extended the second-order model of Sawford (1991) by incorporating a dependence on local dissipation. A Gaussian acceleration model, but conditioned on dissipation, produces a non-Gaussian distribution of acceleration statistics. They define $a' = \sigma_{a'|\varepsilon}\tilde{a}$. The system of Sawford (1991) is equivalent to:

$$\begin{cases} \mathrm{d}u' &= a'\,\mathrm{d}t = \sigma_{a'|\varepsilon}\tilde{a}\,\mathrm{d}t \\ \dfrac{\mathrm{d}a'}{\sigma_{a'|\varepsilon}} &= \dfrac{\alpha_1}{\sigma_{a'|\varepsilon}}u'\,\mathrm{d}t + \alpha_2\dfrac{a'}{\sigma_{a'|\varepsilon}}\,\mathrm{d}t + \dfrac{b}{\sigma_{a'|\varepsilon}}\,\mathrm{d}W_t. \end{cases} \tag{3.50}$$

Using $\mathrm{d}\tilde{a} = \dfrac{\mathrm{d}a'}{\sigma_{a'|\varepsilon}} - \dfrac{1}{\sigma_{a'|\varepsilon}}\dfrac{\mathrm{d}\sigma_{a'|\varepsilon}}{\mathrm{d}t}\tilde{a}\,\mathrm{d}t$ we obtain the new system, on $\boldsymbol{Z} = [u', \tilde{a}, \chi]$:

$$\begin{cases} \mathrm{d}u' &= \sigma_{a'|\varepsilon}\tilde{a}\,\mathrm{d}t \\ \mathrm{d}\tilde{a} &= -\left((T_L^\star)^{-1} + (t_\eta^\star)^{-1} - \dfrac{1}{\sigma_{a'|\varepsilon}}\dfrac{\mathrm{d}\sigma_{a'|\varepsilon}}{\mathrm{d}t}\right)\tilde{a}\,\mathrm{d}t - (T_L^\star)^{-1}(t_\eta^\star)^{-1}u'\,\mathrm{d}t \\ &\quad + \dfrac{1}{\sigma_{a'|\varepsilon}}\sqrt{2\sigma_\star^2\left((T_L^\star)^{-1} + (t_\eta^\star)^{-1}\right)(T_L^\star)^{-1}(t_\eta^\star)^{-1}}\,\mathrm{d}W_t \\ \mathrm{d}\chi &= -\dfrac{1}{T_\chi}\chi\,\mathrm{d}t + \sqrt{\dfrac{2\sigma_\chi^2}{T_\chi}}\,\mathrm{d}W_t', \end{cases} \tag{3.51}$$

where the last equation on $\chi = \ln(\varepsilon_\star/\mathbb{E}\left[\varepsilon_\star\right])$ is taken from the model of Pope and Chen (1990). The conditional acceleration variance is prescribed by K62 first hypothesis: $\sigma_{a'|\varepsilon}^2 = \overline{a_0}\varepsilon_\star^{3/2}\nu^{-1/2}$.

Both time scales are defined in terms of the modeled instantaneous dissipation rate $\varepsilon_\star$. The velocity time scale is $T_L^\star = 2\sigma_\star^2/\mathcal{C}_0\varepsilon^\star$ and the acceleration time scale can be obtained consistently with K62 first hypothesis: $t_\eta^\star = \mathcal{C}_0/2\overline{a_0}\,(\nu/\varepsilon_\star)^{1/2}$. The proposed model reproduces almost a Tsallis distribution for Lagrangian accelerations and approaches DNS and experimental data (Beck 2001a; Beck 2001b; Beck 2003). Several models for the dissipation were proposed in Reynolds (2003a) and Reynolds (2003b) and will be developed in Sec. 3.4.

3.3.4 Conditional Non-Gaussian acceleration

Lamorgese, Pope, Yeung, and Sawford (2007) considered conditionally cubic-Gaussian acceleration statistics. Their model captures the effects of small-scale intermittency on acceleration and the conditional dependence of acceleration on pseudo-dissipation

$$\begin{cases} \mathrm{d}u' &= a'\,\mathrm{d}t = \sigma_{a'|\varepsilon} C\left[(1-p)\overline{a} + p\overline{a}^3\right]\mathrm{d}t, \\ \mathrm{d}\overline{a} &= \overline{\theta}\,\mathrm{d}t + \overline{b}\,\mathrm{d}W_t, \end{cases} \tag{3.52}$$

where $\overline{\theta}$ and $\overline{b}$ are drift and diffusion coefficients specified below. All of the other coefficients are $p = 0.1$, $C = \sqrt{2/3}$ and $\sigma_{a'|\varepsilon}$ is not given by K62 but rather with the following expression, first presented by Yeung, Pope, Lamorgese, and Donzis (2006):

$$\frac{\sigma^2_{a'|\varepsilon}}{a_\eta^2} = \frac{1.2}{\mathrm{Re}_{\lambda_I}^{0.2}}\left(\frac{\varepsilon_\star}{\mathbb{E}\left[\varepsilon_\star\right]}\right)^{0.15} + \ln\left(\frac{\mathrm{Re}_{\lambda_I}}{20}\right)\left(\frac{\varepsilon_\star}{\mathbb{E}\left[\varepsilon_\star\right]}\right)^{1.25}, \tag{3.53}$$

and the process of Pope and Chen (1990) drives the stochastic trajectory of $\varepsilon_\star$.

Another original model for sub-filter acceleration was proposed by Sabel'nikov, Chtab-Desportes, and Gorokhovski (2011), for which two distinct stochastic processes drive the norm and direction of the acceleration vector. The LES-SSAM model leads to the following stochastic Navier-Stokes equation, where the total acceleration $\hat{a}_i$ of a surrogate field $\hat{u}_i$ is modeled by:

$$\hat{a}_i = \frac{\mathrm{d}\hat{u}_i}{\mathrm{d}t} = \frac{\partial\hat{u}_i}{\partial t} + \hat{u}_k\frac{\partial\hat{u}_i}{\partial x_k} = -\frac{1}{\rho}\frac{\partial\hat{P}}{\partial x_i} + \frac{\partial}{\partial x_k}\left[(\nu+\nu_t)\left(\frac{\partial\hat{u}_i}{\partial x_k} + \frac{\partial\hat{u}_k}{\partial x_i}\right)\right] + a_i' \tag{3.54}$$

relying on a Smagorinsky SGS assumption for the turbulent viscosity ν_t. The pressure $\hat{P}$ maintains the incompressibility of the process and a_i' is represented by two independent stochastic processes, one for its norm $a^*(t)$ and another for its direction $e_i^*(t)$:

$$\left\langle (a^*)^2|\varepsilon\right\rangle = \overline{a_0}\varepsilon^{3/2}\nu^{-1/2}, \tag{3.55}$$

so that the norm of the acceleration is in accordance with the K62 theory. The dissipation is modeled with Eq. (3.47), and applying the Itô transformation, one can obtain:

$$\frac{\mathrm{d}a^*}{a^*} = \left(\ln\frac{a^*}{a_\eta} - \frac{3}{16}\sigma_\chi^2\right)T_\chi^{-1}\,\mathrm{d}t + \frac{3}{4}\sqrt{2\sigma_\chi^2 T_\chi^{-1}}\,\mathrm{d}W_t. \tag{3.56}$$

A stochastic model for the vector of the acceleration direction is proposed, with a Brownian random walk on the surface of a unit radius sphere, which expression is not given here. This model produces non-Gaussian acceleration statistics, thanks to the modeling of local dissipation. By introducing two distinct characteristic times, one for the fast decorrelation of the acceleration components, the other for the longer term memory of its norm, it is also consistent with theories and experiments (Monin and Yaglom 1975; Xu, Ouellette, Vincenzi, and Bodenschatz 2007).

3.3.5 Velocity-conditioned acceleration

One can also introduce a vectorial stochastic model for the dynamics of a fluid particle in turbulent flows, looking for a stochastic process of the form:

$$\mathrm{d}a_i' = M_i\,\mathrm{d}t + D_{ij}\,\mathrm{d}W_j. \tag{3.57}$$

Both closure terms M_i and D_{ij} necessarily involves the acceleration a' and the velocity u' to maintain a stationary solution. All the models presented so far have also involved the dissipation $\varepsilon_\star$. On the other hand, some models are based on velocity-conditioned acceleration, such as that of Biferale, Boffetta, Celani, Devenish, Lanotte, and Toschi (2004) which predicts $\left\langle a^2|u\right\rangle \sim |u|^{4.6}$. Indeed, this is also consistent with Kolmogorov's hypotheses, since $\varepsilon \sim \sigma_u^3/L \sim \langle k\rangle^{3/2}/L$, where L is the characteristic size of the largest structures.

Zamansky (2021) developed a model for conditional acceleration involving not only dissipation, but also kinetic energy:

$$\left\langle a^2|\varepsilon,k\right\rangle = f(k,\varepsilon) = A^{-1}a_\eta^2\left(\frac{\varepsilon}{\langle\varepsilon\rangle}\right)^{3/2}\exp\left(\alpha\frac{k}{\langle k\rangle}\right). \tag{3.58}$$

Writing Itô's formula on the process, we get a formula for the increments of a^2:

$$\mathrm{d}a^2 = \frac{\partial f}{\partial k}\,\mathrm{d}k + \frac{\partial f}{\partial \varepsilon}\,\mathrm{d}\varepsilon + \frac{1}{2}\frac{\partial^2 f}{\partial k^2}\,\mathrm{d}k^2 + \frac{1}{2}\frac{\partial^2 f}{\partial \varepsilon^2}\,\mathrm{d}\varepsilon^2 + \frac{\partial^2 f}{\partial\varepsilon\partial k}\,\mathrm{d}\varepsilon\,\mathrm{d}k, \tag{3.59}$$

where we note that $\mathrm{d}k = u_i\,\mathrm{d}u_i = u_i a_i\,\mathrm{d}t = P\,\mathrm{d}t$, where P is the mechanical power per unit mass exchanged by the fluid particle. Stochastic models for $\mathrm{d}\varepsilon$ are developed in Sec. 3.4. With various assumptions, he derived a shape for the vector model of the acceleration $\mathrm{d}a_i$ and thus noting that $a^2 = a_i a_i$ it is possible to obtain the closures through Eq. (3.59).

3.3.6 Conclusion on models compliant with K62

By conditioning the parameters of the Gaussian or non-Gaussian models to the local dissipation, it is possible to produce non-Gaussian statistics, sometimes close to the distributions observed in the experiments.

However, this is not sufficient to reproduce the intermittent character of the statistics: the dissipation model must also be itself intermittent. Hence it is necessary to highlight some existing properties for intermittent dissipation, that we will ascertain on the famous model of Pope and Chen (1990) as well as other models.

3.4 Intermittent stochastic models

This section is focused on stochastic models of dissipation along the trajectory of fluid particles and in particular on the intermittency of their statistics. In Sec. 3.4.1, we first introduce the pseudo-dissipation, which Pope and Chen (1990) have shown that it is more suitable to assess K62 theories. In Sec. 3.4.2, in agreement with experiments, DNS results and K62 theory, we propose a list of properties that the statistics of the modeled dissipation must verify. Section 3.4.3 introduces a

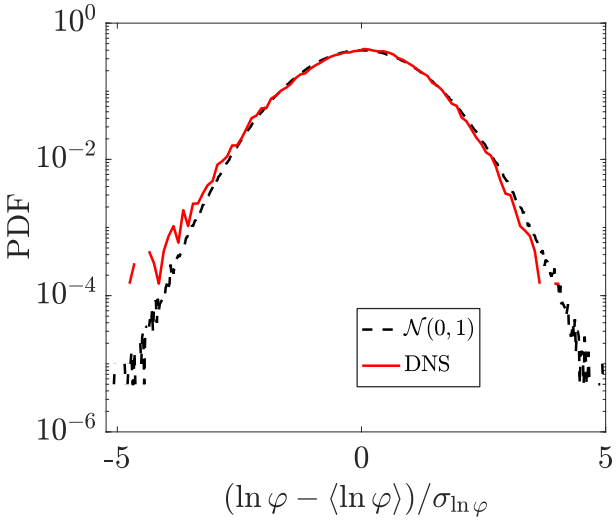

Figure 3.5. Probability density function of the normalized variable $\ln\varphi$ compared to the Gaussian distribution (dashed black line). The y-axis is on a logarithmic scale. Dataset from (Lanotte et al. 2011).

general formalism to establish a stochastic model of pseudo-dissipation. In Sec. 3.4.4.1, we verify whether the dissipation model of Pope and Chen (1990) verifies the list of criteria. Section 3.4.4.2 introduces another class of models, compatible with the cascade model of Yaglom (1966).

3.4.1 Modeling the pseudo-dissipation

According to the third refined similarity hypothesis of K62, the dissipation ε is log-normal. Actually, the PDF of the pseudo-dissipation φ is in better agreement with the log-normal distribution than the classical dissipation, as shown in Pope and Chen (1990). It is defined as:

$$\varphi := \nu \frac{\partial u_i}{\partial x_j}\frac{\partial u_i}{\partial x_j}. \tag{3.60}$$

As noted in Pope and Chen (1990), for homogeneous flows we have $\langle\varphi\rangle = \langle\varepsilon\rangle$. The Lagrangian variable is related to the Eulerian field by: $\varphi(t) = \varphi(\boldsymbol{x}_f(t), t)$, where $\boldsymbol{x}_f(t)$ denotes the position of a fluid particle at time t.

Figure 3.5 compares the PDF of $\ln\varphi$ obtained from the data of Lanotte, Calzavarini, Toschi, Bec, Biferale, and Cencini (2011) with a normal distribution and we find good agreement. As suggested in K62 and measured in DNS by Yeung, Pope, and Sawford (2006), we have $\sigma^2_{\ln\varphi} = A + B\ln\mathrm{Re}$.

The locally-averaged dissipation (also called coarse-grained dissipation) can be defined similarly to ε^τ in Eq. (1.41) by:

$$\varphi^\tau(t) = \frac{1}{\tau}\int_t^{t+\tau} \varphi(s)\,\mathrm{d}s. \tag{3.61}$$

3.4.2 Multifractal properties of the pseudo-dissipation

Numerous studies on data analysis of intermittency in turbulence reveal the multifractal nature of the pseudo-dissipation. The seminal work of Frisch (1995) to characterize intermittency based

on Kolmogorov theories was followed among others by Chevillard, Robert, and Vargas (2009), Chevillard, Robert, and Vargas (2011), Chevillard (2017), Schmitt and Marsan (2001), Schmitt (2003), Pereira, Moriconi, and Chevillard (2018). Combining all the properties of intermittency mentioned in their work, we propose the following criteria for the pseudo-dissipation to exhibit intermittency.

Properties of the intermittent pseudo-dissipation:

(i) Kolmogorov 1941 scaling: $\mathbb{E}[\varphi] = \nu\tau_\eta^{-2}$

(ii) Kolmogorov 1962: φ is log-normal with $\sigma^2_{\ln\varphi} \sim \ln \dfrac{T_L}{\tau_\eta}$

(iii) Multiscaling of the one-point statistics: $\mathbb{E}[\varphi^p] \sim \left(\dfrac{T_L}{\tau_\eta}\right)^{\xi(p)}$, where $\xi(p)$ is a non-linear function.

(iv) Power-law scaling for the coarse-grained dissipation, in the inertial range:
for $\tau_\eta \ll \tau \ll T_L$, $\quad \mathbb{E}[(\varphi^\tau)^p] \sim \left(\dfrac{T_L}{\tau}\right)^{\xi(p)}$

Remark that if the lognormal distribution is a good approximation of the PDF distribution, the numerical data shown in Fig. 3.5 suggest deviations. Assumption (ii) is therefore a reasonable working approximation for modeling but it is not foolproof.
The last two points (iii) and (iv) are precisely the main characteristics of multifractal systems, which were considered for the modeling of the dissipation.

Multifractal random fields are of primary interest for modeling intermittent fields since they possess high variability on a wide range of time or space scales, associated with intermittent fluctuations and long-range power-law correlations (Borgas 1993; Frisch 1995; Sreenivasan and Antonia 1997). Self-similar and complex structures observed in DNS and experimental studies are well reproduced by multifractal random fields, as opposed to monofractal ones.

3.4.3 General formalism for the pseudo-dissipation

In order to compare stochastic models for pseudo-dissipation φ_t, we introduce a general formalism that simplifies the verification of the properties given in Sec. 3.4.2. In the following, models are in the form:

$$\varphi_t = \mathbb{E}[\varphi]\exp(\chi_t), \tag{3.62}$$

where $\mathbb{E}[\varphi] = \nu/\tau_\eta^2$ to fulfill Kolmogorov scaling (i). The stationary process χ_t is Gaussian of variance σ_χ^2 and its mean $\mu_\chi = -\sigma_\chi^2/2$ is determined with the constraint that $\mathbb{E}[\exp(\chi_t)] = 1$. We can parametrize this process by a zero-average Gaussian process X_t and an intermittency coefficient λ_I:

$$\chi_t = \sqrt{\lambda_I} X_t - \frac{\lambda_I}{2}\mathbb{E}\left[X_t^2\right]. \tag{3.63}$$

Without loss of generality, we can therefore rewrite the process φ_t as a function of X_t:

$$\varphi_t = \langle\varphi\rangle \exp\left(\sqrt{\lambda_I} X_t - \frac{\lambda_I}{2}\mathbb{E}\left[X_t^2\right]\right). \tag{3.64}$$

The challenge is to determine the process X_t so that φ_t can satisfy the multifractal properties defined in Sec. 3.4.2. We therefore derive below the expressions for the variance, the moments of the pseudo-dissipation and the locally-averaged pseudo-dissipation as functions of the covariance function of X_t.

Variance:

$$\sigma^2_{\ln\varphi} = \sigma^2_\chi = \lambda_I \sigma^2_X. \tag{3.65}$$

Moments of the pseudo-dissipation:
χ_t is a Gaussian variable, with moments generating function equal to:

$$\mathbb{E}\left[\exp(p\chi)\right] = \exp\left(p\mu_\chi + \frac{1}{2}p^2\sigma^2_\chi\right). \tag{3.66}$$

Using $\mu_\chi = -\sigma^2_\chi/2$, this simplifies to:

$$\mathbb{E}\left[\varphi^p\right] = \mathbb{E}\left[\varphi\right]^p \exp\left(\lambda_I \frac{p(p-1)}{2}\sigma^2_X\right). \tag{3.67}$$

Moments of the coarse-grained dissipation:

$$\begin{aligned}(\varphi^\tau)^p &= \frac{1}{\tau^p}\int_{[t,t+\tau]^p}\prod_{i=1}^p \varphi(s_i)\,\mathrm{d}s_i,\\ &= \frac{\mathbb{E}\left[\varphi\right]^p}{\tau^p}\int_{[t,t+\tau]^p}\exp\left(\sum_{i=1}^p \sqrt{\lambda_I}X_{s_i} - p\frac{\lambda_I}{2}\sigma^2_X\right)\prod_{i=1}^p \mathrm{d}s_i.\end{aligned} \tag{3.68}$$

The process appearing in the exponential is a zero-average Gaussian process. Applying to it the identity of Eq. (3.66), we have:

$$\mathbb{E}\left[(\varphi^\tau)^p\right] = \frac{\mathbb{E}\left[\varphi\right]^p}{\tau^p}\exp\left(-p\frac{\lambda_I}{2}\sigma^2_X\right)\int_{[t,t+\tau]^p}\exp\Big(\frac{1}{2}\sum_{i,j=1}^p \lambda_I\mathbb{E}\left[X_{s_i}X_{s_j}\right]\Big)\prod_{i=1}^p \mathrm{d}s_i \tag{3.69}$$

$$= \frac{\mathbb{E}\left[\varphi\right]^p}{\tau^p}\exp\left(-p\frac{\lambda_I}{2}\sigma^2_X\right)\int_{[t,t+\tau]^p}\exp\Big(\sum_{i<j}\lambda_I\mathbb{E}\left[X_{s_i}X_{s_j}\right] + p\frac{\lambda_I}{2}\sigma^2_X\Big)\prod_{i=1}^p \mathrm{d}s_i \tag{3.70}$$

$$= \mathbb{E}\left[\varphi\right]^p\int_{[0,1]^p}\exp\Big(\lambda_I\sum_{i<j}\mathbb{E}\left[X_{\tau s_i}X_{\tau s_j}\right]\Big)\prod_{i=1}^p \mathrm{d}s_i. \tag{3.71}$$

The expressions obtained in Eq. (3.65), (3.67) and (3.71) only depend on the parameter λ_I and the covariance function of X_t. Those calculations will be useful to assess properties of Sec. 3.4.2 on models of literature. Let us start with the model of Pope and Chen (1990), already introduced in previous section.

3.4.4 A review of existing dissipation processes

3.4.4.1 An Ornstein-Uhlenbeck process

Starting from Eq. (3.47), the corresponding normalized stochastic process X_t^{OU} for the model of Pope and Chen (1990) is:

$$\mathrm{d}X_t^{OU} = -X_t^{OU}\frac{\mathrm{d}t}{T_\chi} + \left(2\frac{\sigma_X^2}{T_\chi}\right)^{1/2}\mathrm{d}W_t. \tag{3.72}$$

The autocorrelation of this process is well-know: following Eq. (3.11) it has an exponential decay in the form $\mathbb{E}\left[X_t X_{t+\tau}\right] = \sigma_X^2 \exp\left(-t/T_\chi\right)$.

Let us examine if this model yields the expected multifractal properties for intermittent dissipation defined in Sec. 3.4.2. The three parameters of the models are T_χ, σ_χ^2 and the intermittency coefficient λ_I.

- The first requirement (i) is fulfilled by taking $\mathbb{E}\left[\varphi\right] = \nu\tau_\eta^{-2}$.
- The second one (ii) provides a general form for $\sigma_\chi^2 = \lambda_I \ln(T_L/\tau_\eta)$. Such dependency in the Reynolds number was already prescribed in Pope and Chen (1990), who noted that $\sigma_\chi^2 = 0.29\ln \mathrm{Re}_\lambda - 0.36$ was a good fit to their DNS data.
- Starting from Eq. (3.67), we have:

$$\mathbb{E}\left[\varphi^p\right] = \mathbb{E}\left[\varphi\right]^p \exp\left(p(p-1)\frac{\sigma_\chi^2}{2}\right) = \mathbb{E}\left[\varphi\right]^p \left(\frac{T_L}{\tau_\eta}\right)^{\frac{\lambda_I}{2}p(p-1)}, \tag{3.73}$$

  which ensures point (iii).
- However, the scaling of the two-points statistics (iv) cannot be obtained with an exponential decay of the autocorrelation function. According to Eq. (3.71), we have:

$$\begin{aligned}\mathbb{E}\left[(\varphi^\tau)^p\right] &= \mathbb{E}\left[\varphi\right]^p \int_{[0,1]^p} \exp\left(\lambda_I \sum_{i<j} \mathbb{E}\left[X_{\tau s_i} X_{\tau s_j}\right]\right) \prod_{i=1}^p \mathrm{d}s_i \\ &= \mathbb{E}\left[\varphi\right]^p \int_{[0,1]^p} \exp\left(\sigma_\chi^2 \sum_{i<j} \exp\left(-\frac{\tau(s_j - s_i)}{T_\chi}\right)\right) \prod_{i=1}^p \mathrm{d}s_i.\end{aligned} \tag{3.74}$$

  Such moments are diverging with the Reynolds number, which is not consistent with the fact that velocity increments are independent on Reynolds number in the inertial range.

We will see in the following section that, on the other hand, a pseudo-dissipation model given by a multiplicative cascade allows one to obtain (iii) moments $\mathbb{E}\left[\varphi^p\right]$ that scale as a power of the Reynolds number, and (iv) bounded moments of φ^τ when $\mathrm{Re} \to \infty$. Let us introduce cascade models with their genesis, the model of Yaglom (1966).

3.4.4.2 Log-correlated processes

The multiplicative cascade model of Yaglom (1966), presented in Sec. 1.3.2 pictures turbulence as an ensemble of discrete length scales, in which the energy transfers from a "mother" to a "daughter" eddy in a recursive and multiplicative manner. In this way, large fluctuations recursively

generate correlations over long distances.

Two main criticisms of these models are made by Mandelbrot (1999). The first concerns the absence of spatio-temporal structure in these Eulerian representations of the dissipation fields which lacks causality, a necessary ingredient. Equivalent Lagrangian models were then proposed, following the formalism of Lagrangian intermittency developed by Borgas (1993). The model of Biferale, Boffetta, Celani, Crisanti, and Vulpiani (1998) is defined via a multiplicative process of independent stationary random processes with given correlation times. Properties (iii) and (iv) can here again only be verified for a finite number of scales depending on the constant scale ratio of the model λ_I.

This brings us to the second critic raised by Mandelbrot (1999) who suggested to consider continuous cascade models such as Gaussian multiplicative chaos (GMC) (Kahane 1985; Robert and Vargas 2010) for which no arbitrary scale is chosen. Stochastic integrals can be interpreted as an infinite sum, with continuous values of scales. Taking the exponential of stochastic integrals gives a "continuous product" instead of the discrete one defined in Eq. (1.50). Several models (Schmitt and Marsan 2001; Muzy and Bacry 2002; Chevillard 2017; Pereira, Moriconi, and Chevillard 2018) are based on this formalism which allows to combine the continuous vision of a cascade and a causal structure of the process. GMC rely on a log-correlated process X_t that requires special attention for its derivation. In the following, we do not attempt to construct this process (this will be detailed in Chap. 4) but rather focus on its properties in the inertial range and we verify that its statistics are indeed intermittent.

Let us introduce X_t, a zero-average Gaussian process with the following variance and covariance scalings:

$$\mathbb{E}\left[X_t^2\right] \sim \ln \frac{T_L}{\tau_\eta}, \tag{3.75}$$

$$\mathbb{E}\left[X_t X_s\right] \sim \ln \frac{T_L}{t-s}, \quad \text{for} \quad \tau_\eta < t-s < T_L \tag{3.76}$$

The mathematical construction of such process will be the focus of the next chapter. In this chapter, we only give the scaling of the covariance function for increments in the inertial zone since this is the range of interest for establishing the intermittency properties of Sec. 3.4.2. In the following, we verify that the requirements are fulfilled with such process.

Following Eq. (3.65), it is immediate that requirement (ii) is satisfied. Also, replacing the variance $\sigma_X^2 \sim \ln(T_L/\tau_\eta)$ in Eq. (3.67) readily ensures requirement (iii):

$$\mathbb{E}\left[\varphi^p\right] \sim \mathbb{E}\left[\varphi\right]^p \exp\left(\frac{\lambda_I}{2} p(p-1) \ln \frac{T_L}{\tau_\eta}\right) \sim \left(\frac{T_L}{\tau_\eta}\right)^{\xi(p)}, \tag{3.77}$$

with the non-linear scaling power law $\xi(p) = \dfrac{\lambda_I}{2} p(p-1)$.

As opposed to the Ornstein-Uhlenbeck model of Sec. 3.4.4.1, the multifractal property of the coarse-grained dissipation (iv) is ensured by the log-correlated autocorrelation of X_t in the inertial

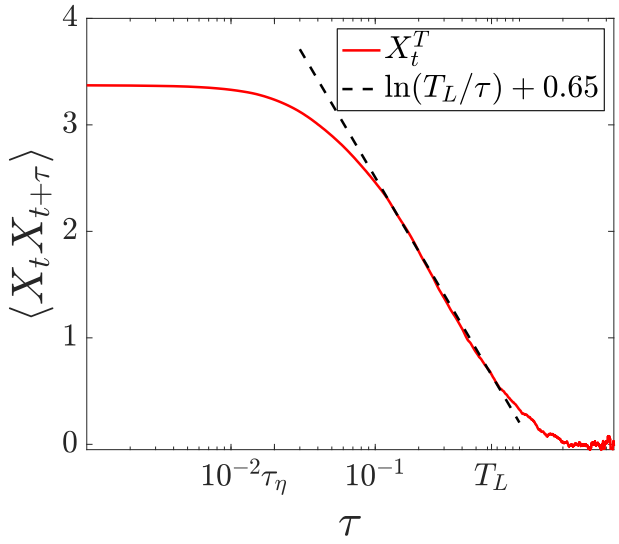

Figure 3.6. Autocorrelation of X_t^T (red line) compared with expected logarithmic behavior (black dotted line). The x-axis is on a logarithmic scale.

range.

$$\begin{aligned}
\mathbb{E}\left[(\varphi^\tau)^p\right] &= \mathbb{E}\left[\varphi\right]^p \int_{[0,1]^p} \exp\left(\lambda_I \sum_{i<j} \mathbb{E}\left[X_{\tau s_i} X_{\tau s_j}\right]\right) \prod_{i=1}^p \mathrm{d}s_i \\
\frac{\mathbb{E}\left[(\varphi^\tau)^p\right]}{\mathbb{E}\left[\varphi\right]^p} &= \int_{[0,1]^p} \exp\left(\lambda_I \sum_{i<j} \ln \frac{T_L}{\tau(s_j - s_i)}\right) \prod_{k=1}^p \mathrm{d}s_k \\
&= \int_{[0,1]^p} \exp\left(\lambda_I \frac{p(p-1)}{2} \ln \frac{T_L}{\tau} - \lambda_I \sum_{i<j} \ln(s_j - s_i)\right) \prod_{k=1}^p \mathrm{d}s_k \\
&= \left(\frac{T_L}{\tau}\right)^{\xi(p)} \int_{[0,1]^p} \prod_{i<j} \frac{1}{(s_j - s_i)^{\lambda_I}} \prod_{k=1}^p \mathrm{d}s_k.
\end{aligned} \tag{3.78}$$

Taking the limit $\mathrm{Re} \to \infty$, the moments of φ diverge in Eq. (3.77) because φ is correlated over the large energy containing scales, whereas at a given scale τ, moments of φ^τ converge in Eq. (3.78), fulfilling the statistical properties of intermittency. It becomes independent of the Reynolds number and behaves as power law at small scales.

3.4.4.3 Comparison of models with DNS

We illustrate this logarithmic behavior of the autocorrelation on DNS of Lanotte et al. (2011). Their simulations were run at $\tau_\eta = 0.02$. The Lagrangian integral time scale is found to be $T_L = 0.64$ which gives, according to Zhang, Legendre, and Zamansky (2019), $\mathrm{Re}_\lambda = (T_L/\tau_\eta)/0.08 = 400$. For each fluid particle, the process χ_t is obtained by taking the logarithm of the pseudo-dissipation along the particle trajectory. X_t^T is retrieved with the normalization of Eq. (3.63) and we plot in Fig. 3.6 its autocorrelation. One can easily verify by comparison with the logarithmic behavior in dashed line that the autocorrelation follows a logarithmic behavior in the inertial range, i.e. between the τ_η and T_L of the simulation.

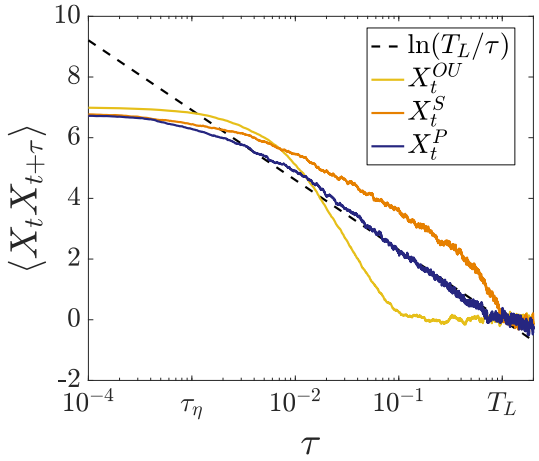

Figure 3.7. Comparison of autocorrelation of processes of (a) Pope X_t^{OU}, (b) Schmitt X_t^S and (c) Pereira X_t^P with logarithmic behavior. Processes are rescaled for comparable variance of $\ln(T_L/\tau_\eta)$.

Figure 3.7 compares the autocorrelation of several dissipation models for X_t, with the logarithmic prediction in the inertial range $[\tau_\eta, T_L] = [10^{-3}, 10^0]$ that was observed in Sec. 3.4.4.3. We have already seen that the model of Pope and Chen (1990) has an exponential autocorrelation. It is plotted in blue in Fig. 3.7 and as expected, the exponential decay does not reproduce a long-range correlation. Two other log-correlated processes, based on the GMC, X_t^P (Pereira, Moriconi, and Chevillard 2018) and X_t^S (Schmitt 2003) display long-range power-law correlation, as opposed to the Ornstein-Uhlenbeck process of Pope X_t^{OU} (Pope and Chen 1990).

A characterization of the intermittency has been proposed in Sec. 3.4.2 and we ensured that the proposed criteria are verified by a log-correlated process X_t. The remaining question to be addressed concerns the construction of such processes. In the literature, it is derived from multifractal processes such as fractional Brownian motions (FBM) which are well-known for their long range correlation properties. Schmitt (2003), Pereira, Moriconi, and Chevillard (2018) developed models for X_t based on FBM and these processes are discussed in detail in the next chapter.

3.4.5 Extension to the LES framework

Dissipation models introduced so far are adapted to RANS formulation, and are based on the Lagrangian integral time scales T_L and T_χ. In the LES framework, more information is available about the resolved field, in particular, we have models on ε_{sgs} or equivalently φ_{sgs}. We can define

$$\begin{aligned} \chi &= \ln(\varphi/\mathbb{E}[\varphi]) = \underbrace{\ln(\varphi/\varphi_{\text{sgs}})}_{\chi'} + \underbrace{\ln(\varphi_{\text{sgs}}/\mathbb{E}[\varphi])}_{\overline{\chi}} \\ \mathrm{d}\chi &= \mathrm{d}\chi' + \frac{\mathrm{d}\varphi_{\text{sgs}}}{\varphi_{\text{sgs}}}, \end{aligned} \tag{3.79}$$

where $\mathrm{d}\chi'$ corresponds to the stochastic equation for the pseudo-dissipation discussed above and $\mathrm{d}\varphi_{\text{sgs}}$ is the increment of the resolved pseudo-dissipation seen by the fluid particle.

In that case, parameters for the model of χ' involve $T_L^\star$ instead of T_L. In Gorokhovski and Zamansky (2018), $T_L^\star = \tau_{\text{sgs}}$ and σ_X^2 should be Reynolds dependent as follows: $\sigma_X^2 \sim \ln \dfrac{\tau_{\text{sgs}}}{\tau_\eta} = \dfrac{1}{2} \ln \mathrm{Re}_\Delta$

Modeling	**K41**	**K62**
Velocity u'	Generalized Langevin model	Conditional Gaussian GLM
Acceleration a'	Second-order model	Conditional Gaussian acceleration Conditional Non-Gaussian acceleration Velocity and dissipation-conditioned acceleration
Normalized logarithm of dissipation X	SGS information	Ornstein-Uhlenbeck Log-correlated process

Table 3.1. Hierarchy of stochastic models for turbulent flows. The two columns K41 and K62 classify models according to their ability to reproduce intermittency.

.

Conclusion

In this chapter, we first introduced mathematical tools to define stochastic processes and their properties. In particular, we have presented the stochastic Langevin equation, which is commonly used in many stochastic models of fluid particle velocity.

We have reviewed a number of stochastic models and examined their ability to reproduce the fundamental theories of turbulence, namely K41 and K62. In particular, we have introduced a classification, according to the level of their modeling (velocity, acceleration, dissipation). This is summarized in Table 3.1.

Finally, in order to reproduce the intermittent statistics of turbulence, we have established a list of properties for the pseudo-dissipation. The Gaussian multiplicative chaos formalism is introduced and the derivation of the process X_t must be carefully considered. The construction of such processes requires a precise mathematical framework, which will be developed in the next chapter.

Chapter 4

A new mathematical framework for the Gaussian multiplicative chaos

In Chap. 3, we have established a set of properties that a dissipation model must satisfy to exhibit the intermittent statistics identified in turbulence by K62. The aim of this chapter is to show how to construct such processes in a generic and elegant manner.

In particular, we have introduced a general formalism for the pseudo-dissipation φ, that can be related to the Gaussian multiplicative chaos (GMC) (Kahane 1985). The construction of the GMC is based on a singular process, denoted X_t in the previous chapter, and for which a logarithmic covariance function is expected. The singularity of its covariance requires the introduction of a regularization on the process X_t^τ, itself derived from regularized fractional Brownian motion (FBM).

In this chapter, we propose an original framework for the construction of regularized FBM. This general formalism allows to easily derive associated stationary processes X_t^τ and we show that it encompasses existing processes of literature, as well as a new one further detailed in Chap. 5. Furthermore, our result proves our process to be very efficient to simplify the usually complex technical computations of variance and autocorrelation. For this reason, we can characterize sufficient conditions to obtain a large family of processes satisfying properties fixed by practitioners.

The chapter is organized as follows: Sec. 4.1 introduces the general framework for deriving intermittent stochastic processes. We define the "approximated" GMC relying on an "approximately" log-correlated process X_t^τ. Such process can be obtained from regularized FBM. We give several examples of such FBM and we introduce their Laplace representation. Based on this representation, Sec. 4.2 proposes a general framework for FBM and Sec. 4.3 extends it to stationnary processes X_t^τ. Finally, we show in Sec. 4.4 the convergence of such regularized processes towards the universal GMC.

4.1 Construction of a stochastic process with intermittent statistics

We have seen in Chap. 3 that intermittent models are based on velocities or accelerations conditioned on local dissipation φ_t, a driving process that should exhibit a singular behavior. The

classical approach is to construct a Gaussian multiplicative chaos (GMC).

4.1.1 Gaussian multiplicative chaos

This section reviews the Gaussian multiplicative chaos (GMC) formalism, introduced by Kahane (1985). According to the definition given by Rhodes and Vargas (2014), Shamov (2016):

Definition 4.1.1 (Gaussian multiplicative chaos) *Let $(\mathcal{T}, \mu)$ be a finite measure space, and let $X = (X(\omega, t)_{\omega\in\Omega, t\in\mathcal{T}})$ be a Gaussian field parametrized by $t \in \mathcal{T}$ and defined on probability space $(\Omega, \mathbb{P})$. A standard Gaussian multiplicative chaos is a random measure that can be formally written:*

$$M_\lambda(\mathrm{d}t) := \exp\left(\lambda_I X_t - \frac{\lambda_I^2}{2}\mathbb{E}\left[X_t^2\right]\right)\mu(\mathrm{d}t), \tag{4.1}$$

where X possesses a covariance kernel of the form:

$$\mathbb{E}\left[X(t)X(s)\right] = \ln_+\frac{1}{|t-s|} + g(t,s), \tag{4.2}$$

with $\ln_+(u) = \max(\ln u, 0)$ and g a continuous function.

The covariance kernel thus possesses a singularity and a standard approach consists in regularizing X by applying a cut-off, based on a small parameter τ such that, in the limit of $\tau \to 0$, φ_t is a GMC in a well-posed abstract framework. Let us define φ_t^τ, an approximated GMC, written as:

$$\varphi_t^\tau := \langle\varphi\rangle \exp\left(\lambda_I X_t^\tau - \frac{\lambda_I^2}{2}\mathbb{E}\left[(X_t^\tau)^2\right]\right), \tag{4.3}$$

where $\langle\varphi\rangle$ and λ_I are given values, and X_t^τ is a well-defined stochastic process which must approximate a Gaussian log-correlated process.

Let us now introduce an example of construction of such process.

4.1.2 A fractional Ornstein-Uhlenbeck process X^τ based on W^τ

It is natural to expect that the process X_t^τ is causal, and thus it will follow a stochastic differential equation with initial condition $X_{t_0}^\tau$ at time t_0 such that

$$\mathrm{d}X_t^\tau = b_\tau(t, X_t^\tau)\,\mathrm{d}t + \sigma_\tau(t, X_t^\tau)\,\mathrm{d}W_t^\tau. \tag{4.4}$$

The drift b_τ, the volatility σ_τ and the driving process W^τ could be chosen to become singular at the limit $\tau \to 0$, but also to ensure stationarity of the process X_t^τ. However the more natural and simple choice for the drift and the volatility will be to set

$$b_\tau(t,x) := -\frac{x}{T}, \qquad \sigma_\tau(t,x) := 1, \text{ for all } x \in \mathbb{R}, \tag{4.5}$$

where T is a parameter. We obtain the stochastic differential equation:

$$\mathrm{d}X_t^\tau = -\frac{X^\tau}{T}\,\mathrm{d}t + \mathrm{d}W_t^\tau, \tag{4.6}$$

whose unique solution with initial data $X^\tau_{t_0}$ at time t_0 is given by

$$X^\tau_t = \mathrm{e}^{-\frac{t-t_0}{T}} X_{t_0} + \int_{t_0}^t \mathrm{e}^{-\frac{t-s}{T}} \, \mathrm{d}W^\tau_s. \tag{4.7}$$

To obtain a stationary solution, it is tempting to let $t_0 \to -\infty$, but justifying the convergence requires heavy covariance computations and will depend on the choice of W^τ. Let us now discuss this choice.

4.1.3 Regularized fractional Brownian motion

A fruitful approach is to consider W^τ as a regularized fractional Brownian motion of Hurst 0. Appropriate formalism for fractional Brownian motion (hereafter denoted FBM) was proposed by Mandelbrot and Van Ness (1968). They defined the FBM of exponent H as *a moving average of* $\mathrm{d}W_t$*, in which past increments of* W_t*, a Brownian motion, are weighted by the kernel* $(t-s)^{H-1/2}$. The parameter $H \in (0,1)$ is called the Hurst parameter and defines the roughness of the path. Standard Brownian motion corresponds to $H = 1/2$ and is noted $W^{1/2}_t = W_t$. A classic expression for the Holmgren-Riemann-Liouville fractional Brownian motion is the following one:

$$\widetilde{W}^H_t = \frac{1}{\Gamma(H+1/2)} \int_0^t (t-s)^{H-1/2} \, \mathrm{d}W_s, \tag{4.8}$$

where Γ is the gamma function. The particular case of Hurst parameter $H = 0$ has a logarithmic autocorrelation (Chevillard 2017) but it is not well-defined because of the singularity of its autocorrelation in time $t = 0$.

Mandelbrot and Van Ness (1968) proposed a different regularization of this FBM, for $\tau > 0$:

$$\widetilde{W}^\tau_t = \frac{1}{\sqrt{\pi}} \int_0^t (t-s+\tau)^{-1/2} \, \mathrm{d}W_s. \tag{4.9}$$

Note that the factor $1/\sqrt{\pi}$ is for normalization purposes and equals $\Gamma(1/2)$, the gamma function being frequently used in this context.

The increments of this regularized fractional Brownian motion satisfy:

$$\mathrm{d}\widetilde{W}^\tau_t = -\frac{1}{2\sqrt{\pi}} \int_0^t (t-s+\tau)^{-3/2} \, \mathrm{d}W_s \, \mathrm{d}t + \frac{\tau^{-1/2}}{\sqrt{\pi}} \, \mathrm{d}W_t. \tag{4.10}$$

and are not stationary. However, according to McCauley, Gunaratne, and Bassler (2007), stationary increments are needed to ensure the stationarity of the X^τ process defined in Eq. (4.6). Let us rather consider the following stationary increments:

$$\begin{aligned} \mathrm{d}W^\tau_t &:= -\frac{1}{2\sqrt{\pi}} \int_{-\infty}^t (t-s+\tau)^{-3/2} \, \mathrm{d}W_s \, \mathrm{d}t + \frac{\tau^{-1/2}}{\sqrt{\pi}} \, \mathrm{d}W_t, \\ &:= \beta^\tau_t \, \mathrm{d}t + \frac{\tau^{-1/2}}{\sqrt{\pi}} \, \mathrm{d}W_t, \end{aligned} \tag{4.11}$$

with the well-defined process β^τ driven by Brownian motion W with kernel $(\cdot+\tau)^{-3/2}$. This definition of $\mathrm{d}W_t^\tau$ describes the increments of the regularized (with parameter $\tau>0$) fractional Brownian motion of Hurst parameter 0:

$$\boxed{W_t^\tau := \frac{1}{\sqrt{\pi}}\left(\int_{-\infty}^0 \left((t-s+\tau)^{-1/2}-(-s+\tau)^{-1/2}\right)\,\mathrm{d}W_s + \int_0^t (t-s+\tau)^{-1/2}\,\mathrm{d}W_s\right)}. \quad (4.12)$$

Similarly, we now retrieve the regularized FBM W_t^H with stationary increments by:

$$\boxed{W_t^H := \frac{1}{\Gamma(H+1/2)}\left\{\int_{-\infty}^0 \left[(t-s)^{H-1/2}-(-s)^{H-1/2}\right]\mathrm{d}W_s + \int_0^t (t-s)^{H-1/2}\,\mathrm{d}W_s,\right\}}. \quad (4.13)$$

which is the Mandelbrot-Van Ness integral representation already introduced in Sec. 3.1.6 and defined for all $t\in\mathbb{R}$.

We will see later that these two processes are good candidates for the construction of X_t^τ, for instance through Eq. (4.6), especially because of their singular behavior in $\tau=0$ (or $H=0$). The expressions (4.11) and (4.13) are based on moving averages of Gaussian increments weighted by a kernel carrying the whole singularity. This corresponds actually to the way these processes are implemented in the literature (Chevillard 2017). However, this vision of the FBM lacks readability, and we will see that with such definition, the numerical simulation can be costly in memory (see Chap. 5). This is the reason why we consider another approach of FBM.

4.1.4 Representation in the Laplace domain

We will now describe a generic representation of these two processes in a unified framework in order to simplify the calculations, to enlighten the dependency in the parameter τ, and to introduce new processes that are regularized FBM of Hurst parameter 0.

4.1.4.1 Laplace representation of W^τ

Let us consider first the process W^τ defined in Eq. (4.12) and for this purpose, remark that the Laplace transform of $\dfrac{1}{\sqrt{x}}$ is given by:

$$\mathcal{L}\left\{\frac{1}{\sqrt{x}}\right\}(s) = \int_{\mathbb{R}_+}\frac{1}{\sqrt{x}}\mathrm{e}^{-sx}\,\mathrm{d}x = \sqrt{\pi}s^{-1/2}, \quad (4.14)$$

thus,

$$\begin{aligned}\pi\, W_t^\tau &= \int_{-\infty}^0\int_{\mathbb{R}_+}\frac{1}{\sqrt{x}}\left(\mathrm{e}^{-(t-s+\tau)x}-\mathrm{e}^{-(-s+\tau)x}\right)\,\mathrm{d}x\;\mathrm{d}W_s\\ &\quad+\int_0^t\int_{\mathbb{R}_+}\frac{1}{\sqrt{x}}\mathrm{e}^{-(t-s+\tau)x}\,\mathrm{d}x\;\mathrm{d}W_s.\end{aligned}$$

Using the stochastic Fubini theorem (Revuz and Yor 2013), we can write for all $\tau>0$:

$$\begin{aligned}W_t^\tau &= \int_{\mathbb{R}_+}\frac{1}{\pi\sqrt{x}}\mathrm{e}^{-\tau x}\left\{\int_{-\infty}^t \mathrm{e}^{-x(t-s)}\,\mathrm{d}W_s - \int_{-\infty}^0 \mathrm{e}^{sx}\,\mathrm{d}W_s\right\}\mathrm{d}x,\\ &= \int_{\mathbb{R}_+}\frac{1}{\pi\sqrt{x}}\mathrm{e}^{-\tau x}\left(Y_t^x - Y_0^x\right)\mathrm{d}x, \quad (4.15)\end{aligned}$$

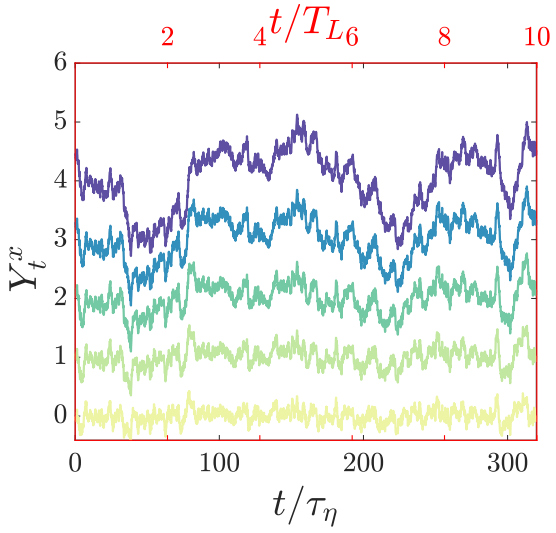

Figure 4.1. 5 correlated Ornstein-Uhlenbeck processes, driven by the same Wiener increments: $Y^x_{t+\Delta t} = Y^x_t - xY^x_t\Delta t + \sqrt{\Delta t}\xi$, with $x_i \sim \mathcal{N}(0,1)$. Plots are shifted up for a better visualization and the color shades are darker with increasing characteristic times $x^{-1} \in [\tau_\eta = 0.02; 0.048; 0.11; 0.27; T_L = 0.64]$. Times are normalized by τ_η and T_L in the x-axis to help visualize the characteristic times of the upper trajectory (T_L) and lower one (τ_η).

where $(Y^x_t)_{x\in\mathbb{R}}$ is a family of stationary Ornstein-Uhlenbeck processes constructed on the same Brownian motion W and with the parameter x being their speed of return to the mean, such that for all $x \in \mathbb{R}$,

$$\mathrm{d}Y^x_t = -xY^x_t\,\mathrm{d}t + \mathrm{d}W_t. \tag{4.16}$$

Let us insist on the fact that all the Ornstein-Uhlenbeck processes appearing in the integrand are driven by the same Wiener increments $\mathrm{d}W_t$ and are thus correlated to each other. Figure 4.1 shows 5 correlated processes Y^x_t with time scales ranging from $\tau_\eta = 0.02$ to $T_L = 0.64$. The process W^τ is therefore a linear combination of standard Ornstein-Uhlenbeck processes, weighted by the kernel $k_\tau = \dfrac{\mathrm{e}^{-\tau x}}{\pi\sqrt{x}}$.

Using this expression in Laplace domain, it is very simple to derive the increments of the FBM. Starting from Eq. (4.15), we differentiate the process Y^x_t and we obtain:

$$\begin{aligned}
\mathrm{d}W^\tau_t &= \int_{\mathbb{R}_+} \mathrm{d}Y^x_t k_\tau(x)\,\mathrm{d}x, \\
&= \int_{\mathbb{R}_+} (-xY^x_t\,\mathrm{d}t + \mathrm{d}W_t)k_\tau(x)\,\mathrm{d}x, \\
&= \int_{\mathbb{R}_+} -xk_\tau(x)\int_{-\infty}^{t} \mathrm{e}^{-(t-s)x}\,\mathrm{d}W_s\,\mathrm{d}x\,\mathrm{d}t + \int_0^\infty k_\tau(x)\,\mathrm{d}x\,\mathrm{d}W_t.
\end{aligned}$$

Using the Laplace transform $\mathcal{L}\left\{x^{1/2}\right\}(s) = \sqrt{\pi}/2s^{-3/2}$ for the first integral and $\mathcal{L}\left\{x^{-1/2}\right\}(s) =$

$\sqrt{\pi}s^{-1/2}$ for the second integral, this yields:

$$\begin{aligned} \mathrm{d}W_t^\tau &= \int_0^t \frac{-1}{2\sqrt{\pi}}(t-s+\tau)^{-3/2}\,\mathrm{d}W_s\,\mathrm{d}t + \tau^{-1/2}\,\mathrm{d}W_t, \\ &= \beta_t^\tau\,\mathrm{d}t + \frac{1}{\sqrt{\pi\tau}}\,\mathrm{d}W_t, \end{aligned}$$

where $\beta_t^\tau := \dfrac{-1}{2\sqrt{\pi}}\displaystyle\int_{-\infty}^t (t-s+\tau)^{-3/2}\,\mathrm{d}W_s$, which gives us Eq. (4.11) as defined by Chevillard (2017).

4.1.4.2 Laplace representation of W^H

We can consider the Laplace transformation of $x^{-H-1/2}$:

$$\mathcal{L}\left\{\frac{1}{x^{H+1/2}}\right\}(s) = \int_{\mathbb{R}_+} \frac{1}{x^{H+1/2}}\mathrm{e}^{-sx}\,\mathrm{d}x = \Gamma(1/2-H)s^{H-1/2}, \tag{4.17}$$

for $H \in [0, 1/2)$. Then, let us introduce the process W^H defined in Eq. (4.13). Applying similar transformation to W^H than in Sec. 4.1.4.1, we obtain:

$$\begin{aligned} \Gamma(H+1/2)\,\Gamma(1/2-H)\,W_t^H = &\int_{-\infty}^0 \int_{\mathbb{R}_+} \frac{1}{x^{H+1/2}}\left(\mathrm{e}^{-(t-s)x} - \mathrm{e}^{sx}\right)\,\mathrm{d}x\;\mathrm{d}W_s \\ &+ \int_0^t \int_{\mathbb{R}_+} \frac{1}{x^{H+1/2}}\mathrm{e}^{-(t-s)x}\,\mathrm{d}x\;\mathrm{d}W_s, \end{aligned} \tag{4.18}$$

and using the stochastic Fubini theorem (which can only be applied for $H > 0$), it comes

$$\Gamma(H+1/2)\,\Gamma(1/2-H)\,W_t^H = \int_{\mathbb{R}_+} \frac{1}{x^{H+1/2}}(Y_t^x - Y_0^x)\,\mathrm{d}x.$$

Now by the Euler reflection formula: $\Gamma(1-z)\Gamma(z) = \dfrac{\pi}{\sin(\pi z)}$, we obtain:

$$\begin{aligned} W_t^H &= \int_{\mathbb{R}_+} \frac{\sin(\pi(H+1/2))}{\pi x^{H+1/2}}(Y_t^x - Y_0^x)\,\mathrm{d}x, \\ &= \int_{\mathbb{R}_+} \frac{\cos(\pi H)}{\pi x^{H+1/2}}(Y_t^x - Y_0^x)\,\mathrm{d}x. \end{aligned} \tag{4.19}$$

The process W_t^H is therefore a linear combination of correlated standard Ornstein-Uhlenbeck processes, weighted by the kernel $k_H = \dfrac{\cos(\pi H)}{\pi x^{H+1/2}}$.

Be careful that, despite the fact that the formula Eq. (4.14) is valid for $\tau = 0$, the stochastic Fubini theorem does not apply for $\tau = 0$, thus it is not possible to write:

$$W_t^0 \overset{!}{=} \int_0^{+\infty} \frac{1}{\pi\sqrt{x}}(Y_t^x - Y_0^x)\,\mathrm{d}x. \tag{4.20}$$

The scheme appearing from the representation of Eq. (4.15) and Eq. (4.19) is that fractional Brownian motion of Hurst parameter 0 can be approximated by processes of the form:

$$\left\{ \int_{\mathbb{R}_+} \kappa_\epsilon(x) \left(Y_t^x - Y_0^x\right) \, \mathrm{d}x \right\}_{t \geq 0}, \tag{4.21}$$

for some kernels $\{\kappa_\epsilon(x),\, x \in \mathbb{R}_+\}_{\epsilon>0}$. The regularization parameter ϵ corresponds to τ in Sec. 4.1.4.1 and H in Sec. 4.1.4.2. We will develop this idea in the next sections and extend it to the associated Ornstein-Uhlenbeck processes. The challenge will then be to identify the limit processes (whenever they exist) as $\epsilon \to 0$.

4.2 A new framework for FBM

Based on the similarities of the representations in the Laplace domain of the two previous FBM, we propose in Sec. 4.2.1 to generalize their writing following Eq. (4.21). We will therefore formally introduce on the one hand the Ornstein-Uhlenbeck process Y_t^x , and on the other hand the Laplace transform. We show in Sec. 4.2.2 under which assumption the kernel κ_ϵ gives a FBM, and thus we obtain a generator set of FBM.

4.2.1 A generic representation encompassing existing FBM

Let us introduce the following transforms:

$$\forall x > 0, \quad \Phi_{t,x}(Z) = \int_{-\infty}^{t} \mathrm{e}^{-x(t-r)} \, \mathrm{d}Z_r, \tag{4.22}$$

where Z is a Gaussian process and the integral is in the sense of Wiener. These are stationary Ornstein-Uhlenbeck processes with x as the speed of return to the mean.

We also introduce a generalized Laplace transform with kernel $k : \mathbb{R}_+^* \to \mathbb{R}$. For any stochastic process $(\Phi_{t,x})_{t\geq 0, x>0}$ which is almost surely $k(x) \, \mathrm{d}x$ integrable,

$$\mathcal{L}(\Phi, k)(t) = \int_0^{+\infty} k(x) \, \Phi_{t,x} \, \mathrm{d}x. \tag{4.23}$$

We then notice that the FBM introduced in Sec. 1 can be written in the general form:

$$\boxed{\mathcal{W}_t := \mathcal{L}\left(\Phi_{t,\cdot} - \Phi_{0,\cdot}, \kappa\right) = \int_{\mathbb{R}_+} \left(\Phi_{t,x} - \Phi_{0,x}\right) \, \kappa(x) \, \mathrm{d}x}. \tag{4.24}$$

Table 4.1 gives the FBM and their increments written with the previous formalism. We detail below the processes involved in the Laplace transform.
Let us note that the process $Y_t^x = \Phi_{t,x}(W)$ is a stationary Ornstein-Uhlenbeck process with:

$$\Phi_{t,x}(W) = Y_t^x \begin{cases} \mathrm{d}Y_t^x &= -x Y_t^x \, \mathrm{d}t + \mathrm{d}W_t \\ Y_t^x &= \displaystyle\int_{-\infty}^{t} \mathrm{e}^{-(t-s)x} \, \mathrm{d}W_s \end{cases} \tag{4.25}$$

Z_t^x	Kernel $\kappa(x)$	FBM
$\Phi_{t,x}(W) - \Phi_{0,x}(W)$	$\frac{\mathrm{e}^{-\tau x}}{\pi\sqrt{x}}$	$\mathcal{L}(Z_t^x, k) = W_t^\tau$ = Eq. (4.12)
$\mathrm{d}\Phi_{t,x}(W) = -x\Phi_{t,x}(W) + \mathrm{d}W_t$	$\frac{\mathrm{e}^{-\tau x}}{\pi\sqrt{x}}$	$\mathcal{L}(Z_t^x, k) = \mathrm{d}W_t^\tau$ = Eq. (4.11)
$\Phi_{t,x}(W) - \Phi_{0,x}(W)$	$\frac{\cos(\pi H)}{\pi x^{H+1/2}}$	$\mathcal{L}(Z_t^x, k) = W_t^H$ = Eq. (4.13)

Table 4.1. Laplace representation of fractional Brownian motions

We can also explicit the process $Z_t^x = Y_t^x - Y_0^x$:

$$\Phi_{t,x}(W) - \Phi_{0,x}(W) = Z_t^x : \begin{cases} \mathrm{d}Z_t^x &= -x(Z_t^x + Y_0^x)\,\mathrm{d}t + \mathrm{d}W_t \\ Z_0^x &= 0 \\ Z_t^x &= Y_t^x - Y_0^x \\ &= \displaystyle\int_{-\infty}^t \mathrm{e}^{-(t-s)x}\,\mathrm{d}W_s - \int_{-\infty}^0 \mathrm{e}^{sx}\,\mathrm{d}W_s \\ &= \displaystyle\int_0^t \mathrm{e}^{-(t-s)x}\,\mathrm{d}W_s + (\mathrm{e}^{-tx} - 1)\int_{-\infty}^0 \mathrm{e}^{sx}\,\mathrm{d}W_s \\ &= \displaystyle\int_0^t \mathrm{e}^{-(t-s)x}\,\mathrm{d}W_s + (\mathrm{e}^{-tx} - 1)Y_0^x \end{cases} \tag{4.26}$$

4.2.2 Computation of covariance of $\mathcal{W}$

Such formalism can simplify calculations of covariance. Consider a stationary process $\psi_{t,x}$ with:

$$\mathbb{E}\left[\psi_{t,x}\psi_{s,y}\right] := K(t-s; x, y), \tag{4.27}$$

then the process $\mathcal{W}_t$ defined with kernel κ such that:

$$\mathcal{W}_t := \mathcal{L}\left(\psi_{t,\cdot} - \psi_{0,\cdot}, \kappa\right) = \int_{\mathbb{R}_+} \left(\psi_{t,x} - \psi_{0,x}\right)\,\kappa(x)\,\mathrm{d}x, \tag{4.28}$$

satisfies:

$$\mathbb{E}\left[\mathcal{W}_t\mathcal{W}_s\right] = \int_{\mathbb{R}_+}\int_{\mathbb{R}_+} \left(K(t-s;x,y) - K(s;y,x) - K(t;x,y) + K(0;x,y)\right)\kappa(x)\kappa(y)\,\mathrm{d}y\,\mathrm{d}x, \tag{4.29}$$

provided that the above quantity is integrable.

From now on we will consider only the stationary process $\psi_{t,x} \equiv Y_t^x = \Phi_{t,x}(W)$. We have, for any $t \geq 0$:

$$K(t;x,y) := \mathbb{E}\left[Y_0^x Y_t^y\right] = \int_{-\infty}^0 \mathrm{e}^{xu}\mathrm{e}^{-y(t-u)}\,\mathrm{d}u = \frac{\mathrm{e}^{-ty}}{x+y}. \tag{4.30}$$

Assumption 4.2.1 *For a mapping $\kappa : \mathbb{R} \to \mathbb{R}$, define the following quadratic form of $|\kappa|$:*

$$\mathcal{Q}(y) := |\kappa(y)| \int_0^1 \theta^{-1} \left| \kappa\left(y\frac{1-\theta}{\theta} \right) \right| \, \mathrm{d}\theta.$$

We assume that for all $t > 0$,

$$\int_{\mathbb{R}_+} (1 \wedge ty)\, \mathcal{Q}(y) \, \mathrm{d}y < \infty.$$

Proposition 4.2.2 *Assume κ satisfies Assumption 4.2.1. Then the following quantity:*

$$\mathcal{W}_t := \int_{\mathbb{R}_+} (Y_t^x - Y_0^x)\, \kappa(x) \, \mathrm{d}x, \quad t \in \mathbb{R}, \tag{4.31}$$

is a well-defined process in $L^2(\Omega)$. Moreover, it is increment stationary, Gaussian and its covariance satisfies for any $s < t$,

$$\mathbb{E}\left[\mathcal{W}_t \, \mathcal{W}_s\right] = \int_{\mathbb{R}_+} \int_{\mathbb{R}_+} \left(\mathrm{e}^{-(t-s)y} - \mathrm{e}^{-sx} - \mathrm{e}^{-ty} + 1 \right) \frac{\kappa(x)\kappa(y)}{x+y} \, \mathrm{d}y \, \mathrm{d}x. \tag{4.32}$$

Proof 4.2.3 We start by proving that for any t, the mapping $(x, y) \mapsto \left(2 - \mathrm{e}^{-tx} - \mathrm{e}^{-ty}\right) \frac{\kappa(x)\kappa(y)}{x+y}$ is integrable on $\mathbb{R}_+^2$. For $t = 0$ this is obvious, so fix $t > 0$. We have

$$\int_{\mathbb{R}_+} \int_{\mathbb{R}_+} \left(2 - \mathrm{e}^{-tx} - \mathrm{e}^{-ty}\right) \frac{|\kappa(x)\kappa(y)|}{x+y} \, \mathrm{d}y \, \mathrm{d}x = 2 \int_{\mathbb{R}_+} \left(1 - \mathrm{e}^{-ty}\right) |\kappa(y)| \int_{\mathbb{R}_+} \frac{|\kappa(x)|}{x+y} \, \mathrm{d}x \, \mathrm{d}y.$$

By the change of variables $x = y\frac{1-\theta}{\theta}$, we get

$$\int_{\mathbb{R}_+} \int_{\mathbb{R}_+} \left(2 - \mathrm{e}^{-tx} - \mathrm{e}^{-ty}\right) \frac{|\kappa(x)\kappa(y)|}{x+y} \, \mathrm{d}y \, \mathrm{d}x = 2 \int_{\mathbb{R}_+} \left(1 - \mathrm{e}^{-ty}\right) \mathcal{Q}(y) \, \mathrm{d}y.$$

Hence the inequality $1 - \mathrm{e}^{-x} \leq 1 \wedge x$, $x \geq 0$, yields

$$\int_{\mathbb{R}_+} \int_{\mathbb{R}_+} \left(2 - \mathrm{e}^{-tx} - \mathrm{e}^{-ty}\right) \frac{|\kappa(x)\kappa(y)|}{x+y} \, \mathrm{d}y \, \mathrm{d}x \leq 2 \int_{\mathbb{R}_+} (1 \wedge ty)\, \mathcal{Q}(y) \, \mathrm{d}y,$$

which is finite by assumption. Hence using that for any $x \neq -y$,

$$\mathbb{E}\left[(Y_t^x - Y_0^x)\,(Y_t^y - Y_0^y)\right] = \frac{1}{x+y}\left(2 - \mathrm{e}^{-tx} - \mathrm{e}^{-ty}\right),$$

we deduce from the integrability of $(x, y) \mapsto \left(2 - \mathrm{e}^{-tx} - \mathrm{e}^{-ty}\right) \frac{\kappa(x)\kappa(y)}{x+y}$ and Fubini's theorem that $\mathcal{W}_t \in L^2(\Omega)$. One then easily deduces that the process $\mathcal{W}$ is increment stationary and Gaussian, and that its covariance is given by Eq. (4.32). ■

Example 4.2.4 The two kernels presented in Sec. 4.1.4, namely $k_\tau(x) = \frac{\mathrm{e}^{-\tau x}}{\sqrt{x}}$ and $k_H(x) = \frac{\cos(\pi H)}{x^{H+1/2}}$, satisfy assumption 4.2.1.

Proposition 4.2.2 thus allows not only to unify the expression of existing FBM but also to derive new ones, under the assumption 4.2.1 for the kernel in the Laplace representation. Now that a general framework for FBM has been introduced, let us study the stationary processes that follow from it.

4.3 A new framework for approximated GMC

The objective being to construct an approximately log-correlated stationary X_t^τ process, different models in the literature have been developed in order to stationarize the FBM $\mathcal{W}$. In this section, we propose a non-exhaustive review of these processes and most importantly, we show how the general framework encompasses those processes in Sec. 4.3.1. Then, a stationary Ornstein-Uhlenbeck process is derived in Sec. 4.3.2 driven by the general fractional Gaussian noise $\mathrm{d}\mathcal{W}_t$.

4.3.1 Generic representation of X^τ

A temporal moving average

In their work, Schmitt and Marsan (2001), Schmitt (2003) developed the following stochastic process, inspired from the kernel of W_t^τ and made stationary with the use of a temporal moving window:

$$X_t^{\tau,S} := \int_{t+\tau-T}^{t} (t-s+\tau)^{-1/2}\,\mathrm{d}W_s. \tag{4.33}$$

They showed its multi-fractal properties (scaling laws of the random process, of the coarse-grained process, logarithmic correlation of the logarithm of the process etc.).

Let us rewrite this process using the same procedure as in Sec. 4.1.4:

$$\begin{aligned} X_t^{\tau,S} &= \int_{t+\tau-T}^{t}\int_{\mathbb{R}_+} \frac{\mathrm{e}^{-(t-s+\tau)x}}{\sqrt{\pi x}}\,\mathrm{d}x\,\mathrm{d}W_s, \\ &= \int_{\mathbb{R}_+}\left(\int_{t+\tau_\eta-T}^{t} \mathrm{e}^{-(t-s)x}\,\mathrm{d}W_s\right)\frac{\mathrm{e}^{-\tau x}}{\sqrt{\pi x}}\,\mathrm{d}x, \\ &= \int_{\mathbb{R}_+}\left(\Phi_{t,x}(W) - \mathrm{e}^{(T-\tau)x}\Phi_{t+\tau-T,x}(W)\right)k_\tau(x)\,\mathrm{d}x. \end{aligned} \tag{4.34}$$

To ensure finiteness of the variance, the Ornstein-Uhlenbeck processes must have a finite memory. In this case, the integral is truncated and the regularization consists in replacing the Ornstein-Uhlenbeck $Y_t^x - Y_0^x$ of Eq. (4.15), by $Y_t^x - \mathrm{e}^{(T-\tau)x}Y_{t+\tau-T}^x$.

A stochastic differential equation

Pereira, Moriconi, and Chevillard (2018) chose to define $X_t^{\tau,P}$ as the stationary solution of Eq. (4.6), more precisely:

$$\mathrm{d}X_t^{\tau,P} = -\frac{1}{T}X_t^{\tau,P}\,\mathrm{d}t + \sqrt{\pi}\,\mathrm{d}W_t^\tau. \tag{4.35}$$

Replacing the expression of increments of $W_t^\tau = \mathcal{L}(\Phi_{t,\cdot}(W) - \Phi_{0,\cdot}(W), k_\tau)$ derived in Eq. (4.11), we obtain a well-defined SDE with a stochastic drift:

$$\mathrm{d}X_t^{\tau,P} = -\frac{1}{T}X_t^{\tau,P}\,\mathrm{d}t + \beta_t^\tau\,\mathrm{d}t + \frac{\tau^{-1/2}}{\sqrt{\pi}}\,\mathrm{d}W_t, \tag{4.36}$$

and its solution is fully described by the formula:

$$X_t^{\tau,P} = \mathrm{e}^{-\frac{t-t_0}{T}} X_{t_0} + \int_{t_0}^{t} \mathrm{e}^{-\frac{t-s}{T}} \, \mathrm{d}W_s^\tau, \tag{4.37}$$

$$= \mathrm{e}^{-\frac{t-t_0}{T}} X_{t_0} + \int_{t_0}^{t} \mathrm{e}^{-\frac{t-s}{T}} \, \beta_s^\tau \, \mathrm{d}s + \frac{\tau^{-1/2}}{\sqrt{\pi}} \int_{t_0}^{t} \mathrm{e}^{-\frac{t-s}{T}} \, \mathrm{d}W_s. \tag{4.38}$$

The stationary solution is therefore straightforward and corresponds to the one given by Pereira, Moriconi, and Chevillard (2018):

$$X_t^{\tau,P} = \int_{-\infty}^{t} \mathrm{e}^{-\frac{t-s}{T}} \beta_s^\tau \, \mathrm{d}s + \tau^{-1/2} \int_{-\infty}^{t} \mathrm{e}^{-\frac{t-s}{T}} \, \mathrm{d}W_s. \tag{4.39}$$

Now, to obtain the expression of $X_t^{\tau,P}$ with the Laplace formalism, we start from Eq. (4.37) and replace the increment $\mathrm{d}W_t^\tau$ by its Laplace formulation:

$$\begin{aligned} X_t^{\tau,P} &= \mathrm{e}^{-\frac{t-t_0}{T}} X_{t_0}^\tau + \int_{t_0}^{t} \mathrm{e}^{-\frac{t-s}{T}} \, \mathrm{d}W_s^\tau, \\ &= \mathrm{e}^{-\frac{t-t_0}{T}} X_{t_0}^\tau + \int_0^{+\infty} \left(\int_{t_0}^{t} \mathrm{e}^{-\frac{t-s}{T}} \, \mathrm{d}\Phi_{s,x}(W) \right) k_\tau(x) \, \mathrm{d}x. \end{aligned}$$

Since the integrand is not random, we can write using an integration-by-parts:

$$\begin{aligned} \int_{t_0}^{t} \mathrm{e}^{-\frac{t-s}{T}} \, \mathrm{d}\Phi_{s,x}(W) &= \left[\mathrm{e}^{-\frac{t-s}{T}} \Phi_{s,x}(W) \right]_{t_0}^{t} - \frac{1}{T} \int_{t_0}^{t} \mathrm{e}^{-\frac{t-s}{T}} \Phi_{s,x}(W) \, \mathrm{d}s, \\ &= \Phi_{t,x}(W) - \mathrm{e}^{-\frac{t-t_0}{T}} \Phi_{t_0,x}(W) - \frac{1}{T} \int_{t_0}^{t} \mathrm{e}^{-\frac{t-s}{T}} \Phi_{s,x}(W) \, \mathrm{d}s. \end{aligned}$$

The stationary version of these processes, which we only consider from now on, reads:

$$X_t^{\tau,P} = \int_{\mathbb{R}_+} \left(\Phi_{t,x}(W) - \frac{1}{T} \int_{-\infty}^{t} \mathrm{e}^{-\frac{t-s}{T}} \Phi_{s,x}(W) \, \mathrm{d}s \right) k_\tau(x) \, \mathrm{d}x. \tag{4.40}$$

Observe that the process $\{\Phi_{t,x}(W) - \frac{1}{T} \int_{-\infty}^{t} \mathrm{e}^{-\frac{t-s}{T}} \Phi_{s,x}(W) \, \mathrm{d}s\}_{t \geq 0}$ is a stationary Ornstein-Uhlenbeck process driven by $\Phi_{\cdot,x}(W)$, hence with our notations, we get:

$$X_t^{\tau,P} = \int_{\mathbb{R}_+} \Phi_{t,\frac{1}{T}} \left(\Phi_{\cdot,x}(W) \right) k_\tau(x) \, \mathrm{d}x. \tag{4.41}$$

An Ornstein-Uhlenbeck process

Note that the model of Pope and Chen (1990), that consists of a single Ornstein-Uhlenbeck process for X^τ, can also be trivially written under this formalism using a dirac as the kernel function in the

Laplace transform:

$$\begin{aligned} \mathrm{d}X_t^{OU} &= -\frac{1}{T_\chi} X_t^{OU}\,\mathrm{d}t + \sqrt{\frac{2\sigma_\chi^2}{T_\chi}}\,\mathrm{d}W_t, \\ X_t^{OU} &= \int_{-\infty}^{t} \sqrt{\frac{2\sigma_\chi^2}{T_\chi}} \mathrm{e}^{-(t-s)/T_\chi}\,\mathrm{d}W_s, \\ &= \int_{\mathbb{R}_+} \omega_\chi \delta(t - T_\chi^{-1}) \Phi_{t,x}(W)\,\mathrm{d}x. \end{aligned} \tag{4.42}$$

An original model

Finally, we mention another model developed throughout this thesis, that we will further detail in Chap. 5. Its particularity lies in the stationary condition directly enforced via the shape of the kernel.

$$X_t^{\tau,\infty} = \int_{\mathbb{R}_+} \Phi_{t,x}(W)\, k_{\tau,T}(x)\ \mathrm{d}x, \tag{4.43}$$

where $k_{\tau,T}$ applies roughly a cut-off below τ and above T, and behaves as $\frac{1}{\sqrt{x}}$ as $\tau \to 0$. For example, $k_{\tau,T} = k_\tau - k_T$.

Remark 4.3.1 *$X_t^{\tau,\infty}$ can be written as a SDE with stochastic drift:*

$$\begin{aligned} \mathrm{d}X_t^{\tau,\infty} &= \int_{\mathbb{R}_+} \mathrm{d}Y_t^x (k_\tau - k_T)\,\mathrm{d}x, \\ &= \left(\beta_t^\tau - \beta_t^T\right)\mathrm{d}t + \left(\frac{1}{\sqrt{\pi\tau}} - \frac{1}{\sqrt{\pi T}}\right)\mathrm{d}W_t, \end{aligned}$$

or as a trivial SDE with fractional Gaussian noise:

$$\mathrm{d}X_t^{\tau,\infty} = \mathrm{d}W_t^\tau - \mathrm{d}W_t^T. \tag{4.44}$$

Using this formalism, we can retrieve the processes which are proposed in the literature and summarized in Table 4.2. We notice that either the process Z_t^x or the kernel k must involve not only the regularization parameter τ, but also a characteristic time T or T_χ which allows to stationarize the process X_t^τ. In the following, we propose to study more particularly the solution X_t^τ given by the stationary solution of an Ornstein-Uhlenbeck driven by any FBM $\mathcal{W}$ in the form of Eq. (4.24). In that case, it will be noted $\mathcal{X}$.

4.3.2 General stationary Ornstein-Uhlenbeck processes

We want to construct the stationary solution $\mathcal{X}$ of Eq. (4.6) and characterize its covariance. The uniqueness for this equation is straightforward, so we focus on the construction and integral representation of a stationary solution.

Remark that the process $X_t^{\tau,P}$ defined in Eq. 4.39 corresponds to the specific case $\kappa(x) = \frac{\mathrm{e}^{-\tau x}}{\sqrt{\pi x}}$.

Z_t^x	Kernel $k(x)$	$X_t^\tau = \mathcal{L}(Z_t^x, k)$
$\Phi_{t,x}(W) - \mathrm{e}^{(T-\tau)x}\Phi_{t+\tau-T,x}(W)$ $= \int_{t+\tau-T}^t \mathrm{e}^{-(t-s)x}\,\mathrm{d}W_s$	$\frac{\mathrm{e}^{-\tau x}}{\sqrt{\pi x}}$	(Schmitt and Marsan 2001), Eq. (4.34) $X_t^{\tau,S} = \int_{t+\tau-T}^t (t-s+\tau)^{-1/2}\,\mathrm{d}W_s$
$\Phi_{t,1/T}(Y_\cdot^x)$ $= \int_{-\infty}^t \mathrm{e}^{-(t-s)/T}\,\mathrm{d}Y_s^x$	$\frac{\mathrm{e}^{-\tau x}}{\sqrt{\pi x}}$	(Pereira et al. 2018), Eq. (4.41) $X_t^{\tau,P} = \int_{-\infty}^t \mathrm{e}^{-(t-s)/T}\,\mathrm{d}W_s^\tau$
$\Phi_{t,x}(W)$	$\omega_\chi \delta(x - T^{-1})$	(Pope and Chen 1990), Eq. (4.42) $X_t^{OU} = \omega_\chi \int_0^t \mathrm{e}^{-(t-s)/T}\,\mathrm{d}W_s$
$\Phi_{t,x}(W)$	$\frac{\mathrm{e}^{-\tau x} - \mathrm{e}^{-Tx}}{\sqrt{\pi x}}$	(Letournel et al. 2021), Eq. (4.43) $X_t^{\tau,\infty} = \int_{-\infty}^t (t-s+\tau)^{-1/2} - (t-s+T)^{-1/2}\,\mathrm{d}W_s$

Table 4.2. Laplace representation of stochastic processes X_t^τ.

Theorem 4.3.2 *Under Assumption 4.2.1, there exists a unique stationary solution $\mathcal{X}$ to Eq.* (4.6)*. It is a Gaussian process with covariance:*

$$\mathcal{C}(t) := \int_{\mathbb{R}_+}\int_{\mathbb{R}_+} \left(\mathrm{e}^{-\frac{t}{T}} - Ty\,\mathrm{e}^{-yt}\right) \frac{Ty}{(1+Ty)(1-Ty)} \frac{\kappa(x)\kappa(y)}{x+y}\,\mathrm{d}x\,\mathrm{d}y. \tag{4.45}$$

The proof of this theorem will be organised as follows:

- In Subsection 4.3.2.1, we introduce a candidate stationary process $\widetilde{\mathcal{X}}$ which is a linear combination of Ornstein-Uhlenbeck processes. We study the candidate covariance $\mathcal{C}$ associated to $\widetilde{\mathcal{X}}$ and prove that it is well defined under Assumption 4.2.1 on κ;
- In Subsection 4.3.2.2, we establish that $\widetilde{\mathcal{X}}$ is solution to the SDE (4.6), which concludes the proof.

4.3.2.1 Covariance of the general stationary Ornstein-Uhlenbeck processes

We do not work immediately on the process $\mathcal{X}$. Instead we introduce:

$$\widetilde{\mathcal{X}}_t := \int_{\mathbb{R}_+} \left(Y_t^x - \frac{1}{T}\int_{-\infty}^t \mathrm{e}^{-\frac{t-s}{T}} Y_s^x\,\mathrm{d}s\right) \kappa(x)\,\mathrm{d}x, \tag{4.46}$$

and prove in the next proposition that it is in $L^2(\Omega)$.

Proposition 4.3.3 *Assume κ satisfies Assumption 4.2.1. Then $(\widetilde{\mathcal{X}}_t)_{t\in\mathbb{R}}$ is a well defined process such that for any $t \in \mathbb{R}$, $\widetilde{\mathcal{X}}_t \in L^2(\Omega)$. Moreover it is a stationary Gaussian process with covariance* (4.45)*.*

Proof 4.3.4 We prove first that for any $t \in \mathbb{R}_+$, $\widetilde{\mathcal{X}}_t\widetilde{\mathcal{X}}_0 \in L^1(\Omega)$. For any $t \in \mathbb{R}_+$ and $x \in \mathbb{R}_+$,

$Y_t^x - \frac{1}{T}\int_{-\infty}^t \mathrm{e}^{-\frac{t-s}{T}} Y_s^x \,\mathrm{d}s \in L^2(\Omega)$. Hence in view of Eq. (4.30), we have:

$$\begin{aligned}
&\mathbb{E}\left[\left(Y_t^x - \frac{1}{T}\int_{-\infty}^t \mathrm{e}^{-\frac{t-s}{T}} Y_s^x \,\mathrm{d}s\right)\left(Y_0^y - \frac{1}{T}\int_{-\infty}^0 \mathrm{e}^{\frac{s}{T}} Y_s^y \,\mathrm{d}s\right)\right] \\
&\quad= \frac{1}{x+y}\Bigg(\mathrm{e}^{-tx} - \frac{1}{T}\int_{-\infty}^0 \mathrm{e}^{\frac{s}{T}-(t-s)x}\,\mathrm{d}s - \frac{1}{T}\int_{-\infty}^0 \mathrm{e}^{-\frac{t-s}{T}+sy}\,\mathrm{d}s - \frac{1}{T}\int_0^t \mathrm{e}^{-\frac{t-s}{T}-sx}\,\mathrm{d}s \\
&\qquad+\frac{\mathrm{e}^{-\frac{t}{T}}}{T^2}\left\{\int_{-\infty}^t\int_{-\infty}^{s_2\wedge 0} \mathrm{e}^{\frac{s_1+s_2}{T}-x(s_2-s_1)}\,\mathrm{d}s_1\,\mathrm{d}s_2 + \int_{-\infty}^0\int_{s_2}^0 \mathrm{e}^{\frac{s_1+s_2}{T}-y(s_1-s_2)}\,\mathrm{d}s_1\,\mathrm{d}s_2\right\}\Bigg) \\
&\quad= \frac{1}{x+y}\Bigg(\mathrm{e}^{-tx} - \frac{\mathrm{e}^{-tx}}{1+Tx} - \frac{\mathrm{e}^{-\frac{t}{T}}}{1+Ty} + \frac{\mathrm{e}^{-\frac{t}{T}}-\mathrm{e}^{-tx}}{1-Tx} \\
&\qquad\qquad+\left\{\frac{\mathrm{e}^{-\frac{t}{T}}}{2(1+Tx)} + \frac{\mathrm{e}^{-\frac{t}{T}}}{2(1+Ty)} + \frac{\mathrm{e}^{-tx}-\mathrm{e}^{-\frac{t}{T}}}{(1+Tx)(1-Tx)}\right\}\Bigg) \\
&\quad= \frac{1}{x+y}\left(\mathrm{e}^{-tx}\frac{Tx}{1+Tx} + (\mathrm{e}^{-\frac{t}{T}}-\mathrm{e}^{-tx})\frac{Tx}{(1-Tx)(1+Tx)} + \mathrm{e}^{-\frac{t}{T}}\left(\frac{1}{2(1+Tx)} - \frac{1}{2(1+Ty)}\right)\right).
\end{aligned}$$

We will now prove that each term in the above sum can be integrated against $\kappa(x)\kappa(y)\,\mathrm{d}x\,\mathrm{d}y$. For the first term, we have:

$$\int_{\mathbb{R}_+}\int_{\mathbb{R}_+} \mathrm{e}^{-tx}\frac{Tx}{1+Tx}\frac{|\kappa(x)\kappa(y)|}{x+y}\,\mathrm{d}x\,\mathrm{d}y = \int_{\mathbb{R}_+} \mathrm{e}^{-tx}\frac{Tx}{1+Tx}\mathcal{Q}(x)\,\mathrm{d}x,$$

performing the same change of variables as in the proof of Proposition 4.2.2. Hence bounding the exponential by 1 and $\frac{Tx}{1+Tx}$ by $1\wedge(Tx)$, we get:

$$\int_{\mathbb{R}_+}\int_{\mathbb{R}_+} \mathrm{e}^{-tx}\frac{Tx}{1+Tx}\frac{|\kappa(x)\kappa(y)|}{x+y}\,\mathrm{d}x\,\mathrm{d}y \le \int_{\mathbb{R}_+} (1\wedge Tx)\,\mathcal{Q}(x)\,\mathrm{d}x,$$

which is finite, by Assumption 4.2.1. For the second term, we use the fact that $1-\mathrm{e}^{-x}\le x$, $\forall x\in\mathbb{R}$ to deduce that

$$\left|\frac{\mathrm{e}^{-tx}-\mathrm{e}^{-t/T}}{1-Tx}\right| \le \begin{cases} 4 & \text{if } x\notin(\frac{1}{2T},\frac{3}{2T}), \\ \mathrm{e}^{-\frac{t}{T}}\dfrac{t}{T} & \text{if } x\in(\frac{1}{2T},\frac{3}{2T})\setminus\{\frac{1}{T}\}. \end{cases} \tag{4.47}$$

Hence by the same argument as the first term, the second term is also integrable. For the last term, observe that if $y>x$, then $\frac{|y-x|T}{(1+Tx)(1+Ty)} \le 1\wedge Ty$. Thus we have:

$$\begin{aligned}
&\int_{\mathbb{R}_+}\int_{\mathbb{R}_+} \mathrm{e}^{-\frac{t}{T}}\frac{|y-x|T}{2(1+Tx)(1+Ty)}\frac{|\kappa(x)\kappa(y)|}{x+y}\,\mathrm{d}x\,\mathrm{d}y \\
&\qquad= \mathrm{e}^{-\frac{t}{T}}\int_{\mathbb{R}_+}\int_{\mathbb{R}_+} \mathbb{1}_{y>x}\frac{|y-x|T}{(1+Tx)(1+Ty)}\frac{|\kappa(x)\kappa(y)|}{x+y}\,\mathrm{d}x\,\mathrm{d}y, \\
&\qquad\le \mathrm{e}^{-\frac{t}{T}}\int_{\mathbb{R}_+} (1\wedge Ty)\,\mathcal{Q}(y)\,\mathrm{d}y,
\end{aligned}$$

which is again finite by assumption. Hence we have proven that $\widetilde{\mathcal{X}}_t\widetilde{\mathcal{X}}_0 \in L^1(\Omega)$. By Fubini's theorem, we also deduce that

$$\mathbb{E}\left[\widetilde{\mathcal{X}}_t\widetilde{\mathcal{X}}_0\right] = \int_{\mathbb{R}_+}\int_{\mathbb{R}_+}\left(\mathrm{e}^{-tx}\frac{Tx}{1+Tx} + (\mathrm{e}^{-tx} - \mathrm{e}^{-\frac{t}{T}})\frac{Tx}{(1-Tx)(1+Tx)} \right.$$
$$\left. +\mathrm{e}^{-\frac{t}{T}}\left(\frac{1}{2(1+Tx)} - \frac{1}{2(1+Ty)}\right)\right)\frac{\kappa(x)\kappa(y)}{x+y}\,\mathrm{d}x\,\mathrm{d}y.$$

Now by symmetry, the last part of the equation with factor $\mathrm{e}^{-\frac{t}{T}}$ vanishes and the first and second part can be simplified to obtain that $\mathbb{E}\left[\widetilde{\mathcal{X}}_t\widetilde{\mathcal{X}}_0\right] = \mathcal{C}(t)$. Finally, the properties of the family of Ornstein-Uhlenbeck processes $(Y^x)_{x\in\mathbb{R}_+}$ and the previous integrability properties ensure that $\widetilde{\mathcal{X}}$ is Gaussian and stationary. ■

This concludes the first step of the proof the candidate process $\widetilde{\mathcal{X}}$ is well-defined, stationary, Gaussian with covariance given by Eq. (4.45).

4.3.2.2 The general stationary OU process as a solution to a SDE

Our goal here is to prove that $\widetilde{\mathcal{X}}$ solves Eq. (4.6):

Proposition 4.3.5 *Assume κ satisfies assumption 4.2.1 and $\widetilde{\mathcal{X}}$ is given by Eq.* (4.46)*:*

$$\widetilde{\mathcal{X}}_t := \int_{\mathbb{R}_+}\left(Y_t^x - \frac{1}{T}\int_{-\infty}^t \mathrm{e}^{-\frac{t-s}{T}}Y_s^x\,\mathrm{d}s\right)\kappa(x)\,\mathrm{d}x.$$

Then $\widetilde{\mathcal{X}}$ satisfies Eq. (4.6)*:*

$$\mathrm{d}\widetilde{\mathcal{X}}_t = -\frac{\widetilde{\mathcal{X}}_t}{T}\,\mathrm{d}t + \mathrm{d}\mathcal{W}_t.$$

Proof 4.3.6 Consider the process Z^x given by

$$Z_t^x = Y_t^x - \frac{1}{T}\int_{-\infty}^t \mathrm{e}^{-\frac{t-s}{T}}Y_s^x\,\mathrm{d}s.$$

This process is the unique stationary solution to the equation:

$$\mathrm{d}Z_t^x = -\frac{1}{T}Z_t^x\,\mathrm{d}t + \mathrm{d}Y_t^x.$$

Hence we can also write:

$$\begin{aligned} Z_t^x &= Z_0^x - \frac{1}{T}\int_0^t Z_s^x\,\mathrm{d}s + Y_t^x - Y_0^x, \\ &= Y_t^x - \frac{1}{T}\int_{-\infty}^0 \mathrm{e}^{\frac{s}{T}}Y_s^x\,\mathrm{d}s - \frac{1}{T}\int_0^t Z_s^x\,\mathrm{d}s. \end{aligned}$$

Hence from the previous equation and Eq. (4.46), we get the following decomposition of $\widetilde{\mathcal{X}}$:

$$\begin{aligned} \widetilde{\mathcal{X}}_t &= \int_{\mathbb{R}_+}\left(\{Y_t^x - Y_0^x\} + \{Y_0^x - \frac{1}{T}\int_{-\infty}^0 \mathrm{e}^{\frac{s}{T}}Y_s^x\,\mathrm{d}s\} - \frac{1}{T}\int_0^t Z_s^x\,\mathrm{d}s\right)\kappa(x)\,\mathrm{d}x, \\ &= \mathcal{W}_t + \widetilde{\mathcal{X}}_0 - \frac{1}{T}\int_{\mathbb{R}_+}\int_0^t\left(Y_s^x - \frac{1}{T}\int_{-\infty}^s \mathrm{e}^{-\frac{s-r}{T}}Y_r^x\,\mathrm{d}r\right)\mathrm{d}s\,\kappa(x)\,\mathrm{d}x. \end{aligned}$$

Now by Fubini's theorem we have

$$\widetilde{\mathcal{X}}_t = \widetilde{\mathcal{X}}_0 + \mathcal{W}_t - \frac{1}{T}\int_0^t \widetilde{\mathcal{X}}_s \, \mathrm{d}s.$$

Thus $\widetilde{\mathcal{X}}$ satisfies Eq. (4.6), and this concludes the proof of Theorem 4.3.2. ■

We have thus constructed a family of FBM processes, and their associated Ornstein-Uhlenbeck processes. We must now ensure that their limit covariance for $\tau \to 0$ satisfies Eq. (4.2) and that they are thus eligible to define a GMC.

4.4 Convergence to the Gaussian multiplicative chaos

4.4.1 The limit covariance

To ensure that the limit covariance $\mathcal{C}_0$ for $\tau \to 0$ in Theorem (4.3.2) is well-defined and has a logarithmic behavior, we formulate an additional assumption on the limit kernel κ_0:

Assumption 4.4.1 *For a nonnegative mapping $\kappa_0 : \mathbb{R} \to \mathbb{R}_+$, define the following quadratic form of κ_0:*

$$\mathcal{Q}_0(y) := \kappa_0(y) \int_0^1 \theta^{-1} \, \kappa_0\left(y\frac{1-\theta}{\theta}\right) \, d\theta.$$

We assume that

(a) $\displaystyle\int_{\mathbb{R}_+} \left(y \wedge \frac{1}{y}\right) \mathcal{Q}_0(y) \, \mathrm{d}y < \infty$*;*

(b) $\displaystyle\int_1^{+\infty} \mathcal{Q}_0(y) \, \mathrm{d}y = +\infty$ *and there exists $\alpha_0 > 0$ such that, for*

$$w_A := T \exp\left(-\frac{1}{\alpha_0}\int_1^A \mathcal{Q}_0(y) \, \mathrm{d}y\right), \tag{4.48}$$

the following quantities are bounded in $A \geq 1$:

$$\int_1^A \left(1 - \mathrm{e}^{-yw_A}\right) \mathcal{Q}_0(y) \, \mathrm{d}y \quad \textit{and} \quad \int_A^\infty e^{-yw_A} \mathcal{Q}_0(y) \, \mathrm{d}y.$$

Proposition 4.4.2 *Assume κ_0 satisfies Assumption 4.4.1. Then the covariance $\mathcal{C}_0$ defined by Eq.* (4.45) *with kernel κ_0 is well-defined for any $t \neq 0$ and we have:*

$$\mathcal{C}_0(t) = \alpha_0 \ln_+\left(\frac{T}{|t|}\right) + \mathcal{R}_0(t), \tag{4.49}$$

where $\mathcal{R}_0$ is a locally bounded function given by:

$$\mathcal{R}_0(t) = \begin{cases} \displaystyle\int_{\mathbb{R}_+} \left(\frac{Ty\left(\mathrm{e}^{-\frac{|t|}{T}} - Ty\mathrm{e}^{-y|t|}\right)}{(1+Ty)(1-Ty)} - \mathbb{1}_{[1,A_{|t|}]}(y)\right) \mathcal{Q}_0(y) \, \mathrm{d}y, & \textit{if } |t| \leq T \\ \mathcal{C}_0(t), & \textit{if } |t| > T \end{cases}$$

with $A_t := \inf\{A \geq 1 : \displaystyle\int_1^A \mathcal{Q}_0(y) \, \mathrm{d}y = \alpha_0 \ln(T/t)\}$ defined for $t \in (0, T]$ (see Eq. (4.51) *below).*

Proof 4.4.3 First step. In the first part of this proof, we check that under Assumption 4.4.1(a), $\mathcal{C}_0(t)$ is well defined for $t \neq 0$.
Without loss of generality, assume that $t > 0$. In view of Eq. (4.45), we study the integrability of the following mapping on $\mathbb{R}_+^2$:

$$(x, y) \mapsto \left(\mathrm{e}^{-\frac{t}{T}} - Ty\,\mathrm{e}^{-yt}\right) \frac{Ty}{(1+Ty)(1-Ty)} \frac{\kappa_0(x)\,\kappa_0(y)}{x+y}.$$

By the change of variables $x = y\dfrac{1-\theta}{\theta}$, this is equivalent to the integrability of:

$$\Phi : y \mapsto \left|\mathrm{e}^{-\frac{t}{T}} - Ty\,\mathrm{e}^{-yt}\right| \frac{Ty}{(1+Ty)|1-Ty|}\,\mathcal{Q}_0(y),$$

for $y \in \mathbb{R}_+$. For $A > 1 \vee \dfrac{2}{T}$, we decompose the domain of integration into the following subdomains: $D_1 = [0, 1]$, $D_2 = (1, A]$ and $D_3 = (A, +\infty)$.
Since $\dfrac{\mathrm{e}^{-\frac{t}{T}} - Ty\,\mathrm{e}^{-yt}}{1-Ty} = \mathrm{e}^{-\frac{t}{T}} + Ty\dfrac{\mathrm{e}^{-\frac{t}{T}} - \mathrm{e}^{-ty}}{1-Ty}$, we have similarly to Eq. (4.47) that:

$$\left|\frac{\mathrm{e}^{-\frac{t}{T}} - Ty\,\mathrm{e}^{-yt}}{1-Ty}\right| \leq \begin{cases} \dfrac{1+Ty}{|1-Ty|} \leq C & \text{if } y \notin (\frac{1}{2T}, \frac{3}{2T}) \\ \\ \mathrm{e}^{-\frac{t}{T}}\,(1+ty) \leq \mathrm{e}^{-\frac{t}{T}}\left(1 + \dfrac{3t}{2T}\right) & \text{if } y \in (\frac{1}{2T}, \frac{3}{2T}) \setminus \{\frac{1}{T}\} \end{cases}. \tag{4.50}$$

Hence there exists a constant $C > 0$ (that may depend on t, A and T) such that for any $y \in [0, A]$, we have:

$$|\Phi(y)| \leq C\,y\,\mathcal{Q}_0(y).$$

It follows that:

$$\int_{D_1 \cup D_2} |\Phi(y)|\,\mathrm{d}y \leq C \int_{[0,A]} y\,\mathcal{Q}_0(y)\,\mathrm{d}y < \infty.$$

Finally on D_3, since $A > \dfrac{2}{T}$, we have $\dfrac{Ty}{|Ty-1|} \leq 2$ for any $y > A$. Since $t \neq 0$, we also have that there exists a constant $C > 0$ (that may depend on t, A and T) such that for $y \in (A, +\infty)$,

$$\left|\mathrm{e}^{-\frac{t}{T}} - Ty\,\mathrm{e}^{-yt}\right| \leq C.$$

Using the two previous inequalities, we get:

$$\int_{D_3} |\Phi(y)|\,\mathrm{d}y \leq C \int_A^{+\infty} \frac{1}{y}\,\mathcal{Q}_0(y)\,\mathrm{d}y < \infty.$$

Second step. We will now prove that for a suitable choice of parameter A depending on t, the integral on D_2 diverges logarithmically, while the integrals on D_1 and D_3 remain bounded.

By Assumption 4.4.1(b), we have that for any $t \in (0, T]$, there exists $A_t > 1$ such that

$$\int_1^{A_t} \mathcal{Q}_0(y)\ \mathrm{d}y = \alpha_0\ \ln\left(\frac{T}{t}\right). \tag{4.51}$$

Then

$$\begin{aligned}
&\int_1^{A_t} \int_{\mathbb{R}_+} \left(\mathrm{e}^{-\frac{t}{T}} - Ty\,\mathrm{e}^{-yt}\right) \frac{Ty}{(1+Ty)(1-Ty)} \frac{\kappa_0(x)\,\kappa_0(y)}{x+y}\ \mathrm{d}x\ \mathrm{d}y, \\
&\quad = \int_1^{A_t} \mathcal{Q}_0(y)\ \mathrm{d}y + \int_1^{A_t} \left(\left(\mathrm{e}^{-\frac{t}{T}} - Ty\,\mathrm{e}^{-yt}\right) \frac{Ty}{(1+Ty)(1-Ty)} - 1\right) \mathcal{Q}_0(y)\ \mathrm{d}y, \\
&\quad =: \alpha_0\ \ln\left(\frac{T}{t}\right) + \mathcal{R}_2(t).
\end{aligned}$$

For $\mathcal{R}_2$, we have

$$\begin{aligned}
\mathcal{R}_2(t) &= \int_1^{A_t} \left(\frac{(\mathrm{e}^{-\frac{t}{T}} - \mathrm{e}^{-yt})Ty}{1-T^2y^2} + \frac{Ty\mathrm{e}^{-yt}}{1+Ty} - 1\right) \mathcal{Q}_0(y)\ \mathrm{d}y, \\
&= \int_1^{A_t} \frac{(\mathrm{e}^{-\frac{t}{T}} - \mathrm{e}^{-yt})Ty}{1-T^2y^2} \mathcal{Q}_0(y)\ \mathrm{d}y + \int_1^{A_t} \frac{Ty(\mathrm{e}^{-yt}-1)-1}{1+Ty} \mathcal{Q}_0(y)\ \mathrm{d}y.
\end{aligned} \tag{4.52}$$

For the first integral in Eq. (4.52), we will use Eq. (4.47) when $y \in (\frac{1}{2T}, \frac{3}{2T})$, and the bound $|\frac{(\mathrm{e}^{-\frac{t}{T}} - \mathrm{e}^{-yt})Ty}{Ty-1}| \leq 3$ when $y \geq \frac{3}{2T}$. We get:

$$\begin{aligned}
\left|\int_1^{A_t} \frac{(\mathrm{e}^{-\frac{t}{T}} - \mathrm{e}^{-yt})Ty}{1-T^2y^2} \mathcal{Q}_0(y)\ \mathrm{d}y\right| &\leq C \int_1^{A_t} \frac{1}{1+Ty} \mathcal{Q}_0(y)\ \mathrm{d}y \\
&\leq C \int_1^{\infty} \frac{1}{y} \mathcal{Q}_0(y)\ \mathrm{d}y,
\end{aligned}$$

which is finite by assumption. For the second integral in Eq. (4.52), we have by inverting Eq. (4.51) that for w_A defined in Eq. (4.48), $w_{A_t} = t$. Hence it comes:

$$\begin{aligned}
\left|\int_1^{A_t} \frac{Ty(\mathrm{e}^{-yt}-1)-1}{1+Ty} \mathcal{Q}_0(y)\ \mathrm{d}y\right| &\leq C \int_1^{A_t} (1-\mathrm{e}^{-yt}) \mathcal{Q}_0(y)\ \mathrm{d}y + C \int_1^{A_t} \frac{1}{y} \mathcal{Q}_0(y)\ \mathrm{d}y, \\
&\leq C \int_1^{A_t} (1-\mathrm{e}^{-yw_{A_t}}) \mathcal{Q}_0(y)\ \mathrm{d}y + C \int_1^{\infty} \frac{1}{y} \mathcal{Q}_0(y)\ \mathrm{d}y.
\end{aligned}$$

By Assumption 4.4.1(a) and (b), both terms are finite and bounded uniformly in $t \in (0, T]$. Extending $\mathcal{R}_2$ to $\mathcal{R}_2(0) = 0$ and by symmetry on $[-T, 0]$, we have proven that $\mathcal{R}_2$ is a bounded function on $[-T, T]$. On $\mathbb{R} \setminus [-T, T]$, we extend $\mathcal{R}_2$ by:

$$\mathcal{R}_2(t) = \int_1^{A_t} \left(\mathrm{e}^{-\frac{|t|}{T}} - Ty\,\mathrm{e}^{-y|t|}\right) \frac{Ty}{(1+Ty)(1-Ty)}\ \mathcal{Q}_0(y)\ \mathrm{d}y, \quad t \in \mathbb{R} \setminus [-T, T].$$

Hence $\mathcal{R}_2$ is a bounded function on $\mathbb{R}$.

It remains to prove the boundedness of the integrals on D_1 and D_3. Define now for any $t \in \mathbb{R}$:

$$\mathcal{R}_1(t) := \int_0^1 \left(\mathrm{e}^{-\frac{|t|}{T}} - Ty\,\mathrm{e}^{-y|t|}\right) \frac{Ty}{(1+Ty)(1-Ty)}\,\mathcal{Q}_0(y)\,\mathrm{d}y$$
$$\mathcal{R}_3(t) := \int_{A_t}^\infty \left(\mathrm{e}^{-\frac{|t|}{T}} - Ty\,\mathrm{e}^{-y|t|}\right) \frac{Ty}{(1+Ty)(1-Ty)}\,\mathcal{Q}_0(y)\,\mathrm{d}y.$$

Using again Eq. (4.50), we get that $\mathcal{R}_1$ is bounded on $\mathbb{R}$. Without loss of generality, let $t > 0$. For $\mathcal{R}_3$, we bound (for A_t large enough) $\dfrac{Ty}{(1+Ty)(1-Ty)}$ by $\dfrac{C}{y}$ to get:

$$\begin{aligned}
|\mathcal{R}_3(t)| &\le C\int_{A_t}^\infty \left|\mathrm{e}^{-\frac{t}{T}} - Ty\,\mathrm{e}^{-yt}\right| \frac{1}{y}\,\mathcal{Q}_0(y)\,\mathrm{d}y,\\
&\le C\int_{A_t}^\infty \frac{1}{y}\,\mathcal{Q}_0(y)\,\mathrm{d}y + C\int_{A_t}^\infty \mathrm{e}^{-yt}\,\mathcal{Q}_0(y)\,\mathrm{d}y,\\
&\le C\int_1^\infty \frac{1}{y}\,\mathcal{Q}_0(y)\,\mathrm{d}y + C\int_{A_t}^\infty \mathrm{e}^{-yw_{A_t}}\,\mathcal{Q}_0(y)\,\mathrm{d}y,
\end{aligned}$$

using again the definition of w_A in Eq. (4.48). By Assumption 4.4.1, the above terms are finite and bounded uniformly in $t \in (0,T]$, and by symmetry on $[-T,T]\setminus\{0\}$ as well. The boundedness on $\mathbb{R}\setminus[-T,T]$ can be treated more simply with Assumption 4.4.1(a) and we omit the details.
Finally the function $\mathcal{R}_0$ is given by te following sum:

$$\mathcal{R}_0 := \mathcal{R}_1 + \mathcal{R}_2 + \mathcal{R}_3.$$

■

4.4.2 Convergence to the log-correlated process

We consider the positive definite kernel K introduced in Eq. (4.2):

$$\forall t,s \in \mathcal{T},\quad K(t,s) = \ln_+ \frac{1}{|t-s|} + g(t,s), \tag{4.53}$$

where g is a bounded function. Let X be a random centered Gaussian distribution with covariance given by Eq. (4.2). According to the definition of Rhodes and Vargas (2014), a smooth approximation of K is defined by:

Definition 4.4.4 (Smooth Gaussian approximation) *We say that a sequence of centered Gaussian fields $(X^\epsilon)_{\epsilon>0}$ is a smooth Gaussian approximation of K if:*

- $\forall t,s \in \mathcal{T},\quad \mathbb{E}\left[X_t^\epsilon X_s^\epsilon\right]$ *converges to $K(t,s)$ as ϵ goes to 0 ;*

- $\forall \tau > 0$*, there exists some constant $C > 0$ and $\alpha > 0$ such that $\forall \epsilon > 0$:*

$$|t-s| \le \tau, \Rightarrow \mathbb{E}\left[\left(X_t^\epsilon - X_s^\epsilon\right)^2\right] \le X|t-s|^\alpha \epsilon^{-\alpha} \tag{4.54}$$

Proposition 4.4.5 *Let $(\kappa_\epsilon)_{\epsilon>0}$ be a family of kernels such that κ_ϵ satisfies Assumption 4.2.1 for all $\epsilon > 0$ and κ_0 a kernel which satisfies Assumption 4.4.1. Assume further that κ_ϵ converges pointwise to κ_0. Then $(\mathcal{X}^\epsilon)_{\epsilon>0}$ is a smooth Gaussian approximation. Moreover, it converges weakly in law to a log-correlated process $\mathcal{X}^0$, in the sense that*

$$\forall \varphi,\psi \in \mathcal{S}(\mathbb{R}),\quad \mathbb{E}\left[\langle \mathcal{X}^\epsilon,\varphi\rangle\,\langle \mathcal{X}^\epsilon,\psi\rangle\right] \longrightarrow \mathbb{E}\left[\langle \mathcal{X}^0,\varphi\rangle\,\langle \mathcal{X}^0,\psi\rangle\right] = \int_{\mathbb{R}}\int_{\mathbb{R}} \mathcal{C}_0(t-s)\,\varphi(s)\,\psi(t)\,ds\,dt$$

Proof of this proposition is still an ongoing work, that will be published in Goudenège, Letournel, and Richard (2022). Therefore, we have derived assumptions on the kernel κ_ϵ to ensure that any associated family of processes $\mathcal{X}^\epsilon$, defined from a SDE driven by $\mathcal{W}^\epsilon$ converges toward the singular process in the GMC.

Conclusion

In this chapter, we have developed a general mathematical framework for the construction of an intermittent stochastic process, based on a Gaussian multiplicative chaos approach. We have proposed an original approach to generate log-correlated processes which converge towards the GMC. These processes are based on regularized fractional Brownian motion $\mathcal{W}$.

In particular, we have proposed an original formalism to generate families of FBM, based on a Laplace transform and consisting of an infinite sum of standard Ornstein-Uhlenbeck processes weighted by a regularized kernel κ_ϵ. This formalism encompasses existing processes of literature, and opens the way to new ones along with new approaches for numerical implementations of such processes that will be detailed in Chap. 5.

In particular, we have focused in this chapter on $\mathcal{X}$, a regularized stationary process following a SDE and we have shown its existence, uniqueness and convergence towards the GMC. The stochastic process defined in the next chapter uses a different regularization, but leads to the same unique GMC.

Chapter 5

An original and versatile numerical approach for intermittent stochastic processes

In Chap. 4, we have established a mathematical framework to build a sequence of regularized processes converging to the universal Gaussian multiplicative chaos. Inspired by the approximation of fractional Brownian motion by an infinite weighted sum of correlated Ornstein-Uhlenbeck processes, we develop a new stochastic model: $X_t = \int_0^\infty Y_t^x k(x)\,\mathrm{d}x$, where Y_t^x is an Ornstein-Uhlenbeck process with speed of mean reversion x and k is a kernel. A regularization of $k(x)$ is proposed to ensure stationarity, finite variance and logarithmic autocorrelation. To simulate the process, we eventually design a new approach relying on a limited number of modes for approximating the integral through a quadrature $X_t^N = \sum_i \omega_i Y_t^{x_i}$, using a conventional quadrature method. This method can retrieve the expected behavior with only one mode per decade, making this strategy versatile and computationally attractive for simulating such processes, while remaining within the proposed framework for a proper description of intermittency.

In Sec. 5.1, the steps to build a new process X_t, inspired by the formalism developed in the previous chapter, are detailed. The covariance computations allow to verify the successful convergence of this regularized process to the GMC. Section 5.2 gives an original and efficient method to implement the process in a discrete way. Other numerical aspects are discussed and a comparison with existing models is made.

5.1 Infinite sum of correlated Ornstein-Uhlenbeck processes

We have shown that the FBM can be expressed as an infinite sum of correlated Ornstein-Uhlenbeck processes, weighted by a kernel function k (see Sec. 4.2.1). This formulation has the advantage that no convolution product appears, and therefore the simulation of such a process does not require long-term memory. Inspired from this formalism, we propose a new process for X_t.

The regularization scales τ and T that we introduced in Chap. 4 for the sake of existence and convergence of processes can be identified with the characteristic scales of turbulence introduced in Chap. 1, according to the following argument:

- The Kolmogorov scale τ_η, below which dissipation prevails over transport phenomena, corresponds to τ, the regularization scale of the FBM. Turbulence theories predict that fluctu-

ations of variables on scales smaller than τ_η are negligible, and the fields or processes are regular under this scale.

- The Lagrangian integral scale T_L, the correlation scale of the velocities of the fluid particles, beyond which the particles "lose" the memory of their history, corresponds to T, which was introduced for the stationarity of the processes X_t and therefore φ_t.

It becomes clear that the GMC, corresponding to the limit process φ_t^0 provides a model of turbulence at infinite Reynolds number. For a finite inertial zone, $\mathrm{Re}_L^{1/2} \sim T_L/\tau_\eta < \infty$, the dissipation can rather be modeled by the approximated GMC $\varphi_t^{\tau_\eta}$. Therefore, in the following, we omit the τ regularization superscript by considering that all introduced X_t are in fact $X_t^{\tau_\eta}$, regularized to the τ_η time scale.

5.1.1 A new stochastic process with appropriate regularizations

As shown in Sec. 3.4.4.3, FBM have been successfully used to reproduce multi-fractal properties and we therefore use Laplace representation derived in Chap. 4 to suggest the following stochastic model for X_t:

$$X_t = \int_0^\infty Y_t^x k(x)\,\mathrm{d}x, \tag{5.1}$$

where Y_t^x is an Ornstein-Uhlenbeck process of parameter x and $k(x)$ has to be determined. We now give the constraints on such model to ensure the stationarity, the finite variance and the logarithmic autocorrelation of X_t.

1. **Stationarity**
   A sufficient condition of stationarity for X_t is to impose stationarity for all the Ornstein-Uhlenbeck processes Y_t^x:

$$Y_t^x = \int_{-\infty}^t \mathrm{e}^{-x(t-s)}\,\mathrm{d}W_s. \tag{5.2}$$

2. **Logarithmic autocorrelation**
   The autocorrelation of this process is:

$$\mathbb{E}\left[X_t X_{t+\tau}\right] = \int_0^\infty \int_0^\infty \mathbb{E}\left[Y_t^x Y_{t+\tau}^y\right] k(x)k(y)\,\mathrm{d}x\,\mathrm{d}y. \tag{5.3}$$

   Let us first derive the covariance functions of two correlated Ornstein-Uhlenbeck processes. We recall that $Y_t^x = \int_{-\infty}^t \mathrm{e}^{-(t-x)x}\,\mathrm{d}W_s$. For any $x, y \in [0, +\infty[$ and $t > 0$ and $\tau > 0$, we have:

$$\begin{aligned}
\mathbb{E}\left[Y_t^x Y_{t+\tau}^y\right] &= \mathbb{E}\left[\int_{-\infty}^t \mathrm{e}^{-x(t-s)}\,\mathrm{d}W_s \int_{-\infty}^{t+\tau} \mathrm{e}^{-y(t+\tau-s)}\,\mathrm{d}W_s\right], \\
&= \mathrm{e}^{-(x+y)t}\mathrm{e}^{-y\tau} \int_{-\infty}^t \mathrm{e}^{(x+y)s}\,\mathrm{d}s, \\
&= \frac{\mathrm{e}^{-y\tau}}{x+y}.
\end{aligned} \tag{5.4}$$

This gives us:

$$\mathbb{E}\left[X_t X_{t+\tau}\right] = \int_0^\infty \int_0^\infty \frac{\mathrm{e}^{-\tau y}}{x+y} k(x)k(y)\,\mathrm{d}x\,\mathrm{d}y. \tag{5.5}$$

We have seen that a FBM of Hurst $H = 0$ has a logarithmic autocorrelation, at least approximately i.e., apart from the singularity. Based on the inverse Laplace transformation of the kernel $K(t) \sim t^{-1/2}$, we propose $k(x) \sim x^{-1/2}$. However, this kernel possesses a singularity at 0 and we need to introduce regularizations to ensure a finite variance.

3. **Finite variance**
   X_t is zero-averaged and its autocorrelation function only depends on the delay τ because of stationarity. The variance of the process can be expressed as:

$$\int_0^\infty \int_0^\infty \frac{k(x)k(y)}{x+y}\,\mathrm{d}x\,\mathrm{d}y < \infty. \tag{5.6}$$

To satisfy and combine these three requirements, we propose to regularize the kernel k in the following way. Here we give physical and qualitative arguments to introduce the regularizations, while the next section is devoted to the mathematical demonstration:

- One can see on the autocorrelation of Eq. (5.5) that any contribution of the function $k(y)$ for $y \gg 1/\tau$ will vanish because of the term $\mathrm{e}^{-\tau y}$. Therefore, we introduce τ_η and we can assume $k(x) \sim x^{-1/2}$ only for $x \ll \tau_\eta^{-1}$, which is now compliant with the integrability on $\mathbb{R}^+$. From a physical point of view, this regularization can be thought as a viscous cut-off.
- A second regularization step is needed to ensure a finite variance of the process X_t, which corresponds to the need to introduce a large scale. More precisely, the second requirement (iii) in Sec. 3.4.2 specifies $\mathbb{E}\left[X_t^2\right] \sim \ln(T_L/\tau_\eta)$. It implies the integrability of $(x,y) \to \dfrac{k(x)k(y)}{x+y}$ on $(\mathbb{R}^+)^2$ and the logarithmic behavior in the inertial range is ensured by the requirement of $k(x) \sim x^{-1/2}$ for $T_L^{-1} \ll x \ll \tau_\eta^{-1}$.

In light of these regularizations, we propose a new model for the process X_t^∞. Note that we use the superscript "∞" because it highlights the use of an infinite sum of Ornstein-Uhlenbeck processes.

$$X_t^\infty = \int_0^\infty Y_t^x \frac{1}{\sqrt{\pi x}} \left(g_{T_L}(x) - g_{\tau_\eta}(x)\right) \mathrm{d}x, \tag{5.7}$$

where g is such that the integral defined by the autocorrelation in Eq. (5.6) converges. A sufficient condition would be:

$$g_\alpha(x) \to \begin{cases} 0 & \text{if } x \ll 1/\alpha \\ 1 & \text{if } x \gg 1/\alpha. \end{cases} \tag{5.8}$$

Examples of possible regularizations of the kernel $k(x) \sim x^{-1/2}$ are shown in Fig. 5.1: Cutting functions are $g_\alpha(x) = 1 - \mathrm{e}^{-\alpha x}$ or $g_\alpha(x) = H(x - 1/\alpha)$ where H is the heaviside function.

5.1.2 Autocorrelation function of X_t^∞

Proposition 5.1.1 *X_t^∞, defined by*

$$X_t^\infty = \int_0^\infty Y_t^x \frac{1}{\sqrt{\pi x}} \left(g_{T_L}(x) - g_{\tau_\eta}(x)\right) \mathrm{d}x, \tag{5.9}$$

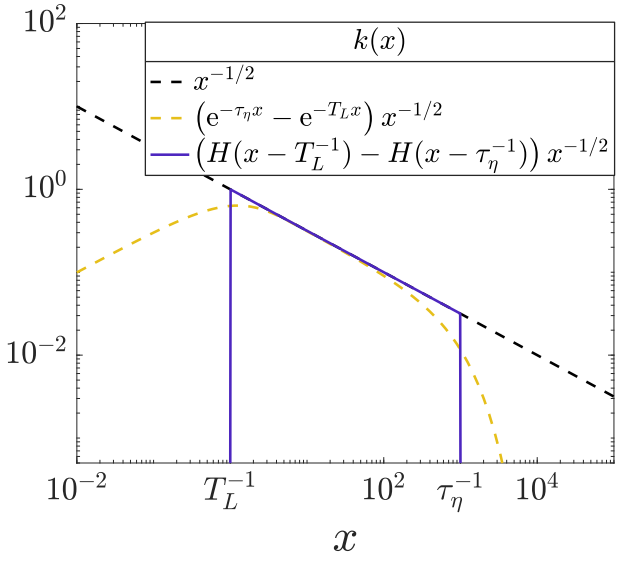

Figure 5.1. Possible regularizations of the kernel $k(x)$ in a log-log scale.

is a smooth Gaussian approximation (see Def. 4.4.4), with $\mathbb{E}\left[X_t^\infty X_{t+\tau}^\infty\right] \sim \ln \dfrac{T_L}{\tau}$.

Proof 5.1.2 We calculate the autocorrelation of the process, that we denote $A = \mathbb{E}\left[X_t^\infty X_{t+\tau}^\infty\right]$. We can consider, without loss of generality: $\mathrm{e}^{-\tau y} = 1 - g_\tau(y)$.

$$\begin{aligned} A &= \frac{1}{\pi}\int_0^\infty\int_0^\infty \frac{\mathrm{e}^{-\tau y}}{(x+y)\sqrt{xy}}\big(g_{T_L}(x) - g_{\tau_\eta}(x)\big)\big(g_{T_L}(y) - g_{\tau_\eta}(y)\big)\,\mathrm{d}x\,\mathrm{d}y \\ &= \frac{1}{\pi}\int_0^\infty\int_0^\infty \frac{1}{(x+y)\sqrt{xy}}\big(g_{T_L}(x) - g_{\tau_\eta}(x)\big)\big(g_{T_L}(y) - g_{\tau}(y)\big)\,\mathrm{d}x\,\mathrm{d}y \\ &= \frac{4}{\pi}\int_0^{\pi/2}\int_{r=0}^\infty \frac{\Big(g_{T_L}(r^2) - g_\tau(r^2)\Big)\Big(g_{T_L/\tan^2\theta}(r^2) - g_{\tau_\eta/\tan^2\theta}(r^2)\Big)}{r}\,\mathrm{d}r\,\mathrm{d}\theta \end{aligned} \tag{5.10}$$

by using the transformation $(x, y) = (r^2\cos^2\theta, r^2\sin^2\theta)$, the Jacobian of which is $4r^3\cos(\theta)\sin(\theta)$. We introduce the function

$$f_{\tau_\eta,T_L} : (r,\theta) \mapsto \Big(g_{T_L}(r) - g_\tau(r)\Big)\Big(g_{T_L/\tan^2\theta}(r) - g_{\tau_\eta/\tan^2\theta}(r)\Big). \tag{5.11}$$

Because g_τ is a cut-off function for values higher than τ^{-1}, the function $g_{\tau_2} - g_{\tau_1}$ can be seen as a band-pass function for values between τ_2^{-1} and τ_1^{-1}. The product of the band-pass functions $f_{\tau_\eta,T_L}(r^2,\theta)$ is also a band-pass function, whose passing-band depends on the values of θ.
The interval of integration of θ can be divided in 5 parts:

$$\begin{aligned} [0;\pi/2] = &\left[0;\tan^{-1}\left(\sqrt{\tau_\eta/T_L}\right)\right] \cup \left[\tan^{-1}\left(\sqrt{\tau_\eta/T_L}\right);\tan^{-1}\left(\sqrt{\tau_\eta/\tau}\right)\right] \\ &\cup \left[\tan^{-1}\left(\sqrt{\tau_\eta/\tau}\right);\pi/4\right] \cup \left[\pi/4;\tan^{-1}\left(\sqrt{T_L/\tau}\right)\right] \\ &\cup \left[\tan^{-1}\left(\sqrt{T_L/\tau}\right);\pi/2\right] \\ &=: I_1 \cup I_2 \cup I_3 \cup I_4 \cup I_5. \end{aligned}$$

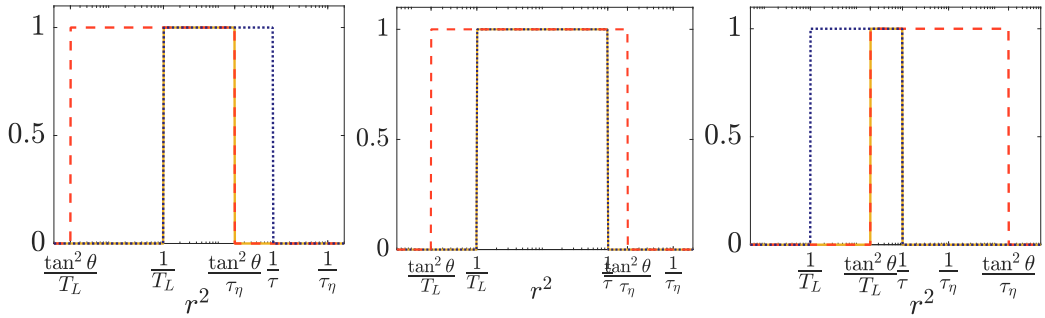

(a) $\theta \in I_2$ (b) $\theta \in I_3$ (c) $\theta \in I_4$

Figure 5.2. The yellow line represents the functions $f(r^2, \theta)$ for three examples of θ, each of them being included in the intervals I_2 (a) ; I_3 (b) ; I_4 (c). The dotted blue line is $\left(g_{T_L}(r^2) - g_\tau(r^2)\right)$, the dashed red line is $\left(g_{T_L/\tan^2\theta}(r^2) - g_{\tau_\eta/\tan^2\theta}(r^2)\right)$.

The integral A can accordingly be split in 5 parts:

$$\begin{aligned}\frac{\pi}{4}A &= \int_{I_1}\int_{r=0}^{\infty}\frac{f(r^2)}{r}\,\mathrm{d}r\,\mathrm{d}\theta + \int_{I_2}\int_{r=0}^{\infty}\frac{f(r^2)}{r}\,\mathrm{d}r\,\mathrm{d}\theta \\ &+ \int_{I_3}\int_{r=0}^{\infty}\frac{f(r^2)}{r}\,\mathrm{d}r\,\mathrm{d}\theta + \int_{I_4}\int_{r=0}^{\infty}\frac{f(r^2)}{r}\,\mathrm{d}r\,\mathrm{d}\theta \\ &+ \int_{I_5}\int_{r=0}^{\infty}\frac{f(r^2)}{r}\,\mathrm{d}r\,\mathrm{d}\theta.\end{aligned} \tag{5.12}$$

The first and last integral are equal to zero because the band-pass functions do not have any superposition when $\theta \in I_1$ or $\theta \in I_5$.

To help the reader visualize the products of the regularized g-functions, we show in Fig. 5.2 the schemes for the resulting product of the g-functions, i.e. f for different values of θ. We can see from Fig. 5.2 that the function $f_{\tau_\eta,T_L}(r^2,\theta)$ for θ in I_2, I_3 and I_4 can be simplified to:

$$\begin{aligned}f_{\tau_\eta,T_L}(r^2,\theta)\mathcal{I}_{I_2}(\theta) &= g_{T_L}(r^2) - g_{\tau_\eta/\tan^2\theta}(r^2), \\ f_{\tau_\eta,T_L}(r^2,\theta)\mathcal{I}_{I_3}(\theta) &= g_{T_L}(r^2) - g_{\tau}(r^2), \\ f_{\tau_\eta,T_L}(r^2,\theta)\mathcal{I}_{I_4}(\theta) &= g_{T_L/\tan^2\theta}(r^2) - g_{\tau}(r^2),\end{aligned} \tag{5.13}$$

where $\mathcal{I}_I$ is the characteristic function of the interval I. We use the property of the regularizing functions g_α, for $0 < \tau_1 \leq \tau_2$, we have:

$$\int_0^\infty \frac{g_{\tau_2}(r^2) - g_{\tau_1}(r^2)}{r}\,\mathrm{d}r \approx \int_{\sqrt{\tau_2^{-1}}}^{\sqrt{\tau_1^{-1}}} \frac{1}{r}\,\mathrm{d}r = \frac{1}{2}\ln\frac{\tau_2}{\tau_1}. \tag{5.14}$$

$$\begin{aligned}\frac{\pi}{4}A &= \int_{I_2}\frac{1}{2}\ln\left(\frac{T_L\tan^2\theta}{\tau_\eta}\right)\mathrm{d}\theta + \int_{I_3}\frac{1}{2}\ln\left(\frac{T_L}{\tau}\right)\mathrm{d}\theta + \int_{I_4}\frac{1}{2}\ln\left(\frac{T_L}{\tau\tan^2\theta}\right)\mathrm{d}\theta,\\ &= \frac{1}{2}\ln\frac{T_L}{\tau_\eta}\left(\tan^{-1}\sqrt{\frac{\tau_\eta}{\tau}} - \tan^{-1}\sqrt{\frac{\tau_\eta}{T_L}}\right) + \int_{\tan^{-1}\sqrt{\tau_\eta/T_L}}^{\tan^{-1}\sqrt{\tau_\eta/\tau}}\ln(\tan\theta)\,\mathrm{d}\theta\\ &+ \frac{1}{2}\ln\frac{T_L}{\tau}\left(\frac{\pi}{4} - \tan^{-1}\sqrt{\frac{\tau_\eta}{\tau}}\right)\\ &+ \frac{1}{2}\ln\frac{T_L}{\tau}\left(\tan^{-1}\sqrt{\frac{T_L}{\tau}} - \frac{\pi}{4}\right) - \int_{\pi/4}^{\tan^{-1}\sqrt{T_L/\tau}}\ln(\tan\theta)\,\mathrm{d}\theta,\end{aligned}$$

and in the inertial range, using $T_L/\tau \to \infty$ and $\tau/\tau_\eta \to \infty$:

$$\begin{aligned}A &= \ln\frac{T_L}{\tau} \qquad (5.15)\\ &- \frac{2}{\pi}\ln\frac{T_L}{\tau}\left[\sqrt{\frac{\tau_\eta}{\tau}} + \sqrt{\frac{\tau}{T_L}} + \mathcal{O}\left(\left(\frac{\tau_\eta}{\tau}\right)^{1/2}\right) + \mathcal{O}\left(\left(\frac{\tau}{T_L}\right)^{3/2}\right)\right]\\ &+ \frac{2}{\pi}\ln\frac{T_L}{\tau_\eta}\left[\sqrt{\frac{\tau_\eta}{\tau}} - \sqrt{\frac{\tau_\eta}{T_L}} + \mathcal{O}\left(\left(\frac{\tau_\eta}{\tau}\right)^{1/2}\right) + \mathcal{O}\left(\left(\frac{\tau_\eta}{T_L}\right)^{1/2}\right)\right]\\ &+ \int_{\tan^{-1}\sqrt{\tau_\eta/T_L}}^{\tan^{-1}\sqrt{\tau_\eta/\tau}}\ln(\tan\theta)\,\mathrm{d}\theta - \int_{\pi/4}^{\tan^{-1}\sqrt{T_L/\tau}}\ln(\tan\theta)\,\mathrm{d}\theta.\end{aligned}$$

The second and third lines are bounded functions and tend towards 0 in the limit of $T_L/\tau \to \infty$ and $\tau/\tau_\eta \to \infty$. The last line tends towards the constant $\frac{4}{\pi}\int_0^{\pi/4}\ln(\tan\theta)\,\mathrm{d}\theta$.

The variance can be deduced from this calculation:

$$\mathbb{E}\left[(X_t^\infty)^2\right] = \frac{1}{\pi}\int_0^\infty\int_0^\infty \frac{1}{(x+y)\sqrt{xy}}\left(g_{T_L}(x) - g_{\tau_\eta}(x)\right)\left(g_{T_L}(y) - g_{\tau_\eta}(y)\right)\mathrm{d}x\,\mathrm{d}y. \quad (5.16)$$

We remark that this expression is similar to the one obtained in Eq.(5.10) where τ is replaced by τ_η. Therefore, we obtain:

$$\mathbb{E}\left[(X_t^\infty)^2\right] \underset{T_L/\tau_\eta\to\infty}{\sim} \ln\left(\frac{T_L}{\tau_\eta}\right) + \frac{8}{\pi}\int_0^{\pi/4}\ln(\tan\theta)\,\mathrm{d}\theta. \quad (5.17)$$

■

We have shown that $\mathbb{E}\left[(X_t^\infty)^2\right] \sim \ln(T_L/\tau_\eta)$ and $\mathbb{E}\left[X_t^\infty X_{t+\tau}^\infty\right] \sim \ln(T_L/\tau)$.

The following section presents the choices of regularization made for the other processes for which spectral representation has been introduced in Sec. 4.3.1.

5.1.3 A framework encompassing existing processes

In this section, we show that previous stochastic processes can be obtained from Eq. (5.1) with appropriate regularizations.

The process W_t^τ is obtained by replacing the stationary process of Ornstein-Uhlenbeck Y_t^x by $Y_t^x - Y_0^x$. Well defined thanks to its regularizing kernel $k_\tau = \dfrac{\mathrm{e}^{-\tau\cdot}}{\pi\sqrt{\cdot}}$, it is however not stationary. We have verified in Sec. 4.2.2 that its covariance function is of logarithmic form, but it is not bounded.

In the spectral representation, we have seen that the process developed by Schmitt and Marsan (2001) can be written, following Eq. (4.34):

$$\int_{\mathbb{R}_+} \left(\int_{t+\tau_\eta - T_L}^{t} \mathrm{e}^{-(t-s)x}\, \mathrm{d}W_s \right) k_{\tau_\eta}(x)\, \mathrm{d}x.$$

Here, the regularization resulting in the stationarity of the process is carried by the process $\displaystyle\int_{t+\tau_\eta - T_L}^{t} \mathrm{e}^{-(t-s)x}\, \mathrm{d}W_s$ which replaces Y_t^x in Eq. (5.1).

According to Eq. (4.41), the process introduced by Pereira, Moriconi, and Chevillard (2018) can be written as

$$\int_{\mathbb{R}_+} \left(\int_{-\infty}^{t} \mathrm{e}^{-(t-s)/T_L}\, \mathrm{d}Y_s^x \right) k_{\tau_\eta}(x)\, \mathrm{d}x.$$

Therefore, the regularization for stationarity consists in replacing the Ornstein-Uhlenbeck Y_t^x of Eq. (5.1), by $\displaystyle\int_{-\infty}^{t} \mathrm{e}^{-(t-s)/T_L}\, \mathrm{d}Y_s^x$. For both processes, the kernel $k_{\tau_\eta} = \dfrac{\mathrm{e}^{-\tau_\eta\cdot}}{\sqrt{\pi\cdot}}$ produces a log-correlated covariance function.

As for the single Ornstein-Uhlenbeck process of Pope and Chen (1990), it can be written as in Eq. (4.42):

$$\int_0^\infty Y_t^x \delta(x - T_\chi^{-1})\, \mathrm{d}x.$$

Though it is stationary, this kernel representation does not exhibit a behavior in $x^{-1/2}$, and we already know that the single Ornstein-Uhlenbeck process is not log-correlated.

Table 5.1 summarizes the different regularizations for all these processes. It shows that the general formalism of Eq. (5.1) is a framework that encompasses existing processes depending on the three criteria for the regularization.

If the general formalism proposed in Eq. (5.1) gives the possibility to represent and simulate these processes using Ornstein-Uhlenbeck processes, one can see that their simulation is not equivalent. Processes of Schmitt (2003) and Pereira, Moriconi, and Chevillard (2018) require to keep in memory the history of the process since at each time t, the set of realizations of W_s and Y_s^x respectively, for s in the intervals $[t + \tau_\eta - T_L, t]$ and $]-\infty, t]$ respectively should be involved in the computation (it is actually truncated for the numerical simulation). It is not the case for the one we propose in Eq. (5.7) and we develop in the following section a numerical approach to implement such a process with no long-term memory.

Process	Definition	Spectral representation
$W_t^{\tau_\eta}$	Eq. (4.12)	$\int_0^\infty (Y_t^x - Y_0^x)\,\frac{\mathrm{e}^{-\tau_\eta x}}{\pi\sqrt{x}}\,\mathrm{d}x$
X_t^S	$\int_{t+\tau_\eta-T_L}^t (t-s+\tau_\eta)^{-1/2}\,\mathrm{d}W_s$	$\int_0^\infty \left(\int_{t+\tau_\eta-T_L}^t \mathrm{e}^{-(t-s)x}\,\mathrm{d}W_s\right)\frac{\mathrm{e}^{-\tau_\eta x}}{\sqrt{\pi x}}\,\mathrm{d}x$
X_t^P	$\sqrt{\pi}\int_{-\infty}^t \mathrm{e}^{-(t-s)/T_L}\,\mathrm{d}W_s^{\tau_\eta}$	$\int_0^\infty \left(\int_{-\infty}^t \mathrm{e}^{-(t-s)/T_L}\,\mathrm{d}Y_s^x\right)\frac{\mathrm{e}^{-\tau_\eta x}}{\sqrt{\pi x}}\,\mathrm{d}x$
X_t^{OU}	$\int_{-\infty}^t \omega\mathrm{e}^{-(t-s)/T_\chi}\,\mathrm{d}W_s$	$\int_0^\infty Y_t^x \omega\delta(x-T_\chi^{-1})\,\mathrm{d}x$
X_t^∞	$\int_{-\infty}^t (t-s+\tau_\eta)^{-1/2} - (t-s+T_L)^{-1/2}\,\mathrm{d}W_s$	$\int_0^\infty Y_t^x \frac{\left(g_{T_L}(x)-g_{\tau_\eta}(x)\right)}{\sqrt{\pi x}}\,\mathrm{d}x$

Table 5.1. Regularizations applied on the spectral representation of different processes. The logarithmic behavior of the autocorrelation of the process comes from the kernel behavior $x^{-1/2}$ in brown, its stationarity comes from the blue term and the red terms ensures the finite variance.

5.2 Finite sum of correlated Ornstein-Uhlenbeck processes

5.2.1 Quadrature

Following the idea of Harms (2020), with an appropriate quadrature, the integral can be replaced by a system of finite number of Ornstein-Uhlenbeck processes. We call X_t^∞ the process defined with the infinite sum and X_t^N the one obtained with N points of quadrature:

$$X_t^\infty \equiv \int_0^\infty Y_t^x \frac{1}{\sqrt{\pi x}}\left(g_{T_L}(x)-g_{\tau_\eta}(x)\right)\mathrm{d}x \approx X_t^N \equiv \sum_{i=1}^N \omega_i Y_t^{x_i}. \tag{5.18}$$

Because of the regularizing functions $g_{T_L} - g_{\tau_\eta}$, it is useless to compute quadrature points far outside the inertial range $[T_L^{-1};\tau_\eta^{-1}]$. In the following, for simplicity, we consider an Heaviside functions for g. Considering the logarithmic shape of the kernel, we propose a geometric partition of this domain, along with a middle-Riemann sum for the weights:

$$\text{for} \quad i=1,...,N \begin{cases} x_i &= \frac{1}{T_L}\left(\frac{T_L}{\tau_\eta}\right)^{\frac{i-1/2}{N}} \\ \omega_i &= \frac{1}{\sqrt{\pi x_i}}\Delta x_i \end{cases}, \quad \text{where } \Delta x_i = \frac{1}{T_L}\left(\frac{T_L}{\tau_\eta}\right)^{\frac{i}{N}} - \frac{1}{T_L}\left(\frac{T_L}{\tau_\eta}\right)^{\frac{i-1}{N}}. \tag{5.19}$$

Figure 5.3 shows the kernel approximation with $N = 10$ points of quadrature. The kernel $x^{-1/2}$ is approached by step functions all along the inertial range. The weights can be normalized to match the variance of the analytic process $\mathbb{E}\left[(X_t^\infty)^2\right]$. The normalizing factor R is given by:

$$R = \frac{\sigma_{X_t^\infty}}{\sigma_{X_t^N}} = \sqrt{\mathbb{E}\left[(X_t^\infty)^2\right]}\left(\sum_{i,j}\frac{\omega_i\omega_j}{x_i+x_j}\right)^{-1/2}. \tag{5.20}$$

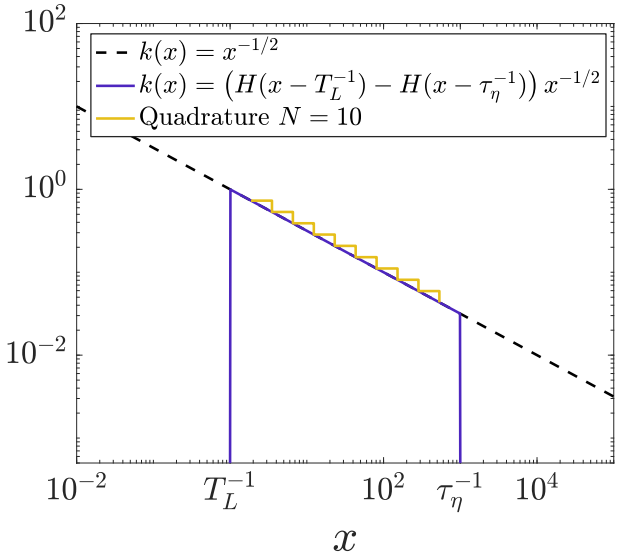

Figure 5.3. The kernel behavior $k(x) \sim x^{-1/2}$ in dashed line is regularized with Heaviside cutting functions in dark blue and compared to its quadrature representation in light yellow. The x and y scales are logarithmic.

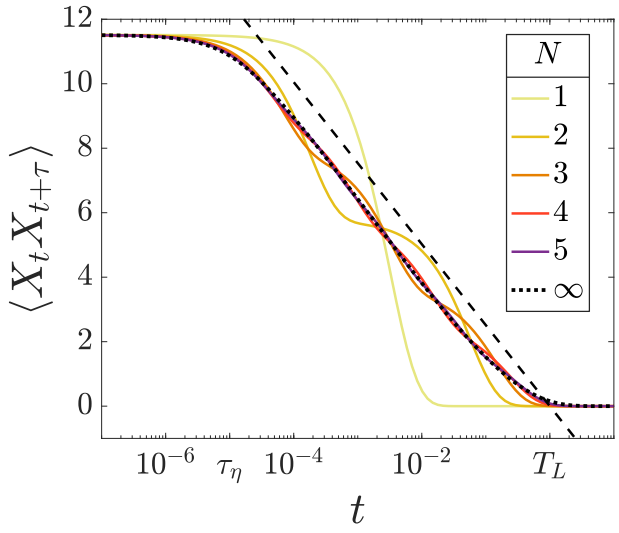

Figure 5.4. Comparison of the autocorrelations of the analytical process (dotted black line) and the discrete one for a finite number of modes. The inertial range covers 5 decades. The x-axis is on a logarithmic scale and the dashed line represents the expected logarithmic behavior.

Figure 5.4 shows the autocorrelation of the process X_t^∞ compared with the discrete one X_t^N. As demonstrated in Sec. 5.1.2, it is clear that the infinite sum has a logarithmic autocorrelation, it follows indeed the dashed line all along the inertial range. A one-point quadrature corresponding to a single Ornstein-Uhlenbeck process is plotted in the lightest yellow in the figure. As discussed above, this specific process corresponds to $X_t^1 = X_t^{OU}$ and does not have a logarithmic autocorrelation all along the inertial range. With two points of quadrature, the autocorrelation displays two bumps, around the two time scales of the Ornstein-Uhlenbeck processes. The autocorrelation range has been extended but it is not yet clear that it follows a logarithmic behavior. With more quadrature points (darker lines), the autocorrelation of X_t^N is getting closer to the analytical one.

This convergence of the autocorrelation can be explicit introducing the relative difference between the analytical autocorrelation $\rho^\infty(\tau)$ and the one obtained from the quadrature $\rho^N(\tau)$:

$$\begin{aligned} \rho^\infty(\tau) &\equiv \int_{T_L^{-1}}^{\tau_\eta^{-1}} \int_{T_L^{-1}}^{\tau_\eta^{-1}} f(\tau, x, y)\, \mathrm{d}x\, \mathrm{d}y \\ \rho^N(\tau) &\equiv \sum_{i=1}^{N} \sum_{j=1}^{N} f(\tau, x_i, x_j) \Delta x_i \Delta x_j, \end{aligned} \tag{5.21}$$

where $f(\tau, x, y) = \dfrac{\mathrm{e}^{-\tau y}}{(x+y)\sqrt{xy}}$. The numerical convergence is verified in Fig. 5.5 with the error defined as:

$$\text{Error} = \sqrt{\int_{\tau_\eta}^{T_L} \left(\frac{\rho^\infty(\tau) - \rho^N(\tau)}{\rho^\infty(\tau)} \right)^2 \mathrm{d}\tau}. \tag{5.22}$$

As observed in Fig. 5.5, the order of convergence is 2. The value of the error is shifted when increasing the inertial range. With one Ornstein-Uhlenbeck per decade, the relative error is below 10%. We can therefore postulate that an acceptable number of processes would be one or two per decade. Figure 5.6 illustrates this choice, with different inertial ranges. The number of points for the discrete process is chosen accordingly and we verify the logarithmic behavior of such processes all along the inertial range. For instance, with an inertial range covering 20 decades (upper yellow line in Fig. 5.6), that corresponds to $\mathrm{Re}_\lambda \sim 10^{11}$, only 20 Ornstein-Uhlenbeck processes are needed to approach a logarithmic behavior of the autocorrelation all along the inertial range.

5.2.2 Discussion

A new log-correlated process X_t^∞ and its discrete version with N Ornstein-Uhlenbeck processes X_t^N have been presented. In this section, we will discuss their physical interpretation and their advantage over existing processes.

5.2.2.1 Physical interpretation

X_t^N can be seen as an extension of Pope's process (Pope and Chen 1990). We recall that the latter corresponds to $N = 1$ with quadrature points taken as:

$$x_1 = \frac{1}{T_\chi}, \quad \omega_1 = \sqrt{\frac{2\sigma_\chi^2}{\mu^\ell T_\chi}}. \tag{5.23}$$

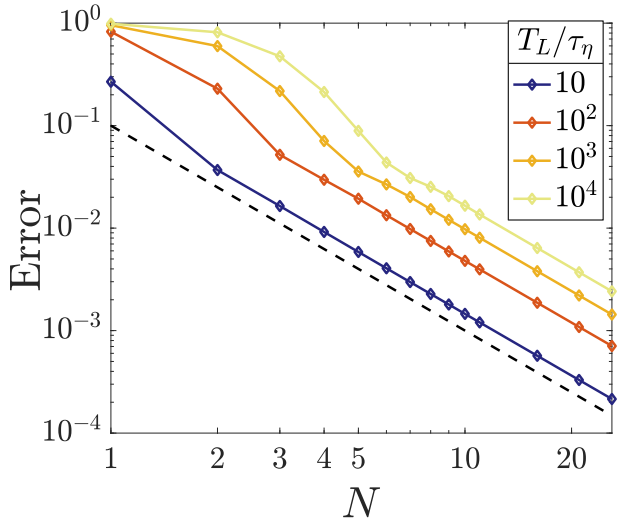

Figure 5.5. Error in log-log scale between the L_2-norm of the discrete process X_t^N and the analytical process X_t^∞. The dashed line represents a slope of -2.

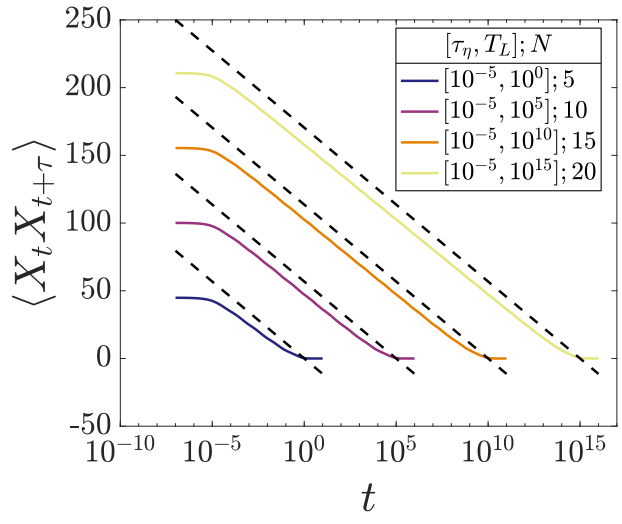

Figure 5.6. Autocorrelation of X_t for different inertial ranges in log-log scale, compared with logarithmic behavior in dashed lines. The number of points chosen in the quadrature N corresponds to the number of decades covered by the inertial range $[\tau_\eta, T_L]$.

Pope and Chen (1990) observed that T_χ scales with the Lagrangian integral time scale T_L and σ_χ scales with logarithm of Reynolds number. By comparison with our proposition of quadrature, we would suggest to use: $T_\chi = \sqrt{T_L \tau_\eta}$, and σ_χ is indeed scaling as $\sigma_\chi \sim \ln(T_L/\tau_\eta)$ to ensure requirement (iii) of Sec. 3.4.2.
For Reynolds number $\mathrm{Re}_\lambda \sim T_L/(0.08\tau_\eta) \lessapprox 125$, we have seen that a single Ornstein-Uhlenbeck is enough to cover the entire inertial range and the exponential decay mimics the logarithmic behavior in such small interval. However, for larger Reynolds number, it is necessary to extend the long-range of the autocorrelation by adding other Ornstein-Uhlenbeck processes, evenly distributed all along the inertial range. A perfect logarithmic scaling is retrieved with an infinity of Ornstein-Uhlenbeck processes.

This new process also makes a very simple link between "continuous" processes with no time scale (or here, an infinity), corresponding to X_t^∞ and "discrete" cascade models X_t^N, where arbitrary time scales are chosen to each represent a turbulent structure. A turbulent cascade is often represented as a product of independent processes defined at each scale, each one presenting a characteristic time scale. The approximation of X_t^∞ by X_t^N exactly consists in selecting representative time scales, and the coherence of the whole cascade is ensured by the fact that every Ornstein-Uhlenbeck process is correlated to each other because driven by the exact same Gaussian Noise.

5.2.2.2 Implementation

Unlike the models of (Schmitt 2003; Pereira, Moriconi, and Chevillard 2018), the process has no 'self-memory'. It is the combination of several Ornstein-Uhlenbeck processes, with adapted characteristic time scales that can mimic this long-range correlation. The closer are the characteristic times of the Ornstein-Uhlenbeck processes, the better is the logarithmic approximation (quadrature with a large number of points) but we show that one time scale per decade is already enough to retrieve the approximate long-range behavior. This should considerably reduce the computational cost of the simulation of such process. Simulating Ornstein-Uhlenbeck processes is very common, rapid and does not require to keep a memory of the whole history of the path, as opposed to the convolution form used in Schmitt (2003), Pereira, Moriconi, and Chevillard (2018).

5.2.2.3 A causal multi-fractal process for pseudo-dissipation

An analytical stochastic equation can be derived for the pseudo-dissipation, which is the variable of interest used in Lagrangian stochastic models. First, we can retrieve an analogous formulation for the incremenents of X_t^∞, introducing the β function already used in Pereira, Moriconi, and Chevillard (2018).

$$\begin{aligned}
\mathrm{d}X_t^\infty &= \int_0^\infty \mathrm{d}Y_t^x \frac{\mathrm{e}^{-x\tau_\eta} - \mathrm{e}^{-xT_L}}{\sqrt{\pi x}}\,\mathrm{d}x, \\
&= \int_0^\infty (-xY_t^x\,\mathrm{d}t + \mathrm{d}W_t)\frac{\mathrm{e}^{-x\tau_\eta} - \mathrm{e}^{-xT_L}}{\sqrt{\pi x}}\,\mathrm{d}x, \\
&= \frac{-1}{2}\int_{-\infty}^t \Big((t-s+\tau_\eta)^{-3/2} - (t-s+T_L)^{-3/2}\Big)\,\mathrm{d}W_s\,\mathrm{d}t + \left(\frac{1}{\sqrt{\tau_\eta}} - \frac{1}{\sqrt{T_L}}\right)\mathrm{d}W_t, \\
&= \left(\beta_t^{\tau_\eta} - \beta_t^{T_L}\right)\mathrm{d}t + \left(\frac{1}{\sqrt{\tau_\eta}} - \frac{1}{\sqrt{T_L}}\right)\mathrm{d}W_t.
\end{aligned}$$

(5.24)

We recall that the Lagrangian multiplicative chaos, which is causal and stationary, is readily obtained while exponentiating the Gaussian process X_t^∞: $\varphi = \langle\varphi\rangle \exp\left(\sqrt{\mu^\ell} X_t^\infty - \frac{\mu^\ell \sigma_X^2}{2}\right)$. Application of Ito's lemma gives the Lagrangian stochastic dynamics of the pseudo-dissipation, namely:

$$\begin{aligned}\frac{\mathrm{d}\varphi}{\varphi} = &\left[\sqrt{\mu^\ell}\left(\beta_t^{\tau_\eta} - \beta_t^{T_L}\right) + \frac{\mu^\ell}{2}\left(\frac{1}{\sqrt{\tau_\eta}} - \frac{1}{\sqrt{T_L}}\right)^2\right]\mathrm{d}t,\\ &+\sqrt{\mu^\ell}\left(\frac{1}{\sqrt{\tau_\eta}} - \frac{1}{\sqrt{T_L}}\right)\mathrm{d}W_t.\end{aligned} \tag{5.25}$$

Of course, the implementation of this stochastic equation preferentially uses the expression of β in the Laplace domain and we recall that the same Wiener process is used in the N Ornstein-Uhlenbeck processes $Y_t^{x_i}$ but also in $\mathrm{d}W_t$ in Eq. (5.25). Numerically, we replace the β-function by its quadrature:

$$\begin{aligned}\beta_t^{\tau_\eta} - \beta_t^{T_L} &= \int_0^\infty -x Y_t^x \frac{g_{T_L}(x) - g_{\tau_\eta}(x)}{\sqrt{\pi x}}\,\mathrm{d}x,\\ &\underset{N}{\approx} \sum_{i=1} -x_i\omega_i Y_t^{x_i}.\end{aligned} \tag{5.26}$$

Numerical implementation is straightforward and leads to a limited memory load compared to the classical approach of discretization of the β function, for example as proposed by Zamansky (2021).

Conclusion

Intermittency in turbulence can be characterized by multi-fractal properties of the dissipation. A Gaussian multiplicative chaos formalism allows us to model such dissipation process, but relies on the introduction of a zero-average Gaussian and log-correlated process, X_t. In the literature, such processes were defined based on a regularized FBM ; they lack physical interpretation and can be computationally expensive in simulations.

In this contribution, we have introduced another way of building such processes, with a general form Eq. (5.1) that requires regularizations. We have shown that specific regularizations yield existing processes, and we propose a new one, which has the benefits of relying on an infinite combination of Ornstein-Uhlenbeck processes. Characteristic time scales of those Ornstein-Uhlenbeck are covering the inertial range, between Kolmogorov time scale and the Lagrangian integral time scale. Each of them represents a specific turbulence structure, collectively representing a continuous cascade model where no arbitrary time scale is needed.

A discrete version of this process is proposed, based on a selection of few specific modes, corresponding to representative characteristic time scales. The quadrature of the infinite sum is therefore a finite sum of Ornstein-Uhlenbeck processes, logarithmically distributed in the inertial range. This corresponds to a discrete cascade model.

Beside its simplicity of simulation, this model is also very adaptive, and could lead to other promising applications: dissipation along trajectory of inertial particles is not logarithmic anymore but the model can actually fit any autocorrelation function. The extension of this model to the case of inertial particles will be addressed in Sec. 8.4.2 in Chap. 8. Thanks to the versatility of the process, application to LES can also be considered, with different regularizing functions, where the cut-off could be based on the sub-grid time scale for instance.

Part III

One-way coupled turbulent disperse two-phase flows

Part III introduces the physical phenomena and the issues involved in modeling a disperse phase transported by a turbulent carrier phase in a one-way coupling context. Chapter 6 presents the equations governing the motion of the particles in the flow and highlights the main physical phenomena occurring as a result of the collective behavior of the particles: the particles preferential concentration trajectory crossing. If the equations of the disperse phase are naturally derived in a Lagrangian framework, these phenomena are based on Eulerian dynamics, which must be introduced. This Eulerian formalism also reduces the dimensionality of the problem in Chap. 7 while proposing a statistical approach for the disperse phase. Finally, we present in this same chapter the strategies for coupling the disperse phase with reduced-order turbulence modeling. We show that in the absence of a particle sub-filter model, the statistics of the disperse phase are altered, and we expose the two strategies for particle models: stochastic and structural models.

Chapter 6

Transport of particles by turbulence

In this chapter, we are interested in the transport of particles by a turbulent flow, the velocity of which is known, in a one-way coupling context. The equations governing the motion of a spherical particle in interaction with the turbulent carrier phase are established according to classical Newtonian mechanics. The expression of the different forces applied to the particle is simplified under a set of assumptions that reduces the difficulty of the problem while encompassing a wide range of natural and industrial applications. In particular, we only consider one-way coupling by neglecting the effect of particles on turbulence. Two-way coupling will be studied and characterized in Part V of this thesis. The final model only takes into account the drag force with point-particle assumption.

In order to study the collective behavior of the particles and to characterize the physics of the disperse phase, we introduce an Eulerian vision. This framework highlights particular behaviors such as the particle preferential concentration (PPC) or the particle trajectory crossing (PTC). The first corresponds to the accumulation of particles in specific regions of the flow; the second describes the occurrence of very close particles with very different velocities. The Stokes number, the ratio of the characteristic time of the particle to that of the fluid, controls the regimes in which these singularities appear. These play a key role in various processes, in particular the collision between particles (Sundaram and Collins 1997). In some cases, which will be detailed in Part V, the PPC plays a key role in the modulation of turbulence.

Section 6.1 of this chapter focuses on establishing the equation of the particle in a flow in the Lagrangian framework. Section 6.2 introduces the Eulerian macroscopic fields, and consequently the main associated statistics that characterize disperse two-phase flows and their behaviors, namely the PPC and the PTC.

6.1 A particle in a flow

We study a single particle motion in a turbulent flow. The particle is considered spherical with diameter d_p and density ρ_p. Its position is defined in space by coordinates $\boldsymbol{x}_p$ of the particle center, and it has a velocity $\boldsymbol{v}_p$. For a spherical and isolated particle (i.e. not influenced by its neighbors), one can derive simple and classical models for the forces that are applied to it and studies have been conducted experimentally and numerically to validate them (Tenneti, Garg, and Subramaniam 2011).

6.1.1 Forces acting on a particle

The external forces applying to a particle are obtained by integration of the Navier-Stokes equations around the surface of this sphere. These forces can be separated into two categories: stationary forces, resulting from a well established condition around the particle, and unsteady forces, related to the history of the particle.

- **The stationary drag force $\boldsymbol{F}_D$** is the force acting on the sphere, in the absence of acceleration of the sphere relative to the flow, in a uniform pressure environment. This force is expressed using a drag coefficient C_D:

$$\boldsymbol{F}_D = \frac{1}{2}\rho C_D A \|\boldsymbol{u} - \boldsymbol{v}_p\| \left(\boldsymbol{u} - \boldsymbol{v}_p\right), \tag{6.1}$$

  where $\boldsymbol{u}$ is the undisturbed flow velocity, $\boldsymbol{v}_p$ is the particle velocity, $A = \dfrac{\pi d_p^2}{4}$ the particle projected area and ρ the density of the carrier phase. The difficulty lies in the determination of the drag coefficient C_D which varies strongly with the intensity of the flow. The latter is characterized by the particle Reynolds number $\mathrm{Re}_p = \dfrac{d_p\|\boldsymbol{u} - \boldsymbol{v}_p\|}{\nu}$, which compares the inertial forces to the viscous forces in the particle referential. In the following, we will consider flows with low Reynolds number $\mathrm{Re}_p \leq 1$ for which we can estimate: $C_D = 24/\mathrm{Re}_p$. This simplifies the drag force expression as follows:

$$\boldsymbol{F}_D = 3\pi\mu d_p \left(\boldsymbol{u} - \boldsymbol{v}_p\right). \tag{6.2}$$

- **A local pressure gradient** at particle location generates a force in the direction of this gradient. In the particular case of a hydrostatic pressure gradient (linked to gravity for example), the associated pressure force is the Archimedean force:

$$\boldsymbol{F}_P = -\nabla P V_p = -\rho \boldsymbol{g} V_p, \tag{6.3}$$

  where $\boldsymbol{g}$ is the gravity and $V_p = \dfrac{\pi}{6} d_p^3$ the volume of the particle.
- **Unsteady forces** due to the history of the particles: the added mass or the Basset force, respectively

$$\boldsymbol{F}_{AM} = \frac{\pi}{12}\rho d_p^3 \frac{\mathrm{d}}{\mathrm{d}t}\left(\boldsymbol{u} - \boldsymbol{v}_p\right), \tag{6.4}$$

  and

$$\boldsymbol{F}_B = \frac{3}{2} d_p^2 \sqrt{\pi\rho\mu} \int_{t_0}^{t} \frac{1}{\sqrt{t-\tau}} \frac{\mathrm{d}}{\mathrm{d}\tau}\left(\boldsymbol{u} - \boldsymbol{v}_p\right) \mathrm{d}\tau. \tag{6.5}$$

- Other forces acting on particle such as the **gravity**, etc...

Taking into account these forces results in the famous Basset-Boussinesq-Oseen (BBO) equation:

$$m_p \frac{\mathrm{d}\boldsymbol{v}_p}{\mathrm{d}t} = \frac{\pi}{6}\rho_p d_p^3 \frac{\mathrm{d}\boldsymbol{v}_p}{\mathrm{d}t} = \boldsymbol{F}_D + \boldsymbol{F}_P + \boldsymbol{F}_{AM} + \boldsymbol{F}_B + \sum_k \boldsymbol{F}_k. \tag{6.6}$$

6.1.2 The Stokes drag for point-particle tracking

Throughout this work, we consider simplifying assumptions to minimize the number of parameters describing the disperse phase. The assumptions on the disperse phase are the following:

- We consider spherical particles of fixed size.
- We do not solve energy or mass transfers: no phase changes is taken into account here (no evaporation).
- We neglect gravity: $\boldsymbol{g} = 0$.
- The density ratio between the particles and the fluid is large ($\rho_p \gg \rho$) and the Reynolds number of the particle is smaller than one ($\mathrm{Re}_p \leq 1$), therefore, all the remaining forces in the original Basset-Boussinesq-Oseen equation Eq. (6.6) are assumed negligible compared to the drag force.
- The volume fraction α is small enough to consider particle-particle collisions as negligible (dilute regime: $\alpha < 10^{-3}$).
- Particles diameter is smaller than the Kolmogorov length scale ($d_p \ll \eta$), thus particle-resolved DNS is not necessary (Fröhlich, Schneiders, Meinke, and Schröder 2018), and a point-particle approximation is adopted.
- In this chapter and throughout Part III and IV, we consider that the particles do not modify the carrier phase (one-way coupling regime). The associated assumptions are detailed in Part V.

The drag force obeys Stokes' law, the equation of motion is linear in the velocity difference between fluid and particle. The drag force of Eq. (6.2) can be simplified. This results in the Lagrangian equations for the particles:

$$\left\{ \begin{array}{rcl} \dfrac{\mathrm{d}\boldsymbol{x}_p(t)}{\mathrm{d}t} & = & \boldsymbol{v}_p(t) \\ \dfrac{\mathrm{d}\boldsymbol{v}_p(t)}{\mathrm{d}t} & = & \boldsymbol{F}_p(t) = \dfrac{\boldsymbol{u}_{@p}(t) - \boldsymbol{v}_p(t)}{\tau_p}, \end{array} \right. \tag{6.7}$$

where $\boldsymbol{x}_p(t)$ and $\boldsymbol{v}_p(t)$ stand for particle position and velocity at time t, and $\boldsymbol{u}_{@p}(t) = \boldsymbol{u}(\boldsymbol{x}_p(t), t)$ is the undisturbed fluid velocity evaluated at the particle position. The particle relaxation time τ_p is defined as $\tau_p = \dfrac{\rho_p d_p^2}{18\mu}$ where μ is the dynamic viscosity of the fluid.

This characteristic time of the particles can be related to that of the fluid, using the Stokes number. In a turbulent flow, we have however established the existence of different characteristic times for the fluid, in Chap. 1, in particular τ_η, the Kolmogorov time, T_L, the Lagrangian integral time scale. These define respectively $\mathrm{St}_\eta := \tau_p/\tau_\eta$ and $\mathrm{St}_L = \tau_p/T_L$. These Stokes numbers play a major role in the collective behavior of the disperse phase, which can be studied using an Eulerian framework.

6.2 Eulerian description of the disperse phase

We have so far introduced the disperse phase according to a Lagrangian vision, i.e. by following each particle in the flow moving in space and time. When the number of particles is important, it may be relevant to consider an Eulerian description of the disperse phase, i.e. describing the properties of the disperse phase at any point in space and time.

Note that these frameworks are related to each other, and that similar to the carrier phase, if one of them is more adapted to the derivation of the equations governing the behavior of the phase, the other one can be introduced *a posteriori* in order to study some macroscopic quantities of interest.

A given realization R of the disperse phase can be described by a number density function (NDF), representing N_p interchangeable particles:

$$f_R(t, \boldsymbol{x}, \boldsymbol{v}) = \sum_{k=1}^{N_p} \delta(\boldsymbol{x} - \boldsymbol{x}_{p,k}(t))\delta(\boldsymbol{v} - \boldsymbol{v}_{p,k}(t)). \tag{6.8}$$

The time evolution of this NDF is governed by Eq. (6.7) and with the knowledge of its initial distribution $f_R(0, \boldsymbol{x}, \boldsymbol{v})$. Because it is unrealistic to have an accurate knowledge of all the initial conditions of the particles except in academic and canonical configurations, they are considered random: $f_R(0, \boldsymbol{x}, \boldsymbol{v}) = f_R^0(\omega; \boldsymbol{x}, \boldsymbol{v})$. With the same formalism as in Sec. 1.1.6.1, it is then possible to define mesoscopic Eulerian quantities at time t from the expectations of the NDF by integrating over the associated probability space: $\mathbb{E}\left[f_R(\omega; t, \boldsymbol{x}, \boldsymbol{v})\right] = f(t, \boldsymbol{x}, \boldsymbol{v})$. Practically speaking, this expectation is estimated with empirical means, for example with N_R realizations:

$$f(t, \boldsymbol{x}, \boldsymbol{v}) \approx \frac{1}{N_R} \sum_R f_R(\omega; t, \boldsymbol{x}, \boldsymbol{v}). \tag{6.9}$$

The Eulerian fields can be obtained by ensemble averaging over several realizations of the particle phase, for a given realization of the turbulent phase (Février, Simonin, and Squires 2005). However, in practice, the number of realizations is finite and for numerical purposes, this local average must have a certain thickness. The Eulerian quantities will therefore be obtained by a projection method based on a volume filtering of the Lagrangian quantities, as shown in Fig. 6.1(a) and 6.1(b). There are several projection kernels Δ: for example the "box" projection, which consists in averaging the properties of the particles present in a cell of the Eulerian mesh, the volume or Gaussian projections, which weight the information according to the distance to the computational node. The box projection is implemented in Asphodele, and we have implemented the Gaussian one (see Sec. 2.4). In his thesis, Moreau (2006) compares those methods of projection and classifies them depending on their characteristic length. This length must be smaller than the spatial scale of variation of the quantities, but also large enough to have enough particles to perform the average.

From the knowledge of f, or its estimation through ensemble averages, macroscopic quantities can then be obtained. We define the particle number density:

$$n(\boldsymbol{x}, t) = \int_{\mathbb{R}} f(t, \boldsymbol{x}, \boldsymbol{v}) \, \mathrm{d}\boldsymbol{v}, \tag{6.10}$$

but it is rather estimated from Lagrangian simulations with:

$$n(\boldsymbol{x}, t) = \frac{1}{N_R} \sum_R \sum_{k=1}^{N_p} \Delta(\boldsymbol{x} - \boldsymbol{x}_{p,k}(t)), \tag{6.11}$$

Similarly, the mean particle velocity is calculated using:

$$n(\boldsymbol{x}, t)\boldsymbol{u}_p(\boldsymbol{x}, t) = \frac{1}{N_R} \sum_R \sum_{k=1}^{N_p} \boldsymbol{v}_{p,k}(t)\Delta(\boldsymbol{x} - \boldsymbol{x}_{p,k}(t)), \tag{6.12}$$

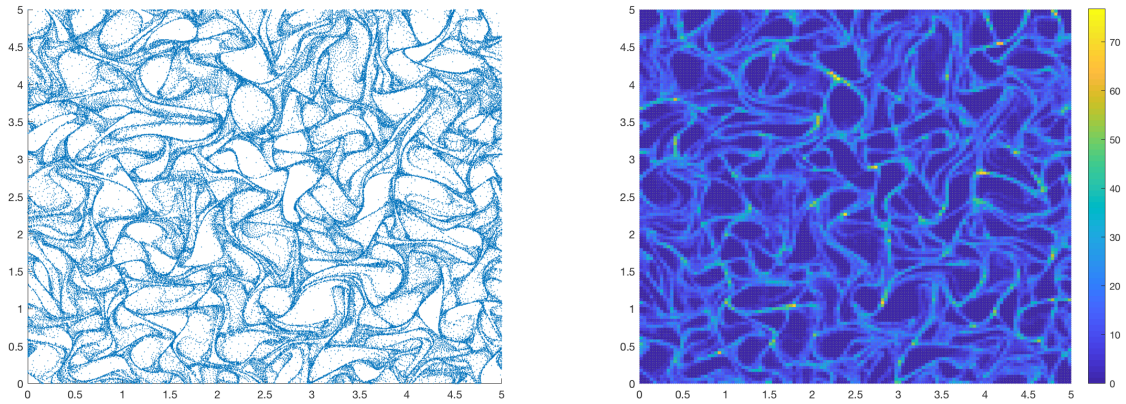

(a) Lagrangian snapshot

(b) Eulerian field

Figure 6.1. (a) Snapshot of particles in a HIT and (b) corresponding particle number density field obtained by projection on a mesh. DNS performed with Asphodele.

In one-way coupling and dilute regime, inter-particle influences (directly through collisions or through a modification of the fluid field by the presence of the particles) are neglected. Under these conditions, simulating a realization with a large number of particles is equivalent to simulating a large number of single-particle realizations.

Eulerian fields provide insights on physical phenomena related to the collective behavior of particles. Unlike the carrier phase, which is a continuous medium, the disperse phase presents singularities such as its spatial heterogeneity or local velocity dispersion (Simonin, Février, and Laviéville 2002). These singularities result from the transport of particles by turbulent eddies and are presented in the following subsections.

6.2.1 Particle preferential concentration

6.2.1.1 Evidence of particle preferential concentration

Figure 6.1(a) is a snapshot of particles in a HIT obtained by DNS. Particles were initially injected with uniform distribution in the domain, and with an initial velocity equal to the one of the fluid. After some time evolving with the flow according to the Stokes drag law, they are preferentially concentrated in specific regions and do not fill the domain uniformly anymore.

We illustrate the disperse phase heterogeneity on a Taylor Green periodic vortex flow, a steady solution of the inviscid incompressible Euler equations. Such two-dimensional flow is described by an analytic expression and its velocity field is shown in Fig. 6.2(a):

$$\begin{cases} u_x(x,y) &= \sin(2\pi x)\cos(2\pi y) \\ u_y(x,y) &= -\cos(2\pi x)\sin(2\pi y). \end{cases} \tag{6.13}$$

Such a configuration is representative of the vortex structure of turbulent flows and help visualize the behavior of the particles according to the Stokes number $\mathrm{St} = \tau_p/\tau_c$, where $\tau_c = 1/8\pi$ is the

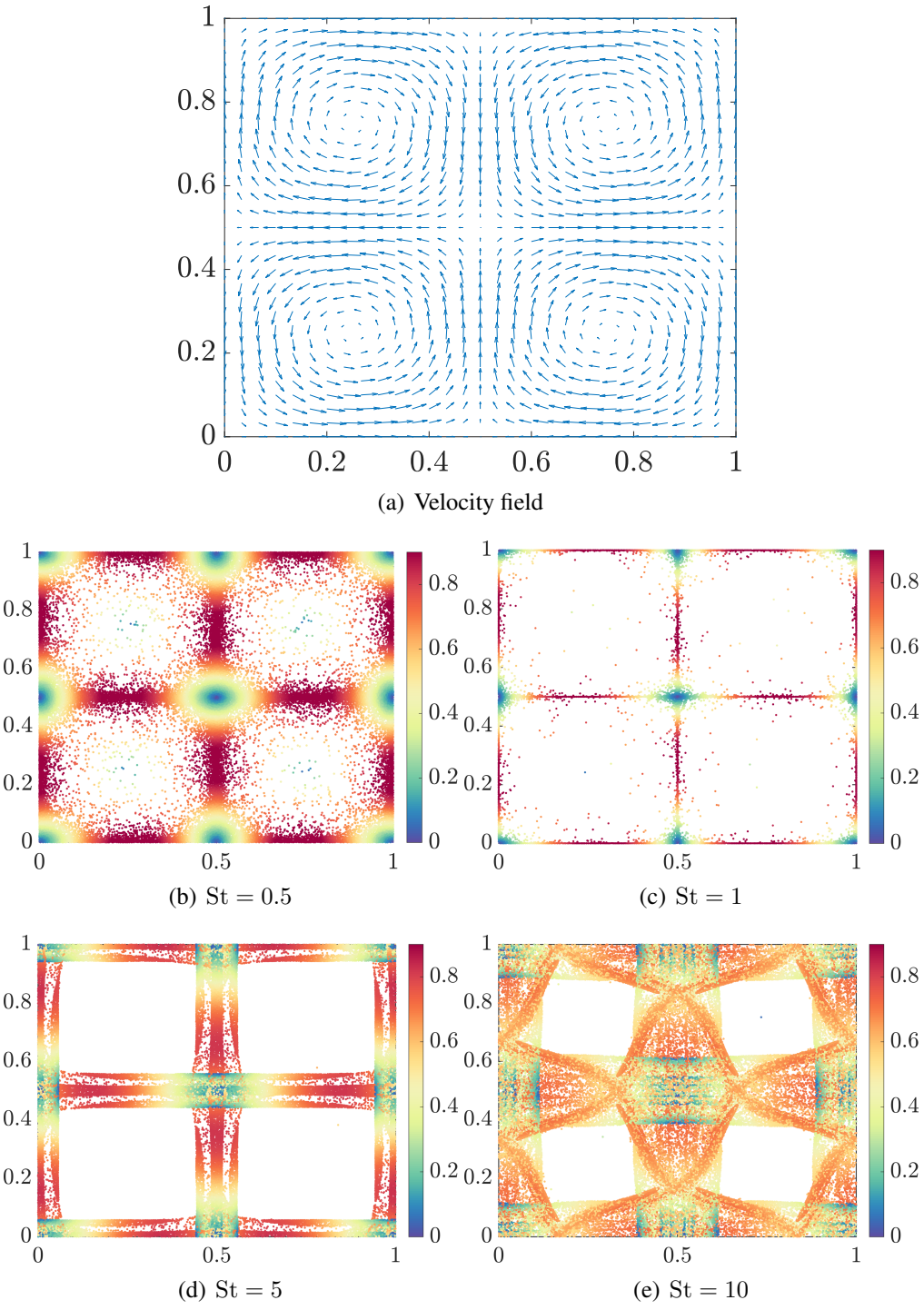

Figure 6.2. Taylor Green velocity field (a) ; and particles at time $t_f = 30\tau_c$ with different Stokes numbers (b-e). Particles are colored according to their final velocity.

characteristic time of the flow. In order to observe the evolution of the particles, we randomly distribute 10000 particles in the square space $[0;1] \times [0;1]$ and compute their evolution according to Eq.(6.7). We observe that:

- Low-inertia particles ($\mathrm{St} \ll 1$) have a behavior very close to tracers (fluid particles). Since they are injected with uniform distribution at initial time, fluid particles tend to fill the space uniformly, producing no spatial heterogeneity thanks to divergence-free of the carrier phase.
- For small Stokes numbers ($\mathrm{St} \lesssim 1$), the trajectories of inertial and fluid particles are drifting apart. The particles are ejected from the vortices because of their inertia but do not acquire enough energy to pass through the regions of low vorticity or high strain rate. They therefore accumulate there, at the periphery of the vortex zones. We then see the phenomenon of preferential concentration of particles, also referred as segregation (Eaton and Fessler 1994). Large regions without particles appear in the centers of vortices for small Stokes numbers in Fig. 6.2(b) and the particle preferential concentration reaches its highest point for $\mathrm{St} \approx 1$, as observed in Fig. 6.2(c).
- With increasing Stokes number ($\mathrm{St} \gtrsim 1$), the particles are less and less influenced by the carrier phase. Their inertia allows them to cross high strain rate or low vorticity regions and they can thus cross vortices with a ballistic trajectory. The preferential concentration decreases.
- For very high-inertia particles ($\mathrm{St} \gg 1$), particles fill again the space uniformly after a sufficient long time.

More specifically, particles sample preferentially the periphery of strong vortical regions and segregate into straining regions as a result of their interaction with the vortical coherent structures.

In turbulent flows, preferential concentration of particles is a major aspect that can strongly lead the physics (Capecelatro and Desjardins 2015). Particle accumulation is not only a concern for flow dynamics but also for the numerical computation of the disperse phase. For example, the impact of PPC in a two-way context will be investigated in Chap. 13. The increase of the collision rate in overpopulated regions or the large vacuum zones and strong gradients in Eulerian representations can be challenging.

6.2.1.2 Measure of particle preferential concentration

In the literature, several methods have been proposed to measure preferential concentration, and an exhaustive review is proposed by Monchaux, Bourgoin, and Cartellier (2012), Hogan and Cuzzi (2001).

The parameter $\left\langle n(\boldsymbol{x},t)^2 \right\rangle / \left\langle n(\boldsymbol{x},t) \right\rangle^2$ is a measure that quantifies the preferential concentration (Kaufmann, Simonin, and Poinsot 2004). It has often been used to study Eulerian fields, for instance by Vié, Pouransari, Zamansky, and Mani (2016). The measure is close to unity for a uniformly distributed particle system. Applied to the Taylor Green vortices, we obtain in Fig. 6.3(a) the evolution of the segregation as a function of the Stokes number and we observe the characteristic peak around Stokes number $\mathrm{St} \approx 1$.
Another common measure is the two-point spatial distribution function. For a statistically homogeneous system of particles, Reade and Collins (2000) introduced the radial distribution function of the interparticle distance, $\langle n(\boldsymbol{x},t) n(\boldsymbol{x}+\boldsymbol{r},t) \rangle / \langle n(\boldsymbol{x},t) \rangle^2$. Moreover, this measure can provide

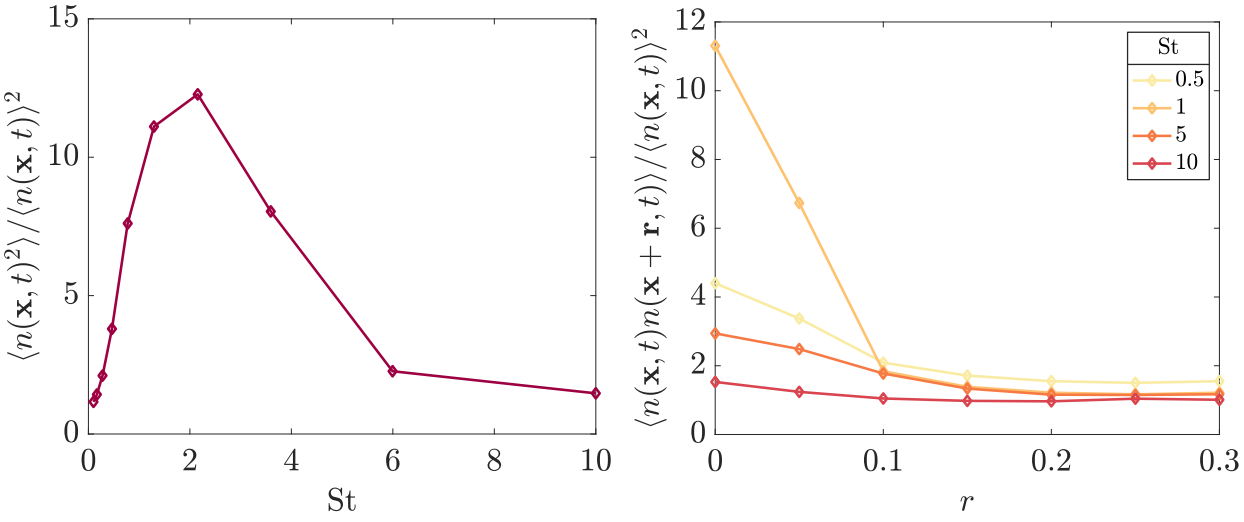

(a) (b)

Figure 6.3. Measures of particle preferential concentration in two-dimensional Taylor Green vortices: (a) Radial distribution function at origin for different Stokes numbers ; (b) Radial distribution function plotted for different Stokes numbers.

a clear estimation of the characteristic length scale of preferential concentration. Note that the first measure is in fact the evaluation of the radial distribution function at the origin. Figure 6.3(b) plots the radial distribution function for different Stokes numbers. Unlike the others, the curve for $\mathrm{St} = 1$ has higher value at origin and a rapid decay is then observed. It is possible to determine the slope at the origin, and to evaluate in this case a characteristic distance of the order of $r = 0.1$.

Both measures depend quantitatively on the mesh chosen for the representation of the number density field. Indeed, in practice the measurement of the radial distribution function is discrete and the resolution step can mask the characteristic scales of the PPC. On the other hand, these measurements can depend on the number of particles simulated, especially when the disperse phase is not statistically converged (average number of particles per box too low). Other measures will be introduced and discussed in Chap. 13 to overcome these biases.

6.2.2 Particle velocity dispersion

6.2.2.1 Evidence of particle trajectory crossing

Particle velocity dispersion is characterized by a multi-valued Eulerian field of particle velocity (Desjardins, Fox, and Villedieu 2008; Ijzermans, Meneguz, and Reeks 2010; Massot 2007; Kah 2011). Since the particles have no volume occupancy and we have neglected inter-particle collisions, particles can be at the same location in the flow. At a given point or neighborhood in space, particles can have different velocities due to their inertia, as illustrated in Fig. 6.4. Let's examine further the behavior of the disperse phase carried by the Taylor Green vortices, this time in terms of velocity dispersion.

- Low-inertia particles ($\mathrm{St} \lesssim 1$) have a behavior very close to tracers (fluid particles). Thus, very close particles will not have any velocity dispersion since they have the same history in the flow.

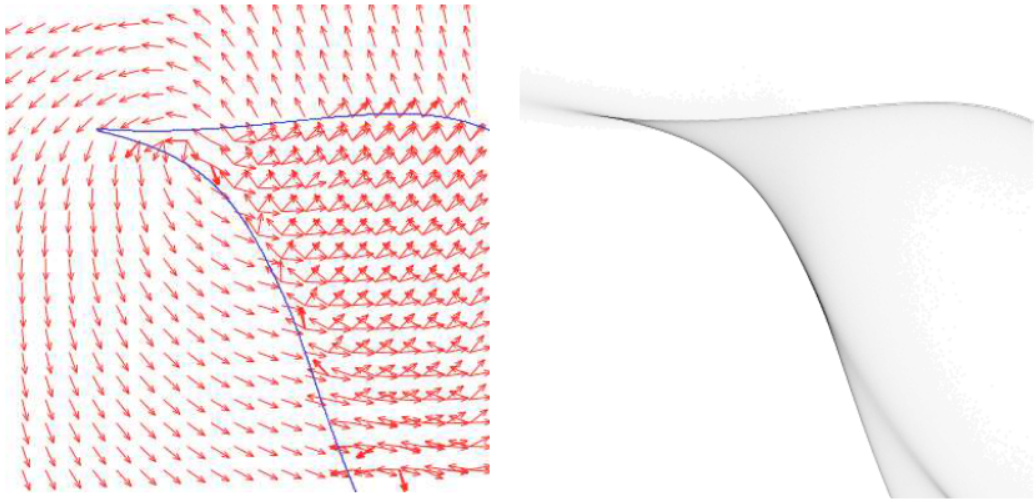

Figure 6.4. (Left) Velocity quiver plot of particles suspended in a two-dimensional random flow with $\mathrm{St} = 10$. (Right) particle density showing significantly enhanced particle-number density in the vicinity of the multi-valued field. Black corresponds to high density, white to low density. Figure from Gustavsson, Meneguz, Reeks, and Mehlig (2012).

- With increasing Stokes number ($\mathrm{St} \gtrsim 1$), the particles are less and less influenced by the dynamics of the carrier phase. The velocities of the particles and the tracers are decorrelated and their trajectories separate rapidly. In particular, particles that are initially far apart (coming from different vortices) can then cross each other, with a very different velocity. This is called particle trajectory crossing (PTC): at a point in space, it is possible to observe a dispersion in velocity of the disperse phase. In some regions of the space of Fig. 6.2(d), one can see a superposition of particles at very different velocities. This phenomenon is all the more visible at very high Stokes, on Fig. 6.2(e)

Taylor Green vortices are a very particular case of flow, but illustrative because they have a unique and steady scale. However, we have seen in Chap. 1 that turbulence is actually composed of a very broad range of scales. The appropriate Stokes number to qualify the PTC regime is based on large scales (Février, Simonin, and Squires 2005). Indeed, the phenomenon becomes significant when $\mathrm{St}_L = \tau_p / T_L > 1$, i.e. the relaxation time of the particles is large compared to the correlation time of particles. In fact, this criterion can even be based on the Lagrangian integral time experienced by the particles, $T_L^{u_{@p}}$, characterizing the correlation time of the fluid velocity along the trajectory of the inertial particles (Fede and Simonin 2006).
In the literature, these phenomena are also referred to as multivelocity (Massot 2007) or multi-valued (Liu, Osher, and Tsai 2006) solutions. PTC considerably complicates the task of Eulerian models since it is necessary to be able to characterize this dispersion in velocity.

6.2.2.2 Measure of particle velocity dispersion

A characterization of relative velocities of inertial particles was proposed by Février, Simonin, and Squires (2005). They decomposed particle velocities into two contributions: a spatially correlated velocity field $\boldsymbol{u}_p(\boldsymbol{x}, t)$, and a random, spatially and temporally uncorrelated contribution, commonly referred to as "random uncorrelated motion" (RUM) $\delta \boldsymbol{v}_p(t)$, a Lagrangian quantity such

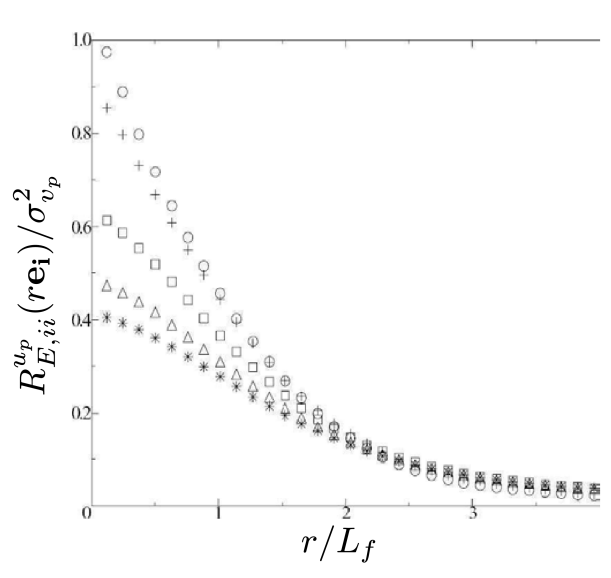

Figure 6.5. Influence of particle inertia (symbols) on the Eulerian longitudinal spatial autocorrelation $R^{u_p}_{E,ii}/\sigma^2_{v_p}$ function in stationary HIT. Stokes numbers St_L are 0.05 for $\circ$, 0.3 for $+$, 1.47 for $\square$, 3.4 for $\triangle$ and 4.8 for $*$. Figure from Février, Simonin, and Squires (2005).

that:

$$\boldsymbol{v}_p(t) = \boldsymbol{u}_p(\boldsymbol{x}_p(t), t) + \delta\boldsymbol{v}_p(t). \tag{6.14}$$

Figure 6.5 shows that the Eulerian correlation of Lagrangian velocities $R^{u_p}_{E,ii} = \langle u_p(\boldsymbol{x} + r\boldsymbol{e}_i)u_p(\boldsymbol{x})\rangle$ varies for the different Stokes numbers considered. For small Stokes numbers, this correlation is close to an exponential form (similar to the longitudinal Eulerian correlations of the fluid). For heavier particles, very close particles have very different velocities: the velocity field of the particles is not continuous. This effect increases with the inertia (the Stokes number) of the particles.

The decomposition of the velocity into two components in Eq. (6.14) also gives two components to the kinetic energy of the particle:

- the mean correlated energy (MCE), given by $\left\langle n(\boldsymbol{x})\boldsymbol{u}_p^2(\boldsymbol{x})\right\rangle / \langle n(\boldsymbol{x})\rangle$;
- the mean internal energy (MIE), given by $\langle n(\boldsymbol{x})\delta\theta_p(\boldsymbol{x})\rangle / \langle n(\boldsymbol{x})\rangle$;

where $\delta\theta_p(\boldsymbol{x})$ is the kinetic energy of the RUM, defined as the Eulerian projection of $\langle\delta v_{p,i}(t)\delta v_{p,i}(t)\rangle$. The mean total energy (MTE) corresponds to the sum of both terms. The evolution of these two correlated and uncorrelated kinetic energies is given in Fig. 6.6. For low Stokes number, the energy is mainly in correlated form. When the inertia of the particles increases, the energy of the particles mainly comes from the uncorrelated motion. The points overlap whatever the Reynolds number of the simulation and this highlights the role of St_L on the PTC.

Note that the meaning given to the RUM tensor is not the same depending on whether the $\langle.\rangle$ represents an ensemble average or a volume average. Indeed, in the first case, the measure gives a statistical variance between several realizations while in the second, it gives a local particle agitation, which can generate collisions between particles of the same simulation.

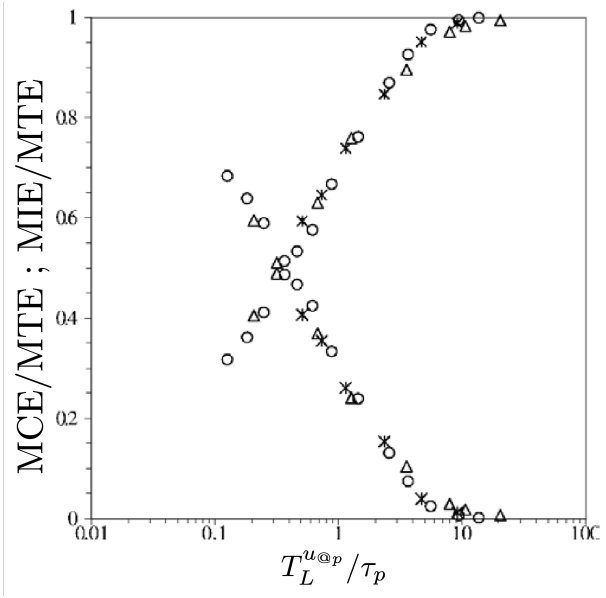

Figure 6.6. Evolution of particle correlated and uncorrelated energy fractions with particle inertia (several turbulent Reynolds numbers are represented with symbols) in stationary HIT. Figure from Février, Simonin, and Squires (2005).

Conclusion

This chapter introduces the main characteristics of a disperse phase flow, and in particular specifies the assumptions that lead to a Lagrangian point-particle modeling. From Lagrangian simulations, Eulerian macroscopic fields can be derived and different methods are presented. This framework gives insights on the dynamics of the disperse phase and more specifically to particle collective behavior through two-point statistics.

For small and intermediate Stokes numbers, particle preferential concentration yields heterogeneous spatial distribution of particles and can generate overpopulated and depletion zones. This quantity is of paramount importance in the combustion domain since it can strongly affect the evolution of the mean vapor mixture fraction. On the other hand, for large Stokes numbers, we observe large velocity differences between nearby particles, which could also enhance collision rate of particles. As a consequence, particle velocity fields become multi-valued, which requires specific numerical methods for the disperse phase, which are the subject of next chapter.

On the other hand, the phenomena described in this chapter were evidenced with a perfect knowledge of the turbulent carrier phase. However, DNS are not affordable for industrial configurations and Chap. 7 is therefore interested in the effects of under-resolved turbulence (by ROS) on the dynamics identified in this chapter.

Chapter 7

Modeling and simulation of the disperse phase

In this chapter, we review existing models of disperse two-phase flows. We introduce different levels of description of the disperse phase and review their benefits and drawbacks in terms of numerical cost, prediction compared to a given experiment, and self-contained statistical information. Two-way coupling will only be discussed in Part V of this thesis and for the moment, we focus on one-way coupled models.

Due to the highly multiscale nature of disperse phase flows, modeling strategies must be designed to achieve their simulation in industrial configurations. Dimensionality reduction can be applied to both phases:

- The numerical cost of Lagrangian approaches as presented in the previous chapter becomes unaffordable in the presence of a large number of particles. We briefly present the different steps to derive Eulerian models (microscopic, mesoscopic and then macroscopic). Euler-Euler representations solve the carrier phase and inertial particles on a common Eulerian grid, greatly reducing the computational cost, as individual particles do not need to be tracked. On the other hand, the Eulerian treatment of the disperse phase can raise other issues (PPC, PTC as seen in Chap. 6), and special attention must be paid to closures of macroscopic equations and numerical schemes.
- We have already investigated in Chap. 2 the reduced-order simulations for the turbulent phase. For two-phase flows, such a reduced description has implications on the particle equations, and additional models should be developed in order to overcome the lack of information resulting from the reduction of the carrier phase.

Section 7.1 first presents mesoscopic and macroscopic approaches for the disperse phase, assuming the carrier phase is fully resolved (DNS). Section 7.2 deals with the treatment of the disperse phase when the turbulence is under-resolved (ROS). Here we detail how the lack of small-scale information can affect the dynamics and statistics of the disperse phase, and we present two classes of models that address this issue: stochastic and structural models. We discuss the advantages and drawbacks of each of these approaches, without going into the details as these models will be further detailed in Chap. 8 and 9 respectively.

7.1 Dimensionality reduction for the disperse phase

7.1.1 Microscopic approaches

For liquid droplets, the best description of multiphase flows is given by a full direct numerical simulation of both phases, for which the dynamics of interface is modeled, as well as the exchanges between the two phases. For solid particles, the shape of the interface of particles is assumed to be simple and known in order to be described with a finite number of parameters, specific to each particle. This is the particle-resolved DNS, for which the boundary is not resolved but imposed: the particle is assimilated to a sphere of diameter d_p, and it is located in space by its center of mass. The interaction with the carrier phase is then resolved precisely for the fluid around the particle. A recent review article on such methods can be found in Tenneti and Subramaniam (2014). These two methods are very rich in information but computationally expensive and their use is restricted to a limited number of tracked particles.

A first dimensionality reduction can be derived by considering point-particles, under the set of assumptions proposed in Chap. 6. The discrete particle simulation (DPS) was first introduced by Riley and Patterson Jr (1974) and later extended to evaporating droplets and combustion (Reveillon and Vervisch 2005). Since this method focuses on tracking every particle, the approach is clearly deterministic and can also be referred as point-particle DNS (Pai and Subramaniam 2012).

The cost of such simulations remains too high in the presence of a large number of particles, since it is based on the resolution of the N_p deterministic ODEs of Eq. (6.7). Moreover, we have seen that the chaotic character of the system implies a resolution of the flow in terms of statistics. It is then common to adopt a mesoscopic point of view, which allows a statistical description of the disperse phase in particular by computing a number density function (NDF), as done in kinetic theory of gases.

7.1.2 Mesoscopic approaches

Already introduced in Sec. 6.2, the NDF f gives the probability of having particles at a given point in space and time and at a given state (temperature, size, velocity...). This NDF satisfies a population balance equation, the Williams-Bolzmann equation (WBE) (Williams 1958), which describes its evolution in phase space. In the particular case considered here of monodisperse particles undergoing only a Stokes drag force, the WBE is derived in App. A:

$$\frac{\partial f}{\partial t} + \boldsymbol{v} \cdot \nabla_{\boldsymbol{x}} f + \nabla_{\boldsymbol{v}} \cdot \left(\frac{\boldsymbol{u}(\boldsymbol{x}, t) - \boldsymbol{v}}{\tau_p} f \right) = 0, \tag{7.1}$$

where $\boldsymbol{x}$ is the the physical space variable, and $\boldsymbol{v}$ the total velocity vector for the particle in the phase space. The work of Février, Simonin, and Squires (2005) establishes in particular the Mesoscopic Eulerian Formalism (MEF), for which a particular NDF is thus conditioned to a given fluid realization. As opposed to the DPS approach, which gives a single realization of the disperse phase, the NDF contains statistical information about all the possible realizations of the disperse phase in a given carrier phase. With notations introduced in the previous chapter, $f_R = f_{DPS}$ and $f = f_{MEF}$.

In order to solve the WBE, we have 3 choices:

- **Direct resolution**, after discretization in the phase space. By considering only the phase space in velocity, we have nevertheless 6 dimensions to solve in 3D, which is not practicable from a computational cost point of view. This technique is limited to low-dimensional problems (at best 2D).
- **Lagrangian sampling**: The NDF is approximated by sampling using the Lagrangian particle tracking techniques described in Sec. 6.1.2. Two classes of methods exist: the direct simulation Monte-Carlo method (Bird 1994), which consists in tracking fictive particles to represent the distribution. This provides statistical information if enough particles are tracked to achieve statistical convergence. The second one, the stochastic parcel method (O'Rourke 1981), consists on the contrary in representing a group of particles by a computational particle, of equivalent weight. In both cases, these Lagrangian simulations remain proportional to the number of the tracked parcels and do not take advantage of the Eulerian formulation of the problem.
- **Method of moments**: By integrating the WBE in the phase space, we reduce the dimensionality of the problem until we obtain a problem in the physical space only. The resulting equations, after closure, can be solved by classical finite volume methods. This is further developed in the next section, as it represents a higher level of reduction.

7.1.3 Macroscopic approaches

Derived from the mesoscopic formulation, this level of resolution gives access to the macroscopic variables of the system. The number density, particle density, particle velocity fields are defined using the integration of the NDF over their respective phase space:

$$\begin{aligned} n(t,\boldsymbol{x}) &:= \int_{\mathbb{R}^3} f(t,\boldsymbol{x},\boldsymbol{v})\,\mathrm{d}\boldsymbol{v}, \\ \rho_p(t,\boldsymbol{x}) &:= \int_{\mathbb{R}^3} m_p f\,\mathrm{d}\boldsymbol{v}, \\ \rho_p(t,\boldsymbol{x})\boldsymbol{u}_p(t,\boldsymbol{x}) &:= \int_{\mathbb{R}^3} m_p \boldsymbol{v} f\,\mathrm{d}\boldsymbol{v}, \end{aligned} \tag{7.2}$$

with m_p the mass of a single particle. The notation $\langle . \rangle_{\boldsymbol{v}}$ is used to denote the integration over the velocity phase space. Higher order moments are expressed in App. A along with a general formalism for the derivation of Eulerian moments equations. The set of obtained equations always involves a moment of higher order which requires an additional model for closure. If the closure is exact, the moments equations formulation is equivalent to the WBE.

Unlike Lagrangian methods, the Eulerian fields obtained are naturally statistically converged. The Eulerian framework being similar to that of the continuous carrier phase, the two-way coupling terms can be easily derived. Compared to Lagrangian methods with a large number of particles, their numerical simulation is less expensive, but special attention must be paid to the numerical methods because of singular behaviors exposed in the previous chapter (PPC, PTC or polydispersion in size). Since the local concentration of particles is modeled as a "fluid", the segregation can be interpreted as a hypercompressibility feature of this "fluid", and PTC results in multi-valued fields (De Chaisemartin 2009).

Balachandar and Eaton (2010) classified the different approaches to the disperse phase based on

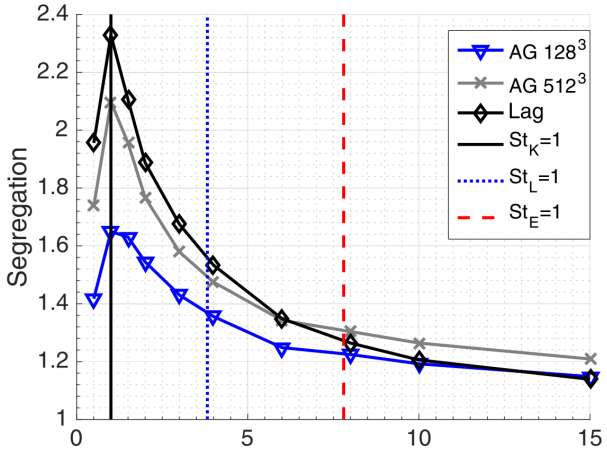

Figure 7.1. Segregation as a function of the Stokes number for Lagrangian result and Anisotropic Gaussian results on 128^3 and 512^3 meshes with projection on the same 64^3 mesh. Figure from Sabat, Vié, Larat, and Massot (2019)

the Stokes number. A robust Eulerian-Eulerian formulation is possible in the limit of a dilute distribution of small particles: it is the Eulerian Equilibrium approach (Maxey 1987; Druzhinin 1995; Ferry and Balachandar 2001). The Eulerian approach is mostly suitable for low inertial particles $\mathrm{St} < 1$, for which the modeling of the PTC is not an outstanding issue. Recently works aim at extending their applicability to intermediate Stokes numbers (Sabat 2016; Chalons, Fox, Laurent, Massot, and Vié 2017; Fox, Laurent, and Vié 2018).

Several closures are reviewed in App. A and some of them are compared on a two-dimensional HIT test case, especially in terms of their ability to reproduce particle preferential concentration and particle trajectory crossing. The reader is referred to Kaufmann, Moreau, Simonin, and Helie (2008), Laurent, Vié, Chalons, Fox, and Massot (2012), Masi, Simonin, Riber, Sierra, and Gicquel (2014), Sabat (2016), Sabat, Vié, Larat, and Massot (2019). In particular, Fig. 7.1 shows the segregation levels obtained by a method of moments, the anisotropic Gaussian method (Vié, Doisneau, and Massot 2015), for different resolutions. Segregation is here defined as the normalized variance of the particle density field, as introduced in Sec. 6.2.1.2. The Lagrangian PPC, considered as a reference and obtained with a 128^3 DNS mesh, can only be approximated by very fine meshes, more than four times finer, because of the hypercompressibilty of the Eulerian model that leads to strong numerical constraints, degenerating the order of convergence close to one in accumulation regions.

7.2 Particles dynamics in under-resolved turbulence

In Chap. 2, we have discussed the limitations of using very high fidelity methods such as DNS for the carrier phase resolution, which is computationally too expensive for industrial applications. We have therefore introduced reduced-order models, resolving the large scales of the flow, and modeling the small ones.

While reduced-order approaches are justified in practical applications dominated by large-scale mixing, their validation is more challenging when the process of interest occurs at smallest scales

(molecular mixing, chemical reaction in turbulent combustion, droplet break up in spray atomization, momentum transfer in near-wall flows). In disperse two-phase flows, the dynamics is intricately linked to the interplay occurring between the two phases. However, the reduction modifies this interaction, preventing the particles from interacting with the structures thus filtered. The use of reduced-order models for flows with disperse phase requires new models in order to correct the dynamics of particles, biased by the partial knowledge of the carrier phase.

In this section, we are therefore first interested in the impact of under-resolved turbulence on the disperse phase. Then, looking for a way to recover the DNS statistics, we present two categories of particle sub-filter scale models: the stochastic and the structural models. We also suggest another approach, based on retrieving not DNS statistics but filtered DNS statistics.

7.2.1 Impact of under-resolved turbulence on particles dynamics

We have seen that the particles Eq. (6.7) involves the velocity of the surrounding fluid at the particle position: $\boldsymbol{u}(\boldsymbol{x}_p(t), t)$. In ROS, only the large scales are resolved and the only available information is $\boldsymbol{U}$, the resolved velocity field of the carrier phase. In some studies (Uijttewaal and Oliemans 1996; Wang and Squires 1996; Yeh and Lei 1991) it was assumed that the unresolved fluctuations $\boldsymbol{u}'$ could be neglected in regard to the inertial particle velocity, since the drag force can be considered as a low-pass filter which thus reject small-scales fluctuations of the fluid. Only recent studies have pointed out the need to take into account these fluctuations and quantified their influence on the dynamics of particles such as particle kinetic energy and/or particle preferential concentration (Marchioli, Salvetti, and Soldati 2008b; Minier 2015; Kuerten 2016).

According to Balachandar (2009), Urzay, Bassenne, Park, and Moin (2014), two types of sub-filter effects are observed: the effect of sub-filter turbulence on the particles, and in some two-way coupling configurations, the effect of the energy delivered by the particles to the fluid at the sub-filter scale. In this chapter, we will deal first with the one-way case and save discussions on the two-way effects for the Part V of this manuscript, which are analyzed in Chap. 13 and modeled in Chap. 14.

In order to identify the shortcomings of the reduced simulations from the point of view of the disperse phase, we compare these effects between a DNS and *a priori* ROS. In the following, we will establish according to which criteria and how the dynamics of the disperse phase can be altered in the absence of a compensatory particle model.

7.2.1.1 Simulation set-up: Euler-Lagrange disperse flows

Consistent with the general working assumptions in this thesis, we consider a mono-disperse phase such that the point-particle approximation is verified and we track the particles with a Lagrangian approach, following the DPS method. DNS and LES point-particle modeling challenges have been reviewed in Subramaniam (2013), Kuerten (2016).

In order to investigate the influence of a reduced-order fluid resolution, we compare the effect of turbulence on the particles between a DNS, and *a priori* reduced-order simulation, i.e. a ROS obtained by filtering the DNS velocity fields. The set-up case is a forced HIT, at $\mathrm{Re}_\lambda = 150$, resolved with DNS performed by Fieldz (see Sec. 2.4). We give as an example in Fig. 7.2(a) a velocity field obtained with DNS, and its associated filtered velocity field in Fig. 7.2(b). Small scales have been

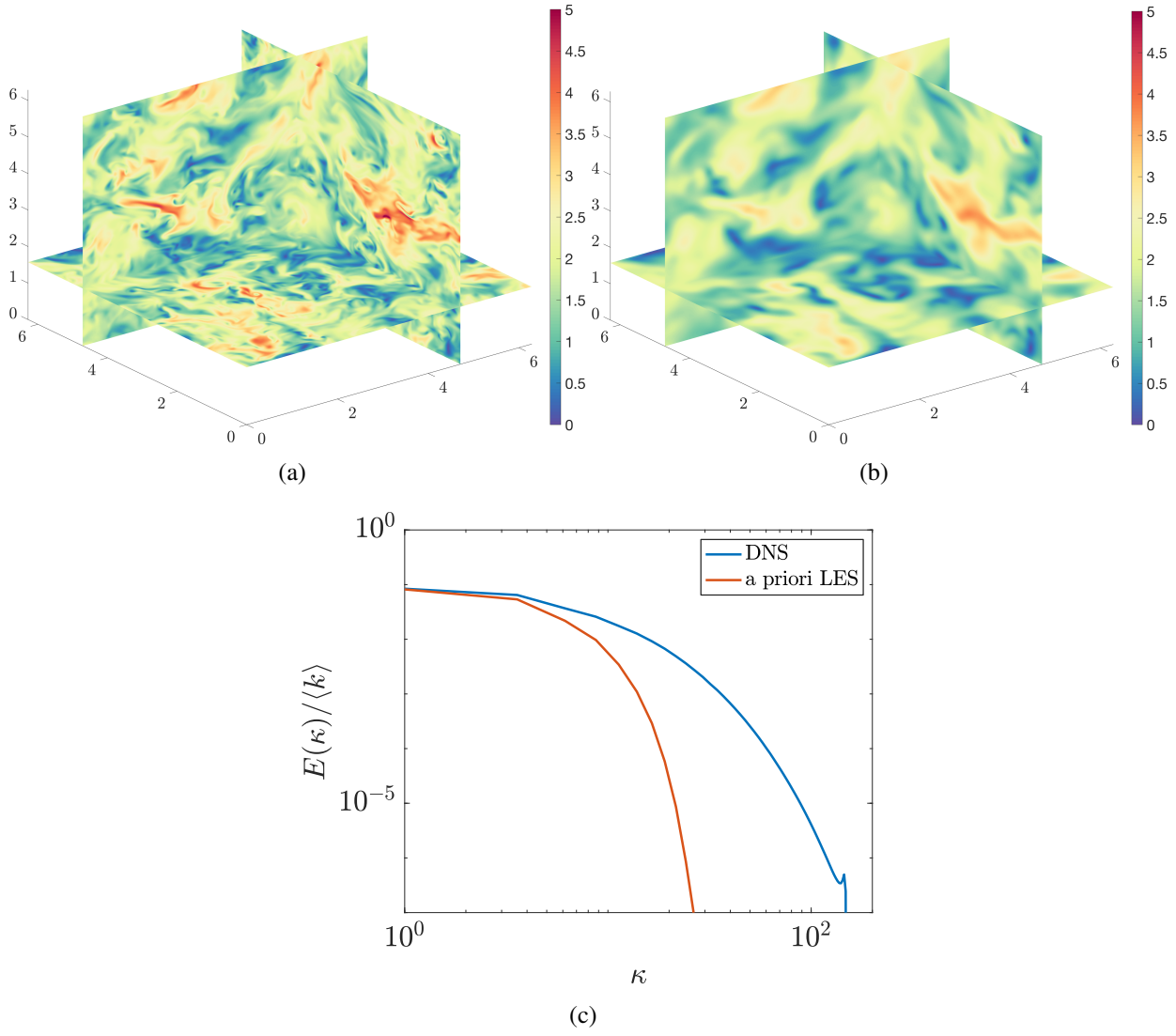

Figure 7.2. Snapshot of the velocity field of (a) DNS ; (b) a priori ROS i.e. filtered DNS (with Gaussian filter). (c) is the energy spectra of the two fields. DNS at $\mathrm{Re}_\lambda = 150$ performed with Fieldz.

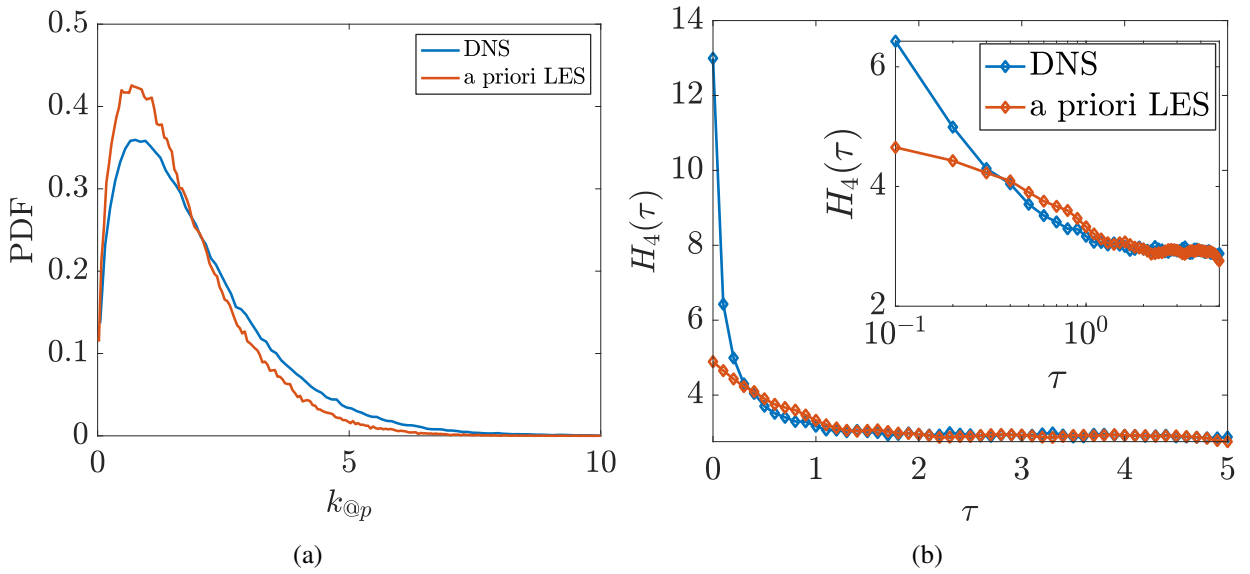

Figure 7.3. Comparison between DNS and a priori ROS fields obtained with Fieldz of (a) particle turbulent kinetic energy PDF ; (b) Flatness of velocity increments. The inset is the same plot with x-axis in log-scale.

filtered out by the Gaussian filtering, which is quantified in the energy spectrum of Fig. 7.2(c). The cut-off wavenumber of the filter is around $\kappa \approx 10$.

Thus, we reproduce the effects of a reduced simulation while knowing the exact velocity fields and we can estimate and quantify the information loss, especially with different levels of reduction of the fluid.

7.2.1.2 Intermittency

There is a general agreement on the limited effects of sub-filter fluid turbulence on particle dispersion, particle Lagrangian time scale, particle velocity fluctuations (Fede and Simonin 2006; Armenio, Piomelli, and Fiorotto 1999), those statistics being mainly driven by large scales (hence resolved) of the fluid. However, filtering the velocity field obviously reduces the amount of energy in the system. This loss is estimated and modeled in the sub-filter terms of the ROS but it is naturally missing in the resolved velocity fields and is therefore not transmitted to the particles. This results in lower values of the turbulent kinetic energy seen by the particles, as can be seen in Fig. 7.3(a). The distribution of kinetic energies $k_{@p}$ in DNS extends to larger values than the one in ROS.

As a consequence, fluid and inertial particles responding to the reduced fluid do not experience such extreme accelerations than with DNS. We have seen in Chap. 3 how such behaviors are characteristics of intermittency. Figure 7.3(b) compares the flatness of velocity increments in a DNS, and in the associated *a priori* ROS. As explained in Chap. 1, this flatness is a good indicator of the intermittency, and we expect far-from-Gaussian statistics (i.e. $H_4(\tau) \neq 3$). The particle velocity fluctuations are very clearly intermittent for DNS, which reaches a flatness of 13 for the acceleration. On the other hand, these levels of intermittency are not reached in the ROS,

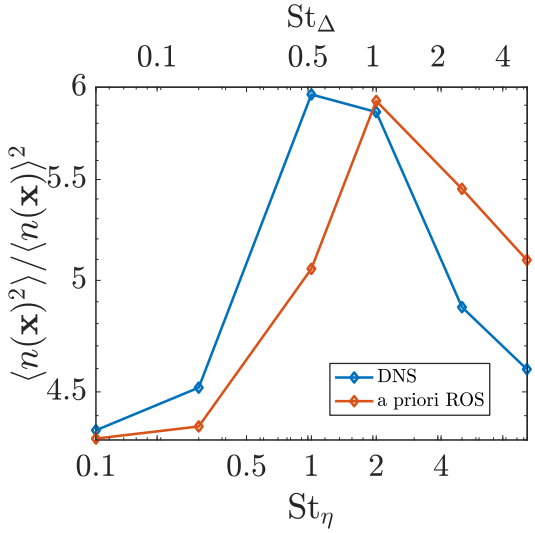

Figure 7.4. Segregation measure for particles in DNS and filtered DNS (*a priori* ROS) as a function of Stokes numbers.

for which the flatness of small velocity increments τ is much lower than that of the DNS. These correspond indeed to the unresolved scales, filtered in the ROS approach and which is thus not able to reproduce strong velocity fluctuations at these scales. It is then necessary to develop appropriate models to reconstruct these statistics at small scales.

7.2.1.3 Segregation

The velocity field seen by the particles being filtered, the scales of the smallest vortices do not correspond to the Kolmogorov lengths but rather to the cut-off lengths of the chosen filter Δ. Thus, the relevant Stokes number for these simulations corresponds to the ratio of the particle relaxation time to the characteristic sub-filter time: $\mathrm{St} = \tau_p/\tau_\Delta$ (Balachandar 2009; Urzay, Bassenne, Park, and Moin 2014).
Comparing the PPC in DNS and ROS, we indeed observe in Fig. 7.4 a shift towards larger Stokes numbers of the characteristic peak when the velocity field seen by the particles is filtered. By plotting the segregation with respect to St_Δ, we find a maximum reached for a unitary St_Δ as expected. This Stokes number is intermediate between St_η and St_L.

- When $\mathrm{St}_\Delta \ll 1$, particles are highly sensitive to unresolved turbulence while behaving as tracers with respect to large resolved eddies. PPC is therefore under-predicted in ROS.
- For $\mathrm{St}_\Delta \approx 1$, sub-filter turbulence results in a randomization of particle distribution mainly driven by intermediate scales. PPC is overpredicted in ROS and a diffusion process for particle modeling could help reducing the PPC in that case.
- When $\mathrm{St}_\Delta \gg 1$, particles are inertial with respect to sub-filter fluctuations and their interaction with resolved scales is sufficient to reproduce the level of segregation of DNS and no additional modeling is required.

Note that Fede and Simonin (2006) have observed similar behaviors by considering a Stokes number related to the Lagrangian integral time of the sub-filter velocity seen by the particle: $\mathrm{St}^\star_\Delta = \tau_p/T_L^{u'_{@p}}$.

Following the classification taken from Marchioli (2017) in Fig. 7.5, we can summarize the need

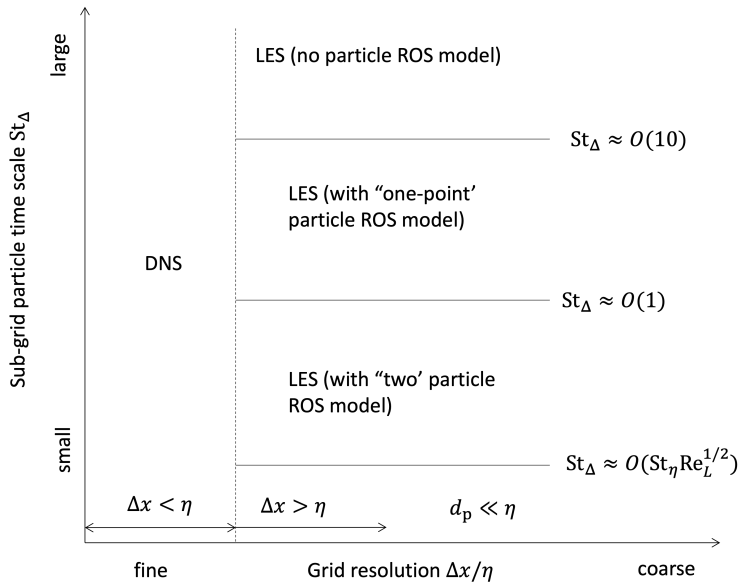

Figure 7.5. Classification of modeling approaches depending on the Stokes number St_Δ and the grid resolution. Figure reproduced from Marchioli (2017).

for an additional model on particles:

- For very large Stokes numbers, particles are not affected by the filtered scales and no additional model is needed;
- For intermediate Stokes numbers, preferential concentration might be approximately retrieved, however, particles do not experience the correct level of intermittency. "One-point" particle models should be considered to retrieve intermittent statistics;
- Particles with inertia lower than the sub-filter time scale obviously miss the interaction with filtered structures, and PPC is therefore not well reproduced in such ROS. Given the importance of the two-point dynamic of the disperse phase for combustion application, a "two-point" model is required.

7.2.2 Overview of existing particle sub-filter scale models

Today, the LES is widely used to understand and predict turbulent particle-laden flows. The most classical way consists in combining a single-phase LES model to describe the gas phase, with an additional sub-filter scale model for the particulate phase. The reader is referred to Kuerten (2016) for an exhaustive review of particle SFS models. These models are actually suitable either for LES or RANS or both (Marchioli 2017).

Models have been proposed in the literature, which can be classified into two categories:

- **Stochastic models** (Minier, Chibbaro, and Pope 2014; Bini and Jones 2008; Shotorban and Mashayek 2006; Zamansky, Vinkovic, and Gorokhovski 2013), the objective of which is to mimic the effect of sub-filter scale flow on particle paths using additional random process on Lagrangian quantities.
- **Structural models** that aims at reconstructing the sub-filter scales of the flow. Among them are the approximate deconvolution models (ADM), the fractal interpolation, or kinematic simulations (Murray, Lightstone, and Tullis 2016a). The latter approach is based on the

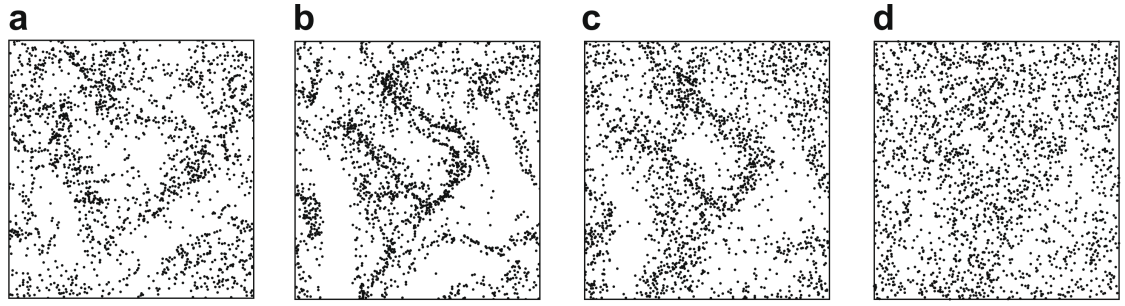

Figure 7.6. Snapshots of particle positions; $\mathrm{St} = 2$. (a) DNS; (b) a priori LES with no SGS dispersion model; (c) a priori LES with model and $C = 0.05$; (d) with $C = 1$. Figure from Pozorski and Apte (2009).

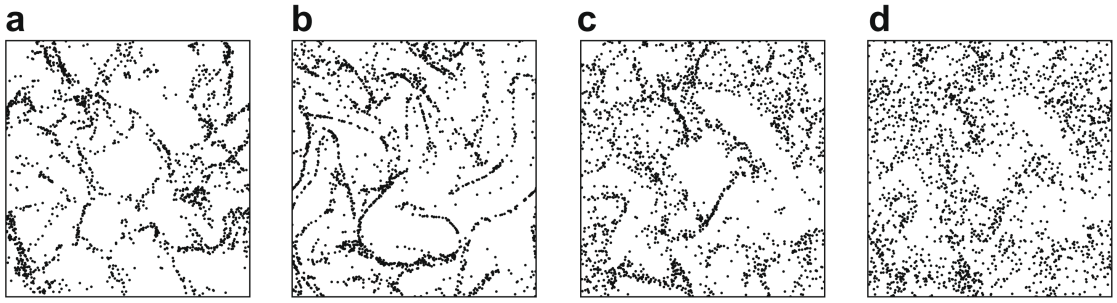

Figure 7.7. Snapshots of particle positions; $\mathrm{St} = 0.7$. (a) DNS; (b) a priori LES with with no SGS dispersion model; (c) a priori LES with model and $C = 0$; (d) with $C = 0.05$. Figure from Pozorski and Apte (2009).

reconstruction of the field from an Eulerian point of view.

7.2.2.1 Stochastic models

Historically, Lagrangian approaches were first developed with the use of random walks for particle trajectories. In the context of RANS models for turbulence, we have already seen some of these Lagrangian models applied to fluid particles in Chap. 3 and they can be adapted to the case of inertial particles, which will be the focus of Chap. 8. From this arises the general formalism for PDF which has been developed among others by Reeks (1992), Pozorski and Minier (1999), Minier and Peirano (2001).

Pozorski and Apte (2009) have investigated the use of stochastic Langevin models. They concluded that they could produce the right amount of particle kinetic energy and any one-point statistics by construction. Indeed, parameters of stochastic models can tune the expectations, variances, covariances of the modeled processes. We will see how the intermittency can be faithfully reproduced in such models and we will discuss these choices in Chap. 8.

However, all stochastic models rely somehow on uncorrelated Gaussian noises and therefore assume a Markovian nature of velocity histories. They cannot enforce any spatial correlations, as a consequence, very close particles can see very different noises. Pozorski and Apte (2009) investigated the influence of the stochastic model of Pozorski and Minier (1999), driven by the factor C involved in the sub-filter characteristic time $\tau_{\mathrm{sgs}} = C\Delta/\sigma_{\mathrm{sgs}}$. They noticed in Fig. 7.6 that for

large-inertia particles, the diffusion introduced by the stochastic models can replace the randomizing effect of small scales and thus roughly recover the preferential concentration levels of the particles in DNS. However, for small-inertial particles, those models cannot recreate the small-scale patterns solely based on coarse sub-filter information. This is shown in Fig. 7.7, were no fitting of C allows to recover the small-scale particle concentration. To conclude, they suggested that two-points statistics (Eaton, Squires, and Eaton 1991) can only be found in structural models to ensure particle-fluid and particle-particle velocity correlations. This motivates the need for a structural approach to use more information about how real turbulence is known to behave, in particular its spatial and temporal organization.

7.2.2.2 Structural models

Structural models consist in reconstructing a velocity field similar to the fully resolved field for the particles to evolve in. As opposed to stochastic models, this implies reconstructing information in the whole space, and not only for each particle. This method has the advantage of preserving the spatial correlation, so that neighboring particles can experience a similar fluid velocity.

Approximate deconvolution method (ADM) seeks to recover the original field precisely, by reversing the effects of the reduction operator on the fluid field. Compared to ROS without a particle SFS model, it has been shown that ADM improves the particle results. However, since the reduction operator is not injective, it is not possible to rigorously invert it and the information lost when projecting the filtered or averaged field onto the coarse grid cannot thus be recovered. In fact, it is found that only the scales close to the cutoff scale can be reconstructed by the ADM method and therefore the sub-filter kinetic energy is only partially retrieved (Shotorban and Mashayek 2005). Cernick, Tullis, and Lightstone (2015) compared simulations with different stochastic models, ADM, and no particle SFS model. They observe that although it is possible to partially recover the preferential concentration in the absence of a model, this is clearly improved with a structural model such as the ADM. However, it does not reach the segregation observed in DNS due to the limitations of the ADM model, which can only reconstruct scales close to the cut-off scale. Stochastic models, on the other hand fails to predict any particle clustering due to the random components applied to particles.

Fractal interpolation consists in reconstructing the velocity field on a finer mesh by interpolating the filtered field, interpolation which depends on the fractal dimension of the signal which should either be known or assumed a priori. More details on this technique can be found in Scotti and Meneveau (1999). Marchioli, Salvetti, and Soldati (2008a) considered models based on fractal interpolation and concluded that this technique is not systematically able to recover the amount of SGS turbulent kinetic energy for the fluid velocity field and hence does not recover the particle segregation.

Kinematic simulation (KS) is a computationally attractive method to reconstruct the small-scales field. By imposing a turbulent kinetic energy spectrum, a random velocity field is generated by means of orthogonal and random Fourier modes (Kraichnan 1970; Murray, Lightstone, and Tullis 2016a; Ijzermans, Meneguz, and Reeks 2010). We detail this method in Chap. 9 and discuss its advantages and drawbacks.

7.2.3 Capturing reduced-order statistics of the disperse phase

In general, the scope of modeling strategies for ROS of particle-laden flows is to capture particles dynamics. Such dynamics require a correct description of the particle localization (preferential concentration) as well as particle acceleration. Following the conclusions of Pozorski and Apte (2009), we would expect that stochastic models are not an acceptable choice because they lack a correct prediction of preferential accumulation. This conclusion is based on a specific strategy for validation: the authors validate ROS against the DNS statistics. However, this choice is open to discussion since one can also decide to validate the ROS on the filtered DNS statistics. These two options differ by the objective of the model in sight: describing the PDF or the filtered PDF.

We perform a DNS of particle-laden turbulent flows, and we show the particle number density field in Fig. 7.8(a). The same field is filtered and presented in Fig. 7.8(b). Such particle number density fields are the two possible references to validate a particle SFS model. The PPC of the filtered density field is lower and can be compared to that produced by the ROS in Fig. 7.8(c). Quantitatively, the PPC as a function of Stokes number (Fig. 7.8(e)) of ROS is of the order of magnitude of the filtered DNS field, with a shift towards higher Stokes numbers. This is consistent with the loss of smallest structures in ROS, and the PPC peak is obtained at St_Δ. Nonetheless, we can now have excessive PPC prediction in ROS. Adding a stochastic process (in Fig. 7.8(d)) could reduce the segregation and eventually recover the missing physics.

Other techniques can be used to obtain filtered statistics, in particular to obtain filtered Eulerian moments. The main distinction concerns the stage at which the reduction operation is applied:

- **by filtering the WBE**, an additional term appears that represents the diffusion transport caused by the interaction of particles with small-scale sub-filter turbulent eddies (Pandya and Mashayek 2002; Sabat 2016; Zaichik, Simonin, and Alipchenkov 2009). Adopting a similar type of closure problem than in Reeks (1992), they derive the corresponding set of moments;
- **by filtering the moment equations** obtained from the MEF: particle number density, momentum and internal energy. The resulting moment equations exhibit a similar structure to that of gaseous compressible flows and Moreau, Simonin, and Bédat (2010) used similar approximations as closures.

Conclusion

In this chapter, we have first examined the reduction strategies for the disperse phase, considering a fully resolved carrier phase.

However, we have previously established that it is not possible to completely resolve the turbulence when the Reynolds number becomes too large, which is the case in most industrial applications. It is then necessary to consider new models for the disperse phase, aiming at reproducing the effect of unresolved scales of the flow on the particles.

Two categories of particulate SFS models are available in the literature: stochastic models, which by means of Brownian motions allow to recover the one-point statistics of the disperse phase and we detail this approach in the next chapter. However, these diffusive models do not allow to repro-

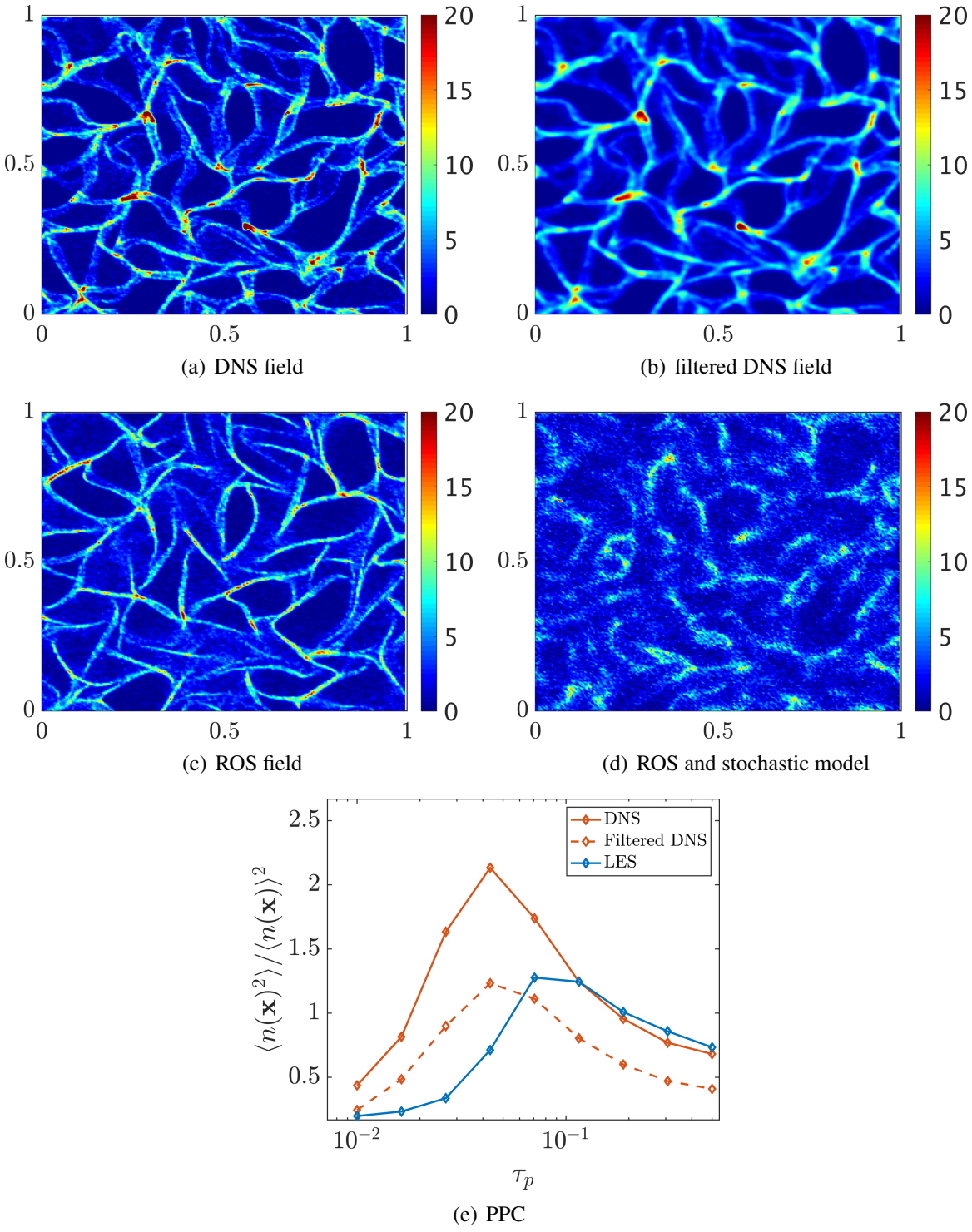

Figure 7.8. Particle number density field for (a) DNS ; (b) filtered field of DNS ; (c) ROS with no particle SFS mode ; (d) ROS with stochastic modeling ; and (e) PPC.

	DPS	**Mesoscopic Lagrangian**	**Mesoscopic Eulerian**	**Eulerian Moments**
DNS	DNS / DPS	Lagrangian methods (DMCS, SP)	WBE $\rightarrow$ MEF	NDF-shape or algebraic closures
ROS	Structural models	Stochastic models	(Modified) WBE and EMEF	Reduced-order Eulerian moments

Table 7.1. One-way coupling between reduced descriptions of turbulence and disperse phase.

duce the dispersion of the particles and to retrieve the preferential concentration levels obtained in DNS. On the other hand, structural models focus on reconstructing the sub-filter velocity field while keeping only a limited number of parameters to not increase the dimensionality.

In order to complete the overview of the possible couplings between the reduced descriptions of each phase, which we give in Table. 7.1, we have also mentioned coupling strategies between ROS and Eulerian equations of the disperse phase but they are not studied further in our work.

We have not addressed in this chapter the modeling aspects related to two-way coupling, these will be treated in the last part and the dedicated Chap. 14: new models must also be considered not only for the particles, but also for the sub-filtered flow since the particles can have an impact on the resolved and unresolved scales.

Part IV

Reproducing segregation and intermittency in turbulent disperse two-phase flows

Part IV aims at developing particle sub-filter models in the context of under-redolved turbulence. The objective is to overcome the biases introduced by the reduced-order simulation of the turbulence, and to reproduce the unresolved velocity fluctuations of the inertial particles, still in a one-way context. Chapter 8 first introduces stochastic models on inertial particles, and different choices of the literature are discussed: particle velocity, fluid velocity seen by the particles, dissipation seen by the particles. Then, dissipation along the inertial particles trajectory is considered using the intermittent stochastic model introduced in Chap. 5 in the framework of fluid particles and thus adapted in this chapter to inertial particles. Chapter 9 introduces particle sub-filter modeling from another perspective to reproduce two-point statistics of the disperse phase, namely the preferential concentration. Kinematic simulation (KS) based on Fourier series is classically used in the literature to address this problem. We propose another paradigm of kinematic simulation based on wavelets with particular properties. Like the Fourier-based KS, we build a synthetic divergence-free turbulent field capable of reproducing the energy spectra and other specific features of turbulence. After validating such a model from a strictly turbulent point of view, we study in Chap. 10 the behavior of a disperse phase transported by such a dynamic synthetic field. We verify that collective behaviors such as segregation and random uncorrelated motion are correctly reproduced. Finally, Chap. 11 gives some perspectives for such a kinematic model, by studying, in particular, its intermittency and by verifying its suitability for LES applications.

Chapter 8

Two-phase flow stochastic models

In the previous chapter, we have demonstrated the need to introduce a particle SFS model when turbulence is resolved relying on reduced-order simulations. Stochastic methods allow to add information directly to the particle trajectory to mimic the effect of the filtered scales on the particles. Several choices are then to be considered: which kind of stochastic equation to use? What type of random noise? At what level should we introduce the randomness? On the position, velocity, acceleration, dissipation of the particle?

Several reviews of stochastic models are proposed in (Balachandar and Eaton 2010; Kuerten 2016; Marchioli 2017), and the objective of this chapter is not to propose an exhaustive list but rather to discuss the main ones and identify their shortcomings based on the tools already introduced in the study of fluid particles (Chap. 3). Then we introduce a new model, consistent with the intermittent one developed in Chap. 5.

As in Chap. 3, we propose a classification of the models according to the level of modeling and study in each case their compatibility with the K41 or K62 theories:

- We present in Sec. 8.1 the main requirements and statistics to validate a stochastic model for inertial particles;
- Section 8.2 introduces the stochastic models dealing with the particle velocity;
- In Sec. 8.3, we review stochastic acceleration models (or equivalently models based on the fluid velocity seen by the particle) and we highlight the differences with fluid particles models;
- Intermittency can be accurately modeled by considering conditional acceleration with a stochastic model for dissipation. We discuss the limits of existing models in Sec. 8.4 and we propose a new intermittent model for inertial particle, as an extension of the fluid one introduced in Chap. 5 .

8.1 Criteria for the assessment of stochastic models

Minier, Chibbaro, and Pope (2014) have proposed a list of criteria for the formulation of Lagrangian stochastic models for disperse two-phase turbulent flows when modeling the fluid seen by inertial particles:

- Expression of drift and diffusion terms must be explicit so that the model is predictive;
- The inertial particles model should revert to an acceptable stochastic model in the particle tracer limit;

- For homogeneously distributed particles, the fluid seen is such that the predicted mean kinetic energy of the fluid seen by particles respects the same statistical evolution as the mean fluid kinetic energy;
- The model should be consistent with the equilibrium Eulerian approach formulated in the limit of small particle Stokes numbers (Balachandar and Eaton 2010).

This list of formal criteria is a basis for the construction of stochastic models. In order to compare the different models and by reviewing the literature on the subject, we propose a list of quantities of interest to be assessed and compared in order to validate the stochastic particle models. This list is not exhaustive, it includes the main metrics of interest compared in the different studies:

- Particle velocity (kinetic energy, autocorrelation, PDF) (Fede and Simonin 2006; Shotorban and Mashayek 2006; Pozorski and Apte 2009; Berrouk et al. 2007)
- Particle acceleration (PDF, variance, flatness, autocorrelation) (Gorokhovski and Zamansky 2018; Bini and Jones 2007)
- Mean square displacement of particles or particle dispersion (Shotorban and Mashayek 2006; Berrouk et al. 2007)
- Particle preferential concentration (Fede and Simonin 2006; Pozorski and Apte 2009; Berrouk et al. 2007)
- Lagrangian velocity increments (PDF) (Bini and Jones 2007)
- Power exchange with the fluid (PDF) (Gorokhovski and Zamansky 2018)

Following the general notations of Sec. 2.2.3, in a framework of reduced description of turbulence, we decompose the instantaneous fluid velocity as: $\boldsymbol{u}(\boldsymbol{x},t) = \boldsymbol{U}(\boldsymbol{x},t) + \boldsymbol{u}'(\boldsymbol{x},t)$, where $\boldsymbol{U}$ is numerically solved, but $\boldsymbol{u}'$ requires modeling. The objective is to correct the particle velocity $\boldsymbol{v}_p$ altered by the reduced representation of the fluid velocity, with stochastic model in agreement with the list of criteria of Minier, Chibbaro, and Pope (2014). Models will be assessed according to DNS disperse phase statistics, in particular the ones listed above.

In the following, we present the different modeling strategies (velocity, acceleration, dissipation models) by giving examples of literature models. We have generalized and standardized the notations of the models we review in this chapter to include any type of closure (RANS or LES) but we will mention each time, which closures are chosen by the authors of these models.

8.2 Stochastic models for particle velocity

Since trajectory divergence between particles in reduced-order models and in DNS is mainly due to inaccurate estimation of the forces acting on the particles, a first class of stochastic models introduces the stochastic noise directly on the particle velocity equation, justifying this additional term as a model representing the missing fluctuating force.

Fukagata, Zahrai, and Bark (2004) proposed to account for sub-grid turbulence effects on particle by adding a Brownian force in the particle velocity equation, following the model:

$$\frac{\mathrm{d}\boldsymbol{v}_p}{\mathrm{d}t} = \frac{\boldsymbol{U}_{@p} - \boldsymbol{v}_p}{\tau_p} + \boldsymbol{F'}_p, \quad \text{with } \boldsymbol{F'}_p = \frac{\sigma_S}{\Delta t}\boldsymbol{\xi}, \tag{8.1}$$

and σ_S is the increment in standard deviation of particle velocity due to velocity fluctuations during the simulation time step Δt and $\xi_i \sim \mathcal{N}(0,1)$ is a standardized Gaussian variable. The parameter

σ_S is rescaled according to the kinetic theory for particle motion in isotropic turbulence (Reeks 1991): $\sigma_S^2 = \sigma_{\star@p}^2 \lambda$, where λ is a parameter depending on the particle relaxation time τ_p and on the sub-grid integral time scale $T_L^{\star@p}$. The parameters $\sigma_{\star@p}$ and $T_L^{\star@p}$ are analogous to $\sigma_\star$ and $T_L^\star$ but sampled along the trajectories of inertial particles.

According to Cernick, Tullis, and Lightstone (2015), this model correctly reproduces DNS statistics (particle and fluid seen turbulent kinetic energy) for particles with intermediate Stokes numbers but overpredicts the energy for smaller and larger Stokes numbers. The model also underpredicts the particle Lagrangian integral timescale, leading to a large range of dispersion results.

The model of Bini and Jones (2008) also provides a Langevin equation for the particle velocity, with the drift term still corresponding to the "large scales" acceleration, and the diffusion term fitted based on the sub-grid scale kinetic energy $k_{\star@p} = 3/2\sigma_{\star@p}^2$:

$$\mathrm{d}\boldsymbol{v}_p = \frac{\boldsymbol{U}_{@p} - \boldsymbol{v}_p}{\tau_p}\,\mathrm{d}t + \sqrt{\mathcal{C}_0 \frac{k_{\star@p}}{\tau_t}}\,\mathrm{d}W_t. \tag{8.2}$$

They introduced a time scale τ_t and studied several forms:

$$\tau_t = \frac{\tau_p^{2\alpha}}{(\Delta/\sqrt{k_{\star@p}})^{2\alpha-1}}, \quad \tau_t = \frac{\Delta^{1/3}}{|v_p|}, \quad \tau_t = \frac{\Delta^{1/3}}{\sqrt{k_{\star@p}}} \tag{8.3}$$

They stated that it is necessary to have a non-linearity in the diffusion term (involving the particle velocity $\boldsymbol{v}_p$) to introduce the far-from-Gaussian behavior of particle acceleration statistics.

Two main criticisms can be raised regarding those models:

- Both introduced in a LES framework, parameters were taken identical to the sub-grid parameters of the Smagorinsky model: $\sigma_{\star@p} = \sigma_\star = \sigma_{\mathrm{sgs}}$ and $T_L^{\star@p} = T_L^\star = 2\sigma_{\mathrm{sgs}}^2/\mathcal{C}_0\varepsilon_{\mathrm{sgs}}$. However, these parameters are supposed to represent characteristics along the trajectories of inertial particles, and therefore, we expect them to capture different velocity fluctuations along their trajectory than fluid particles, due to their inertia.
- Such Brownian-like models can hardly converge to fluid particle models in the limit of $\tau_p \to 0$, since they do not model the velocity of the fluid seen by the particles but directly the velocity of the inertial particles. The next section therefore focuses on modeling fluid velocity seen by inertial particles.

8.3 Stochastic models for particle acceleration

Let us first note that stochastic models for particle acceleration are equivalent to stochastic models on fluid velocity seen by particles, which is denoted $\boldsymbol{u}_{@p}(t) = \boldsymbol{u}(\boldsymbol{x}_p(t), t)$. We have:

$$\mathrm{d}\boldsymbol{v}_p = \frac{\boldsymbol{u}_{@p} - \boldsymbol{v}_p}{\tau_p}\,\mathrm{d}t = \frac{\boldsymbol{U}_{@p} - \boldsymbol{v}_p}{\tau_p}\,\mathrm{d}t + \frac{\boldsymbol{u}'_{@p}}{\tau_p}\,\mathrm{d}t \tag{8.4}$$

Therefore particle acceleration can be decomposed into two parts:

$$\begin{aligned} \boldsymbol{A}_p &:= \frac{\boldsymbol{U}_{@p} - \boldsymbol{v}_p}{\tau_p}, \quad \text{and} \\ \boldsymbol{a'}_p &:= \frac{\boldsymbol{u}'_{@p}}{\tau_p}, \end{aligned} \tag{8.5}$$

and the increment of the fluctuating part is given by $\mathrm{d}\boldsymbol{a}'_p = \mathrm{d}\boldsymbol{u}'_{@p}/\tau_p$. Let us decompose the fluid velocity along inertial particle trajectory and examine models for the increments.

8.3.1 Velocity along inertial particle trajectory

Let us express the velocity increment along a solid particle trajectory, considering a first order development of the particle position $\boldsymbol{x}_p$ at time $t + \mathrm{d}t$, as performed in Simonin, Deutsch, and Minier (1993), Simonin, Deutsch, and Boivin (1995), Zeren (2010):

$$\boldsymbol{u}_{@p}(t+\mathrm{d}t) = \boldsymbol{u}(\boldsymbol{x}_p(t+\mathrm{d}t), t+\mathrm{d}t) = \boldsymbol{u}(\boldsymbol{x}_p(t) + \boldsymbol{v}_p(t)\,\mathrm{d}t, t+\mathrm{d}t). \tag{8.6}$$

They express the increments, and they introduce and reorganize terms:

$$\begin{aligned}
\mathrm{d}\boldsymbol{u}_{@p} &= \boldsymbol{u}(\boldsymbol{x}_p + \boldsymbol{v}_p\,\mathrm{d}t, t+\mathrm{d}t) - \boldsymbol{u}(\boldsymbol{x}_p, t) \\
&= \boldsymbol{u}(\boldsymbol{x}_p + \boldsymbol{u}_{@p}\,\mathrm{d}t, t+\mathrm{d}t) - \boldsymbol{u}(\boldsymbol{x}_p, t) \\
&+\boldsymbol{u}(\boldsymbol{x}_p + \boldsymbol{v}_p\,\mathrm{d}t, t+\mathrm{d}t) - \boldsymbol{u}(\boldsymbol{x}_p + \boldsymbol{u}_{@p}\,\mathrm{d}t, t+\mathrm{d}t) \\
&= \boldsymbol{U}(\boldsymbol{x}_p + \boldsymbol{u}_{@p}\,\mathrm{d}t, t+\mathrm{d}t) - \boldsymbol{U}(\boldsymbol{x}_p, t) \qquad (1) \\
&+\boldsymbol{u}'(\boldsymbol{x}_p + \boldsymbol{u}_{@p}\,\mathrm{d}t, t+\mathrm{d}t) - \boldsymbol{u}'(\boldsymbol{x}_p, t) \qquad (1)' \\
&+\boldsymbol{U}(\boldsymbol{x}_p + \boldsymbol{v}_p\,\mathrm{d}t, t+\mathrm{d}t) - \boldsymbol{U}(\boldsymbol{x}_p + \boldsymbol{u}_{@p}\,\mathrm{d}t, t+\mathrm{d}t) \qquad (2) \\
&+\boldsymbol{u}'(\boldsymbol{x}_p + \boldsymbol{v}_p\,\mathrm{d}t, t+\mathrm{d}t) - \boldsymbol{u}'(\boldsymbol{x}_p + \boldsymbol{u}_{@p}\,\mathrm{d}t, t+\mathrm{d}t). \qquad (3)
\end{aligned} \tag{8.7}$$

- (1) + (1)' is the Lagrangian increment along fluid trajectory. We have an explicit expression for (1):

$$(1) = \big(\frac{-1}{\rho}\nabla P + \nu\nabla^2\boldsymbol{U}\big)\,\mathrm{d}t$$

- (2) is the Eulerian increment of mean fluid velocity.

$$(2) = (\boldsymbol{v}_p - \boldsymbol{u}_{@p}) \cdot \nabla\boldsymbol{U}\,\mathrm{d}t + O(\mathrm{d}t)$$

- (3) is the Eulerian increment of fluctuating fluid velocity. It can be modeled along with the fluctuating part (1)' following the generalized Langevin model for fluid tracers:

$$(1)' + (3) = \boldsymbol{u}'(\boldsymbol{x}_p + \boldsymbol{v}_p\,\mathrm{d}t, t+\mathrm{d}t) - \boldsymbol{u}'(\boldsymbol{x}_p, t) = \mathrm{d}\boldsymbol{u}'_{@p} \sim \mathbb{G}_{fp}\boldsymbol{u}'_{@p}\,\mathrm{d}t + \mathbb{B}_{fp}\,\mathrm{d}\boldsymbol{W}_t$$

  where $\mathbb{G}_{fp}$ and $\mathbb{B}_{fp}$ must be determined.

$$\boxed{\mathrm{d}\boldsymbol{u}_{@p} = \left(\frac{-1}{\rho}\nabla P + \nu\nabla^2\boldsymbol{U}\right)\mathrm{d}t + (\boldsymbol{v}_p - \boldsymbol{u}_{@p}) \cdot \nabla\boldsymbol{U}\,\mathrm{d}t + \mathbb{G}_{fp}\boldsymbol{u}'_{@p}\,\mathrm{d}t + \mathbb{B}_{fp}\,\mathrm{d}\boldsymbol{W}_t.} \tag{8.8}$$

In the limit of particle tracers $\boldsymbol{v}_p \to \boldsymbol{u}_{@p}$, we should retrieve the stochastic equation Eq. (3.31).

In order to write a stochastic equation on the fluctuating velocity seen by an inertial particle, they identify $\boldsymbol{u}'_{@p} = \boldsymbol{u}_{@p} - \boldsymbol{U}$ and its increments verify:

$$\begin{aligned} \mathrm{d}\boldsymbol{u}'_{@p} &= \mathrm{d}\boldsymbol{u}_{@p} - \mathrm{d}\boldsymbol{U} \\ &= \mathrm{d}\boldsymbol{u}_{@p} - (\boldsymbol{U}(\boldsymbol{x}_p + \boldsymbol{v}_p\,\mathrm{d}t, t + \mathrm{d}t) - \boldsymbol{U}(\boldsymbol{x}_p, t + dt) + \boldsymbol{U}(\boldsymbol{x}_p, t + dt) - \boldsymbol{U}(\boldsymbol{x}_p, t)) \\ &= \mathrm{d}\boldsymbol{u}_{@p} - \boldsymbol{v}_p \nabla \boldsymbol{U}\,\mathrm{d}t - \partial_t \boldsymbol{U}(\boldsymbol{x}_p, t)\,\mathrm{d}t. \end{aligned} \tag{8.9}$$

Knowing that

$$\partial_t \boldsymbol{U}(\boldsymbol{x}_p, t) = -\boldsymbol{U}\cdot\nabla\boldsymbol{U} - \frac{1}{\rho}\nabla P + \nu\nabla^2\boldsymbol{U} + \frac{1}{\rho}\nabla\tau^r, \tag{8.10}$$

where τ^r is the sub-grid stress tensor. They finally obtain the stochastic equation for the fluctuating velocity seen by particle:

$$\boxed{\mathrm{d}\boldsymbol{u}'_{@p} = \left(-\frac{1}{\rho}\nabla\tau^r - \boldsymbol{u}'_{@p}\nabla\boldsymbol{U}\right)\mathrm{d}t + \mathbb{G}_{fp}\boldsymbol{u}'_{@p}\,\mathrm{d}t + \mathbb{B}_{fp}\,\mathrm{d}\boldsymbol{W}_t.} \tag{8.11}$$

Several models are proposed in the literature, corresponding to closures for $\mathbb{G}_{fp}$ and $\mathbb{B}_{fp}$. Those are directly consistent with the formulation of the stochastic equation of fluid velocity seen by particles, as required by Minier, Chibbaro, and Pope (2014) in Sec. 8.1. In the following, closures of such models are discussed.

8.3.2 Stochastic models for the velocity seen

Following the approach established in Chap. 3, one can obtain a similar expression with adapted parameters:

$$\mathrm{d}u_{@p} = \left(\frac{-1}{\rho}\nabla P + \nu\nabla^2 U - \frac{1}{T_L^{\star@p}}(u_{@p} - U_{@p})\right)\mathrm{d}t + \sqrt{\mathcal{C}_0\varepsilon_{\star@p}}\,\mathrm{d}W_t. \tag{8.12}$$

This naturally ensures to retrieve the well known generalized Langevin model in the limit of fluid particles. Such models were derived for isotropic turbulence in LES context by Shotorban and Mashayek (2006), Fede, Simonin, Villedieu, and Squires (2006) and in RANS framework by Pozorski and Minier (1998), Minier and Peirano (2001).

However, the above-mentioned models still considered similar parameters than for fluid particles, not tacking into account the inertial effect of particles:

- For RANS models, $\varepsilon_{\star@p} = \langle\varepsilon\rangle$ and $T_L^{\star@p} = 2\sigma_u^2/\mathcal{C}_0\,\langle\varepsilon\rangle$;
- For LES models, $\varepsilon_{\star@p} = \varepsilon_{\mathrm{sgs}}$ and $T_L^{\star@p} = 2\sigma_{\mathrm{sgs}}^2/\mathcal{C}_0\varepsilon_{\mathrm{sgs}}$

Berrouk, Laurence, Riley, and Stock (2007) were the first to propose a model taking into account the difference in trajectory between fluid and inertial particles. The Lagrangian integral time scale along particle trajectory $T_L^{\star@p}$ is modeled with a correlation developed by Wang and Stock (1993) that takes into account particle inertia:

$$T_L^{\star@p} = \frac{T_L^\star}{\beta}\left[1 - (1-\beta)\,(1 + \mathrm{St}_E^\star)^{-0.4\left(1+0.01\mathrm{St}_E^\star\right)}\right], \tag{8.13}$$

where $\beta = T_L^\star/T_E^\star$ is the ratio of the Lagrangian and Eulerian sub-grid time scales (definitions given in Chap. 1 can be extended to sub-grid velocity). For this model, β is a parameter and we define $\mathrm{St}_E^\star = \tau_p/T_E^\star$. The diffusion term is accordingly modified to maintain a stationary flow by introducing the constant $\mathcal{C}_0^\star = \mathcal{C}_0 T_L^\star/T_L^{\star@p}$. Finally, we have:

$$\mathrm{d}u_{@p} = \left(\frac{-1}{\rho}\nabla P + \nu\nabla^2 U - \frac{1}{T_L^{\star@p}}(u_{@p} - U)\right)\mathrm{d}t + \sqrt{\mathcal{C}_0^\star \varepsilon_\star}\,\mathrm{d}W_t. \tag{8.14}$$

Similarly, Pozorski and Apte (2009) derived a stochastic formulation for the fluctuating velocity (see Eq. (8.11)):

$$\mathrm{d}\boldsymbol{u}'_{@p} = \left(-\frac{1}{\rho}\nabla\tau^r - \boldsymbol{u}'_{@p}\nabla\boldsymbol{U}\right)\mathrm{d}t - \frac{1}{T_L^{\star@p}}\boldsymbol{u}'_{@p}\,\mathrm{d}t + \sqrt{\frac{2\sigma^2_{\star@p}}{T_L^{\star@p}}}\,\mathrm{d}\boldsymbol{W}_t, \tag{8.15}$$

with $\sigma_{\star@p} = \sigma_{\mathrm{sgs}}$, and $T_L^{\star@p}$ being a function of $T_L^\star = C\Delta/\sigma_{\mathrm{sgs}}$ and β, and also taking into account crossing-trajectory effect with Csanady's factors.

However, Eq. (8.13) was obtained for the large turbulent scales only and β is actually a function of the Reynolds number. The model is highly sensitive to that parameter. Eq. (8.13) retrieves the correct asymptotic behavior for very small particle inertial $T_L^{\star@p} \to T_L^\star$ and for very high particle inertia $T_L^{\star@p} \to T_E^\star$. Cernick, Tullis, and Lightstone (2015) compared stochastic models of Fukagata et al. (2004), Shotorban and Mashayek (2006) and Berrouk et al. (2007) and although satisfying results were obtained for low Stokes numbers, these models have a strong sensitivity to the Stokes number and to the filter size.

Let us also recall that Langevin's fluid velocity models do not reproduce small-scale fluctuations since only the Lagrangian integral time scale is introduced in the model, and no dissipative scale: that certainly explains the strong dependence on the filter size. Moreover, as it stands, only the sub-grid dissipation is introduced in the diffusion term, which does not reproduce the intermittency of the statistics, as explained in Chap. 3. An acceleration model conditioned on dissipation can be developed to tackle these two limitations.

8.3.3 Stochastic model for the acceleration

An other model for the fluctuating part of the acceleration was proposed by Gorokhovski and Zamansky (2018), Zhang, Legendre, and Zamansky (2019), as an extension of the fluid model of Sabel'nikov, Chtab-Desportes, and Gorokhovski (2011). This original model consists in two separate stochastic models for the norm and the direction of the vector: $\boldsymbol{a}'_p = a^*\boldsymbol{e}^*$, where $a^* = \overline{a_0^{1/2}}\varepsilon_{\star@p}^{3/4}\nu^{-1/4} f(\mathrm{St}, \mathrm{Re}_\Delta)$ and we define $\mathrm{Re}_\Delta = (T_L^\star/\tau_\eta)^2$.

There are two main differences with previous approaches:

- Following the proposition of Sabel'nikov, Chtab-Desportes, and Gorokhovski (2011), the orientation $\boldsymbol{e}$ is not given by an isotropic Wiener process but a more complex stochastic process with a shorter correlation time than the norm.
- Dissipation along particle trajectory is reconstructed instead of considering the local sub-grid scale dissipation. We have seen in Chap. 3 the importance of modeling the dissipation along

the particle trajectory with appropriate stochastic models that allow to recover intermittent statistics. Using a specific stochastic process for $\varepsilon_{\star@p}$, it is therefore possible to retrieve stochastic properties and especially intermittency: in the following, we seek to derive such intermittent stochastic models.

By ensuring multifractal properties (see Sec. 3.4.2) of the modeled dissipation $\varepsilon_{\star@p}$, all the models presented in Sec. 8.3.3 could readily be adapted to retrieve intermittent statistics.

8.4 Dissipation along inertial particle trajectory

We propose to apply the same decomposition as in Sec. 8.3.1 on the variable $\chi = \overline{\chi} + \chi' = \ln(\varphi_\star/\langle\varphi\rangle) + \ln(\varphi/\varphi_\star)$.

$$\begin{aligned}
\mathrm{d}\chi_{@p} &= \chi(\boldsymbol{x}_p + \boldsymbol{v}_p\,\mathrm{d}t, t+\mathrm{d}t) - \chi(\boldsymbol{x}_p, t) \\
&= \overline{\chi}(\boldsymbol{x}_p + \boldsymbol{u}_{@p}\,\mathrm{d}t, t+\mathrm{d}t) - \overline{\chi}(\boldsymbol{x}_p, t) && (1)\\
&+\chi'(\boldsymbol{x}_p + \boldsymbol{u}_{@p}\,\mathrm{d}t, t+\mathrm{d}t) - \chi'(\boldsymbol{x}_p, t) && (1)'\\
&+\overline{\chi}(\boldsymbol{x}_p + \boldsymbol{v}_p\,\mathrm{d}t, t+\mathrm{d}t) - \overline{\chi}(\boldsymbol{x}_p + \boldsymbol{u}_{@p}\,\mathrm{d}t, t+\mathrm{d}t) && (2)\\
&+\chi'(\boldsymbol{x}_p + \boldsymbol{v}_p\,\mathrm{d}t, t+\mathrm{d}t) - \chi'(\boldsymbol{x}_p + \boldsymbol{u}_{@p}\,\mathrm{d}t, t+\mathrm{d}t) && (3)
\end{aligned}$$

- (1) is the Lagrangian increment of the filtered dissipation along fluid trajectory. It is given by the simulation:

$$(1) = \mathrm{d}\overline{\chi} = \frac{\mathrm{d}\varphi_\star}{\varphi_\star}.$$

- (2) is the Eulerian increment of the filtered dissipation:

$$(2) = (\boldsymbol{v}_p - \boldsymbol{u}_{@p}) \cdot \nabla\overline{\chi}\,\mathrm{d}t + O(\mathrm{d}t).$$

- (3) is the Eulerian increment of fluctuating dissipation. It can be modeled along with (1)' with a new stochastic process.

In Chap. 3 we have derived stochastic models for $\mathrm{d}\chi'$ along fluid particles and we want to extent this modeling to inertial particles: $(1)' + (3) = \mathrm{d}\chi'_{@p}$.

8.4.1 An Ornstein-Uhlenbeck process for the dissipation seen by particles

Inspired by the model of Pope and Chen (1990) for the fluid dissipation, Gorokhovski and Zamansky (2018) have extended the Ornstein-Uhlenbeck process for inertial particles by adapting the parameters in the model:

$$\mathrm{d}\chi'_{@p} = -\frac{\chi'_{@p}}{T_\chi^{@p}}\,\mathrm{d}t + \sqrt{\frac{2\sigma^2_{\chi@p}}{T_\chi^{@p}}}\,\mathrm{d}W_t. \tag{8.16}$$

They chose to retain the same characteristic time as for fluid particles, i.e. $T_\chi^{@p} = T_L^\star$. The variance of the process is set to $\sigma^2_{\chi@p} = \ln\left(T_L^\star/(\tau_\eta + \tau_p)\right)/2$. One can verify that for fluid particles,

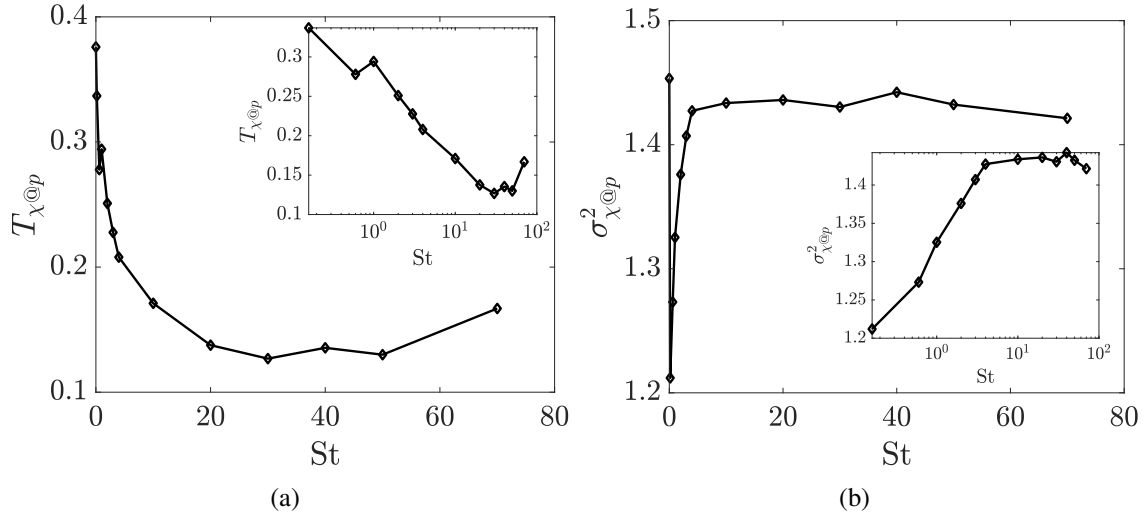

(a) (b)

Figure 8.1. Characteristic time scale (a) and variance (b) for dissipation along particles' trajectory. Insets show the same plots with a log-scale for the x-axis. Dataset of Lanotte et al. (2011).

we retrieve $\sigma^2_\chi = \ln(T^\star_L/\tau_\eta)/2$ and therefore $\sigma^2_\chi \sim \ln \mathrm{Re}_L$ for RANS and $\sigma^2_\chi \sim \ln \mathrm{Re}_\Delta$ in LES, as expected in Sec. 3.4.5.

Applying Itô formula, they obtain the final stochastic equation for the local dissipation $\varepsilon_{\star@p}$:

$$\frac{\mathrm{d}\varepsilon^{3/4}_{\star@p}}{\varepsilon^{3/4}_{\star@p}} = \frac{\mathrm{d}\varepsilon^{3/4}_{\star}}{\varepsilon^{3/4}_{\star}} - \left(\ln \frac{\varepsilon^{3/4}_{\star@p}}{\varepsilon^{3/4}_{\star}} - \frac{3}{16}\sigma^2_{\chi@p} \right) \frac{\mathrm{d}t}{T^{@p}_\chi} + \sqrt{\frac{9}{8}\frac{\sigma^2_{\chi@p}}{T^{@p}_\chi}}\,\mathrm{d}W_t, \tag{8.17}$$

where $\varepsilon_\star$ is either replaced by $\langle\varepsilon\rangle$ or $\varepsilon_{\mathrm{sgs}}$, depending on the ROS context.

Several remarks can be raised regarding this model:

- First, the choice $T^{@p}_\chi = T^\star_L$ can be questioned. We measure this characteristic time in a DNS by defining

$$T_{\chi@p} := \frac{1}{\sigma^2_{\chi@p}} \int_0^\infty R^{\chi@p}_L(\tau)\,\mathrm{d}\tau, \quad \text{where } R^{\chi@p}_L(\tau) := \langle \chi_{@p}(t)\chi_{@p}(t+\tau)\rangle\,. \tag{8.18}$$

  Its evolution with the Stokes numbers is reported in Fig. 8.1(a). Although the limit value of $T_{\chi@p}$ for $\mathrm{St} \to 0$ is of the order of magnitude of $T_L = 0.64$, an important decrease is observed for small and intermediate Stokes numbers. This characteristic time collapses for high Stokes numbers because inertial particles pass through high velocity vortices with widely different dissipations and the decorrelation is therefore faster than for fluid particles.

- On the other hand, Fig. 8.1(b) shows that the variance of the dissipation along the inertial particle trajectories varies with the Stokes number, first decreasing for very low St and then increasing, rather than the monotonic decrease predicted in the model of Gorokhovski and Zamansky (2018). This is due to the sampling of the fluid dissipation by the particles. This sampling is uniform for tracers and for particles with a very high Stokes number, since these are the two extreme cases for which no PPC occurs. Indeed, in Fig. 8.1(b), we can see that for $\mathrm{St} \gg 1$, the value of $\sigma_{\chi@p}$ reaches the same value as for $\mathrm{St} = 0$. For lower Stokes on

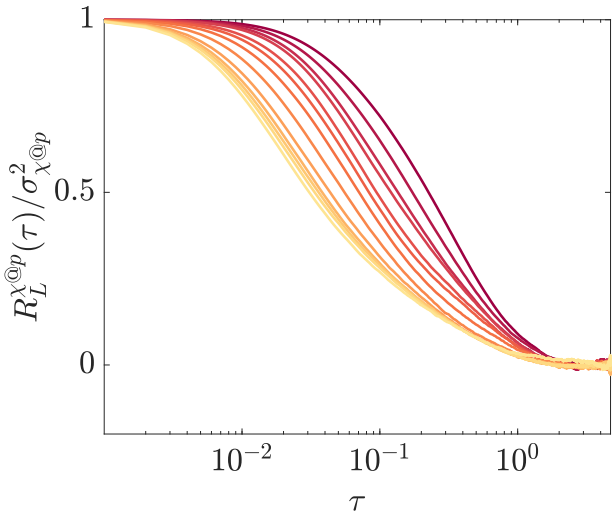

Figure 8.2. Autocorrelation of the dissipation along inertial particles $\chi_{@p}$. Increasing Stokes number from dark to light colors. $\mathrm{St} \in \{0, 0.16, 0.6, 1, 2, 3, 4, 10, 20, 30, 40, 50, 70\}$. Dataset of Lanotte et al. (2011).

the other hand, the particles concentrate in areas of low vorticity, and the sampling of the dissipation field is therefore reduced with a bias, since fewer areas of high dissipation are sampled by the particles. Thus, the variance decreases for these particles.

- Finally, we also showed in Sec. 3.4.4.1 that the model of Pope and Chen (1990), although producing non-Gaussian statistics, does not yield intermittent statistics in the strict mathematical sense (as defined in Chap. 4): the coarse-grained dissipation exhibits no multifractal properties.

These observations have motivated the development of a new model for the dissipation seen by inertial particles, naturally derived from the one developed in Sec. 3.2 for fluid particles.

8.4.2 A multifractal process for the dissipation seen by particles

In the same way that we extended Pope's model (Pope and Chen 1990) for fluid particles in Chap. 3 using a linear combination of Ornstein-Uhlenbeck processes, we propose here a multifractal model adapted to the dissipation seen by inertial particles. We recall that the idea of such a process is to reproduce by means of Ornstein Uhlenbeck processes the infinity of characteristic scales of vortices between the largest scale, and the smallest scales (respectively T_L and τ_η, in the case of fluid particles).

Figure 8.2 shows the autocorrelation function of the process $\chi_{@p}$ for different Stokes numbers. A rapid reading of this graph allows to identify two remarkable times for each plot: an initial time for which the autocorrelation remains very strong and approximately equal to 1, and the final time for which the autocorrelation reaches null values. The maximum correlation time, T_L is unchanged whatever the relaxation time of the particles. On the other hand, the smallest characteristic time, referred to as $t_{\chi@p}$, decreases with the Stokes number. It is approximately τ_η for fluid particles, but clearly decreases for inertial particles, since the latter do not maintain the correlation over such a "long" time. We have seen in Chap. 5 how, for a high Reynolds number, a sum of correlated Ornstein-Uhlenbeck processes could better reproduce the process χ for fluid particles. It is quite

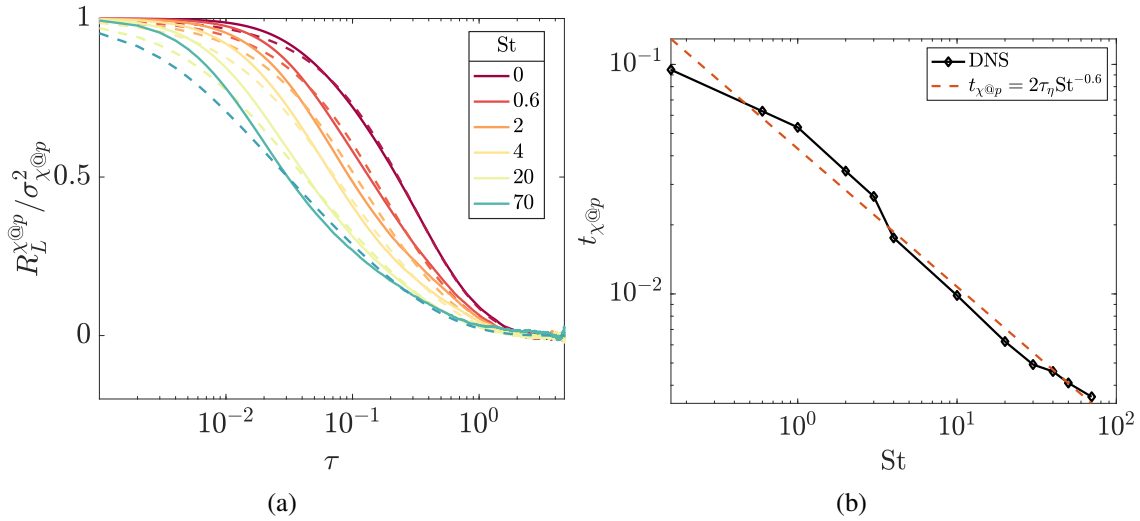

Figure 8.3. Autocorrelation of $\chi_{@p}$ for different Stokes number with associated models in dotted lines (a). Corresponding minimum characteristic time scales are plotted in (b) and compared with an empirical model in dotted line. The dataset is from Lanotte et al. (2011)

clear that the same holds for the processes following inertial particles, and is even more relevant as the correlation range is extended in Fig. 8.2.

We propose the following model, already established in Sec. 5.2.1, and for which we replace τ_η by $t_{\chi@p}$:

$$X_t^{@p} \equiv \int_0^\infty Y_t^x \frac{1}{\sqrt{\pi x}} \left(g_{T_L}(x) - g_{t_{\chi@p}}(x)\right) \mathrm{d}x \approx \sum_{i=1}^{N} \omega_i Y_t^{x_i}. \tag{8.19}$$

The geometric quadrature with N points gives:

$$\text{for} \quad i = 1, ..., N \begin{cases} x_i &= \dfrac{1}{T_L}\left(\dfrac{T_L}{t_{\chi@p}}\right)^{\frac{i-1/2}{N}} \\ \tilde{\omega}_i &= \dfrac{1}{\sqrt{x_i}}\Delta x_i, \end{cases} \quad , \quad \text{where } \Delta x_i = \frac{1}{T_L}\left(\frac{T_L}{t_{\chi@p}}\right)^{\frac{i}{N}} - \frac{1}{T_L}\left(\frac{T_L}{t_{\chi@p}}\right)^{\frac{i-1}{N}}. \tag{8.20}$$

The weights are normalized to match a unit variance. The normalizing factor R is given by:

$$R = \left(\sum_{i,j} \frac{\omega_i \omega_j}{x_i + x_j}\right)^{-1/2}, \tag{8.21}$$

and the final weights are $\omega_i = R\tilde{\omega}_i$.

The best fit for the autocorrelations in Fig. 8.3(a) are obtained for the characteristic times $t_{\chi@p}$ reported in Fig. 8.3(b). A large number of quadrature points N were used to optimize the convergence towards the analytic process. The optimal time scales are obtained by minimizing the least square error between the autocorrelation of the model and the one of the data.

The characteristic time scales are reported in Fig. 8.3(b), and an interpolation is performed to obtain the dashed line with a power law scaling $t_{\chi@p} = 2\tau_\eta \mathrm{St}^{-0.6}$. This scaling holds for intermediate and large Stokes numbers, but it is not consistent for very small Stokes numbers and for tracers. Therefore, we suggest

$$t_{\chi@p} = \min(2\tau_\eta, 2\tau_\eta \mathrm{St}^{-0.6}). \tag{8.22}$$

More accurate models could certainly be proposed, in particular to better predict the behavior of particles for $0 \leq \mathrm{St} \leq 1$, but the number of such Stokes numbers in the database of Lanotte et al. (2011) is not sufficient to propose a model on this range. However, the proposed model of Eq. (8.22) is consistent with the tracer limit: as seen in Chap. 5, the smallest scale introduced in the fluid particle model is of the order of magnitude of τ_η, and the inertial particle model predicts $t_{\chi@p} \to 2\tau_\eta$.

Let us also note that the dependence on the Reynolds number is naturally integrated since we recall that $\mathrm{Re} \sim T_L/\tau_\eta$ and that these two time scales are precisely the two parameters of the model. For large Reynolds and large Stokes numbers, the use of several processes becomes all the more relevant compared to a single process as proposed by Pope and Chen (1990) since in this case, the logarithmic autocorrelation range can extend on several decades.

Conclusion

This chapter presents the main stochastic modeling strategies for inertial particles in reduced-order turbulence simulations, and reviews some common processes of the literature. A similar classification to that proposed in Chap. 3 has been established and we summarize the main conclusions:

- A Brownian force added to particle velocity equation cannot retrieve the fluid particle limit behavior. A model on the velocity or the acceleration of the fluid seen by inertial particles is preferred.
- Parameters of the model $T_L^{\star@p}$ and $\sigma_{\star@p}$ should be adapted to take into account particle inertia, and existing models fail to predict particles statistics with intermediate Stokes numbers.
- Models consistent with K62 require the modeling of the local dissipation sampled along inertial particles trajectory: $\varepsilon_{\star@p}$. Stochastic processes inspired from the model of Pope and Chen (1990) are actually not thoroughly intermittent.

Therefore, we propose to extend the formalism developed in Chap. 5 in order to propose a multifractal model for the dissipation seen by inertial particles. The empirical law for the model parameter should be further investigated, especially with different Reynolds numbers.

Obtaining stochastic equations for the particles is a key element in the derivation of associated kinetic equations (Reeks 1991): they allow not only to model and simulate the probability density functions of the variables of interest, but also provide a Monte Carlo evaluation of the PDF (Minier and Peirano 2001).

However, let us insist on the fact that all these models, by nature diffusive, cannot reproduce the statistics in two points of the disperse phase, namely the segregation of the particles. This is the reason why we consider in the next chapters another strategy of particle models, based on structural methods.

Chapter 9

Wavelet-based kinematic simulation

Following the conclusions of Chap. 7, establishing the necessity to use structural models to obtain DNS statistics of particles while using ROS, we propose in this chapter a discussion on the kinematic simulation (KS) as classically used in the literature and we identify the potential flaws of such an approach. In order to tackle them, we then suggest a new strategy, which makes use of divergence-free wavelets random fields with enforced temporal evolution.

Wavelets, with compact support, are a powerful tool that, similar to sinusoidal functions, allow to decompose any function in a Hilbert space. In addition, they are spatially localized, which is a necessary condition in a two-way coupling context since the coupling between particles and fluid can occur at local scales.

We show that the wavelet-based KS can reproduce the characteristic time and length scales of turbulence and, thanks to a temporal evolution scheme of the synthetic field, Lagrangian statistics.

In this chapter, we are only interested in the dynamics and statistics of the carrier phase velocity field, and the behavior of the particles in it (our final goal) will be treated in the next chapter. After having pointed out the advantages and drawbacks of Fourier-based kinematic simulation in Sec 9.1, we introduce wavelets in Sec. 9.2, and more specifically divergence-free wavelets, since we intend to preserve the incompressibility of the flow. In Sec. 9.3, we develop the construction of the new kinematic field, based on a wavelet representation. Sec. 9.4 validates the new KS against 3D DNS data.

9.1 Fourier-based kinematic simulation

The kinematic simulation (KS), introduced by Kraichnan (1970), Fung, Hunt, Malik, and Perkins (1992), was widely studied in the literature as a model for stationary HIT, for example in Ijzermans, Meneguz, and Reeks (2010), Gustavsson, Meneguz, Reeks, and Mehlig (2012), Murray, Lightstone, and Tullis (2016a), Murray, Lightstone, and Tullis (2016b), Mercier (2020): it consists of a superposition of sinus and cosinus functions, such as Fourier series synthesis:

$$\boldsymbol{u}(\boldsymbol{x},t) = \sum_{n=1}^{N_\kappa} \boldsymbol{a_n}\cos(\boldsymbol{\kappa_n}\cdot\boldsymbol{x}+\omega_n t) + \boldsymbol{b_n}\sin(\boldsymbol{\kappa_n}\cdot\boldsymbol{x}+\omega_n t) \tag{9.1}$$

where N_κ is the number of modes, $\boldsymbol{\kappa_n}$ and ω_n are the wavenumber vector and frequency of the nth mode, and $\boldsymbol{a_n}$ and $\boldsymbol{b_n}$ are the mode amplitudes. Spatial and weight coefficients $\boldsymbol{a_n}$, $\boldsymbol{b_n}$ and $\boldsymbol{\kappa_n}$ are

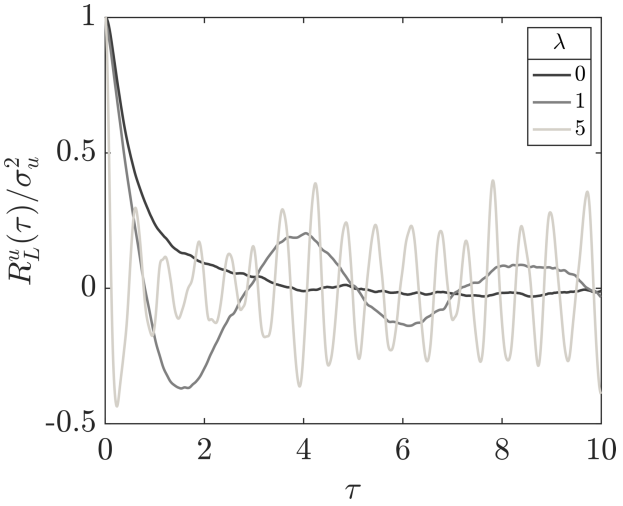

Figure 9.1. Autocorrelation of the velocity of fluid particles along their trajectory on a KS of fluid for different values of eddy turnover times.

chosen to match a given energy spectrum and to create a divergence-free flow. The wavenumber vectors $\boldsymbol{\kappa_n} = \kappa_n \boldsymbol{e_n}$ are chosen according to a geometric sequence for κ_n, ranging in the inertial range and $\boldsymbol{e_n}$ is a unit vector in a random direction (i.e. a vector uniformly distributed over the unit sphere). The amplitudes $\boldsymbol{a_n}$ and $\boldsymbol{b_n}$ are chosen to have random directions perpendicular to $\boldsymbol{e_n}$ such that: $\boldsymbol{a_n} = \boldsymbol{A_n} \times \boldsymbol{\kappa_n}$ and $\boldsymbol{b_n} = \boldsymbol{B_n} \times \boldsymbol{\kappa_n}$ where $\boldsymbol{A_n}$ and $\boldsymbol{B_n}$ are random vectors with independent, normally distributed components, each with zero mean and variance given by:

$$\sigma_n^2 = E(\kappa_n)\Delta\kappa_n, \tag{9.2}$$

in order to reproduce an energy spectrum prescribed by a model. Temporal coefficients ω_n are meant to represent the eddy turnover time associated to each wavelength.

In our opinion, there are some limitations to the use of such a KS, especially in the context where it is used to mimic the turbulent carrier phase seen by some inertial particles:

- Figure 9.1 shows the autocorrelation of fluid particle velocity for different values of λ, where $\omega_n \propto \lambda$. The oscillating behavior observed for $\lambda \neq 0$ is highly unrealistic, we have already seen in Chap. 3 that the autocorrelation function of the particle velocity can be modeled by a decreasing exponential function. This oscillating behavior was also reported by Murray, Lightstone, and Tullis (2016b) who prescribed using $\lambda = 0$.
- However, a frozen fluid is not an appropriate turbulence model: without sweeping, the nature of particle clustering is fundamentally changed. In the absence of collisions, particles with $\mathrm{St}_\eta < 1$ will therefore accumulate indefinitely around the equilibrium points of the flow. The lack of temporality could also explain the difficulty in mapping Eulerian and Lagrangian scales, a problem raised in the conclusion of Murray, Lightstone, and Tullis (2016a).
- Enforcing a periodic condition on such a synthetic field considerably reduces the realizable phases space for the κ_n. The simulation method chosen here consists in considering only κ_n wavevectors with integer coordinates. The number of degrees of freedom for the random sampling of the small κ_n is very limited in this case, and the obtained energy spectra are discrete and very noisy.

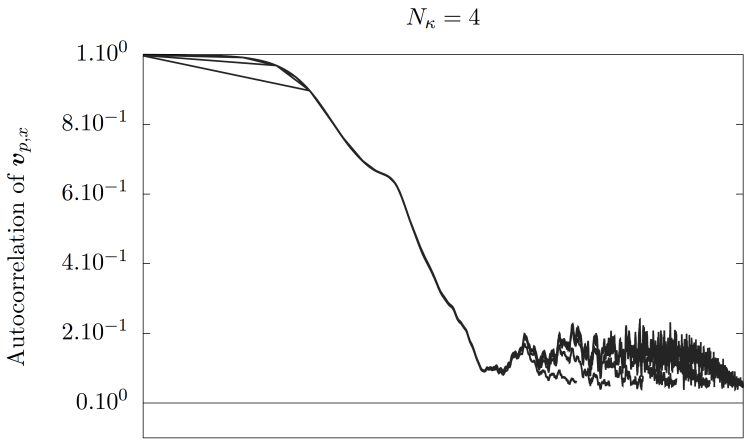

Figure 9.2. Autocorrelation of the velocity of fluid particles along their trajectory on a Fourier-based KS of fluid. Figure from Mercier (2020).

- The Eulerian spectrum of the synthetic fluid is sparse by construction, which is not the case for real turbulence

- In his thesis, Mercier (2020) used KS to investigate reduction of fluid description, since KS allow to master the probability space associated to the set of turbulent fluids, which is not possible with solutions of the Navier-Stokes equations. KS provides satisfying agreement with turbulence statistics for his study (Thomson and Devenish 2005), but he pointed out the divergence of the velocity autocorrelation of tracers $R_L^{v_p}(\tau)/\sigma_{v_p}^2 = \langle v_p(t)v_p(t+\tau)\rangle/\langle v_p(t)^2\rangle$, reported in Fig. 9.2. Normally, fluid particle velocities should be completely uncorrelated after a very long time, and the autocorrelation should tend towards 0.

We assume that the oscillating and divergent behavior of the Lagrangian statistics could be attributed to the non-compactness of the cosinus and sinus modes. Therefore, we are exploring a different approach for kinematic simulation, and we present a new framework with the following specifications:

(i) The synthetic fluid is spatially correlated with compact modes ;
(ii) It is a divergence-free flow, to recover the correct fluid particle behavior ;
(iii) It can reproduce any energy spectrum ;
(iv) The temporal correlation can be fitted to map Eulerian scales with Lagrangian ones ;
(v) Particles one and two-point DNS-like statistics can be recovered ;
(vi) The flow must be compatible with LES framework and computationally affordable (of the order of magnitude of the LES computational cost).

In App. B, we propose a first approach to kinematic simulation, based on the superposition of Gaussian fields, whose numerical modes are compact. Although the classic Lagrangian and Eulerian statistics of fluid and inertial particles can be recovered, the use of such a tool requires a large memory. In the following, we explore the use of wavelets to define a new kinematic simulation framework and next section introduces the main tools for wavelets.

9.2 Multiresolution Analysis

Multiresolution analysis (MRA) wavelets are approximation spaces generated by function bases. In the literature, the wavelet decomposition was first used for the analysis of turbulent flows (Farge 1992; Meneveau 1991) then later for the resolution of the 2D Navier-Stokes equations (Farge, Kevlahan, Perrier, and Goirand 1996), based on Galerkin approaches. However, the incompressibility of the flow is not guaranteed and recent works propose an extension to 3D equations in which the resolution of the Poisson equation is necessary to ensure the divergence-free of the flow (Kevlahan and Vasilyev 2005).

Another strategy relying on divergence-free wavelets, first introduced by Lemarié-Rieusset (1992), have been used for the analysis of 2D/3D turbulent flows (Albukrek, Urban, Rempfer, and Lumley 2002; Deriaz and Perrier 2006). With a compact support, they can take into account boundary conditions, contrary to classical approaches only applicable for periodic flows (Urban 2002).

After having recalled some definitions and properties essential to the understanding of the wavelets transform, we focus on its implementation. The reader is referred to the book of Kahane and Lemarié-Rieusset (1995) for a detailed description of wavelets. We first consider the case of one-dimensional real functions. Then we extend the construction to multi-dimensional spaces. Finally, we introduce the divergence-free wavelets.

9.2.1 Introduction to wavelets

Definition 9.2.1 *A Riesz basis $\{b_n, n \in \mathbb{N}\}$ of a real Hilbert space E is a set of elements of E verifying:*

$$\forall f \in E, \quad \exists\, (c_n)_{n\in\mathbb{N}} \in E^{\mathbb{N}} \quad \textit{such that} \quad \lim_{n\to+\infty} \left\| f - \sum_{k=0}^{n} c_k b_k \right\| = 0 \tag{9.3}$$

and

$$\exists A, B \in \mathbb{R}_+^* \quad \textit{such that} \quad A \sum_{n=0}^{+\infty} |c_n|^2 \leq \|f\|^2 \leq B \sum_{n=0}^{+\infty} |c_n|^2. \tag{9.4}$$

First, we consider the space of one-dimensional square-integrable functions $L_2(\mathbb{R})$. MRA is defined as a sequence of embedded sub-spaces that goes from the finest (small scale or high resolution) to the coarsest (large scale or low resolution) and such that if a function belongs to one of these spaces V_j, the function zoomed by a factor of 2 belongs to the next space. More precisely, we have:

Definition 9.2.2 *A sequence of closed sub-spaces $(V_j)_{j\in\mathbb{Z}}$ of $L_2(\mathbb{R})$ is a MRA if $\forall j \in \mathbb{Z}$,*

- $V_j \subset V_{j-1}$
- $\bigcap_{j\in\mathbb{Z}} V_j = \{0\}$ *and* $\overline{\bigcup_{j\in\mathbb{Z}} V_j} = L_2(\mathbb{R})$
- *Dilatation:* $f \in V_j \quad \Leftrightarrow \quad f(2\cdot) \in V_{j-1}$
- *Translation:* $f \in V_j \quad \Rightarrow \quad \forall k \in \mathbb{Z}, \quad f(. - k) \in V_j$

Remark 9.2.3 The invariance by dilatation and translation implies that there exists a function $\varphi \in V_0$, called scaling function, such that the family $\{\varphi(\cdot - k)\}_{k\in\mathbb{Z}}$ is a Riesz basis. Therefore, each space V_j is generated by the family of functions $\{\varphi_{j,k}; k \in \mathbb{Z}\}$ with $\varphi_{j,k}(x) = 2^{j/2}\varphi\left(2^j x - k\right)$, where the parameter j defines the level of detail.

It follows that any function $f_J \in V_J$ can be decomposed into the basis of functions:

$$f_J(x) = 2^{J/2} \sum_{k\in\mathbb{Z}} c_{J,k}\varphi(2^J x - k). \tag{9.5}$$

Let us define the basis of the supplementary spaces W_j:

$$V_{j+1} = V_j \oplus W_j, \tag{9.6}$$

where the sum $V_j \oplus W_j$ is direct. Let us introduce a function ψ, called mother wavelet such that the family of functions $\{\psi(. - k); k \in \mathbb{Z}\}$ generates a space W_0. Here again, the successive spaces W_j can be generated by the families of functions $\psi_{j,k} = 2^{j/2}\psi\left(2^j \cdot -k\right)$, the so-called daughter wavelets. Iterating this decomposition of V_j provides the MRA (V_j) and the associated wavelet spaces W_ℓ:

$$V_j = V_0 \bigoplus_{\ell=0}^{j-1} W_\ell, \tag{9.7}$$

which allows to write when j tends to infinity, the wavelet decomposition of the whole space $L^2(\mathbb{R})$:

$$L^2(\mathbb{R}) = V_0 \bigoplus_{\ell=0}^{+\infty} W_\ell. \tag{9.8}$$

Thus, it follows that any function $f \in L^2(\mathbb{R})$ can be decomposed into the basis of functions $\{\varphi_k, \psi_{j,k}; j \geq 0, k \in \mathbb{Z}\}$, with $\varphi_k = \varphi(\cdot - k)$ and $\psi_{j,k} = 2^{j/2}\psi\left(2^j \cdot -k\right)$:

$$f = \sum_{k\in\mathbb{Z}} c_k\varphi_k + \sum_{j\geq 0}\sum_{k\in\mathbb{Z}} d_{j,k}\psi_{j,k}. \tag{9.9}$$

An example of a MRA basis, the Haar family, is given in Fig. 9.3 where we plot the scaling and wavelet functions. An other example of wavelet, the spline function of degree 1, is given in Fig. 9.4 to illustrate the dilatation and translation. In dotted lines, four possible translations of the wavelet at level $j = 2$ are plotted, for a periodic function in $[0, 1]$. At level $j = 3$, the support of the wavelet (in dashed lines) is twice as small and its amplitude is twice as large to preserve its norm. The same goes for the higher levels and we notice that the information is more and more localized in space, and the generated field is less regular.

9.2.2 Multi-dimensional wavelets

One can extend the notion of multiresolution analysis to spaces of any dimension. The simplest way is to perform tensor products between wavelets and scale functions of the same level (isotropic wavelets). In the following, we consider the case of two-dimensional spaces which can be directly generalized to higher dimensions.

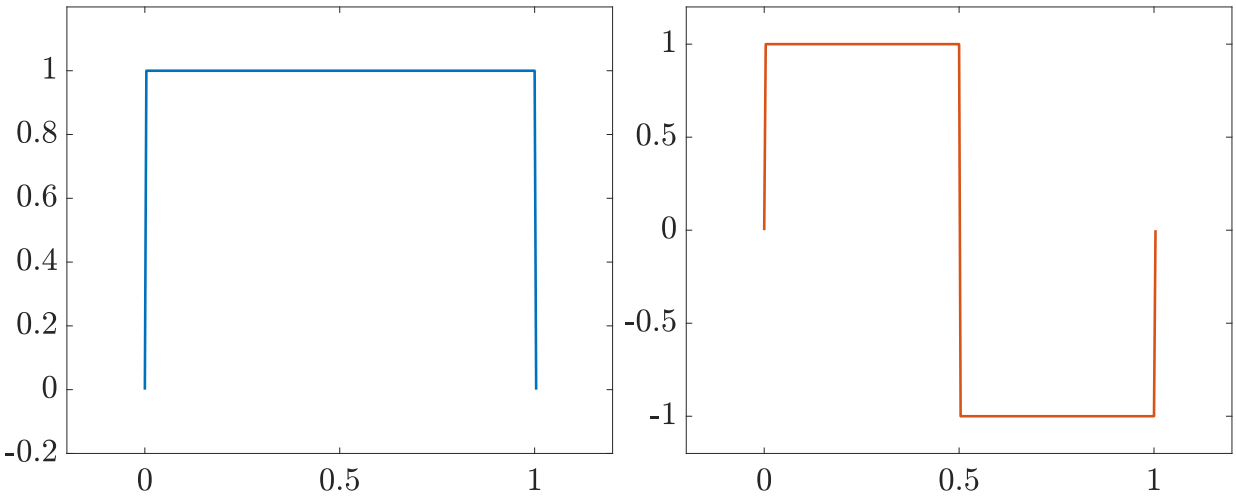

(a) Scaling function φ (b) Wavelet function ψ

Figure 9.3. Scaling function (a) and wavelet function (b) for the Haar family.

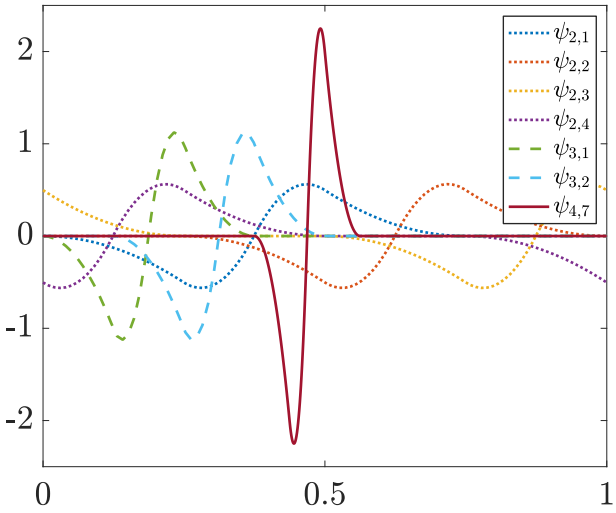

Figure 9.4. Example of translated and dilated wavelets of level 2 (dotted lines), 3 (dashed lines), 4 (full line).

9.2.2.1 Decomposition of a scalar field

We consider two MRA of $L^2(\mathbb{R})$: (V_j^0) and (V_j^1) respectively associated to the scale and wavelets couple-functions (φ_0, ψ_0) and (φ_1, ψ_1). The MRA space tensor product $V_J^0 \otimes V_J^1$ is generated by the scale functions $\left\{\varphi_{0j,k_1}(x)\varphi_{1j,k_2}(y); (k_1,k_2) \in \mathbb{Z}^2\right\}$, where $\varphi_{0j,k_1}(x) = 2^{j/2}\varphi_0\left(2^j x - k_1\right)$ and the same goes for φ_{1j,k_2}. The first coordinate is decomposed in the MRA (V_j^0), and the second one into (V_j^1). Then any function f_J of $V_J^0 \otimes V_J^1$ can be written as:

$$f_J(x,y) = \sum_{k_1,k_2 \in \mathbb{Z}} c_{J,k_1,k_2} 2^J \varphi_0\left(2^J x - k_1\right)\varphi_1\left(2^J y - k_2\right). \tag{9.10}$$

Iterating the decomposition of V_{J+1} using the supplementary spaces, we have:

$$\begin{aligned} V_{J+1}^0 \otimes V_{J+1}^1 &= (V_J^0 \oplus W_J^0) \otimes (V_J^1 \oplus W_J^1) \\ &= (V_J^0 \otimes V_J^1) \oplus (W_J^0 \otimes V_J^1) \oplus (V_J^0 \otimes W_J^1) \oplus (W_J^0 \otimes W_J^1) \\ &= (V_0^0 \otimes V_0^1) \\ &\oplus (W_0^0 \otimes V_0^1) \oplus (V_0^0 \otimes W_0^1) \oplus (W_0^0 \otimes W_0^1) \\ &\oplus ... \\ &\oplus (W_J^0 \otimes V_J^1) \oplus (V_J^0 \otimes W_J^1) \oplus (W_J^0 \otimes W_J^1), \end{aligned} \tag{9.11}$$

which leads to the following decomposition of f_J, introducing the daughter wavelets $\psi_{1j,k}$ and $\psi_{0,j,k}$:

$$\begin{aligned} f_J(x,y) = &\sum_{(k_1,k_2)\in\mathbb{Z}^2} c_{k_1,k_2}\varphi_0(x-k_1)\varphi_1(y-k_2) \\ &+ \sum_{j=0}^{J-1}\left(\sum_{k_1,k_2} d_{j,k_1,k_2}^{(1,0)}\psi_{0j,k_1}(x)\varphi_{1j,k_2}(y) + \sum_{k_1,k_2} d_{j,k_1,k_2}^{(0,1)}\varphi_{0j,k_1}(x)\psi_{1j,k_2}(y)\right. \\ &\left. + \sum_{k_1,k_2} d_{j,k_1,k_2}^{(1,1)}\psi_{0j,k_1}(x)\psi_{1j,k_2}(y)\right) \end{aligned} \tag{9.12}$$

This decomposition involves three types of wavelets:

- one along the x direction: $\psi^{(1,0)}(x,y) = \psi_0(x)\varphi_1(y)$. Coefficients in the decomposition associated to such terms are called horizontal detail coefficients, because the wavelet function is applied in the horizontal direction;
- one along the y direction: $\psi^{(0,1)}(x,y) = \varphi_0(x)\psi_1(y)$, respectively with vertical detail coefficients;
- one along both directions at once: $\psi^{(1,1)}(x,y) = \psi_0(x)\psi_1(y)$, associated to diagonal coefficients;

and one scaling function: $\varphi^{(0,0)}(x,y) = \varphi_0(x)\varphi_1(y)$.

Let us consider the decomposition of an image of size $\left(2^J \times 2^J\right)$, given in Fig. 9.5(a). The first decomposition generates image fields of size $\left(2^{J-1} \times 2^{J-1}\right)$, whose horizontal, vertical and diagonal coefficients are represented in the upper right, lower left and lower right quarters of Fig. 9.5(b). The second level decomposition is given in the same way in the upper left quarter, with the same

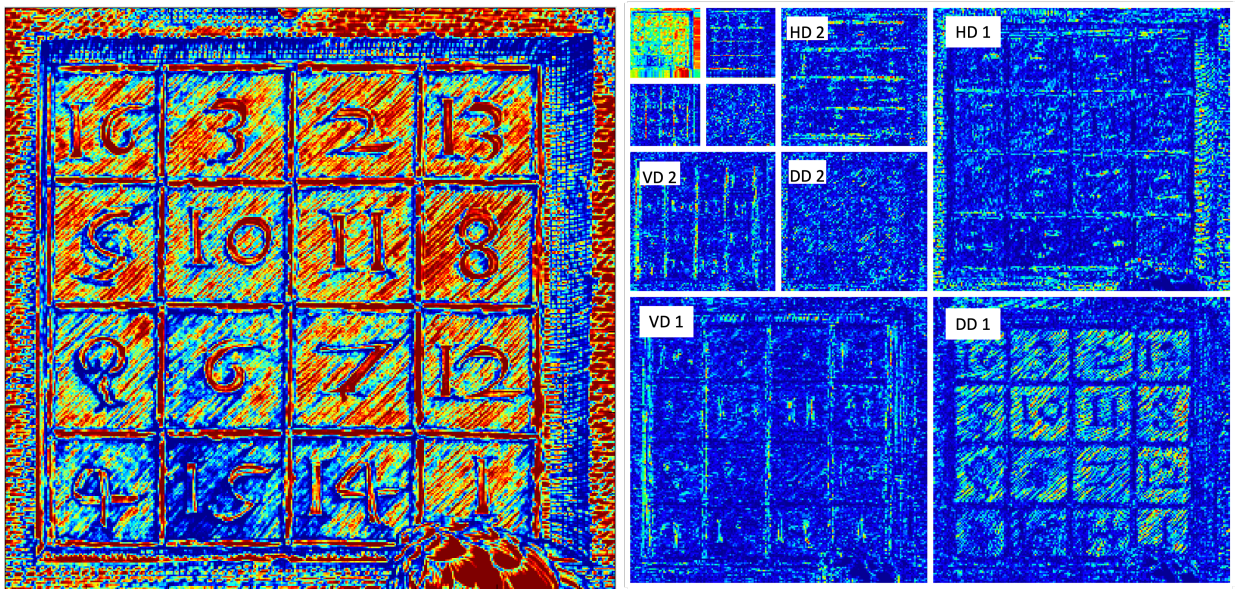

(a) Original image (b) Decomposition on three levels

Figure 9.5. An original image from Matlab library (a) is decomposed on three levels (b). Coefficients of the decomposition are displayed in the following order: upper-left are successive level of decomposition and extreme upper left are the approximation coefficients. Upper-right are the horizontal detail (HD) coefficients, bottom left are the vertical detail (VD) coefficients and bottom right corresponds to the diagonal detail (DD) coefficients.

pattern. These fields are naturally of size $\left(2^{J-2} \times 2^{J-2}\right)$. As the decomposition stops at level 3, it remains the so-called approximation coefficients of level 3: c_{J-3,k_1,k_2}. They are given by the partial decomposition:

$$\begin{aligned} f_J(x,y) = & \sum_{(k_1,k_2)\in\mathbb{Z}^2} c_{J-3,k_1,k_2}\varphi_{0,J-3,k_1}(x)\,\varphi_{1,J-3,k_2}(y) \\ & + \sum_{j=J-3}^{J-1}\left(\sum_{k_1,k_2} d^{(1,0)}_{j,k_1,k_2}\psi_{0j,k_1}(x)\varphi_{1j,k_2}(y) + \sum_{k_1,k_2} d^{(0,1)}_{j,k_1,k_2}\varphi_{0j,k_1}(x)\psi_{1j,k_2}(y)\right. \\ & \left. + \sum_{k_1,k_2} d^{(1,1)}_{j,k_1,k_2}\psi_{0j,k_1}(x)\psi_{1j,k_2}(y)\right) \end{aligned} \tag{9.13}$$

The interest of this wavelet basis lies in the fact that their support is proportional to 2^{-j} in each direction, and thus preserves a spatial and frequency localization, level by level, in all directions at once. This is why this decomposition is called isotropic.

9.2.2.2 Decomposition of a vector field

To decompose a vector field $\boldsymbol{u} \in L^2(\mathbb{R})^2$, we assume that we have two MRA (V_j^0) and (V_j^1). We then decompose the two-dimensional function into the MRA tensor $(V_j^1 \otimes V_j^0) \times (V_j^0 \otimes V_j^1)$: the first component of the field, u_x, is decomposed in the $(V_j^1 \otimes V_j^0)$ basis, and the second one, u_y, in

the $(V_j^0 \otimes V_j^1)$ basis.

In the case of 2D isotropic wavelets, the two-dimensional scaling functions Φ_1, Φ_2 and canonical wavelets $\Psi_1^\varepsilon, \Psi_2^\varepsilon$ are given by:

$$\begin{array}{lll} \Phi_1(x,y) & = \begin{pmatrix} \varphi_1(x)\varphi_0(y) \\ 0 \end{pmatrix} & \Phi_2(x,y) & = \begin{pmatrix} 0 \\ \varphi_0(x)\varphi_1(y) \end{pmatrix} \\ \Psi_1^{(1,0)}(x,y) & = \begin{pmatrix} \psi_1(x)\varphi_0(y) \\ 0 \end{pmatrix} & \Psi_2^{(1,0)}(x,y) & = \begin{pmatrix} 0 \\ \psi_0(x)\varphi_1(y) \end{pmatrix} \\ \Psi_1^{(0,1)}(x,y) & = \begin{pmatrix} \varphi_1(x)\psi_0(y) \\ 0 \end{pmatrix} & \Psi_2^{(0,1)}(x,y) & = \begin{pmatrix} 0 \\ \varphi_0(x)\psi_1(y) \end{pmatrix} \\ \Psi_1^{(1,1)}(x,y) & = \begin{pmatrix} \psi_1(x)\psi_0(y) \\ 0 \end{pmatrix} & \Psi_2^{(1,1)}(x,y) & = \begin{pmatrix} 0 \\ \psi_0(x)\psi_1(y) \end{pmatrix} \end{array} \tag{9.14}$$

The functions $\left\{\Psi_{ij,\boldsymbol{k}}^\varepsilon(x,y) = 2^j \Psi_i^\varepsilon\left(2^j x - k_1, 2^j y - k_2\right)\right\}$ with $j \in \mathbb{Z}, \boldsymbol{k} = (k_1,k_2) \in \mathbb{Z}^2, \varepsilon \in \{(0,1),(1,0),(1,1)\}, i = 1,2$, form a Riesz basis of $\left(L^2\left(\mathbb{R}^2\right)\right)^2$. Any vectorial function $\mathbf{u} = (u_x,u_y) \in \left(L^2\left(\mathbb{R}^2\right)\right)^2$ can be decomposed in this basis:

$$\begin{aligned} u_x &= \sum_{j\in\mathbb{Z}} \sum_{\boldsymbol{k}\in\mathbb{Z}^2} \left(d_{1,j,\boldsymbol{k}}^{(1,0)} \Psi_{1,j,\boldsymbol{k}}^{(1,0)} + d_{1,j,\boldsymbol{k}}^{(0,1)} \Psi_{1,j,\boldsymbol{k}}^{(0,1)} + d_{1,j,\boldsymbol{k}}^{(1,1)} \Psi_{1,j,\boldsymbol{k}}^{(1,1)} \right), \\ u_y &= \sum_{j\in\mathbb{Z}} \sum_{\boldsymbol{k}\in\mathbb{Z}^2} \left(d_{2,j,\boldsymbol{k}}^{(1,0)} \Psi_{2,j,\boldsymbol{k}}^{(1,0)} + d_{2,j,\boldsymbol{k}}^{(0,1)} \Psi_{2,j,\boldsymbol{k}}^{(0,1)} + d_{2,j,\boldsymbol{k}}^{(1,1)} \Psi_{2,j,\boldsymbol{k}}^{(1,1)} \right). \end{aligned} \tag{9.15}$$

One can note that the terms in u_x represent the wavelet decomposition in the MRA $\left(V_j^1 \otimes V_j^0\right)$, while the terms in u_y correspond to the decomposition in the MRA $\left(V_j^0 \otimes V_j^1\right)$.

9.2.3 Divergence-free wavelets

Divergence-free wavelets were introduced by Lemarié-Rieusset (1992) in order to provide bases suitable to represent the incompressible Navier-Stokes solution, in two and three dimensions. In that case, Lemarié-Rieusset (1994) has shown that compactly supported wavelets, used for non-periodic problems, can only be supported by biorthogonal wavelet bases. This means that the sum $V_j \oplus W_j$ is direct, but not orthogonal, and the choice of W_j is not unique. For the definition and properties of biorthogonal MRA and associated wavelets, the reader is referred to Kahane (1985).

9.2.3.1 Definition

The construction of divergence-free wavelets relies on the existence of two MRA related by differentiation and integration.

Proposition 9.2.4 *Let (V_j^1) be a multiresolution analysis associated to the scaling function φ_1, such that $\varphi_1 \in C^{1+\epsilon}$ for any $\epsilon > 0$ and a wavelet ψ_1. Then there exists a MRA (V_j^0) associated to a scaling function φ_0 and a wavelet function ψ_0 verifying:*

$$\varphi_1'(x) = \varphi_0(x) - \varphi_0(x-1), \quad \psi_1'(x) = 4\psi_0(x) \tag{9.16}$$

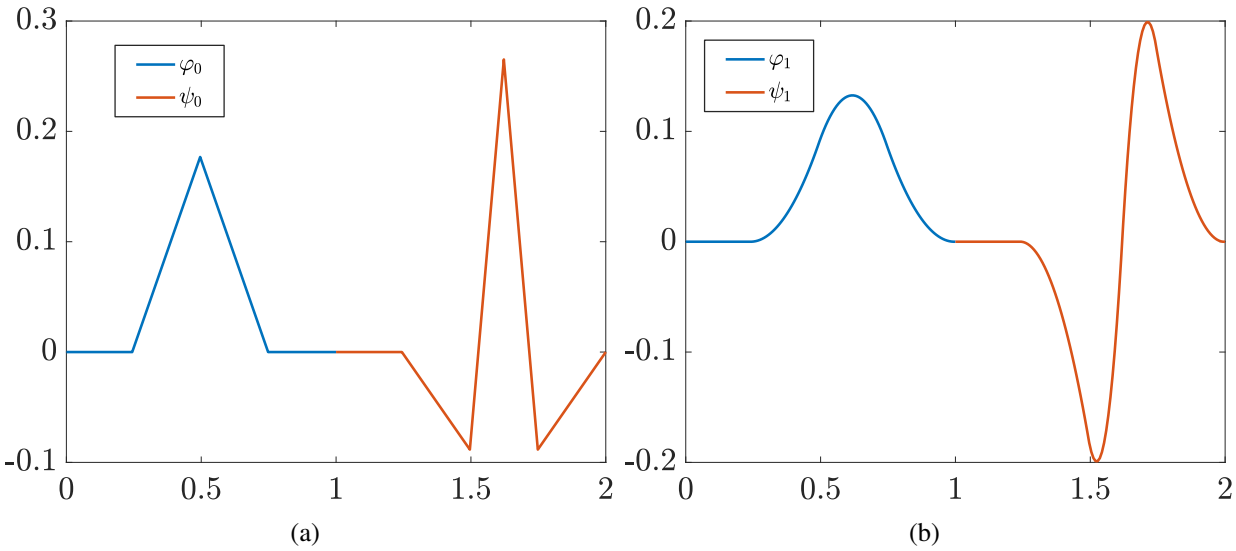

Figure 9.6. Scaling functions and wavelets for splines of degree 1 (a) and degree 2 (b.

The proof of this property and the construction of such ARMs is given in Deriaz (2006) and we are only interested in the following particular case:

Example 9.2.5 Biorthogonal splines functions, used in Kahane and Lemarié-Rieusset (1995), provide a simple framework for such MRAs. Their scaling functions are B-splines, which are defined piecewise by polynomials and the associated wavelets can be obtained by linear and translated combination of B-splines. For example, B-splines of degree 1 and 2, φ_0 and φ_1, associated to wavelets ψ_0 and ψ_1 are represented in Fig. 9.6 and verify property 9.2.4.

Definition 9.2.6 *Let two MRAs (V_j^0) and (V_j^1), verifying Prop. 9.2.4. We define the following two-dimensional scaling function:*

$$\Phi_{\text{div}}(x,y) = \begin{pmatrix} \varphi_1(x)\varphi_1'(y) \\ -\varphi_1'(x)\varphi_1(y) \end{pmatrix} = \begin{pmatrix} \varphi_1(x)[\varphi_0(y) - \varphi_0(y-1)] \\ -[\varphi_0(x) - \varphi_0(x-1)]\varphi_1(y) \end{pmatrix}, \tag{9.17}$$

along with the divergence-free vector wavelets, given by:

$$\begin{aligned} \Psi_{\text{div}}^{(1,0)}(x,y) &= -\frac{1}{4}\begin{pmatrix} \psi_1(x)\varphi_1'(y) \\ -\psi_1'(x)\varphi_1(y) \end{pmatrix} = -\frac{1}{4}\begin{pmatrix} \psi_1(x)[\varphi_0(y) - \varphi_0(y-1)] \\ -4\psi_0(x)\varphi_1(y) \end{pmatrix} \\ \Psi_{\text{div}}^{(0,1)}(x,y) &= \frac{1}{4}\begin{pmatrix} \varphi_1(x)\psi_1'(y) \\ -\varphi_1'(x)\psi_1(y) \end{pmatrix} = \frac{1}{4}\begin{pmatrix} 4\varphi_1(x)\psi_0(y) \\ -[\varphi_0(x) - \varphi_0(x-1)]\psi_1(y) \end{pmatrix} \\ \Psi_{\text{div}}^{(1,1)}(x,y) &= \frac{1}{4}\begin{pmatrix} \psi_1(x)\psi_1'(y) \\ -\psi_1'(x)\psi_1(y) \end{pmatrix} = \frac{1}{4}\begin{pmatrix} 4\psi_1(x)\psi_0(y) \\ -4\psi_0(x)\psi_1(y) \end{pmatrix} \end{aligned} \tag{9.18}$$

These define isotropic divergence-free wavelets in $\mathbb{R}^2$.

Taking the example 9.2.5 of spline functions, Fig. 9.7(a) shows the two-dimensional isotropic scale function. The resulting field looks like a symmetric vortex. Figures 9.7(b) and 9.7(c) shows

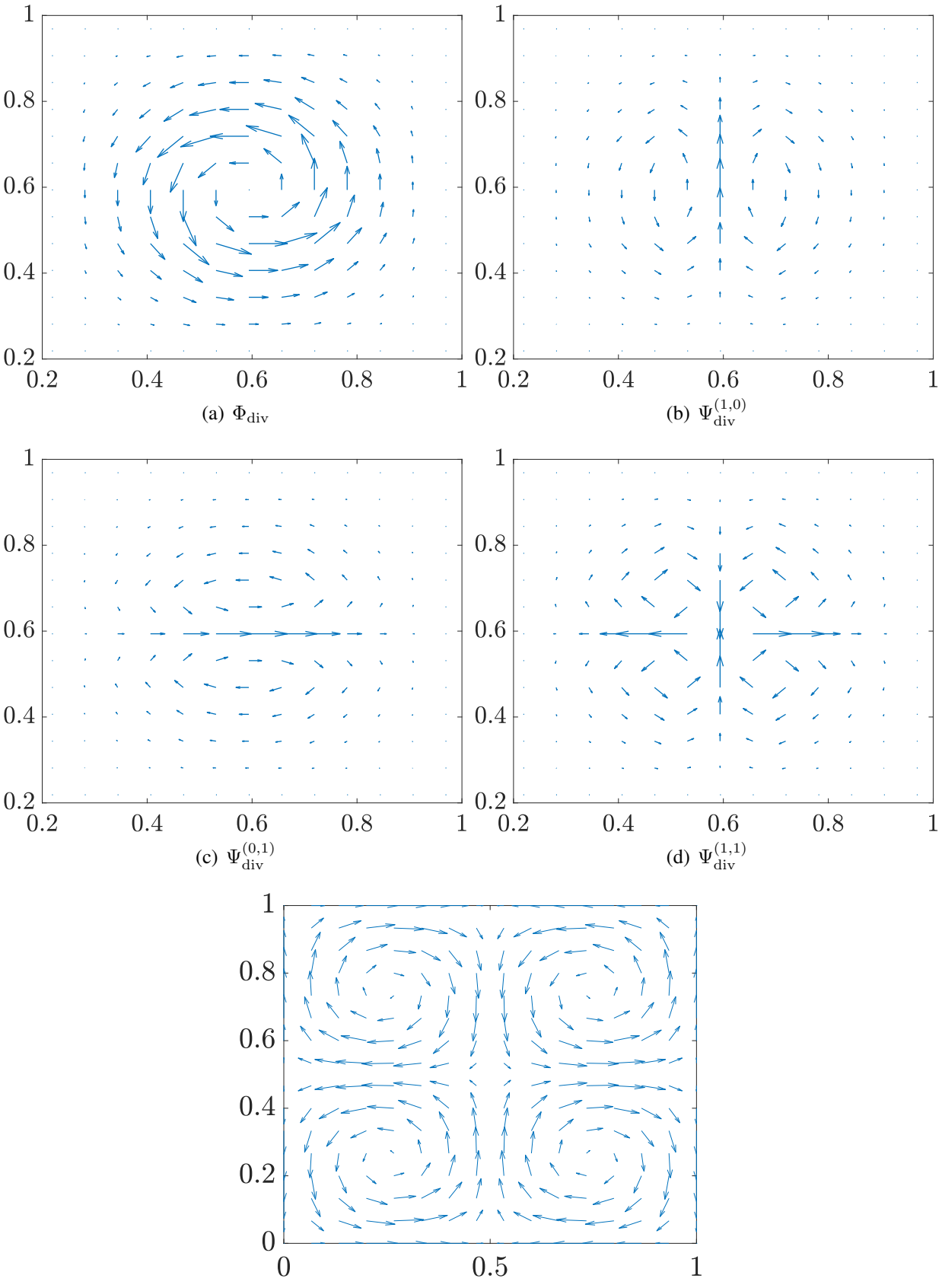

(a) Φ_{div} (b) $\Psi_{\text{div}}^{(1,0)}$

(c) $\Psi_{\text{div}}^{(0,1)}$ (d) $\Psi_{\text{div}}^{(1,1)}$

(e) Taylor Green vortices

Figure 9.7. (a-d) Scaling functions and divergence-free 2D wavelets for the MRA spline functions and (d) Taylor Green vortices.

the $\Psi^{(1,0)}_{\text{div}}$ and $\Psi^{(0,1)}_{\text{div}}$ functions respectively. We observe two opposite vortices, stretched in the preferential direction. Finally, Fig. 9.7(d) shows the last wavelet function, $\Psi^{(1,1)}_{\text{div}}$, and we observe four vortices. The resulting field looks like Taylor Green vortices of Fig. 9.7(e), but with compact support: the field is fading on the edges.

9.2.3.2 Change of basis

Divergence-free wavelets can be expressed in terms of linear combinations of canonical wavelets Ψ^{ε}_{i}. More precisely, for each $\varepsilon \in \{(0,1),(1,0),(1,1)\}$, the divergence-free wavelet $\Psi^{\varepsilon}_{\text{div}}$ is defined above and an additional function Ψ^{ε}_{n} can be introduced such that:

$$\text{vect}\left\{\Psi^{\varepsilon}_{1,j,\boldsymbol{k}}, \Psi^{\varepsilon}_{2,j,\boldsymbol{k}} | \boldsymbol{k} \in \mathbb{Z}^2\right\} = \text{vect}\left\{\Psi^{\varepsilon}_{\text{div}j,\boldsymbol{k}} | \boldsymbol{k} \in \mathbb{Z}^2\right\} \oplus \text{vect}\left\{\Psi^{\varepsilon}_{\text{n}j,\boldsymbol{k}} | \boldsymbol{k} \in \mathbb{Z}^2\right\}, \tag{9.19}$$

where the sum is direct but not orthogonal: the wavelet Ψ^{ε}_{n} is not divergence-free and many options for change-of-basis exist. For example, following Deriaz and Perrier (2006), we can have:

$$\begin{aligned}
&\left\{\begin{array}{l}\Psi^{(1,0)}_{1}\\ \Psi^{(1,0)}_{2}\end{array}\right. \longrightarrow \left\{\begin{array}{l}\Psi^{(1,0)}_{\text{div}} = \Psi^{(1,0)}_{2} - \frac{1}{4}\left[\Psi^{(1,0)}_{1} - \Psi^{(1,0)}_{1}(x, y-1)\right]\\ \Psi^{(1,0)}_{\text{n}} = \Psi^{(1,0)}_{1}\end{array}\right.\\
&\left\{\begin{array}{l}\Psi^{(0,1)}_{1}\\ \Psi^{(0,1)}_{2}\end{array}\right. \longrightarrow \left\{\begin{array}{l}\Psi^{(0,1)}_{\text{div}} = \Psi^{(0,1)}_{1} - \frac{1}{4}\left[\Psi^{(0,1)}_{2} - \Psi^{(0,1)}_{2}(x-1, y)\right]\\ \Psi^{(0,1)}_{\text{n}} = \Psi^{(0,1)}_{2}\end{array}\right.\\
&\left\{\begin{array}{l}\Psi^{(1,1)}_{1}\\ \Psi^{(1,1)}_{2}\end{array}\right. \longrightarrow \left\{\begin{array}{l}\Psi^{(1,1)}_{\text{div}} = \Psi^{(1,1)}_{1} - \Psi^{(1,1)}_{2}\\ \Psi^{(1,1)}_{\text{n}} = \Psi^{(1,1)}_{1} + \Psi^{(1,1)}_{2}\end{array}\right.
\end{aligned} \tag{9.20}$$

We can then rewrite the decomposition of $\boldsymbol{u}$ in such basis:

$$\begin{aligned}
\boldsymbol{u} = &\sum_{j\in\mathbb{Z}}\sum_{\boldsymbol{k}\in\mathbb{Z}^2}\left(d^{(1,0)}_{\text{div}j,\boldsymbol{k}}\Psi^{(1,0)}_{\text{div}j,\boldsymbol{k}} + d^{(0,1)}_{\text{div}j,\boldsymbol{k}}\Psi^{(0,1)}_{\text{div}j,\boldsymbol{k}} + d^{(1,1)}_{\text{div}j,\boldsymbol{k}}\Psi^{(1,1)}_{\text{div}j,\boldsymbol{k}}\right)\\
&+\sum_{j\in\mathbb{Z}}\sum_{\boldsymbol{k}\in\mathbb{Z}^2}\left(d^{(1,0)}_{\text{n}j,\boldsymbol{k}}\Psi^{(1,0)}_{\text{n}j,\boldsymbol{k}} + d^{(0,1)}_{\text{n}j,\boldsymbol{k}}\Psi^{(0,1)}_{\text{n}j,\boldsymbol{k}} + d^{(1,1)}_{\text{n}j,\boldsymbol{k}}\Psi^{(1,1)}_{\text{n}j,\boldsymbol{k}}\right)
\end{aligned} \tag{9.21}$$

where the new coefficients $d^{\varepsilon}_{\text{div}j,\boldsymbol{k}}$ and $d^{\varepsilon}_{\text{n}j,\boldsymbol{k}}$ are expressed directly as a function of the canonical coefficients :

$$(d_{\text{div}})\left\{\begin{array}{l}d^{(1,0)}_{\text{div}\,j,\boldsymbol{k}} = d^{(1,0)}_{2,j,\boldsymbol{k}}\\ d^{(0,1)}_{\text{div}\,j,\boldsymbol{k}} = d^{(0,1)}_{1,j,\boldsymbol{k}}\\ d^{(1,1)}_{\text{div}\,j,\boldsymbol{k}} = \frac{1}{2}d^{(1,1)}_{1,j,\boldsymbol{k}} - \frac{1}{2}d^{(1,1)}_{2,j,\boldsymbol{k}}\end{array}\right. \qquad (d_n)\left\{\begin{array}{l}d^{(1,0)}_{\text{n}j,\boldsymbol{k}} = d^{(1,0)}_{1,j,\boldsymbol{k}} + \frac{1}{4}d^{(1,0)}_{2,j,\boldsymbol{k}} - \frac{1}{4}d^{(1,0)}_{2,j,k_1,k_2-1}\\ d^{(0,1)}_{\text{n}j,\boldsymbol{k}} = d^{(0,1)}_{2,j,\boldsymbol{k}} + \frac{1}{4}d^{(0,1)}_{1,j,\boldsymbol{k}} - \frac{1}{4}d^{(0,1)}_{1,j,k_1-1,k_2}\\ d^{(1,1)}_{\text{n}j,\boldsymbol{k}} = \frac{1}{2}d^{(1,1)}_{1,j,\boldsymbol{k}} + \frac{1}{2}d^{(1,1)}_{2,j,\boldsymbol{k}}\end{array}\right. \tag{9.22}$$

By construction, the incompressibility condition $\text{div}\boldsymbol{u} = 0$ is equivalent to $d^{\varepsilon}_{\text{n}j,\boldsymbol{k}} = 0, \quad \forall j, \boldsymbol{k}, \varepsilon$. The decomposition in the divergence-free wavelet basis has been successfully used for the analysis of turbulent fields by Deriaz and Perrier (2006), and in our case we are rather interested in the generation of divergence-free synthetic fields.

9.2.3.3 Extension to the 3D case

In three dimension, the decomposition of $(L(\mathbb{R}^3))^3)$ is given by:

$$(V_j^1 \otimes V_j^0 \otimes V_j^0) \times (V_j^0 \otimes V_j^1 \otimes V_j^0) \times (V_j^0 \otimes V_j^0 \otimes V_j^1). \tag{9.23}$$

There are 21 canonical wavelets, with the following type:

$$\varepsilon \in \{(0,0,1),(0,1,0),(1,0,0),(0,1,1),(1,1,0),(1,0,1),(1,1,1)\},$$

which can lead to 14 generating divergence-free wavelets $\Psi^{\varepsilon}_{\mathrm{div}}$, and 7 supplementary wavelets Ψ^{ε}_{n}. The construction of these wavelets is not detailed here and the reader is referred to the appendices of the thesis of Deriaz (2006) for their implementation.

Now that we have introduced this multi-dimensional divergence-free wavelet basis, let us investigate how to apply it to propose a new structural turbulence model.

9.3 A new kinematic simulation based on wavelets

9.3.1 Construction of a new synthetic velocity field

We have already discussed the drawbacks of the Fourier-based kinematic simulation, which relies on a Fourier decomposition in Eq. (9.1) and involves sinus and cosinus functions, which are non-compact functions. Instead of sine functions, we want to use a wavelet decomposition, to take advantage of the compactness of the modes and the locality of the information. In the following, we investigate this change of formalism and we show how the parameters of the model can be adjusted to retrieve DNS statistics.

We aim to generate a N_d-dimensional velocity field in a box of length $\mathcal{L}$. We suggest the following form for the velocity field, replacing the Fourier decomposition with a multiresolution analysis:

$$\boxed{\boldsymbol{u} = \sum_{j=j_{\min}}^{j_{\max}} \sum_{\boldsymbol{k}} \sum_{\varepsilon} d^{\varepsilon}_{\mathrm{div}j,\boldsymbol{k}} \Psi^{\varepsilon}_{\mathrm{div}j,\boldsymbol{k}}}. \tag{9.24}$$

Compared to the general decomposition derived in Eq. (9.21), all coefficients $d^{\varepsilon}_{n,j,\boldsymbol{k}}$ are set to 0 to ensure divergence-free, the sum is truncated between $j_{\min}$ and $j_{\max}$ in order to define finite scale sizes, and $\boldsymbol{k}$ does not run over all natural integers of dimension N_d: it is limited in spatial dimension to the box of length $\mathcal{L}$.

The divergence-free wavelet $\Psi^{\varepsilon}_{\mathrm{div}j,\boldsymbol{k}}$, of size $\ell_j = \mathcal{L}/2^j$ and of type ε is located at position $\ell\boldsymbol{k}$, with $\boldsymbol{k} \in [\![1\ ;\ 2^j]\!]^{N_d}$. It is weighted by a random coefficient $d^{\varepsilon}_{\mathrm{div}j,\boldsymbol{k}}$ whose distribution will be presented in the following. By superposing different wavelet functions of different sizes and at different positions, one can obtain as an example the typical flow represented in Fig. 9.8.

Note that for a periodic flow, we impose a periodic condition on the wavelets:

$$\forall \varepsilon, \forall \boldsymbol{k}, \forall j, \forall i \in \{1,...,N_d\}, \quad \Psi^{\varepsilon}_{\mathrm{div}j,\boldsymbol{k}}(\boldsymbol{x} + \mathcal{L}\boldsymbol{e}_i) = \Psi^{\varepsilon}_{\mathrm{div}j,\boldsymbol{k}}(\boldsymbol{x}). \tag{9.25}$$

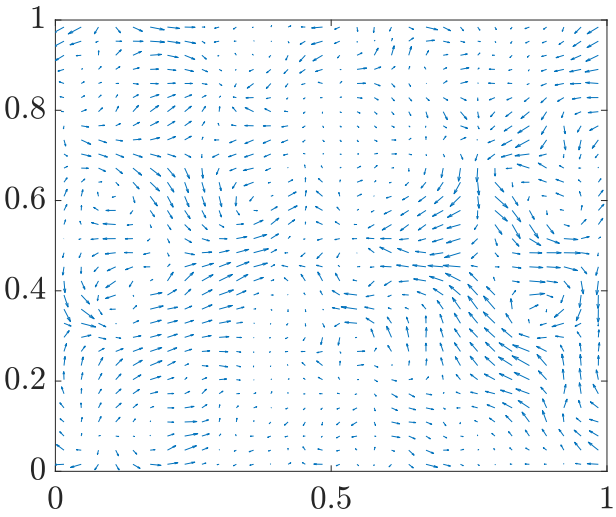

Figure 9.8. 2D velocity field generated with random coefficients $d^{\varepsilon}_{\mathrm{div}}$ in Eq. (9.24).

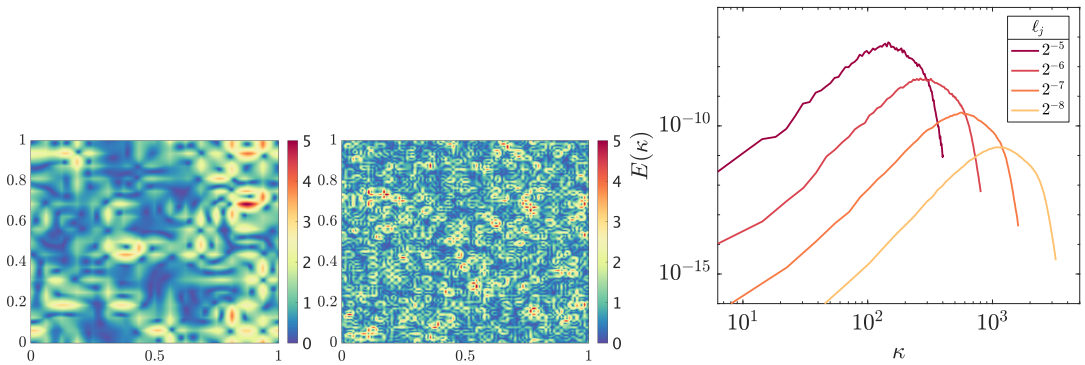

(a) $\ell_j = 2^{-3}$ (b) $\ell_j = 2^{-5}$ (c) Energy Spectrum

Figure 9.9. Snapshots of a velocity component for 2D flows generated with a single level $j = 3$ (a) and $j = 5$ (b). (c) is the energy spectra of $\boldsymbol{u}$ generated with single levels j.

This amounts to imposing periodicity on the basis wavelets and scaling functions :

$$\psi_i(x + \mathcal{L}) = \psi_i(x), \quad \text{and } \varphi_i(x + \mathcal{L}) = \varphi_i(x), \quad \text{with } i = 0, 1 \tag{9.26}$$

Conversely, for particular geometries with boundary conditions, such as in Urban (1994), it may be useful to define specific wavelets which ensure zero velocity conditions at the boundary for the function and for its derivatives. The reader is referred to Deriaz (2006) for the construction of such wavelets.

The model described by Eq. (9.24) ensures the spatial correlation of the flow, and as opposed to the Fourier-based KS, the velocity field has compact modes, inherited from wavelets properties. Moreover, the use of divergence-free wavelets naturally ensures the divergence free nature of the sum. Those properties satisfy points (i) and (ii) of the requirements of Sec. 9.1.

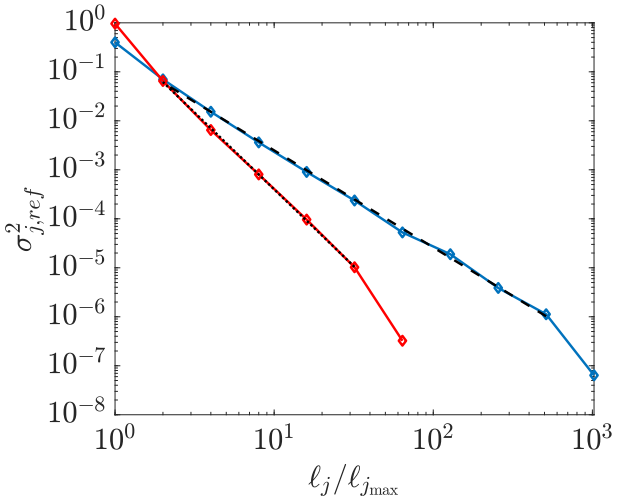

Figure 9.10. Reference variances computed for single-level wavelet fields. The blue curve is for the 2D field, while the red one represents the 3D reference values. The dashed and dotted lines represent their respective analytical law given in Eq. (9.28).

9.3.1.1 Energy spectrum and characteristic length scales

Each level of detail j is associated with vortices of size $\ell_j = \mathcal{L}/2^j$, where $\mathcal{L}$ is the dimension of the box, each vortex of level j having thus a specific contribution to the global energy spectrum. This is illustrated in Fig. 9.9(a) and 9.9(b), where two examples of synthetic fluids reconstructed with a single level j are given. Their corresponding energy spectra are plotted in Fig. 9.9(c) and the maximum of the energy is found for a wavenumber of the order of magnitude $\kappa_j = 2\pi/\ell_j$.

The energy associated with level j thus depends directly on the values of $d^{\varepsilon}_{\mathrm{div}j,\boldsymbol{k}}$. Their distribution must have zero mean, because we want to model a HIT, whose mean velocity is zero. On the other hand, we can control the variance of the distribution: the higher it is, the higher the associated energy level is. Therefore, we propose a Gaussian distribution of coefficients, with variance depending on the associated level: $d^{\varepsilon}_{\mathrm{div}j,\boldsymbol{k}} \sim \mathcal{N}(0, \sigma_j^2)$. The objective is to find a model for σ_j to reproduce a given energy spectrum.

We recall that in the Fourier-based KS, the amplitudes of the vectors $\boldsymbol{a}_n$ and $\boldsymbol{b}_n$ are chosen such that the appropriate energy density at each particular scale is enforced:

$$|\boldsymbol{a}_n^2| = |\boldsymbol{b}_n^2| = 2E(\kappa_n)\Delta\kappa_n, \quad \text{where } \Delta\kappa_n = \begin{cases} \dfrac{\kappa_{n+1} - \kappa_n}{2}, & \text{if } n = 1, \\ \dfrac{\kappa_{n+1} - \kappa_{n-1}}{2}, & \text{if } 2 \leq n \leq N-1, \\ \dfrac{\kappa_n - \kappa_{n-1}}{2}, & \text{if } n = N. \end{cases} \tag{9.27}$$

For the wavelet-based KS, we want to enforce the discrete level of energy at level j, but unlike the case of Fourier modes, we do not know analytically the energy level of each mode. We therefore calculate the energy of each level for a normalized distribution of coefficients $d^{\varepsilon}_{\mathrm{div}j,\boldsymbol{k}} \sim \mathcal{N}(0,1)$. Figure 9.10 shows the measured variance of single-level wavelet fields (i.e. $j_{\min} = j_{\max}$). An empirical law can be obtained for two and three-dimensional flows:

$$\begin{aligned}\sigma^2_{j,\text{ref}} &= 0.24\left(\frac{\ell_j}{\ell_{j_{\max}}}\right)^{-2}, \quad \text{in 2D} \\ \sigma^2_{j,\text{ref}} &= 0.54\left(\frac{\ell_j}{\ell_{j_{\max}}}\right)^{-3.1}, \quad \text{in 3D.}\end{aligned} \tag{9.28}$$

Note that these laws are only valid for the spline wavelet we have chosen, and that they will have to be recalculated for a different choice of MRA.

In the wavelet-based KS, the energy of each level j is controlled by adapting the variance of the Gaussian law for the coefficient of this level: $d^{\varepsilon}_{\text{div}j,\boldsymbol{k}} \sim \mathcal{N}(0,\sigma_j^2)$. We therefore propose the following scaling law for σ_j :

$$\sigma_j^2 = E(\kappa_j)\Delta\kappa_j/\sigma^2_{j,\text{ref}}. \tag{9.29}$$

Energy spectrum models can be reproduced, for example following

$$E(\kappa) = \sigma_u^2\kappa_0^{2/3}\kappa^{-5/3}, \quad \forall\kappa \in [\kappa_{\min};\kappa_{\max}] \tag{9.30}$$

which is commonly used in the literature (Murray, Lightstone, and Tullis 2016b). Figure 9.11(a) compares the model with energy spectra obtained with wavelet and Fourier-based KS. The energy spectrum obtained with wavelet fields reproduces well the prescribed model, except for the largest and smallest values of the wavenumbers. Indeed, the degrees of freedom of the wavelet model do not allow to control independently each wavenumber, but rather the bench of wavenumbers involved in the representation of a given wavelet. The smallest and biggest wavelets (first and last level) therefore the first and last wavelets will thus give the trends of the energy spectrum at the smallest and largest wavenumbers.

Compared to the Fourier one, the wavelet spectrum is considerably smoother. In this comparison lies the intrinsic difference between the Fourier and the wavelet approaches: the first one is very resolved in frequency but does not give local information, while the second gives a less detailed spectral resolution but a better information in space. Each of the wavelengths appearing in the Fourier representation contributes to the spectrum at the associated discrete energy. In contrast, each wavelet already covers a continuous set of wavelengths (Fig. 9.9(c)) and superimposed, these spectra populate the spectrum continuously. The effect is all the more statistically converged by the presence of these wavelets everywhere in the domain, since they are distributed in space.

The range of the spectrum model (and thus of the scales to represent) determines the parameters $j_{\min}$ and $j_{\max}$. Indeed, the levels of each wavelet j are related to their maximum wavenumber by the following expression:

$$j = \log_2\left(\frac{\mathcal{L}}{2\pi}\kappa_j\right) \tag{9.31}$$

and the knowledge of $\kappa_{\min}$ and $\kappa_{\max}$ thus sets the parameters $j_{\min}$ and $j_{\max}$. For the spectrum model given in Eq. (9.30), these wavenumbers are linked respectively to the integral scales $L = 2\pi/\kappa_{\min}$ and Kolmogorov scales $\eta \sim 2\pi/\kappa_{\max}$. One can verify in Fig. 9.11(b) the change of the inertial range when changing the extreme levels.

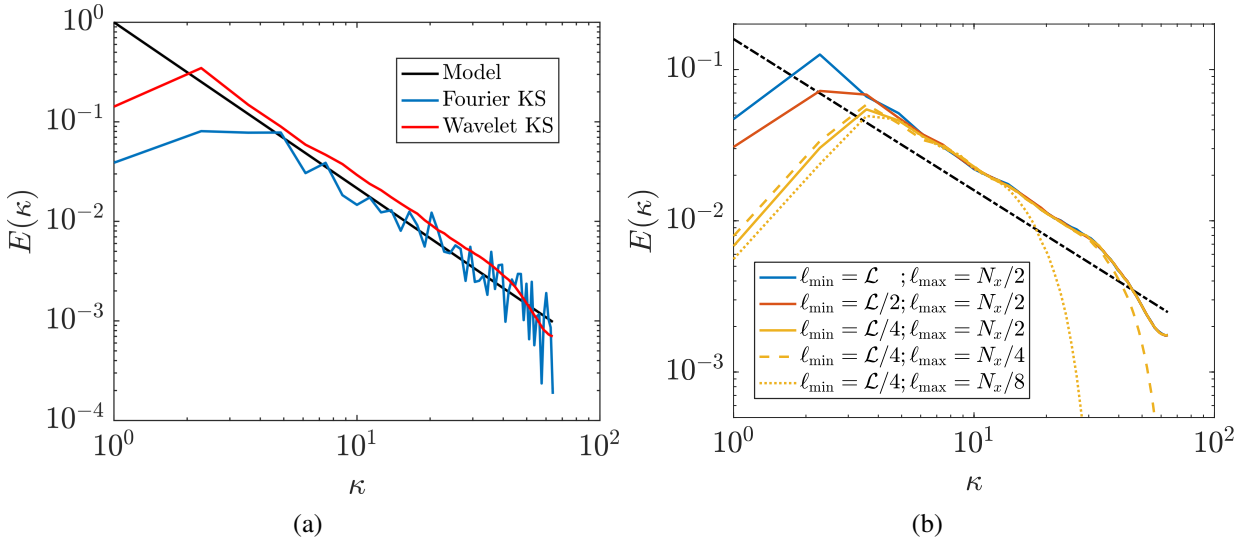

Figure 9.11. Energy spectrum for linear model (a) ; and different inertial ranges obtained by changing $j_{\min}$ and $j_{\max}$ (b). The black lines represent the characteristic slope $-5/3$.

Figure 9.12 represents one velocity component of the synthetic flow described by Eq. (9.24), with different values of $\ell_{\max}$. The lower $\ell_{\max}$, the more details are present in the simulation, revealing the presence of small and very located vortices.

9.3.1.2 Characteristic time scales

We can verify the scaling of the time scales with the parameters of the model. In Fig. 9.13, we study the dependency of the Kolmogorov time scale with the two parameters, $\ell_{\min}$ and $\ell_{\max}$, which are respectively the smallest and the largest length scales in the flow. We obtain scaling in power laws:

$$\tau_\eta = \sqrt{\nu / \langle \varepsilon \rangle} \sim \sigma_u^{-1} \ell_{\min}^{0.4} \ell_{\max}^{0.6}, \tag{9.32}$$

which are close to the theoretical ones, predicted by the Kolmogorov phenomenology in Sec. 1.2.4:

$$\tau_\eta \sim \sigma_u^{-1} L^{1/3} \eta^{2/3}. \tag{9.33}$$

We recall that the largest time scale in the flow is the autocorrelation time of the fluid particle velocities, i.e. the Lagrangian integral time scale defined in Sec.1.2.4 by:

$$T_L = \frac{1}{\sigma_u^2} \int_0^{+\infty} R_L^u(\tau)\, \mathrm{d}\tau \tag{9.34}$$

Since $T_L \sim \sigma_u^{-1} L$, it is also expected to scale with the largest scales in the flow. Figure 9.14 shows the autocorrelation function of the velocity, for different values of $\ell_{\min}$ and $\ell_{\max}$. The overlap of dashed and full lines confirms the independence of the autocorrelation, hence T_L, with the small scales. On the other hand, there is a clear impact of the parameter $j_{\min}$ on the characteristic time

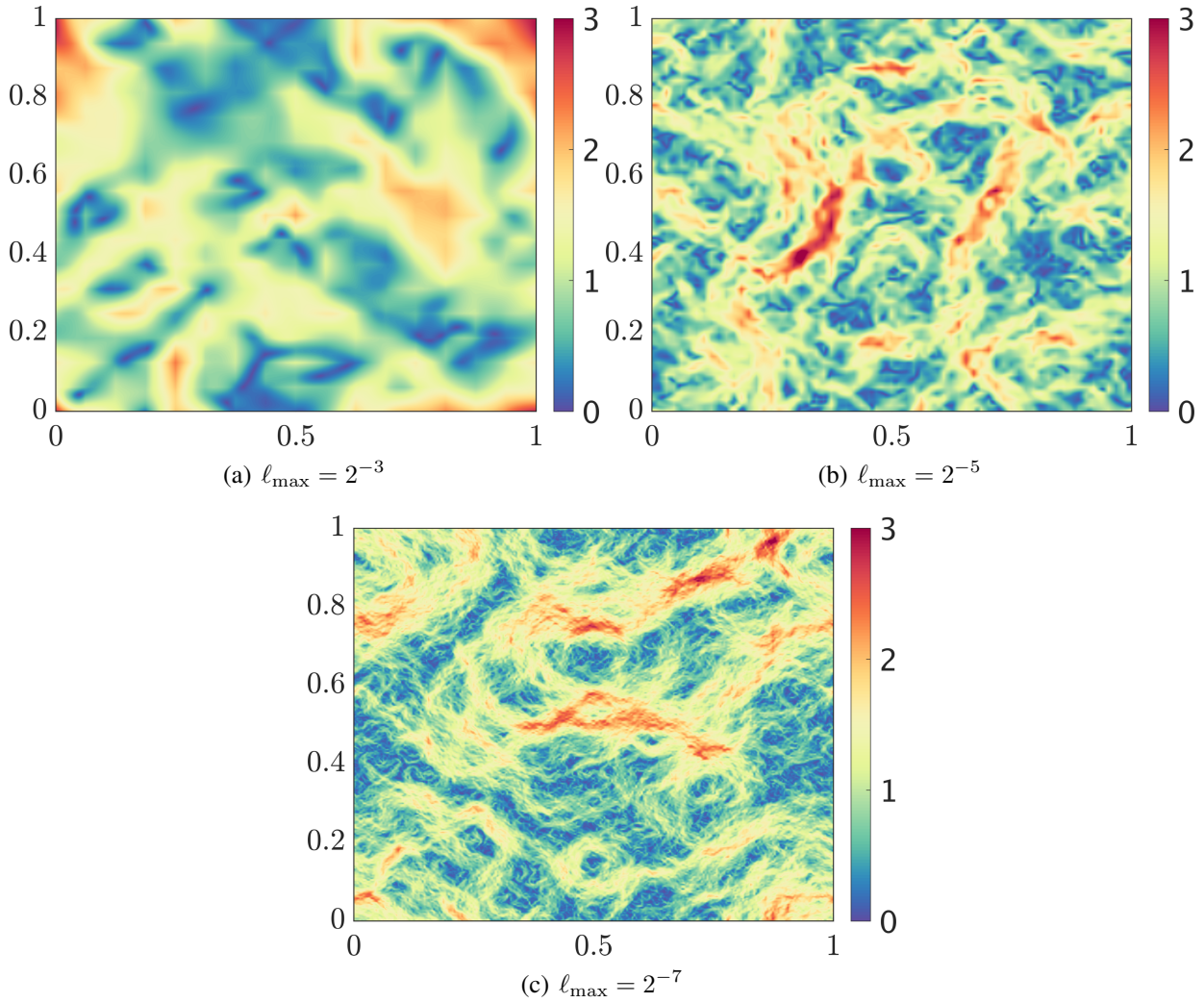

(a) $\ell_{\max} = 2^{-3}$ (b) $\ell_{\max} = 2^{-5}$

(c) $\ell_{\max} = 2^{-7}$

Figure 9.12. Snapshot of a 2D velocity field obtained for different values of $j_{\max} \in \{3, 5, 7\}$ and fixed $j_{\min} = 0$ in a cubic box of size $\mathcal{L} = 1$.

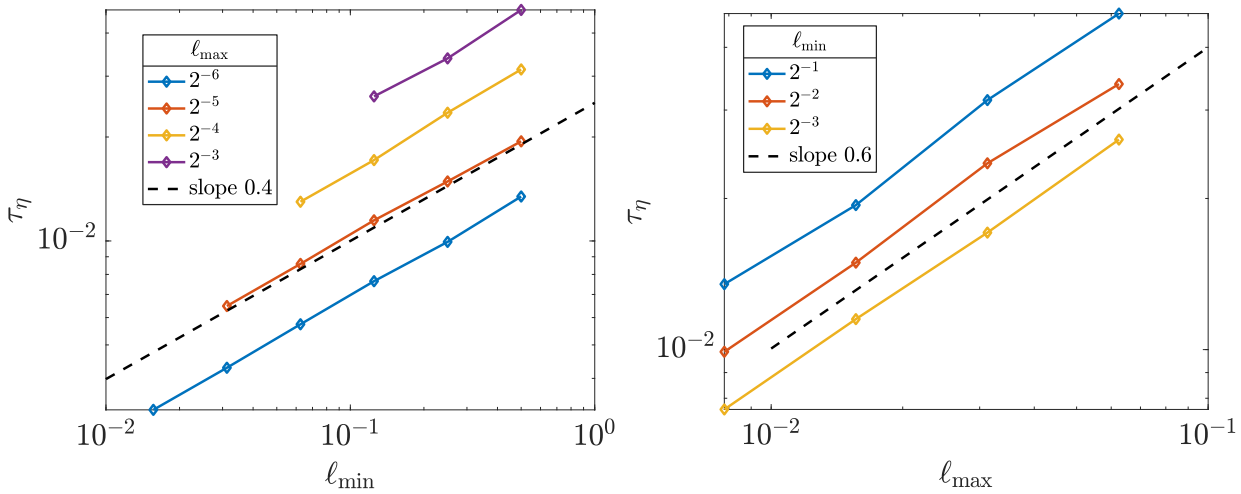

(a) Scaling of τ_η with L (b) Scaling of τ_η with η

Figure 9.13. Kolmogorov time scale τ_η measured for different values of $L \sim \ell_{\min}$ and compared with a scaling law of power 0.4 (a) and different values of $\eta \sim \ell_{\max}$, compared with a scaling law of power 0.6.

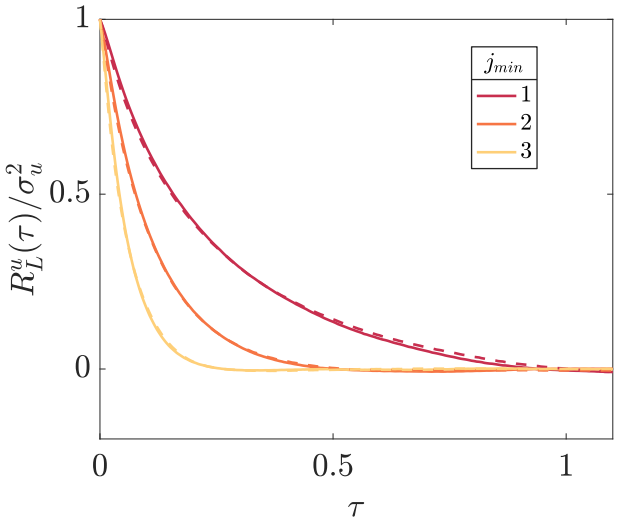

Figure 9.14. Autocorrelation of the fluid particle velocity for different values of $j_{\min}$ (in the legend), and $j_{\max}$ (full line: $j_{\max} = 5$, dashed line: $j_{\max} = 6$).

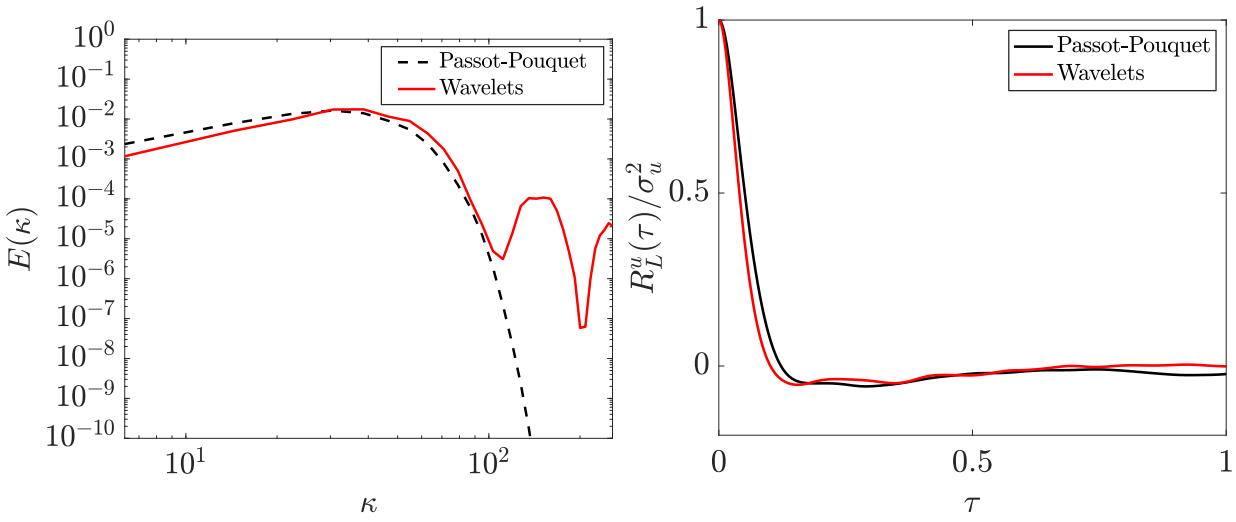

(a) Energy spectrum (b) Autocorrelation

Figure 9.15. Comparison of the energy spectra (a) and Lagrangian velocity autocorrelation (b) between the Passot-Pouquet turbulence and the wavelet model.

of autocorrelation T_L.

We have thus shown that for a velocity field generated with Eq. (9.24), it is possible to adjust the characteristic lengths and times of the model and to reproduce the universal behavior of the inertial range. Before introducing a temporal evolution on this velocity field, let us validate this surrogate as a frozen turbulence.

9.3.1.3 Validation with 2D frozen turbulence

We first validate the model by comparing the statistics observed in a two-dimensional frozen HIT generated from the exponential spectral model introduced in Sec 2.3.2. The velocity field is produced on a 256^2 grid and we enforce a variance $\sigma_u = 1$.

The wavelet-based KS is parametrized to reproduce the energy spectrum and the coefficients are then fixed at $j_{\min} = j_{\max} = 3$. Figure 9.15(a) compares the two spectra, the one generated by the spectral model and the one obtained with the wavelets. We notice peaks for large wavenumbers on the wavelet spectrum. Indeed, as soon as the field is projected on a mesh such that $N_x > 2^{j_{\max}+1}$, we can see these residual energies appearing at small scales. Their energy is however negligible compared to the energy of the smallest scales at $\kappa_{\max}$ and there is actually no interest in using such a detailed resolution.

The Kolmogorov time scale of the spectral model is $\tau_\eta = 0.023$, that of the wavelet model $\tau_\eta = 0.021$. Figure 9.15(b) compares the autocorrelation functions of the fluid particle velocities in the two simulations and finds good agreement. This confirms that the wavelet field is able to reproduce not only Eulerian statistics such as the energy spectra, the TKE, the global dissipation, but also Lagrangian statistics such as the velocity autocorrelation of fluid particles.

The comparison with a frozen DNS turbulence field being satisfying, we are now interested in

reproducing the dynamics of the flow. Let us introduce the time evolution of this velocity field, which is also a matter of improvement in the Fourier-based KS.

9.3.2 Evolution of the wavelet field

First, we propose to write a time evolution law directly on the coefficients. The constraints on the evolution model are such that the stationarity of the flow must be preserved, as well as the energy spectrum. Thus, at any time, the distribution of the coefficients must remain a Gaussian of variance σ_j. We propose a stochastic Langevin model for each coefficient, which guarantees the two properties mentioned above, and introduces an additional control parameter: the eddy turnover time of that level $T_{E,j}$:

$$\mathrm{d}(d^{\varepsilon}_{\mathrm{div}j,k_1,k_2}) = -\frac{1}{T_{E,j}} d^{\varepsilon}_{\mathrm{div}j,k_1,k_2}\,\mathrm{d}t + \sqrt{\frac{2\sigma_j^2}{T_{E,j}}}\,\mathrm{d}W_t. \tag{9.35}$$

The random variables are Gaussian, and driven by Ornstein-Uhlenbeck processes. They are stationary by construction (see Sec. 3.1.5), with variance σ_j and time scales $T_{E,j}$. We introduce the eddy turnover frequency $\omega_j = T_{E,j}^{-1}$ for which some models are already proposed in the literature, in the framework of Fourier-based KS. The most common expression for the eddy turnover frequency is the following (Fung et al. 1992; Malik 1996):

$$\omega_j = \lambda\sqrt{\kappa_j^3 E(\kappa_j)}, \tag{9.36}$$

which becomes $\omega_j = \lambda\sigma_u\kappa_0^{1/3}\kappa_j^{2/3}$ considering the energy spectrum model of Eq. (9.30). More recently, Osborne, Vassilicos, and Haigh (2005) suggested another form to improve the scalings of Eulerian one-point two-time velocity structure functions:

$$\omega_j = \lambda\sigma_u\kappa_j. \tag{9.37}$$

In both models, the parameter λ controls the overall eddy turnover time. For very small values of λ, all the eddies turnover times are very large and turbulence is almost frozen. In the following, we will choose model of Eq. (9.36) but further investigations could be performed to examine the impact of this choice on the overall statistics.

Figure 9.16 shows the velocity autocorrelation for different values of λ. We remark that for very small values of λ (up to a frozen turbulence), the velocity can be negatively correlated and a brief oscillating behavior can occur before reaching the total decorrelation. For larger values of λ, the decrease of the autocorrelation function is monotonic and more rapid, and the Lagrangian integral time scale T_L is hence reduced. This is expected because the dynamic introduced in the temporal equation decorrelates fluid particles velocities faster.

We notice, with an analysis similar to the one done in the previous chapter for Fig. 8.2, that the parameter λ essentially impacts the first characteristic time of decorrelation, the one related to small scales. Further studies should consider other models of ω_j, with a weaker increase in κ_j to avoid the rapid forcing of the small scales eddy turnover time.

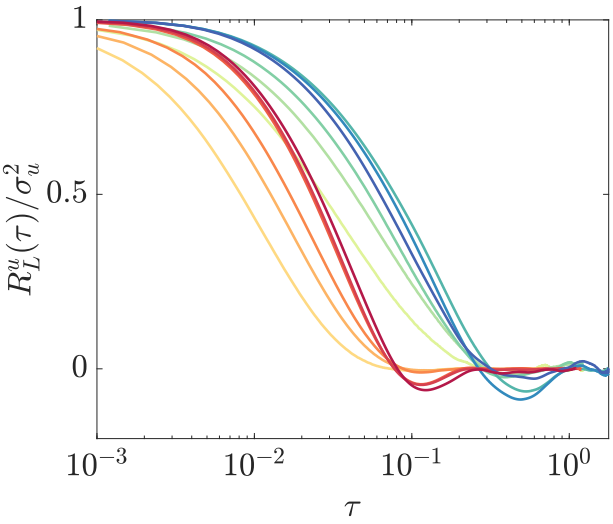

Figure 9.16. Lagrangian velocity autocorrelation, for $j_{\min} = 1$ (hot colors) and $j_{\min} = 3$ (cold colors), with fixed $j_{\max} = 6$. From dark to light shades, increasing values of $\lambda \in \{0.01, 0.05, 0.1, 0.5, 1, 2, 5\}$.

9.4 Validation with DNS

We also validate the wavelet-based KS by verifying its ability to reproduce some statistics of a 3D flow obtained by DNS. The reference fields are simulated on a 128^3 and 256^3 mesh, using the DNS Fieldz code.

First, we adapt the variance σ_j, following Eq. (9.29) in order to reproduce the reference energy spectrum as closely as possible. These are given in Fig. 9.17(a) and 9.17(b) and we manage to reproduce a very large part of the spectral scales, except the smallest scales, at the limit of the resolution, for which the wavelet field does not reproduce the decrease of the energy content of the DNS field.

Snapshots of velocity fields obtained in DNS (Figs. 9.18(a) and 9.18(b)), with the wavelet-based KS (respectively Figs. 9.18(c) and 9.18(d)) and with a Fourier-based KS (Figs. 9.18(e) and 9.18(f)) for the two meshes can be compared, and we observe structures of similar size and intensity between the DNS and wavelet-based KS. The patterns appearing in the Fourier-based KS are very stretched, and this anisotropy probably comes from discrete forcing at certain wavenumbers to impose periodicity. Isotropic wavelets (Deriaz and Perrier 2006) allows on the contrary to avoid the existence of elongated structures, which do not appear visibly in the DNS reference for HIT. Note however that the use of anisotropic wavelets could be appropriate for flows with more singular geometry or physics, for which a stretch or shear is resolved, and a preferential direction can be better represented using these wavelets.

Although the wavelet field seems visually more similar to the reference one, it is necessary to establish proper metrics to assess it objectively. We have for example introduced the characteristic quantities of turbulent systems in Chap. 1, which we can then compare. The Kolmogorov time τ_η is respectively 0.17 for the DNS, 0.16 with the wavelet field and 0.14 with the Fourier one. Figure 9.19 compares the autocorrelation functions of DNS, wavelet and Fourier-based KS for a frozen and a dynamic flow. Both methods retrieve the exponential behavior of the DNS autocorre-

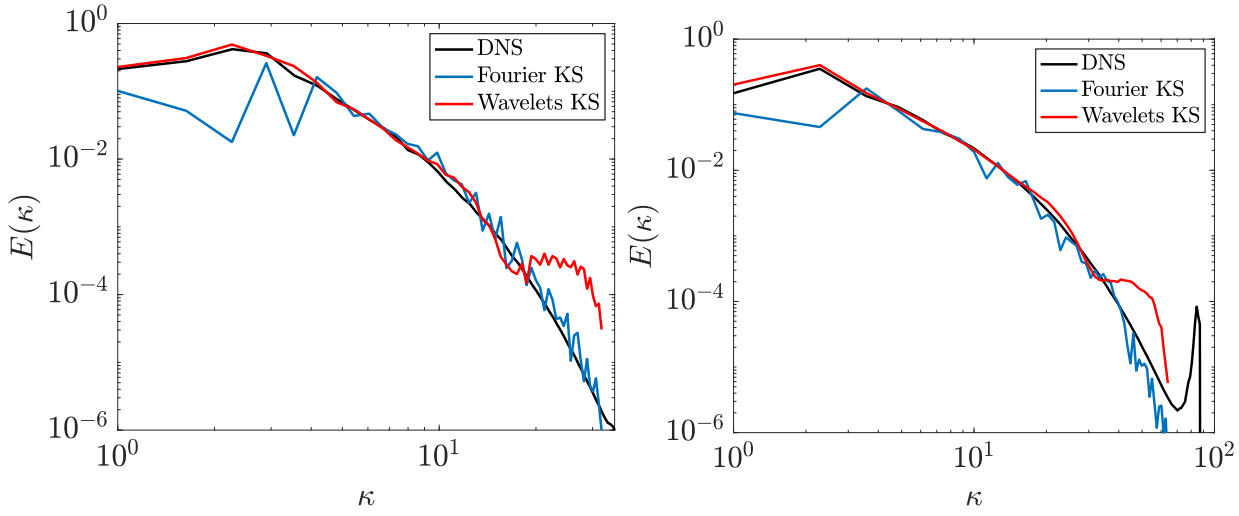

(a) $N_x = 128$ (b) $N_x = 256$

Figure 9.17. Comparison of energy spectra between DNS, wavelet and Fourier-based KS for $N_x = 128$ (a), and $N_x = 256$ (b).

lation for $\lambda = 0$. We thus conclude that ensuring the faithful reproduction of the energy spectrum, i.e. the spatial scales, is sufficient to reproduce also the small and large temporal character scales (namely τ_η and T_L).

However, $\lambda = 0$ yields a field with unphysical steadiness and in the next chapter, we will fit its value according to the expected particle preferential concentration. For $\lambda = 0.5$, the autocorrelation function of the wavelet-based KS decreases faster, thus reducing the Lagrangian integral time scale of the simulation, as observed in Sec. 9.3.2, whereas the Fourier-based KS produces oscillations. This spurious behavior of Fourier-based KS motivates the further investigation of the wavelet model.

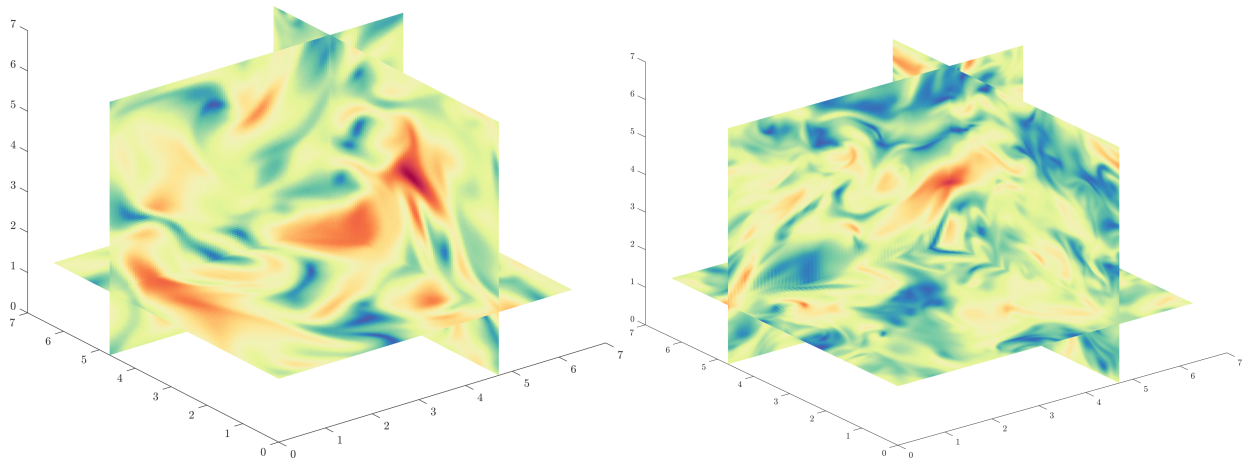

(a) DNS with $N_x = 128$

(b) DNS with $N_x = 256$

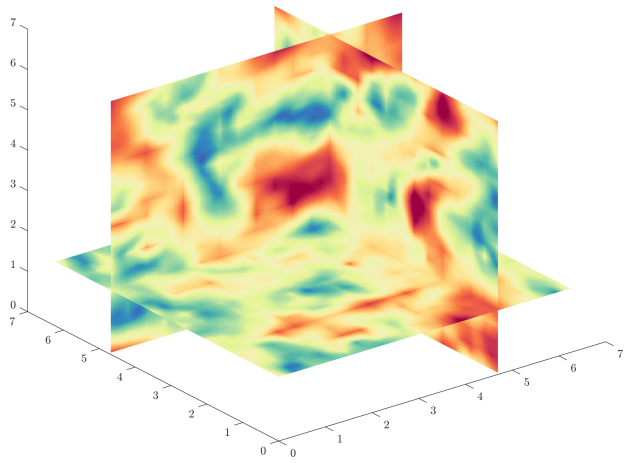

(c) Wavelet field, $N_x = 128$

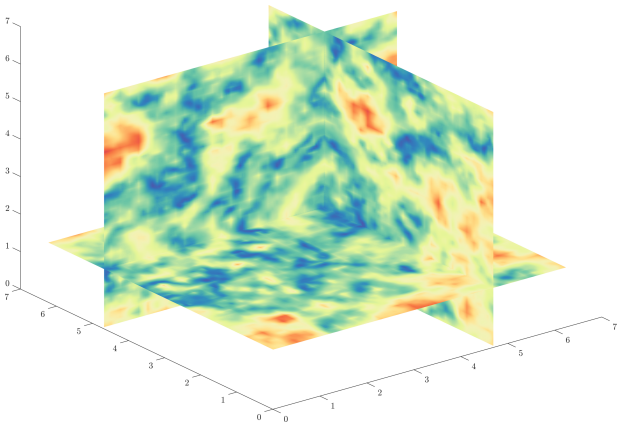

(d) Wavelet field, $N_x = 256$

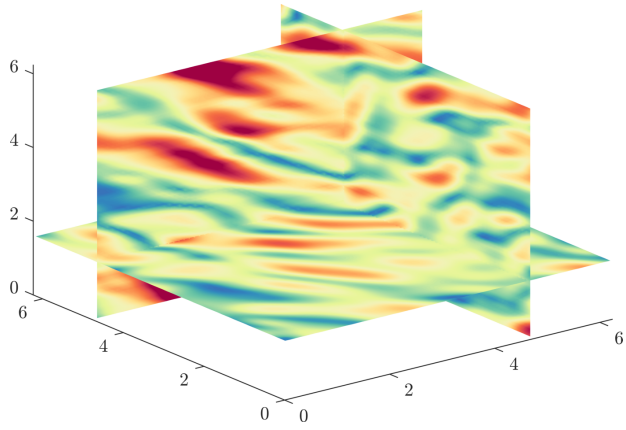

(e) Fourier field, $N_x = 128$

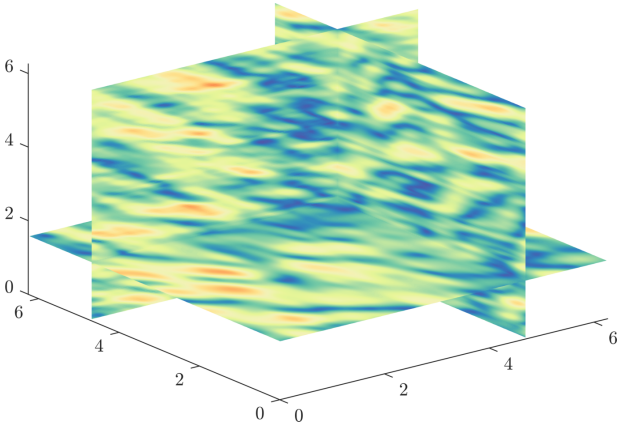

(f) Fourier field, $N_x = 256$

Figure 9.18. Comparison of velocity snapshots for $N_x = 128$ (on the left), and $N_x = 256$ (on the right). (a) and (b) correspond to DNS; (c) and (d) to wavelet-based KS; (e) and (f) to Fourier-based KS.

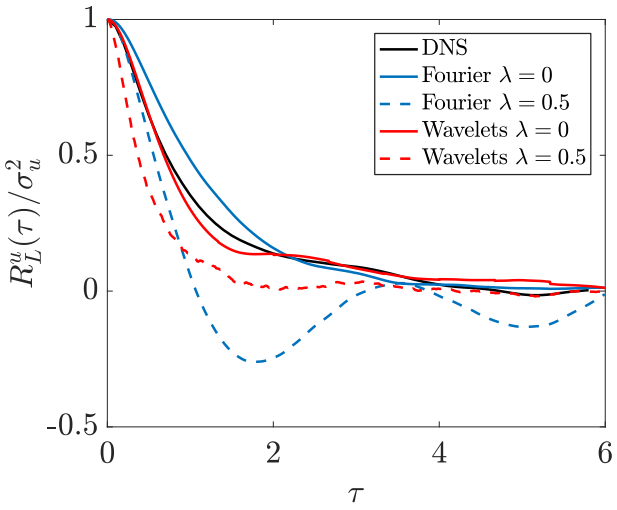

Figure 9.19. Autocorrelation function of fluid particle velocity for DNS and both kinematic models, in a frozen fluid and with $\lambda = 0.5$.

Conclusion

In conclusion, we have designed a new framework for kinematic simulation, based on divergence-free wavelets. We have proposed an analytic expression for the synthetic flow, with a stochastic Langevin equation for the temporal evolution of the coefficients. We have shown that parameters of the model can be adjusted to retrieve all the important DNS features. Parameters are summarized in Tab. 9.1.

This formalism has the same advantages as a Fourier-based kinematic simulation, namely its analytic formulation and numerical simplicity, its similarity with the Kolmogorov picture of turbulence. But as opposed to the sinus and cosinus functions used in the Fourier decomposition, wavelets have a compact support and seem more adapted to represent other characteristics of real turbulent flows.

Many additional studies could be conducted to validate such a surrogate by measuring fluid particle dispersion, velocity increment statistics (intermittency measure), dissipation, enstrophy, Q criterion etc. The objective of our work is not necessarily to develop the most realistic turbulence model, but rather to use it as a sub-filter model for the particles. In the next chapter, we are therefore interested in kinematic modeling in an attempt to recover the statistics of the disperse phase, and in particular the segregation.

Parameter	Description and control	Model
$j_{\min}$	Lowest level of wavelets (largest length scales)	Integral length scale $L = \mathcal{L}/2^{j_{\min}}$
$j_{\max}$	Higher level of wavelets (smallest length scales)	Kolmogorov length scale $\eta = \mathcal{L}/2^{j_{\max}}$
σ_j	Variance of velocity at scale ℓ_j, depends on the mode of energy spectrum	$\sigma_j = E(\kappa_j)\Delta\kappa_j/\sigma^2_{j,\text{ref}}$.
$d^{\varepsilon}_{\text{div}j,\boldsymbol{k}}$	Details coefficients	$d^{\varepsilon}_{\text{div}j,\boldsymbol{k}} \sim \mathcal{N}(0, \sigma_j^2)$
$T_{E,j} = 1/\omega_j$	Eddy turnover time scales	$\omega_j = \lambda\sqrt{\kappa_j^3 E(\kappa_j)}$ or $\omega_j = \lambda\sigma_u\kappa_j$
λ	Factor of turnover velocity	Fit to retrieve Lagrangian autocorrelation
Evolution	Temporal evolution of the detailed coefficients	$\mathrm{d}(d^{\varepsilon}_{\text{div}j}) = -\dfrac{1}{T_{E,j}} d^{\varepsilon}_{\text{div}j}\,\mathrm{d}t + \sqrt{\dfrac{2\sigma_j^2}{T_{E,j}}}\,\mathrm{d}W_t$

Table 9.1. Summary of the wavelet-based KS model parameters

Chapter 10

Particles dynamics in wavelet-based kinematic simulation

This chapter studies the statistics of the disperse phase carried by a wavelet-based kinematic field. In particular, we aim at evaluating the particle preferential concentration (PPC) and trajectory crossing (PTC), which are key elements to model in view of a two-way context. We remind the reader that the two-way coupling will be the subject of Part. V.

We highlight the influence of the Reynolds number on particle dynamics in wavelet-based kinematic simulations. In particular, the extent of the inertial zone produces PPC and PTC on a broader range of scales. We then study the effect of the KS dynamics, using the time evolution scheme for the coefficients introduced in Chap. 9. We observe that wavelet-based KS can reproduce results of DNS by adjusting the control parameter of the model, λ.

In Sec. 10.1, we investigate the influence of the Reynolds number on the disperse phase statistics in frozen turbulence, and Sec. 10.2 validates them quantitatively in a two-dimensional frozen flow. Section 10.3 investigates the effect of λ, the parameter controlling the turnover time of vortices. Validation against DNS and comparison with Fourier-based KS of particles statistics in HIT with 3D stationary turbulence are performed in Sec. 10.4.

10.1 Influence of the Reynolds number

We have seen in Chap. 6 that the preferential concentration of particles occurs when the relaxation time of the particles is close to the Kolmogorov time: $\mathrm{St}_\eta \approx 1$. Actually, for an isolated vortex of size ℓ_j, its proper characteristic time τ_j can be introduced and the relevant Stokes number to characterize its interaction with particles is $\mathrm{St}_j = \tau_p/\tau_j$ (as this was done for Taylor Green vortices in Sec. 6.2.1).

In turbulence, we recall that the Reynolds number is related to the separation of scales $\mathrm{Re}_\lambda sim T_L/\tau_\eta$, and the turbulence theories (Chap. 1) describe a cascade of vortices of different sizes and time scales, ranging from the Kolmogorov time scale τ_η to the Lagrangian integral time scale T_L. By associating a Stokes number to each scale, we have $\mathrm{St}_L \leq \mathrm{St}_j \leq \mathrm{St}_\eta$. We already know from Chap. 6 that St_η mainly characterizes PPC while St_L controls PTC. Let us detail those phenomena for increasing particle relaxation times:

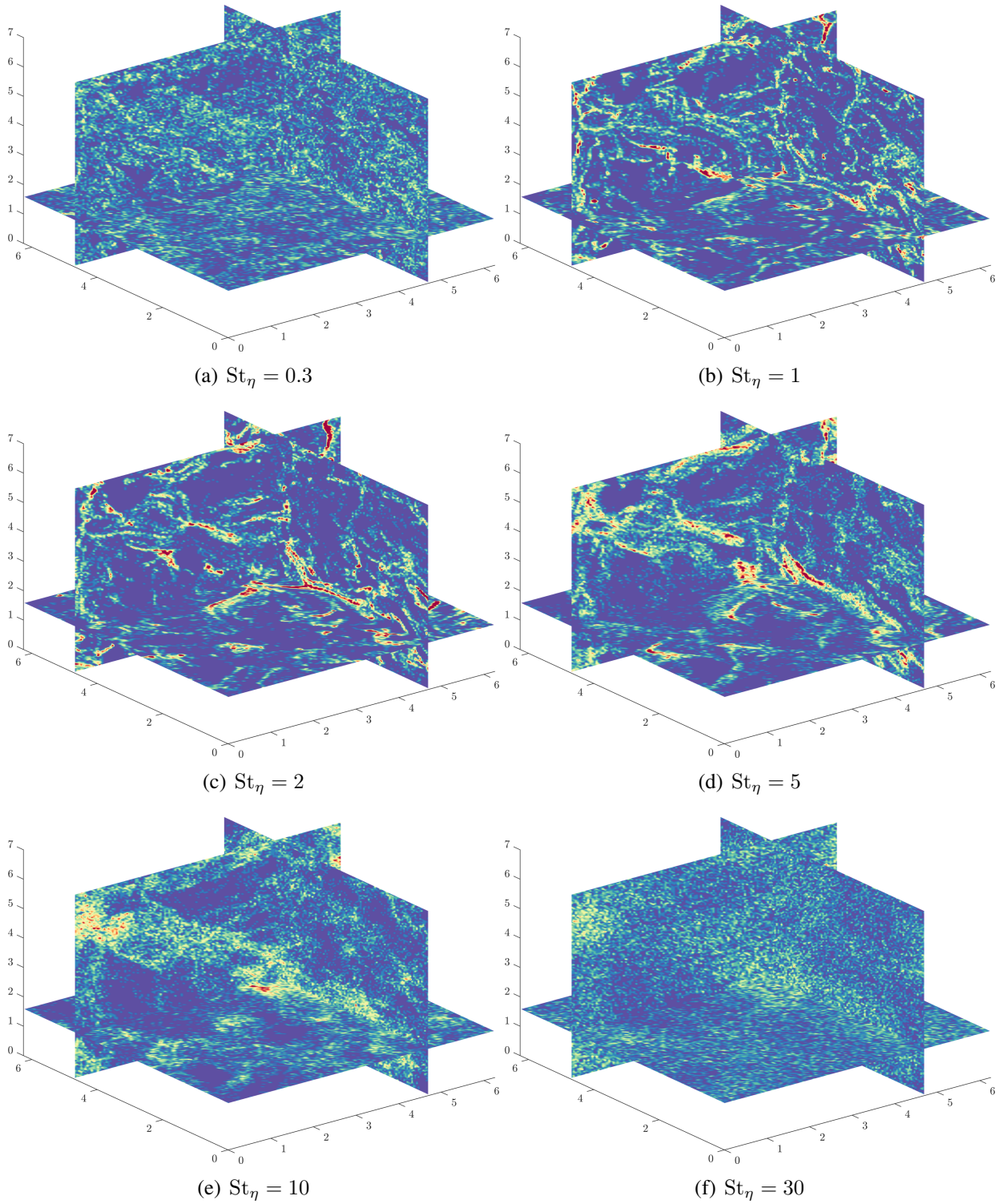

(a) $\mathrm{St}_\eta = 0.3$ (b) $\mathrm{St}_\eta = 1$

(c) $\mathrm{St}_\eta = 2$ (d) $\mathrm{St}_\eta = 5$

(e) $\mathrm{St}_\eta = 10$ (f) $\mathrm{St}_\eta = 30$

Figure 10.1. Particle number density fields obtained with wavelet-based KS with $\lambda = 0$, $j_{\min} = 1$, $j_{\max} = 5$ at $t_f = 6$. Eulerian fields are obtained with box projection on a 2^7 grid.

- For $\mathrm{St} = 0$, particles trace the fluid: if the divergence-free condition is well reproduced in the simulation, particles should fill the space with the same distribution that the one initially drawn.
- For $\mathrm{St}_\eta < 1$, all the particles tend to align their velocity with the flow, and are ejected from the center of vortices, as observed in Fig. 10.1(a).
- For $\mathrm{St}_\eta = 1$, the segregation of particles is maximal in the Kolmogorov vortices, but for bigger vortices, we have $\mathrm{St}_j < 1$. Figure 10.1(b) shows strong heterogeneity of the disperse phase with accumulation of particles around small vortices. This results in characteristic small scales patterns in the number density field.
- For $\mathrm{St}_j = 1$, particles mostly interact with vortices of size ℓ_j: they are ejected from the larger vortices, hence increasing PPC, but they cross the smaller one, producing PTC. Depending on the balance between those two phenomena, we can observe large scale patterns of PPC but random uncorrelated motion at small scales. Figures 10.1(c) and 10.1(d) show the particle number density fields for those intermediate Stokes numbers. Particle segregates around larger vortices, resulting in bigger patterns in the density field.
- For $\mathrm{St}_L > 1$, all Stokes numbers are now larger than one, and all particles will pass through vortices of any size without being greatly affected. The PTC occurs for all particles anywhere in the flow. This is illustrated in Figs. 10.1(e) and 10.1(f) in which particles tend to sample the space uniformly again.

Thus, the larger the Reynolds number, the more PPC and PTC phenomena are involved in a wide range of scales, resulting in different type of patterns in the heterogeneity of the disperse phase. Kinematic simulations can produce velocity fields with large inertial ranges at a very low cost and thus we can observe a PPC and PTC specific to each scale (or Stokes number).

10.1.1 Particle preferential concentration

Figure 10.2 shows the evolution of particle preferential concentration with Stokes number St_η for different inertial ranges, adapted with parameters $j_{\min}$ and $j_{\max}$. The segregation is measured with a box counting method, defined in Sec. 6.2.1.2, with resolution $N_x = 2^6$. The time of measurement is adapted to each simulation, based on the Lagrangian integral time scale. We observe a shift of the PPC curve towards larger Stokes numbers when extending the inertial range. In particular, for $T_L/\tau_\eta \geq 3.75$, the maximum of PPC is not reached for $\mathrm{St}_\eta = 1$ anymore but rather for another $\mathrm{St}_j = 1$. This enhancement of PPC at larger Stokes numbers can be attributed to the interaction of these large-inertial particles with larger scales introduced with the increase of $j_{\max} - j_{\min}$.

10.1.2 Random uncorrelated motion

In Chap. 6 we have introduced a measure of the random uncorrelated motion based on the mean correlated and uncorrelated energies. The ratio of the mean correlated energy (MCE) with the mean total energy (MTE) is plotted for different configurations in Fig. 10.3. As explained in Sec. 6.2.2, we expect this measure to tend towards 1 for particles with very low inertia and to decrease as the Stokes number rises.

Note that the ratio is not always exactly 1 for fluid particles and this discrepancy is related to the chosen projection kernel. If it is too large compared to the smallest vortices, several particles in one

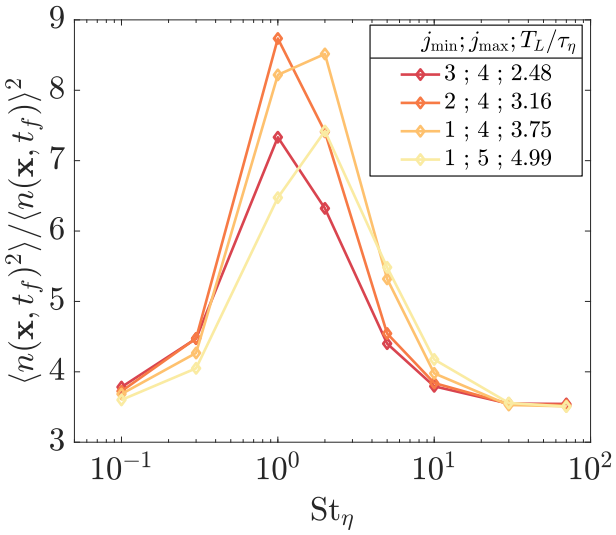

Figure 10.2. PPC as a function of Stokes number St_η for different values of $j_{\min}$ and $j_{\max}$. Inertial ranges are enlarged (from dark to light colors). Corresponding Reynolds numbers can be estimated: $\mathrm{Re}_\lambda = \{31, 40, 47, 62\}$. The parameter λ is set to 0 (frozen turbulence). Particle number density fields are measured on a grid of size 2^6 at time $t_f = 10T_L$.

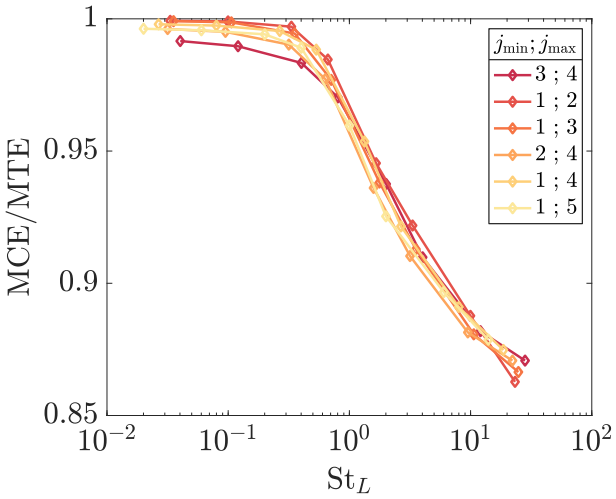

Figure 10.3. Evolution of mean correlated energies (MCE) with the Stokes number for different inertial ranges. The parameter λ is set to 0 (frozen turbulence). Eulerian particle velocity fields are projected on a grid of size 2^6. MCE as a function of Stokes number St_L for different values of $j_{\min}$ and $j_{\max}$. Inertial ranges are enlarged (from dark to light colors). The parameter λ is set to 0 (frozen turbulence). MCE fields are measured on a grid of size 2^6 when staionnary regime is reached.

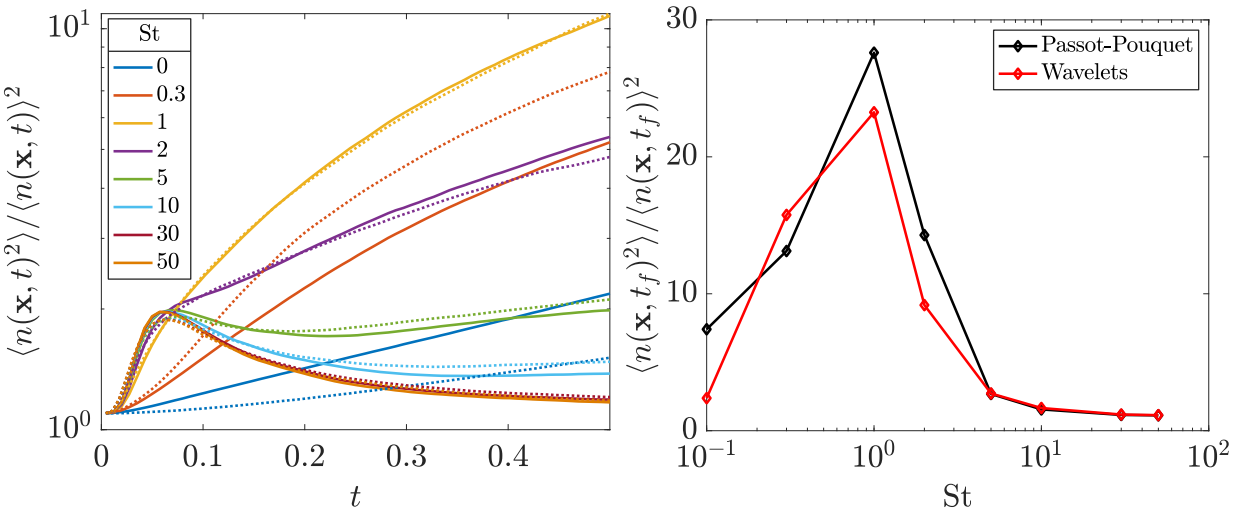

(a) Temporal evolution (b) Final segregation

Figure 10.4. (a) Comparison of the temporal evolution of segregation between the Passot-Pouquet turbulence (full lines) and the wavelet model (dotted line). (b) Final segregation at $t_f \approx 10T_L$.

"box" can have velocity dispersion, hence producing "uncorrelated energy". Apart from this phenomenon, which is indeed noticeable for the configurations with the smallest vortices, we observe a good scaling of all curves when plotted as a function of Stokes numbers St_L. This is consistent with observations of the literature (Février, Simonin, and Squires 2005), showing no dependency on the Reynolds number (see Fig. 6.5).

In Sec. 10.1, we have investigated the influence of the Reynolds number on the disperse phase statistics in a frozen wavelet-based KS, and we show how the interaction between the particles and the vortex structures control the dynamics of the disperse phase. A quantitative comparison is performed using a two-dimensional flow obtained with DNS.

10.2 Validation with 2D frozen turbulence

In frozen turbulence, the characteristic times of vortices are relatively simple to estimate and are related to characteristic length scales. This is already established for the Lagrangian integral time scale, for which $T_L \sim \sigma_u^{-1} L$, and for the Kolmogorov time scale: $\tau_\eta \sim \sigma_u^{-1} L^{1/3} \eta^{2/3}$. Thus, we can argue similarly with intermediate time scales, and we suppose that a vortex of size ℓ_j has a characteristic time related to L and ℓ_j: $\tau_j \sim \sigma_u^{-1} L^{1/3} \ell_j^{2/3}$.

We consider again the case of 2D frozen turbulence described in previous chapter, in Sec. 9.3.1.3. Inertial particles are initially injected at equilibrium with the carrier phase velocity. The temporal evolution of the segregation is shown in Fig. 10.4(a) and we find very comparable trends for the two simulations, for the whole duration of the simulation.

We give in Fig. 10.4(b) the PPC as a function of the Stokes number, at a given time in the simulation such that $t_f \approx 10T_L$. The maximum of PPC is reached for a Stokes number close to 1. This is consistent with conclusions of Sec. 10.1 since there is no separation of scales in the Passot-Pouquet

spectrum. The final segregation, in Fig. 10.4(b) shows that the wavelet model is also qualitatively satisfying for recovering the segregation in frozen turbulence. We observe that for fluid particles, the divergence-free condition is better reproduced with the wavelet-based KS than with the Passot-Pouquet spectrum. This could be due to interpolation schemes: we use spline interpolation with the wavelet-based KS, which is naturally the most adapted since wavelets are based on spline functions of degree 0 and 1. For small-inertia particles, the wavelet-based KS overestimates a bit the segregation. We presume it might be caused by the spurious peaks of large wavenumbers observed in the energy spectrum in Fig. 9.15(a).

Still, this comparison validates the behavior of particles in the synthetic wavelet field before introducing the additional complexity related to the modeling of its dynamics.

10.3 Influence of λ

In dynamic turbulence, vortices are created, transformed, deformed and die, and their characteristic time is therefore much more difficult to estimate. However, we know that it is necessarily reduced compared to that in frozen turbulence. The particles in a vortex do not necessarily have the time to reach their maximum segregation, the vortex having changed in the meantime.

Figure 10.5(a) compares the time evolution of PPC in a frozen ($\lambda = 0$) and in a dynamic wavelet-based KS ($\lambda = 0.5$). We observe that the disperse phase reaches a stationary regime for PPC when $\lambda \neq 0$. We expect the stationary regime to be reached for $t > \max(T_{E,j})$, the maximum eddy turnover time of wavelet-based KS. On the other hand, with $\lambda = 0$, PPC keeps increasing for particles such that $\mathrm{St}_L < 1$.

Figure 10.5(b) shows the segregation for different values of λ, measured at time $30T_L$. We can clearly see that λ controls the intensity of PPC. As expected, the dynamics introduced by the eddy turnover time slows down the segregation of particles.

In Fig. 10.6(a), we compare the temporal evolution with a logarithmic scale of the MCE for a frozen and a dynamic wavelet-based KS. Both simulations reach stationary statistics, and we notice that large-inertia particles reach their stationary MCE later than small ones. The stationary statistics obtained with $\lambda \neq 0$ are more noisy, due to the stochastic Langevin equation for coefficients. Figure 10.6(b) shows the influence of the parameter λ on the mean correlated energies of the disperse phase. It seems that the particle trajectory crossing is not strongly affected by the sweeping phenomena induced by λ. It will not possible to adapt this parameter in order to control the prediction for this statistics.

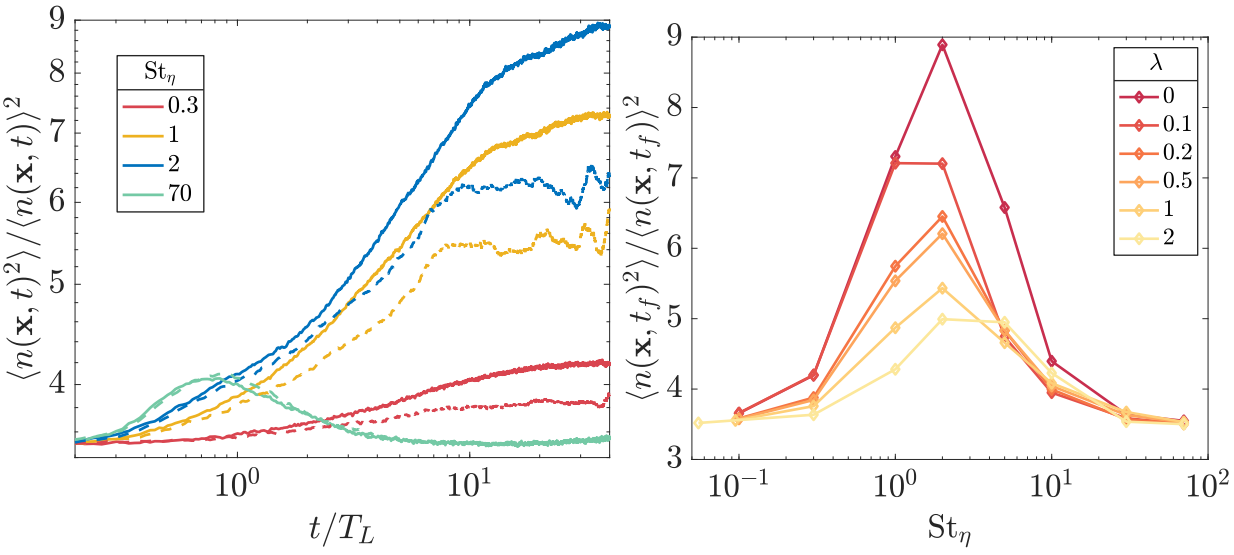

(a) $\lambda = 0$ (b) $\lambda = 0.2$

Figure 10.5. (a) Temporal evolution of PPC for $\lambda = 0$ (full lines) and $\lambda = 0.5$ (dotted lines), with logarithmic temporal scale. (b) Influence of λ on the PPC as a function of the Stokes number St_η. PPC is measured at time $30T_L$, with a grid resolution of 2^6.

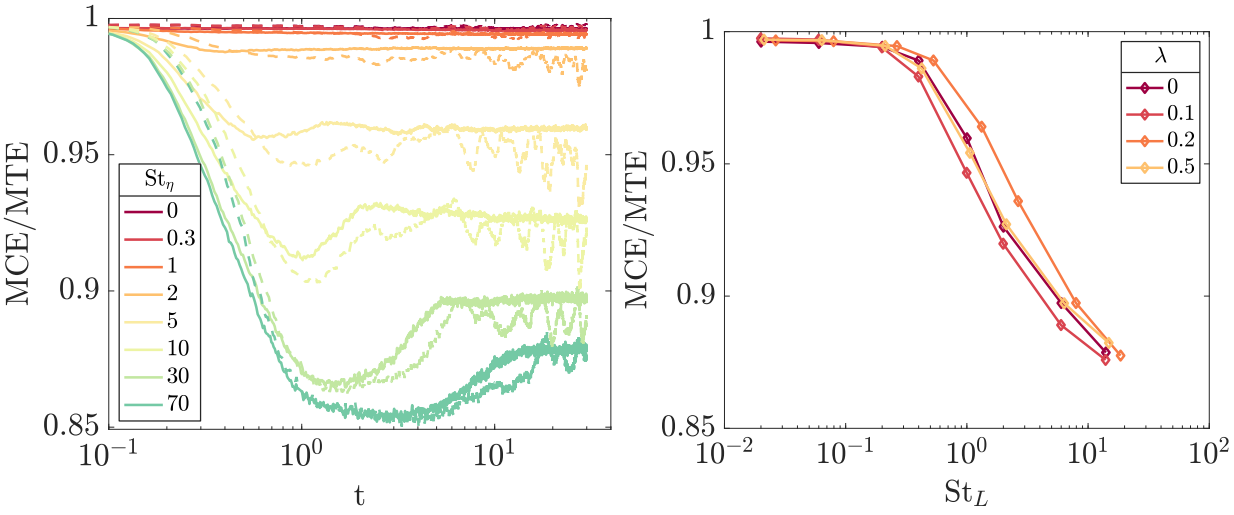

(a) Temporal evolution (b) Stokes number dependency

Figure 10.6. (a) Comparison of the temporal evolution of the MCE for $\lambda = 0$ (full lines) and $\lambda = 0.1$ (dotted lines), plotted for different Stokes numbers with logarithmic temporal scale. (b) Stationary MCE as a function of the Stokes number, plotted for different values λ. $j_{\min} = 1$ and $j_{\max} = 5$. Eulerian particle velocity fields are projected on a grid of size 2^6.

10.4 Validation with DNS of 3D HIT and comparison with Fourier-based KS

We now seek to validate the 3D wavelet-based KS with time evolution, which ensures stationarity of the disperse phase statistics. We consider the DNS case described in the previous chapter, in Sec. 9.4, on the 128^3 mesh. Energy spectra, snapshots of the velocity field and autocorrelation of fluid particles have already been compared with Fourier-based KS and wavelet-based KS and the latter shows better agreement with the DNS of HIT.

We plot in Fig. 10.7 the segregation according to the inertia of the particles and compare the results obtained in DNS, with stationary wavelet and Fourier-based KS. The best agreement is obtained with the wavelet-based KS, for $\lambda \approx 0.5$, which not only predicts the correct peak of segregation, but also correctly reproduces the preferential concentration for all $\mathrm{St}_\eta > 1$. The PPC is underpredicted for small Stokes numbers, and this might be related to the rapid decorrelation of small scales observed in Chap. 9. The eddy turnover of small scales is probably too high and this excessively reduces the segregation at those specific scales.
We can see that in this case, there is no scale separation because the peak is reached at $\mathrm{St}_\eta = 1$. Indeed, the Reynolds number of this DNS is $\mathrm{Re}_\lambda = 50$. However, the segregation obtained with Fourier-based KS is shifted towards larger values of Stokes numbers. This shift was already observed in Murray, Lightstone, and Tullis (2016a). This shows that small scales are probably not well reproduced.

Figure 10.8 shows the evolution of the mean correlated energy with the Stokes number for the three simulations (DNS, wavelets, Fourier). Overall, we observe a satisfactory agreement with DNS for both wavelets and Fourier. A small shift of the curve towards larger Stokes numbers is present, and is more significant in the case of the Fourier-based KS, consistent with the shift in the PPC.

The collective behavior of the particles, measured through particle segregation and trajectory crossing, seems to be better predicted qualitatively and quantitatively by wavelet-based KS than with Fourier-based KS. In addition, recall that in the dynamic case, the field obtained with a Fourier-based KS produces nonphysical oscillating Lagrangian statistics (see Chap. 9).

Conclusion

This chapter has demonstrated that the wavelet-based kinematic model can recover the main properties of the disperse phase in a turbulent flow. High Reynolds number simulations show that the PPC and PTC phenomena can affect a wide range of scales, which indicates that the particles interact with all scales of the turbulent surrogate model. The parameter λ, characterizing the eddy turnover velocity, can be fitted to retrieve the accurate PPC of a reference DNS.

The wavelet model has been validated on a two-dimensional frozen turbulence, and displays a similar temporal evolution compared to the one in the DNS field. The wavelet-based KS can recover qualitatively and quantitatively the PPC of a 3D stationary HIT, while the Fourier-based KS shifts the segregation towards higher Stokes numbers. The eddy turnover time of small scales might be mispredicted by the proposed model for ω_j and further investigations could be made to improve

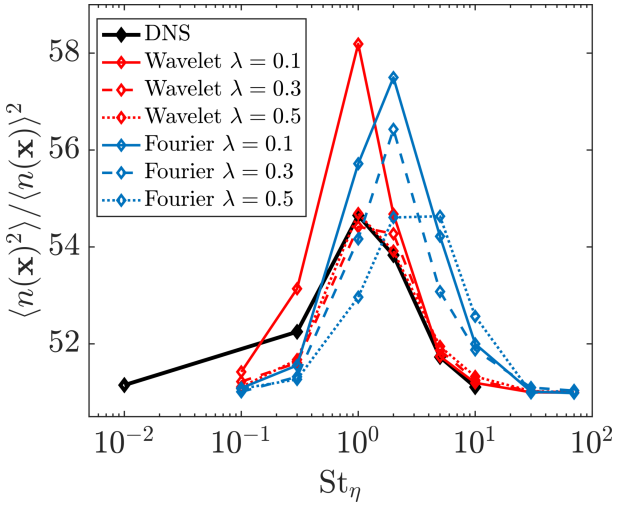

Figure 10.7. Evolution of particle preferential concentration with Stokes number obtained with DNS, wavelet and Fourier-based KS for different values of λ.

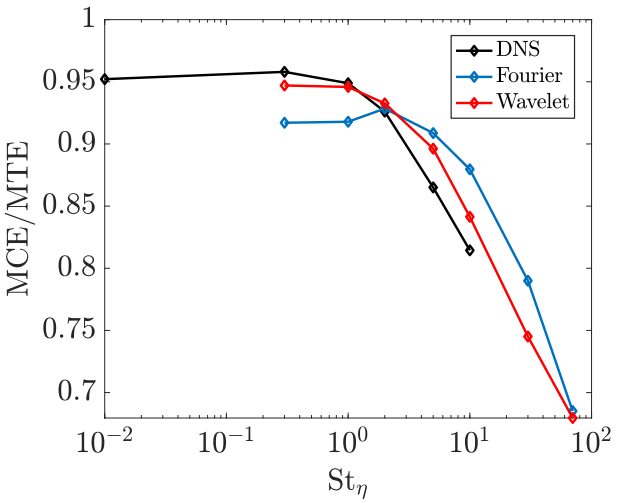

Figure 10.8. Measure of the normalized mean correlated energy for DNS, Fourier-based and wavelet-based KS ($\lambda = 0.5$). Eulerian particle velocity fields are projected on a grid of size 2^4.

their modeling.

The wavelet-based kinematic model can thus reproduce the segregation of particles in a HIT, and the proposed temporal evolution scheme for the coefficients ensures stationary statistics and control of the sweeping level. Many perspectives remain to be explored for the use of such a particle SFS model in the framework of a ROS. Improvements, in particular concerning the temporal evolution model, can be considered. These are discussed in the next chapter in view of reproducing the intermittent statistics of the velocity field or reducing the dimensionality of the model.

Chapter 11

Perspectives for wavelet-based kinematic simulation

This thesis aims at developing a particle SFS model for reduced-order simulations of turbulence in a two-way coupling context; the key point is to reproduce in particular segregation and intermittency. The wavelet-based KS is validated as a DNS surrogate for respectively basic turbulent statistics in Chap. 9 and particles statistics in Chap. 10. We still need to verify the higher-order statistics (i.e., intermittency) and discuss the applicability of such a model in reduced-order simulations constrained by computational cost (in time and memory). The two-way aspects are left to Chap. 14.

In Sec. 11.1, we show that although naturally intermittent, the wavelet-based kinematic model should be adapted in order to reproduce the level of intermittency obtained in DNS. Section 11.2 focuses on the adaptation of wavelet-based KS into ROS framework. In particular, similar to Fourier framework, compression is well suited for wavelet fields (Farge and Schneider 2005) and can be used to reduce the dimensionality of the synthetic fluid significantly.

11.1 Intermittency in wavelet-based KS

11.1.1 Comparing intermittency in kinematic simulations

We measure the flatness of the velocity increments along the fluid particle trajectories for the DNS and the kinematic models and compare the results in Fig. 11.1. We have displayed the characteristic times τ_η and T_L to identify the inertial zone on the abscissa. Consistent with the DNS results of Chap. 1, the flatness of the DNS is very high for small increments and decreases down to the Gaussian value 3, reached for increments such that $\tau \gg T_L$. We can notice that none of the two kinematic models, whatever the parameter λ, reaches the level of intermittency of DNS in the dissipation zone.

The flatness of the wavelet-based KS initially decreases slightly in the dissipative zone, then stabilizes at a constant value in the inertial zone before decreasing to 3, the Gaussian-like value. We notice that the wavelet model is not very sensitive to the parameter λ. Only a small shift is observed for models with $\lambda \neq 0$, departing sooner from the plateau, consistent with the observation made in Chap. 9 that the value of T_L decreases slightly when $\lambda \neq 0$.

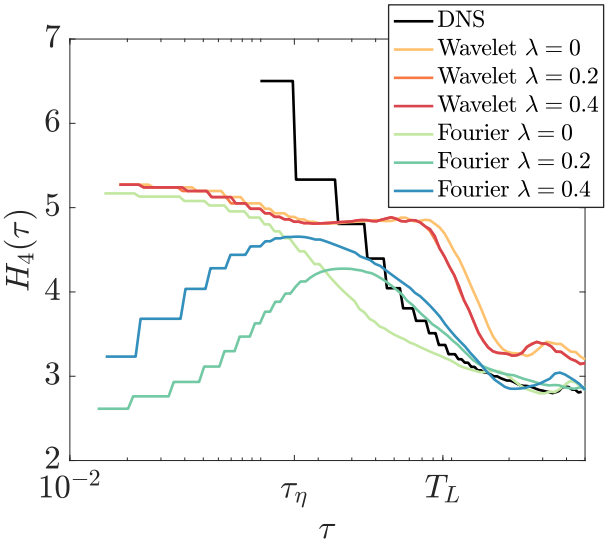

Figure 11.1. Flatness of the Lagrangian fluid velocity increments obtained with DNS, wavelet and Fourier-based KS for different values of λ.

The Fourier model at $\lambda = 0$ follows the same decrease along the inertial range. We observe that the two kinematic models have a quasi-identical flatness along the entire dissipative zone, and that it is underestimated compared to the reference flatness of the DNS. Moreover, it should be noted that the sampling time step of the DNS is not small enough to capture the behavior in the dissipative range and therefore the flatness in this zone, but it is at least higher than 6.5. The flatness of the Fourier model is much more surprising for $\lambda \neq 0$: it is close to 3 for the acceleration (or small increments). It rises to reach its maximum in the inertial zone and then decreases as expected for large increments. The initial value of 3 is highly criticizable, it shows a Gaussian behavior of the acceleration, revealing a new limitation of the dynamic Fourier model.

We seek to propose an adapted wavelet-based kinematic model by introducing a coherent cascade of energy that enhances the intermittency of the acceleration statistics and reproduces the progressive decay observed in the DNS along the inertial zone.

11.1.2 Towards an intermittent cascade of wavelets

The forcing scheme proposed in Sec. 9.3.2, based on a Langevin equation for each coefficient, ensures the stationarity of all scales by enforcing a spectral model. It consists of superimposed images of turbulence but the vortices do not interact with each other. However, we know that intermittency comes from the transfer of energy between the different scales of the flow. In particular, processing all scales in the same way probably leads to the typical plateau in the inertial zone observed in Fig. 11.1 instead of a gradual decay. Therefore, another scheme of evolution for the wavelet-based KS, capable of reproducing the energy transfer between scales, could be developed.

In order to propose such a model, we are interested in the Eulerian cascade models of intermittent dissipation proposed in the literature and we compare their predictions with the statistics of a DNS. Afterwards, we discuss a possible approach for implementing these models in the wavelet-based kinematic simulation.

11.1.3 An overview of discrete cascade models

The reader is referred to Chap. 1, Sec. 1.3.2 for an introduction on the discrete cascade model formalism. We recall that in such approaches, the domain is subdivided into cells of size $\mathcal{L}/2^j$ and the dissipation at scale ℓ_j is given by:

$$\varepsilon_{\ell_j} = \alpha_1\alpha_2...\alpha_j\mathbb{E}\left[\varepsilon\right], \tag{11.1}$$

where the random variable α_i yield different models of intermittency. Indeed, we obtained a scaling for the moments of coarse-grained dissipation as follows:

$$\mathbb{E}\left[(\varepsilon_{\ell_j})^p\right] = \mathbb{E}\left[\varepsilon\right]^p \left(\frac{\ell_j}{L}\right)^{K(p)}, \tag{11.2}$$

where $K(p) = -\ln_2 \mathbb{E}\left[\alpha^p\right]$. This exponent can be related with the structure function exponent $\xi(p) = K(p/3) + p/3$. In the following, we present three models for α.

The log-normal model

Yaglom (1966) assumed a log-normal distribution for α. We have already explored this model in a Lagrangian framework and we retrieve a quadratic form for $K(p) = \dfrac{\lambda_I}{2}(p^2 - p)$, where $\lambda_I = K(2)$ is the so-called intermittency parameter. The structure function exponent in this case is $\xi(p) = \dfrac{p}{3} - \dfrac{\lambda_I}{18}(p^2 - 3p)$

The β-model

The initial assumption is to consider that only a fraction β^n of the domain has energy. Assuming that the smaller eddies, the less space they fill, we introduce ψ the probability for an eddy to generate an "active" eddy. If the largest eddies are space filling, then after n iterations, only a fraction of the space is occupied by active fluid. Introduced by Frisch, Sulem, and Nelkin (1978), the random variable α can only take two values according to the following probabilities:

$$P(\alpha = 0) = 1 - \psi \tag{11.3}$$
$$P(\alpha = \gamma) = \psi, \tag{11.4}$$

and conservation of mean dissipation implies $\gamma = 1/\psi$. We introduce the fractal dimension D also called self-similarity dimension $\psi = 2^{D-3}$. In the well-known cases where $D = 1$, 2 or 3, the objects are therefore intervals, squares or cubes. This model leads to:

$$K(p) = \lambda_I(p-1), \quad \xi(p) = \frac{p}{3} - \lambda_I(\frac{p}{3} - 1), \tag{11.5}$$

where $\lambda_I = K(2)$ is still defined as the intermittency parameter and we note here that $D = 3 - \lambda_I$, where λ_I is equivalent to a codimension.

The random β-model

Benzi, Paladin, Parisi, and Vulpiani (1984) suggested to improve the β-model by considering a random factor ψ instead of a fixed one. The factor is independently selected at each step of the

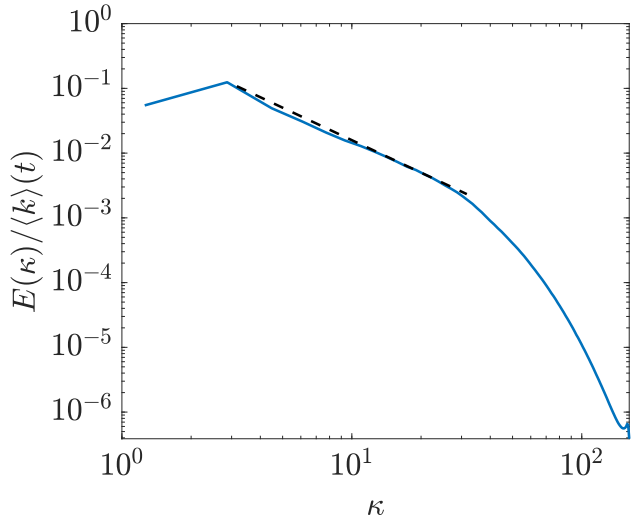

Figure 11.2. Normalized energy spectrum. Dotted line shows the $-5/3$ slope characteristic of the inertial range.

cascade following a binomial distribution:

$$\begin{aligned} P(\psi = \frac{1}{2}) &= 1 - x \\ P(\psi = 1) &= x \end{aligned} \tag{11.6}$$

This gives:

$$\begin{aligned} K(p) &= \log_2(1 - x + x2^{p-1}) \\ \xi(p) &= \frac{p}{3} - \log_2(1 - x + x2^{p/3-1}) \end{aligned} \tag{11.7}$$

A reasonable agreement was found for $x = 0.125$ for low order exponents.

Comparison of discrete models

The validation of these models can only be done by comparison with experimental or DNS results. However, as mentioned in Chap. 2, simulations at high Reynolds number, for which a large inertial zone can give sufficient statistics, are very expensive. It is therefore difficult to find results on high order statistics of velocity increments in the literature.

We perform DNS to solve the unsteady three-dimensional Navier-Stokes and continuity equations with Asphodele (see Sec. 2.4). Figure 11.2 shows the energy spectrum of the flow at a given time and exhibits a clear inertial range for $\kappa \in [5; 30]$, corresponding to length scales of $[0.21; 1.26]$ and grid spacing size $r/\Delta x \in [10; 60]$. Figure 11.3(a) shows the longitudinal velocity increments of different orders p. We interpolate the curves in the inertial range with linear expressions in log-log scale and obtain the exponents of the velocity increments $\xi(p)$ in Fig. 11.3(b). The different models of literature are compared to the DNS measures and to K41 model where no intermittency is modeled.

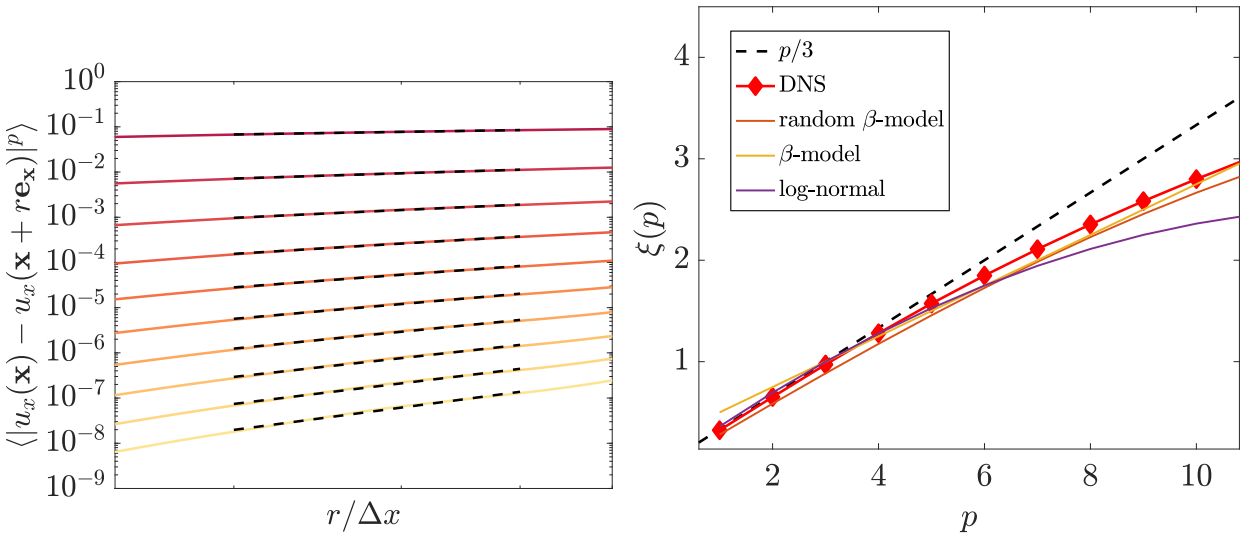

Figure 11.3. (a) Structure functions of order $p \in [1; 10]$ (from dark to light colors) with linear fitting in the inertial range (dashed black lines). (b) Scaling exponents of the structure functions. The dotted line shows the K41 law: $\xi(p) = p/3$ and the solid red line is the DNS measure.

First of all, models predict approximately the same evolution for the first 6 moments, and the behaviors diverge for moments of higher orders, for which unfortunately the measurement uncertainty on the DNS results is also increased. However, and this is confirmed in the literature, the log-normal model and the β-model are less satisfying than the random β-model (Anselmet, Gagne, Hopfinger, and Antonia 1984). Let us now give some perspectives on the use of such models in wavelet-based KS.

11.1.4 A perspective for intermittent KS

Such Eulerian model apply well to the case of discrete wavelets, since in both cases, the domain is divided into sub-domains of size $\ell_j = \mathcal{L}/2^j$. In the wavelet-based KS framework, each cell $\{j, \boldsymbol{k}\}$ is associated to a velocity coefficient $d^{\varepsilon}_{\text{div},j,\boldsymbol{k}}$. In the cascade model, each cell $\{j, \boldsymbol{k}\}$ is associated to a local dissipation, and more precisely to a random variable $\alpha_{j,\boldsymbol{k}}$, which represents the ratio between the local dissipation of the cell $\varepsilon_{j,\boldsymbol{k}}$ and its mother cell's dissipation $\varepsilon_{j-1,\boldsymbol{k}'}$.

In future works, one can design a law of evolution of the vortices of size $j+1$ according to the local vortices of size j which corresponds to an intermittent model. Thus, forcing the largest scales would naturally dissipate and feed the smaller vortices. This could result for instance in an "inter-level" conditional Gaussian distribution for the coefficients $d^{\varepsilon}_{\text{div},j,\boldsymbol{k}}$, in the sense that the PDF of a coefficient $\{j+1, \boldsymbol{k}\}$ would depend on the value of its mother cell's coefficient $\{j, \boldsymbol{k}\}$.

The random β-model provides good agreement of the intermittency coefficient with DNS measures and is promising in terms of memory cost, since "dead" eddies correspond to zero wavelet coefficients. Indeed, the dimensionality of the problem is one of the key aspects to handle if we want to apply the KS in the framework of reduced-order and numerically affordable models.

11.2 Towards reduced-order simulations

This section focuses on the implementation of the wavelet-based KS into ROS. Two of the main issues for ROS are the computational and the memory cost. The generation of random coefficients and their stochastic evolution according to an Ornstein-Uhlenbeck process is straightforward and certainly avoids the complexity of the numerical solution of the Navier-Stokes equations. However, in its current form, it requires storing a large number of coefficients. The compression of the wavelet fields is therefore studied in Sec. 11.2.1 and 11.2.2 and a time evolution scheme for the coefficients is proposed in Sec. 11.2.3.

Finally, so far we have considered the kinematic simulation as a RANS model, i.e., in a way that reproduces the whole turbulent flow. For LES applications, we intend to adapt the KS to a sub-grid model consistent with the resolved scales in Sec. 11.2.4.

11.2.1 Compression of the wavelet field

We have to consider the memory space necessary to store all the coefficients. For a cubic periodic box, the number of coefficients is as follows:

$$N_c = \sum_{j=j_{\min}}^{j_{\max}} (2^j)^{N_d} = \frac{2^{N_d(j_{\max}+1)} - 2^{N_d j_{\min}}}{2^{N_d} - 1} \sim (2^{j_{\max}})^{N_d} \tag{11.8}$$

where we note N_d the number of dimensions on the physical domain to consider.
However, if we aim at reproducing the smallest scales, up to the Kolmogorov scale for example, we have to set $\ell_{max} = \mathcal{L}/2^{j_{\max}} \leq \eta$, which is therefore equivalent to the criterion for solving a DNS, given in Sec. 2.1: $\mathcal{L}/N_x \leq \eta$. We would need at least $(N_x)^{N_d}$ coefficients, which is the same amount of information as for a DNS. Therefore, we are interested in dimensionality reduction.

One idea is to take advantage of wavelet compression. So far, for each level, the idea was to draw random coefficients according to a normal law. This operation is not as computationally expensive as the Navier-Stokes resolution can be, however it requires a lot of memory, since all coefficients of each level must be stored. The idea with compression is to threshold coefficients below a certain absolute value. This way, most coefficients are set to 0 and do not need to be kept in memory. In that case, detailed coefficients can be drawn according to a truncated normal distribution.

11.2.2 Truncated normal distribution

We introduce the truncated normal distribution, derived from a normally distributed random variable by bounding the random variable.

Suppose X has a normal distribution with mean μ and variance σ^2. For a given interval $-\infty \leq a \leq b \leq +\infty$, we build the truncated normal distribution of Y that rejects all random values inside

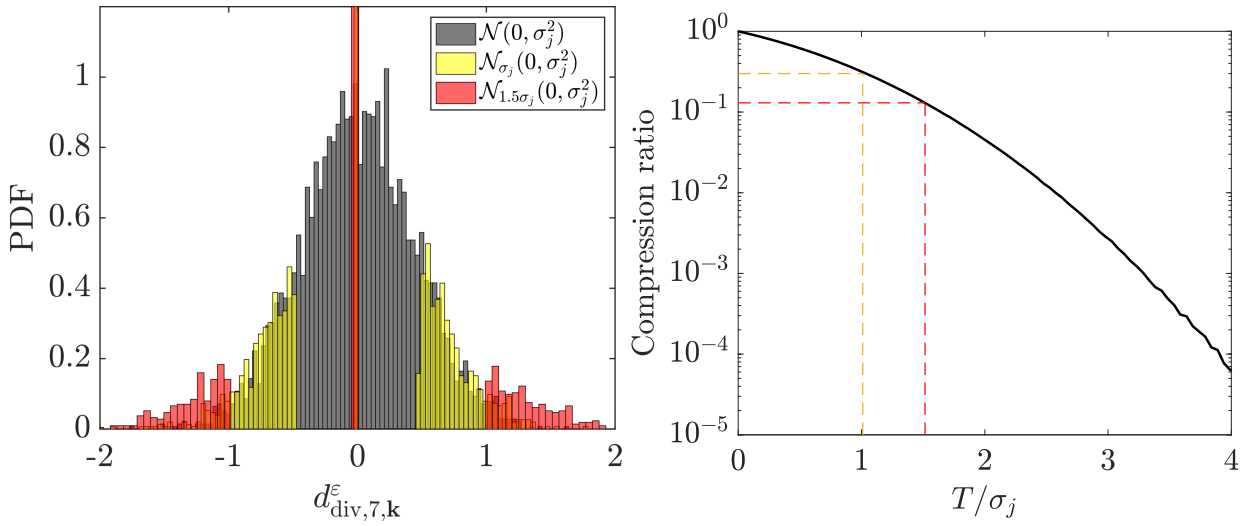

(a) (b)

Figure 11.4. (a) PDF of detailed coefficients $d^{\varepsilon}_{\mathrm{div},7,\boldsymbol{k}}$ in black, following a normal distribution. The yellow distribution corresponds to a compression ratio of 0.3 and the red one to 0.13 with the threshold method. (b) Compression ratio as a function of the threshold normalized by σ_j. Corresponding values of $T = \sigma_j$ and $T = 1.5\sigma_j$ are reported in yellow and red.

the interval $[a, b]$ and sets them to 0:

$$\begin{cases} P(Y \leq a) &= F_X(a), \\ P(Y \geq b) &= 1 - F_X(b), \\ P(Y = 0) &= F_X(b) - F_X(a), \end{cases} \tag{11.9}$$

where F_X is the cumulative distribution function of the Gaussian distribution:

$$F_X(x) = \frac{1}{2}\left[1 + \mathrm{erf}\left(\frac{x-\mu}{\sigma\sqrt{2}}\right)\right]. \tag{11.10}$$

In the following, we consider the symmetric truncated normal distribution of threshold T, with rejection interval given by $[-T; T]$ and noted $\mathcal{N}_T$.

The distribution of coefficients at level $j = 7$ is given for different thresholds in Fig. 11.4(a). The dark distribution is the normal one, with a storage capacity of 100%: it follows a Gaussian distribution. The yellow distribution of coefficients is thresholded at $T = \sigma_j$, and only retains 30% of the total coefficients. The red distribution which is thresholded at $1.5\sigma_j$ requires to store only 13% of the total number of coefficients: one can notice the peak in the histogram for the zero values: 87% of coefficients are null in that case.

Let us compare the velocity fields obtained after such compression. Figure 11.5(a) represents the velocity field obtained with normal distribution of all coefficients for all levels and its memory storage is therefore given by Eq. (11.8). Thresholding those distributions up to $T = \sigma_j$ produces the velocity field in Fig. 11.5(b), and we can see only few qualitative changes between the two snapchots. Considering their respective energy spectrum, no change can be reported from Fig. 11.5(d):

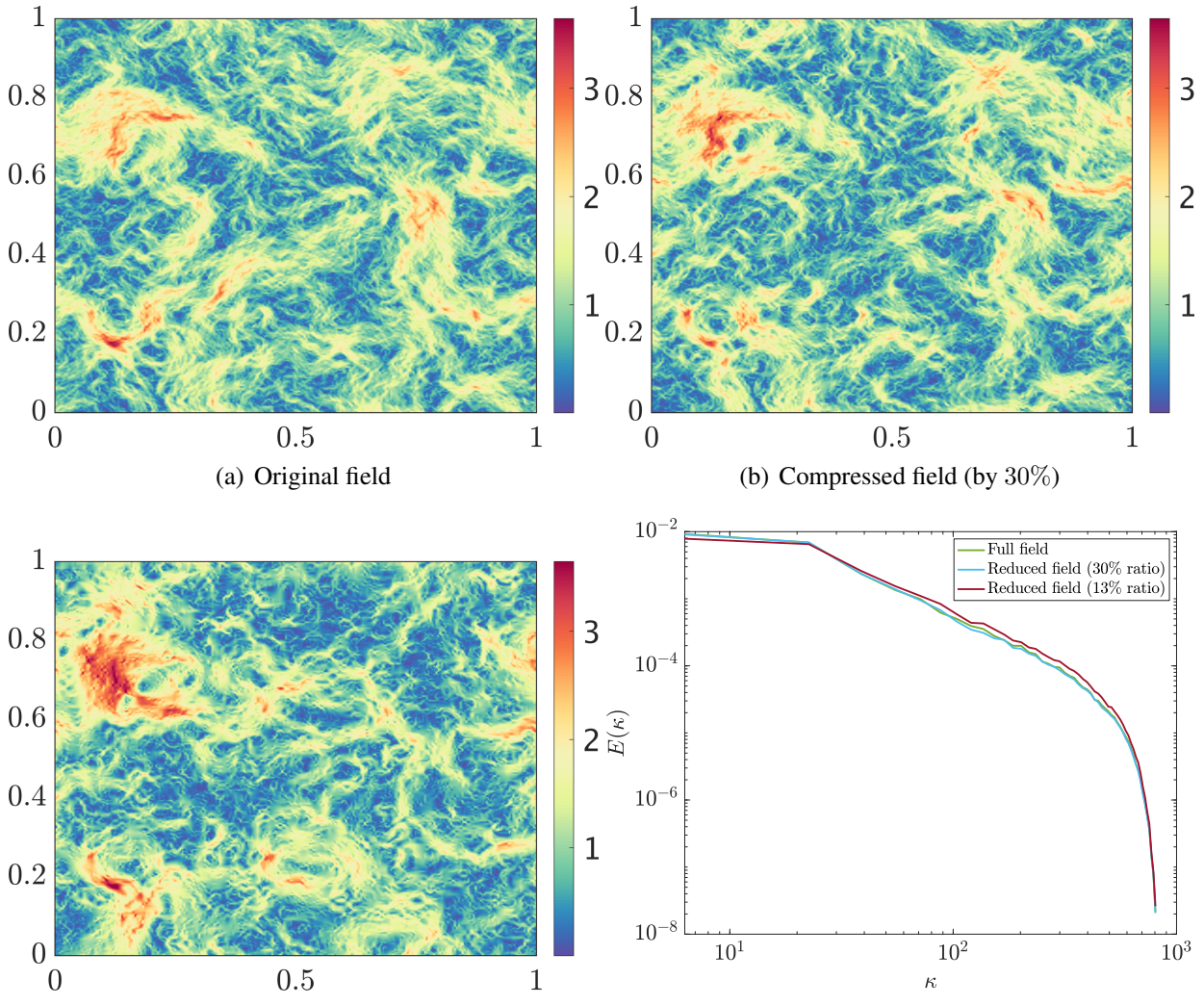

(a) Original field (b) Compressed field (by 30%)

(c) Compressed field (by 13%) (d) Energy spectra

Figure 11.5. Snapshots of the velocity field with 100% (a), 30% (b) and 13% (c) of the wavelet coefficients. Associated energy spectra (d).

all scales are still well-reproduced with the appropriate level of energy. This is consistent with the fact that at all wavenumbers, only insignificant energetic vortices have been removed. With higher compression rate, if we retain only 13% of total coefficients, we observe more differences in the field, although some typical vortices can still be identifiable. Regarding its energy spectrum, the behavior is still well reproduced at all scales.

The compression significantly reduces the memory cost, as quantified in Fig. 11.4(b) where the ratio of compression is plotted. It would be worth further investigating the impact of compression on the velocity field with appropriate metrics. Of course, larger values of T reduce the storage, but a trade-off must be found so that the number of non-zero coefficients remains statistically significant (i.e. enough to obtain converged statistics).

11.2.3 Sinusoidal temporal evolution of coefficients

Such a compression of the coefficients is not compatible with the stochastic time evolution law. Indeed, after that the initial field has been drawn with thresholds coefficients, what temporal evolution should be applied to the zero coefficients? If we apply the Langevin equation Eq. (9.35) to all coefficients, they immediately risk to become non zero and therefore we loose the compression effect. Non-zero coefficients, on the other hand, can see their energy decrease and fall below the threshold criterion. Ornstein-Uhlenbeck processes are stationary only if a normal distribution is chosen as the initial distribution. Otherwise, it will progressively relax the distribution of the statistics towards a normal distribution. However, we would like to keep a small number of coefficients to be stored throughout the simulation. Another approach for the evolution must be considered.

This technique is inspired by the proper orthogonal decomposition, where the spatio-temporal field is decomposed into a deterministic spatial function modulated by a temporal coefficient. Let us consider two velocity fields, generated by truncated normal distributions of coefficients $d^{\varepsilon,1}_{\mathrm{div},j,\boldsymbol{k}}$ and $d^{\varepsilon,2}_{\mathrm{div},j,\boldsymbol{k}}$ thus both having a reduced form and a low storage cost. We then define the coefficients of the model as a linear combination of these two fields:

$$d^{\varepsilon}_{\mathrm{div},j,\boldsymbol{k}} = \cos(2\pi\omega_j t) d^{\varepsilon,1}_{\mathrm{div},j,\boldsymbol{k}} + \sin(2\pi\omega_j t) d^{\varepsilon,2}_{\mathrm{div},j,\boldsymbol{k}}. \tag{11.11}$$

With this approach, we only have to store twice as many coefficients as for a single draw of the truncated normal distribution.

To avoid a time periodicity of the field, it is necessary to regularly renew the two coefficients $d^{\varepsilon,1}_{\mathrm{div},j,\boldsymbol{k}}$ and $d^{\varepsilon,2}_{\mathrm{div},j,\boldsymbol{k}}$. We propose to draw new coefficients as follows:

- when $2\omega_j t \in \mathbb{N}$ (i.e. $\sin(2\pi\omega_j t) = 0$) we draw $d^{\varepsilon,2}_{\mathrm{div},j,\boldsymbol{k}} \sim \mathcal{N}_T(0, \sigma_j^2)$;
- when $2\omega_j t - 1/2 \in \mathbb{N}$ (i.e. $\cos(2\pi\omega_j t) = 0$) we draw $d^{\varepsilon,1}_{\mathrm{div},j,\boldsymbol{k}} \sim \mathcal{N}_T(0, \sigma_j^2)$.

This temporal evolution is illustrated for one coefficient $d^{\varepsilon}_{\mathrm{div},j,\boldsymbol{k}}$ given as an example, in Fig. 11.6(a). The dashed lines represent coefficients $d^{\varepsilon,1}_{\mathrm{div},j,\boldsymbol{k}}$ and $d^{\varepsilon,2}_{\mathrm{div},j,\boldsymbol{k}}$, the evolution of which is incremental, due to a new draw at each period. Periods of the two coefficients are shifted so that the coefficient is changed when the sinus or cosinus becomes zero. The dotted lines display these fields with a sinusoidal multiplicative factor and their sum gives the final coefficient in black line.
Figure 11.6(b) details the same construction but with a truncated normal law for $d^{\varepsilon}_{\mathrm{div},j}$. In that case, $d^{\varepsilon,1}_{\mathrm{div},j}$ or $d^{\varepsilon,2}_{\mathrm{div},j}$ are more often drawn as zero, and therefore $d^{\varepsilon}_{\mathrm{div},j}$ can also sometimes become null.

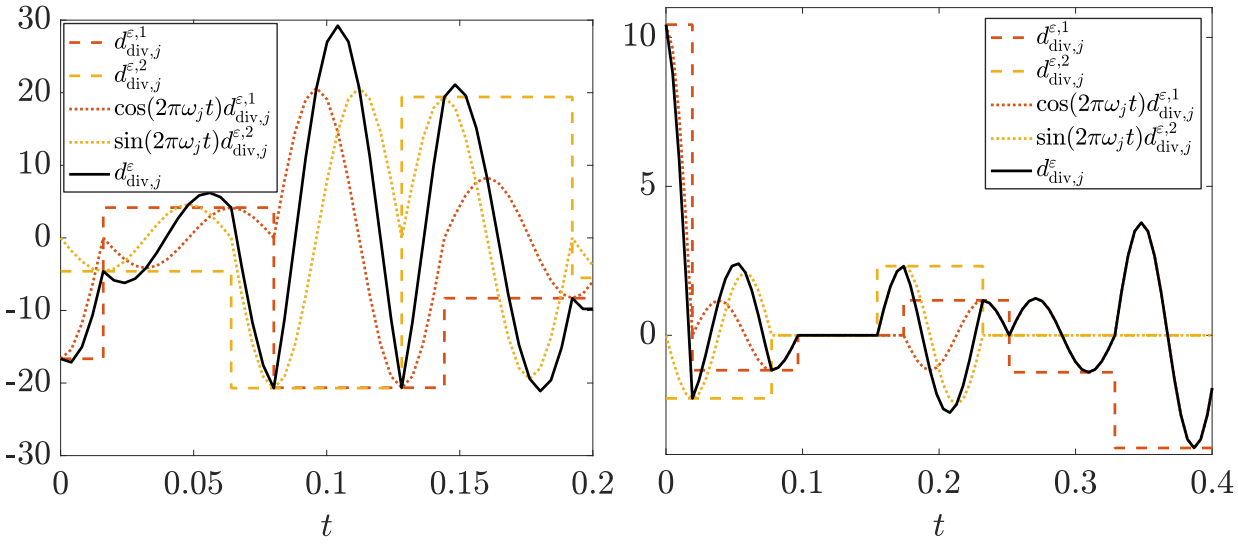

(a) $d^{\varepsilon}_{\mathrm{div},j} \sim \mathcal{N}(0, \sigma_j^2)$ (b) $d^{\varepsilon}_{\mathrm{div},j} \sim \mathcal{N}_{0.5\sigma_j}(0, \sigma_j^2)$

Figure 11.6. Black line represents the temporal evolution of one coefficient following Eq. (11.11). We show the evolution of the two coefficients used in its construction in dashed lines, and weighted by cosinus and sinus function in dotted lines. Distributions are Gaussian (a), truncated Gaussian (b).

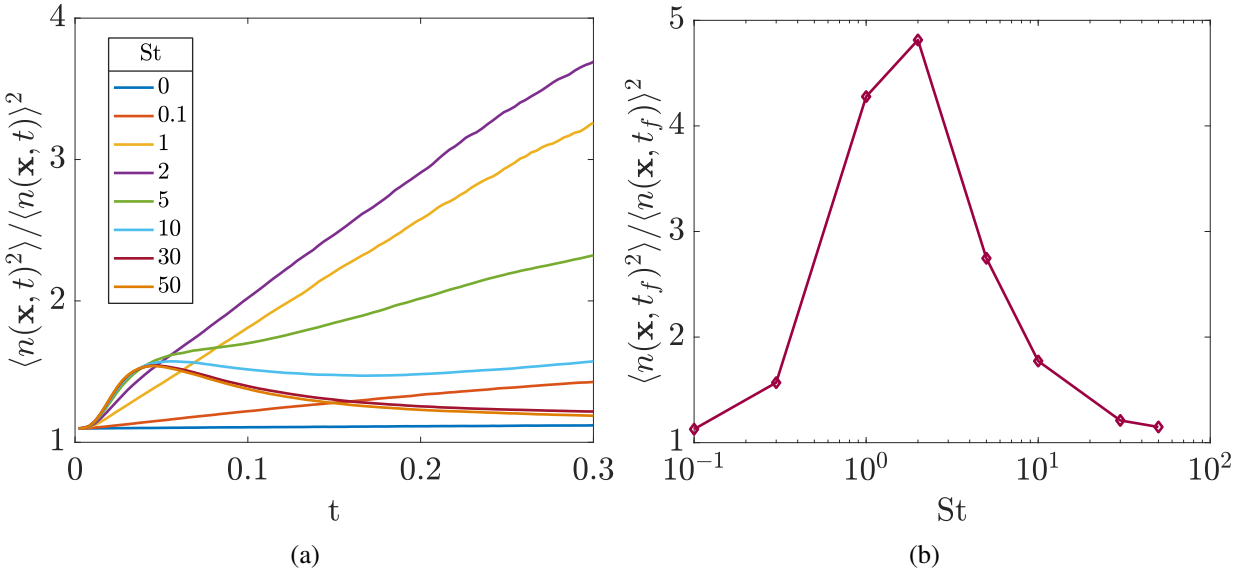

(a) (b)

Figure 11.7. (a) Temporal evolution of PPC and (b) PPC at $t_f = 10T_L$ as a function of Stokes number. Parameters of the model are $j_{\min} = 2$, $j_{\max} = 6$, $\lambda = 0.1$. The evolution of coefficients is following Eq. (11.11).

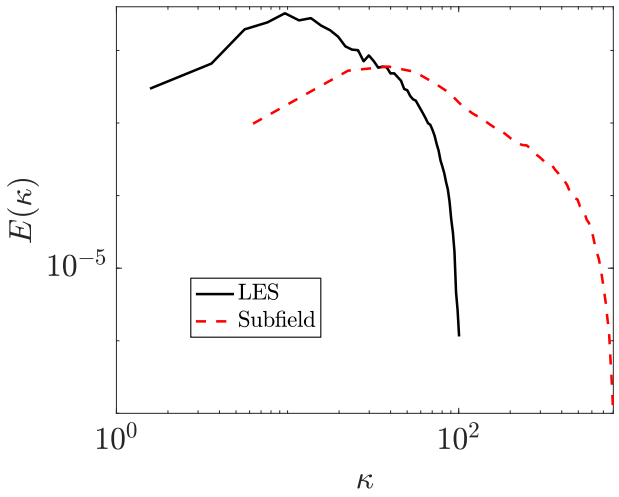

Figure 11.8. A LES-like energy spectrum completed with a synthetic flow, with $\kappa_0 = 1/2$, $\kappa_{\min}$ corresponding to $\kappa_c = 64$ and $\kappa_{\max} = 512$.

Such temporal evolution scheme is implemented and PPC is analyzed. Even though more thorough validations should be conducted (following the analyses of previous chapter), we can already observe on the test case presented in Figs. 11.7(a) and 11.7(b) the same temporal trend and final PPC as with the stochastic Langevin model.

11.2.4 A sub-grid velocity model for LES

Wavelet-based KS can be considered as a velocity sub-grid model for LES. This strategy has been first developed by Flohr and Vassilicos (2000) for Fourier-based KS but can be adapted with the use of wavelets. The sub-grid velocity field of the flow has its spectral model extended from κ_c, the LES cut-off wavelength, to the Kolmogorov length κ_η. However, instead of prescribing a unique law σ_j for the coefficients of the whole space, they take into account the local information of the sub-grid to which they belong. The local variance is hence given by:

$$\sigma_j^2 = \sigma_\star^2 \kappa_0^{2/3} \kappa_j^{-5/3} \Delta\kappa_j / \sigma_{j,\text{ref}}^2. \tag{11.12}$$

We set $\ell_{min} = \Delta$, or equivalently $\kappa_{\min} = \kappa_c$, so that the largest scale of the sub-grid field corresponds to the smallest scale of resolution of the LES field, and $\kappa_{\max}$ can also be locally adapted to retrieve the correct sub-grid scale dissipation $\varepsilon_\star$. This ensures the continuity of the energy spectrum. An example of the energy spectrum reconstruction is shown in Fig. 9.9(c) and retrieves a large inertial range, similar to a DNS-like energy spectrum.

Conclusion

This chapter gives some perspectives for improving the wavelet-based kinematic model. It is found that the velocity field statistics do not reproduce the expected intermittency in a DNS, and new patterns of evolution and relationship between coefficients of each level can be imagined, in agreement with intermittent Eulerian models in the literature.

Objective	**Coefficients distribution**	**Temporal evolution**
Retrieve disperse phase statistics	Gaussian $\mathcal{N}(0, \sigma_j^2)$	Ornstein-Uhlenbeck process
Retrieve intermittency	Inter-level conditional Gaussian	Inspired from cascade model
Reduce dimensionality	Truncated Gaussian $\mathcal{N}_T(0, \sigma_j^2)$	Sinusoidal temporal evolution

Table 11.1. Summary of the main wavelet-based KS schemes

On the other hand, an essential step for this method to be computationally attractive is the dimensionality reduction, and wavelet compression is investigated to reduce the storage of information. The use of truncated normal distribution allows for a satisfying compression ratio and another temporal evolution is proposed in this chapter, consistent with the dimensionality reduction. Their use in the LES framework seems natural, since one can adapt parameters of the models to local sub-grid information.

We summarize in Table 11.1 the different strategies introduced for wavelet-based KS in the three last chapters:

- A Gaussian distribution with Ornstein-Uhlenbeck processes can retrieve accurate fluid and disperse phase statistics (Chap. 9 and 10);
- Inter-level conditional Gaussian distributions could be derived following intermittent cascade models;
- Truncated Gaussian distribution with adapted temporal evolution scheme allows for dimensionality reduction.

Wavelet-based kinematic models offer promising perspectives for two-way coupling approaches, which will be detailed in Chap. 14. Other perspectives can also be considered, such as more complex geometries or near-wall flows, thanks to the spatial localization of wavelets.

Part V

Towards two-way coupling in turbulent disperse two-phase flows

Part V with two-way coupling between the disperse and the turbulent carrier phase in an Euler-Lagrange framework. Chapters 12 and 13 are adapted from Letournel, Laurent, Massot, and Vié (2020). In particular, Chap. 12 introduces the main issues of such a coupling: the numerical challenges but also the insufficient knowledge on the mechanisms responsible for the attenuation or the enhancement of the turbulence by the particles. A dimensional analysis allows to identify a set of dimensionless parameters: the mass loading, the Stokes number, and the particle number density. The influence of these parameters is established in turn in Chap. 13 within the framework of an exhaustive DNS/DPS study. In particular, this study highlights a parameter never studied before, the heterogeneity of the disperse phase, which strongly influences the scales at which the energy transfer between the two phases occurs. We will introduce different metrics to evaluate this spatial heterogeneity. Finally, based on these results, Chap. 14 proposes a review of coupling strategies depending on the chosen approach for the two phases, and we develop an extension of the kinematic wavelet model in the two-way coupling context, with three distinct coupling levels.

Chapter 12

Modeling two-way coupling

We have so far highlighted that turbulence governs particles behavior. Conversely, when the mass loading of the disperse phase is not negligible, the presence of particles can also influence the turbulence (Squires and Eaton 1990; Boivin, Simonin, and Squires 1998). This chapter introduces the two-way coupling framework and presents the challenges related to its numerical treatment, and the understanding of the physical mechanisms governing the modulation of energy of the turbulent carrier phase. We propose a review of existing studies on the subject, and then develop a new framework for the study of two-way coupling based on three dimensionless numbers: mass loading, Stokes number, and particle number density.

In Sec. 12.1, we discuss the different regimes of interaction between the disperse and the carrier phase. Section 12.2 presents an overview of the literature, specifying the parameters already clearly identified and those less certain that play a role in the modulation of turbulence Section. 12.3 presents the assumptions and governing equations of our study, as well as the numerical methods. Then, the target HIT configuration and the parameter set are presented in Sec. 12.4, with an emphasis on the other parametric studies in the literature.

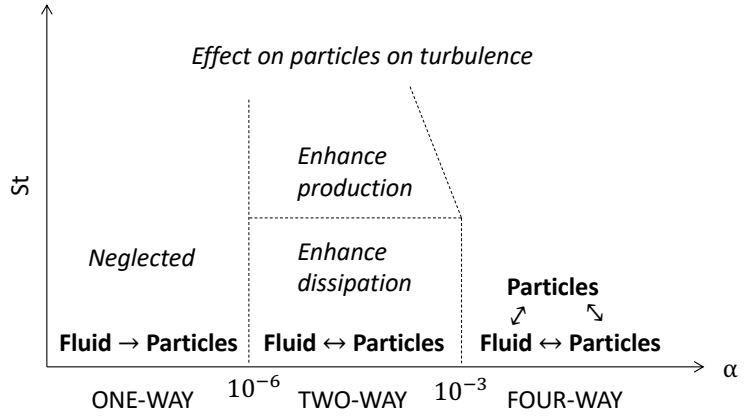

Figure 12.1. Map of regimes of interaction between particles and turbulence adapted from Elghobashi (1994)

12.1 Impact of volume and mass fractions

In previous chapters, we were interested in the main characteristics of a disperse phase transported by a turbulent flow. The interactions between the two phases can actually be much more complex, when the inertial particles interact with each other or with the carrier phase. A classification of these interactions is proposed by Elghobashi (1994) in Fig. 12.1 based on the volume fraction α of the disperse phase. This classification can be refined also considering the mass loading ϕ:

- **One-way coupling**: For $\alpha < 10^{-3}$ and $\phi < 10^{-2}$, the regime is known as "one-way": the disperse phase is sufficiently diluted to neglect collisions between particles and the mass loading is too small to modify the carrier phase. The motion of the particles is entirely controlled by the continuous phase and many studies focus on the spatial dispersion of the particles.
- **Two-way coupling**: For $\alpha < 10^{-3}$ and $\phi > 10^{-2}$, the regime is "two-way": the disperse phase can modify the carrier phase. Statistics and spectral structure of the turbulence can be altered depending on the type of particles. Despite numerous studies (Squires and Eaton 1990; Elghobashi and Truesdell 1994; Ferrante and Elghobashi 2003), this type of regime still lacks insight, regarding both parameters that control it and the dynamics of turbulence modulation. Chapter 13 proposes a new insight on this regime, in particular as a function of the dimensionless numbers introduced in Sec. 12.4.2.
- **Four-way coupling**: two-way coupling with extra interactions between the particles. The volume fraction is no longer small enough to neglect collisions, which must be taken into account. More specifically
  - For $10^{-3} < \alpha < 10^{-1}$, inter-particle collisions can induce significant new physical phenomena: momentum transfer, heat transfer, modification of the preferential concentration of particles, coalescence, agglomeration. The collision mechanism is a very complex phenomenon, governed by the relative velocity of the particles, which can be induced by a shear of the carrier phase, a high Stokes number (PTC), or also particles with different properties.
  - For $\alpha > 10^{-1}$, we refer to dense (or granular) flows for which particle-particle interactions govern most of the dynamics of the disperse phase.

In the following, we will study the two-way coupling framework that is relevant for instance for combustion applications. We start by giving the reader an overview of the literature.

12.2 Overview of existing studies

In the literature, the interactions between a turbulent carrier phase and a particulate phase in the point-particle limit have been extensively studied. In the one-way coupled context, for which the particles do not affect the carrier phase, the importance of Stokes number based on Kolmogorov or Lagrangian integral time scales have been demonstrated: the former characterizes the occurence of preferential concentration (Eaton and Fessler 1994) while the latter is representative of the transition to particle-trajectory-crossing dominated flows (Février, Simonin, and Squires 2005).

In the case of two-way coupling, turbulence modulation by particles has been also investigated in homogeneous isotropic turbulence (HIT), focusing on the effect of the Stokes number and mass

loading. On the one hand, studies on stationary HIT of Squires and Eaton (1990), Boivin et al. (1998), Mallouppas et al. (2017) showed that the turbulent kinetic energy of the carrier phase is reduced by particles. They concluded that inertial particles inject energy in the turbulent motion at high wavenumbers with a corresponding increase in the dissipation, which was also described by Squires and Eaton (1994) with respect to mass loading.
On the other hand, Elghobashi and Truesdell (1994), Druzhinin and Elghobashi (1999), Druzhinin (2001), Ferrante and Elghobashi (2003), Abdelsamie and Lee (2012) worked with a decaying HIT and found that particles with low Stokes number can slow the decay of fluid energy. Indeed, studies on the fluid-particle interaction spectrum reveal a negative contribution at low wave numbers where intensity is reduced when Stokes number increases, whereas the energy rate at large wavenumbers remains positive. More generally, Ferrante and Elghobashi (2003) classified particles according to their Stokes number and described the evolution of turbulent energy and dissipation of the flow, and Sundaram and Collins (1999) showed that the shift in energy to high wavenumbers in the fluid phase increases the viscous dissipation rate. The focus of all these studies was the influence of the Stokes number and mass loading: the former parameter globally determines the dynamics of particles in a given fluid and the latter plays a role in the inverse-coupling force that the particles exert on the fluid. Table 12.1 summarizes some of the previous works, and the parameters studied.

A dimensional analysis leads to the identification of a third controlling parameter, the particle number density. In fact, this parameter plays a key-role: for high number density, the proximity of particles can lead to a continuous phase behavior, while for low number density, distant particles can produce strong local effects on the surrounding fluid and the exact location of the particles may have a great impact on the dynamics of the flow, depending on the realization. In the literature, this parameter has been first studied in the objective of reaching statistical convergence for one-way coupled simulations (Vié, Pouransari, Zamansky, and Mani 2016). Strutt, Tullis, and Lightstone (2011) observed the lack of consensus regarding the number of particles that must be considered in simulations. A common definition for statistical convergence is the point at which the particle dispersion statistics do not change significantly (i.e. become independent on the number of particles). On the other hand, Sundaram and Collins (1999) studied a regime with very low particle number density, for which each particle acts independently and observed that their collective effect on the fluid scales linearly with the total number of particles.

In the following, we present the assumptions and governing equations of the two-phase flows, as well as the numerical methods.

12.3 Modeling and numerical frameworks

12.3.1 Fluid and particles equations

We assume the set of assumptions described in Sec. 6.1.2 are verified, which allows us to write a system of ordinary differential equations for each p particle like the one in Eq. (6.7).
In the framework of two-way coupling, we must also define the effect of the particles on the carrier phase. This one is expressed through an additional force in the momentum equation of the fluid.

Reference	**Forcing**	M_r/M_c	**Fixed**	**Changed**
(Squires and Eaton 1990)	YES	100	St, n_η	$\boldsymbol{\phi}$, α, ρ_p/ρ, d_p/η
(Elghobashi and Truesdell 1994)	NO	100	α, St	$\boldsymbol{d_p/\eta}$, ρ_p/ρ, n_η , ϕ
			α, d_p/η, n_η	**St**, ρ_p/ρ, ϕ
			St, ρ_p/ρ, d_p/η	$\boldsymbol{\alpha}$, ϕ, n_η
(Squires and Eaton 1994)	YES	1	St, n_η	$\boldsymbol{\phi}$, α, ρ_p/ρ, d_p/η
(Boivin, Simonin, and Squires 1998)	YES	> 1	α, ϕ, ρ_p/ρ	**St**, d_p/η, n_η
			St, n_η	$\boldsymbol{\phi}$, ρ_p/ρ, α, d_p/η
(Druzhinin and Elghobashi 1999)	NO	1	St, ρ_p/ρ, d_p/η	$\boldsymbol{\phi}$, α, n_η
(Sundaram and Collins 1999)	NO	1	α, ϕ, ρ_p/ρ	**St**, d_p/η, n_η
			St, d_p/η, ρ_p/ρ	$\boldsymbol{\alpha}$, ϕ, n_η
(Druzhinin 2001)	NO	1	α, ϕ, ρ_p/ρ	**St**, d_p/η, n_η
(Ferrante and Elghobashi 2003)	NO	47	α, ϕ, ρ_p/ρ	**St**, d_p/η, n_η
(Abdelsamie and Lee 2012)	YES / NO	95	α, ϕ, ρ_p/ρ	**St**, d_p/η, n_η
(Mallouppas, George, and van Wachem 2017)	YES	1	α, d_p/η, n_η	**St**, ρ_p/ρ, ϕ
			St, ρ_p/ρ, d_p/η	$\boldsymbol{\phi}$, α, n_η

Table 12.1. Previous studies of the modulation of turbulence by disperse phase. Forcing scheme for stationary HIT and ratio of real particles per computational particle are specified for each study. Choices of fixed parameters and studied parameters are displayed in the two last columns. In the table, St is the Stokes number, α is the volume fraction, n_η is the particle number density, ϕ is the mass fraction, ρ_p/ρ is the ratio of particle and fluid densities and d_p/η is the ratio of particle diameter and Kolmogorov scale. M_r/M_c is the ratio of the number of real particles per computational particle.

For an incompressible fluid, the equations of motion for the carrier fluid are:

$$\left\{\begin{array}{rcl} \dfrac{\partial u_i}{\partial x_i} & = & 0 \\ \dfrac{\partial u_i}{\partial t} + \dfrac{\partial u_i u_j}{\partial x_j} & = & \dfrac{-1}{\rho}\dfrac{\partial P}{\partial x_i} + \nu \dfrac{\partial^2 u_i}{\partial x_j \partial x_j} + \dfrac{1}{\rho} f_i, \end{array}\right. \tag{12.1}$$

where $\boldsymbol{f}$ is the force exerted by particles on the fluid.

12.3.2 Coupling equations

A projection kernel Δ is introduced to give a local average of the feedback force. This function is positive, monotically decreasing and normalized such that its integral over the entire physical space is unity. The source term $\boldsymbol{f}$ in Eq.(12.1) is then written as:

$$\boldsymbol{f}(\boldsymbol{x}, t) = -\sum_p \boldsymbol{F}_D^{(p)} \Delta(\boldsymbol{x} - \boldsymbol{x}_p(t)), \tag{12.2}$$

where $-\boldsymbol{F}_D^{(p)} = -m_p \boldsymbol{F}_p = m_p \dfrac{\boldsymbol{v}_p(t) - \boldsymbol{u}_{@p}(t)}{\tau_p}$ is the resultant force exerted by a particle p of mass m_p on the fluid derived in Sec. 6.1.2.
Other Eulerian spatial fields can therefore be defined as:

$$\begin{array}{ll} n(\boldsymbol{x}, t) & = \sum_p \Delta(\boldsymbol{x} - \boldsymbol{x}_p(t)) \\ n(\boldsymbol{x}, t)\tilde{\boldsymbol{v}}_p(\boldsymbol{x}, t) & = \sum_p \boldsymbol{v}_p \Delta(\boldsymbol{x} - \boldsymbol{x}_p(t)) \\ n(\boldsymbol{x}, t)\tilde{\boldsymbol{u}}_{@p}(\boldsymbol{x}, t) & = \sum_p \boldsymbol{u}_{@p} \Delta(\boldsymbol{x} - \boldsymbol{x}_p(t)). \end{array} \tag{12.3}$$

For monodisperse spherical particles, $m_p = \rho_p \pi d_p^3/6$ and global volume fraction is defined as $\alpha = n_0 \pi d_p^3/6$, where n_0 is the mean particle number density $\langle n(\boldsymbol{x}, t)\rangle = n_0$. The mass loading of the disperse phase is therefore defined as $\phi = \alpha \rho_p/\rho$. To highlight the effect of these parameters, the coupling term is expressed as:

$$\frac{1}{\rho}\boldsymbol{f}(\boldsymbol{x}, t) = \phi \frac{n(\boldsymbol{x}, t)}{n_0} \frac{\tilde{\boldsymbol{v}}_p(\boldsymbol{x}, t) - \tilde{\boldsymbol{u}}_{@p}(\boldsymbol{x}, t)}{\tau_p}. \tag{12.4}$$

The mass fraction term is thus a factor in the expression, the fraction $n(\boldsymbol{x}, t)/n_0$ contains information about the spatial distribution of particles and the last term is related to the Stokes number.

12.3.3 Numerical methods

We performed direct numerical simulation to solve the unsteady three-dimensional Navier-Stokes and continuity equations with the Asphodele code using a low Mach formulation of the Navier-Stokes equations and a Lagrangian formulation for the particles (see Sec. 2.4).
One of the key aspects of in Euler-Lagrange simulation is the coupling between the particle equations and the carrier phase. Two elements are required: an interpolation scheme to evaluate the carrier phase properties at the particle locations, and a projection scheme to compute the feedback of particles to the carrier phase or to compute particle Eulerian fields.

For the interpolation step, the Asphodele solver uses a second-order trilinear algorithm to compute the carrier phase quantities at particle location. Strutt, Tullis, and Lightstone (2011) discussed the accuracy of interpolation schemes such as the fourth-order cubic spline, the fifth-order Lagrange or the third-order Hermite polynomials interpolation and they concluded that the three schemes gave similar mean square particle displacements, advising to use the least computationally expensive Hermite polynomials interpolation. Moreover, a recent work has also shown that a lower-order interpolation combined with uncorrected fluid velocity could lead to an improved drag estimation (Horwitz and Mani 2016). Regarding these works, the choice of a second-order algorithm seems to be a reasonable solution with respect to the up-to-date literature.

The choice of the projection kernel depends on the particles properties and the desired precision. The PSI-Cell method of Crowe, Sharma, and Stock (1977) was originally implemented in Asphodele code. The Lagrangian contributions are instantaneously allocated to neighboring nodes, weighted by the distance to the nodes. This procedure is sometimes controversial because it leads to significant error that depends on the ratio of particle diameter to the grid spacing. This approach requires for the mesh size to be much larger than the particle diameter, as demonstrated by Capecelatro et al. (2015), Horwitz and Mani (2016), Ireland and Desjardins (2017), Balachandar et al. (2019). Various mollification kernels can be used to transfer particle data on the Eulerian mesh, depending on the quantity of interest. Some of them are described by Capecelatro and Desjardins (2013). Diffusion operation might also be necessary to deal with finer grids (Poustis, Senoner, Zuzio, and Villedieu 2019). Maxey, Patel, Chang, and Wang (1997) proposed a "narrow envelope function" in the form $\Delta(\boldsymbol{x}) = (2\pi\sigma^2)^{-3/2}\exp(-\boldsymbol{x}^2/2\sigma^2)$, which was used by other works (Capecelatro and Desjardins 2013; Zamansky, Coletti, Massot, and Mani 2014). The length scale σ is a parameter that can be adjusted to reflect the finite size of the particle. A Gaussian envelope for the source term was also implemented in the code and a comparison of the influence of the projection kernels is provided in App. C: the effect of the coupling kernel is limited to the smallest scales and does not impact the qualitative results that are reported in this work.

Another concern discussed in literature is about recovering the undisturbed velocity of the fluid at particle position. This was extensively studied by Gualtieri, Picano, Sardina, and Casciola (2015), Horwitz and Mani (2016), Ireland and Desjardins (2017), Balachandar, Liu, and Lakhote (2019), Zamansky (2019) who have developed models to estimate this quantity in two-way coupled problems. Based on their results, given the ratio of particle diameter with grid spacing of our simulations ($d_p \ll \Delta x$), we do not require this level of modeling.

12.4 Target configuration and parameter sets

12.4.1 Homogeneous isotropic turbulence

Among the works mentioned in Sec. 12.2, we can distinguish studies with forced stationary turbulence, for which statistics are therefore easier to carry out, from naturally decreasing turbulences, as reported in the first column of Table 12.1. A comparison of these turbulences is proposed by Abdelsamie and Lee (2012), who noted a number of difficulties in the attempt to study the impact of particles on the energy spectrum when it is artificially forced. Many differences are observed, including significant changes in the influence of small particles that do not allow energy to be reintroduced to the fluid in forced turbulence. And although Mallouppas, George, and van Wachem

time	$\langle k \rangle$	$\langle \varepsilon \rangle$	τ_k	η	τ_f	L_f	Re_L	Re_λ
t_0	0.015	0.0089	0.335	0.018	2.11	0.21	21.13	15.9
$t_{inj} = 3$	0.054	0.0014	0.854	0.029	4.55	0.27	16.45	14.6
$t_f = 6$	0.003	0.00052	1.38	0.037	6.95	0.31	13.47	12.7

Table 12.2. Turbulence properties of the HIT

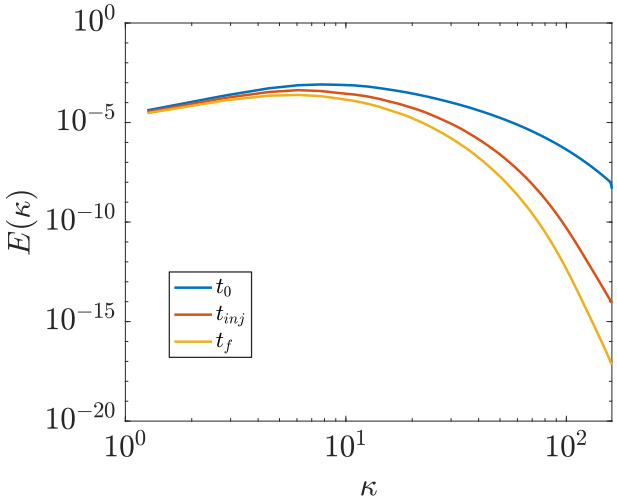

Figure 12.2. Energy spectra at initial time, injection time and final time.

(2013) introduced a new forcing model, the same biases observed for small particles are found in their results. We have therefore chosen a configuration of decaying turbulence, for which we normalize the observed quantities by the total kinetic energy at each instant and thus retrieve more stationary trends in the evolution of components of the energy decay rate.

The proposed test case is a decaying homogeneous isotropic turbulence loaded with particles. The results presented in this work were obtained using the 256^3 grid. The turbulent characteristics of the decaying HIT are given in Table 12.2 for initial time, injection time and final time. It shows the mean turbulent kinetic energy $\langle k \rangle$, the dissipation $\langle \varepsilon \rangle$, the Kolmogorov time and length scales (τ_k and η), the Eulerian eddy turn-over time τ_f , the longitudinal integral length scale L_f, and the turbulent Reynolds number based on the integral length scales $\mathrm{Re}_L = \sigma_u L_f / \nu$, where $\sigma_u = \sqrt{2/3 \langle k \rangle}$ is the fluid velocity fluctuations. The energy spectrum is plotted for the corresponding times in Fig. 12.2.

To evaluate turbulence modulation by particles, statistical quantities and spectrum of energy are studied. As presented in Sec. 1.1.6.2, the homogeneous isotropic field allows us to use the spatial average instead of the ensemble averaging. It is numerically implemented as the discrete average over all the cells in the domain.

$$\langle \phi \rangle (t) = \frac{1}{|\mathcal{V}|} \int_{\mathcal{V}} \phi(\boldsymbol{x}, t) \, \mathrm{d}\boldsymbol{x}, \tag{12.5}$$

where $\mathcal{V}$ indicates that the integral is taken over the whole domain of fluid $|\mathcal{V}| = \mathcal{L}^3$. The time dependency is conserved because the turbulence is not stationary.

The fluid energy equation is obtained by multiplying fluid momentum equation by u_j and ensemble averaging.

$$\frac{\mathrm{d}\,\langle k\rangle}{\mathrm{d}t} = -\,\langle\varepsilon\rangle\,(t) + \langle\psi_p\rangle\,(t), \tag{12.6}$$

where $\langle\varepsilon\rangle\,(t) = 2\nu\langle S_{ij}S_{ij}\rangle$ is the viscous dissipation rate of energy with $S_{ij} = \frac{1}{2}\Big(\frac{\partial u_i}{\partial x_j} + \frac{\partial u_j}{\partial x_i}\Big)$ and ν is the dimensionless kinematic viscosity. $\langle\psi_p\rangle\,(t)$ represents the energy rate of change due to the particles drag force:

$$\langle\psi_p\rangle\,(t) = \frac{\phi}{\tau_p n_0}\Big\langle n(\boldsymbol{x},t)u_i(\boldsymbol{x},t)[\tilde{v}_{p,i}(\boldsymbol{x},t) - \tilde{u}_{@p,i}(\boldsymbol{x},t)]\Big\rangle. \tag{12.7}$$

It is also called the two-way interaction energy rate.

Performing the Fourier transform of the fluid momentum equation, we obtain the equation for the energy spectrum $E(\kappa)$:

$$\frac{\partial E(\kappa,t)}{\partial t} = T(\kappa,t) - D(\kappa,t) + \Psi_p(\kappa,t), \tag{12.8}$$

where the spectral dissipation rate is $D(\kappa) = 2\nu\kappa^2 E(\kappa)$ and $T(\kappa)$ is the spectral energy transfer rate. The fluid-particle energy interaction term $\Psi_p(\kappa)$ produced by particles is responsible for the modulation in the turbulence energy spectrum. It is defined by:

$$\Psi_p(\kappa,t) = -\sum_{\kappa\leq|\boldsymbol{\kappa}|\leq\kappa+1} \Re\Big\{\hat{u}_i^{\star}(\boldsymbol{\kappa},t)\frac{\hat{f}_i(\boldsymbol{\kappa},t)}{\rho}\Big\}, \tag{12.9}$$

where "$\hat{}$" denotes Fourier transform, "$\star$" the complex conjugate, and $\Re\{\}$ denotes the real part.

12.4.2 Key-parameters and dimensional analysis

The dynamics of the disperse phase depends on many phenomena and interactions. In this section, we introduce the dimensionless numbers that allow to study different interaction regimes.
The dimensionless numbers of interest can be deduced from the Pi theorem from the characteristic numbers of the problem.

- The disperse phase is completely defined with three parameters : particle diameter d_p, particle density ρ_p and the mean particle number density n_0. Those parameters are highlighted in the diagram of Fig. 12.3(a).
- The carrier phase is more complex. Physical parameters are its density ρ and its viscosity μ, but a number of scales and other characteristics are required to completely define turbulence. Actually, the entire initial energy spectrum should be taken into consideration. As seen in Chap. 1, the universality of turbulence in the inertial range allows us to only characterize the largest scales and the smallest ones. σ_u characterizes the velocity of the fluctuations (related to the kinetic energy) and the mean dissipation rate $\langle\varepsilon\rangle$ is also necessary to introduce the Kolmogorov scales.

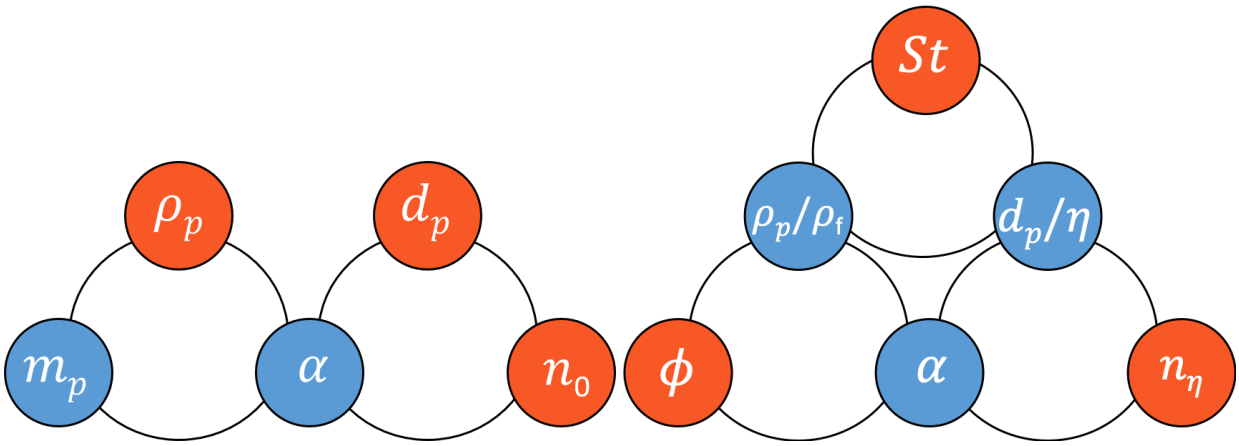

Figure 12.3. Controlling dimensional (a) and non-dimensional (b) parameters for particles in turbulence.

According to the Pi-theorem, the problem with seven parameters expressed in three fundamental units (mass, length, time) can thus be expressed with four dimensionless numbers. Three of them combine the parameters of the two phases such as the dark ones in Fig. 12.3(b) and the last one only characterizes the carrier phase: the Reynolds number $\mathrm{Re}_L = \sigma_u L/\nu$.

Note that the relaxation time of the particles τ_p involves the dynamic viscosity of the carrier phase μ, but is not a dimensionless number. Its ratio with the Kolmogorov time scale yields the Stokes number $\mathrm{St} = \tau_p/\tau_\eta$ which quantifies the intensity of the inertia of the droplets. Other classical dimensionless numbers can be retrieved, like the volume fraction $\alpha = n_0 \pi d_p^3/6$, or the mass loading $\phi = \alpha\rho_p/\rho$. We also propose to consider as a parameter of interest ratios of density ρ_p/ρ or of length d_p/η. Finally, we will also see in Chap. 13 the role of the density in number of particles $n_\eta = n_0\eta^3$, which corresponds to the number of particles per Kolmogorov eddy. All those parameters are related to each other in Fig. 12.3(b).

These dimensionless numbers are fundamental to understand the mechanisms that govern the interactions between the two phases. We detail in the next chapter the role of the Stokes number in the preferential concentration of the particles and we examine the importance of each of these parameters in the coupling terms between the two phases.

The reader can re-examine previous publications with this diagram in mind. Table 12.1 shows the parameters that were fixed and changed between their different simulations. The parameters in bold font were those identified by the authors as responsible for turbulence modulation. The only consistent and exhaustive study of a given triplet was completed by Elghobashi and Truesdell (1994) who successively observed the separate influence of τ_p, α and d_p. However, the use of computational particles to represent several real particles ($M_r/M_c = 100$) can mimic the characteristics of an heterogeneous disperse phase, though aiming at representing a highly-concentrated one (high "real" particle number density but low "computational" particle number density). As already noticed by Boivin, Simonin, and Squires (1998), neither simulations of Squires and Eaton (1990), Elghobashi and Truesdell (1994) nor their own calculations met the condition of $n_\eta \gg 1$,

required for correspondence between computational and actual particles. Therefore, only "real" particles ($M_r/M_c = 1$) are used in our study.

Attempts to assess the importance of some dimensionless parameters on turbulence modification have been made. Gore and Crowe (1989) claimed that the ratio of particle diameter to a turbulent length scale provides an estimate of whether the turbulent intensity of the carrier phase will be increased or decreased. Kenning and Crowe (1997) introduced a criterion based on a hybrid length scale defined with the dissipation length scale of the single-phase flow and average interparticle spacing. Tanaka and Eaton (2008) introduced a new dimensionless parameter Pa, the particle momentum number, involving the Stokes number, the ratio of particle and fluid densities, the Reynolds number, the ratio of particle diameter to a flow length scale. However, there is no general consensus on a single parameter responsible or not for the modulation of turbulence and their respective conclusions were sometimes contradictory: Tanaka and Eaton (2008) claimed that the Stokes number does not control turbulence modification whereas most of the other studies highlight its role. It thus seems clear that a single parameter is not sufficient in order to characterize the physics of such flows and we need to identify the ones to be considered.

We propose to describe the disperse phase by the orange triplet in Fig. 12.3(b). The choice of these three parameters was made in view of the form of the interaction term. Indeed, in Eq. (12.7), mass loading is a factor as well as the inverse of the relaxation time of the particles. We therefore naturally wanted to be able to study the influence of each of these terms in modifying turbulence.
For the description of the system, we see in Fig. 12.3(b) that the third parameter can be the volume fraction, the particle diameter or the particle number density. From a modeling point of view, we have already seen that the number of particles plays a role in the description of the disperse phase in single-phase flows (Vié, Pouransari, Zamansky, and Mani 2016). We will see through this work that at fixed Stokes number and mass loading, particle distribution in space is essential to quantify the impact on the carrier phase.
In some of previous works such as those of Druzhinin and Elghobashi (1999) or Druzhinin (2001), particle field has been considered as perfectly homogeneous when $\mathrm{St} \ll 1$. This assumption was justified by considering that in the case of microparticles the preferential concentration is negligible. However, if particle number density is not large enough, the disperse phase cannot be considered as homogeneous even though the distribution of particles is uniform in the domain. One of the objectives of the present work is to give a criterion on particle number density to determine the appropriate mean particle number density to consider the two-way exchanges as independent of this parameter.

Conclusion

In this chapter, we have reported the Navier-Stokes equations, fluid turbulent kinetic energy and turbulent energy spectrum equations with source term added by the exchange of momentum or turbulent energy with the disperse phase.

According to all the studies presented, enhancement or attenuation of the turbulence do not have a consensus on specific particle parameters and the modulation of the turbulent spectrum requires further investigations to be fully understood.

Dimensionless parameters for the two-way problem were introduced and related to each other, and the lack of a complete study of the influence of each of them on modulation of turbulence is noticed. In the next chapter, such an exhaustive study is carried out and sheds new light on previous results in literature.

Chapter 13

Modulation of turbulence by particles

Following the identification of dimensionless parameters governing the interaction between the carrier and the disperse phase in Chap. 12, we investigate the effect of the particle number density along with the mass loading and the Stokes number. We will see that one of the main mechanisms responsible for the exchange of energy at different scales is the particle preferential concentration, and more specifically, we introduce the notion of heterogeneity of the disperse phase.

A definition of heterogeneity is detailed in Sec. 13.1 along with the way to measure it unequivocally when preferential concentration occurs. Results of the extensive study are presented in Sec. 13.2, in the following order: turbulence modulation by particles is measured through the analysis of global energy transfers (Sec. 13.2.2). Then, deeper insight is given by an analysis in the spectral domain (Sec. 13.2.3), permitting to identify specific regimes with respect to the number density of the particulate phase. These regimes are further analyzed in Sec. 13.2.4, in particular with regard to coupling mechanisms.

13.1 A measure of disperse phase spatial heterogeneity

In turbulent flows, preferential concentration of particles is a major aspect that can strongly control the physics (Capecelatro and Desjardins 2015). However, preferential concentration is not the only source of phase heterogeneity. Actually, when particle concentration is not high enough, the particulate phase cannot be seen as a continuum, and must therefore be considered as a set of individual particles, and this can have an impact on the form of the coupling (Zamansky, Coletti, Massot, and Mani 2016). This introduces an additional level of heterogeneity.

We thus define the heterogeneity of the disperse phase as the combination of the preferential concentration, consequence of the interactions between particles and turbulence, and the lack of continuum, consequence of the large particle interspace. In the following, we propose methods that allow to separate both sources, and we also propose a way to identify isolated particles.

13.1.1 Box counting measure

We have seen in Chap. 6 that a classical tool to quantify preferential concentration is the PDF of particle number density based on box counting, which depends on the box size, as demonstrated by Monchaux, Bourgoin, and Cartellier (2012) and Hogan and Cuzzi (2001).

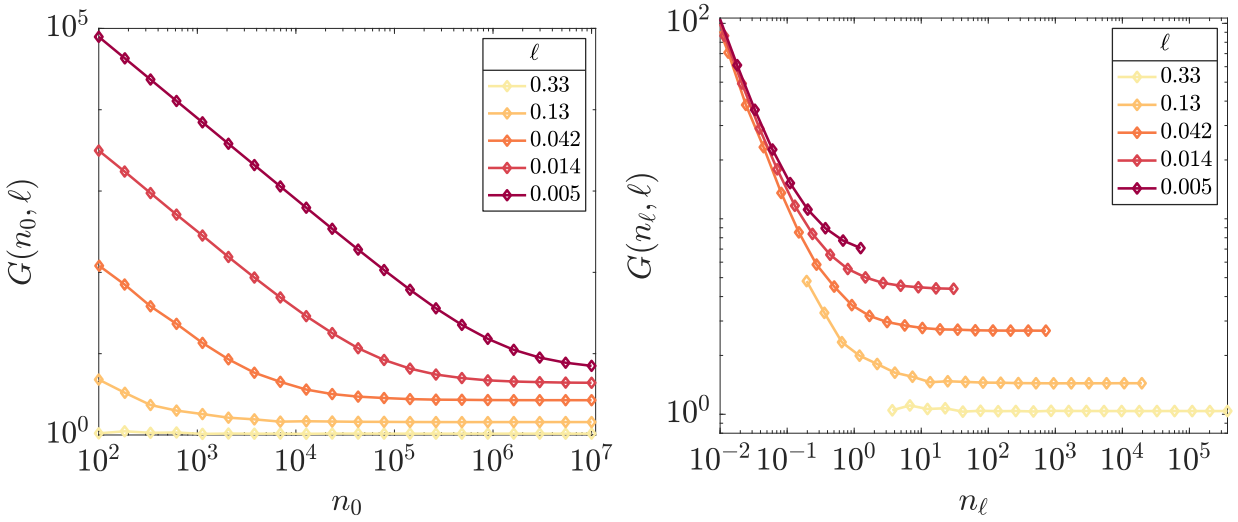

Figure 13.1. Evolution of the measure of segregation G with the normalized particle number density n_0 (a); n_ℓ (b). Different box sizes ℓ are tested. The Stokes number is $\mathrm{St} = 1$.

Let us define $\mathcal{B}$ a set of N_b boxes partitioning the domain and N_{pb}^b the number of particles in the box b. We introduce N_p the total number of particles in the domain. A possible index to quantify the preferential concentration is the normalized variance of the discrete number density field:

$$g(N_p, N_b) = \frac{\langle N_{pb}^2 \rangle}{\langle N_{pb} \rangle^2} = \frac{N_b}{N_p^2} \sum_{b \in \mathcal{B}} (N_{pb}^b)^2. \tag{13.1}$$

We provide a probabilistic analysis of the box counting measure in App. D: for one-way coupled simulations, it is possible to detail the asymptotic behavior of the measure.

Let us rewrite this measure and rather consider:

$$G : (n_\ell, \ell_b) \mapsto g\left(n_\ell \frac{\mathcal{L}^3}{\ell^3}, \frac{\mathcal{L}^3}{\ell_b^3} \right). \tag{13.2}$$

Figure 13.1(a) not only confirms the dependency of the measure with the box size ℓ, but also highlights its dependency on particle number density n_0. For a given box size, the measure appears to converge when increasing the number of particles. For sufficiently high particle number densities, the statistical sampling becomes redundant and saturated and increasing the number of particles does not add any information in the measure. This is confirmed by plotting the measure against the particle density in the chosen box size ℓ, in Fig. 13.1(b). Thus, it seems that for any box size, the convergence of the measure is established for $n_\ell \gg 1$. The mathematical proof of the convergence of the measure with the number of particles is shown in App. D, as well as its linear behavior for small number of particles.

The choice of the box size remains a degree of freedom and we want to characterize the scaling of the measure with this parameter. Ensuring $n_\ell = 10$ (i.e. the measure can be considered as independent on the particle number density), we plot in Fig. 13.2(a) the measure G as a function of

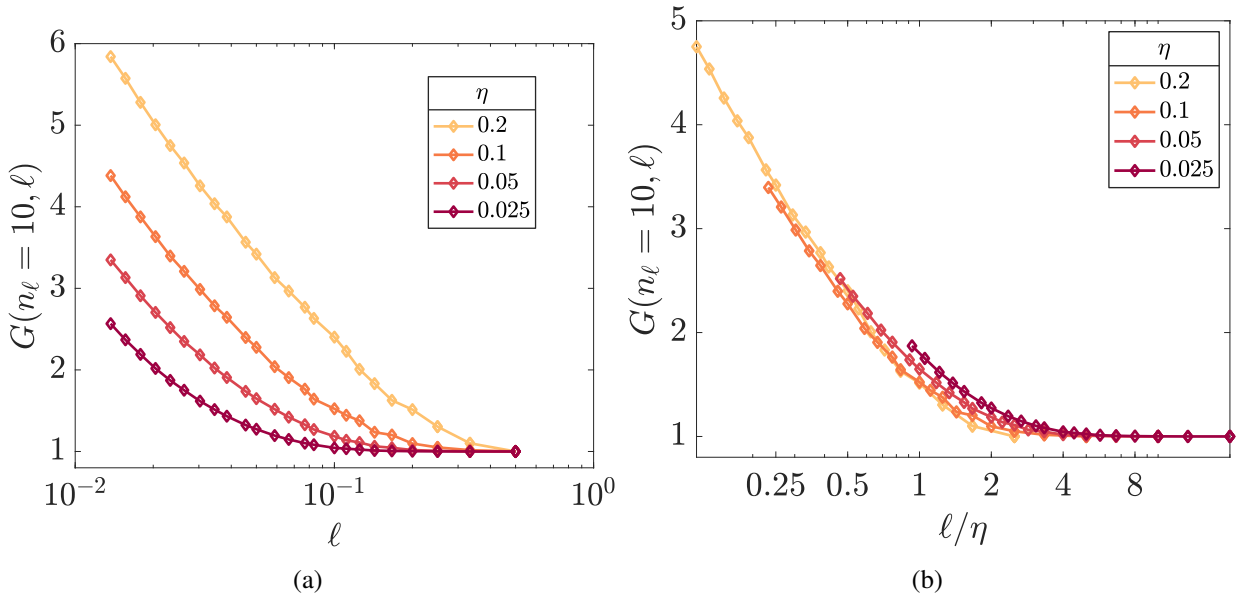

(a) (b)

Figure 13.2. Segregation measure G as a function of the box size ℓ (a) ; and the normalized box size ℓ/η (b).

the box size ℓ for different simulations. We observe two regimes in the obtained trends. For very large boxes, the measure tends to 1 and is not representative. On the other hand, the segregation increases with the logarithmic decrease of ℓ. Rescaling the measure as a function of ℓ/η, the curves in Fig. 13.3(b) overlap.
We can see that the linear regime is established for $\ell \leq \eta/2$. Thus, choosing smaller ℓ will not improve the accuracy. On the other hand, for ℓ larger than this critical value, the measure is not converged.

The choice of ℓ must therefore result in a compromise between the cost of the simulation (limited number of particles), and the sufficient sampling of the small scales η. This way, the segregation metric $G(n_\eta = 10, \ell = \eta/2)$ is independent of the number of particles, of the box size (chosen according to η), and adapted to the characteristic fluid scale η. Figure 13.3(b) shows the scaling of G for different simulations, and the characteristic peak obtained for unitary Stokes.

However, it is not always possible to simulate so many particles, and most of the simulations obtained do not reach statistical convergence. In this case, another measure of the segregation must be considered in order to get rid of the dependence on the size of the boxes.

13.1.2 Voronoï measure

Another solution proposed in the literature is the use of Voronoï diagrams based on the Lagrangian point-particle cloud. The local particle concentration is the inverse of the volume of Voronoï cells v and unlike other segregation calculation methods such as box counting, they do not depend on the size of the box arbitrarily chosen. A direct measure for the preferential concentration is the standard deviation of Voronoï volume distributions: when clusters and vacuum regions are formed, the tails of the distributions are enhanced and the standard deviation increases.

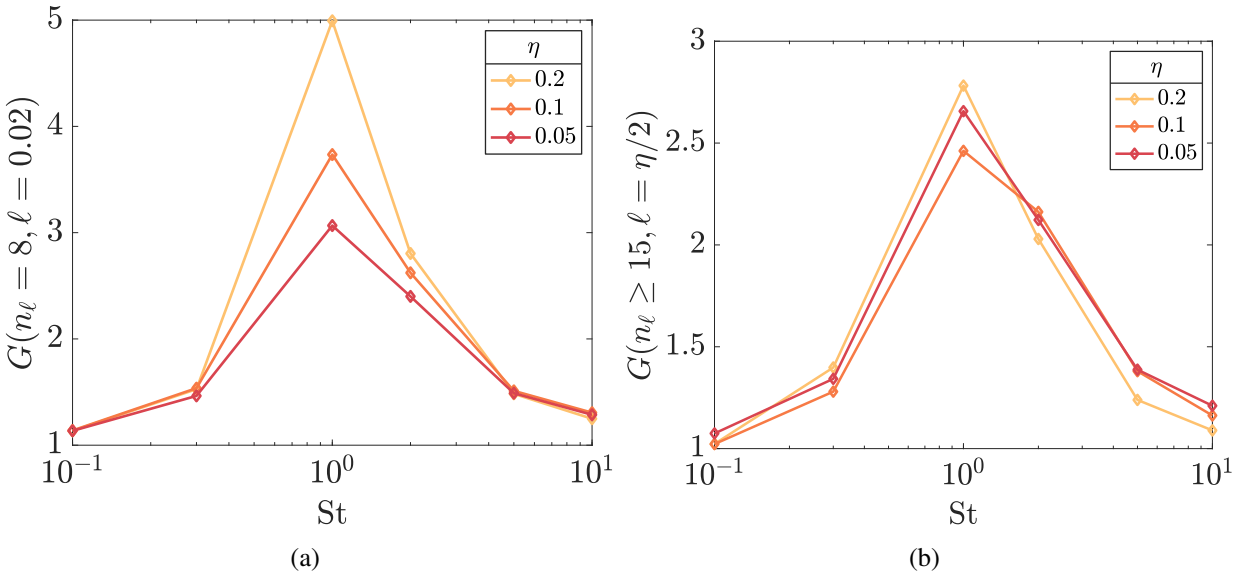

Figure 13.3. Segregation as a function of Stokes number for different Kolmogorov length scales with (a) classic box counting measure ; (b) scaled box-counting measure

Figure 13.4(a) shows the distribution of the normalized Voronoï volumes normalized by the average particle density[1], introduced by Monchaux, Bourgoin, and Cartellier (2010). Three one-way coupled simulations are compared with different Stokes numbers and particle number densities at final time. Figure 13.4(a) also shows the distribution generated by a random Poisson process (RPP), which corresponds to the perfectly homogeneous case. For all three cases, the standard deviation is greater than for the RPP, and it is maximal for a Stokes number close to unity, when the highest preferential concentration occurs.

In Fig. 13.4(b), we show the standard deviation of the Voronoï volume distribution $\sigma(\log(vn_0))$ for three original simulations with different particle number densities: $n_\eta = 0.07, 0.33, 3.3$, respectively the full, dashed and dotted lines. Similar to the box counting method, this measure also depends on the particle number density, and thus does not differentiate the source of heterogeneity between preferential concentration and the lack of continuum. Such bias has already been studied by Monchaux (2012) who suggested to artificially sub-sample highly concentrated simulations in post-processing. Particles are randomly chosen and removed from the original data set. Sub-sampled simulations exhibit the same $\sigma(\log(vn_0))$ behavior for one-way simulations in Fig. 13.4(b). This is expected because the carrier phase is identical for all three simulations (one-way coupling) and the sub-sampling process before or after running the simulation leads to the same particulate field. In order to compare preferential concentration of particles between simulations with different number of particles, we apply the sub-sampling procedure to each simulation up to a number of particles of reference $N_p = 10^5$ (corresponding to $n_\eta = 0.02$). Note that this sub-sampling procedure was also used by Monchaux and Dejoan (2017).

To summarize, we compare the different measures of preferential concentration introduced above in Fig. 13.5(a), for several Stokes numbers. The box counting method based on the smallest boxes ($l_{box} = \Delta x$) reveals a strong statistical bias that can mask the preferential concentration of particles

[1]We recall that the average particle density is independent of the spatial organization of particles.

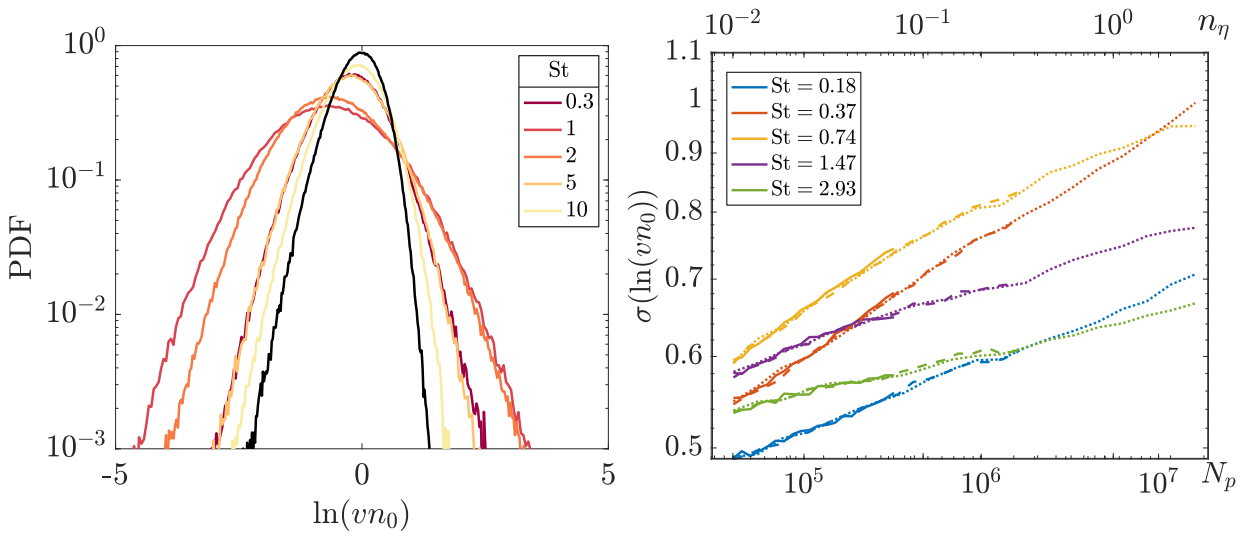

Figure 13.4. (a) PDF of normalized Voronoï volumes for different Stokes number and compared to the random Poisson process (RPP) in black line ; (b) Evolution of the standard deviation of the PDF with the number of particles in simulations, for successive sub-sampling in post-processing. Dotted lines (·····) : $n_\eta = 3.3$, dashed lines (- - -): $n_\eta = 0.33$ and solid lines (——): $n_\eta = 0.07$.

for very low particle number densities: the Stokes number dependency is not evident for the dotted curve in Fig. 13.5(a). This is corrected in the measure introduced by Monchaux, plotted in red in Fig. 13.5(b). Even for very low particle number densities, the Voronoï diagrams are well defined and the shape of the correct dependency on Stokes number is captured. However, there is still the statistical bias due to the mean particle number density. The black lines represents the unbiased measure after sub-sampling. The scaling of those black curves is consistent with the fact that the Stokes number rules the preferential concentration, and that the only difference between the red curves is due to the additional sampling. Note that the value of the depleted measure still contains the effect of particle number density because it depends on the reference n_η chosen, but it is now independent of the particle number density of the original simulation. This quantifies the tendency for particles to gather in specific regions of the fluid.

13.1.3 Identification of isolated particles

Several works are interested in the identification of clusters with the Voronoï tesselation. For example, Monchaux, Bourgoin, and Cartellier (2010) suggested a methodology to identify clusters as a connected set of low Voronoï volumes. This was used for instance by Zamansky, Coletti, Massot, and Mani (2016) and improved by Baker, Frankel, Mani, and Coletti (2017). However, we seek here to identify isolated particles, which do not form a complementary set to clusters.

Voronoï cells produce a partition of the domain and thus, even in a regime where all particles are visibly part of a well-converged cluster as in the schematic example of Fig. 13.6(a), the cells of particles located at the border of the high density area will include the vacuum domain separating the other clusters. From the definition proposed by Monchaux, Bourgoin, and Cartellier (2010), those specific particles are therefore not part of any clusters. However, we would like to include

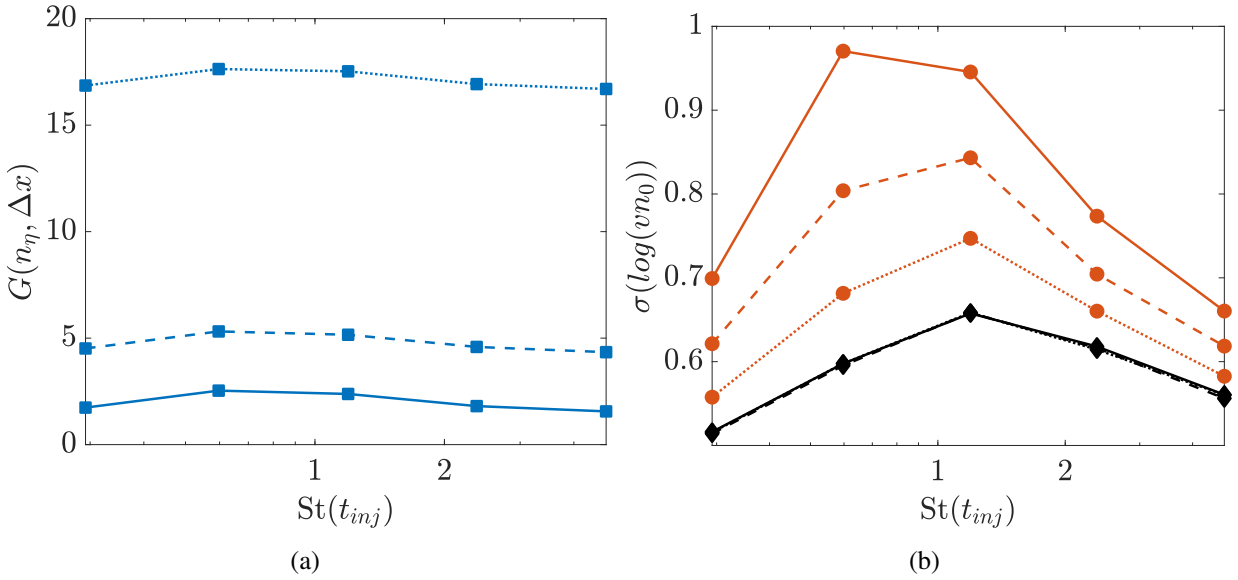

Figure 13.5. Comparison of preferential concentration for one-way coupled simulations. Dotted lines (·····) : $n_\eta = 0.07$, dashed lines (- - -): $n_\eta = 0.33$ and solid lines (——): $n_\eta = 3.3$. (a) Normalized variance of the number density field with box counting method; (b) Standard deviation of normalized Voronoï PDF before (red lines) and after (black lines) sub-sampling in post-processing.

them in the cluster given that they are located in the high-density area. On the other hand, we would like to identify if particles are completely isolated from a cluster, and Voronoï volumes fail to provide this information because a large cell volume does not necessarily mean that the associated particle is in a void region. This is why we are considering a different distribution than the Voronoï volumes to avoid this eventuality.

Let us introduce the minimum interparticle distance δ_{min}, defined for each particle as the distance between the particle and its closest neighbor. Thus, even for particles on the boundary of a cluster, the minimum distance is small enough to consider that those particles belong to it, while the Voronoï criterion reflects the fact that they belong to a vacuum region. The distributions of minimum interparticle distances are given in Fig. 13.6(b) for several particle number densities. Naturally, an increase in the particle number density results in a shift of the distribution towards lower values of interparticle distances.

13.1.4 Summary of proposed measures

We have introduced several measures of particle concentration. We have verified that the box counting measure of segregation converges with the number of particles (see App. D), and that particle preferential concentration can be compared between simulations with different number densities using the method of sub-sampling and volume Voronoï PDF. We will therefore use the box counting method to estimate the convergence of exchanges between particles and fluids at a given scale, and the volume Voronoï PDF will be helpful to compare particle preferential concentration in two-way coupled simulations in Chap. 13. The minimum interparticle distance gives another characterization of the heterogeneity of the particulate phase, by allowing to identify isolated particles with large interparticle distances.

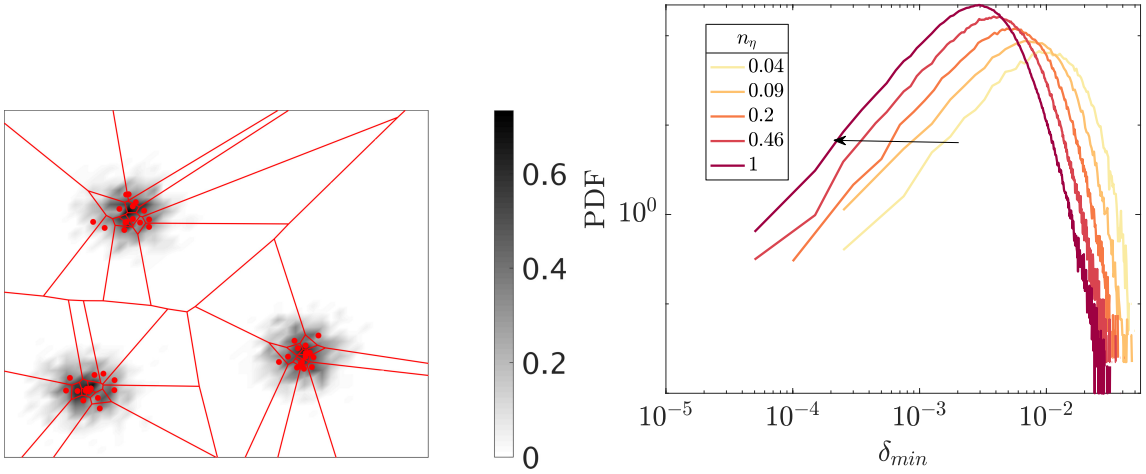

(a) (b)

Figure 13.6. (a) 2D Voronoï cells (red polygons) associated to particles (red points) superimposed with particle number density field (grey scale) ; (b) Probability density function of minimum interparticle distance for simulation with $\mathrm{St} = 1$ and $\eta = 0.01$.

13.2 Modulation of turbulence by particles: an exhaustive study

An overview of the evolution of statistical quantities and spectra is presented in this section according to the three parameters St, ϕ and n_η. The results already observed in the literature for the influence of Stokes number and mass loading are retrieved. Focus is on the role played by the particle number density, and the importance of taking it into consideration for a heterogeneous disperse phase.

13.2.1 Methodology

The carrier phase simulation is described in Sec. 12.4.1. Particles are injected at $t = 1$, with particles' location randomly sampled according to a uniform distribution law in the domain, and the particle velocities are set equal to the ones of the carrier phase at the particle locations. Natural turbulence is established at that time: the relation $\dfrac{\mathrm{d}\left\langle k\right\rangle}{\mathrm{d}t} = -\left\langle \varepsilon\right\rangle (t)$ is satisfied.
The simulation is run under one-way coupling during approximately one eddy turn over time to "thermalize" the particles. Then the two-way coupling is activated at $t_{inj} = 3$. This delay for the activation of the two-way coupling allows the influence of the particles to be studied once they have been naturally segregated. This removes an inconvenient transitional regime observed otherwise, already mentioned by Ferrante and Elghobashi (2003), especially visible for particles with large Stokes number.

In the present work, we apply direct numerical simulations to investigate turbulence modulation by inertial particles in decaying isotropic turbulence. Parameters of the disperse phase were successively varied to provide data on modulation of turbulence features and energy spectra according to Table 13.1. In order to cover the entire parameters space, the exhaustive study of the three selected parameters is carried out according to the parameter values in the first line of Table 13.1. To emphasize the role played by the particle number density parameter, another set of simulations is performed, with a very large range of values for n_η. To satisfy the assumptions of sub-Kolmogorov particles and dilute regime, the mass fraction is set at a sufficiently low value $\phi = 0.001$.

13.2.2 Two-way interaction energy rate

Despite the lack of consensus on a unique criterion for turbulence modulation by particles, the Stokes number has often been identified as one of the key parameters. For instance, Elghobashi (1994) provided a diagram showing the regimes of production or dissipation of turbulence by particles according to the Stokes number based on Kolmogorov time scale. Ferrante and Elghobashi

Figures	$\mathrm{St}(t_{inj})$	ϕ	n_η
Fig. 13.7 to 13.13, 13.17	$[0.3, 0.6, 1.2, 2.4, 4.8]$	$[0.1, 0.2, 0.3]$	$[0.07, 0.7, 7]$
Fig. 13.18, 13.14	$[0.6, 2.4]$	$[0.1, 0.2, 0.3]$	$[0.07, 0.17, 0.7, 1.7, 7, 17]$
Fig. 13.15, 13.19, 13.20	0.6	0.001	8.4×2^j, $j = -15, ..., 0$

Table 13.1. Set of parameters for particles.

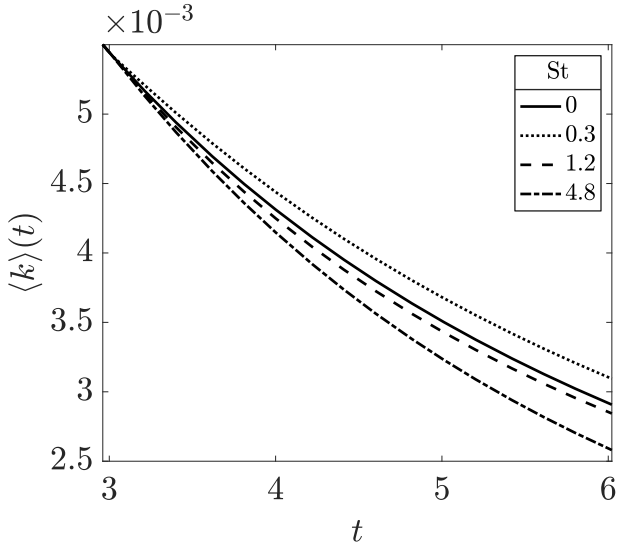

Figure 13.7. Turbulent kinetic energy temporal evolution for $\phi = 0.3$ and $n_\eta = 0.7$ from injection time $t_{inj} = 3$ to final time $t_f = 6$.

(2003) also identified a critical Stokes number (based on the Kolmogorov time scale at injection time) for which particles do not change the total energy of the carrier phase (thereby named "ghosts particles"). Figure 13.7 shows similar results: the Stokes number does play a role in the modulation of the kinetic energy of the fluid, with a tendency to slow down the rate of energy decrease for low Stokes numbers, and to increase it for more inertial particles. The evolution equation of this decay rate (Eq. 12.7) is related to the dissipation term $-\langle\varepsilon\rangle(t)$, to which is added the energy rate of change due to particle drag force $\langle\psi_p\rangle(t)$.

Figure 13.8 describes the evolution of the two components of the decay rate: the fluid-particle coupling energy rate (Fig. 13.8(a)) and the dissipation rate (Fig. 13.8(b)) at a given time $t_f = 6$ and as a function of the final Stokes number. Both are normalized by the total energy budget of the carrier phase $\langle k\rangle(t_f)$ and plotted with the same amplitude of y-axis in order to compare their relative magnitude.

The two-way interaction energy rate $\langle\psi_p\rangle$ depends on the velocity difference between the particle and its surrounding fluid, whereas $\langle\varepsilon\rangle$ depends on the strain rate only involving fluid gradients. Therefore, the only term accounting for the transfer of energy between the two phases is $\langle\psi_p\rangle$ as opposed to the modulation of $\langle\varepsilon\rangle$ which is the consequence of the propagation of the fluid perturbation around each particle. The two energy rates have very similar behaviors, and this correspondence is highlighted in Fig. 13.9 which groups the fluid dissipation values according to those of the fluid-particle exchange term. We believe that this strong correlation is a consequence of the fact that the dissipation rate is somehow a measure of the velocity gradients. As particle source term implies a perturbation of the velocity field, any modification due to particles leads to an immediate modification of the dissipation rate, in a strongly correlated manner. The reader can refer to the work of Ferrante and Elghobashi (2003), who gave a comprehensive analysis of the effect of particles on the dissipation $\langle\varepsilon\rangle$ by considering their impact on the vorticity field.
The comparison of Figs. 13.8(a) and 13.8(b) shows that the magnitude of the change in dissipation $(\langle\varepsilon\rangle_{\text{2-way}} - \langle\varepsilon\rangle_{\text{1-way}})/\langle k\rangle$ is always smaller than the normalized source term $\langle\psi_p\rangle/\langle k\rangle$. There-

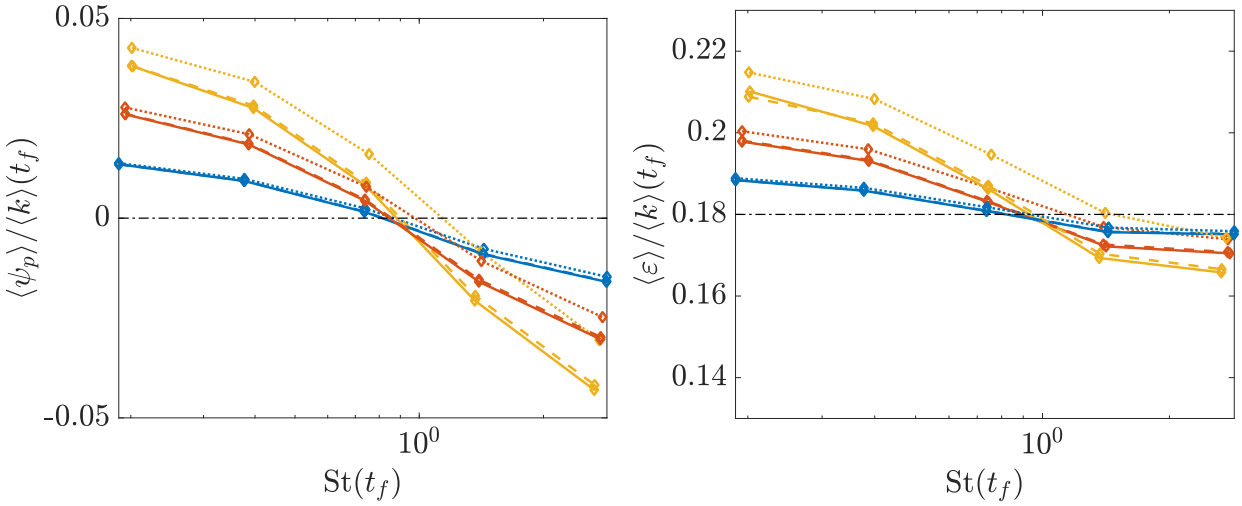

Figure 13.8. (a) Normalized fluid-particle exchange energy rate ; (b) Normalized dissipation rate versus Stokes number at time $t_f = 6$. Lines blue: $\phi = 0.1$, red: $\phi = 0.2$, yellow: $\phi = 0.3$, —: $n_\eta = 7$, - - -: $n_\eta = 0.7$, ·····: $n_\eta = 0.07$. The black dash-dotted line stands for the single-phase flow.

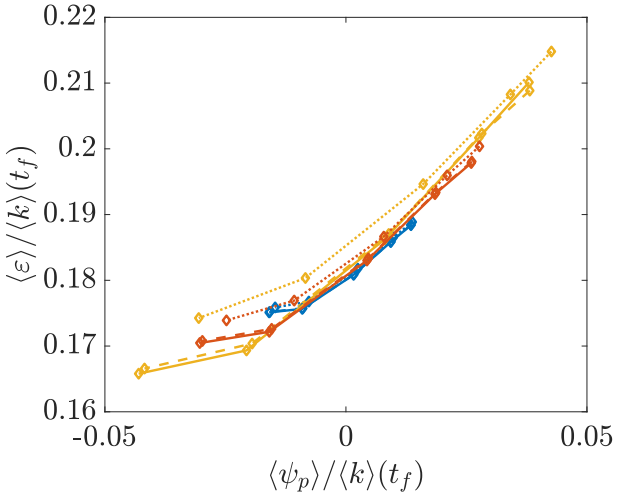

Figure 13.9. Normalized dissipation rate $\langle\varepsilon\rangle$ / $\langle k\rangle$ as a function of $\langle\psi_p\rangle$ / $\langle k\rangle$. at time $t_f = 6$. Lines blue: $\phi = 0.1$, red: $\phi = 0.2$, yellow: $\phi = 0.3$, —: $n_\eta = 7$, - - -: $n_\eta = 0.7$, ·····: $n_\eta = 0.07$. .

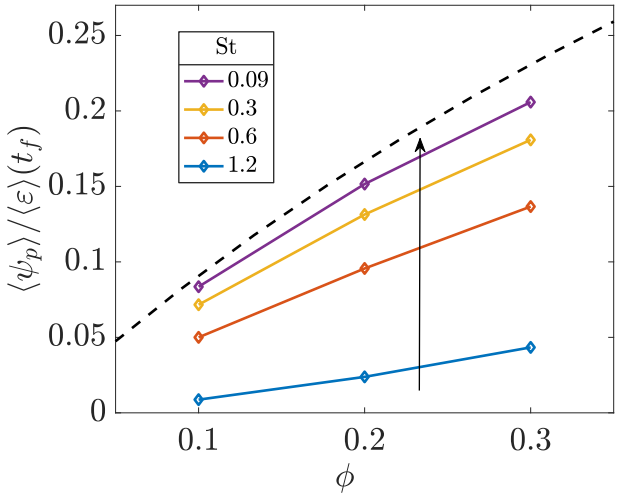

Figure 13.10. Fluid-particle coupling energy rate normalized by dissipation rate as a function of mass loading at $t_f = 6$. The arrow shows the decrease in Stokes number. The dashed line is the asymptotic limit analytically predicted by the model in Eq. (13.3).

fore, we will mainly focus on the two-way interaction energy rate and consider the dissipation as a consequence of this term.

We measure a change in the sign of $\langle\psi_p\rangle$ around Stokes number close to unity[2] in Fig. 13.8(a). In the case of $\mathrm{St} < 1$, the fluid-particle coupling energy rate $\langle\psi_p\rangle$ is positive, because the fluid-particle correlation along the particles paths $\langle u_i(\boldsymbol{x},t)\tilde{v}_{p,i}(\boldsymbol{x},t)\rangle$ is larger than the autocorrelation of the fluid $\langle u_i(\boldsymbol{x},t)\tilde{u}_{@p,i}(\boldsymbol{x},t)\rangle$ (Ferrante and Elghobashi 2003). With the inverse coupling, particle energy is given to the fluid resulting in an attenuation of the energy decay rate.

For Stokes numbers close to unity, particles are ejected from the large-vorticity cores but remain in their periphery. Even though fluid-particle energy rate is close to zero, the concentration of particles in those peripheric areas of vortices increases the dissipation.
Conversely, when the inertia of the particles increases, the fluid-particle coupling energy rate becomes negative due to a decorrelation between the velocities of the fluid and the particles. Inertial particles escape from their initial vortices and "cross" the trajectories of fluid points. Accordingly, $\langle\psi_p\rangle$ becomes negative and thus enhances the decay rate of turbulent kinetic energy.

In the scalar limit (for microparticles, i.e. $\mathrm{St} \ll 1$), the particle distribution is relatively uniform and particles behave like fluid-tracers. They are not ejected from the vortex cores and they retain their kinetic energy longer than the surrounding fluid. This is called "dusty gas", a phenomenon already described by Saffman (1962) and quantified analytically by Druzhinin (2001). The zeroth-order solution of the two-way coupling source term is in the form:

$$\langle\psi_p\rangle(t) = \frac{\phi}{1+\phi}\langle\varepsilon\rangle(t) + O(St). \tag{13.3}$$

This asymptotic behavior is retrieved in Fig. 13.10.

[2]The Stokes number calculated in our study is based on Kolmogorov scale at the measuring time $\tau_k = \sqrt{\nu/\langle\varepsilon\rangle(t_f)}$, and not the injection time as it is defined by Ferrante and Elghobashi (2003)

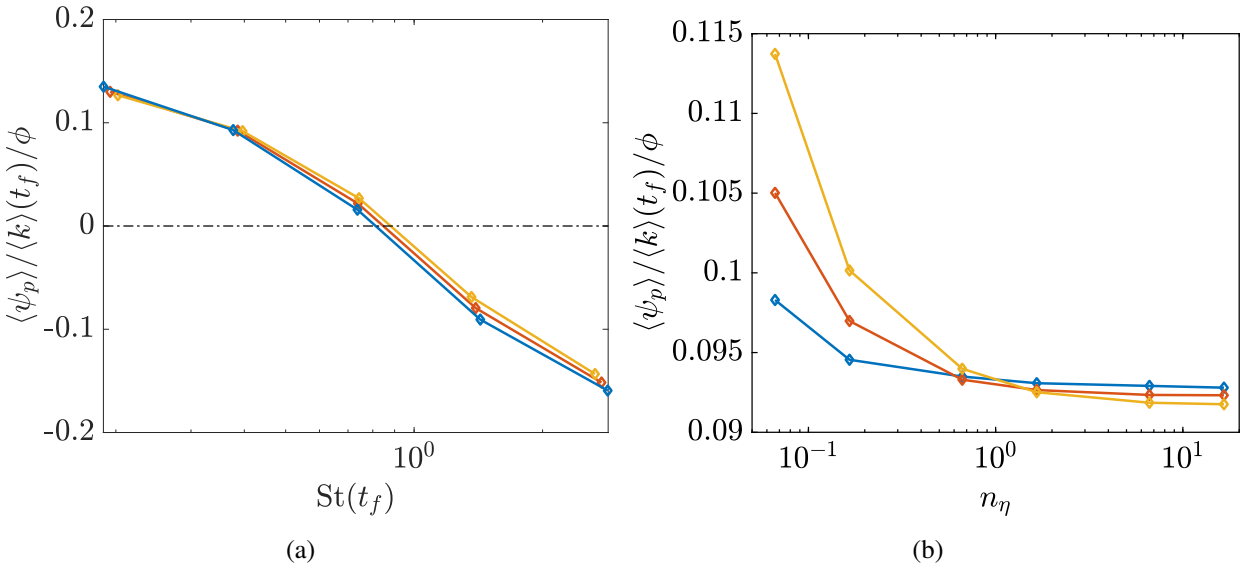

Figure 13.11. (a) Fluid-particle coupling energy rate normalized by mass loading for a fixed $n_\eta = 7$; (b) Two-way interaction energy rate normalized by total kinetic energy and mass loading at $t_f = 6$ with fixed $\mathrm{St}(t_{inj}) = 0.6$. Lines blue: $\phi = 0.1$, red: $\phi = 0.2$, yellow: $\phi = 0.3$.

As expected, an increase in mass loading produces a more significant fluid-particle coupling term. Figure 13.11(a) suggests that a normalization by ϕ yields a scaling independent of mass loading. Thus, at high Stokes numbers, an increase in mass loading enhances the suppression of kinetic energy. On the contrary, at low Stokes numbers, $\langle\psi_p\rangle$ remains positive, and its absolute value increases, which slows down the natural decrease in the turbulent kinetic energy of the fluid. The particles with low Stokes number follow the fluid particles and thus uniformly charge the vortices, which therefore retain their vorticity longer. However this scaling is verified here for a very high particle number density $n_\eta = 7$ and we show in Fig. 13.11(b) that the behavior is not that simple for heterogeneous particle phases.

Figure 13.11(b), which shows the evolution of the normalized fluid-particle energy rate as a function of the particle number density, confirms that an heterogeneous disperse phase enhances the fluid-particle exchange term contribution. For a very high number of particles, the source term is almost proportional to mass loading (the normalized plots are almost overlapping). However, for lower number of particles, the normalized two-way interaction term is stronger for high mass loadings than for low ϕ. For one-way coupled simulations, at fixed St, the dynamics of the particles is identical and thus the (hypothetical) two-way interaction term is strictly linear with the mass loading. For two-way coupled flows, the velocity of the fluid is locally modified by particles, thus changing the velocity correlations in the two-way interaction term. Even though the mass loading is in factor in the expression of $\langle\psi_p\rangle$ (see Eq. 12.7), the non-linear dependency of velocity correlations yields this non-overlapping of the curves. This figure precisely highlights the role played by particle number density in momentum exchanges between particle and carrier phases.

The asymptotic behavior of the exchange term at very high particle number densities is reminiscent of the dependency of the box counting method with particle number density. We show that the source terms in Fig. 13.11(b) converge towards an asymptotic limit value. It is assumed that convergence is based on the average volume of Voronoï cells i.e. $v(N_p) = L^3/N_p$. In order

ϕ	p	$\psi_p(N_{p,max})$	ψ_p^∞
0.1	0.7219	0.0928	0.0931
0.2	1.1210	0.0923	0.0927
0.3	1.0050	0.0918	0.0926

Table 13.2. Estimation of the converged values using Richardson's extrapolation.

to evaluate the level of convergence in terms of particle number density, we apply a Richardson's extrapolation considering the parameter to be varied is not the mesh size, but the number of particle. We thus postulate

$$\psi_p(N_p) - \psi_p^\infty = Cv(N_p)^p$$

where $\psi_p(N_p)$ is the two-way interaction energy rate with N_p particles in the domain, ψ_p^∞ is the theoretical value of the quantity ψ_p at convergence, C is a constant, and p is an estimate of the order of convergence. If we are in the asymptotic regime, these two constants, C, p are fixed and we use the Richardson extrapolation to obtain the values of the constants as well as an estimate of the two-way interaction value at convergence. With three values of $\psi_p(N_p)$ taken with a constant ratio $r = 10$ between the $v(N_p)$, we estimate:

$$p = -\frac{1}{\ln(r)} \ln\Big(\frac{|\psi_p(r^2 N_p) - \psi_p(rN_p)|}{|\psi_p(rN_p) - \psi_p(N_p)|}\Big)$$

$$C = \frac{\psi_p(r^2 N_p) - \psi_p(rN_p)}{v(r^2 N_p)^p - v(rN_p)^p}$$

Values at convergence are listed in Table 13.2. We observed that the estimated converged value is very close to the value obtained with the maximum number of particles in our study.

13.2.3 Spectral space analysis of two-way coupling energy rate

The consequence on the coupling can be further examined by taking the evolution of the energy and forcing spectra. As already observed by Ferrante and Elghobashi (2003), even if the change in the total energy budget is not affected by the presence of small particles (in the case of ghost particles), it does not necessarily imply that the distribution of this energy in the different scales is uniformly zero.

In Fig. 13.12, the turbulence spectrum is plotted at time $t_f = 6$ for cases without particles, and in the two-way coupled cases for a fixed mass loading and Stokes number $\mathrm{St}(t_{inj})$, and six different values of mean particle number densities n_η. The presence of particles enhances the energy at small scales while decreasing the energy at large scales, the overall turbulent kinetic energy being reduced because of the promoted turbulent dissipation. Furthermore, as the particle number density is increased, the spectrum tends to a limit which corresponds to the highly-concentrated regime, as already discussed in Sec. 13.2.2.

The fluid-particle interaction spectrum has been extensively studied in the literature (Ferrante and Elghobashi 2003; Fröhlich, Schneiders, Meinke, and Schröder 2018; Mallouppas, George, and

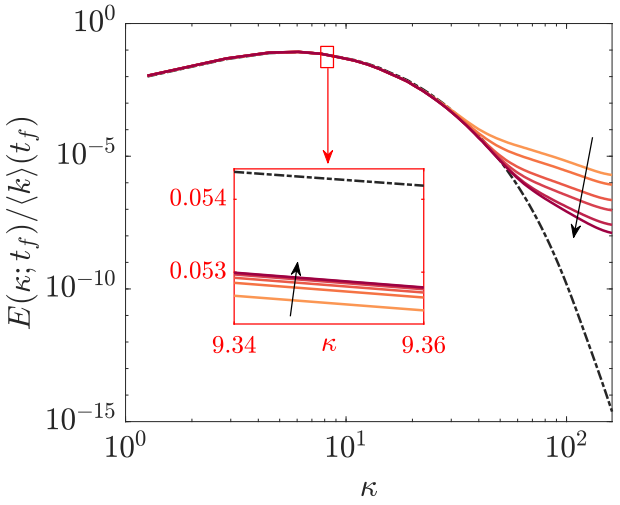

Figure 13.12. Normalized Energy spectrum $E(\kappa)/\langle k\rangle$ at $t_f = 6$ for $\phi = 0.3$ and $\mathrm{St}(t_{inj}) = 2.4$. The arrows show the increase in the particle number density following this order: $n_\eta = 0.07, 0.17, 0.7, 1.7, 7, 17$. The dash-dotted line stands for the single-phase flow spectrum. The inset is a zoom on small wavenumbers.

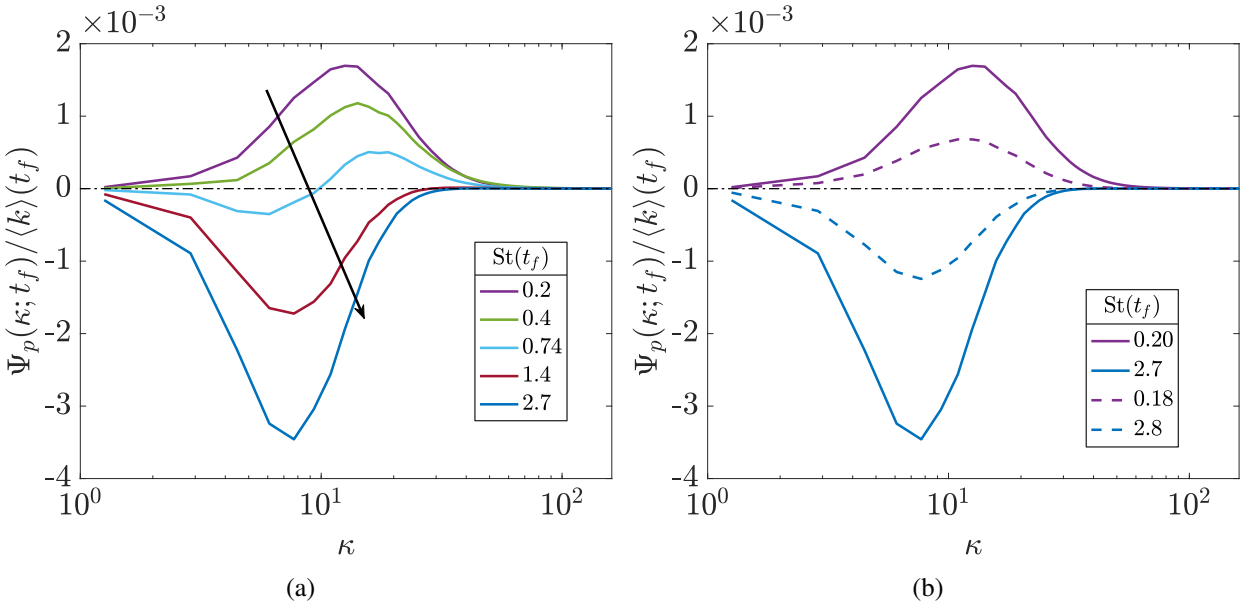

Figure 13.13. Normalized two-way interaction spectra $\Psi_p(\kappa)/\langle k\rangle$ at $t_f = 6$ for $n_\eta = 7$. Influence of the Stokes number based on final time (a) and of mass loading (b). Full lines (——): $\phi = 0.3$, dashed lines (- - -): $\phi = 0.1$

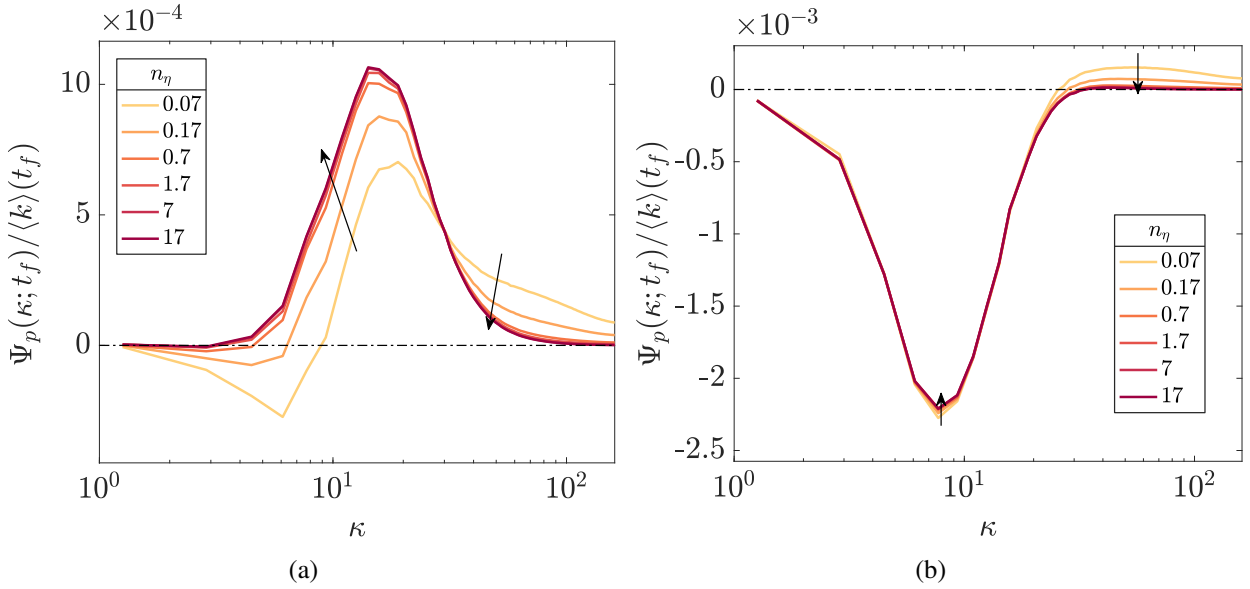

Figure 13.14. Spectral fluid-particle interaction plotted for different particle number densities n_η and fixed $\phi = 0.3$. (a) $\mathrm{St}(t_{inj}) = 0.60$; (b) $\mathrm{St}(t_{inj}) = 2.4$

van Wachem 2017; Abdelsamie and Lee 2012; Druzhinin 2001). In particular, Ferrante and Elghobashi (2003) compared $\Psi_p(\kappa)$ for different Stokes number and found similar results. Figure 13.13(a) shows that for particles with small Stokes number (microparticles), $\Psi_p(\kappa)$ is positive at almost all wavenumbers and thus produces a positive contribution to the decay rate $\partial E(\kappa)/\partial t$. On the other hand, the term is negative at almost all wavenumbers for larger Stokes numbers. For intermediate and large Stokes numbers, $\Psi_p(\kappa)$ remains positive for large κ while a negative peak appears in the spectrum for small κ.

Figure 13.13(b) shows the spectral fluid-particle interaction for two different Stokes numbers and two different mass loading. As mentioned in Sec. 13.2.2, the scaling between spectra with same Stokes number but different mass loading is close to the ratio of mass loading, but because of the non-linearity, we do not expect such scaling for higher mass loading.

Previous results show that a low particle number density results in an increase in the fluid-particle interaction energy rate $\langle \psi_p \rangle (t)$, especially when the mass loading is high. Let us study the spectrum of this exchange term to identify at what scales the interactions between particles and fluid are located and how the distribution of mass loading can modify the fluid energy. We can see in Figs. 13.13(a) and 13.13(b) that a heterogeneous disperse phase ($n_\eta = 0.07$) systematically produces a larger $\Psi_p(\kappa)$ at small scales than a highly-concentrated one ($n_\eta = 17$). At large scales however, a heterogenous disperse phase reduces the two-way interaction contribution compared to higher particle number densities simulations.

We observe that the two-way interaction spectra are positive at the largest wavenumbers, even for large Stokes numbers (Fig. 13.13(b)). The feedback force in the momentum equation always results in a local alignment of fluid velocity around a particle with the particle velocity. The intensity of the feedback modulates this tendency to alignment. It is more obvious for low Stokes number, but it can also become important at high Stokes number and large mass loading.

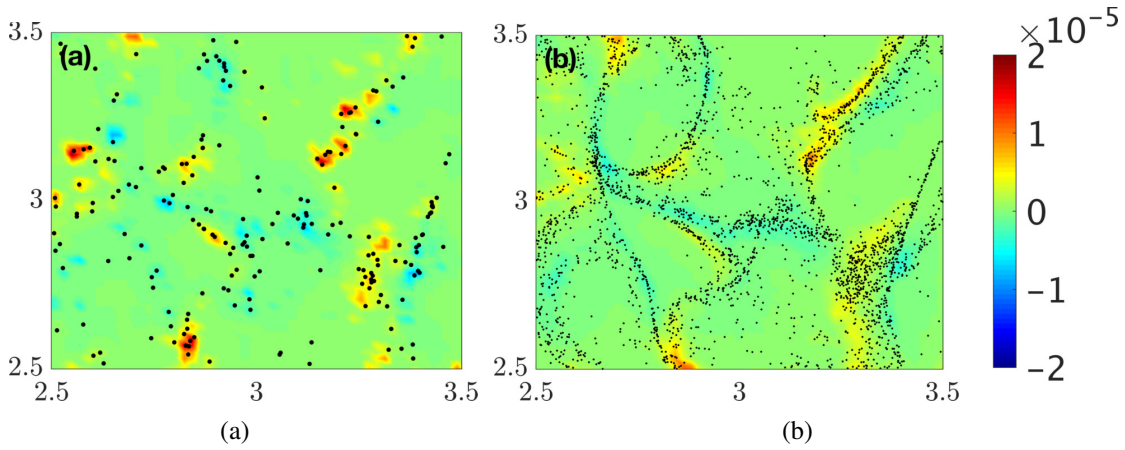

Figure 13.15. Distribution of two-way interaction energy rate ψ_p at $t = 6$ superimposed with particles parametrized by $\phi = 0.001$ and $\mathrm{St} = 1$. (a) $n_\eta = 0.12$; (b) $n_\eta = 2$

13.2.4 Particle field heterogeneity

For a physical intuition of the interpretation of the spectra in Sec. 13.2.3, the spatial distribution of the corresponding fields before the Fourier transform can be examined. Figure 13.15 compares the spatial distribution of the local two-way interaction energy rate $\psi_p(\boldsymbol{x}, t) = u_i(\boldsymbol{x}, t) f_i(\boldsymbol{x}, t)/\rho$, with superimposed particles in a part of the flow domain at time $t = 6$. Particles parameters were set to the same Stokes number $\mathrm{St} = 1$, and global mass loading $\phi = 0.001$, but different particle number densities. Figure 13.14(a) shows that each isolated particle produces a localized contribution to the two-way interaction term, and therefore the two-way interaction field is more heterogeneous than for the case with higher n_η, accordingly to the corresponding particle concentration field. By increasing the particle number density n_η without changing the total mass ϕ nor the behavior of each particle defined by St, see Fig. 13.14(b), each particle produces a smaller individual effect on the fluid. On the other hand, the collective effect of segregated particles results in a smoother and well-distributed two-way interaction field.

The probability distribution function of the corresponding spatial two-way interaction terms is plotted in Fig. 13.16, and the reduction of the tails indicates a better distributed interaction term for highly-concentrated disperse phase.

13.2.4.1 Preferential concentration

Figure 13.17 shows the standard deviation of the normalized Voronoï volume distributions for the different configurations. As explained in Sec. 13.1, the simulations were depleted in post-processing to equalize to the same number of particles in order to be able to compare them without statistical bias. The quasi-scaling of those curves is consistent with the fact that the Stokes number based on up-to-date time governs the preferential concentration, revealing that the adaptation is faster than the decrease in energy. Only simulations with low particle number density and low Stokes number increase the preferential particle concentration effect. We can conclude that all the two-way coupling effects that we analyze in our simulations are not a consequence of a modification of the clustering.

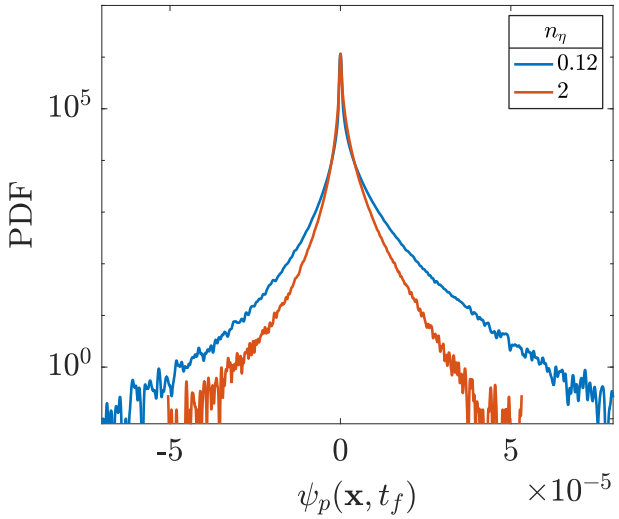

Figure 13.16. Distribution of the two-way interaction energy rate field $\psi_p(\boldsymbol{x}, t)$ for the heterogeneous and highly-concentrated cases.

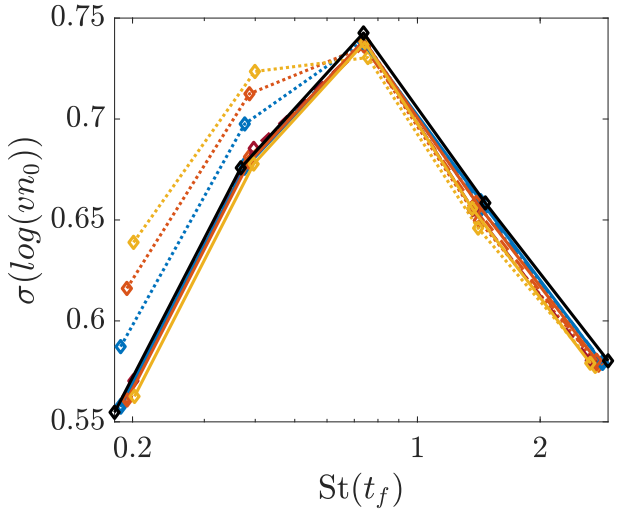

Figure 13.17. Comparison of preferential concentration for all simulations. Lines blue: $\phi = 0.1$, red: $\phi = 0.2$, yellow: $\phi = 0.3$, ——: $n_\eta = 7$, - - -: $n_\eta = 0.7$, ·····: $n_\eta = 0.07$. The black dash-dotted line stands for the single-phase flow.

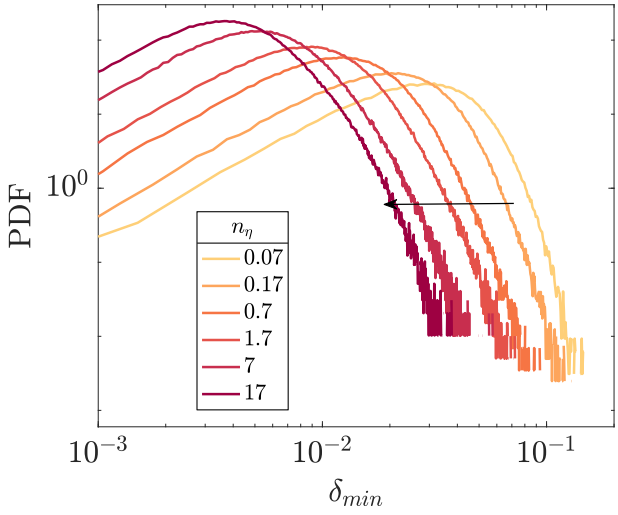

Figure 13.18. Probability density function of minimum interparticle distance for simulation with $\mathrm{St}(t_{inj}) = 0.6$ and $\phi = 0.3$ at $t_f = 6$. In our simulations, with the PSI-Cell approach, $2\delta_i = 2\Delta x = 0.04$.

13.2.4.2 Collective and isolated regimes

A single particle will interact and exchange energy with the surrounding fluid up to a characteristic length of δ_i, which is directly related to the size of the projection kernel[3]. The source term introduced in the fluid momentum equation is limited to the kernel envelope δ_i and we will consider that a particle is "isolated" if it is distant from others of more than $2\delta_i$ (the interaction zones of the two particles do not overlap). On the contrary, if two particles are closer than this length scale, their corresponding source terms can overlap and these two particles form a "cluster".

Let us consider the two limit regimes where particles are either all isolated to each other, or all part of a cluster. Those two configurations correspond to the PDF of the minimal interparticle distance being respectively on the right or on the left side of the $2\delta_i = 2\Delta x$ boundary, see Fig. 13.18. These limit behaviors are indeed observed in Fig. 13.14: green and light blue distributions of Fig. 13.18 are on the left of $2\delta_i$ and produced in Fig. 13.14 almost identical spectra, because the particulate phase is already converged and increasing particle number density do not change the interaction spectrum anymore. However, for the other distributions, on the other side of the threshold, one can see in Fig. 13.14 that the spectra are strongly dependent on particle number density, especially at the smallest scales, the last ones to reach convergence.

Let us explained these limit behaviors. If particles are all isolated from each other, then the particles properties locally determine the amount of energy exchanged with the fluid and the global budget is a statistical average of all the exchanges. Thus, if we modify the properties of this particle, for example by decreasing the particle number density of the simulation while ensuring that we keep isolated particles, then the mass m_p of the single particle is now larger and the amount of energy transferred will be locally larger. In this regime, the two-way interaction spectrum is highly sensitive to particle number density, especially at the smallest scales of the fluid, where particles inject an energy almost proportional to their mass.

[3]Using a trilinear projection, we verify that $\delta_i = \Delta x < \eta$

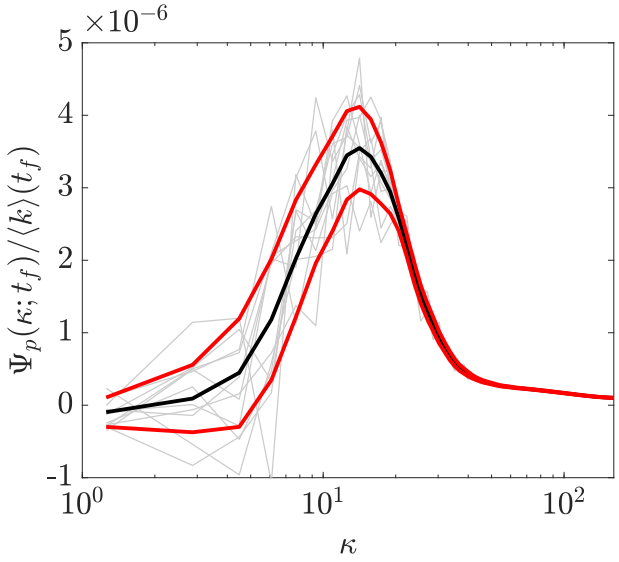

Figure 13.19. Normalized two-way interaction spectra $\Psi_p(\kappa)/\langle k\rangle$ for 11 realizations of simulation with $n_\eta = 8.4\times 2^{-14}$ (grey lines), the average spectrum $\langle\Psi_p\rangle(\kappa)/\langle k\rangle$ (black full line) and the standard deviation (red full lines).

On the contrary, if every particle is part of a cluster, the force exerted by particles on the fluid can be assimilated to a continuous force on the cluster domain. By increasing particle number density but maintaining the mass loading, the total mass and therefore the energy contained in each cluster is unchanged. Therefore, the two-way interaction spectrum is unchanged, this collective regime leads to the two-way limit behavior observed for spectra.

This criterion is very restrictive, those two limit regimes are rarely reached and we propose in the next section another approach to characterize the transition from the isolated to collective regime, scale by scale.

13.2.4.3 Scale by scale convergence

The two-way interaction spectrum indicates for each wavenumber the amount of energy introduced into the spectral equation. More precisely, each wave-number κ_l is associated to a physical size $l = 2\pi/\kappa_l$. Thus, the term $\Psi_p(\kappa_l)$ specifies the average energy provided by the exchange term in boxes of size l contained in the domain.

Figure 13.19 shows several realizations (grey lines) of the interaction spectrum of a very heterogeneous disperse phase ($n_\eta = 8.4\times 2^{-14} = 5.13\times 10^{-4}$). The spectra are noisy at the largest scales due to a lack of samples available for the corresponding box sizes. We define a reconstructed spectrum, in black line, as the mean spectrum of all the realizations $\langle\Psi_p\rangle(\kappa) = \dfrac{1}{N_R}\sum_R \Psi_p(\kappa)$, where N_r is the number of realizations of the simulation (same parameters of the disperse phase and the gas phase but different initial particle distribution). The standard deviation is also plotted in red lines in Fig. 13.19. The variability between the different realizations is reduced at the smallest scales because one flow realization contains a sufficiently large sample of small eddies to ensure a meaningful sampling.

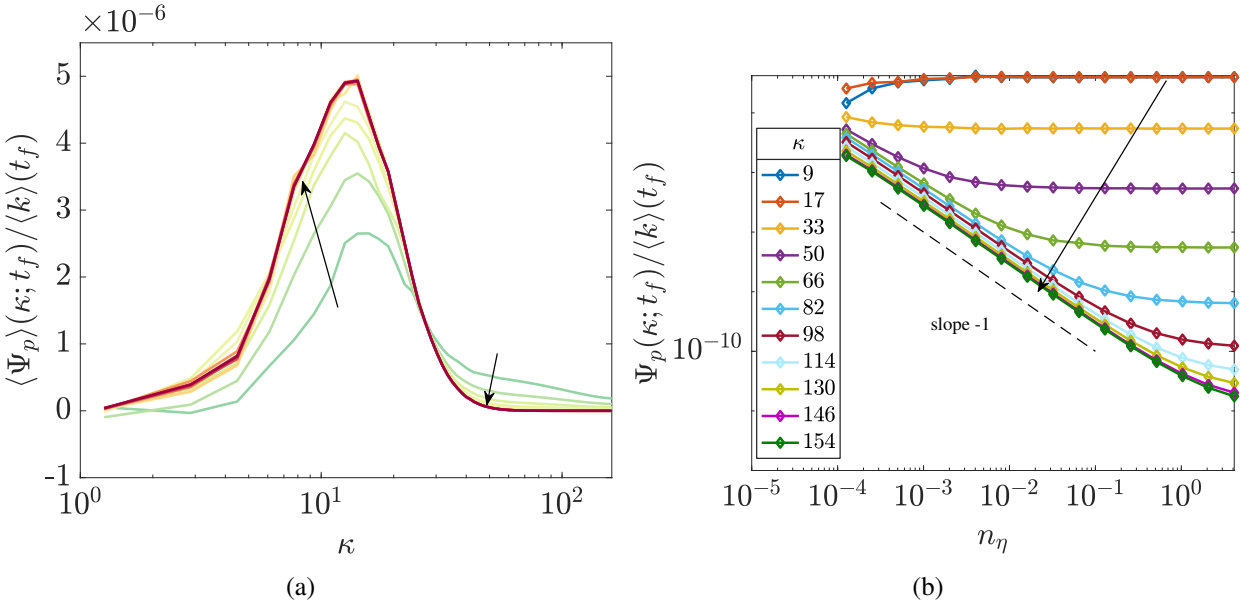

(a) (b)

Figure 13.20. (a) Normalized two-way interaction spectra averaged between several realizations with increasing particle number densities. (b) Evolution with n_η of the spectral values for different wavenumbers (the arrow indicates increasing wavenumbers).

In the following, to only take into consideration the effect of a representative realization of a highly heterogeneous disperse phase, we consider the average spectrum associated with several realizations (black spectrum). We thus obtain smoothed spectra in Fig. 13.20(a) even for very low particle number densities.

In Fig. 13.20(b), we have plotted for several wavenumbers the evolution of the spectrum values at those scales when n_η increases.
For each graph in this figure, we observe two very distinct regimes: a first linear zone of slope -1 for low n_η, and a second zone for high n_η, in which the spectrum values are converged and are therefore no longer modified when the particle number density increases. Those regimes are respectively the isolated (linear) and collective (converged) regime introduced before. This scale-by-scale convergence can be correlated with the convergence of the segregation measure defined with bin counting in Sec. 13.1.1, and is also a consequence of the statistical sampling related to the scale in consideration: the large scales reach their asymptotic value for smaller n_η than small scales, because the number of particles per scale is larger.

Conclusion

An exhaustive study of the influence of the three parameters describing a monodispersed phase on isotropic homogeneous turbulence has been carried out. Classical results from the literature have been retrieved, in particular the global trends in energy and spectral statistics with the Stokes number and mass loading. The study of the two-way coupling term here normalized by fluid kinetic energy and the use of a Stokes number based on instantaneous Kolmogorov scales have permitted to clearly identify two regimes: a first regime for $\mathrm{St} < 1$ in which particles reduce the decay of turbulent energy, and a second regime for $\mathrm{St} > 1$ in which particles enhance the decay.

Additionally to the existing literature, the present study has emphasized the influence of the particle number density on the coupling term. First, we ensured with a Voronoï analysis that the structure of turbulence is not strongly modified by the presence of particles: turbulence is sustained or dissipated but particle preferential concentration remains directly correlated to the updated Stokes number.

Numerical simulations have revealed that a highly heterogeneous particulate phase tends to increase the energy transmitted to the fluid. In particular, a spectral analysis showed that isolated particles inject energy at the finest scales while a continuous particulate phase no longer produces energy at these scales but rather at smaller wavenumbers. Those two regimes are reflected in the behavior of the energy spectra:

- At "small" scales, the spectrum is strongly dependent on particle number density and behave almost linearly with this parameter: the energy injected by particles is almost proportional to individual particle mass because particles are isolated regarding those specific scales.
- At "large" scales, the spectrum is no longer modified by the number of particles since the sampling is significant enough, all these scales necessarily contain a large number of particles.
- The limits for "small" and "large" scales depend on the mean particle number density.
- If the distribution of minimal interparticle distance is on the left side of η, the spectrum is completely converged: increasing particle number density does not modify the spectrum.

Furthermore, due to the high variability of the spectrum at large scales for low particle concentration, we have highlighted the necessity to construct statistics over several flow-particles realizations.

This study therefore made it possible to determine precisely the conditions of partial or total convergence of the spectrum as a function of the particle number density, and more precisely of the distribution of interparticle distances.

As a conclusion, it must be noted that such regimes, whereas being intrinsically present in Lagrangian point-particle approaches, must be included and modeled when the carrier phase description is given by a reduced description such as Large Eddy Simulation. The use of adapted Lagrangian stochastic models must be considered. For Eulerian approaches, even with a fully resolved carrier phase, accounting for heterogeneous regime requires new developments and closures at the kinetic level.

Chapter 14

Towards two-way coupling

Throughout this thesis, we have been particularly interested in Lagrangian approaches for particle SFS models with the aim of reproducing disperse phase statistics, in particular intermittency and particle preferential concentration. The objective of this chapter is to present the issues and objectives for extending these models to two-way coupling approaches.

The particle SFS models considered so far can be applied to one-way coupling, since the reduced-order model of the turbulence does not require any modification due to the presence of particles. Within a two-way coupling context, things are considerably more complicated. In Chap. 13, we have studied the implications of the two-way coupling in terms of turbulence modulation, which apparently affects all scales of the energy spectrum. Indeed, the presence of particles affects not only the large scales of the turbulence (leading to an additional term in the filtered velocity equation), but also the small scales, which is then a matter of sub-filter modeling for the fluid itself. The models will have to be adjusted accordingly.

Section 14.1 first reviews the consequence of accounting for two-way coupling when reductions are applied on the disperse phase, using the example of a combustor simulation. Then, Section 14.2 will clarify the possible statistically-consistent formalisms. Finally, an extension of the wavelet-based kinematic model to two-way coupling is proposed in Section 14.3.

14.1 Challenges with two-way coupled simulations

Apart from the discussions about the point-particle model itself, the two-way coupling does not add any complexity to DPS-DNS, except from numerical issues due to stiff source terms and interpolation and projection, and it stands as the reference simulation. The problem rises when we switch to a mesoscopic statistical description of the disperse phase, which is necessarily based on an ensemble-average in some sense to be clarified. In a one-way coupling framework, one can consider the ensemble-average of his choice for the disperse phase, as it has no consequence on the carrier phase, in the spirit of the Mesoscopic Eulerian Formalism of Février, Simonin, and Squires (2005). However, with two-way coupling, any ensemble-average on the particle will propagate to the carrier phase, as stated in Mercier (2020). Therefore, whatever the reduction technique applied to the carrier phase, there is an additional ensemble-average that is applied to it, and the statistical description of the gas phase will depend on the chosen particle ensemble (initial conditions, boundary conditions...). In the worst case scenario, this particle ensemble would permit, coupled to the carrier phase, to cover the whole space of possible states for the system of interest. It will

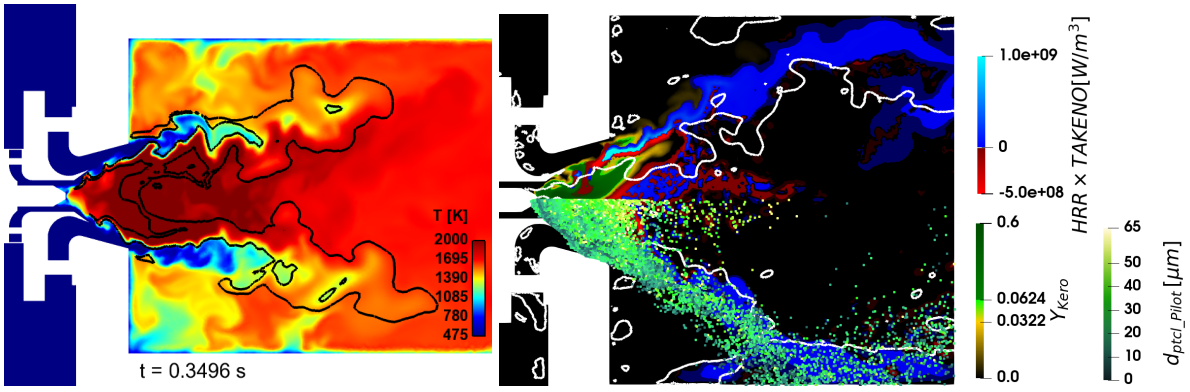

(a) (b)

Figure 14.1. Simulation of the BIMER combustor with (a) an Eulerian Moment Method (Cheneau, Vié, and Ducruix 2019) and (b) a Lagrangian Particle Tracking (Cunha Caldeira Mesquita, Vié, and Ducruix 2017) with Large Eddy Simulation. In (a), the represented field is the gas temperature with an isoline of heat release rate to identify the flame. In (b), we represent the combustion regime with the Takeno index, the fuel mass fraction, along with particle position in a slice, colored by their diameter.

therefore turn to a RANS formalism. Therefore, great care must be given to the interpretation of the resolved quantities and to the closure of the models, as defining the statistical ensemble is mandatory.

For instance, some simulations of two-way coupled combustion systems have been performed using Eulerian moment methods (Eleonore Riber 2007; Sanjosé, Senoner, Jaegle, Cuenot, Moreau, and Poinsot 2011; Cheneau, Vié, and Ducruix 2019; Lancien, Prieur, Durox, Candel, and Vicquelin 2018), see Fig. 14.1(a). The simulations were two-way coupled in mass, momentum and energy. Even if the particle ensemble-average is expected to apply to the gas phase, no specific care has been taken in this optics: the moment method has not been designed considering this aspect. So what can we expect from this kind of simulations? This is discussed in the following[1]:

- **Homogeneous limit**: as shown in Chap. 12, when the density of particles becomes high enough, each realization will lead to the same Eulerian fields, and thus the same coupling with the carrier phase. Therefore, the ensemble-averaging will have no impact on the carrier phase statistics, as demonstrated in the previous chapter, and its resolution will remain unaffected [2]. However, in the case of aeronautical combustors, the Lagrangian simulations exhibit several isolated droplets (see Fig. 14.1(b) as an example). This excludes a possible homogeneous regime for most of the combustion chambers (in that case after the divergent exit, far enough from the injector). So the "meaning" of the resolved quantities must be related to the statistical ensemble of the particle, which is not the case in actual combustor simulations.
- **Single realization**: another solution is to no longer perform an ensemble of realizations for the particles. This way, the resulting formalism will become a one-shot simulation. In a Lagrangian context, this turns out to be a DPS. In an Eulerian framework, this corresponds to the resolution of the equation on the fine-grain NDF, for which no ensemble average is

[1] Here we take aside the related numerical issues

[2] It stays that if the gas phase resolution is based on ensemble-averaging such as in RANS, it will lead to an ensemble-average on the particle that must be accounted for.

applied, which could be performed using adapted moment methods. If we take aside the question of the numerics, there is one specific aspect that must be adapted: the boundary conditions. Actually, such Eulerian simulations make use of deported injection conditions, for which the atomization process is embedded into a 0D model, which gives spatial profiles of droplets in the disperse phase region. Existing injection models consider for instance a Gaussian profile of liquid volume fraction. Such a continuous profile is not representative of a one-shot simulation, as the droplet injection rate is not high enough to reach converged profiles. Furthermore, constructing a one-shot injection model would also require to model the particle-turbulence correlations, which are here missing. Thus, even if we forget about the adaptation of the closure models and the numerical issues, the injection condition prevents from interpreting such simulations with respect to a single realization.

- **Extended Mesoscopic Eulerian Formalism (EMEF)**: the last solution has been investigated in Février, Simonin, and Squires (2005), and further explored by Mercier (2020): the conditional average. As stated in Chap. 12, the two-way coupling can occur in certain conditions at small length scale. If we consider that resolved scales in the ROS are larger than the coupling scale, the coupling will be limited to unresolved scales and the additional modeling due to two-way coupling will be limited to sub-filter scales. Looking at the Large Eddy Simulations of Fig. 14.1, this is this last interpretation that could hold, but under several assumptions, as stated in Mercier (2020). This is discussed in the next section.

14.2 Statistically-consistent two-phase formalisms with two-way coupling

If many efforts have been devoted to particle SFS modeling in one-way framework, there are few studies conducted on two-way coupling with a reduced description of the turbulence. Among them, Boivin, Simonin, and Squires (2000) have performed LES of gas-solid flows in forced HIT with two-way coupling. They applied several sub-grid models in the fluid equations and several LES resolutions in *a priori* and *a posteriori* tests. They were able to capture complex spectral behavior of the source-sink fluid-particle energy exchange only for $\mathrm{St}_\Delta > 1$. We had already noticed that in this case, it is not necessary to add a particulate SFS model and the significant part of the energy exchange with the fluid occurs at large scales, which are resolved. Note that this particular case corresponds to a unique realization of the disperse phase, without reduction on particles, interacting with a reduced description of the fluid.

If we introduce a reduction in the particle description, as mentioned in the previous section, it could lead to a statistical average on the carrier phase, whatever reduction technique initially chosen for the carrier phase. In the following subsection, we discuss the interaction between resolved and unresolved scales, to highlight how reduction on small scales could affect the large scales, and we will naturally go to the Extended Mesoscopic Eulerian Formalism introduced by Mercier (2020).

14.2.1 Interactions between unresolved and resolved scales in ROS

In ROS an operation (filtering or averaging) is performed to reduce the dimensionality of the original set of equations. Applied to a unique carrier phase realization, we obtain a filtered field. At this point, there is a first issue related to the invertibility of the filtering operation: for a given filtered

field, is there a unique unfiltered field that leads to it?

Some filters are invertible, such as the Gaussian filter, for which the filtered field belongs to one and only one unfiltered field. Please note that an invertible filter does not reduce the dimensionality of the problem in terms of wave-numbers, as the energy is simply reduced at small wavelengths, and not discarded.

But some are not, such as the box filter, which loses information that cannot be recover by deconvoluting the filtered field. When projecting a solution on a mesh, information is lost for scales smaller than the mesh size and this information cannot be recovered. For the fully-resolved fields, we can choose a mesh fine enough to capture all details. But with ROS, we expect to use a mesh with significantly less degrees of freedom than for the fully-resolved fields. Therefore we can postulate that ROS are in general based on a non-invertible filtering operation, either because of the mesh or because of the filter itself.

From this statement, when computing the evolution of the filtered field in ROS, the question is to know if the evolution of the filtered field is unique or not, as different sub-filter scales could lead to different evolutions of the large scales. The options are the following:

- The evolution of the large scales is unique: this is only possible if we consider a unique field for the unresolved scales, or if we consider that all possible sub-grid scales have the same impact on the large scales.
- Otherwise, in the general case, the evolution of the large resolved scales must be described statistically, as an ensemble-averaged over all sub-grid scale realizations.

14.2.2 Consequences of two-way coupling on the statistical description

This discussion was made considering a purely single-phase flow, and it should now be extended to coupled two-phase flows. As mentioned before, the presence of particles can significantly affect turbulence. Depending on the regime, this forcing can occur at large resolved scales or at small unresolved scales. If we consider a unique evolution of the large scales, a unique sub-filter scale, and a unique particle realization (one-shot simulation), the simulation is equivalent to a DPS, and no specific issue arises. If on the other hand, we aim at a statistical description of the particles, here are the new options:

- The forcing of particles is at small scales: we can consider statistics conditioned on a unique large scale for all particle realizations and all possible sub-filter scales. This is possible if the sub-filter scales have the same impact on the large scales. If not, the ensemble average over the particle will eventually lead to a ensemble-averaged formalism, with no control on the resolved statistics. This was proposed by the EMEF of Mercier (2020).
- The forcing of particles is at large scales: we cannot take all possible particle realizations, as they will modify the large scales. In that case, we must consider the ensemble of particle realizations that share the same impact on the large scales. Thus the statistics are conditioned on both the large-scale and on a subset of particle realizations.

14.2.3 A classification of possible strategies

With regards to the previous discussion, we propose in Fig. 14.2 a classification of acceptable modeling frameworks.

First of all, if we consider a DPS for the particles, there are only two possible modeling frameworks:

- **The reference DNS-DPS** framework which is the base model for all our derivation;
- **The two-phase single shot ROS**: if we couple a DPS with any ROS of the carrier phase, we have no choice but to consider a one-shot ROS, for example with a time-space explicit reconstruction of the sub-filter scale information. If any random variable is to be accounted for in the ROS description, such as RANS, we must switch to probabilistic ensemble-averaged methods (which can still be solved using stochastic Lagrangian models or Eulerian approaches).

Now, if we switch to an ensemble-averaged description for the particles, the landscape is more complex, and the choice of the modeling framework will be a consequence of the physics to be solved. Here are the options:

- **The Fully-Resolved Point-Particle approach**: in the homogeneous limit, for which all realizations are equivalent with respect to the coupling, i.e. each realization will give the same result. There is in this case no interest in performing any statistics and we have the full statistical content in one realization.
- **The two-phase RANS**: in the general case, without any physical assumption or statistical restriction, a statistically-consistent formalism is to a consider a RANS formalism, which ensemble-averaged is the combination of the gas-phase ensemble average and the disperse phase ensemble average, hence the name two-phase RANS. The required closures will be far more complex than in the single-phase case because of phase interactions.
- **The EMEF**: this formalism considers statistics conditioned on restricted ensembles of the carrier phase or the particle phase. There is however a strong requirement on the impact of carrier phase sub-filter scales on the resolved scales. All small scales must have the same impact on the large scales, so that an ensemble-average over the small scales does not result in an ensemble-average on the large scales. There are also requirements on the particulate phase physics, which leads to two approaches:
  - **Large-scale conditioning**: the EMEF is based on conditioning statistics to a unique large-scale realization. This is only possible if the particulate phase is homogeneous at the large-scale, i.e. all realizations lead to the same large-scale coupling, or if, for an heterogeneous regime, the coupling is active at small scales only, which is not true in the general case.
  - **Large-scale and particle sub-ensemble conditioning**: for an heterogeneous regime, if the coupling is at large scales, we must condition the statistics with both a unique large scale realization and a sub-ensemble of particle realization that shares the same large scale coupling.

This proposed classification does not give a direct resolution of two-phase flows, but intends to give an insight of what can be understood from a two-way coupled simulation and some coarse guidelines to analyze the statistics of such flow, when the objective is to construct models. In the next section, regarding the contributions of this thesis, we propose a modeling strategy making use of kinematic simulations.

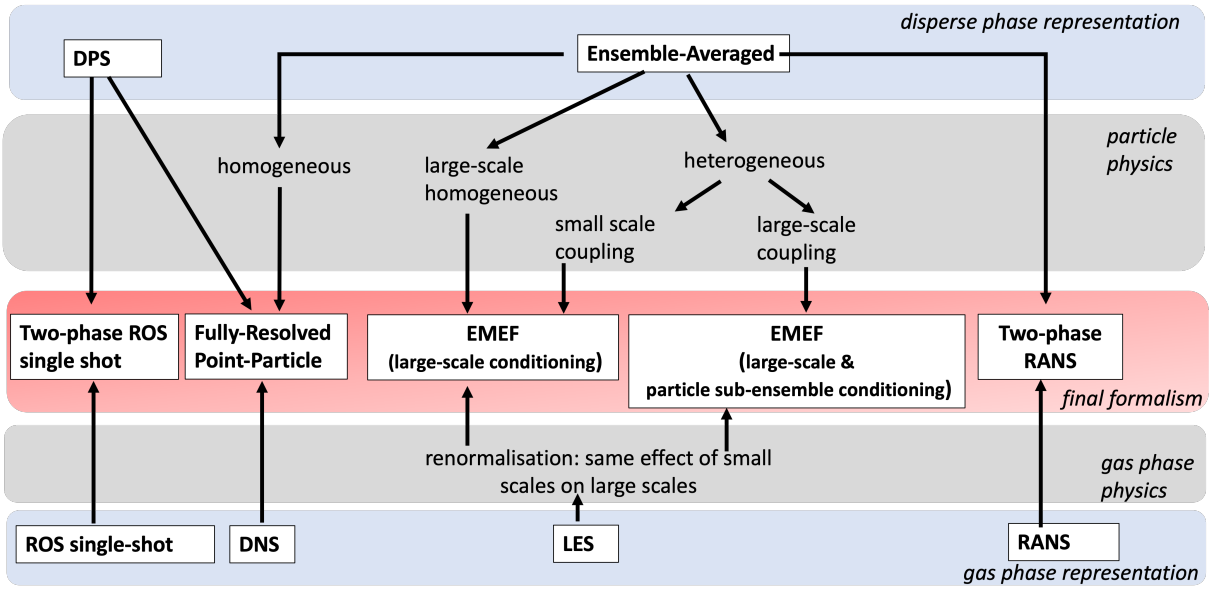

Figure 14.2. Classification of possible modeling strategies with two-way coupling between the particle and the carrier phase. This schematic describes the various paths to get a consistent modeling approach. The reader should choose the options on top and bottom rows, and should follow one of the paths to get to the appropriate formalism, depending on the acceptable physical hypotheses.

14.3 Extension of kinematic simulation for two-way coupled flows

Recall that the wavelet-based kinematic model depends only on a limited number of inputs:

- The spectral model $E(\kappa)$, itself constrained by the kinetic energy $\langle k \rangle$ and the dissipation $\langle \varepsilon \rangle$.
- The model of temporal evolution of the coefficients $d^{\varepsilon}_{\mathrm{div},j,\boldsymbol{k}}$
- The model for the eddy turnover time of each level ω_j

In the following, we assume that the two-way coupling does not modify the temporal evolution of coefficients nor the eddy turnover times. On the other hand, we expect from the study conducted in the previous chapter that the energy spectrum of the fluid is modified by the presence of the particles. We propose three strategies, associated with three levels of coupling:

- **On global statistics:** as observed in Chap. 13, the presence of particles modifies the total dissipation of the fluid, and therefore the system reaches a new stationary state. The target energy spectrum to be reproduced by the KS is hence adapted to produce the total dissipation.
- **On the energy spectrum:** in the previous chapter, we also observed the spectral distribution of the energy associated with the coupling term with the particles, and thus the scale by scale modifications on the energy spectrum of the fluid. The kinematic model then takes as input a two-way energy spectrum perturbed by the presence of the particles.
- **On the momentum:** Unlike the previous two methods, this coupling respects the locality of the particles, by introducing a modification of the fluid velocity precisely at the location of the particle clusters. The two-way coupling term is projected on a wavelet basis and added to the corresponding local wavelet coefficient.

These strategies are detailed in the following subsections.

14.3.1 Global statistics

The target spectrum being fixed $E(\kappa) = C \langle\varepsilon\rangle^{2/3} \kappa^{-5/3}$, there is a bijection between the spectrum and $\langle\varepsilon\rangle$. Let us assume that the dissipation rate of the fluid in the absence of a particle is known, noted $\langle\varepsilon_1\rangle$. The stationarity condition allows us to obtain the energy production term $\langle P_1\rangle$ simulated by the kinematic model:

$$\frac{d\langle k_1\rangle}{dt} = \langle P_1\rangle - \langle\varepsilon_1\rangle = 0 \tag{14.1}$$

In two-way, the particle dissipation source term subtracts from the fluid dissipation, as already derived in Eq. (12.6):

$$\frac{d\langle k_2\rangle}{dt} = \langle P_2\rangle - \langle\varepsilon_2\rangle + \langle\psi_p\rangle \tag{14.2}$$

assuming that in this flow, the same type of external forcing has been applied as in the one-way case, we have $\langle P_2\rangle = \langle P_1\rangle$. By looking for the stationary solution of these statistics, we obtain an equivalent dissipation $\langle P_2\rangle = \langle P_1\rangle - \langle\psi_p\rangle$. The new spectral model is then given by this dissipation $\langle\varepsilon_2\rangle$. The term $\langle\psi_p\rangle$ is obtained (see Chap. 13) by:

$$\langle\psi_p\rangle(t) = \frac{\phi}{\tau_p n_0}\Big\langle n(\boldsymbol{x},t)u_i(\boldsymbol{x},t)[\tilde{v}_{p,i}(\boldsymbol{x},t) - \tilde{u}_{@p,i}(\boldsymbol{x},t)]\Big\rangle \tag{14.3}$$

As for the DNS study performed in the previous chapter and in order to avoid modeling the transient regime, we run the one-way simulation with particles until we reach the steady state, before computing $\langle\psi_p\rangle$.

14.3.2 Global spectrum

Assuming that the particles only modify specific scales of the energy spectrum, we propose here to release the constraint of the original spectral model and to allow the forcing of certain wavelengths by the particle coupling term. Here we are interested in the turbulent energy equation for each wavelength. In one-way coupling, the kinematic model must reproduce the well known behavior:

$$\begin{aligned}\frac{\partial E_1}{\partial t} &= P_1(\kappa) + T_1(\kappa) - D_1(\kappa)\\ \frac{\partial E_1}{\partial t} &= P_1(\kappa) + T_1(\kappa) - 2\nu\kappa^2 E_1(\kappa) = 0\end{aligned} \tag{14.4}$$

This stationarity condition gives us, in the one-way context: $P_1(\kappa) + T_1(\kappa) = 2\nu\kappa^2 E_1(\kappa)$.

For two-way coupled flows, this equation is modified and we add the two-way coupling term, introduced in Eq. (12.8):

$$\begin{aligned}\frac{\partial E_2}{\partial t} &= P_2(\kappa) + T_2(\kappa) - 2\nu\kappa^2 E_2(\kappa) + \Psi_p(\kappa)\\ \frac{\partial E_2}{\partial t} &= P_1(\kappa) + T_1(\kappa) - 2\nu\kappa^2 E_2(\kappa) + \Psi_p(\kappa)\\ \frac{\partial E_2}{\partial t} &= 2\nu\kappa^2(E_1(\kappa) - E_2(\kappa)) + \Psi_p(\kappa) = 0\end{aligned} \tag{14.5}$$

where we assume that the same forcing $P_1(\kappa)$ is applied and that the energy transfer, mainly attributed to the fact that large scales give up their energy to small ones, is also conserved: $P_1(\kappa) + T_1(\kappa) = P_2(\kappa) + T_2(\kappa)$.

This finally gives in steady state the following spectrum for two-way coupled flows:

$$E_2(\kappa) = E_1(\kappa) + \frac{\Psi_p(\kappa)}{2\nu\kappa^2} \tag{14.6}$$

The spectral term $\Psi_p(\kappa)$ is obtained by taking the spectral Fourier transform of the interaction term, following Eq. (12.9):

$$\Psi_p(\kappa, t) = -\sum_{\kappa \leq |\boldsymbol{\kappa}| \leq \kappa+1} \Re\Big\{ \hat{u}_i^\star(\boldsymbol{\kappa}, t) \frac{\hat{f}_i(\boldsymbol{\kappa}, t)}{\rho} \Big\} \tag{14.7}$$

where

$$\frac{1}{\rho}\boldsymbol{f}(\boldsymbol{x}, t) = \phi \frac{n(\boldsymbol{x}, t)}{n_0} \frac{\tilde{\boldsymbol{v}}_p(\boldsymbol{x}, t) - \tilde{\boldsymbol{u}}_{@p}(\boldsymbol{x}, t)}{\tau_p} \tag{14.8}$$

In a RANS context, these "global" couplings do not correspond to a single-shot fluid realization because the target spectrum does not retain the local information of the position of the particles. Thus, the changes in the target spectrum can generate a modification of the fluid which is transmitted to every point in the space.

In a LES context however, as seen in Sec. 11.2.4, the target spectrum can be adapted to the sub-grid scale (given σ_{sgs} and ε_{sgs}), and the locality of the information is thus preserved, at best, at the resolved scales. In that case, such coupled KS can be applied in the framework of EMEF (large-scale conditioning), by assuming that the disperse phase is large-scale homogeneous, i.e. all possible realizations of the disperse phase produce the same effects on the carrier phase.

In order to keep the locality, it is rather necessary to directly modify the fluid field at the position of the particles, which is allowed by the following local model.

14.3.3 Local two-way coupling

In this case, we do not model the energy brought to the fluid by the particles but directly the momentum. The Navier-Stokes equation gives:

$$\mathrm{d}\boldsymbol{u_1} = \left(\boldsymbol{f}_{\text{ext}} - \boldsymbol{u_1} \cdot \nabla \boldsymbol{u_1} - \frac{1}{\rho}\nabla p + \nu \Delta \boldsymbol{u_1} \right) \mathrm{d}t \tag{14.9}$$

and the kinematic model prescribes the evolution model of each wavelet coefficient

$$\mathrm{d}d^{\varepsilon}_{\text{div},j,\boldsymbol{k},1} = -\omega_j d^{\varepsilon}_{\text{div},j,\boldsymbol{k},1}\,\mathrm{d}t + \sqrt{2\sigma_j^2\omega_j}\,\mathrm{d}W_t \tag{14.10}$$

Assuming thus that this evolution equation models the right hand side term of the Navier-Stokes equation and that it is not strongly modified by the presence of particles, the Navier-Stokes equation

to model in two-way framework becomes:

$$\begin{aligned} \partial_t \boldsymbol{u_2} &= \left(\boldsymbol{f}_{\text{ext}} - \boldsymbol{u_2} \cdot \nabla \boldsymbol{u_2} - \frac{1}{\rho} \nabla p + \nu \Delta \boldsymbol{u_2} + \frac{1}{\rho} \boldsymbol{f} \right) \mathrm{d}t \\ \partial_t \boldsymbol{u_2} &= \partial_t \boldsymbol{u_1} + \frac{1}{\rho} \boldsymbol{f} \end{aligned} \tag{14.11}$$

By projecting the coupling term onto the divergence-free wavelet basis:

$$\frac{1}{\rho} \boldsymbol{f} = \sum_j \sum_{\boldsymbol{k}} \sum_{\varepsilon} d^{\varepsilon}_{f,\mathrm{div},j,\boldsymbol{k}} \Psi^{\varepsilon}_{\mathrm{div},j,\boldsymbol{k}} \tag{14.12}$$

We then obtain a modified evolution equation for each local coefficient:

$$\mathrm{d}d^{\varepsilon}_{\mathrm{div},j,\boldsymbol{k},2} = \left(-\omega_j d^{\varepsilon}_{\mathrm{div},j,\boldsymbol{k},2} + d^{\varepsilon}_{f,\mathrm{div},j,\boldsymbol{k}}(t) \right) \mathrm{d}t + \sqrt{2\sigma_j^2 \omega_j}\, \mathrm{d}W_t \tag{14.13}$$

The local coefficient $d^{\varepsilon}_{\mathrm{div},j,\boldsymbol{k},2}$ is now driven by an Ornstein-Uhlenbeck process with an additional drift term coming from the particle momentum: particle fluid velocity will tend to align its velocity on the particle one.

Such approach could result in a "two-phase ROS single-shot", since one realization of the disperse phase interacts with one particular velocity field, fully reconstructed (from large to smallest scales).

14.3.4 Next steps

We have proposed an extension to two-way coupling of our kinematic model based on wavelets, which could also include intermittency effects if the energy cascade is explicitly handled. This final local two-way coupling strategy has the advantage of making use of the whole richness of wavelets. But several assumptions still have to be made in order to close the model, which must be verified. Furthermore, all the developments have been made in HIT cases, and the next step towards applications is to handle realistic geometry and we thus need to investigate how to impose boundary conditions. A last comment would be to mention that this model contains a high level of information compared to what is used in applications, and it will be necessary to ensure that the model that makes use of droplet "output" (evaporated fuel for example) is taking into account all the details that we have added to the disperse phase description.

Conclusion

This chapter outlines the issues at stake in the treatment of the two-way coupling and defines, according to the resolution strategies for each phase, the appropriate framework to perform this coupling.

The statistical treatment of the dispersed phase, through the coupling, necessarily introduces a statistical approach of the carrier phase and it is then essential to establish conditioning strategies according to the scales of the coupling.

The under-resolved turbulence, which already requires the addition of particle SFS models in a one-way context, must also be reconsidered in the two-way framework and we distinguish different strategies depending on the nature of the ROS and of the disperse phase (homogeneous, heterogeneous...).

We are finally considering some ideas for future two-way models, based on the wavelet-based kinematic models, and detail the approaches according to the level of coupling.

Conclusion

This thesis has lifted several critical barriers for the design and use of reduced-order models as predictive tools for applications involving turbulent disperse two-phase flows. Such flows are involved in a wide panel of environmental and industrial applications, which motivates the need for reachable numerical simulation.

The random and multi-scale nature of single-phase turbulent flows requires statistical tools and reduced-order models. The extension of these methods to disperse two-phase flows raises many challenges. This thesis brings some answers: the objective of a particle sub-filter scale model is to recover accurately statistics and macroscopic trends, such as intermittency, segregation, or two-way coupling between the particles and the carrier phase.

We have conducted exhaustive analyses, implemented various tools, and proposed new models to address these challenges. Eventually, let us emphasize some key achievements of this work.

Main analyses

Before developing appropriate models, we have carried out several in-depth analyses to shed new light on the mechanisms identified in such flows (intermittency, segregation, two-way coupling) and the way they are addressed in the literature.

Framework for stochastic models

We have proposed a classification of stochastic models for fluid and inertial particles (Chap. 3 and 8). This review of the existing models identifies different components:

- level of modeling: the stochastic model can address the position, velocity, acceleration, dissipation of the particles. This choice has consequences in particular regarding the order of derivability of the processes obtained;
- compatibility with turbulence theories: the closure of the diffusion term of the Langevin equations can be made compatible with the K41 theory (a global constant for the dissipation must be introduced), or K62 (the local dissipation must be reconstructed);
- type of model used: the Langevin model is often used in the literature, but other choices can be considered, for example by modeling separately the norm and the direction of the stochastic process. Moreover, in order to reproduce intermittent statistics, multi-fractal stochastic processes must be considered, such as fractional Brownian motions;
- sub-filter information: we have established general notations $T_L^\star$, $\sigma_\star$, and $\varepsilon_\star$ which can be adapted to any reduced-order model. RANS simulations result in identified constants T_L, σ_u and $\langle\varepsilon\rangle$, while LES provide modeling of sub-grid terms at the resolved scale.

Identifying and adequately assessing these modeling choices allows us to benchmark the models available in the literature and consider different combinations of choices for future models.

Framework for intermittency

Intermittent processes obtained from Gaussian multiplicative chaos have been studied under an original perspective (Chap. 4).

- General framework: we have derived an original approach for the construction of such processes that encompass existing processes and have also led us to propose a new one.
- Regularization: relying on an infinite sum of correlated Ornstein-Uhlenbeck processes, we have introduced different regularization strategies for FBM to obtain a stationary log-correlated process (Chap. 4 and 5).
- Mathematical definition and turbulence applications: we have established a link between the mathematical definition of an intermittent process and its common use in turbulence. The two visions are reconcilable for zero viscosity (or infinite Reynolds), and processes for turbulence with high but finite Reynolds numbers can be modeled with regularizations of the GMC. This regularization involves two characteristic times, the Kolmogorov time, which enables the existence of the physical process, and the correlation time T_L, which is necessary to stationarize the process.

Such characterization and formalism set up the theoretical background for new stochastic models reproducing intermittency.

Modulation of two-way coupling

The modulation of turbulence by sub-Kolmogorov particles has been thoroughly characterized in the literature, showing either enhancement or reduction of kinetic energy at small or large scale depending on the Stokes number and the mass loading. However, the impact of a third parameter, the number density of particles, had not been independently investigated. In Chap. 13, we have performed DNS of decaying HIT loaded with monodisperse sub-Kolmogorov particles, varying the Stokes number, the mass loading, and the number density of particles independently. Several achievements can be highlighted:

- Retrieving literature results: Like previous investigators, we have observed consistently crossover and modulations of the fluid energy spectra with the change in Stokes number and mass loading.
- Role of particle number density: Additionally, DNS results show an apparent influence of particle number density, promoting the energy at small scales while reducing the energy at large scales. For high particle number density, the turbulence statistics and spectra become insensitive to the increase of this parameter, presenting a two-way asymptotic behavior. Our investigation identifies the energy transfer mechanisms and highlights the differences between the influence of a highly concentrated disperse phase (high particle number density, asymptotic behavior) and that of heterogeneous concentration fields (low particle number density).
- Identification of isolated and collective regimes: In particular, a measure of this heterogeneity is proposed and discussed, enabling the identification of specific regimes in the evolution of turbulence statistics and spectra.

We were thus able to identify the scales and mechanisms of these energy transfers, in order to bring in new ingredients for the design of a model in the framework of ROS.

New constructions

Based on these analyses, we have proposed original models, techniques, and tools to enrich the ROS, paving the way for accurate two-way coupled simulations

A versatile Lagrangian stochastic intermittent process

Following the framework established for the construction of intermittent processes, we have proposed in Chap. 5 a new stochastic model X_t^∞, based on an infinite sum of correlated Ornstein-Uhlenbeck processes. A regularization of $k(x)$ is required to ensure stationarity, finite variance, and logarithmic autocorrelation. A variety of regularizations are conceivable, and we have shown that they lead to the aforementioned multifractal models. To simulate the process, we eventually designed a new approach relying on a limited number of modes for approximating the integral using a conventional quadrature method. This method can retrieve the expected behavior with only one mode per decade, making this strategy versatile and computationally attractive for simulating such processes, while remaining within the proposed framework for a proper description of intermittency.

This construction can also be adapted to inertial particles by adjusting the characteristic time parameters according to the relaxation time of the particles (Chap. 8).

Adapted measures of segregation

In order to quantify the preferential concentration of particles, we have compared and developed suitable metrics and convergence criteria for these measurements (Chap. 13). The first one, $G(n, \ell)$ is a box-counting measure which converges for $n_\ell \gg 1$ and is particularly appropriate when $\ell < \eta$. However, in most simulations, these criteria are not met and the simulations can be compared to each other only after depopulation. The Voronoï measure allows to overcome the drawbacks of using fixed box size.
Finally, the measurement of the interparticle distance gives information on the heterogeneity of the disperse phase. This has two distinct origins: the preferential concentration of particles and the average density of particles.

Kinematic models

We have proposed two different models in the spirit of kinematic simulations (App. B and Chap. 9). For both Gaussian and wavelets fields, the idea is to generate synthetic divergence-free fields with a spatial correlation that can be adjusted to retrieve Eulerian and Lagrangian DNS statistics. Temporal evolution of the flow is then proposed, with stochastic evolution of the parameters. By controlling the model's characteristic length and time scales, we can reproduce the flow statistics and the particles segregation obtained by DNS with a better agreement than with Fourier-based kinematic simulation. The wavelet-based KS is promising both for data compression purposes and because it can be adapted to existing LES models, as wavelets allow to keep the locality of the sub-grid information.

Main perspectives

The perspectives can be twofold:

- Future works will consist in extending and improving the models developed in this thesis. The difficulties can already be identified and are only a technical matter. Their achievement should require comparative studies or more advanced analyses, similar to those conducted in this thesis.
- Future challenges, however, require new model developments or to address broader questions.

Extension of this work

- **Wavelet-based KS as a single-phase ROS**
  The question of the validity of the wavelet model itself as a single-phase LES model can be raised. Many properties on the kinematic field remain to be observed, and analytical quantities such as σ^2_{ref}, the dissipation or the turbulent kinetic energy could be derived. Furthermore, it would be interesting to conduct a comparative study with existing functional and structural LES models (e.g., Smagorinsky) regarding fidelity and numerical cost. Perspectives of compression mentioned in Chap. 11 can be further extended for this purpose.

- **An intermittent kinematic model**
  A logical extension of this work would be to introduce suitable stochastic processes within the kinematic wavelet model to obtain an intermittent velocity field, in line with the suggestion of Chap. 11. This requires redefining the properties of an Eulerian intermittent field by considering the multifractal nature of the spatial locally averaged dissipation instead of the temporal one. The idea is to identify some correlations between the random distributions of the local coefficients of different levels to reproduce a given cascade model.

- **Two-way coupling in Lagrangian framework**
  Based on the analysis of the coupling terms between the two phases carried out in this thesis, it is now possible to recognize the configurations for which this coupling only affects the small scales, or on the contrary, in which cases the source term introduced by the particles also affects the large scales. An extension of models developed in this thesis to two-way coupled flows could be performed in future works. The ideas for such models presented in Chap. 14 could be developed, implemented, and compared to the results of the DNS studies.

Next challenges

- **Modeling assumptions**
  Models of this thesis have been validated under strong and restrictive assumptions: the disperse phase is handled in a point-particle approach, and the turbulent carrier phase is homogeneous and isotropic. The physical cases often push these approximations to the limit of their validity. On the one hand, the complexity of the geometry and the turbulence's nature may require the use of specific models (near-wall models, inhomogeneous turbulence...). On the other hand, the geometry of the particles can also be much more complex, ranging from polydisperse sprays to separated phase flows, which are processed today with a different approach. In atomization jets, flows include all these geometries, and the question of a

unified model for the description of multiphase flows is a strong and open challenge for the community (Cordesse 2020; Loison 2024).

- **Objective of the modeling strategy**
  In general, the scope of modeling strategies for LES of particle-laden flows is to capture particles dynamics. Such dynamics require an accurate description of particle localization (preferential concentration) and particle acceleration. However, it is necessary to give meaning to "accurate description", and in particular to define the metric to compare and validate the results. The notions of measures and ensemble-averages must therefore be clarified. For example, following the conclusions of Pozorski and Apte (2009), we would expect that stochastic models are not an acceptable choice because they lack a correct prediction of preferential accumulation. This conclusion is based on a specific strategy for validation: the authors validate LES models against the DNS statistics. However, this choice is open to discussion since one can also validate the LES models on the filtered DNS statistics. These two options differ by the objective of the model in sight: describing the PDF or the filtered PDF.

- **A statistical approach**
  The kinematic models give a plausible realization of the disperse phase flow. Indeed, because it models the unresolved velocity field, the result is comparable to an experiment or a DNS and it does not contain all the possible statistics of the disperse phase. Mesoscopic approaches should be derived for this purpose. In particular, the EMEF developed by Mercier (2020) is a first step in this direction since it precisely takes into account the reduction of the carrier phase. In this context, appropriate kinetic equations could be derived from the intermittent stochastic models developed in this thesis, as for such mesoscopic descriptions, one needs the information on the fluctuations.

Appendix A

Eulerian moment methods

In this appendix, we first derive the mesoscopic formalism and obtain the William-Boltzmann equation. Then, we propose a general formalism for moment methods at any order by introducing in particular a tensor notation at order N. We then review the main closures of moment equations in the literature and compare these different methods on a 2D HIT field.

A.1 Mesoscopic approach

Eulerian representation of a point-particle

The particles are considered as point-like and each particle k has a number of internal variables, such as its velocity $\boldsymbol{v}_{p,k}$, its size $S_{p,k}$, its enthalpy $h_{p,k}$ etc. In this thesis, we consider a monodisperse phase and we do not attempt to solve the energy exchanges.
The Eulerian representation of a point-particle is hence given by the fine-grain distribution (Pope and Ching 1992):

$$f_{p,k}(t,\boldsymbol{x},\boldsymbol{v}) = \delta(\boldsymbol{x}-\boldsymbol{x}_{p,k}(t))\delta(\boldsymbol{v}-\boldsymbol{v}_{p,k}(t)), \tag{A.1}$$

where $\boldsymbol{x}$ is the the physical space variable, and $\boldsymbol{v}$ the total velocity vector for the particle in the phase space. A key assumption in the description of f is the independence of the variables $\boldsymbol{x},\boldsymbol{v}$ and t.

We can write the Liouville equation applied to this density function, since it is necessarily constant along the trajectories in the phase space and in the following we neglect the collisions:

$$\begin{aligned} \frac{\mathrm{d}f_{p,k}}{\mathrm{d}t} &= \frac{\partial f_{p,k}}{\partial t} + \frac{\mathrm{d}\boldsymbol{x}_{p,k}}{\mathrm{d}t}\cdot\nabla_{\boldsymbol{x}} f_{p,k} + \frac{\mathrm{d}\boldsymbol{v}_{p,k}}{\mathrm{d}t}\cdot\nabla_{\boldsymbol{v}} f_{p,k} \\ 0 &= \frac{\partial f_{p,k}}{\partial t} + \nabla_{\boldsymbol{x}}\cdot(\boldsymbol{v} f_{p,k}) + \nabla_{\boldsymbol{v}}\cdot\left(\frac{\boldsymbol{u}(\boldsymbol{x},t)-\boldsymbol{v}}{\tau_p} f_{p,k}\right). \end{aligned} \tag{A.2}$$

Eulerian representation of a disperse phase

For a given fluid-particle realization, the disperse phase can be described by a number density function (NDF), representing N_p particles:

$$f_{DPS} = f_{DPS}(t,\boldsymbol{x}_{p,1},\boldsymbol{v}_{p,1},...,\boldsymbol{x}_{p,N_p},\boldsymbol{v}_{p,N_p}). \tag{A.3}$$

We consider that particles are interchangeable, which simplifies the writing of the NDF:

$$f_{DPS}(t,\boldsymbol{x},\boldsymbol{v}) = \sum_{i=1}^{N_p} \delta(\boldsymbol{x}-\boldsymbol{x}_{p,k}(t))\delta(\boldsymbol{v}-\boldsymbol{v}_{p,k}(t)). \tag{A.4}$$

In the absence of collision, the evolution equation of the NDF of the disperse phase is then written:

$$\frac{\partial f_{DPS}}{\partial t} + \boldsymbol{v}\cdot\nabla_{\boldsymbol{x}} f_{DPS} + \nabla_{\boldsymbol{v}}\cdot\left(\frac{\boldsymbol{u}(\boldsymbol{x},t)-\boldsymbol{v}}{\tau_p} f_{DPS}\right) = 0. \tag{A.5}$$

Mesoscopic Eulerian framework

From a statistical point of view, we are interested in obtaining the NDF of a converged disperse phase defined from an ensemble average. This one encompasses the set of realizations of the carrier phase and of the continuous phase. Février, Simonin, and Squires (2005) introduce the notation $\mathcal{H}_{f,p}$ to define a fluid-particle realization and set the framework for the Mesoscopic Eulerian Formalism. Thus, the NDF we are looking for corresponds to:

$$f(t,\boldsymbol{x},\boldsymbol{v}) = \langle f_{DPS}\rangle = \lim_{N_{f,p}\to\infty} \frac{1}{N_{f,p}} \sum_{k=1}^{N_{f,p}} f_{DPS}(t,\boldsymbol{x},\boldsymbol{v}|\mathcal{H}_{f,p}). \tag{A.6}$$

The limit for an infinite number of realizations of the Liouville equation (A.5) leads to the Williams-Boltzmann equation (WBE), driving the dynamic of the NDF of Eq. (A.6):

$$\frac{\partial f}{\partial t} + \boldsymbol{v}\cdot\nabla_{\boldsymbol{x}} f + \nabla_{\boldsymbol{v}}\cdot\left(\frac{\boldsymbol{u}(\boldsymbol{x},t)-\boldsymbol{v}}{\tau_p} f\right) = 0. \tag{A.7}$$

We find the same form as for the Liouville equations, the difference lies in the interpretation and the form given to the NDF.

A.2 Some notations and definitions

Let us denote, respectively with tensorial and index notations, where $i_1, i_2 ..., i_N$ can represent the physical directions in d dimensions.

- $\otimes^0\boldsymbol{v} = 1$
- $\otimes^1\boldsymbol{v} = \boldsymbol{v} = v_{i_1}$
- $\otimes^2\boldsymbol{v} = \boldsymbol{v}\otimes\boldsymbol{v} = v_{i_1}v_{i_2}$
- $\otimes^3\boldsymbol{v} = \boldsymbol{v}\otimes\boldsymbol{v}\otimes\boldsymbol{v} = v_{i_1}v_{i_2}v_{i_3}$
- $\otimes^N\boldsymbol{v} = \boldsymbol{v}\otimes ...\boldsymbol{v}\otimes\boldsymbol{v} = v_{i_1}v_{i_2}v_{i_3}...v_{i_N}$

We introduce the general form for any velocity tensor set: $\boldsymbol{\mathcal{V}} = m_p[1, \boldsymbol{v}, \otimes^2\boldsymbol{v}, \otimes^3\boldsymbol{v}, ..., \otimes^N\boldsymbol{v}]$

We define the corresponding moments for velocity: $\boldsymbol{\mathcal{M}}^{(N)} = \left\langle \boldsymbol{\mathcal{V}}^{(N)} f \right\rangle_{\boldsymbol{v}}$.

By definition, the following standard values can be specified:

- Zeroth order moment:

  $$\boldsymbol{\mathcal{M}}^{(0)} = \langle m_p f\rangle_{\boldsymbol{v}} = \rho_p(t,\boldsymbol{x}) \tag{A.8}$$

  is the particle density field.

- First order moment:

$$\boldsymbol{\mathcal{M}}^{(1)} = \langle m_p \boldsymbol{v} f \rangle_{\boldsymbol{v}} = \rho_p(t, \boldsymbol{x}) \boldsymbol{u}_p(t, \boldsymbol{x}), \tag{A.9}$$

where $\boldsymbol{u}_p(t, \boldsymbol{x})$ is the average particle velocity field.
We introduce the centered velocity in the phase space: $\boldsymbol{c} = \boldsymbol{v} - \boldsymbol{u}_p$, which corresponds to the deviatoric part of the particle velocity.

- Second order moment:

$$\boldsymbol{\mathcal{M}}^{(2)} = \langle m_p \boldsymbol{v} \otimes \boldsymbol{v} f \rangle_{\boldsymbol{v}} = \rho_p \left(\boldsymbol{u}_p \otimes \boldsymbol{u}_p + \boldsymbol{\Sigma} \right), \tag{A.10}$$

where $\boldsymbol{\Sigma}(t, \boldsymbol{x}) := \langle \boldsymbol{c} \otimes \boldsymbol{c} f \rangle_{\boldsymbol{v}}$ and one can also introduce the velocity pressure $\boldsymbol{P} := \rho_p \boldsymbol{\Sigma} = \langle m_p \boldsymbol{c} \otimes \boldsymbol{c} f \rangle_{\boldsymbol{v}}$.
$\boldsymbol{\Sigma}$ can be found under different names and notations in the literature: the covariant or velocity dispersion matrix, the RUM (random uncorrelated motion) tensor. It is defined as $R_{p,ij}$ in Vié, Masi, Simonin, and Massot (2012), $\delta R_{p,ij}$ in Masi and Simonin (2012), $\delta\tilde{\sigma}_{p,ij}$ in Février, Simonin, and Squires (2005), σ_{ij} in Vié, Doisneau, and Massot (2015)...

The total energy tensor is given by $\boldsymbol{E} := \frac{1}{2}\boldsymbol{u}_p \otimes \boldsymbol{u}_p + \frac{1}{2\rho_p}\boldsymbol{P}$ and therefore we have $\boldsymbol{\mathcal{M}}^{(2)} = \rho_p \boldsymbol{u}_p \otimes \boldsymbol{u}_p + \boldsymbol{P} = 2\rho_p \boldsymbol{E}$.

- Third order moment:

$$\boldsymbol{\mathcal{M}}^{(3)} = \left\langle m_p \otimes^3 \boldsymbol{v} f \right\rangle_{\boldsymbol{v}} = \rho_p \otimes^3 \boldsymbol{u}_p + 3\boldsymbol{u}_p \otimes_s \boldsymbol{P} + \boldsymbol{Q}, \tag{A.11}$$

where $\boldsymbol{Q} = \langle m_p \otimes^3 \boldsymbol{c} f \rangle_{\boldsymbol{v}}$ is the third order heat flux tensor.
The total enthalpy tensor is defined as $\boldsymbol{H} := \boldsymbol{E} + \boldsymbol{\Sigma}$. Therefore:

$$\begin{aligned} \boldsymbol{\mathcal{M}}^{(3)} &= \rho_p \boldsymbol{u}_p \otimes_s \left(\boldsymbol{u}_p \otimes \boldsymbol{u}_p + 3\boldsymbol{\Sigma} \right) + \boldsymbol{Q} \\ &= \boldsymbol{u}_p \otimes_s \left(2\rho_p \boldsymbol{E} + 2\boldsymbol{P} \right) + \boldsymbol{Q} \\ &= 2\rho_p \boldsymbol{H} \otimes_s \boldsymbol{u}_p + \boldsymbol{Q}. \end{aligned} \tag{A.12}$$

Some rules for calculation with tensors:

- The symmetric tensor outer product is introduced and can be defined with the introduction of the cyclic permutation operator $\sigma(S)_{i_1,i_2,i_3,...,i_N} = S_{i_2,i_3,...,i_N,i_1}$:

$$\begin{aligned} \boldsymbol{a} \otimes_s \boldsymbol{b} &= \frac{1}{2}\left[\boldsymbol{a}\otimes\boldsymbol{b} + \boldsymbol{b}\otimes\boldsymbol{a}\right] \\ \boldsymbol{a_1} \otimes_s \boldsymbol{a_2}... \otimes_s \boldsymbol{a_N} &= \frac{1}{N}\sum_{k=0}^{N-1} \sigma^k(\boldsymbol{a_1}\otimes\boldsymbol{a_2}...\otimes\boldsymbol{a_N}). \end{aligned} \tag{A.13}$$

- The divergence of a high-order tensor is implicitly realized on its last "direction". We already know that the divergence of a matrix $\boldsymbol{A}$ is given by: $\nabla_{\boldsymbol{x}}\cdot(\boldsymbol{A}) = \dfrac{\partial A_{ij}}{\partial x_j}$. This can be generalized:

$$\left[\nabla_{\boldsymbol{x}}\cdot(\boldsymbol{T})\right]_{i_1,i_2,...i_{N-1}} = \nabla_{\boldsymbol{x}}\cdot(T_{i_1,i_2,...i_N}) = \frac{\partial T_{i_1,i_2,...i_N}}{\partial x_{i_N}}. \tag{A.14}$$

- The gradient of a high-order tensor is implicitly realized on its last "direction":

$$\left[\nabla_{\boldsymbol{x}}\boldsymbol{T}\right]_{i_1,i_2,...i_{N+1}} = \frac{\partial T_{i_1,i_2,...i_N}}{\partial x_{i_N+1}}. \tag{A.15}$$

- The scalar product with a vector is realized upon its last "direction":

$$\left[\boldsymbol{a}\cdot\boldsymbol{T}\right]_{i_1,i_2,...i_{N-1}} = a_{i_N}T_{i_1,i_2,...i_N}. \tag{A.16}$$

A.3 Moments equation

We multiply the WBE by $\boldsymbol{\mathcal{V}}^{(N)}$ and integrate over the moment space :

$$\begin{array}{llll} \partial_t f & +\nabla_{\boldsymbol{x}}\cdot(\boldsymbol{v}f) & +\nabla_{\boldsymbol{v}}\cdot(\boldsymbol{F}f) & = 0 \\ \left\langle \partial_t(\boldsymbol{\mathcal{V}}^{(N)}f)\right\rangle & +\left\langle \boldsymbol{\mathcal{V}}^{(N)}\nabla_{\boldsymbol{x}}\cdot(\boldsymbol{v}f)\right\rangle_{\boldsymbol{v}} & +\left\langle \boldsymbol{\mathcal{V}}^{(N)}\nabla_{\boldsymbol{v}}\cdot(\boldsymbol{F}f)\right\rangle_{\boldsymbol{v}} & = 0 \\ \partial_t\boldsymbol{\mathcal{M}}^{(N)} & +\nabla_{\boldsymbol{x}}\cdot\left(\boldsymbol{\mathcal{M}}^{(N+1)}\right) & +\left\langle \boldsymbol{\mathcal{V}}^{(N)}\nabla_{\boldsymbol{v}}\cdot(\boldsymbol{F}f)\right\rangle_{\boldsymbol{v}} & = 0. \end{array} \tag{A.17}$$

A generalized integration by parts simplifies the last term:

$$\left\langle \boldsymbol{\mathcal{V}}^{(N)}\nabla_{\boldsymbol{v}}\cdot(\boldsymbol{F}f)\right\rangle_{\boldsymbol{v}} = -\left\langle \boldsymbol{F}\cdot\nabla_{\boldsymbol{v}}\left(\boldsymbol{\mathcal{V}}^{(N)}\right)f\right\rangle_{\boldsymbol{v}}. \tag{A.18}$$

The general moment equation can be written in the form:

$$\boxed{\partial_t\boldsymbol{\mathcal{M}}^{(N)} + \nabla_{\boldsymbol{x}}\cdot\left(\boldsymbol{\mathcal{M}}^{(N+1)}\right) = \left\langle \boldsymbol{F}\cdot\nabla_{\boldsymbol{v}}\left(\boldsymbol{\mathcal{V}}^{(N)}\right)f\right\rangle_{\boldsymbol{v}}}. \tag{A.19}$$

Let us consider the Stokes' drag force $\boldsymbol{F} = \dfrac{\boldsymbol{u}-\boldsymbol{v}}{\tau_p}$.

We have:

$$\begin{aligned}
\boldsymbol{v}\cdot\nabla_{\boldsymbol{v}}\boldsymbol{\mathcal{V}}^{(N)} &= v_{i_{N+1}}\cdot\frac{\partial(v_{i_1}v_{i_2}...v_{i_N})}{\partial v_{i_N+1}} = N(v_{i_1}v_{i_2}...v_{i_N}) \\
&= N\boldsymbol{\mathcal{V}}^{(N)} \\
\boldsymbol{u}\cdot\nabla_{\boldsymbol{v}}\boldsymbol{\mathcal{V}}^{(N)} &= u_{i_{N+1}}\cdot\frac{\partial(v_{i_1}v_{i_2}...v_{i_N})}{\partial v_{i_N+1}} = u_{i_1}v_{i_2}...v_{i_N} + v_{i_1}u_{i_2}...v_{i_N} + ... + v_{i_1}v_{i_2}...u_{i_N} \\
&= N\boldsymbol{u}\otimes_s^{N-1}\boldsymbol{v}.
\end{aligned} \tag{A.20}$$

Corresponding moments are :

- $\left\langle \boldsymbol{v}\cdot\nabla_{\boldsymbol{v}}\boldsymbol{\mathcal{V}}^{(N)}\right\rangle_{\boldsymbol{v}} = N\boldsymbol{\mathcal{M}}^{(N)}$
- $\left\langle \boldsymbol{u}\cdot\nabla_{\boldsymbol{v}}\boldsymbol{\mathcal{V}}^{(N)}\right\rangle_{\boldsymbol{v}} = N\boldsymbol{u}\otimes_s^{N-1}\boldsymbol{\mathcal{M}}^{(N-1)}$

A.4 Closures

Whatever the order N of the moment equations, the expression Eq. (A.19) always involves the moment of order $N+1$ which is not resolved. It is then necessary to propose a model for this additional term in order to obtain a closure of the set of equations.

The ACBMM (Algebraic Closure Based Moments Method) closes the RUM stress tensor $\boldsymbol{\Sigma}$ to be able to solve only a limited set of moments (usually up to second order). The closure involves an algebraic equilibrium assumption, inspired from the RANS turbulence modeling. The simplest closure is the viscosity-like assumption, proposed by Simonin, Février, and Laviéville (2002) (hereinafter referred to as VISCO model). Another model, the 2ϕ-EASM, more accurate, introduced by Masi and Simonin (2012), uses another assumption, similar to the one used in turbulence to close the Reynold stresses.

The KBMM (Kinetic-Based Moment Moment) is based on the choice of reconstruction of an underlying kinetic distribution. A NDF shape is proposed with as many parameters as moments to close. The choice of the NDF depends on the accuracy requirements and calculation capabilities. This method is more expensive than the ACBMM method since it solves all the tensor components. KBMM, on the other hand, for specific NDF reconstruction, can have a well-defined mathematical structure and therefore allows numerical resolution through hyperbolic solvers.

A.4.1 Algebraic closures

To solve the system of equations of moments at first order, it is therefore necessary to find a model for the tensor $\boldsymbol{\Sigma}$ introduced in Eq. (A.10).
Algebraic Closure-Based Moment Method (ACBMM) class of closing methods aims at expressing the missing quantities through physical and mathematical assumptions.

Masi and Simonin (2012) chose to close the RUM stresses by physical assumptions on their evolution. They divide the tensor into two components, a spherical and a deviatoric contributions:

$$\boldsymbol{\Sigma} = \boldsymbol{\Sigma}^\star + \frac{2\delta\theta_p}{N_d}\boldsymbol{I}_d, \tag{A.21}$$

where $\delta\theta_p$ is the RUM kinetic energy (RUE) and N_d the number of physical dimensions.
The RUE is solved by an additional transport equation and the deviatoric part of the RUM stresses is closed with a physical assumption.

The deviatoric part can be closed with a viscosity-like assumption suggested by Simonin, Février, and Laviéville (2002) and Kaufmann, Moreau, Simonin, and Helie (2008), referred to as the VISCO model.

$$\boldsymbol{\Sigma}^\star = -2\nu_{PTC}\boldsymbol{S}^\star, \tag{A.22}$$

having $\nu_{PTC} = \tau_p\delta\theta_p/N_d$ and $S^\star_{ij} = S_{ij} - 1/N_d S_{kk}\delta_{ij}$.
Another possible closure is the 2ϕ-EASM closure proposed by Masi and Simonin (2012). In both closures models, the third-order correlations appearing into the RUE equation is neglected.

A.4.2 Assumed NDF shape

A.4.2.1 Monokinetic closure

For particles with very low inertia, there is no trajectory crossing and it is then possible to define a single local particle velocity at any point in space. The local velocity dispersion being null, we propose the following NDF model:

$$\boxed{^{MK}f(t,\boldsymbol{x},\boldsymbol{v}) = n(t,\boldsymbol{x})\delta(\boldsymbol{v} - \boldsymbol{u}_p(t,\boldsymbol{x}))}. \tag{A.23}$$

One can verify that the second order centered moment $\boldsymbol{P} = \left\langle m_p \otimes^2 \boldsymbol{c}f \right\rangle_{\boldsymbol{v}}$ is null. This model is also referred as the Pressureless Gas Dynamic (PGD) model.
The associated system of equations is:

$$\begin{cases} \partial_t\rho_p & +\nabla_{\boldsymbol{x}}\cdot(\rho_p\boldsymbol{u}_p) & = 0 \\ \partial_t\rho_p\boldsymbol{u}_p & +\nabla_{\boldsymbol{x}}\cdot(\rho_p\boldsymbol{u}_p\otimes\boldsymbol{u}_p) & = \langle \boldsymbol{F}m_p f\rangle_{\boldsymbol{v}} = \rho_p\dfrac{\boldsymbol{u}-\boldsymbol{u}_p}{\tau_p}. \end{cases} \tag{A.24}$$

A.4.2.2 Anisotropic Gaussian closure

For larger inertia particles, PTC can occur and we must define a model for the velocity dispersion. The anisotropic Guassian closure uses for the velocity distribution a multivariate Gaussian form:

$$\boxed{^{AG}f(t,\boldsymbol{x},\boldsymbol{v}) = n(t,\boldsymbol{x})\frac{\det(\boldsymbol{\Sigma})^{-1/2}}{(2\pi)^{N_d/2}}\exp\left(-\frac{1}{2}\boldsymbol{c}^T\boldsymbol{\Sigma}^{-1}\boldsymbol{c}\right)}, \tag{A.25}$$

where N_d is the number of dimension considered. Moments of order 0 to 2 allow to compute the parameters $n(t,\boldsymbol{x})$, $\boldsymbol{u}_p$ and $\boldsymbol{\Sigma}$ which then allow to close the different terms. In particular, the third order centered moment $\boldsymbol{Q} = \left\langle m_p \otimes^3 \boldsymbol{c}f\right\rangle$ is null.

In order to deal with $\rho_p \boldsymbol{E}$ rather than $\boldsymbol{\mathcal{M}}^{(2)}$, equations of the second order are generally multiplied by $\frac{1}{2}$. The AG system becomes:

$$\left\{\begin{array}{lll} \partial_t \rho_p & +\nabla_{\boldsymbol{x}} \cdot (\rho_p \boldsymbol{u}_p) & = 0 \\ \partial_t \rho_p \boldsymbol{u}_p & +\nabla_{\boldsymbol{x}} \cdot (\rho_p \boldsymbol{u}_p \otimes \boldsymbol{u}_p + \boldsymbol{P})) & = \rho_p \dfrac{\boldsymbol{u} - \boldsymbol{u}_p}{\tau_p} \\ \partial_t \rho_p \boldsymbol{E} & +\nabla_{\boldsymbol{x}} \cdot (\rho_p \boldsymbol{H} \otimes_s \boldsymbol{u}_p) & = \rho_p \dfrac{\boldsymbol{u} \otimes_s \boldsymbol{u}_p - 2\boldsymbol{E}}{\tau_p}. \end{array}\right. \tag{A.26}$$

This system is strictly hyperbolic and fulfills an entropy inequality. The equations of the PGD are the asymptotic limit of the AG when pressure tends towards 0.

A.4.2.3 Isotropic Gaussian closure

A simple form of the Gaussian models is obtained when isotropic pressure is considered. In this case, the NDF is assumed to be an isotropic Gaussian distribution centered at $\boldsymbol{u}_p$ and with an isotropic dispersion $\boldsymbol{\Sigma} = \theta \boldsymbol{I} \Rightarrow \boldsymbol{P} = \rho_p \boldsymbol{\Sigma} = \mathcal{P} \boldsymbol{I}$. This gives:

$$\boxed{{}^{IG}f(t, \boldsymbol{x}, \boldsymbol{v}) = n(t, \boldsymbol{x}) \frac{\sigma^{-1/2}}{(2\pi)^{d/2}} \exp\left(-\frac{1}{2\sigma}(\boldsymbol{c} \cdot \boldsymbol{c})\right),} \tag{A.27}$$

with $\sigma = \det(\boldsymbol{\Sigma})$.

The total energy has no deviatoric part and can be expressed with $\mathcal{E} := \mathrm{tr}(\boldsymbol{E}) = \frac{1}{2}\boldsymbol{u}_p \cdot \boldsymbol{u}_p + \frac{N_d}{2}\theta$. The second order equation can be simplified in a scalar equation (the trace of the AG second order equation) with $\mathcal{H} = \mathcal{E} + \theta$. We retrieve the Euler equations with a drag source term:

$$\left\{\begin{array}{lll} \partial_t \rho_p & +\nabla_{\boldsymbol{x}} \cdot (\rho_p \boldsymbol{u}_p) & = 0 \\ \partial_t \rho_p \boldsymbol{u}_p & +\nabla_{\boldsymbol{x}} \cdot (\rho_p \boldsymbol{u}_p \otimes \boldsymbol{u}_p + \mathcal{P} \boldsymbol{I}) & = \rho_p \dfrac{\boldsymbol{u} - \boldsymbol{u}_p}{\tau_p} \\ \partial_t \rho_p \mathcal{E} & +\nabla_{\boldsymbol{x}} \cdot (\rho_p \mathcal{H} \boldsymbol{u}) & = \rho_p \dfrac{\boldsymbol{u} \cdot \boldsymbol{u}_p - 2\mathcal{E}}{\tau_p}. \end{array}\right. \tag{A.28}$$

A.4.2.4 Comparison of the methods on HIT

Figures A.1 depict the instantaneous particle number density for the five differents methods, the Lagrangian one being the reference. Results show that all the models give close prediction to the Lagrangian one for small Stokes number. This was expected given the absence of PTC, models taking into account velocity anisotropism or not do not give significant different results in this case.

Similarly, for a Stokes close to 1, the density field patterns are correctly reproduced with Eulerian models. On the other hand, the fields seem slightly more diffuse than for the Lagrangian simulation, which suggests that a refinement of the mesh size could correct this.

For larger Stokes numbers, real differences appear in the density fields of the different models. Because of the occurence of PTC, it becomes apparent that the isotropic model is not able to capture the velocity dispersion and therefore does not correctly reflect the motions and positions of the

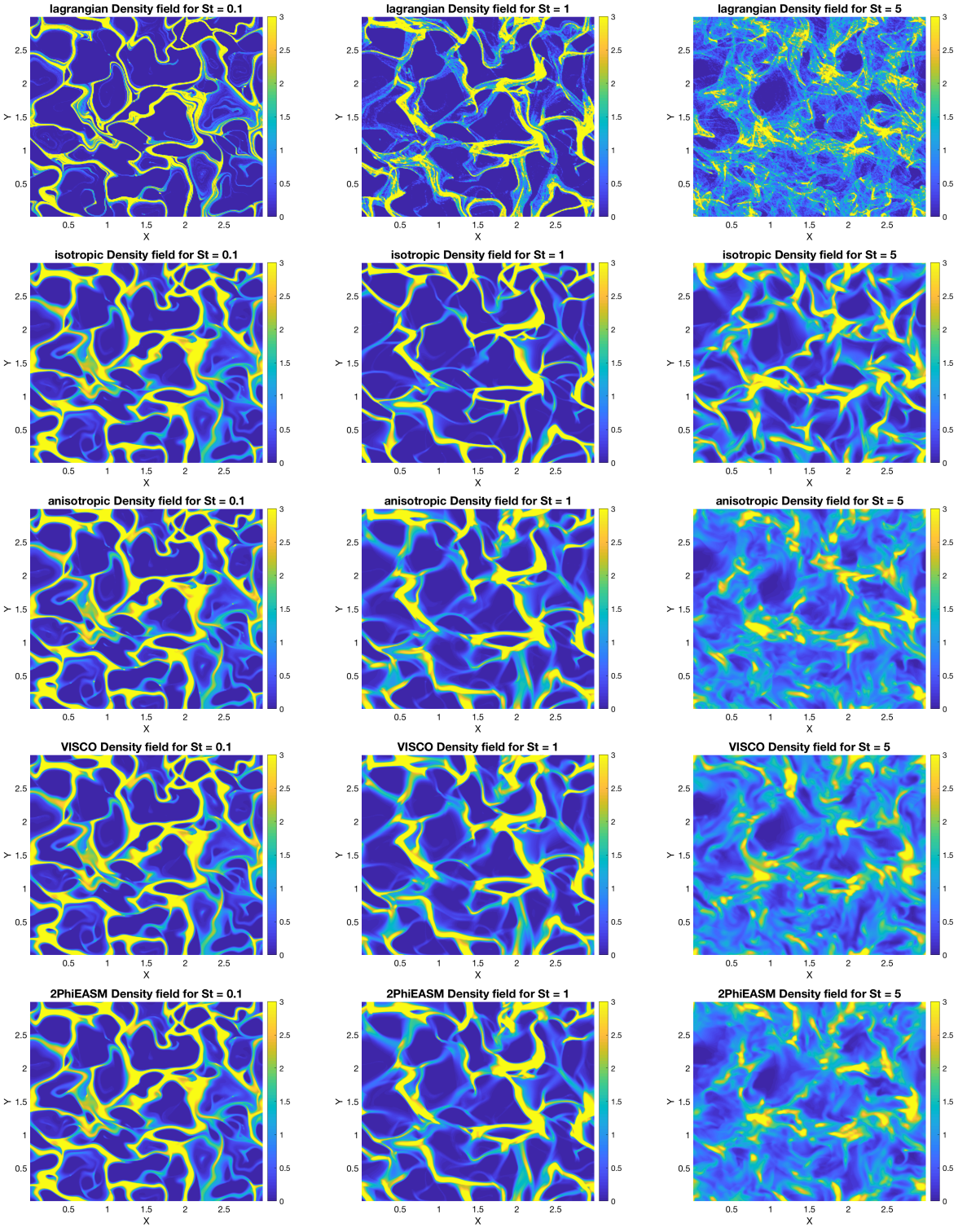

Figure A.1. Particle number density fields for HIT.

particles. The Lagrangian structures have become more complex, and the filaments have expanded.

The two best models are the 2ϕ-EASM and anisotropic models, which manage to better capture segregation.

Appendix B

Kinematic simulation with Gaussian fields

Following the conclusions establishing the necessity to use structural models to obtain DNS statistics of particles, we suggest a new strategy which makes use of a random field with enforced divergence-free condition and spatial and temporal correlations. We show that the model can retrieve some Lagrangian statistics and in particular, particle segregation.
Structural models have the advantage of being able to produce a spatial structure of the flow field. Segregation is strongly related to the existence of small scale and large scale coherent structures, which are not present in stochastic modeling. In the following, we propose to develop a synthetic field as a basis for structural models. The objective is to construct a velocity field $\boldsymbol{u}(\boldsymbol{x}, t)$ without solving the Navier-Stokes equation but keeping all the turbulence statistics of interest such as the Kolmogorov time or the integral time scales. To this aim, we will decompose the problem into two sub-problems: space reconstruction and time evolution.

B.1 Construction of a new synthetic velocity field

We generate the velocity field using the following technique:

- We first generate three Gaussian random fields A_x, A_y, A_z, over which we impose a spatial correlation by applying a spatial filter (here chosen as Gaussian). The size of the filter σ_f determines the length of correlation ℓ_c of the field. As opposed to the Fourier-based KS, the correlation length is compact because it is directly generated with the Gaussian filter of finite size. Therefore, it satisfies the constraint (i).
- We generate a three-dimensional divergence-free flow using $\boldsymbol{v}_{\ell_c}(\boldsymbol{x}) = \nabla \times \boldsymbol{A}$, which naturally ensures (ii).
- By superposing velocity fields with varying filter sizes, we can control the turbulence spectrum according to point (iii). Figure B.1(a) shows that each sub-field v_{ℓ_c} produces an energy spectrum with a maximum located at the correlation length of the field $\kappa_{\text{max}} \sim \ell_c^{-1}$. With an adapted linear combination, it is possible to produce an energy spectrum with slope $-5/3$ in Fig. B.1(b). We normalize it so that its variance is 1. An example of the velocity and vorticity fields obtained are presented in Fig. B.1(c) and Fig. B.1(d).

The obtained field $\boldsymbol{v}(\boldsymbol{x}) = \sum_{n=1}^{N_m} \alpha_n \boldsymbol{v}_{\ell_n}(x)$ is therefore spatially-correlated (with compact modes), divergence-free, and its energy spectrum is controlled with the number of modes (sub-fields) and the range of correlation lengths: from the largest scale $L = \ell_1$, to the smallest $\eta = \ell_{N_m}$. This gives a frozen flow and we add a temporal correlation in the following section.

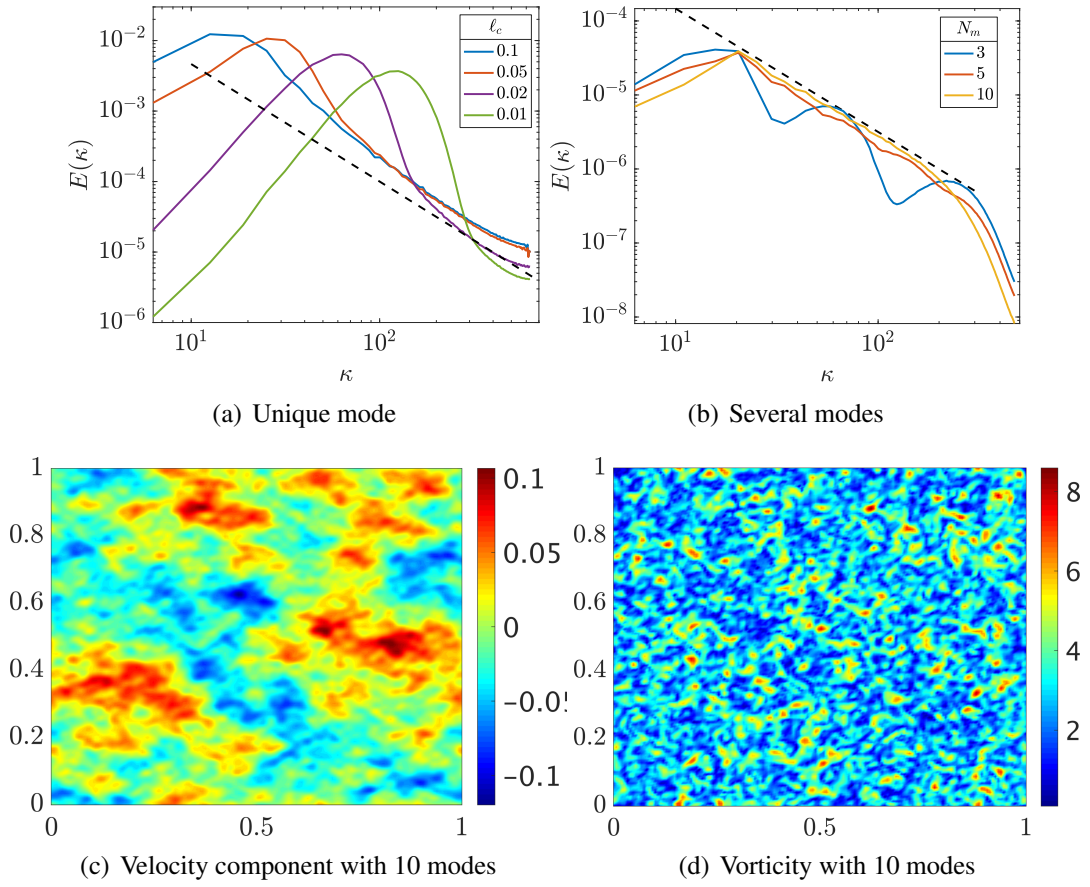

(a) Unique mode

(b) Several modes

(c) Velocity component with 10 modes

(d) Vorticity with 10 modes

Figure B.1. Spatially-correlated random field with zero divergence: (a) influence of the filtering length ℓ_c for a unique field; (b) superposition of different random fields to control the turbulence spectrum; (c) example of the generated velocity field and (d) vorticity field.

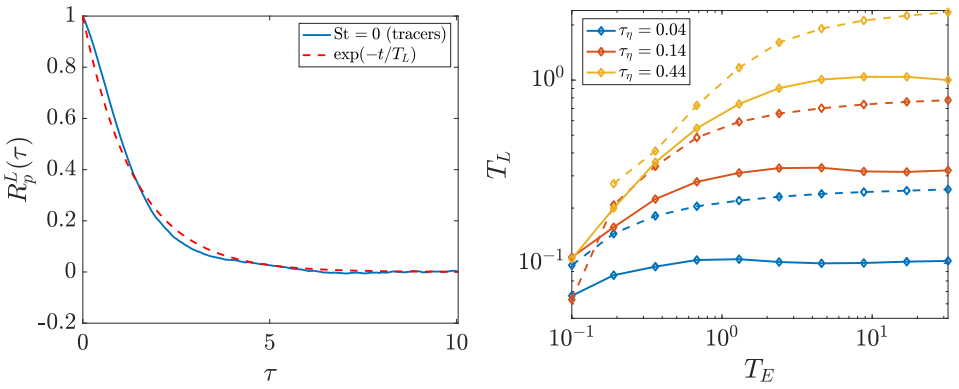

(a) Lagrangian velocity autocorrelation (b) Influence of T_E

Figure B.2. One-point Lagrangian statistics: (a) Lagrangian velocity autocorrelation fitted with an exponential function ($T_E = 3$ and $\tau_\eta = 0.7$); (b) Lagrangian integral time scale as a function of T_E for different τ_η and number of modes: $N_m = 1$ (full lines), $N_m = 3$ (dashed lines).

B.2 Temporal evolution of the velocity field

Compared to Fourier-based KS, we do not have an analytic expression in which we can include time evolution in a straightforward manner. To introduce a temporal correlation as required by point (iv), we decided to use a stochastic equation in which we replace the usual Gaussian noise $\mathrm{d}W_t$ by the spatially correlated field $\boldsymbol{v}(\boldsymbol{x})$ introduced in the previous section. For each spatial point $\boldsymbol{x}$, we have the following Langevin equation for the velocity field, seen as a time process:

$$\mathrm{d}\boldsymbol{u}(\boldsymbol{x}) = -\frac{1}{T_E}\boldsymbol{u}(\boldsymbol{x})\,\mathrm{d}t + \sqrt{\frac{2\sigma_u^2}{T_E}}\boldsymbol{v}_t(\boldsymbol{x})\sqrt{dt} \tag{B.1}$$

where we generate a new Gaussian field $\boldsymbol{v}_t(\boldsymbol{x})$ at each time step and inject it as the random noise in the equation. This has the formalism of a classic Langevin equation since for each point $\boldsymbol{x}$, the "noise" $\boldsymbol{v}(\boldsymbol{x})$ is Gaussian of variance 1. Moreover, increments are uncorrelated because we draw a new field $\boldsymbol{v}_t$ at each time step. Because $\boldsymbol{v}_t(\boldsymbol{x})$ is spatially correlated, $\boldsymbol{u}(\boldsymbol{x}, t)$ keeps this spatial correlation and neighbored points will have a similar evolution.

T_E is an Eulerian correlation time, and it controls the speed of change of the flow. When large, temporal increments $\mathrm{d}\boldsymbol{u}(\boldsymbol{x}, t)$ tend towards 0 and the flow becomes frozen. On the other hand, if T_E is small, the velocity field changes very fast, and the relaxation towards the perturbation $\boldsymbol{v}_t(\boldsymbol{x})$ is immediate.

The coefficient $\sqrt{2\sigma_u^2/T_E}$ before the noise ensures the stationarity of the Langevin Equation (and therefore of the flow statistics), with a given variance σ_u^2. We recall that σ_u gives the intensity of the forcing and is related to the turbulent kinetic energy $\langle k \rangle = 3/2\sigma_u^2$.

The Kolmogorov time scale is related to the fluid variance and the length scales in $\boldsymbol{v}(\boldsymbol{x})$: $\tau_\eta \sim \ell_c/\sigma_u$, where ℓ_c is the mean correlation length of the flow.
We observe that this temporal evolution formalism introduces parameters to control Lagrangian scales, such as T_L, the Lagrangian integral time scale. As opposed to the diverging autocorrelation

Table B.1. Parameters of the fluid model used as a carrier phase

N_m	ℓ_c	σ_u^2	τ_η	T_E	T_L
1	0.03	0.01	0.4	4	1
3	0.01 , 0.03, 0.1	0.01	0.4	4	2

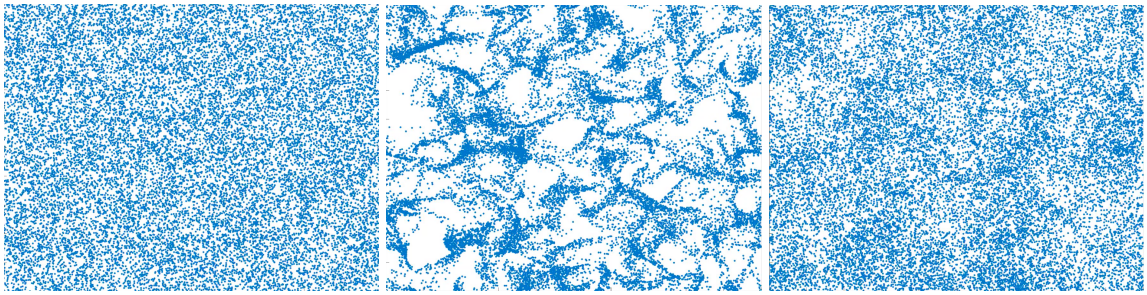

(a) St = 0 (b) St = 2 (c) St = 10

Figure B.3. Particles in a slice of the 3D synthetic turbulence for different Stokes numbers at time $t = 6$ for $\tau_\eta = 0.44$ and one mode ($N_m = 1$ in Table B.1).

with Fourier-based KS in Fig. 9.2, the one obtained in Fig. B.2(a) converges towards 0 with an exponential decrease.
Figure B.2(b) shows the dependency of T_L with T_E and it is clear, even with a single mode, that increasing the Eulerian correlation time of the flow also raises the integral Lagrangian time to a maximum, which is obtained for frozen turbulence. Moreover, keeping the same τ_η but extending the inertial range with additional modes can also increase T_L (dotted lines in Fig. B.2(b)).
An interesting perspective is to imagine having different temporal evolution for each sub-field v_{ℓ_n} for which an adapted T_E could be introduced. This is studied in Chap. 9.

Those additional parameters can be adapted and fitted to retrieve Lagrangian one-point statistics. In the next section, results for two-point statistics are discussed, to complete the validation of point (v).

B.3 Particle segregation in the Gaussian-based KS

Now we have a time and space varying field, and we can use it as a carrier phase for the dynamics of particles. Table B.1 shows the model parameters chosen to simulate the synthetic fluid.

We investigate the effect of Stokes number on the segregation, even with a single mode. First, we show that we retrieve the tracer limit for zero-inertia particles for which no segregation is expected. In Fig. B.3(a), thanks to the divergence-free, the tracers are not preferentially concentrated and fill the space homogeneously. Particles with Stokes number close to 1, in Fig. B.3(b), are preferentially concentrated by the reconstructed scales of the synthetic flow, and the segregation increases with time, as shown in Fig. B.4(a). Particles with high Stokes number (Fig. B.3(c)) are first ejected out of vortices: the segregation rises at the beginning of the simulation, but their large inertia prevents them from evolving with the small scales, and particle trajectory crossing occurs shortly after.

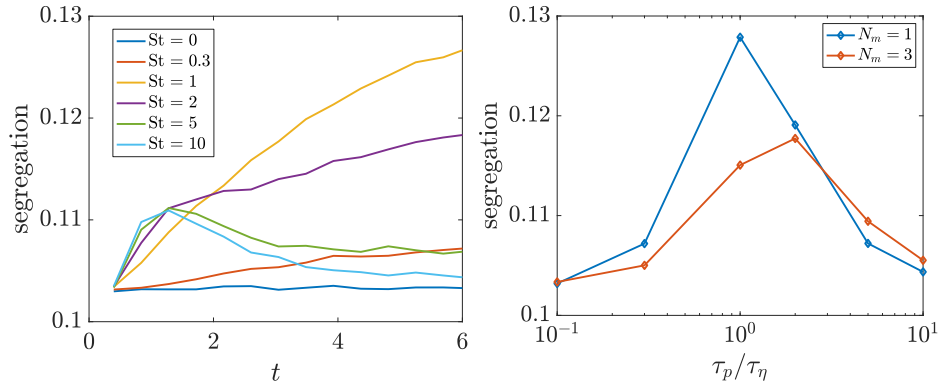

(a) Segregation with one mode (b) segregation with 1 and 3 modes

Figure B.4. Temporal evolution of segregation (variance of the PND) of particles interacting with the kinematic fluid of one mode (a) and segregation at time $t = 6$ for one and 3 modes (b).

The temporal trends of Fig. B.4(a) are similar to what is expected for particles in real turbulence and allow us to conclude that our field is appropriate as a surrogate for Navier-Stokes simulation to predict particle segregation in turbulence.
Figure B.4(b) shows that changing the number of modes in the synthetic fluid can also adjust the intensity of the segregation quantitatively.

B.4 Compatibility with LES framework

The versatility of this method due to the choice of the characteristic lengths allows us to adapt the generated field according to the LES characteristics easily. Indeed, the synthetic field can be generated to complete only the small missing scales and thus reconstruct a complete DNS-like spectrum. This is illustrated in Fig. B.5(a) where a LES spectrum is completed with a sub-grid flow.

However, generating sub-grid scales everywhere requires the same memory space as a DNS. Therefore, we investigate dimensionality reduction strategies. Instead of generating a field on the complete refined mesh, only a part of this field is simulated on a limited area (Fig. B.5(c)), and then replicated on the complete domain in a second step (Fig. B.5(d)). The combination of this reproduced field with the large scales of the LES produces the field in Fig. B.5(e) and reconstructs the spectrum shown in Fig. B.5(a).

Conclusion

In this appendix, we have introduced a structural model well known in the literature, the kinematic simulation based on a reconstruction of the velocity field with a Fourier series. However, the oscillatory behavior of the statistics suggests that the use of sinusoidal functions with infinite support is not suitable for turbulence. Moreover, the models studied so far with particles have been able to use at best a frozen velocity field.

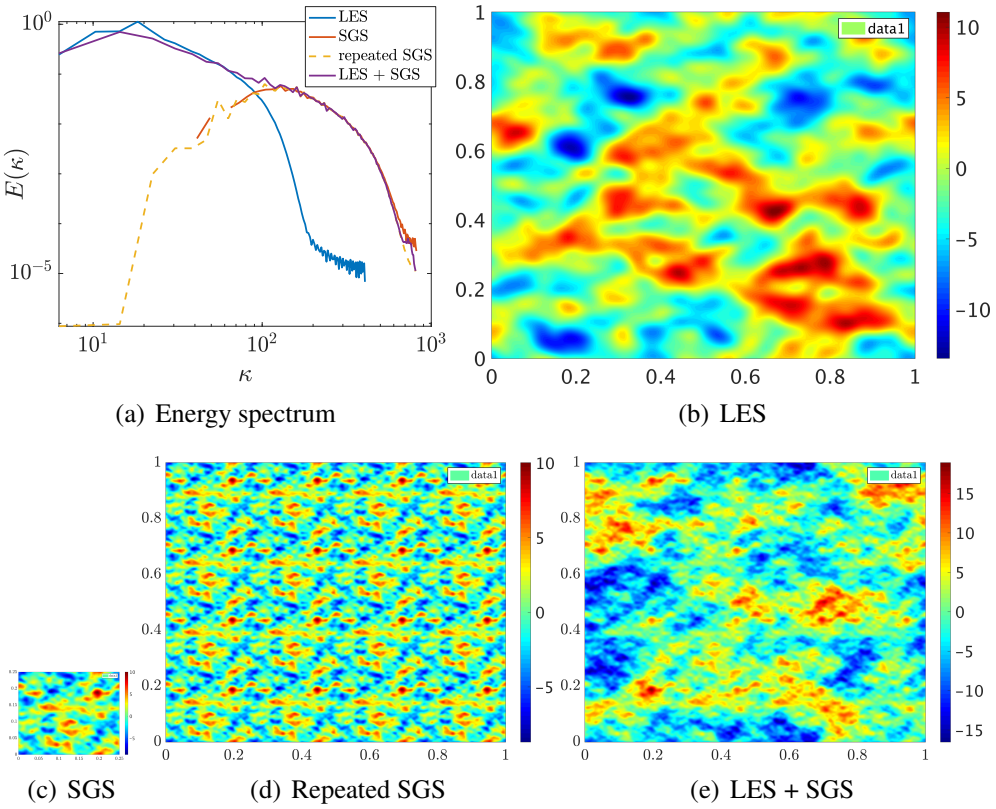

(a) Energy spectrum (b) LES

(c) SGS (d) Repeated SGS (e) LES + SGS

Figure B.5. Energy spectrum of LES and LES combined with the synthetic flow(a), snapshot of LES velocity field (a), synthetic fluid with small scales (b), repeated patterns of the synthetic fluid (c) and LES and synthetic fluid combined (d).

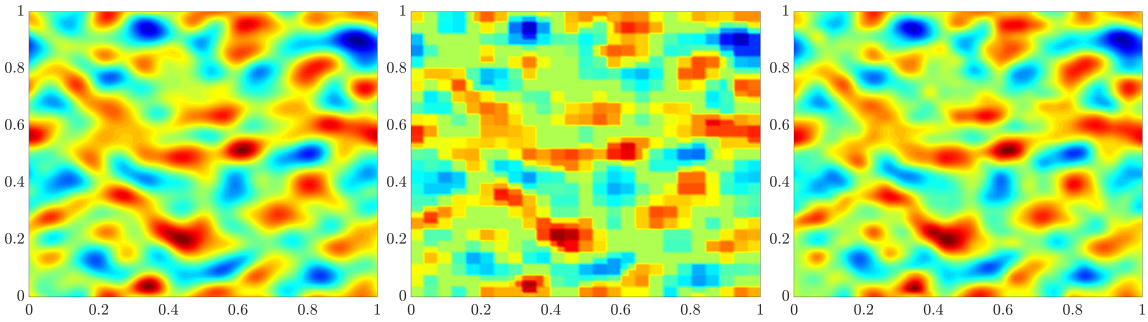

(a) Synthetic field (b) Haar wavelets (c) Daubechies wavelets

Figure B.6. Snapshot of a synthetic field (a), and the same field is decomposed using Haar wavelets (b) or Daubechies wavelets (c) with a compressing ratio of 1%.

We therefore considered a new approach for the development of a synthetic fluid field, based on filtered random fields. The Gaussian filters have such characteristic lengths that the superposition of the filtered fields reconstructs the typical energy spectrum and also allows the control of all scales of the turbulence. The zero divergence is obtained by taking the rotational of three of these scalar fields. The temporal evolution is imposed on the mesh nodes, following a stochastic Langevin equation, thus ensuring the stationarity of the flow and allowing the introduction of an Eulerian time parameter.

We have shown that such a field can faithfully reproduce the dynamics of the particles, in particular their preferential concentration. Although the computational cost of their simulation is very low, the storage cost remains important. Reduction strategies are proposed to address this issue.

This synthetic fluid has also lead us to consider wavelet decomposition (Farge 1992) because unlike Fourier series, wavelets maintain the compacity, and the locality of the information and compression could reduce the cost. Figure B.6 compares a wavelet decomposition using Haar wavelets or Daubechies wavelets. The original field is not only decomposed on a wavelet basis, but also compressed with a compression ratio of 1%: only 1% of the original information is used to reproduce fields of Fig. B.6(b) and B.6(c).

Certainly, the choice of the wavelet mother is crucial to expect a fair representation of the initial field: Daubechies wavelets seem to be a better choice for the decomposition because of their regularity. The level of compression and the amount of information will also be critical. The use of wavelets for a kinematic simulation is the subject of the Chap. 9.

Appendix C

Impact of the coupling kernel

The length scale δ_i is the characteristic size of the domain of influence of a particle on the surrounding fluid. The numerical quantity associated is the size of the volume filtering kernel. Several works are dedicated to the determination of the parameter δ_i for finite size particles (see for instance Maxey and Patel (2001)), the objective being to ensure that the force distributions are completely contained within the interior of the particle. Capecelatro and Desjardins (2013) recommended $\delta_i \approx 3d_p$ but the minimal value for δ_i is the grid spacing to avoid singularities in the carrier phase source term. The PSI-Cell approach implemented in Asphodele naturally yields $\delta_i = \Delta x$. We also implemented another coupling kernel with a Gaussian envelope of size $\sigma = \Delta x/2\sqrt{2\ln(2)}$ such that the full width at half height of the kernel δ_i is equal to the grid spacing. This way, the effect of the particle is typically spread out over the 27 nearest cells. Results are compared with the trilinear projection kernel.

Thus, in Fig. C.1, the comparison of the interaction spectra obtained is consistent with the previous wavenumber analysis: for simulations with a large number of particles, statistical convergence is achieved at all scales and thus the kernel change has no impact on the interaction spectrum. On the other hand, at low particle number density, the small scales are less energetic with the Gaussian kernel which spreads the energy of the particles at these scales over a larger range of cells. It should also be noted that large scales are then more energetic in this case, since the total interaction energy must be preserved.

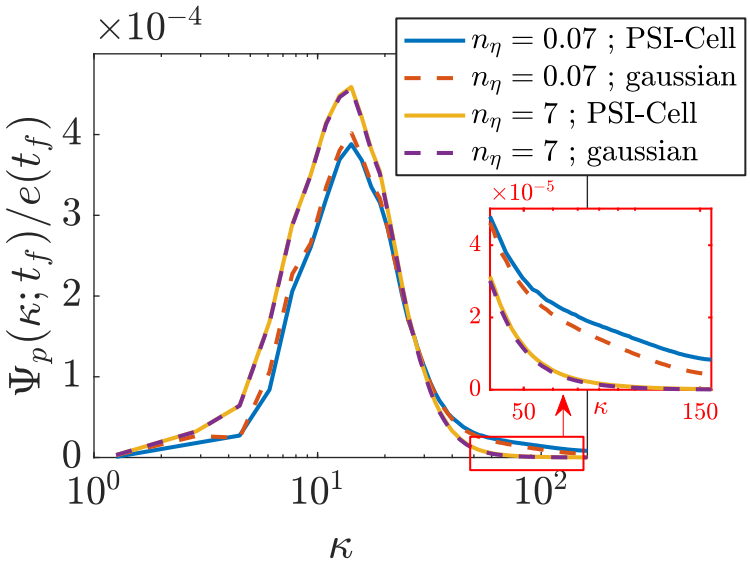

Figure C.1. Normalized two-way interaction spectrum with PSI-Cell (solid lines) and Gaussian (dashed lines) projections. Two different particle number densities are compared. The inset displays a zoom around the smallest scales.

Appendix D

Convergence of the box counting measure

Let us recall that N_{pb}^b is the random variable giving for each box $b \in \mathcal{B}$ the number of particles in the box. We define the box counting measure of particle preferential concentration as the normalized variance of the discrete particle number density field:

$$\begin{aligned} g(N_p, N_b) &= \frac{\frac{1}{N_b}\sum_{b\in\mathcal{B}}(N_{pb}^b)^2}{\left(\frac{1}{N_b}\sum_{b\in\mathcal{B}} N_{pb}^b\right)^2} \\ &= \frac{N_b}{N_p^2}\sum_{b\in\mathcal{B}}(N_{pb}^b)^2 \end{aligned}$$

The dependency of the measure with the total number of particles and the number of boxes is highlighted. One should also note that this measure is itself a random variable. In the following, we explain the asymptotic behaviors of the measure with the number of particles in the domain.

For very low values of N_p and samplings such that $\max_{b\in\mathcal{B}} N_{pb}^b \leq 1$, it is possible to detail the segregation. We have $g(N_p, N_b) = \frac{N_b}{N_p^2}\sum_{b\in\mathcal{B}}\delta_b$, where δ_b is 1 if a particle is in the box b, 0 otherwise. This yields: $g(N_p, N_b) \underset{N_p\to 0}{\sim} N_b N_p^{-1}$, hence the linear behavior with slope -1 of Fig. 13.2(a), and the shift between the different curves.

For very high values of N_p, we can assume that random variables N_{pb}^b are independent. It is known that N_{pb}^b follows a binomial distribution of parameters $B(N_p, p_b)$, where p_b is the probability for a particle to be in the box b (p_b is fixed and independent of N_p for one-way coupled simulations). The mean and variance of N_{pb}^b are respectively $N_p p_b$ and $N_p p_b(1-p_b))$. The expected value of the

measure g is:

$$\begin{aligned}
\mathbf{E}[g] &= \Big(\frac{N_b}{N_p}\Big)^2 \frac{1}{N_b} \sum_{b\in\mathcal{B}} \mathbf{E}[(N_{pb}^b)^2] \\
&= \Big(\frac{N_b}{N_p}\Big)^2 \frac{1}{N_b} \sum_{b\in\mathcal{B}} N_p p_b(1-p_b) + (N_p p_b)^2 \\
&= \frac{N_b}{N_p} \sum_{b\in\mathcal{B}} p_b(1 - p_b + N_p p_b) \\
\mathbf{E}[g] &\xrightarrow{N_p\to\infty} N_b \sum_{b\in\mathcal{B}} p_b^2
\end{aligned}$$

The particular case of uniform distribution, characterized by $p_b = p$ for all k yields a convergence towards 1.
We also verify that the variance of the measure tends to zeros when N_p tends to infinity :

$$\begin{aligned}
\mathrm{Var}[g] &= \mathbf{E}[g^2] - \mathbf{E}[g]^2 \\
&= \Big(\frac{N_b}{N_p}\Big)^4 \Big\{ \mathbf{E}[\langle (N_{pb}^b)^2 \rangle_b^2] - \mathbf{E}[\langle (N_{pb}^b)^2 \rangle_b]^2 \Big\}
\end{aligned}$$

The second term in the variance behaves like:

$$\begin{aligned}
\Big(\frac{N_b}{N_p}\Big)^4 \mathbf{E}[\langle (N_{pb}^b)^2 \rangle_b]^2 &= N_b^2 \Big(\sum_{b\in\mathcal{B}} p_b^2 \Big)^2 + O(N_p^{-1}) \\
&= N_b^2 \sum_{i\in\mathcal{B}} \sum_{j\in\mathcal{B}} p_i^2 p_j^2 + O(N_p^{-1})
\end{aligned}$$

The first term expands as:

$$\Big(\frac{N_b}{N_p}\Big)^4 \mathbf{E}[\langle (N_{pb}^b)^2 \rangle_b^2] = \frac{N_b^2}{N_p^4} \sum_{i\in\mathcal{B}} \sum_{j\in\mathcal{B}} \mathbf{E}[(N_{pb}^i)^2 (N_{pb}^j)^2]$$

The random variables N_{pb}^b are independent, thus:

$$\begin{aligned}
\text{for } i \neq j, \quad \mathbf{E}[(N_{pb}^i)^2 (N_{pb}^j)^2] &= \mathbf{E}[(N_{pb}^i)^2] \mathbf{E}[(N_{pb}^j)^2] \\
&= N_p^4 p_i^2 p_j^2 + O(N_p^3) \\
\text{for } i = j, \quad \mathbf{E}[(N_{pb}^i)^2 (N_{pb}^j)^2] &= \mathbf{E}[(N_{pb}^i)^4] \\
&= \sum_{k=0}^{4} \frac{N_p!}{(N_p - k)!} S(4,k) p_i^k \\
&= N_p^4 p_i^4 + O(N_p^3)
\end{aligned}$$

where $S(n,k)$ are the Stirling numbers of the second kind. The first and second term therefore simplify and we have $\mathrm{Var}[g] = O(N_p^{-1})$. This explains the convergence of the measure for one-way coupled simulations.

References

Abdelsamie, A. H. and C. Lee (2012). Decaying versus stationary turbulence in particle-laden isotropic turbulence: Turbulence modulation mechanism. Physics of Fluids 24(1), 15106. (p. 11, 24, 251, 252, 254, 275)

Abraham, E. R. (1998). The generation of plankton patchiness by turbulent stirring. Nature 391(6667), 577–580. (p. 8, 21)

Albukrek, C. M., K. Urban, D. Rempfer, and J. L. Lumley (2002). Divergence-Free Wavelet Analysis of Turbulent Flows. Journal of Scientific Computing 17(1-4), 49–66. (p. 194)

Anselmet, F., Y. Gagne, E. J. Hopfinger, and R. A. Antonia (1984). High-order velocity structure functions in turbulent shear flows. Journal of Fluid Mechanics 140, 63–89. (p. 235)

Armenio, V., U. Piomelli, and V. Fiorotto (1999). Effect of the subgrid scales on particle motion. Physics of Fluids 11(10), 3030–3042. (p. 165)

Arnèodo, A., R. Benzi, J. Berg, L. Biferale, E. Bodenschatz, A. Busse, E. Calzavarini, B. Castaing, M. Cencini, L. Chevillard, R. T. Fisher, R. Grauer, H. Homann, D. Lamb, A. S. Lanotte, E. Lévèque, B. Lüthi, J. Mann, N. Mordant, W. C. Müller, S. Ott, N. T. Ouellette, J. F. Pinton, S. B. Pope, S. G. Roux, F. Toschi, H. Xu, and P. K. Yeung (2008). Universal intermittent properties of particle trajectories in highly turbulent flows. Physical Review Letters 100(25), 1–5. (p. 49)

Baker, L., A. Frankel, A. Mani, and F. Coletti (2017). Coherent clusters of inertial particles in homogeneous turbulence. Journal of Fluid Mechanics 833, 364–398. (p. 265)

Balachandar, S. (2009). A scaling analysis for point-particle approaches to turbulent multiphase flows. International Journal of Multiphase Flow 35(9), 801–810. (p. 163, 166)

Balachandar, S. and J. K. Eaton (2010). Turbulent Dispersed Multiphase Flow. Annual Review of Fluid Mechanics 42(1), 111–133. (p. 161, 179, 180)

Balachandar, S., K. Liu, and M. Lakhote (2019). Self-induced velocity correction for improved drag estimation in Euler–Lagrange point-particle simulations. Journal of Computational Physics 376(September), 160–185. (p. 254)

Bardina, J., J. Ferziger, and W. C. Reynolds (1980). Improved subgrid-scale models for large-eddy simulation. In 13th fluid and plasmadynamics conference, pp. 1357. (p. 62)

Bardos, C., F. Golse, and C. D. Levermore (1993). Fluid dynamic limits of kinetic equations II convergence proofs for the Boltzmann equation. Communications on pure and applied mathematics 46(5), 667–753. (p. 34)

Beck, C. (2001a). Dynamical foundations of nonextensive statistical mechanics. Physical Review Letters 87(18), 180601–1–180601–4. (p. 94)

Beck, C. (2001b). On the small-scale statistics of lagrangian turbulence. Physics Letters, Section A: General, Atomic and Solid State Physics 287(3-4), 240–244. (p. 94)

Beck, C. (2003). Lagrangian acceleration statistics in turbulent flows. Europhysics Letters 64(2), 151–157. (p. 94)

Benzi, R., S. Ciliberto, R. Tripiccione, C. Baudet, F. Massaioli, and S. Succi (1993). Extended

self-similarity in turbulent flows. Physical Review E 48(1), R29–R32. (p. 50)

Benzi, R., G. Paladin, G. Parisi, and A. Vulpiani (1984). On the multifractal nature of fully developed turbulence and chaotic systems. Journal of Physics A: Mathematical and General 17(18), 3521. (p. 40, 51, 233)

Berrouk, A. S., D. Laurence, J. J. Riley, and D. E. Stock (2007). Stochastic modelling of inertial particle dispersion by subgrid motion for LES of high Reynolds number pipe flow. Journal of Turbulence 8(8), N50. (p. 180, 183, 184)

Biferale, L., E. Bodenschatz, M. Cencini, A. S. Lanotte, N. T. Ouellette, F. Toschi, and H. Xu (2008). Lagrangian structure functions in turbulence: A quantitative comparison between experiment and direct numerical simulation. Physics of Fluids 20(6), 65103. (p. 49)

Biferale, L., G. Boffetta, A. Celani, A. Crisanti, and A. Vulpiani (1998). Mimicking a turbulent signal: Sequential multiaffine processes. Physical Review E 57(6), R6261–R6264. (p. 100)

Biferale, L., G. Boffetta, A. Celani, B. J. Devenish, A. Lanotte, and F. Toschi (2004). Multifractal statistics of lagrangian velocity and acceleration in turbulence. Physical Review Letters 93(6), 1–4. (p. 95)

Biferale, L., G. Boffetta, A. Celani, A. Lanotte, and F. Toschi (2005). Particle trapping in three-dimensional fully developed turbulence. Physics of Fluids 17(2), 1–4. (p. 51)

Bini, M. and W. P. Jones (2007). Particle acceleration in turbulent flows: A class of nonlinear stochastic models for intermittency. Physics of Fluids 19(3). (p. 10, 23, 180)

Bini, M. and W. P. Jones (2008). Large-eddy simulation of particle-laden turbulent flows. Journal of Fluid Mechanics 614, 207–252. (p. 167, 181)

Bird, G. A. (1994). Molecular gas dynamics and the direct simulation of gas flows. Molecular gas dynamics and the direct simulation of gas flows. (p. 6, 20, 161)

Boivin, M., O. Simonin, and K. D. Squires (1998). Direct numerical simulation of turbulence modulation by particles in isotropic turbulence. Journal of Fluid Mechanics 375, 235–263. (p. 11, 24, 249, 251, 252, 257)

Boivin, M., O. Simonin, and K. D. Squires (2000). On the prediction of gas-solid flows with two-way coupling using large eddy simulation. Physics of Fluids 12(8), 2080–2090. (p. 11, 24, 285)

Boniou, V. (2021). On the numerical simulation of evaporating two-phase flows using sharp interface capturing methods. Ph. D. thesis, Université Paris-Saclay. (p. 5, 18)

Borgas, M. S. (1993). The multifractal Lagrangian nature of turbulence. Philosophical Transactions of the Royal Society of London. Series A: Physical and Engineering Sciences 342(1665), 379–411. (p. 11, 24, 47, 97, 100)

Capecelatro, J. and O. Desjardins (2013). An Euler-Lagrange strategy for simulating particle-laden flows. Journal of Computational Physics 238, 1–31. (p. 8, 21, 254, 319)

Capecelatro, J. and O. Desjardins (2015). Mass Loading Effects on Turbulence Modulation by Particle Clustering in Dilute and Moderately Dilute Channel Flows. Journal of Fluids Engineering 137(11), 111102. (p. 153, 261)

Capecelatro, J., O. Desjardins, and R. O. Fox (2015). On fluid-particle dynamics in fully developed cluster-induced turbulence. Journal of Fluid Mechanics 780, 578–635. (p. 254)

Cernick, M. J., S. W. Tullis, and M. F. Lightstone (2015). Particle subgrid scale modelling in large-eddy simulations of particle-laden turbulence. Journal of Turbulence 16(2), 101–135. (p. 11, 24, 169, 181, 184)

Chalons, C., R. O. Fox, F. Laurent, M. Massot, and A. Vié (2017). Multivariate Gaussian extended quadrature method of moments for turbulent disperse multiphase flow. Multiscale

Modeling & Simulation 15(4), 1553–1583. (p. 162)

Chen, S., G. D. Doolen, R. H. Kraichnan, and Z. S. She (1992). On statistical correlations between velocity increments and locally averaged dissipation in homogeneous turbulence. Physics of Fluids A 5(2), 458–463. (p. 71, 72)

Cheneau, B., A. Vié, and S. Ducruix (2019). Numerical study of flame shapes and structures in a two-stage two-injection aeronautical burner with variable fuel staging using eulerian large eddy simulations. Journal of Engineering for Gas Turbines and Power 141(7), 71014. (p. 284)

Chentsov, N. N. (1956). Weak convergence of stochastic processes whose trajectories have no discontinuities of the second kind and the "heuristic" approach to the Kolmogorov-Smirnov tests. Theory of Probability & Its Applications 1(1), 140–144. (p. 85)

Chevillard, L. (2017). Regularized fractional Ornstein-Uhlenbeck processes and their relevance to the modeling of fluid turbulence. Physical Review E 96(3), 1–9. (p. 11, 24, 73, 97, 100, 107, 108, 110)

Chevillard, L., R. Robert, and V. Vargas (2009). A Stochastic Representation of the Local Structure of Turbulence. EPL (Europhysics Letters) 89, 54002. (p. 97)

Chevillard, L., R. Robert, and V. Vargas (2011). Random vectorial fields representing the local structure of turbulence. Journal of Physics: Conference Series 318(4), 42002. (p. 97)

Cordesse, P. (2020). Contribution to the study of combustion instabilities in cryotechnic rocket engines : coupling diffuse interface models with kinetic-based moment methods for primary atomization simulations. Ph. D. thesis, Université Paris-Saclay. (p. 9, 22, 299)

Crowe, C. T., M. P. Sharma, and D. E. Stock (1977). The particle-source-in cell (PSI-CELL) model for gas-droplet flows. Journal of fluids engineering 99(2), 325–332. (p. 70, 254)

Cunha Caldeira Mesquita, L., A. Vié, and S. Ducruix (2017). Two-Phase Flow Large Eddy Simulations of a Staged Multipoint Swirling Burner: Comparison Between Euler-Euler and Euler-Lagrange Descriptions. In Turbo Expo: Power for Land, Sea, and Air, Volume 50855, pp. V04BT04A024. American Society of Mechanical Engineers. (p. 284)

De Chaisemartin, S. (2009). Modèles eulériens et simulation numérique de la dispersion turbulente de brouillards qui s'évaporent. Ph. D. thesis, Ecole Centrale Paris. (p. 7, 20, 70, 161)

Deriaz, E. (2006). Ondelettes pour la simulation des écoulements fluides incompressibles en turbulence. Ph. D. thesis, Institut National Polytechnique de Grenoble. (p. 200, 203, 204)

Deriaz, E. and V. Perrier (2006). Divergence-free and curl-free wavelets in 2D and 3D, application to turbulent flows. J. of Turbulence 7(3). (p. 73, 194, 202, 212)

Desjardins, O., R. O. Fox, and P. Villedieu (2008). A quadrature-based moment method for dilute fluid-particle flows. Journal of Computational Physics 227(4), 2514–2539. (p. 154)

Di Battista, R. (2021). Towards a unified eulerian modeling framework for two-phase flows: geometrical small scale phenomena and associated flexible computing strategies. Ph. D. thesis, Institut Polytechnique de Paris. (p. 9, 22)

Doisneau, F. (2013). Eulerian modeling and simulation of polydisperse moderately dense coalescing spray flows with nanometric-to-inertial droplets: application to Solid Rocket Motors. Ph. D. thesis, Ecole Centrale Paris. (p. 8, 22)

Drew, D. A. and S. L. Passman (2006). Theory of multicomponent fluids, Volume 135. Springer Science & Business Media. (p. 40)

Drui, F. (2017). Modélisation et simulation Eulériennes des écoulements diphasiques à phases séparées et dispersées : développement d ' une modélisation unifiée et de méthodes numériques adaptées au calcul massivement parallèle. Ph. D. thesis, Université Paris-Saclay.

(p. 9, 22)
Druzhinin, O. A. (1995). On the two-way interaction in two-dimensional particle-laden flows: The accumulation of particles and flow modification. Journal of Fluid Mechanics 297, 49–76. (p. 162)
Druzhinin, O. A. (2001). The influence of particle inertia on the two-way coupling and modification of isotropic turbulence by microparticles. Physics of Fluids 13(12), 3738–3755. (p. 251, 252, 258, 271, 275)
Druzhinin, O. A. and S. Elghobashi (1999). On the decay rate of isotropic turbulence laden with microparticles. Physics of Fluids 11, 602. (p. 251, 252, 258)
Dubrulle, B. B. (2019). Beyond kolmogorov cascades. Journal of Fluid Mechanics 867. (p. 49)
Dunkel, J., S. Heidenreich, K. Drescher, H. H. Wensink, M. Bär, and R. E. Goldstein (2013, may). Fluid Dynamics of Bacterial Turbulence. Physical Review Letters 110(22), 228102. (p. 8, 21)
Eaton, J. K. and J. R. Fessler (1994). Preferential concentration of particles by turbulence. International Journal of Multiphase Flow 20, 169–209. (p. 153, 250)
Eaton, J. K., K. D. Squires, and J. K. Eaton (1991). Measurements of particle dispersion obtained from direct numerical simulations of isotropic turbulence. Journal of Fluid Mechanics 226(-1), 1. (p. 169)
Eleonore Riber (2007). Developpement De La Methode De Simulation Aux Grandes Echelles Pour Les éoulements Diphasiques Turbulents. Ph. D. thesis, Institut National Polytechnique de Toulouse. (p. 284)
Elghobashi, S. (1991). Particle-laden turbulent flows: direct simulation and closure models. In Computational fluid dynamics for the petrochemical process industry, pp. 91–104. Springer. (p. 8, 21)
Elghobashi, S. (1994). On predicting particle-laden turbulent flows. Applied Scientific Research 52(4), 309–329. (p. 11, 24, 249, 250, 268)
Elghobashi, S. and G. C. Truesdell (1992). Direct simulation of particle dispersion in a decaying isotropic turbulence. Journal of Fluid Mechanics 242(-1), 655. (p. 6, 19)
Elghobashi, S. and G. C. Truesdell (1994). On the two-way interaction between homogeneous turbulence and dispersed solid particles. II. Particle dispersion. Physics of Fluids A: Fluid Dynamics 6(7), 1790–1801. (p. 250, 251, 252, 257)
Eswaran, V. and S. B. Pope (1988). An examination of forcing in direct numerical simulations of turbulence. Computers & Fluids 16(3), 257–278. (p. 68)
Farge, M. (1992). Wavelet transforms and their applications to turbulence. Annual review of fluid mechanics 24(1), 395–458. (p. 194, 317)
Farge, M., N. Kevlahan, V. Perrier, and E. Goirand (1996). Wavelets and turbulence. Proceedings of the IEEE 84(4), 639–669. (p. 194)
Farge, M. and K. Schneider (2005). Wavelets: application to turbulence. University Warnick, lectures. (p. 231)
Fede, P. and O. Simonin (2006). Numerical study of the subgrid fluid turbulence effects on the statistics of heavy colliding particles. Physics of Fluids 18(4), 45103. (p. 10, 11, 23, 24, 155, 165, 166, 180)
Fede, P., O. Simonin, P. Villedieu, and K. D. Squires (2006). Stochastic modeling of the turbulent subgrid fluid velocity along inertial particle trajectories. In Proceedings of the Summer Program, pp. 247–258. Center for Turbulence Research. (p. 89, 183)
Ferrante, A. and S. Elghobashi (2003). On the physical mechanisms of two-way

coupling in particle-laden isotropic turbulence. Physics of Fluids 15(2), 315–329. (p. 11, 24, 250, 251, 252, 268, 269, 271, 273, 275)

Ferry, J. and S. Balachandar (2001). A fast Eulerian method for disperse two-phase flow. International journal of multiphase flow 27(7), 1199–1226. (p. 162)

Ferziger, J. H., H. G. Kaper, and H. G. Kaper (1972). Mathematical theory of transport processes in gases. North-Holland. (p. 5, 19)

Février, P. (2000). Etude numérique des effets de concentration préférentielle et de corrélation spatiale entre vitesses de particules solides en turbulence homogene isotrope stationnaire. Ph. D. thesis, Toulouse, INPT. (p. 68)

Février, P., O. Simonin, and K. D. Squires (2005). Partitioning of particle velocities in gas-solid turbulent flows into a continuous field and a spatially uncorrelated random distribution: Theoretical formalism and numerical study. Journal of Fluid Mechanics 533, 1–46. (p. 150, 155, 156, 157, 160, 223, 250, 283, 285, 302, 303)

Flohr, P. and J. C. Vassilicos (2000). A scalar subgrid model with flow structure for large-eddy simulations of scalar variances. Journal of Fluid Mechanics 407, 315–349. (p. 241)

Fox, R. O., F. Laurent, and A. Vié (2018). Conditional hyperbolic quadrature method of moments for kinetic equations. Journal of Computational Physics 365, 269–293. (p. 162)

Frisch, U. (1985). Turbulence and predictability of geophysical fluid dynamics and climate dynamics. Proceedings of the International School of Physics" Enrico Fermi", Course LXXXVIII, Varenna, 1985. (p. 50)

Frisch, U. (1995). Turbulence: the legacy of AN Kolmogorov. Cambridge university press. (p. 11, 24, 96, 97)

Frisch, U., P.-L. Sulem, and M. Nelkin (1978). A simple dynamical model of intermittent fully developed turbulence. Journal of Fluid Mechanics 87(4), 719–736. (p. 51, 233)

Fröhlich, K., L. Schneiders, M. Meinke, and W. Schröder (2018). Validation of Lagrangian two-way coupled point-particle models in large-eddy simulations. Flow, Turbulence and Combustion 101(2), 317–341. (p. 149, 275)

Fukagata, K., S. Zahrai, and F. H. Bark (2004). Dynamics of Brownian particles in a turbulent channel flow. Heat and mass transfer 40(9), 715–726. (p. 180, 184)

Fung, J. C. H., J. C. R. Hunt, N. A. Malik, and R. J. Perkins (1992). Kinematic simulation of homogeneous turbulence by unsteady random Fourier modes. Journal of Fluid Mechanics 236(281), 281–318. (p. 66, 191, 211)

George, W. K. (1992). The decay of homogeneous isotropic turbulence. Physics of Fluids A: Fluid Dynamics 4(7), 1492–1509. (p. 65)

Germano, M., U. Piomelli, P. Moin, and W. H. Cabot (1991). A dynamic subgrid-scale eddy viscosity model. Physics of Fluids A: Fluid Dynamics 3(7), 1760–1765. (p. 64)

Gore, R. A. and C. T. Crowe (1989). Effect of particle size on modulating turbulent intensity. International Journal of Multiphase Flow. (p. 258)

Gorokhovski, M. and R. Zamansky (2018). Modeling the effects of small turbulent scales on the drag force for particles below and above the Kolmogorov scale. Physical Review Fluids 3(3), 34602. (p. 102, 180, 184, 185, 186)

Goudenège, L., R. Letournel, and A. Richard (2022). Intermittency in a stochastic modelling of turbulence. Technical report. (p. 13, 26, 124)

Gualtieri, P., F. Picano, G. Sardina, and C. M. Casciola (2015). Exact regularized point particle method for multiphase flows in the two-way coupling regime. Journal of Fluid Mechanics 773, 520–561. (p. 254)

Guichard, L., J. Réveillon, and R. Hauguel (2004). Direct numerical simulation of statistically stationary one- and two-phase turbulent combustion: A turbulent injection procedure. Flow, Turbulence and Combustion 73(2), 133–167. (p. 69)

Gustavsson, K., E. Meneguz, M. Reeks, and B. Mehlig (2012). Inertial-particle dynamics in turbulent flows: caustics, concentration fluctuations and random uncorrelated motion. New Journal of Physics 14(11), 115017. (p. 155, 191)

Harms, P. (2020). Strong convergence rates for markovian representations of fractional processes. Discrete & Continuous Dynamical Systems-B. (p. 134)

Haworth, D. C. and S. B. Pope (1986). A generalized Langevin model for turbulent flows. The Physics of fluids 29(2), 387–405. (p. 61, 86, 88, 89)

Hogan, R. C. and J. N. Cuzzi (2001). Stokes and Reynolds number dependence of preferential particle concentration in simulated three-dimensional turbulence. Physics of Fluids 13(10), 2938–2945. (p. 153, 261)

Horwitz, J. A. and A. Mani (2016). Accurate calculation of Stokes drag for point-particle tracking in two-way coupled flows. Journal of Computational Physics 318, 85–109. (p. 6, 19, 254)

Ijzermans, R. H. A., E. Meneguz, and M. W. Reeks (2010). Segregation of particles in incompressible random flows: singularities, intermittency and random uncorrelated motion. Journal of fluid mechanics 653, 99–136. (p. 154, 169, 191)

Innocenti, A., N. Mordant, N. Stelzenmuller, and S. Chibbaro (2020). Lagrangian stochastic modelling of acceleration in turbulent wall-bounded flows. Journal of Fluid Mechanics. (p. 91)

Ireland, P. J. and O. Desjardins (2017). Improving particle drag predictions in Euler–Lagrange simulations with two-way coupling. Journal of Computational Physics 338, 405–430. (p. 6, 19, 254)

Kah, D. (2011). Taking into account polydispersity for the modeling of liquid fuel injection in internal combustion engines. Ph. D. thesis, Ecole Centrale Paris. (p. 154)

Kahane, J.-P. (1985). Sur le chaos multiplicatif. Ann. Sci. Math. Québec 9(2), 105–150. (p. 11, 24, 100, 105, 106, 199)

Kahane, J.-P. and P.-G. Lemarié-Rieusset (1995). Fourier series and wavelets, Volume 3. Gordon & Breach Science Pub. (p. 194, 200)

Kaufmann, A., M. Moreau, O. Simonin, and J. Helie (2008). Comparison between Lagrangian and mesoscopic Eulerian modelling approaches for inertial particles suspended in decaying isotropic turbulence. Journal of Computational Physics 227(13), 6448–6472. (p. 9, 22, 162, 306)

Kaufmann, A., O. Simonin, and T. Poinsot (2004). Direct numerical simulation of particle-laden homogeneous isotropic turbulent flows using a two-fluid model formulation. In 5th Int. Conf. on Multiphase Flow, Yokohama, Japan, Number 443, pp. 101. (p. 153)

Kenning, V. M. and C. T. Crowe (1997). On the effect of particles on carrier phase turbulence in gas-particle flows. International Journal of Multiphase Flow. (p. 258)

Kevlahan, N. K. R. and O. V. Vasilyev (2005). An adaptive wavelet collocation method for fluid-structure interaction at high Reynolds numbers. SIAM Journal on Scientific Computing 26(6), 1894–1915. (p. 194)

Knorps, M. and J. Pozorski (2015). An Inhomogeneous Stochastic Model for Subgrid-Scale Particle Dispersion in LES. In Direct and large-eddy simulation IX, pp. 671–678. Springer. (p. 89)

Kolmogorov, A. N. (1941a). On degeneration (decay) of isotropic turbulence in an incompressible viscous liquid. In Dokl. Akad. Nauk SSSR, Volume 31, pp. 538–540. (p. 50)

Kolmogorov, A. N. (1941b). The local structure of turbulence in incompressible viscous fluid for very large Reynolds numbers. Cr Acad. Sci. URSS 30(1890), 301–305. (p. 37, 47)

Kolmogorov, A. N. (1962). A refinement of previous hypotheses concerning the local structure of turbulence in a viscous incompressible fluid at high Reynolds number. Journal of Fluid Mechanics 13(1), 82–85. (p. 11, 24, 37, 47, 49, 50)

Kraichnan, R. H. (1970). Diffusion by a random velocity field. Physics of Fluids 13(1), 22–31. (p. 169, 191)

Kuerten, J. G. (2016). Point-Particle DNS and LES of Particle-Laden Turbulent flow - a state-of-the-art review. Flow, Turbulence and Combustion 97(3), 689–713. (p. 163, 167, 179)

La Porta, A., G. A. Voth, A. M. Crawford, J. Alexander, and E. Bodenschatz (2001). Fluid particle accelerations in fully developed turbulence. Nature 409(6823), 1017–1019. (p. 51)

Lamorgese, A. G., S. B. Pope, P. K. Yeung, and B. L. Sawford (2007). A conditionally cubic-Gaussian stochastic Lagrangian model for acceleration in isotropic turbulence. Journal of Fluid Mechanics 582, 423–448. (p. 93, 94)

Lancien, T., K. Prieur, D. Durox, S. Candel, and R. Vicquelin (2018). Large eddy simulation of light-round in an annular combustor with liquid spray injection and comparison with experiments. Journal of Engineering for Gas Turbines and Power 140(2). (p. 284)

Landau, L. D. and E. M. Lifshitz (1944). Course of Theoretical Physics. V. 3 Mechanics of continuous medi Moscow: Nauka. (p. 49)

Landau, L. D. and E. M. Lifshitz (1987). Fluid Mechanics: Course of Theoretical Physics, Volume 6, Volume 6. Pergamon Press, New York. (p. 48)

Landau, L. D., E. M. Lifshitz, and C. H. Holbrow (1963). The classical theory of fields. PhT 16(6), 72. (p. 48)

Lanotte, A., E. Calzavarini, F. Toschi, J. Bec, L. Biferale, and M. Cencini (2011). Heavy particles in turbulent flows RM-2007-GRAD-EULER-2048: https://data.4tu.nl/articles/dataset/Heavy_particles_in_turbulent_flows_RM-2007-GRAD-EULER-2048/12697028. (p. xiii, 38, 39, 46, 48, 53, 69, 72, 88, 96, 101, 186, 187, 188, 189)

Laurent, F., A. Vié, C. Chalons, R. O. Fox, and M. Massot (2012). A hierarchy of Eulerian models for trajectory crossing in particle-laden turbulent flows over a wide range of Stokes numbers. Proceedings of the Summer Program 2012 - Center for Turbulence Research, 193–204. (p. 9, 22, 162)

Lele, S. K. (1992). Compact finite difference schemes with spectral-like resolution. Journal of computational physics 103(1), 16–42. (p. 69)

Lemarié-Rieusset, P. G. (1992). Analyses multi-résolutions non orthogonales, commutation entre projecteurs et derivation et ondelettes vecteurs à divergence nuIIe. Revista Matemática Iberoamericana 8(2), 221–237. (p. 194, 199)

Lemarié-Rieusset, P.-G. (1994). Un théorème d'inexistence pour les ondelettes vecteurs à divergence nulle. Comptes rendus de l'Académie des sciences. Série 1, Mathématique 319(8), 811–813. (p. 199)

Letournel, R., L. Goudenège, R. Zamansky, A. Vié, and M. Massot (2021). Reexamining the framework for intermittency in Lagrangian stochastic models for turbulent flows: A way to an original and versatile numerical approach. Physical Review E 104(1), 15104. (p. 13, 26, 117)

Letournel, R., F. Laurent, M. Massot, and A. Vié (2019). Impact of particle field heterogene-

ity on the dynamics of turbulent two-way coupled particulate flows. 10th International Conference on Multiphase Flow, ICMF 2019. (p. 13, 26)

Letournel, R., F. Laurent, M. Massot, and A. Vié (2020). Modulation of homogeneous and isotropic turbulence by sub-Kolmogorov particles: Impact of particle field heterogeneity. International Journal of Multiphase Flow 125, 103233. (p. 13, 26, 247)

Letournel, R., F. Laurent, M. Massot, and A. Vié (2021). Reproducing segregation and particle dynamics in Large Eddy Simulation of particle-laden flows. In International Conference on Liquid Atomization and Spray Systems (ICLASS), Volume 1. (p. 13, 26)

Letournel, R., M. Massot, and A. Vié (2022). Wavelet-based kinematic simulation of particle-laden turbulent flows. Technical report. (p. 13, 26)

Lilly, D. K. (1992). A proposed modification of the Germano subgrid-scale closure method. Physics of Fluids A: Fluid Dynamics 4(3), 633–635. (p. 64)

Lions, P.-L. and N. Masmoudi (2001). From the Boltzmann Equations to the Equations o Incompressible Fluid Mechanics, I. Archive for Rational Mechanics and Analysis 158(3), 173–193. (p. 34)

Liu, H., S. Osher, and R. Tsai (2006). Multi-valued solution and level set methods in computational high frequency wave propagation. Commun. Comput. Phys 1(5), 765–804. (p. 155)

Loison, A. (2024). Eulerian modeling of separated phases and dispersed phases two-phase flows : development of unified approach based on geometric variables and specific numerical schemes based with massively parallel AMR. Ph. D. thesis, Institut Polytechnique de Paris. (p. 9, 22, 299)

Lundgren, T. S. (2003). Linearly forces isotropic turbulence. Technical report. (p. 68)

Malik, N. A. (1996). Structural diffusion in 2D and 3D random flows. In S. Gavrilakis, L. Machiels, and P. A. Monkewitz (Eds.), Advances In Turbulence VI, Dordrecht, pp. 619–620. Springer Netherlands. (p. 211)

Mallouppas, G., W. K. George, and B. G. M. van Wachem (2013). New forcing scheme to sustain particle-laden homogeneous and isotropic turbulence. Physics of Fluids 25(8), 83304. (p. 255)

Mallouppas, G., W. K. George, and B. G. M. van Wachem (2017). Dissipation and inter-scale transfer in fully coupled particle and fluid motions in homogeneous isotropic forced turbulence. International Journal of Heat and Fluid Flow 67, 74–85. (p. 251, 252, 275)

Mandelbrot, B. B. (1999). Lognormal hypothesis and distribution of energy dissipation in intermittent turbuler Springer. (p. 100)

Mandelbrot, B. B. and J. W. Van Ness (1968). Fractional Brownian motions, fractional noises and applications. SIAM review 10(4), 422–437. (p. 84, 85, 107)

Marchioli, C. (2017). Large-eddy simulation of turbulent dispersed flows: a review of modelling approaches. Acta Mechanica 228(3), 741–771. (p. 89, 166, 167, 179)

Marchioli, C., M. V. Salvetti, and A. Soldati (2008a). Appraisal of energy recovering sub-grid scale models for large-eddy simulation of turbulent dispersed flows. Acta Mechanica 201(1-4), 277–296. (p. 169)

Marchioli, C., M. V. Salvetti, and A. Soldati (2008b). Some issues concerning large-eddy simulation of inertial particle dispersion in turbulent bounded flows. Physics of Fluids 20(4). (p. 163)

Marta, G. (2009). Development and validation of the Euler-Lagrange formulation on a parallel and unstructured solver for large-eddy simulation. Ph. D. thesis, Institut National Polytechnique de Toulouse-INPT. (p. 6, 19)

Masi, E. and O. Simonin (2012). An algebraic-closure-based momentmethod for unsteady Eulerian modeling of non-isothermal particle-laden turbulent flows in very dilute regime and high Stokes number. Proceeding of THMT-12. Proceedings of the Seventh International Symposium On Turbulence, Heat and Mass Transfer Palermo, Italy, 24-27 September, 2012, 12. (p. 303, 305, 306)

Masi, E., O. Simonin, E. Riber, P. Sierra, and L. Y. M. Gicquel (2014). Development of an algebraic-closure-based moment method for unsteady Eulerian simulations of particle-laden turbulent flows in very dilute regime. International Journal of Multiphase Flow 58, 257–278. (p. 9, 22, 162)

Massot, M. (2007). Eulerian multi-fluid models for polydisperse evaporating sprays. In Multiphase reacting flows: modelling and simulation, pp. 79–123. Springer. (p. 154, 155)

Maxey, M. R. (1987). The gravitational settling of aerosol particles in homogeneous turbulence and random flow fields. Journal of Fluid Mechanics 174, 441–465. (p. 162)

Maxey, M. R. and B. K. Patel (2001, sep). Localized force representations for particles sedimenting in Stokes flow. International Journal of Multiphase Flow 27(9), 1603–1626. (p. 319)

Maxey, M. R., B. K. Patel, E. J. Chang, and L. P. Wang (1997). Simulations of dispersed turbulent multiphase flow. Fluid Dynamics Research 20(1), 143–156. (p. 254)

McCauley, J. L., G. H. Gunaratne, and K. E. Bassler (2007). Hurst exponents, Markov processes, and fractional Brownian motion. Physica A: Statistical Mechanics and its Applications 379(1), 1–9. (p. 85, 107)

Meneveau, C. (1991). Analysis of turbulence in the orthonormal wavelet representation. Journal of Fluid Mechanics 232, 469–520. (p. 194)

Meneveau, C. and K. R. Sreenivasan (1987). Simple multifractal cascade model for fully developed turbulence. Physical Review Letters 59(13), 1424–1427. (p. 51)

Mercier, D. (2020). Large eddy simulation of coupled dispersed phase flows: a statistically-consistent formalism. Ph. D. thesis, Université Paris-Saclay. (p. 12, 25, 58, 191, 193, 283, 285, 286, 299)

Mesquita, L. C. C., A. Vié, L. Zimmer, and S. Ducruix (2021). Numerical analysis of flame shape bifurcation in a two-stage swirled liquid burner using Large Eddy Simulation. Proceedings of the Combustion Institute 38(4), 5971–5978. (p. 6, 19)

Minier, J. P. (2015). On Lagrangian stochastic methods for turbulent polydisperse two-phase reactive flows. Progress in Energy and Combustion Science 50, 1–62. (p. 163)

Minier, J. P., S. Chibbaro, and S. B. Pope (2014). Guidelines for the formulation of Lagrangian stochastic models for particle simulations of single-phase and dispersed two-phase turbulent flows. Physics of Fluids 26(11), 113303. (p. 79, 167, 179, 180, 183)

Minier, J.-P. and E. Peirano (2001). The pdf approach to turbulent polydispersed two-phase flows. Physics reports 352(1-3), 1–214. (p. 79, 168, 183, 189)

Monchaux, R. (2012). Measuring concentration with Voronoï diagrams: the study of possible biases. New Journal of Physics 14(9), 95013. (p. 264)

Monchaux, R., M. Bourgoin, and A. Cartellier (2010). Preferential concentration of heavy particles: A Voronoï analysis. Physics of Fluids 22(10), 103304. (p. 264, 265)

Monchaux, R., M. Bourgoin, and A. Cartellier (2012). Analyzing preferential concentration and clustering of inertial particles in turbulence. International Journal of Multiphase Flow 40, 1–18. (p. 153, 261)

Monchaux, R. and A. Dejoan (2017). Settling velocity and preferential concentration of heavy

particles under two-way coupling effects in homogeneous turbulence. Physical Review Fluids 2(10), 104302. (p. 264)

Monin, A. S. and A. M. Yaglom (1975). Statistical Fluid Mechanics. Volume 2. Mechanics of Turbulence. The MIT Press. (p. 38, 42, 47, 48, 94)

Mordant, N., A. M. Crawford, and E. Bodenschatz (2004). Experimental Lagrangian acceleration probability density function measurement. Physica D: Nonlinear Phenomena 193(1-4), 245–251. (p. 49, 51)

Mordant, N., J. Delour, E. Léveque, A. Arnéodo, and J. F. Pinton (2002). Long Time Correlations in Lagrangian Dynamics: A Key to Intermittency in Turbulence. Physical Review Letters 89(25), 2–5. (p. 49)

Mordant, N., P. Metz, O. Michel, and J. F. Pinton (2001). Measurement of lagrangian velocity in fully developed turbulence. Physical Review Letters 87(21), 214501–1–214501–4. (p. 51)

Moreau, M. (2006). Modélisation numérique directe et des grandes échelles des écoulements turbulents gaz-particules dans le formalisme eulérien mésoscopique. Ph. D. thesis, Institut National de Polytechnique de Toulouse. (p. 150)

Moreau, M., O. Simonin, and B. Bédat (2010). Development of gas-particle euler-euler les approach: A priori analysis of particle sub-grid models in homogeneous isotropic turbulence. Flow, Turbulence and Combustion 84(2), 295–324. (p. 170)

Murray, S., M. F. Lightstone, and S. Tullis (2016a). Single-particle Lagrangian and structure statistics in kinematically simulated particle-laden turbulent flows. Physics of Fluids 28(3). (p. 24, 167, 169, 191, 192, 226)

Murray, S., M. F. Lightstone, and S. Tullis (2016b). Target Lagrangian kinematic simulation for particle-laden flows. Physical Review E 94(3), 1–9. (p. 191, 192, 206)

Muzy, J.-F. and E. Bacry (2002). Multifractal stationary random measures and multifractal random walks with log infinitely divisible scaling laws. Physical Review E 66(5), 56121. (p. 100)

Neau, H., M. Pigou, P. Fede, R. Ansart, C. Baudry, N. Mérigoux, J. Laviéville, Y. Fournier, N. Renon, and O. Simonin (2020). Massively parallel numerical simulation using up to 36,000 CPU cores of an industrial-scale polydispersed reactive pressurized fluidized bed with a mesh of one billion cells. Powder Technology 366, 906–924. (p. 9, 22)

O'Rourke, P. J. (1981). Collective drop effects on vaporizing liquid sprays. Ph. D. thesis, Princeton University. (p. 6, 20, 161)

Orszag, S. A. and G. S. Patterson Jr (1972). Numerical simulation of three-dimensional homogeneous isotropic turbulence. Physical Review Letters 28(2), 76. (p. 65)

Osborne, D. R., J. C. Vassilicos, and J. D. Haigh (2005). One-particle two-time diffusion in three-dimensional homogeneous isotropic turbulence. Physics of Fluids 17(3). (p. 211)

Ottino, J. M. (1990). Mixing, chaotic advection, and turbulence. Annual Review of Fluid Mechanics 22(1), 207–254. (p. 40)

Overholt, M. R. and S. B. Pope (1998). A deterministic forcing scheme for direct numerical simulations of turbulence. Computers and Fluids 27(1), 11–28. (p. 66, 67)

Pai, M. G. and S. Subramaniam (2012). Two-way coupled stochastic model for dispersion of inertial particles in turbulence. Journal of Fluid Mechanics 700, 29–62. (p. 160)

Pandya, R. V. and F. Mashayek (2002). Two-fluid large-eddy simulation approach for particle-laden turbulent flows. International Journal of Heat and Mass Transfer 45(24), 4753–4759. (p. 170)

Passot, T. and A. Pouquet (1987). Numerical Simulation of Compressible Homogeneous Flows

in the Turbulent Regime. Journal of Fluid Mechanics 181, 441–466. (p. 68)

Paulhiac, D. (2015). Modélisation de la combustion d'un spray dans un bruleur aéronautique. Ph. D. thesis, Institut National Polytechnique de Toulouse. (p. 21)

Pereira, R. M., L. Moriconi, and L. Chevillard (2018). A multifractal model for the velocity gradient dynamics in turbulent flows. Journal of Fluid Mechanics 839, 430–467. (p. 11, 24, 97, 100, 102, 114, 115, 117, 133, 138)

Pope, S. B. (1994). On the relationship between stochastic Lagrangian models of turbulence and second-moment closures. Physics of Fluids 6(2), 973–985. (p. 61)

Pope, S. B. (2000). Turbulent Flows. Cambridge university press. (p. 34, 42, 45, 57)

Pope, S. B. and Y. L. Chen (1990). The velocity-dissipation probability density function model for turbulent flows. Physics of Fluids A 2(8), 1437–1449. (p. 11, 24, 49, 52, 88, 92, 93, 94, 95, 96, 98, 99, 102, 115, 117, 133, 136, 138, 185, 187, 189)

Pope, S. B. and E. S. Ching (1992). Stationary probability density functions: An exact result. Physics of Fluids A 5(7), 1529–1531. (p. 301)

Poustis, J.-F., J.-M. Senoner, D. Zuzio, and P. Villedieu (2019). Regularization of the Lagrangian point force approximation for deterministic discrete particle simulations. International Journal of Multiphase Flow 117, 138–152. (p. 6, 8, 19, 21, 254)

Pozorski, J. and S. V. Apte (2009). Filtered particle tracking in isotropic turbulence and stochastic modeling of subgrid-scale dispersion. International Journal of Multiphase Flow 35(2), 118–128. (p. 11, 24, 168, 170, 180, 184, 299)

Pozorski, J. and J.-P. Minier (1998). On the Lagrangian turbulent dispersion models based on the Langevin equation. International Journal of Multiphase Flow 24(6), 913–945. (p. 183)

Pozorski, J. and J.-P. P. Minier (1999). Probability density function modeling of dispersed two-phase turbulent flows. Physical Review E 59(1), 855. (p. 168)

Reade, W. C. and L. R. Collins (2000). Effect of preferential concentration on turbulent collision rates. Physics of Fluids 12(10), 2530–2540. (p. 153)

Reeks, M. W. (1991). On a kinetic equation for the transport of particles in turbulent flows. Physics of Fluids A 3(3), 446–456. (p. 181, 189)

Reeks, M. W. (1992). On the continuum equations for dispersed particles in nonuniform flows. Physics of Fluids A 4(6), 1290–1303. (p. 168, 170)

Reveillon, J. and F.-X. Demoulin (2007). Effects of the preferential segregation of droplets on evaporation and turbulent mixing. Journal of Fluid Mechanics 583, 273–302. (p. 69)

Reveillon, J. and L. Vervisch (2005). Analysis of weakly turbulent dilute-spray flames and spray combustion regimes. Journal of Fluid Mechanics 537, 317–347. (p. 160)

Revuz, D. and M. Yor (2013). Continuous martingales and Brownian motion, Volume 293. Springer Science & Business Media. (p. 108)

Reynolds, A. M. (2003a). On the application of nonextensive statistics to Lagrangian turbulence. Physics of Fluids 15(1), L1–L4. (p. 93, 94)

Reynolds, A. M. (2003b). Superstatistical Mechanics of Tracer-Particle Motions in Turbulence. Physical Review Letters 91(8), 1–4. (p. 93, 94)

Reynolds, O. (1883). XXIX. An experimental investigation of the circumstances which determine whether the motion of water shall be direct or sinuous, and of the law of resistance in parallel channels. Philosophical Transactions of the Royal society of London 174(174), 935–982. (p. 35)

Rhodes, R. and V. Vargas (2014). Gaussian multiplicative chaos and applications: A review. Probability Surveys 11(2014), 315–392. (p. 106, 123)

Riley, J. J. and G. S. Patterson Jr (1974). Diffusion experiments with numerically integrated isotropic turbulence. The Physics of Fluids 17(2), 292–297. (p. 5, 19, 160)

Robert, R. and V. Vargas (2010). Gaussian multiplicative chaos revisited. The Annals of Probability 38(2), 605–631. (p. 11, 24, 100)

Rosales, C. and C. Meneveau (2005). Linear forcing in numerical simulations of isotropic turbulence: Physical space implementations and convergence properties. Physics of fluids 17(9), 95106. (p. 68)

Sabat, M. (2016). Eulerian modeling and numerical methods for the description of turbulent polydisperse sprays. Ph. D. thesis, Université de Paris-Saclay. (p. 8, 9, 21, 22, 162, 170)

Sabat, M., A. Vié, A. Larat, and M. Massot (2019). Statistical description of turbulent particle-laden flows in the very dilute regime using the anisotropic Gaussian moment method. International Journal of Multiphase Flow 112, 243–257. (p. 9, 22, 162)

Sabel'nikov, V., A. Chtab-Desportes, and M. Gorokhovski (2011). New sub-grid stochastic acceleration model in les of high-Reynolds-number flows. European Physical Journal B 80(2), 177–187. (p. 94, 184)

Saffman, P. G. (1962). On the stability of laminar flow of a dusty gas. Journal of Fluid Mechanics 13(1), 120–128. (p. 271)

Sagaut, P. (2006). Large eddy simulation for incompressible flows: an introduction. Springer Science & Business Media. (p. 62)

Sanjosé, M., J. M. Senoner, F. Jaegle, B. Cuenot, S. Moreau, and T. Poinsot (2011). Fuel injection model for Euler–Euler and Euler–Lagrange large-eddy simulations of an evaporating spray inside an aeronautical combustor. International Journal of Multiphase Flow 37(5), 514–529. (p. 284)

Sawford, B. L. (1991). Reynolds number effects in Lagrangian stochastic models of turbulent dispersion. Physics of Fluids A 3(6), 1577–1586. (p. 52, 89, 91, 93)

Sawford, B. L., P. K. Yeung, M. S. Borgas, P. Vedula, A. La Porta, A. M. Crawford, and E. Bodenschatz (2003). Conditional and unconditional acceleration statistics in turbulence. Physics of Fluids 15(11), 3478–3489. (p. 52)

Schmitt, F. and D. Marsan (2001). Stochastic equations generating continuous multiplicative cascades. The European Physical Journal B-Condensed Matter and Complex Systems 20(1), 3–6. (p. 11, 24, 97, 100, 114, 117, 133)

Schmitt, F. G. (2003). A causal multifractal stochastic equation and its statistical properties. European Physical Journal B 34(1), 85–98. (p. 97, 102, 114, 133, 138)

Scotti, A. and C. Meneveau (1999). A fractal model for large eddy simulation of turbulent flow. Physica D: Nonlinear Phenomena 127(3-4), 198–232. (p. 169)

Seuront, L., H. Yamazaki, and F. G. Schmitt (2005). Intermittency. Marine turbulence: Theories, observations and models 66, 78. (p. 51)

Shamov, A. (2016). On Gaussian multiplicative chaos. Journal of Functional Analysis 270(9), 3224–3261. (p. 106)

She, Z.-S., E. Jackson, and S. A. Orszag (1990). Intermittent vortex structures in homogeneous isotropic turbulence. Nature 344(6263), 226–228. (p. 65)

Shotorban, B. and F. Mashayek (2005). Modeling subgrid-scale effects on particles by approximate deconvolution. Physics of Fluids 17(8), 81701. (p. 169)

Shotorban, B. and F. Mashayek (2006). A stochastic model for particle motion in large-eddy simulation. Journal of Turbulence 7(7), N18. (p. 88, 89, 167, 180, 183, 184)

Simonin, O., E. Deutsch, and M. Boivin (1995). Turbulent Shear Flows. (p. 182)

Simonin, O., E. Deutsch, and J. P. Minier (1993). Eulerian prediction of the fluid/particle correlated motion in turbulent two-phase flows. Applied Scientific Research 51(1), 275–283. (p. 182)

Simonin, O., P. Février, and J. Laviéville (2002). On the spatial distribution of heavy-particle velocities in turbulent flow: from continuous field to particulate chaos. Journal of Turbulence 3, N40. (p. 151, 305, 306)

Smagorinsky, J. (1963). General circulation experiments with the primitive equations: I. The basic experiment. Monthly weather review 91(3), 99–164. (p. 64)

Squires, K. D. and J. K. Eaton (1990). Particle response and turbulence modification in isotropic turbulence. Physics of Fluids A: Fluid Dynamics 2(7), 1191–1203. (p. 11, 24, 249, 250, 251, 252, 257)

Squires, K. D. and J. K. Eaton (1991). Preferential concentration of particles by turbulence. Physics of Fluids A: Fluid Dynamics 3(5), 1169–1178. (p. 6, 19)

Squires, K. D. and J. K. Eaton (1994). Effect of Selective Modification of Turbulence on Two-Equation Models for Particle-Laden Turbulent Flows. Journal of Fluids Engineering 116, 778. (p. 11, 24, 251, 252)

Sreenivasan, K. R. and R. A. Antonia (1997). The phenomenology of small-scale turbulence. Annual review of fluid mechanics 29(1), 435–472. (p. 11, 24, 97)

Strutt, H. C., S. W. Tullis, and M. F. Lightstone (2011). Numerical methods for particle-laden DNS of homogeneous isotropic turbulence. Computers & Fluids 40(1), 210–220. (p. 251, 254)

Subramaniam, S. (2013). Lagrangian-Eulerian methods for multiphase flows. Progress in Energy and Combustion Science (March). (p. 163)

Sundaram, S. and L. R. Collins (1997). Collision statistics in an isotropic particle-laden turbulent suspension. Part 1. Direct numerical simulations. Journal of Fluid Mechanics 335, 75–109. (p. 147)

Sundaram, S. and L. R. Collins (1999). A numerical study of the modulation of isotropic turbulence by suspended particles. Journal of Fluid Mechanics 379, 105–143. (p. 251, 252)

Tanaka, T. and J. K. Eaton (2008). Classification of turbulence modification by dispersed spheres using a novel dimensionless number. Physical Review Letters 101(11), 114502. (p. 258)

Temam, R. (2001). Navier-Stokes equations: theory and numerical analysis, Volume 343. American Mathematical Soc. (p. 35)

Tenneti, S., R. Garg, and S. Subramaniam (2011). Drag law for monodisperse gas-solid systems using particle-resolved direct numerical simulation of flow past fixed assemblies of spheres. International Journal of Multiphase Flow 37(9), 1072–1092. (p. 147)

Tenneti, S. and S. Subramaniam (2014). Particle-resolved direct numerical simulation for gas-solid flow model development. Annual Review of Fluid Mechanics 46, 199–230. (p. 160)

Thomson, D. J. and B. J. Devenish (2005). Particle pair separation in kinematic simulations. Journal of Fluid Mechanics 526, 277–302. (p. 193)

Toutant, A. (2006). Modélisation physique des interactions entre interfaces et turbulence. Ph. D. thesis, Institut National Polytechnique de Toulouse. (p. 68)

Uijttewaal, W. S. J. and R. Oliemans (1996). Particle dispersion and deposition in direct numerical and large eddy simulations of vertical pipe flows. Physics of Fluids 8(10), 2590–2604. (p. 163)

Urban, K. (1994). A wavelet Galerkin algorithm for the driven cavity stokes problem in two space dimensio

Citeseer. (p. 204)

Urban, K. (2002). Wavelet bases for H (div) and H (curl). In Wavelets in Numerical Simulation, pp. 83–107. Springer. (p. 194)

Urzay, J., M. Bassenne, G. I. Park, and P. Moin (2014). Characteristic regimes of subgrid-scale coupling in LES of particle-laden turbulent flows. Center for Turbulence Research Annual Research Briefs, 3–13. (p. 163, 166)

Vassilicos, J. and S. Laizet (2010, nov). DNS of multiscale-generated turbulence. Bulletin of the American Physical Society 55. (p. 3, 16)

Vedula, P. and P. K. Yeung (1999). Similarity scaling of acceleration and pressure statistics in numerical simulations of isotropic turbulence. Physics of Fluids 11(5), 1208–1220. (p. 51)

Vié, A., F. Doisneau, and M. Massot (2015). On the Anisotropic Gaussian velocity closure for inertial- particle laden flows. Communications in Computational Physics 17, 1–46. (p. 162, 303)

Vié, A., E. Masi, O. Simonin, and M. Massot (2012). On the direct numerical simulation of moderate-stokes number turbulent particulate flows using algebraic closure-based and kinetic-based moment methods. Proceedings of the Summer Program 2012 - Center for Turbulence Research, 355–364. (p. 303)

Vié, A., H. Pouransari, R. Zamansky, and A. Mani (2016). Particle-laden flows forced by the disperse phase: Comparison between Lagrangian and Eulerian simulations. International Journal of Multiphase Flow 79, 144–158. (p. 153, 251, 258)

Viggiano, B., J. Friedrich, R. Volk, M. Bourgoin, R. B. Cal, and L. Chevillard (2020). Modelling Lagrangian velocity and acceleration in turbulent flows as infinitely differentiable stochastic processes. Journal of Fluid Mechanics 900. (p. 92)

Von Karman, T. and L. Howarth (1938). On the statistical theory of isotropic turbulence. Proceedings of the Royal Society of London. Series A-Mathematical and Physical Sciences 164(917), 192–215. (p. 44)

Voth, G. A., K. Satyanarayan, and E. Bodenschatz (1998). Lagrangian acceleration measurements at large Reynolds numbers. Physics of Fluids 10(9), 2268–2280. (p. 51, 92)

Wang, L. P. and M. R. Maxey (1993). Settling velocity and concentration distribution of heavy particles in homogeneous isotropic turbulence. Journal of Fluid Mechanics 256, 27–68. (p. 65)

Wang, L. P. and D. E. Stock (1993). Dispersion of heavy particles by turbulent motion. Journal of the Atmospheric Sciences 50(13), 1897–1913. (p. 183)

Wang, Q. and K. D. Squires (1996). Large eddy simulation of particle deposition in a vertical turbulent channel flow. International Journal of Multiphase Flow 22(4), 667–683. (p. 163)

Williams, F. A. (1958). Spray combustion and atomization. The physics of fluids 1(6), 541–545. (p. 160)

Xu, H., M. Bourgoin, N. T. Ouellette, and E. Bodenschatz (2006). High order Lagrangian velocity statistics in turbulence. Physical review letters 96(2), 24503. (p. 49)

Xu, H., N. T. Ouellette, D. Vincenzi, and E. Bodenschatz (2007). Acceleration correlations and pressure structure functions in high-Reynolds number turbulence. Physical review letters 99(20), 204501. (p. 94)

Xu, Y. and S. Subramaniam (2010). Effect of particle clusters on carrier flow turbulence: A direct numerical simulation study. Flow, Turbulence and Combustion 85(3), 735–761. (p. 5, 18)

Yaglom, A. M. (1966). The influence of fluctuations in energy dissipation on the shape

of turbulence characteristics in the inertial interval. Soviet Physics Doklady 11, 26. (p. 47, 49, 50, 51, 52, 96, 99, 233)

Yeh, F. and U. Lei (1991). On the motion of small particles in a homogeneous isotropic turbulent flow. Physics of Fluids A: Fluid Dynamics 3(11), 2571–2586. (p. 163)

Yeung, P. K. (1997). One- and two-particle Lagrangian acceleration correlations in numerically simulated homogeneous turbulence. Physics of Fluids 9(10), 2981–2990. (p. 51)

Yeung, P. K. and S. B. Pope (1988). An algorithm for tracking fluid particles in numerical simulations of homogeneous turbulence. Journal of Computational Physics 79(2), 373–416. (p. 71)

Yeung, P. K. and S. B. Pope (1989). Lagrangian statistics from direct numerical simulations of isotropic turbulence. Journal of Fluid Mechanics 207, 531–586. (p. 48, 49, 57, 69)

Yeung, P. K., S. B. Pope, E. A. Kurth, and A. G. Lamorgese (2007). Lagrangian conditional statistics, acceleration and local relative motion in numerically simulated isotropic turbulence. Journal of Fluid Mechanics 582, 399–422. (p. 51)

Yeung, P. K., S. B. Pope, A. G. Lamorgese, and D. A. Donzis (2006). Acceleration and dissipation statistics of numerically simulated isotropic turbulence. Physics of Fluids 18(6), 1–14. (p. 49, 94)

Yeung, P. K., S. B. Pope, and B. L. Sawford (2006). Reynolds number dependence of Lagrangian statistics in large numerical simulations of isotropic turbulence. Journal of Turbulence 7, 1–12. (p. 51, 96)

Yoshimoto, H. and S. Goto (2007). Self-similar clustering of inertial particles in homogeneous turbulence. Journal of Fluid Mechanics 577, 275–286. (p. 9, 22)

Zaichik, L. I., O. Simonin, and V. M. Alipchenkov (2009). An Eulerian approach for large eddy simulation of particle transport in turbulent flows. Journal of Turbulence 10, 1–21. (p. 170)

Zamansky, R. (2019). Lecture on Turbulent dispersed multiphase Flows. In CISM Course on "Advances in Dispersed Multi-Phase Flows: from Measuring to Modeling", Udine, Italy. (p. 254)

Zamansky, R. (2021). Acceleration scaling and stochastic dynamics of a fluid particle in turbulence. arXiv preprint arXiv:2111.01467, 1–30. (p. 47, 53, 95, 139)

Zamansky, R., F. Coletti, M. Massot, and A. Mani (2014). Radiation induces turbulence in particle-laden fluids. Physics of Fluids 26(7), 1–8. (p. 8, 21, 254)

Zamansky, R., F. Coletti, M. Massot, and A. Mani (2016). Turbulent thermal convection driven by heated inertial particles. Journal of Fluid Mechanics 809, 390–437. (p. 21, 38, 70, 261, 265)

Zamansky, R., I. Vinkovic, and M. Gorokhovski (2013). Acceleration in turbulent channel flow: Universalities in statistics, subgrid stochastic models and an application. Journal of Fluid Mechanics 721, 627–668. (p. 167)

Zeren, Z. (2010). Modélisation Lagrangienne Stochastique des Écoulements Gaz-Solides Turbulents avec Couplage Inverse en Turbulence Homogène Isotrope Stationnaire. Ph. D. thesis, Institut National Polytechnique de Toulouse. (p. 68, 182)

Zhang, Z. (2019). Micro-bubble dynamics in turbulent flow. Ph. D. thesis, Université de Toulouse (INP). (p. 10, 23)

Zhang, Z., D. Legendre, and R. Zamansky (2019). Model for the dynamics of micro-bubbles in high-Reynolds-number flows. Journal of Fluid Mechanics 879, 554–578. (p. 101, 184)